Université de Montréal

Reactivities of cyclonickelated complexes in the context of C−H functionalization chemistry

Par

Rajib Kumar Sarker

Département de chimie

Faculté des arts et des sciences

Thèse présentée

en vue de l'obtention du grade de Philosophiæ Doctor (Ph.D.)

en Chimie

February 2024

Université de Montréal

Département de chimie, Faculté des arts et des sciences

Cette thèse intitulée

Reactivities of cyclonickelated complexes in the context of C−H functionalization chemistry

Présentée par

Rajib Kumar Sarker

A été évaluée par un jury composé des personnes suivantes

Frank Schaper
Président-rapporteur

Davit Zargarian
Directeur de recherche

Garry Hanan
Membre du jury

Marc-André Légaré
Examinateur externe

Résumé

Ce mémoire décrit les résultats d'une étude conçue pour tester l'efficacité d'une approche particulière visant à étudier le mécanisme de la fonctionnalisation des hétéroatomes C dans les liaisons C-H catalysée par les composés des métaux de transition. L'approche en question consiste à examiner les réactivités d'une famille de complexes nickelacycliques sélectionnés pour servir de système modèle pour les intermédiaires postulés être générés in situ lors de protocoles de fonctionnalisation C−H appelés « one-pot » (en une seule étape). Ainsi, les complexes nickelacycliques susmentionnés, y compris les complexes dimériques κ^C, κ^P-{2-OPR$_2$,4-R'-C$_6$H$_4$}$_2$Ni$_2$(μ-Br)$_2$ et leurs adduits acétonitrile monomères κ^C, κ^P-{2-OPR$_2$,4-R'-C$_6$H$_4$}Ni(Br)(NCMe), obtenus par nickelation C−H des arylphosphinites, R$_2$P(OAr), ont été traités avec des substrats appropriés possédant une liaison faible/labile telle que des liaisons simples N−O et N−N pour déterminer si la rupture des liaisons cibles mènerait à une coupure C–O ou C–N.

En tant que substrats pour les couplages C–O, nous avons testé les réactivités des hydroxylamines (PhCH$_2$)$_2$NOH et (CH$_3$CH$_2$)$_2$NOH, en plus du substrat protégé par le benzyle PhCH$_2$ONH$_2$. Les réactivités observées entre ces substrats et les complexes nickelacycliques modèles susmentionnés ont révélé trois schémas distincts influencés par la nature du complexe de nickel, le solvant utilisé dans la réaction et le substrat spécifique utilisé. Premièrement, pour le substrat protégé par le benzyle PhCH$_2$ONH$_2$, le résultat implique la formation directe d'adduits liés à l'azote avec tous les complexes de nickel testés. Deuxièmement, le complexe dimérique non-substitué (R' = H) réagit avec (CH$_3$CH$_2$)$_2$NOH et (PhCH$_2$)$_2$NOH dans CH$_2$Cl$_2$, produisant l'amine oxyde zwitterionique κ^C, κ^P-{2-OPR$_2$-C$_6$H$_5$}Ni{κ^O-ONH(CH$_3$CH$_2$)$_2$}Br et l'aminooxyde bidente (i-R$_2$POPh)Ni{κ^O,κ^N-ON(CH$_2$Ph)$_2$}Br, respectivement. Enfin, la réaction parallèle de complexes de nickel substitués (R' = Cl, OMe, NMe$_2$) avec des hydroxylamines fournit des adduits à base d'imines résultant de la déshydratation de (CH$_3$CH$_2$)$_2$NOH et (PhCH$_2$)$_2$NOH. Cette dernière réactivité atteint des résultats optimaux en acétonitrile, bien qu'elle se manifeste également dans une moindre mesure en C$_6$D$_6$ si la réaction se poursuit pendant plus de 24 heures.

Divers scénarios mécanistiques ont été explorés pour élucider la transformation observée des hydroxylamines en imines, tous indiquant deux voies mécanistiques possibles. Le mécanisme le

plus en évidence est l'attaque nucléophile sur l'acétonitrile coordonné, résultant en une déshydratation nette de l'hydroxylamine avec l'élimination de la molécule d'acétamide. Dans l'ensemble, cette étude a montré que cette réaction peut également se produire par des voies radicalaires pour lesquelles la coordination de l'acétonitrile au nickel n'est pas nécessaire.

S'appuyant sur les résultats décrits ci-dessus, nous avons réalisé une autre étude de réactivité entre les complexes nickelacycliques susmentionnés et les hydroxylamines en conjonction avec des oxydants, en utilisant spécifiquement le TEMPO (2,2,6,6-tétraméthyl-1-pipéridinyl-N-oxyde). Cette investigation a donné naissance à une série de nouveaux complexes Ni-TEMPOH, où TEMPOH représente le 2,2,6,6-tétraméthyl-1-pipéridinyl-N-hydroxyde. Ces composés intrigants nous ont offert l'occasion unique d'explorer leur chimie de coordination avec divers nucléophiles, comme expliqué dans le chapitre 4. Cette étude a montré que le complexe Ni-TEMPOH peut être obtenu par deux voies distinctes : 1) en convertissant le TEMPO en TEMPOH avant de réagir avec le précurseur dimérique, et 2) en formant un complexe zwitterionique par réaction du dimère avec l'hydroxylamine, suivi du traitement avec le TEMPO.

Les investigations de réactivité mettent en évidence que le MeCN déplace efficacement la fraction TEMPOH des complexes Ni(II)-TEMPOH, tandis que des ligands plus volumineux tels que le PPh$_3$ et le DMSO échouent à montrer une réactivité similaire. Cela souligne le rôle crucial des considérations stériques dans la détermination de la réaction de substitution de ce complexe spécifique. De plus, l'étude révèle qu'en réagissant ces complexes avec d'autres nucléophiles tels que la morpholine et l'imidazole, des produits correspondants sont générés, notamment un adduit de morpholine et un complexe bis-imidazole, respectivement. L'analyse RMN du complexe bis-imidazole montre qu'en solution, il existe sous forme de complexes mono-imidazole, ce qui indique qu'un processus d'échange pourrait avoir lieu en solution. Fait intéressant, un aspect supplémentaire de cette recherche implique des tentatives d'oxydation du complexe Ni(II)-TEMPOH en utilisant l'AgOCOCF$_3$. Ce processus conduit au remplacement du Br par l'OCOCF$_3$, donnant ainsi un complexe acétate.

En plus des enquêtes précédentes concernant les hydroxylamines, nous avons examiné le potentiel de couplage C–N du 4-amino-4H-1,2,4-triazole comportant des liaisons N–N simples lorsqu'il est réagi avec nos complexes nickelacycliques. Bien que nous ayons détecté des indications d'une voie de décomposition qui pourrait impliquer la rupture de la liaison N–N, cette réactivité est un élément

mineur dans le panorama de réactivité observé, la voie principale conduisant à la formation de simples adduits du substrat triazole. En conséquence, nous avons réussi à isoler à la fois des adduits mononucléaires, à savoir {κ^P,κ^C-(i-Pr)$_2$PO-Ar}Ni(Br)(κ^N-4-amino-4H-1,2,4-triazole), et des adduits dinucléaires à pont triazole, spécifiquement [{κ^P,κ^C-(i-Pr)$_2$PO-Ar}Ni(Br)}$_2$(μ,κ^N,κ^N-4-amino-4H-1,2,4-triazole). En utilisant la surveillance par RMN à température variable des réactions impliquant les précurseurs de nickel et le substrat triazole, nous avons révélé que les nouveaux adduits triazoles s'engagent dans un processus d'échange dynamique.

L'analyse des données de RMN a révélé que les adduits triazoles mononucléaires et dinucléaires sont impliqués dans des équilibres dynamiques avec leurs adduits correspondants d'acétonitrile. Une observation intéressante émerge : les espèces cristallines récupérées dans la solution sont systématiquement soit les adduits triazoles mononucléaires, soit les adduits triazoles dinucléaires, jamais les deux simultanément. De plus, il semble que le choix de l'adduit optimal pour la cristallisation dépend du précurseur spécifique utilisé. Les précurseurs [{κ^P,κ^C-(i-Pr)$_2$PO-C$_6$H$_4$}Ni(μ-Br)]$_2$ et [{κ^P,κ^C-(i-Pr)$_2$PO-(4-MeO-C$_{10}$H$_5$)}Ni(μ-Br)]$_2$ produisent exclusivement des produits mononucléaires, tandis que [{κ^P,κ^C-(i-Pr)$_2$PO-(5-OMe-C$_6$H$_3$)}Ni(μ-Br)]$_2$, [{κ^P,κ^C-(i-Pr)$_2$PO-(5-Cl-C$_6$H$_3$)}Ni(μ-Br)]$_2$, et [{κ^P,κ^C-(i-Pr)$_2$PO-(C$_{10}$H$_6$)}Ni(μ-Br)]$_2$ produisent exclusivement les produits dinucléaires.

Mots-clés : Cyclonickellation, Phosphinite, Complexe imine, Complexe Ni-TEMPOH, Complexe Ni-triazole, Mécanisme, Nickellation C-H, Diffraction des Rayons X.

Abstract

This thesis describes the results of a study designed to test the effectiveness of a particular approach for probing the mechanism of transition metal-catalyzed C-heteroatom functionalization of C–H bonds. The approach in question involves examining the reactivities of a family of nickelacyclic complexes selected to serve as a model system for intermediates postulated to be generated in-situ during so-called one-pot C–H functionalization protocols. Thus, the said nickelacyclic complexes, including the dimeric complexes κ^C,κ^P-{2-OPR$_2$,4-R'-C$_6$H$_4$}$_2$Ni$_2$(μ-Br)$_2$ and their monomeric acetonitrile adducts κ^C,κ^P-{2-OPR$_2$,4-R'-C$_6$H$_4$}Ni(Br)(NCMe), which were obtained via the C–H nickelation of arylphosphinites, were treated with suitable substrates possessing a weak/labile bond such as N–O and N–N single bonds to see if rupture of the target bonds would lead to C–O or C–N coupling.

As substrates for studying C–O coupling reactions, we tested the reactivities of the hydroxylamines (PhCH$_2$)$_2$NOH and (CH$_3$CH$_2$)$_2$NOH in addition to the benzyl protected substrate PhCH$_2$ONH$_2$. The reactivities observed between these substrates and the above-mentioned model nickelacyclic complexes revealed three distinct patterns influenced by the nature of the Ni complex, the solvent employed in the reaction, and the specific substrate used. Firstly, for the benzyl-protected substrate PhCH$_2$ONH$_2$, the outcome involves straightforward formation of N-bound adducts with all Ni complexes tested. Secondly, the unsubstituted dimeric complex (R' = H) reacts with (CH$_3$CH$_2$)$_2$NOH and (PhCH$_2$)$_2$NOH in CH$_2$Cl$_2$ to give the zwitterionic amine oxide κ^C,κ^P-{2-OPR$_2$-C$_6$H$_5$}Ni{κ^O-ONH(CH$_3$CH$_2$)$_2$}Br and the bidentate aminoxide (i-R$_2$POPh)Ni{κ^O,κ^N-ON(CH$_2$Ph)$_2$}Br, respectively. Lastly, the parallel reaction of substituted Ni complexes (R' = Cl, OMe, NMe$_2$) with hydroxylamines furnishes imine-based adducts originating from the dehydration of (CH$_3$CH$_2$)$_2$NOH and (PhCH$_2$)$_2$NOH. This latter reactivity attains optimal results in acetonitrile, although it also manifests to a lesser extent in C$_6$D$_6$ if the reaction proceeds for over 24 hours.

Various mechanistic scenarios have been explored to elucidate the observed transformation from hydroxylamines to imines, all of which indicate two possible mechanistic pathways. The most prominent mechanism is the nucleophilic attack on coordinated acetonitrile resulting in net

dehydration of hydroxyl amine with elimination of acetamide molecule. Overall, this study showed that this reaction can also proceed through radical pathways for which coordination of acetonitrile to nickel is not necessary.

Building upon the findings described above, we carried out another reactivity study between the nickellacyclic complexes mentioned above and hydroxylamines in conjunction with oxidants, specifically employing TEMPO (2,2,6,6-tetramethyl-1-piperidinyl-N-oxyl). This investigation yielded a series of new Ni-TEMPOH complexes, where TEMPOH stands for 2,2,6,6-tetramethyl-1-piperidinyl-N-hydroxy. These intriguing compounds have afforded us a unique opportunity to delve into their coordination chemistry with diverse nucleophiles, as elucidated in chapter 4. This study showed that the Ni-TEMPOH complex can be accessed through two distinct pathways: 1) converting TEMPO to TEMPOH prior to reacting with the dimeric precursor, and 2) forming a zwitterionic complex through the reaction of the dimer with hydroxylamine, subsequently treated with TEMPO.

Reactivity investigations highlight that MeCN effectively displaces the TEMPOH moiety from the Ni(II)-TEMPOH complexes, while bulkier ligands such as PPh_3 and DMSO fail to exhibit similar reactivity. This underscores the pivotal role of steric considerations in determining the substitution reaction of this specific complex. Furthermore, the study reveals that treating these complexes with other nucleophiles such as morpholine and imidazole, the corresponding charge-neutral mono(morpholine) adduct and cationic bis-imidazole adduct. NMR analysis of the latter complex indicates that in solution it exists as a mono-imidazole adduct undergoing exchange processes in solution. Interestingly, an additional facet of this research involves attempts to oxidize the Ni(II)-TEMPOH complex using $AgOCOCF_3$. This process leads to the replacement of Br with $OCOCF_3$, yielding an acetate complex.

In addition to the above investigations involving hdroxylamines, we have examined the C–N coupling potential of 4-Amino-4H-1,2,4-triazole featuring N–N single bonds when reacted with our nickelacyclic complexes. Although we have detected indications of a decomposition pathway that could involve N–N bond cleavage, this reactivity is a minor element within the broader reactivity landscape observed, the primary route leading to the formation of simple adducts of the triazole substrate. As a result, we have isolated both mononuclear adducts, namely $\{\kappa^P, \kappa^C$-(i-Pr)$_2$PO-Ar$\}$Ni(Br)(κ^N-4-amino-4H-1,2,4-triazole), and triazole-bridged dinuclear adducts,

specifically $[\{\kappa^P,\kappa^C\text{-}(\text{i-Pr})_2\text{PO-Ar}\}\text{Ni(Br)}\}_2(\mu,\kappa^N,\kappa^N\text{-4-amino-4H-1,2,4-triazole})$. By employing variable temperature NMR monitoring of the reactions involving the Ni precursors and the triazole substrate, we unveiled that the newly formed triazole adducts engage in a dynamic exchange process.

Analysis of the NMR data revealed that both mono- and dinuclear triazole adducts are engaged in dynamic equilibria with their corresponding acetonitrile adducts. Interestingly, a noteworthy observation emerges: the crystalline species retrieved from the solution are consistently either the mononuclear or the dinuclear triazole adduct, never both simultaneously. Moreover, it appears that the selection of the favored adduct for crystallization is contingent upon the specific precursor used. Precursors $[\{\kappa^P,\kappa^C\text{-}(i\text{-Pr})_2\text{PO-}C_6H_4\}\text{Ni}(\mu\text{-Br})]_2$ and $[\{\kappa^P,\kappa^C\text{-}(i\text{-Pr})_2\text{PO-}(4\text{-MeO-}C_{10}H_5)\}\text{Ni}(\mu\text{-Br})]_2$ exclusively yield mononuclear products, whereas $[\{\kappa^P,\kappa^C\text{-}(i\text{-Pr})_2\text{PO-}(5\text{-OMe-}C_6H_3)\}\text{Ni}(\mu\text{-Br})]_2$, $[\{\kappa^P,\kappa^C\text{-}(i\text{-Pr})_2\text{PO-}(5\text{-Cl-}C_6H_3)\}\text{Ni}(\mu\text{-Br})]_2$, and $[\{\kappa^P,\kappa^C\text{-}(i\text{-Pr})_2\text{PO-}(C_{10}H_6)\}\text{Ni}(\mu\text{-Br})]_2$ exclusively yield the dinuclear products.

Keywords: Cyclonickelation, Phosphinite, Imine complex, Ni-TEMPOH complex, Ni-triazole complex, Mechanism, C-H nickelation, X-Ray diffraction.

Table of Contents

List of Schemes

List of Figures

List of Tables

List of abbreviations

Ar : aryl

C−M : carbon-metal

C−Ni : carbon-nickel

C−H : carbon-hydrogen

C−X : carbon-halogen

C−N : carbon- Nitrogen

C−O : carbon-oxygen

C−C : carbon-carbon

CO : carbon monoxide

COD : 1,5-cycloocatdiene

DCM : dichloromethane

M−H : metal-hydride

Ni−H : nickel-hydride

OAc : Acetate

i-Pr : isopropyl

n-pen : n-pentane

Bn : benzyl

Bz : benzoyl

Piv : pivalate / tertbutylcarboxylate

TEMPO : (2,2,6,6-tetramethylpiperidin-1-yl)-oxy

OTf : triflate

OTs : tosylate

acac : acetylacetonate

DG : directing group

8AQ : 8-aminoquinol-N-yl

AQ : quinol-8-yl

XRD : X-Ray diffraction

NMR : nuclear magnetic resonance

IR : infrared

SET : Single electron transfer

CV : cyclic voltammetry

DFT : density functional theory

THF : tetrahydrofuran

Acknowledgement

First and foremost, I would like to express my gratitude to Professor Davit Zargarian for accepting me into his research group and for his exceptional guidance throughout my doctoral studies. I was fascinated by the research done in the Zargarian laboratory and this motivated me to pursue my PhD studies under his guidance. I took up one advanced course on organometallic chemistry given by Professor Zargarian which has enhanced my thirst in this field of chemistry. The best aspect of Professor Zargarian is his appreciation for the opinions of his students. Whenever we make decisions about a project or a manuscript, it becomes a collective choice. He is the person with whom I can discuss both my professional and personal life challenges. Throughout the process of refining my research proposal and up to the moment I submitted my thesis, his steadfast support and abundant wisdom have played a pivotal role in shaping my academic journey.

Besides my supervisors, I owe a great debt of gratitude to my outstanding fellow lab members, whose unwavering support has consistently fueled my motivation. I'd like to mention the interns who passed through the group and were receptive to the knowledge I could share, particularly Zafar Ali and Christian Mina. I would also like to thank all the members of the group, Dr. Loic Mangen and Dr. Naser Rahimi. My special thanks to Prof. Frank Hein Schaper for helping me to analyze XRD data and solving structures.

The research presented in this thesis would not have been possible without the high-quality research facilities available at the University of Montreal. Therefore, I would like to extend my thanks to the members of the NMR service, with a special mention to Dr. Pedro Aguiar, who was always available to set up the specific experiments I needed and to assist me in resolving NMR-related issues I encountered. I would also like to express my gratitude to all the members of the X-ray Diffraction Analysis service for their availability and trust in me, especially Dr. Maris Thierry and Dr. Daniel Chartrand, who trained me in this technique.

Finally, I want to express my heartfelt thanks to my parents, who instilled in me a thirst for knowledge from a young age, who always encouraged me to pursue my ambitions and provided both moral and financial support. I would also like to extend my gratitude to my lovely wife Tithi, for standing by me throughout these years, for unwavering belief in me, and for making me happy every day.

1.1 Chapter 1-Introduction

The carbon-hydrogen bond (C−H) holds a distinctive place in organic chemistry as the ubiquitous unfunctionalized group. Organic molecule representations often reveal the presence of C−H bonds by the absence of other bonds. This "invisibility" of C−H bonds results from their wide prevalence and their generally low reactivity. Considering these attributes, it becomes evident that the advancement of precise methods for selectively functionalizing C−H bonds could represent one of the most versatile and impactful transformations in organic synthesis. Realizing this potential has the capacity to revolutionize the synthesis of organic compounds, ranging from simple substances like methanol to intricately structured natural and synthetic products.

One of the most promising approaches to C−H functionalization is based on so-called "organometallic routes," which involve the formation of a bond between carbon and a metal center. The direct carbon-hydrogen bond activation and subsequent formation of C−C or C−heteroatom (C−X) bonds through transition metal catalysis have shown to be one of the most promising alternatives to traditional cross-coupling reactions that start from an activated C-X bond as opposed to a C-H bond. Indeed, selective functionalization of C−H bonds promoted by transition metal precursors has attracted much attention as it can convert inert alkanes and arenes into valuable functionalized organic products[1,2]. This method does not require pre-functionalization of starting materials to reactive organohalides or organometallic complexes (for example Grignards, organozinc compounds, etc.) making the process simpler and greener[3]. In addition, selective C−H functionalization involves comparatively short synthetic operations and generates less undesired byproducts, rendering the method economically attractive. As a consequent, in the last decade, metal-promoted C−H functionalization has become a trusted tool in organic synthesis[4], medicinal chemistry[5], crop protection[6] and material science[7]. Synthetic procedures based on C−H functionalization are becoming prominent and play a central role in developing sustainable chemical processes.

Transition metal precursors can break C−H bonds in several ways. Low oxidation state metals activate C−H bonds through a classic oxidative addition mechanism to give a new metal complex featuring an organyl and a hydride moiety[8], while other metals follow radical mechanisms[9] to break

C−H bonds. Furthermore, some other metals can follow sigma bond metathesis[10], ambiphilic metal -ligand activation[11], concerted metalation-deprotonation[12] and ligand to ligand hydrogen transfer[13]. In some cases, one metal precursor can react via several competing mechanisms leading to lower yields and lower selectivities.

The less abundant and precious 4d and 5d transition metals like iridium, palladium, rhodium and ruthenium are strongly active towards catalytic functionalization of inert alkanes and arenes through C−H bond activation. However, their low natural availability, high cost and environmental shortcomings have motivated chemists to search for new catalysts form cheaper and more abundant transition metals. Recently, earth abundant first row transition metals have attracted more attention for C−H bond functionalization compared to expensive metals. Among 3d metals nickel catalysts have been found to be highly active towards various organic transformations. Indeed, Ni-based systems have a long history in the activation of C-H bonds. Thus, the first nickel catalyzed selective C−H bond activation was reported by Kleinman and Dubeck in 1963. [14]. Over the past few decades, there has been a growing number of reports highlighting Ni(II)-catalyzed protocols for directly functionalizing unactivated C−H moieties.

The central theme of the present thesis is inspired by the documented efficacy of Ni-based precursors for C−H functionalization applications. More precisely, the vast majority of Ni-promoted C−H functionalization chemistry follows the so-called directing group-assisted C-H functionalization methodologies. Before describing the projects undertaken during the course of my Ph. D. studies, I will provide in the following sections a review of some important nickel catalyzed directing-group-assisted C−H functionalization examples in order to provide some context for the research studies in question.

1.2   Directing group assisted C−H functionalization

Metal-catalyzed C−H bond activation stands as a highly valuable strategy reliant on nucleophilic substituents (in other words directing groups) within the substrate that enable its binding to the metal, thus facilitating the subsequent coordination of the targeted C−H bond. This approach

involves chelation assistance, forming a metallacycle intermediate that reacts with a co-substrate to create C−C or C−X bonds, as illustrated in **Scheme 1.1**.

Scheme 1. 1. Generalized scheme for chelation-assisted C−H bond derivatization.
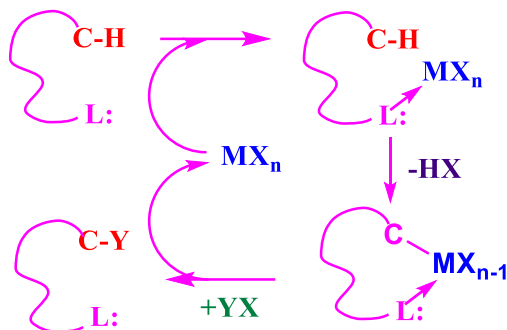
Many different types of functional groups have been evaluated as directing groups to selectively activate a C−H bond and promote its functionalization. The efficiency of metal catalyst C−H functionalization partly depends on the easy installation and removal of these directing groups. Despite the fact that a significant number of monodentate directing groups are available, bidentate directing groups are mostly limited to quinoline and pyridine derivatives. Furthermore, installation and subsequent purification processes of bidentate directing groups are lengthy and economically not feasible. Also, in many cases conventional directing groups are unable to bind the metal propel; as a result, C−H functionalization remains unsuccessful. Therefore, invention of new types of directing groups are crucial in order to functionalize a C−H bond that cannot be derivatize with traditional directing groups.

1.3 Examples of chelation-assisted nickel-catalyzed C−H bond functionalization

1.3.1 Alkylation of C−H bond

Several chelation-assisted systems are applicable in nickel-mediated C−H derivatization. Notably, in 2013, Chatani reported a chelation-assisted alkylation of the C−H bond situated at the ortho position to an 8-aminoquinoline directing group[15]. Although this method is quite efficient, giving 88% yield, it requires a very high temperature (140 $^\circ$C), supporting ligand PPh$_3$, and a base (**Scheme 1.2**).

Scheme 1. 2. Alkylation of Csp^2-H bonds with linear R-X in presence of Ni (II) catalyst.
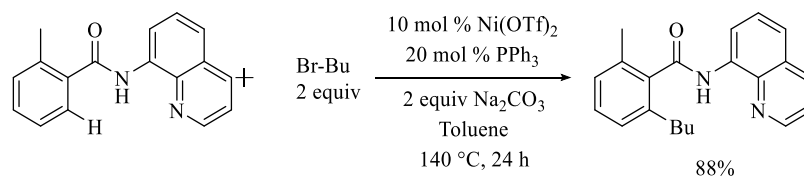
First, this C−H functionalization strategy necessitates the external base (Na$_2$CO$_3$) to neutralize in-situ generated HX. Secondly, the supporting ligand PPh$_3$ likely aids in displacing the ¯OTf ligand, inducing a positive charge on Ni that allows for the binding with the directing group and subsequent coordination of the C−H bond facilitating its activation. Additionally, the supporting ligand (PPh$_3$) serves to coordinatively stabilize the electropositive Ni(IV) intermediate. Lastly, this method requires high temperature, probably because oxidative addition of alkyl halide to Ni(II) is energetically not favorable. It is probable that an excess of RX and base is employed to accelerate the reaction rate. According to the proposed mechanism, the catalyst initially reacts with the directing group (DG), leading to the formation of HX. Subsequently, a cyclometallation occurs through a concerted metalation–deprotonation mechanism to activate the ortho C−H bond. This is followed by the oxidative addition of RX, reductive elimination, and finally, protonation with HX, resulting in the desired product (Scheme **1.3**).

Scheme 1. 3. Mechanism of alkylation of Csp^2-H bonds with linear R-X in presence of Ni (II) catalyst.
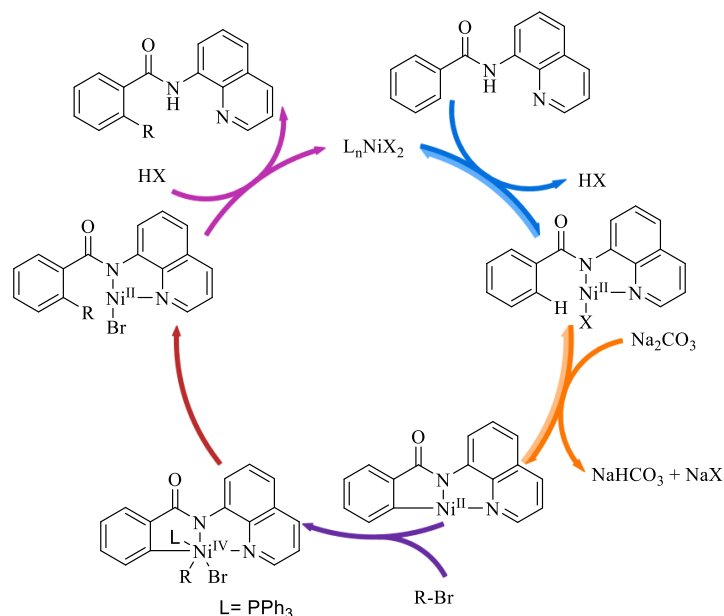
Punji reported another intriguing example of Ni-catalyzed alkylation involving a Csp^2-H bond of a pyridine-substituted indole (**Scheme 1.4**)[16]. Indoles play a crucial role in numerous biologically active compounds, natural products, and pharmaceuticals. Consequently, the selective functionalization of indoles using transition metal catalysis is gaining considerable attention. This method necessitates a catalytic amount of LiHMDS and two equivalents of LiO^{t}Bu for achieving complete conversion (**Scheme 1.4**). Notably, other precursors such as Ni(OAc)$_2$, (DME)NiCl$_2$, and (DME)NiCl$_2$/Phen proved inefficient, failing to yield satisfactory results in the mentioned reaction. The high acidity of the C(2)-H bond suggests an easy activation. The proposed mechanism suggests that the catalyst undergoes initial activation by LiN(SiME$_3$)$_2$, followed by the addition of RX through a radical pathway.

Scheme 1. 4. Alkylation of indoles.
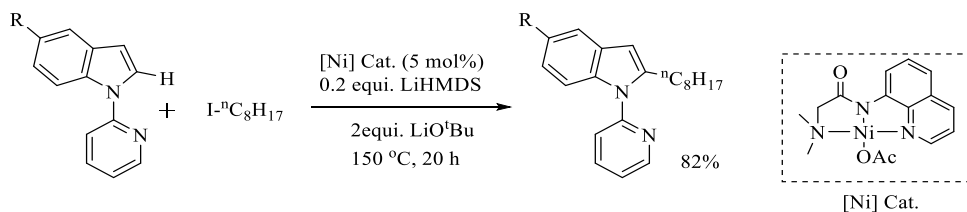
In 2016, Wang introduced a system initially aimed at functionalizing benzoic acid derivatives derived from 8-aminoquinoline (**Scheme 1.5**). Unexpectedly, instead of targeting the phenyl ring as intended, the functionalization occurred at the C5 position of the quinoline[17]. This surprising outcome turned out to be favorable because quinolines constitute essential structural components of numerous biologically active drugs and natural products. Furthermore, the bioactivity of these drugs is significantly influenced by the nature of substituents on the C5 position of the quinoline moiety. Consequently, developing a method allowing selective functionalization of the C(5)-H bond of quinoline holds considerable significance.

Scheme 1. 5. Alkylation of Quinoline.
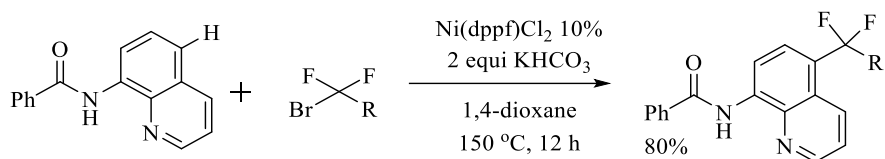
The authors observed lower yields when substituents were installed at the C4, C6, and C7 positions, implying that steric hindrance on the quinoline moiety significantly impacts the above reaction. Also, mechanistic studies show that the presence of a radical scavenger, 2,2,6,6-tetramethyl-1-piperidinyloxy (TEMPO), completely inhibits functionalization. This inhibition suggests the involvement of a radical process in the reaction mechanism. The authors proposed the tentative mechanism shown in Scheme 1.6 to rationalize their findings.

Scheme 1. 6. Mechanism of C(5)-H functionalization of quinoline.
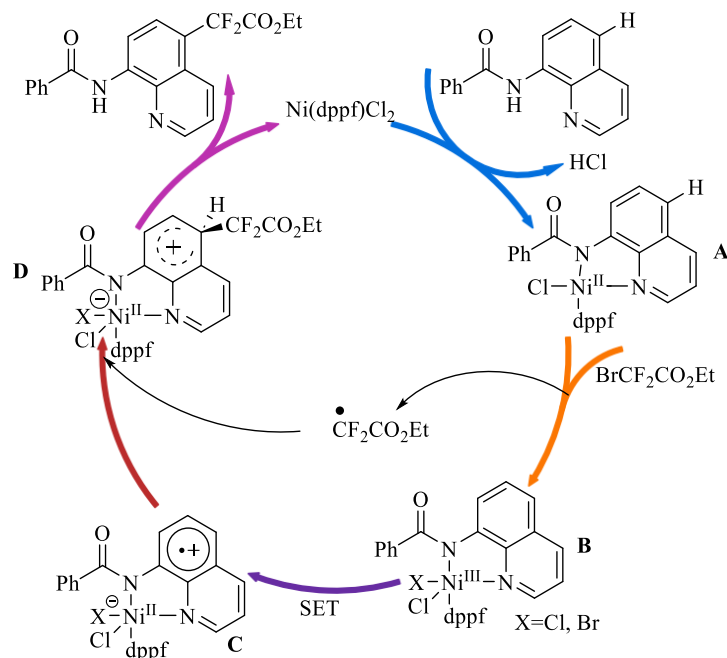
According to this proposed mechanism, intermediate A abstracts a Br• radical, leading to the formation of the •CF_2CO_2Et radical and the oxidized intermediate **B**. The latter then undergoes an intramolecular Single Electron Transfer (SET) process, resulting in Intermediate **C**, which features a radical cation fragment. This species reacts with the in-situ formed radical •CF_2CO_2Et, generating **D**. Finally, a proton transfer/demetallation step leads to the formation of the product.

Ge and his team have reported an effective system for alkylating unactivated Csp^3-H bonds using alkyl halides as electrophiles[18]. When an aliphatic amide and alkyl halide mixture is treated with a Ni(II) precursor in the presence of a base and a robust supporting ligand, the methyl C−H bond undergoes functionalization with the alkyl group (**Scheme 1.7**). In this instance, the strong supporting ligand dppbz most probably stabilizes the electrophilic Ni(IV) intermediate. The authors do not explicitly justify the need for using an excess of base (5 equivalents), but it is likely due to the low solubility of the base in the solvent in which the reaction was conducted (toluene).

Scheme 1. 7. Alkylation of Csp^3-H bond
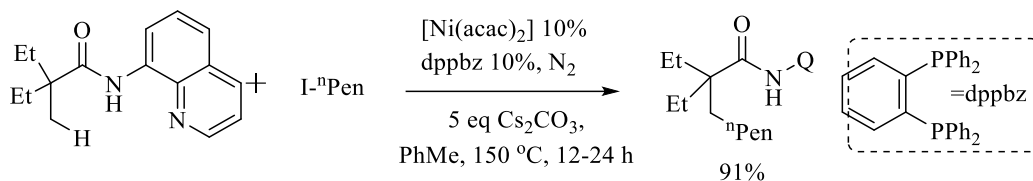
Alkylation of the C−H bond in the methyl group is notably absent in the case of ethyl or propyl groups, suggesting a preference for the formation of a five-membered ring intermediate over six or seven-membered ring intermediates in the cyclometallation step. Bulky alkyl halides such as iso-propyl and iso-butyl iodides also fail to yield the desired products, likely due to the steric instability of the intermediate formed. The proposed mechanism closely resembles the previously discussed alkylation of Csp^2-H bonds.

1.3.2 Arylation of C−H bond

Numerous catalytic systems have emerged for the arylation of C−H bonds, often employing chelation strategies. Hoover's work introduced the Ni-mediated oxidative decarboxylative arylation of Csp^2-H bonds using aromatic carboxylates as coupling partners. This method demonstrates a broad substrate scope for aromatic carboxylates, encompassing compounds such as benzofuran, benzoxazoles, triazole, pyrazole, and benzothiophene. The anticipated product is obtained through a Ni-catalyzed reaction between benzamide and an aromatic carboxylate in the presence of a base and an additive (**Scheme 1.8**)[19].

Scheme 1. 8. Arylation of phenyl group.
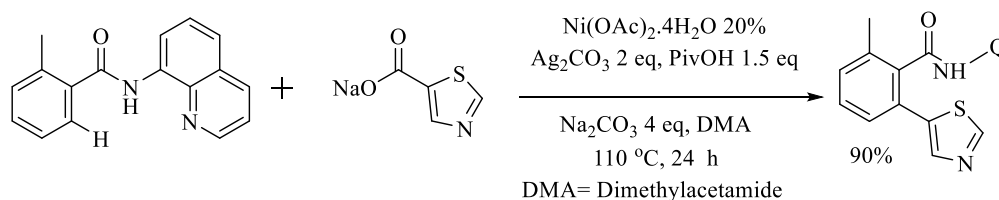
The requirement of fairly expensive Ag$_2$CO$_3$ in this method for obtaining satisfactory results stands as one of its drawbacks. The authors justify the need for silver salts by citing literature reports[20,21] that invoke decarboxylation of carboxylic acids in the presence of these reagents at high temperature. According to the authors, thiazole-5-carboxylate reacts with silver salt to generate Ag-thiazole species with elimination of CO$_2$. Subsequently, this Ag-thiazole species undergoes

transmetalation with Ni^{II} intermediate as shown in **scheme 1.9**. In addition, the involvement of a polar aprotic solvent like DMA can expedite the rate of nickel-mediated C−H bond activation. This phenomenon is attributed to the solvent's ability to stabilize the electropositive nickel center. Another possibility is that the solvent aids in the dissociation of the $^{-}$OAc anion, thereby facilitating the coordination of Ni with the directing group. Notably, the reaction remains unaffected by TEMPO, indicating that a single electron transfer process is not involved. Additionally, the kinetic isotope effect value of 4.3 (obtained from competition experiments with deuterated and nondeuterated amide substrate) suggests an irreversible C−H bond activation step. The proposed mechanism is depicted in **Scheme 1.9**.

Scheme 1. 9. Oxidative decarboxylative arylation of Csp^2-H bond.
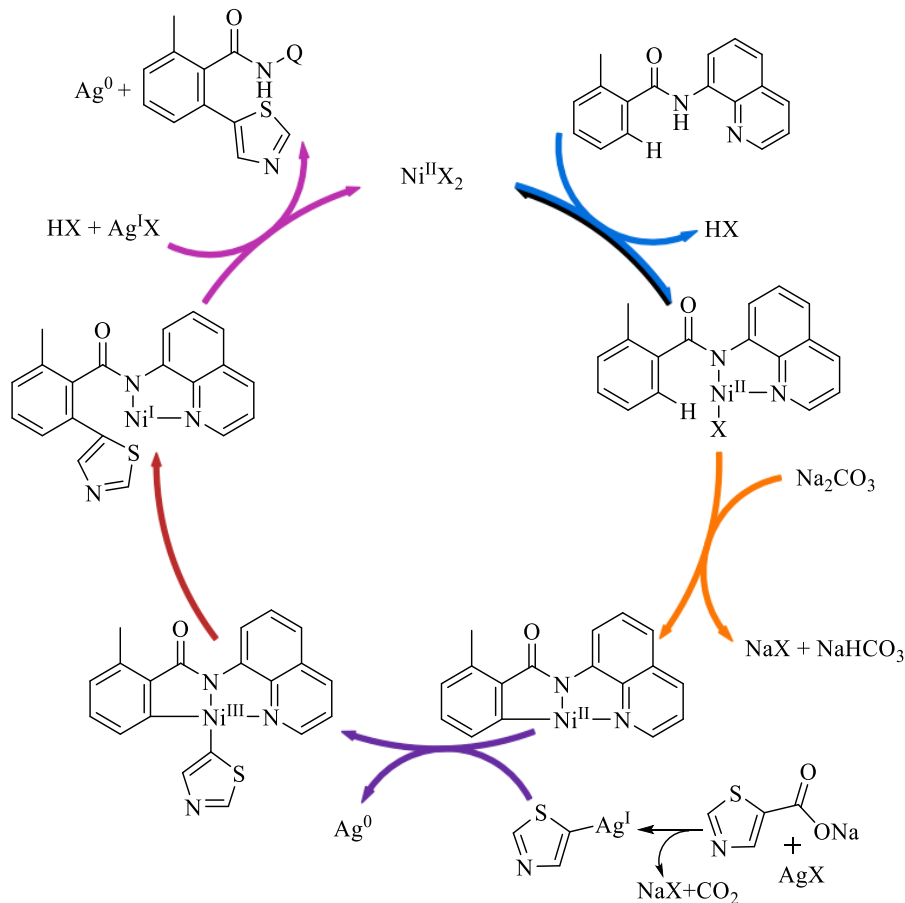
Ong explored the hydroarylation reaction of benzimidazole with styrene, detailing two catalytic conditions that yield either branched or linear coupling products. These conditions involve $Ni(COD)_2$, a supporting ligand (NHC), and $AlMe_3$ as a Lewis acid (**Scheme 1.10**)[22]. The selectivity

in product formation is attributed to the coordination of AlMe$_3$ by the benzimidazole nitrogen, a relationship confirmed through X-ray crystallography. The linear product arises due to steric control during the insertion of styrene into the Ni-H bond, while the branched product results from the electronically favored hydride insertion at the β-carbon of styrene.

Scheme 1. 10. Hydroarylation reaction of benzimidaozle.
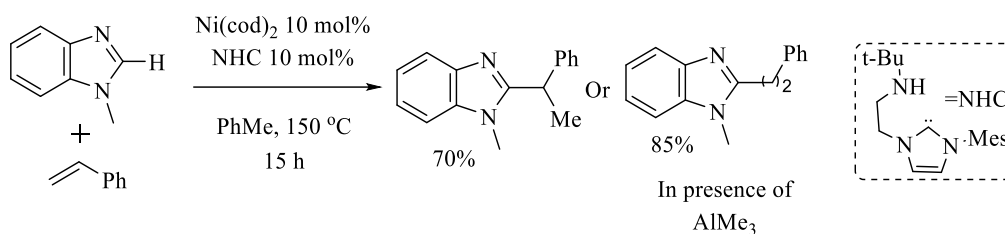
Preceding the activation of the C−H bond, the formation of the NHC-Ni complex occurs through the substitution of the COD ligand with NHC. Notably, the C−H bond at the C-2 position exhibits significant acidity, making the activation of this C−H bond by the nickel center highly facile. The proposed mechanism involves the activation of the C−H bond, followed by coordination and insertion of styrene, ultimately leading to reductive elimination and yielding either linear or branched products (Scheme 1.11). In the presence of AlMe$_3$, the insertion of styrene occurs at the alternate carbon of the double bond, resulting in the linear product. For simplicity, this specific step is omitted in the figure.

Scheme 1. 11. Mechanism of hydroarylation reaction of benzimidazole.
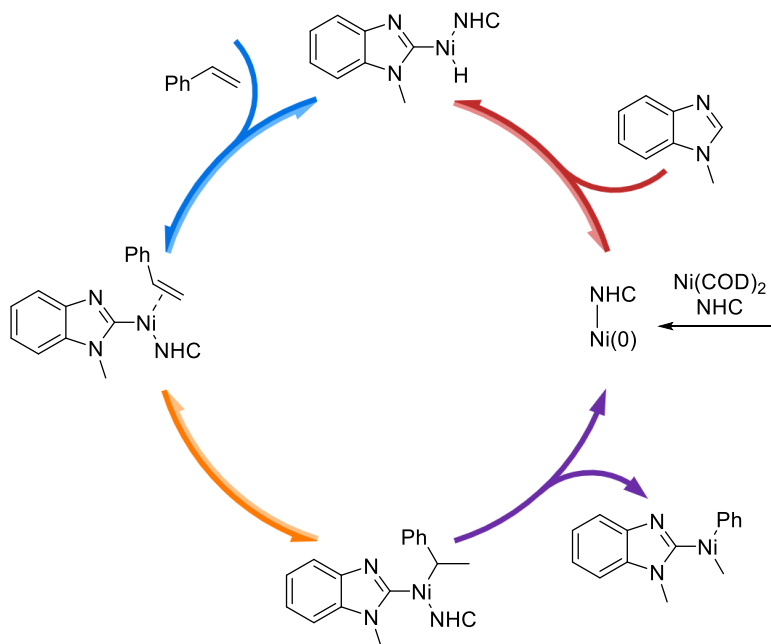
The direct functionalization of an alkyl group with thiophene holds significant promise due to the widespread presence of thiophenes and their analogues in functional materials, pharmaceuticals, and natural products. Kambe detailed a Ni-catalyzed cross-coupling reaction involving an alkyl amide with thiophene. The efficiency of this method is limited by the utilization of many additives like Ag_2CO_3, MesCOOH, TBAB, and KH_2PO_4 (**Scheme 1.12**)[23]. Whereas rule of TBAB and MesCOOH is not clearly understood.

Scheme 1. 12. Cross coupling of alkyl amide with thiophene.

$Ni(OTf)_2$, Ag_2CO_3,
TBAB, KH_2PO_4

MesCOOH, DMSO
160 °C, 24 h

70%
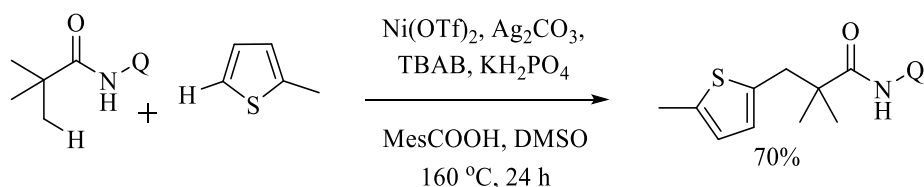
TBAB = tetrabutylammonium bromide

The kinetic isotope effect value of 4.6 (measured by a competition experiment between deuterated and nondeuterated substrates) suggests that the rate-determining step involves the cleavage of the Csp^3-H bond. The proposed mechanism closely resembles the arylation of Csp^2-H bonds, with a few distinctions: (1) prior to cross-coupling, KH_2PO_4 activates the catalyst, converting it to

Ni(H$_2$PO$_4$)$_2$, (2) after the activation of the C−H bond, silver salt oxidizes Ni(II) species to Ni(III) species, and (3) subsequently, Ni(III) undergoes metathesis with thiophene. Finally, reductive elimination yields the arylated product, as illustrated in **Scheme 1.9**.

1.3.3 Alkynylation of C−H bond

Alkynes serve as versatile building blocks in synthetic organic chemistry and find significant utility in material science and biological chemistry as valuable precursors. The oxidative coupling of Csp^3-H bonds with alkynes presents a highly promising approach due to its potential for atom- and step-economy. Shi reported a nickel-catalyzed alkynylation of Csp^3-H bonds using ethynyl(tri-isopropyl)silane, demonstrating excellent yields (**Scheme 1.13**)[24]. However, the method requires additives such as the oxidant Cu(OAc)$_2$, the supporting ligand DavePhos, and the transmetalating reagent Me$_2$S•CuBr, which can be considered a limitation of this approach. The co-solvent PhCN results in marginal improvements in the yield, but its precise contribution to the reaction mechanism remains unclear.

Scheme 1. 13. Alkynylation of Csp^3-H bonds.
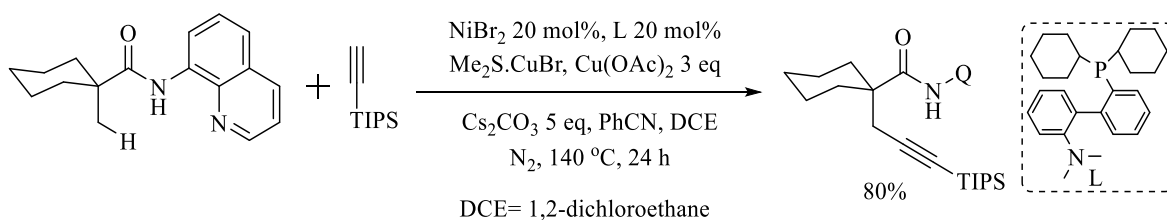
This report also presents some preliminary mechanistic studies. For example, deuterium labeling experiments conducted on the aforementioned system demonstrate an absence of proton-deuterium scrambling, indicating that the C−H activation step is irreversible. In addition, KIE values obtained from both parallel reactions (KIE = 2.8) and competition reactions (KIE = 2.0) support the involvement of C−H bond cleavage in the rate-determining step. Moreover, when a radical scavenger is introduced into the standard reaction, the yield drops to 15%, suggesting a potential radical pathway. Based on these findings, the authors propose the following reaction mechanism (**Scheme 1.14**).

Scheme 1. 14. Mechanism of alkynylation of Csp³-H bond.
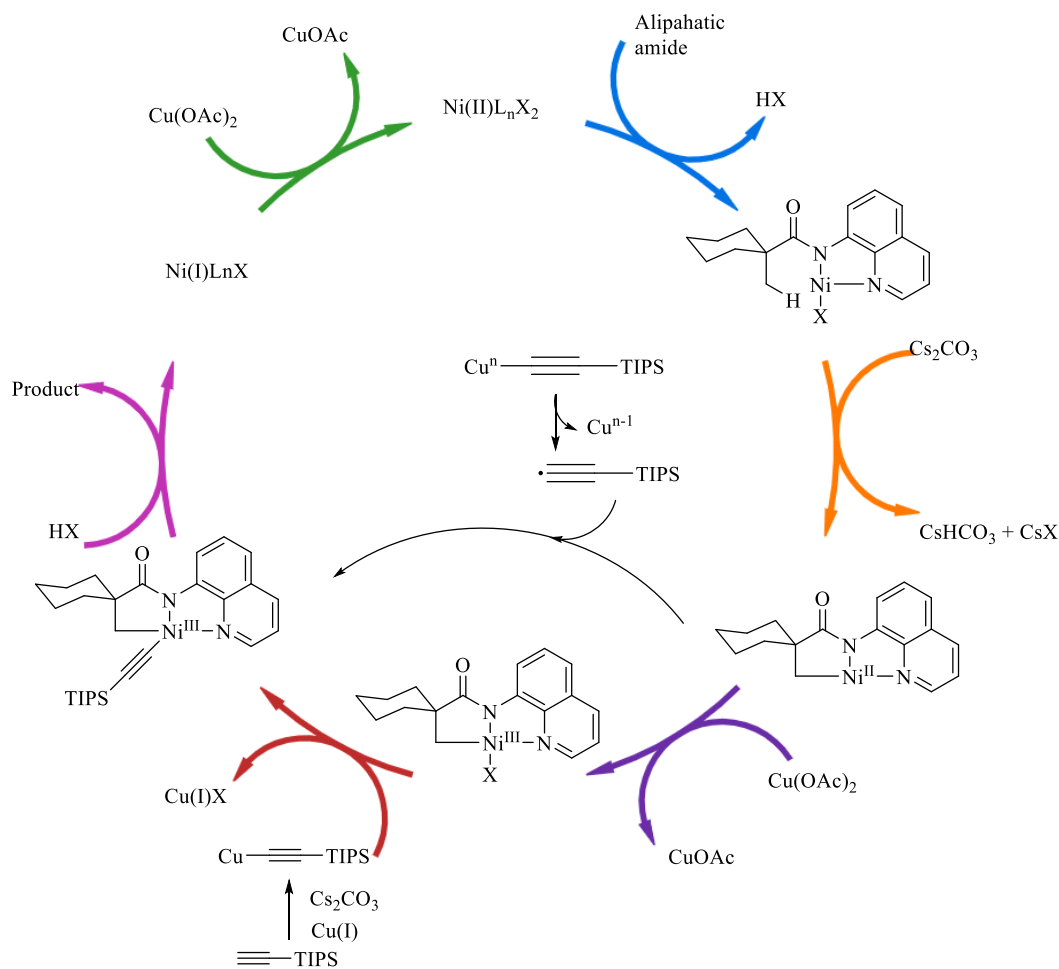
In 2015, Shi devised a nickel-catalyzed direct alkynylation of unactivated aromatic amides with alkyl bromides (**Scheme 1.15**)[25]. Remarkably, this reaction proceeds solely with alkyl halides in the presence of a nickel catalyst and base, without requiring any oxidant, supportive ligand, or additional additives. DME plays a dual role as both a cosolvent and a supportive ligand in this reaction. Notably, only 0.5 mol% of catalyst loading is sufficient to generate yields of 95%, and a broad range of alkynyl bromides featuring different chain lengths and both aromatic and aliphatic alkyne groups could be introduced. An additional advantage lies in the ease of removing the PIP directing group through mild N-nitrosylation/hydrolysis of the functionalized amide.

Scheme 1. 15. Alkynylation of Csp^2-H bonds.
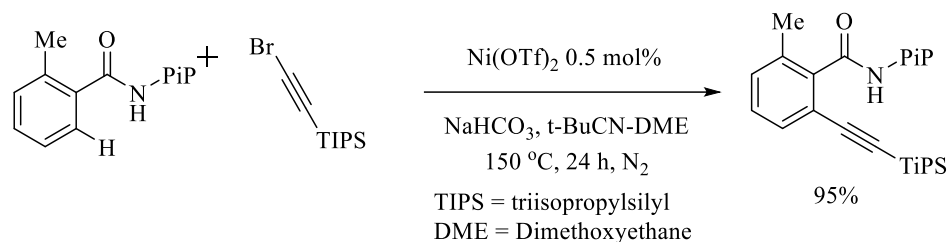
Punji developed a catalytic system employing $(thf)_2NiBr_2/Phen$ precursor for the alkynylation of nitrogen-containing heteroarenes using triisopropylsilylalkynyl bromide as coupling partners. This method demonstrates the capability to couple numerous heteroarenes, including pyrazole, indoles, imidazoles, and pyrroles, with alkynyl bromides (**Scheme 1.16**)[26]. Notably, the reaction tolerates various functional groups such as F, Br, NO_2, OMe, and CN on the heteroarene moiety. However, it is important to note that this method is specifically applicable only to triisopropylsilylalkynyl bromides.

Scheme 1. 16. Alkynylation of heteroarenes.
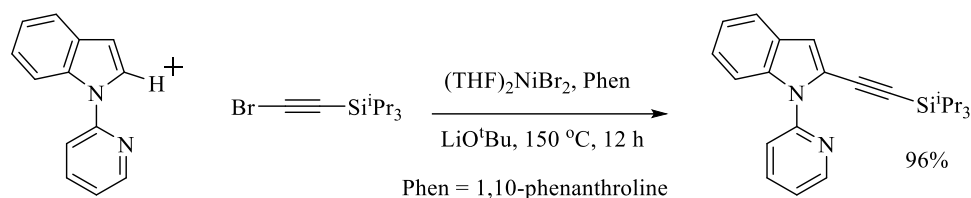
The presence of a crucial stabilizing supporting ligand, 1,10-phenanthroline, significantly impacts the reaction, and without it the yield of the alkynylated product is limited to only 10%. Notably, indoles containing other coordinating groups, such as $-C(O)O^tBu$, $-C(O)Ph$, and 2-thiophenyl, fail to yield the expected product. These observations underscore the significance of a nitrogen group at the 2-position of the N-substituent. The measured kinetic isotope effect ($K_H/K_D = 3.6$) suggests that C−H nickelation might be the rate-determining step. Furthermore, deuterium labeling experiments indicate that C−H nickelation is an irreversible process. The mechanism proposed by the authors is similar to the mechanisms described earlier for the alkylation or arylation of C−H bonds (Schem **1.3** and Scheme **1.10**).

1.3.4 Alkenylation of C−H bond

Functionalized alkene compounds are highly valued as potential building blocks in synthetic organic chemistry, finding utility in diverse reactions such as metathesis, cross-coupling, and cycloaddition reactions. Zhang developed a method involving nickel-mediated alkenylation of β-Csp^3-H bonds with terminal alkynes, facilitated by the chelation assistance of the 8-aminoquinoline group (**Scheme 1.17**)[27]. This method needs multiple additives such as a base, supporting ligand, and a weak acid, giving a moderate yield of final product. The acidic additive, HOAc, appears to be essential for the proton transfer from the concerted metalation-deprotonation step to the base. There is no plausible explanation for the necessity of the supporting ligand (MePh$_2$P).

Scheme 1. 17. Alkenylation of Csp^3-H bond.
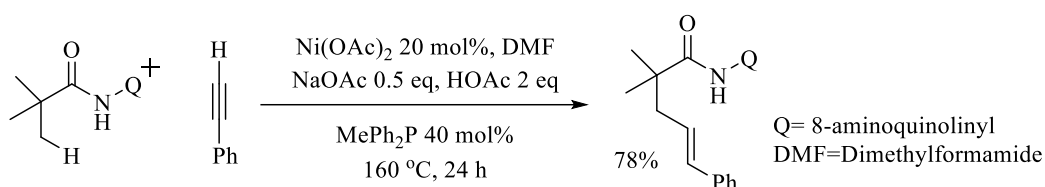
The absence of any influence on reaction yields when using radical scavengers indicates the exclusion of a radical pathway in the mechanism. Additionally, the deuterium labeling experiment revealed no deuterium-proton exchange, supporting the irreversible nature of C−H nickelation. The parallel and competitive KIE values of 3.5 and 4.6, respectively, highlight that C−H activation represents the slowest step in the process. As proposed, the mechanism involves initial coordination of the alkyne, followed by its insertion into the C−Ni bond, ultimately culminating in metathesis to yield the desired product, as depicted in **Scheme 1.18**.

Scheme 1. 18. Mechanism of alkenylation of Csp^3-H bond.
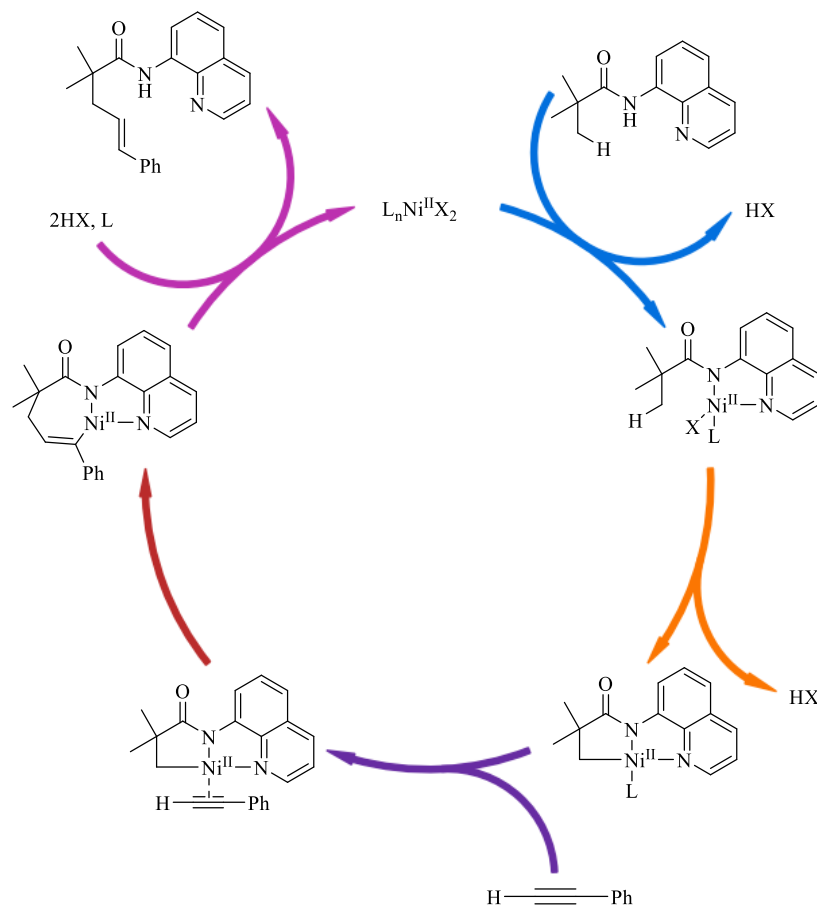
Miura's strategy for alkenylation of 1,3,4-oxadiazole with alkyne or styrene showcases the ease of functionalizing oxadiazole due to the highly acidic nature of its C(5)-H bond. This acidity predicts the straightforward activation of the C(5)-H bond, which indeed facilitates the alkenylation process in the presence of Ni(COD)$_2$ at 100°C within a short span of 3 hours (**Scheme 1.19**)[28]. Notably, this strategy relies solely on the supporting ligand (PCy$_3$), which potentially aids in dissociating the 'COD' ligand. Owing to the absence of in-situ generated HX, the use of a base is not required.

Scheme 1. 19. Alkenylation of 1,3,4-oxadiazole.
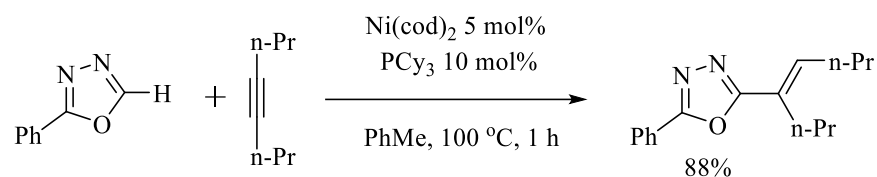
The proposed mechanism involves the protonation of the Ni(0) catalyst by the highly acidic C(5)-H bond. Subsequently, the alkyne coordinates and inserts into the Ni-H bond. Finally, the resulting intermediate undergoes reductive elimination, yielding the desired product.

Shi's method for alkenylation of carboxamides with styrenyl iodide involves the use of the precursor Ni(acac)$_2$, the supporting ligand BINOL, and KTFA as an additive (**Scheme 1.20**)[29]. The supporting ligand potentially aids in forming a highly oxidized nickel intermediate, ensuring coordinative saturation. However, it is worth noting that the article does not detail any mechanistic studies for this particular reaction.

Scheme 1. 20. Direct alkenylation of carboxamide with styrenyl iodide.
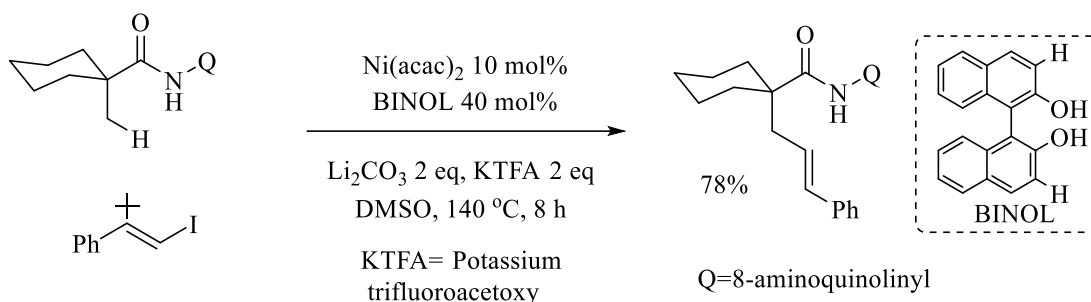
1.3.5   Halogenation of C−H bonds

Chatani's development of an efficient method for iodination of aromatic C−H bonds using molecular iodine showcases the utility of aryl halides in synthesizing compounds relevant to medicinal and material science (**Scheme 1. 21**)[30]. Interestingly, this method necessitates only a catalyst and a base, eliminating the need for supporting ligands or additional oxidants. The presence of a chlorine group at the C5 position of the quinoline moiety acts as a regulator, effectively blocking this site and enhancing the regioselectivity of C−H bond functionalization.

Scheme 1. 21. Iodination aryl C−H bond
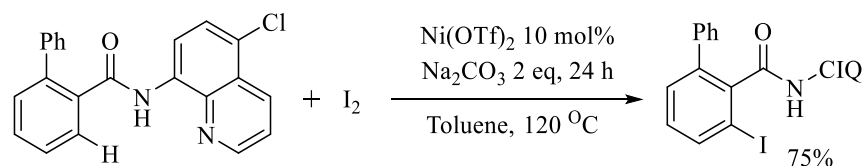
The authors present some mechanistic experiments that provide insights about some key features of the catalytic cycle. For example, the deuterium labeling experiment does not show any proton-deuterium exchange, indicating an irreversible C−H nickelation. Whereas KIE value of 1.8 from competition reactions hints that C−H bond breaking is likely the rate-determining step. Moreover, this reaction fails to proceed in the presence of a radical scavenger (TEMPO, BHT), indicating the involvement of radical species in the reaction. The authors proposed the following reaction mechanism based on the aforementioned mechanistic studies.

Scheme 1. 22. Mechanism of Iodination aryl C−H bond
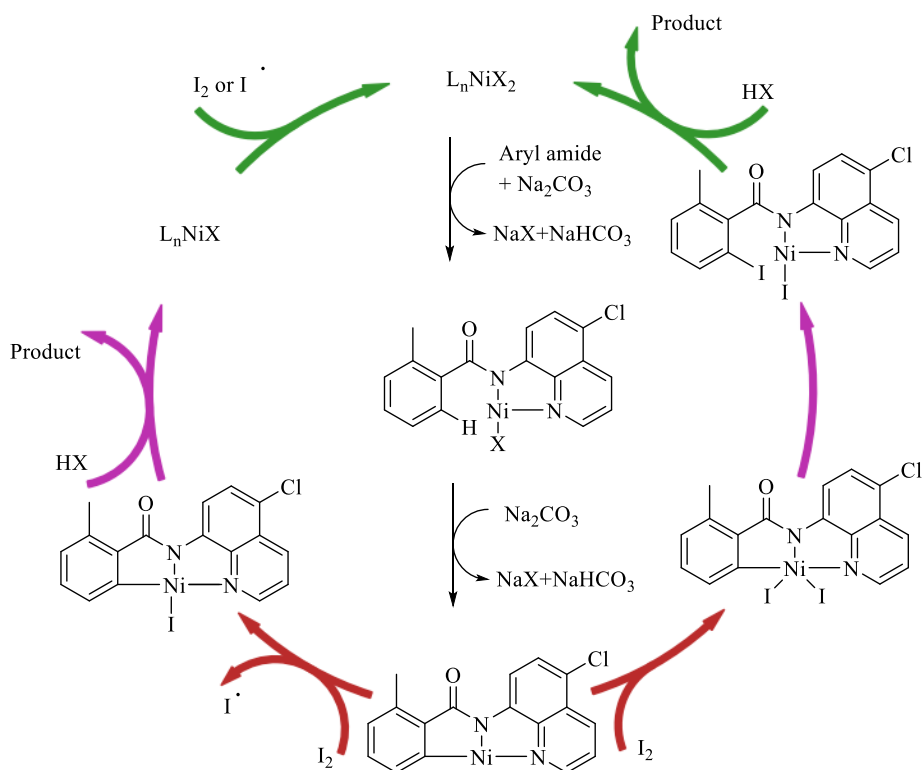
Shi presented a method involving nickel-mediated halogenation of aromatic amides using lithium halide, aided by the PIP directing group (**Scheme 1.23**). This process requires a strong oxidant in the form of $KMnO_4$ and O_2 combined, along with the utilization of a supporting ligand, THP, to achieve the expected yield. It is likely that an excess of LiX (3 eq) is employed to accelerate the reaction rate. The precursor $NiCl_2(PPh_3)_2$ is used instead of $Ni(OTf)_2$ for the generation of chlorinated products.

Scheme 1. 23. Halogenation of Csp^2-H bond with LiBr in presence of $Ni(OTf)_2$.
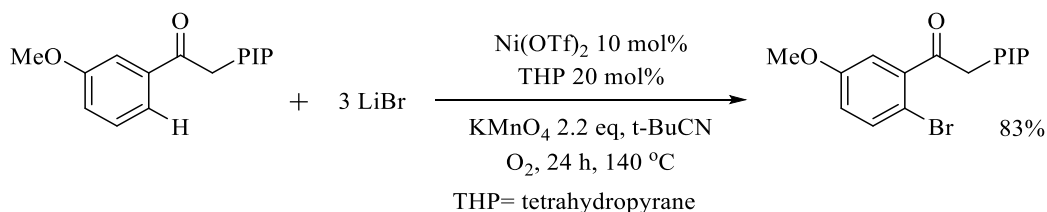
1.3.6 Thiolation and Selenation of C−H bond

2-Aminothiophenols and their selena analogues are important structural units of many bioactive compounds and can be used as intermediates in the synthesis of many heterocycles that are valuable in the pharmaceutical industry and material science. For example, 2-aminothiophenols are present as substituents in benzothiazole, phenothiazines and dibenzothiazepines which are the key functional units of various immunosuppressive, antipsychotic and antidepressant agents.

Ackermann has developed a strategy of chalcogenation of electron rich anilines with the aid of a monodentate pyrimidyl directing group (**Scheme 1. 24**)[31]. This method requires an oxidant (MnO_2) that converts diphenyl disulphide to sulfinyl radical (**Scheme 1. 25**). No extra ligand is required, likely because 1,4-dioxane serves the dual purpose of solvent and supporting ligand. Selena analogues formed following the same strategy.

Scheme 1. 24. Sulfonylation of aryl C−H bond.
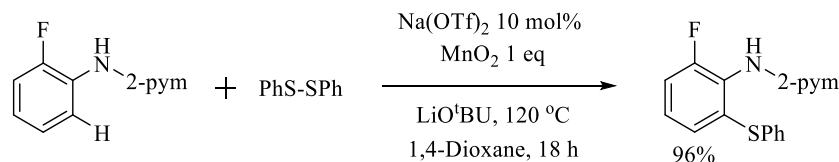
It is observed that an electron withdrawing group on aniline leads to low yields, hinting that a nucleophilic mode of action is operative. Radical scavengers inhibit the reaction, suggesting that a single electron transfer process is involved in the mechanism. In addition, the high value of $K_H/K_D = 5$ proves that C−H bond activation is the rate limiting step. Based on the above information, the following mechanism is proposed (**Scheme 1.25**).

Scheme 1. 25. Mechanism of sulfonylation of aryl C−H bond.
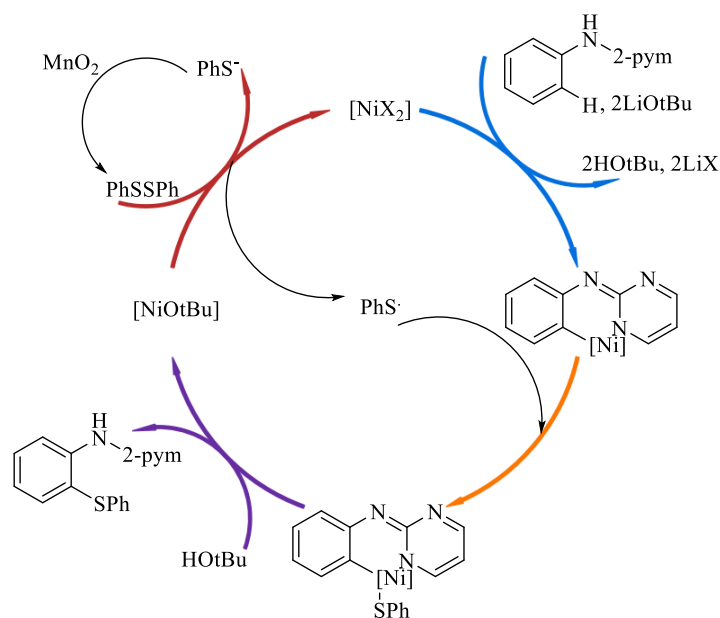
Kambe introduced a straightforward method for the sulfonylation of aromatic C−H bonds using NiCl$_2$ (**Scheme 1.26**)[32]. This process operates without the need for any additives, yet it demands a high catalyst loading, resulting in a moderate yield of 61%. Among various solvents examined, only dioxane demonstrated efficacy, likely due to its polar nature and coordinating properties.

Scheme 1. 26. Sulfonylation of aromatic C−H bond.
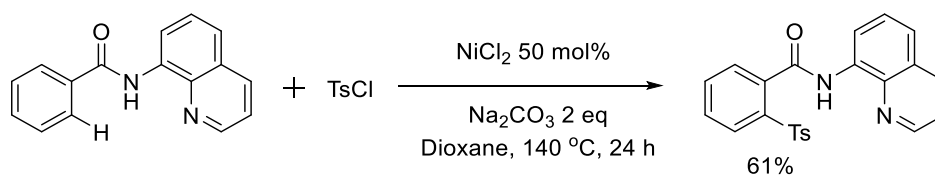
1.3.7 Amination of C−H bond

Arylamines are essential substructures found in natural products and materials used for optoelectronics, agrochemicals, and pharmaceuticals. Hence, research based on facile amination of unreactive C−H bonds is quite attractive. In 2015, Zhang reported an efficient strategy for direct amination of aryl C−H bond[33]. Treatment of 8-aminoquinoline benzamides auxiliary with secondary amines in the presence of nickel precursor, strong oxidants and base delivers ortho-

amination products (**Scheme 1. 27**). The method is compatible with both electron donating and withdrawing groups. Moreover, aryl rings and halogen groups are also tolerated on the substrate. Steric factors play little or no role on the reaction as both para- and meta- substituted carboxamides afford similar yields. Another advantage of this method is that it works with both acyclic and cyclic amines (e.g., 2,6-dimethylmorpholine and substituted piperidines).

Scheme 1. 27. Direct amination of C−H bond.

Q = 8-aminoquinolinyl
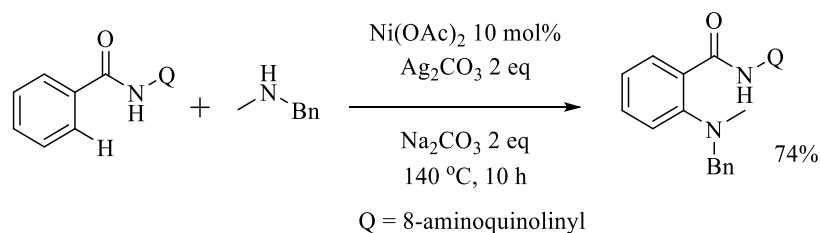
Competitive and parallel KIE values of 4.3 and 4.9, respectively, suggest that C−H bond cleavage of benzamide is the slowest step. A radical scavenger experiment indicated the possibility of involvement of single electron transfer process. Based on preliminary mechanistic studies and literature precedents, the mechanism shown in **Scheme 1.28** was proposed. Intermediate C was detected by MAIDL-TOF-MS, partially supporting the proposed mechanism. SET process may be involved in the formation of intermediate C.

Scheme 1. 28. Mechanism of amination.
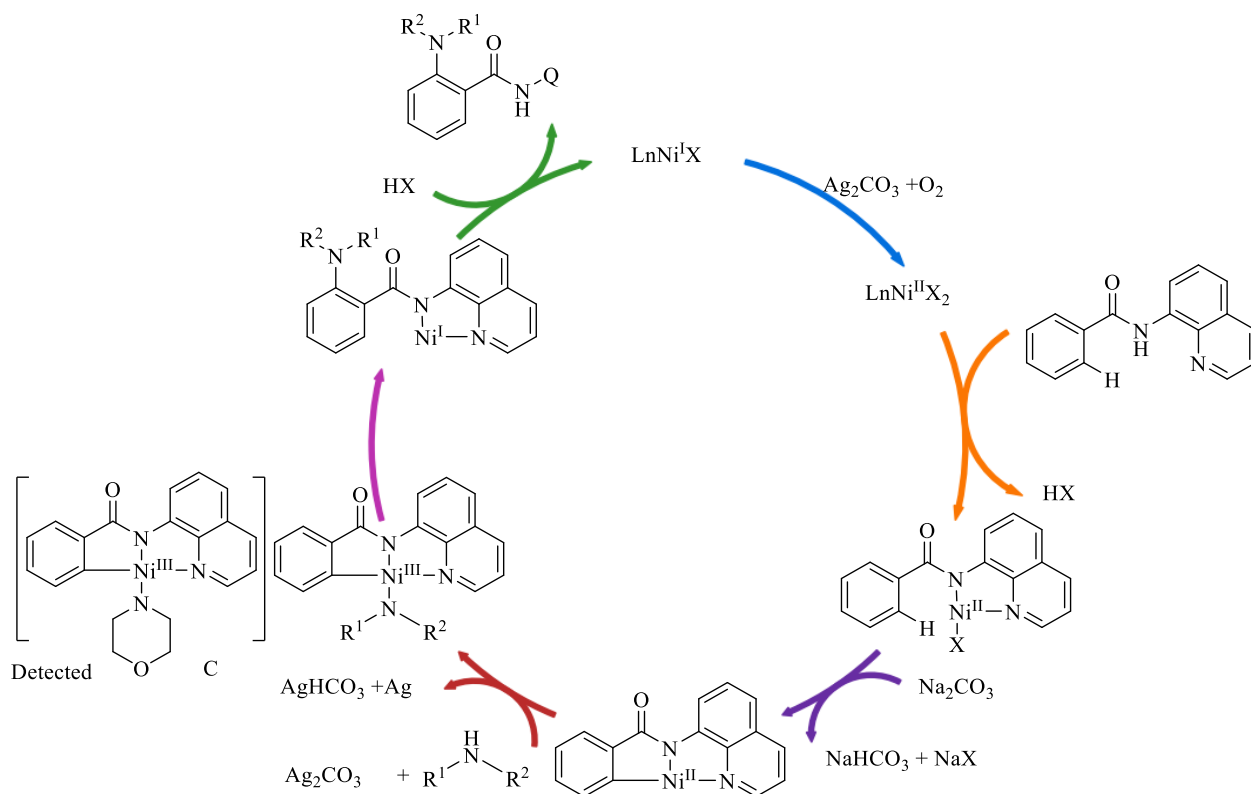
1.3.8 Examples of stoichiometric C−H functionalization

The previous section presented several examples of Ni-catalyzed C−H functionalization strategies involving C-C and C-X (X= O, N, S etc.) bond forming. These precedents showcase the potential of this strategy and establish some of the advantages of these protocols, including: the effectiveness of different directing/binding groups; compatibility with many substrates, metal precursors or catalysts; and tolerance of high temperature. In addition, many of these strategies also afford excellent yields of functionalized products.

However, a significant drawback of these one-pot methods is that they provide limited understanding of the way in which the functionalization reaction works. In many cases, the authors propose mechanisms without substantial experimental evidence, and for this reason many of the mechanistic proposals are general in nature and fairly similar to one another. Indeed, the mechanistic schemes presented above share the following common features: (a) the Ni-organyl intermediate required for the functionalization step is generated via C−H nickelation (for Ni(II) precursors) or C−H activation (for Ni(0) precursors), followed by (b) introduction of a second

intermediate featuring a Ni(II), Ni(III) or Ni(IV) center bonded to an additional organyl ligand R (aryl, alkyl, alkynyl) or a heteroatom-bonded fragment such as OR, NR$_2$, etc., and finally (c) formation of the C-C or C-X bond via reductive elimination. While these proposals are, for the most part, reasonable, there are very few reports supporting these proposals. For instance, only in a limited number of cases has the functionalization of Ni(II)-organyl moiety been substantiated to occur as claimed in the above-cited mechanistic proposals. Demonstrating the feasibility of such coupling steps would require isolation of the postulated intermediate species or analogous model systems and exploring their reactivities. Fortunately, a number of research groups have recently begun conducting such studies involving stoichiometric model reactions, with the express objective of identifying the reaction variables (temperature, base, solvents, ligands, oxidants etc.) that can promote the functionalization step. The present section describes some of these studies and presents the insights they have provided into the underlying C−H functionalization reaction mechanisms for the systems in question. Given the limited number of reports on Ni systems, some examples of Pd-based systems are also included in this discussion.

Pd-based systems. Maiti et al. documented that a stoichiometric amount of Pd(OAc)$_2$ reacts with phenylacetamides of 8-aminoquinoline in acetonitrile at 65 °C, resulting in the formation of the organopalladium species shown in **Scheme 1.29**. This species is isolated through crystallization, and its XRD analysis confirms a distorted square planar Pd(II) geometry for this intermediate.[34,35] The target alkenylated product forms upon treatment of this organopalladium species with styrene. Rate measurements conducted on parallel reactions involving *β,β*-D$_2$-biphenyl styrene and undeuterated biphenyl styrene yielded a kinetic isotope effect of 2.84 (**Scheme 1. 29**). This observation suggests that the rate-determining step might be the product-forming step, which could involve β-hydride elimination. The significance of this report lies in the direct observation of an insertion reaction occurring on an isolated and authenticated Pd−Ar intermediate, thus serving to corroborate the likelihood of such reactivities in a catalytic process.

Scheme 1. 29. Palladium assisted alkenylation.
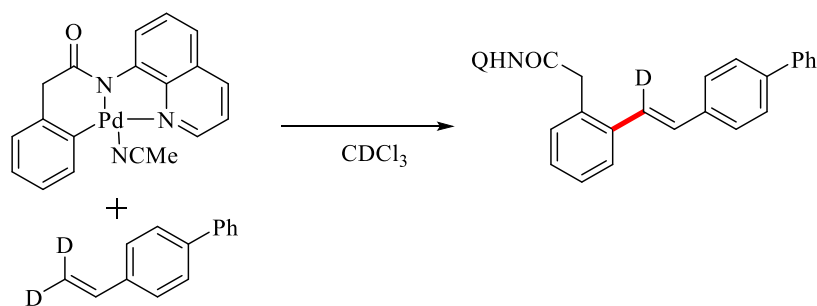
In 2018, Qu et al. provided evidence for the formation of a palladacycle intermediate via a stoichiometric reaction between a pre-formed imine and Pd(OAc)$_2$ in AcOD-d$_4$ at 70 °C.[36] Treatment of this palladacycle intermediate with [F$^+$] in AcOH resulted in the formation of both fluorinated and acylated products featuring opposite configurations at the C−X bond formation site (Scheme 1.30). Based on DFT analysis of transition state energies, the authors proposed that the fluorination occurs via reductive elimination, while acylation follows an S$_N$2 mechanism.

Scheme 1. 30. Reactivity of bicyclic palladacycle [F$^+$]BF$_4^-$
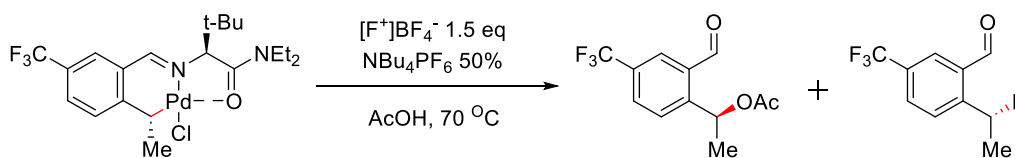
In 2018, Bull and colleagues isolated a palladacycle through the treatment of pyrrolidine with Pd(OAc)$_2$ in pyridine,[37,38] and showed that this palladium intermediate reacts with 4-iodoanisole to give the arylated product in a very low yield (13%) (**Scheme 1. 31**). Also in 2015, Chen reported preparation of similar 5-membered palladacycle intermediate by reacting benzamides with Pd(OAc)$_2$ in CH$_3$CN at 60 °C. Subsequent reaction of this palladacycle with alkyl iodide in ^{t}AmylOH/xylene (1:1) at 130 °C resulted in the formation of the alkylated product, obtained after an acidic aqueous workup (**Scheme 1.32**). Although there was no insight on exactly how the C−C coupling takes place, the study establishes the feasibility of such a reactivity between palladacycles and aryl iodides.

Scheme 1. 31. Arylation of pyrrolidine moiety
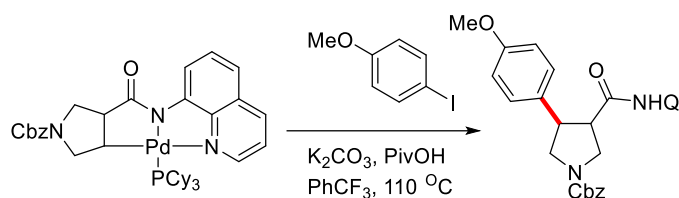
Scheme 1. 32. Reaction of Palladicycle with akyl halide giving alkylation
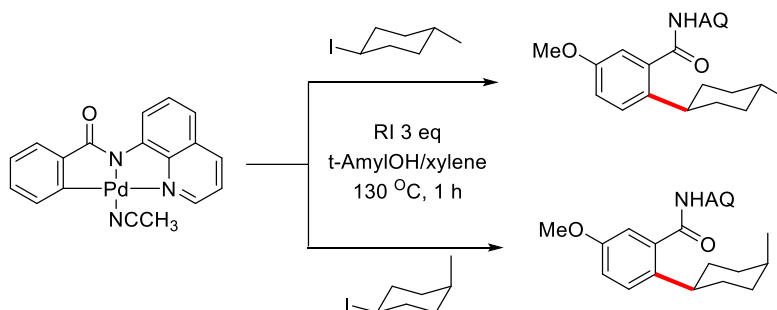
Ni-based systems. In 2019, Sanford's group devised a method based on the reaction of 2-(Quinolin-8-yl)isoindoline-1,3-dione with Ni(OAc)$_2$ in the presence of Ni(PEt$_3$)$_4$ and picoline in benzene-d$_6$ at 100 °C to give a stable nickelacyclic intermediate (**Scheme 1.33**).[39] The subsequent stoichiometric reaction of this Ni^{II} intermediate with I$_2$ resulted in the formation of an iodinated product, as shown below.

Scheme 1. 33. Reaction of Ni(II) intermediate with I$_2$
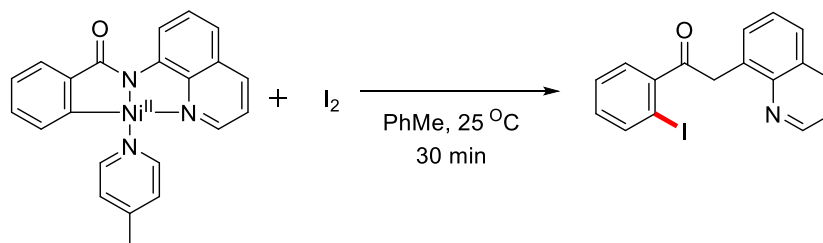
To establish whether the above iodination reaction proceeds through high-valent intermediates, the authors conducted cyclic voltammetry (CV) experiments on the Ni(II) species, showing that a quasi-reversible one-electron redox event occurs at approximately +0.2 V versus Ag/Ag$^+$, identified as the Ni$^{II/III}$ couple. The CV data for the Ni(II) intermediate suggests that Ag^I salts can facilitate the single-electron oxidation of this Ni^{II} complex. Indeed, treating this species with 1

equivalent of AgOTf or AgOTFA resulted in the formation of the Ni^{III} triflate (OTf) and trifluoroacetate (OTFA) complexes **Scheme 1.34**. Curiously, however, these Ni^{III} complexes did not exhibit any reactivity with iodine. This possibly implies that the iodination is initiated by a divalent precursor.

Scheme 1. 34. Oxidation of Ni^{II} species to Ni^{III} complex
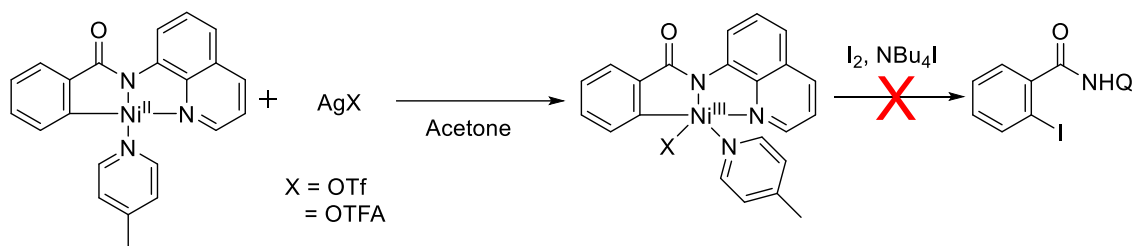
Love and co-workers demonstrated a model nickelacyclic intermediate that shows interesting reactivities with other substrates giving valuable functionalized product (**Scheme 1.35**).[40] For instance, introducing an α-bromoketone resulted in the generation of a new C−C bond, yielding alkylated products in good yields. Similarly, they successfully formed new C−C bonds through the addition of an aryl iodonium salt or PhI, generating arylated products. Productive insertion reactions of CO led to the creation of new C−C and C−N bonds within the cyclized urea.

Scheme 1. 35. Reaction of nickelacycilc intermediate with different coupling partners
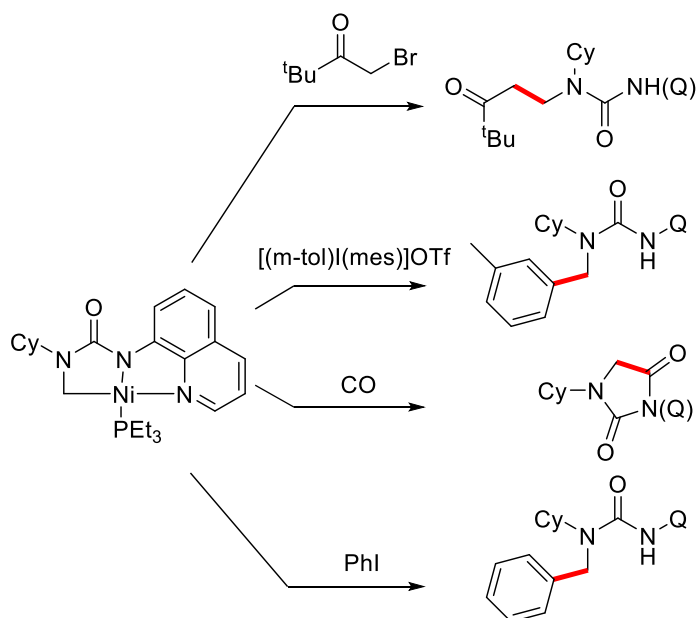
The above precedents present some of the stoicheometric studies carried out on Ni- and Pd-based model systems probing the mechanistic aspects of C–H functionalization reactions. These studies are analogous to our group's investigations on the reactivities of nickellacyclic complexes with various substrates. An overview of these studies is provided in the following section to provide context for the projects that constitute the central theme of the present thesis.

1.3.9 Early results from our group

Over the last decade, a growing number of studies on nickel-catalyzed C−H functionalization reactions have highlighted the potential of Ni precursors as effective substitutes for the more commonly used Pd counterparts. These advancements, coupled with our group's enduring interest and focus on organonickel chemistry, in general, and pincer-type nickel complexes in particular, motivated our team to synthesize nickelacyclic complexes and investigate their structures, stabilities, and potential for functionalization.

Building upon the group's expertise in synthesizing POCOP-type (POCOP= *mer-κP, κC, κP*-(1,3-PR$_2$-C$_6$H$_3$) pincer complexes of nickel through C−H nickelation, a new project was initiated in 2013 with the objective of developing synthetic routes to cyclonickellated complexes derived from aryl phosphinites and investigating their structures, thermal stabilities, and reactivities under conditions pertinent to C−H functionalization chemistry. Mr. Boris Vabre, the first group member who took on this new project, reported in 2014 that phosphinite ligands derived from phenol and its substituted derivatives can undergo relatively facile C-H nickelation to give nickealcyclic dimers and their phosphinite adducts, as shown in **Scheme 1.36**.

Scheme 1. 36. Synthesis of cyclometalated complexes of Ni
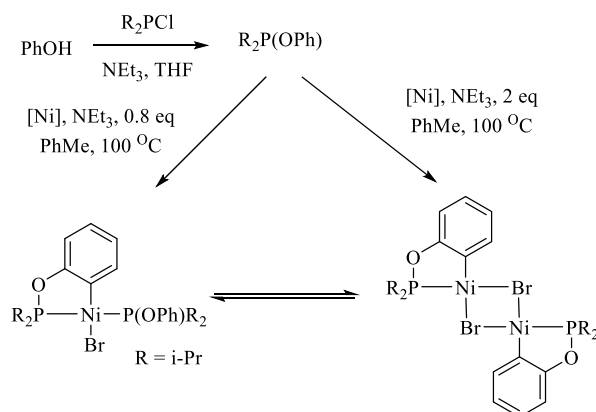
It was shown that the observed C−H nickelation step is influenced by electron-donating groups (OMe > Me > COOMe).[41] These studies indicated an electrophilic C−H nickelation mechanism occurring with a mono(phosphinite) intermediate generated in situ through ligand dissociation (**Scheme 1.37**).

Scheme 1. 37. Proposed mechanism for C-H nickellation
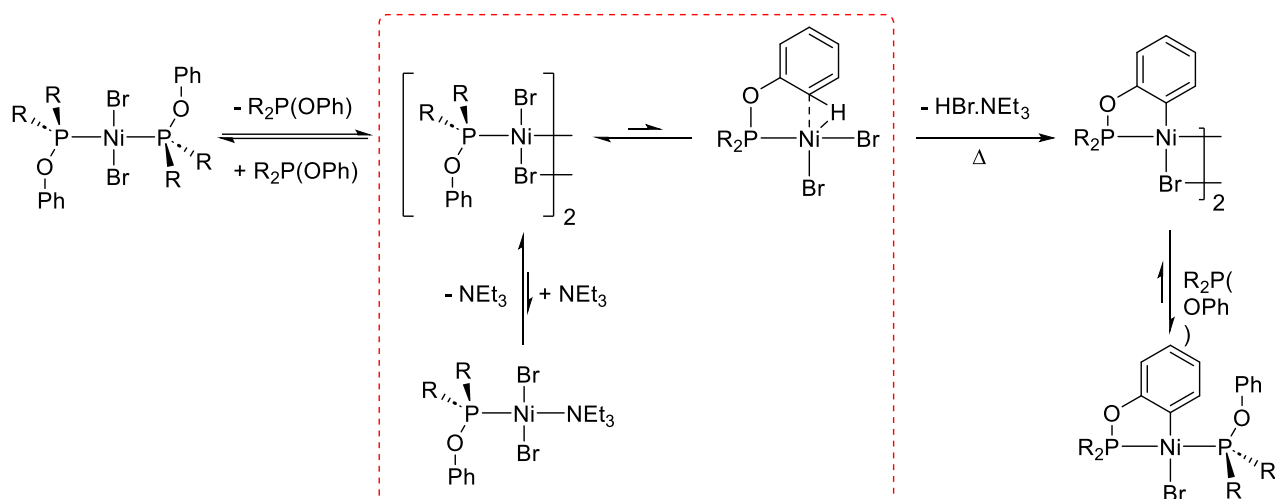
Boris Vabre has also examined the regioselectivity of the C-H nickelation step, showing for instance that cyclonickelation of 3-F-C6H4OP(i-Pr)2 proceeds with a preference for nickelation at the C−H bond para to the fluoro substituent. (**Scheme 1.38**).

Scheme 1. 38. Cyclonickelation of substituted ligand showing site selectivity

5.6 : 1
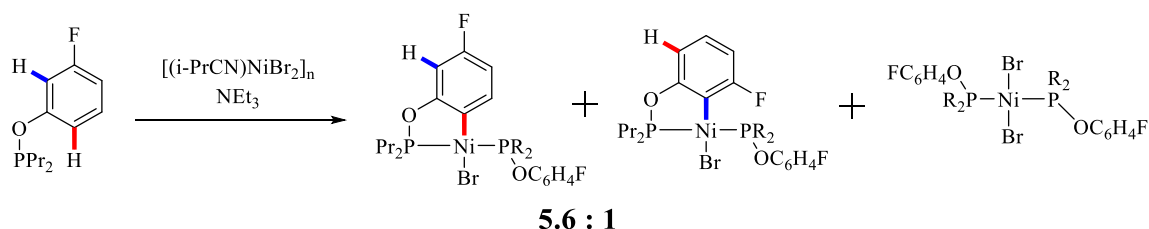
The reactivities of the nickellacyclic complexes prepared by Vabre were also explored briefly to show that reaction with benzyl bromide can result in benzylated products, as shown in **Scheme 1.39**. The confirmation of product identity was achieved through NMR and GC/MS analyses. The benzylation of the ipso-C atom of the nickelacyclic dimer was considered important as it provided evidence supporting the feasibility of the proposed strategy for arenol functionalization. Indeed, several literature reports have shown that Ni-Ar complexes can undergo insertion of SO2, CO, and

alkynes. In addition, there are literature precedents that nickellacyclic intermediates can react with alkyl halides producing alkylated products.[41]

Scheme 1. 39. Benzylation of nickelacyclic dimer
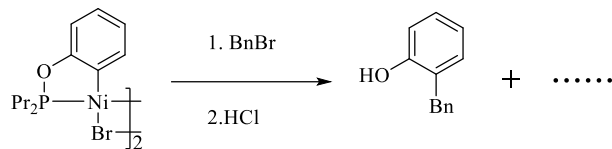
Mr. Vabre's pioneering studies were subsequently pursued by another group member, Mr. Loic Mangin, who conducted further studies on C−H nickelation and functionalization steps. For instance, Mr. Mangin devised a more efficient strategy of C−H activation using acetonitrile as solvent.[42] Thus, he showed that employing acetonitrile as the solvent facilitated orthonickellation at reduced temperatures and within a shorter timeframe for the reaction. This method also required only a slight excess of the Ni(II) precursor to efficiently produce the monomeric MeCN adduct as a stable form of the cyclonickellated species. The acetonitrile reaction mixtures remained homogeneous throughout the entire reaction period, ensuring a higher effective concentration of Ni while preserving a Ni : phosphinite ratio of approximately 1 : 1. Additionally, the undesired formation of the analogous $P(OPh)(i\text{-}Pr)_2$ adduct was avoided by the easy formation of the acetonitrile adduct, whereas the latter could be worked-up to give the target Br-bridged dimer, as shown in **Scheme 1.40**.

Scheme 1. 40. Alternative protocols for preparation of orthonickellated complexes
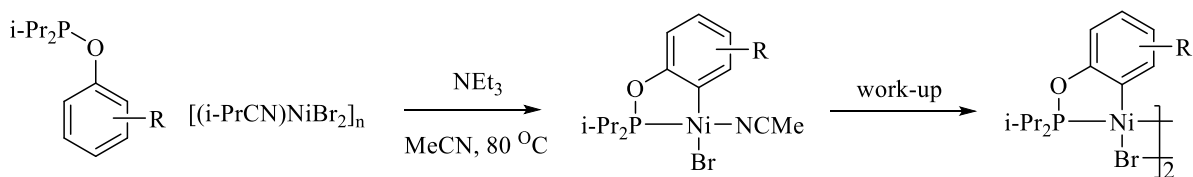
Regioselectivity studies of the new C−H nickellation reaction showed that cyclonickellation of aryl phosphinites derived from 3-Me-, 3-MeO-, and $3\text{-}Cl\text{-}C_6H_4OH$ occurs exclusively at the ortho position farthest from the substituent (**Scheme 1.41**). In light of the observation that the C−H nickellation reactions in question are regioselective regardless of the electron-donating or electron-withdrawing nature of the substituents, it was concluded that the determinant factor determining regioselectivity is sterics, not electronics.

Scheme 1. 41. Cyclonickellation of various mono- or di-orthosubstituted aryl phosphinites

	R	R'	time (h)	%yield
c:	Me	H	16	67
d:	OMe	H	16	60
e:	Cl	H	40	71
f:	F	F	60	62
g:	Me	Me	60	nr
h:	Cl	Cl	60	nr
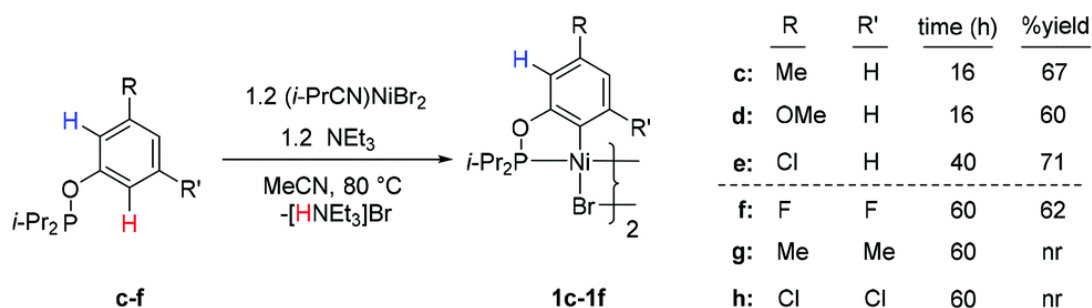
Mr. Mangin also noted that the nickelation of $3,5\text{-}(OMe)_2\text{-}C_6H_3OP(i\text{-}Pr)_2$ followed by the usual workup did not yield the expected μ-Br dimeric species (**Scheme 1.42**). Instead, it produced the monomeric MeCN adduct. This observation suggests that the presence of two MeO substituents in the substrate $3,5\text{-}(OMe)_2\text{-}C_6H_3OP(i\text{-}Pr)_2$ creates significant steric hindrance, discouraging the dimerization of its cyclonickellated derivative and favoring the formation of the acetonitrile adduct.

Scheme 1. 42. Formation of Ni-NCMe from cyclonickellation of $3,5\text{-}(OME)_2\text{-}C_6H_3OP(i\text{-}Pr)_2$
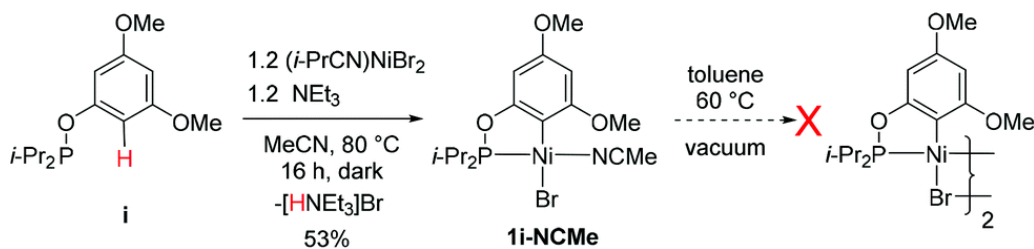
Another important observation was the size variation of the resulting nickellacycles: a pronounced preference for a 5-membered nickellacycle, which hindered nickelation at the phenol substituent C−H sites in 2-substituted and 2,6-disubstituted substrates. This phenomenon is attributed to the more favorable energetics of the 5-membered nickellacycle that are formed at the transition state compared to the alternative 6- or 7-membered nickellacycles (**Scheme 1.43**).

Scheme 1. 43. Formation of 6-memebered nickellacycle is not energetically favored
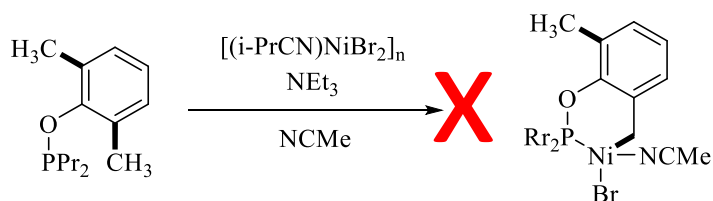
Mr. Mangin has made other mechanistic studies to gain deeper insight to C−H nickelation step in MeCN. And it is seen that when deuterated and nondeuterated cyclonickelated dimer is dissolved in MeCN, H/D scrambling occurs at the ortho position, indicating that the cyclonickelated complex is thermodynamically unstable toward reprotonation by HBr (**Scheme 1.44**).[43]

Scheme 1. 44. Observed Ortho H/D Scrambling between Complexes deuterated and nondeuterated dimer in MeCN
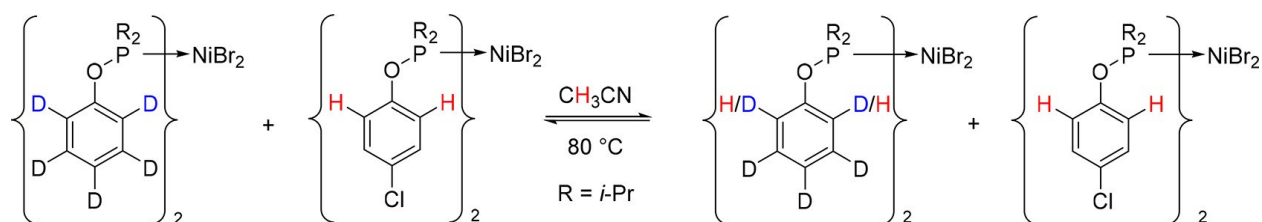
To examine the process of H/D scrambling, a deuterated complex was subjected to reflux in CH₃CN for 24 hours. Analysis of the resulting product revealed that the ligand had assimilated 17% H specifically at the ortho positions (**Scheme 1.45**). This outcome can be explained by considering the exchange of H/D between the DBr formed in situ and the reaction solvent, leading to the generation of HBr. Subsequently, the HBr likely protonates the newly formed Ni−C bond, explaining the incorporation of H into deuterated nickelacycle (**Scheme 1.45**).

Scheme 1. 45. Mechanism of H incorporation into deuterio ligand
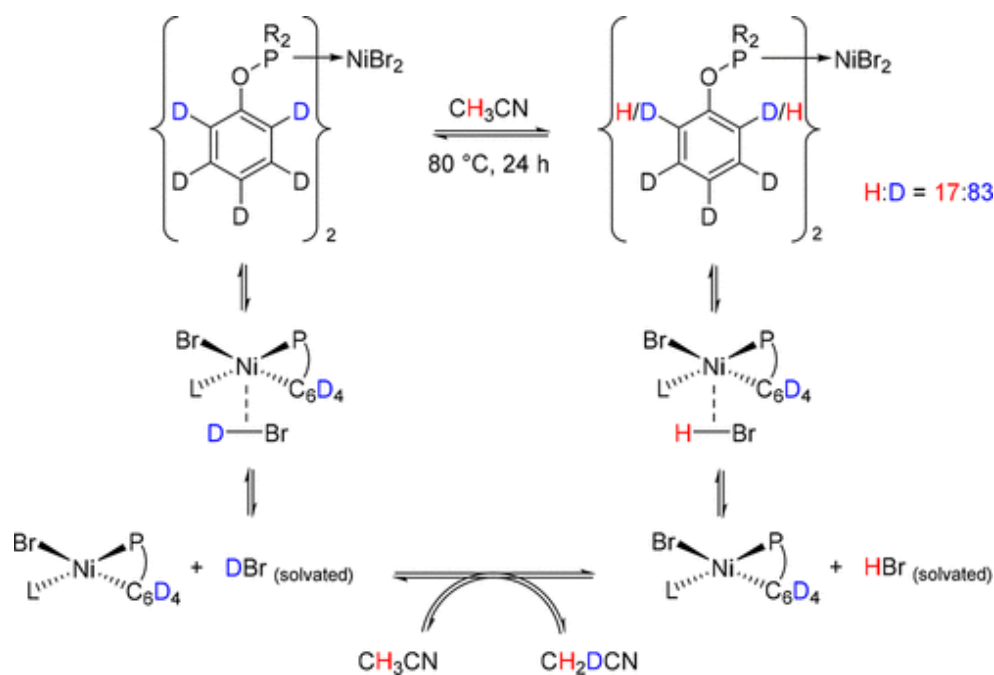
In 2019, Mangin expanded the range of cyclonickelated complexes accessible via C-H nickellation to include phosphinites derived from 1- and 2-naphthol. When these naphthol phosphinites are treated with a Ni^{II} precursor, $\{(i\text{-PrCN})NiBr_2\}_n$ in the presence of Et$_3$N, the resulting cyclonickelated products can be isolated.[44] These products exist either as bromo-bridged dimers or as adducts, which can be either acetonitrile or the phosphinite ligand itself (**Schem 1.46**).

Scheme 1. 46. Nickelation of 4-X-1-naphthyl phosphinites
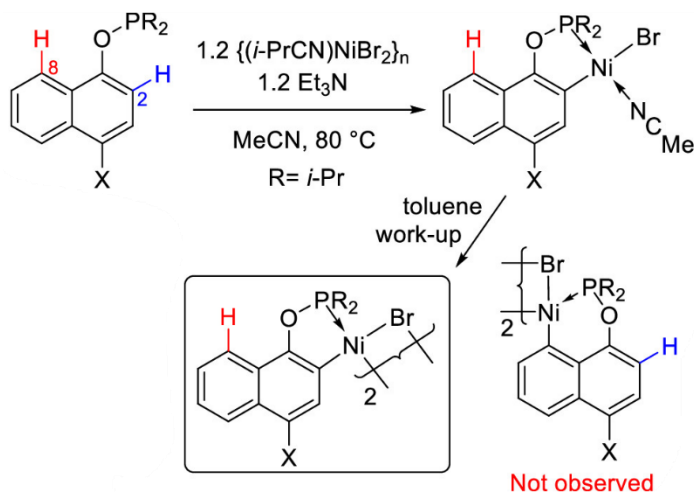
Another approach demonstrated that when 2-allyl-1-naphthyl phosphinite is exposed to a nickel precursor in the presence of a base at room temperature, it triggers the nickelation of the allylic moiety as shown in **scheme 1.47**.

Scheme 1. 47. C−H nickelation of 2-allyl-1-naphthyl

66
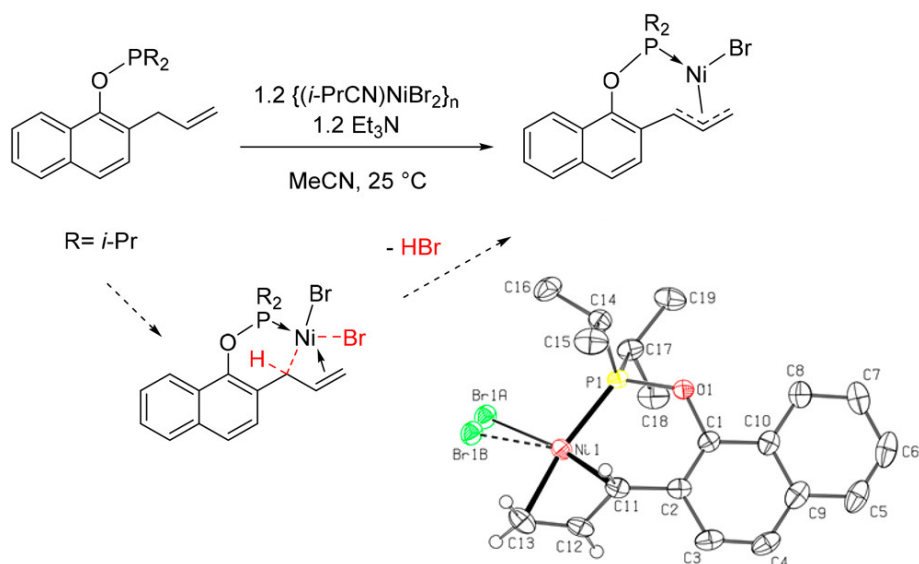
Significantly, Mangin et al. observed an unexpected insertion-type C−P functionalization while investigating the nickelation of the phosphinite derived from 2-Et-1-naphthol at high temperature (**Scheme 1.48**).[44] It was observed that heating an acetonitrile solution of 1-naphthylphosphinite and {(i-PrCN)NiBr$_2$}$_n$ at 160 °C for 4 hours without Et$_3$N resulted in a crude mixture. The isolation process via crystallization and subsequent XRD analysis revealed a C-P functionalized product and some unknown species, as depicted in **Scheme 1.48**.

Scheme 1. 48. C−P Functionalization of phosphinite
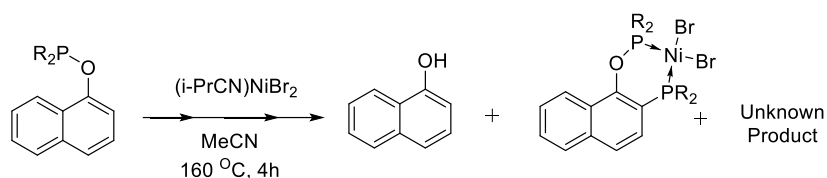
Later, the authors uncovered several aspects concerning this C-P bond formation reaction. For instance, the reaction is expedited by a high concentration of the phosphinite substrate and elevated temperatures. Moreover, alongside the functionalized product, naphthol is also generated. Additionally, heating the product crystal in MeCN at 160−200 °C does not prompt decomposition, suggesting that the unidentified species arises from a distinct side reaction rather than thermal degradation of the insertion product. These observations led to the following proposed mechanism.

Scheme 1. 49. Postulated mechanism for formation of C-P functionalized product
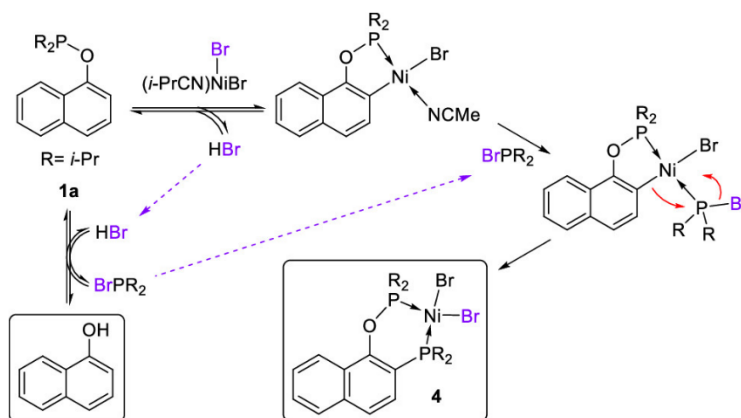
In the aforementioned C−P functionalization reaction, a side product characterized by a ^{31}P singlet at 121 ppm was observed. In an effort to identify this side product, Mr. Mangin explored an alternative route to obtain the C-P functionalized product. Treating 2-Et-8-(i-Pr$_2$P(O))-1-naphthol

with a nickel precursor at 160°C without a base gave phosphorus-containing species shown in **Scheme 1.50**. The proposed mechanism closely resembles the one presented in **Scheme 1.49**.

Scheme 1. 50. Formation of another C−P functionalized product
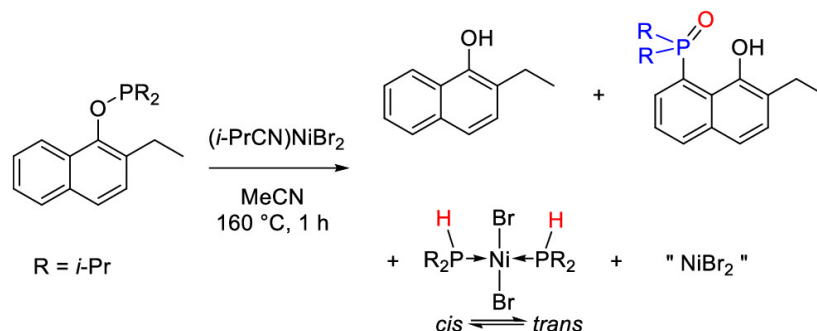
To summarize this subsection, my former colleagues have successfully developed an effective method for activating aromatic C−H bonds, followed by an in-depth exploration of the factors influencing the C−H metalation step. It has been established, for instance, that the C−H nickelation step is reversible in the absence of a base, and electron-donating groups have been observed to accelerate this step. In addition, their work provides a comprehensive approach to isolating and characterizing nickellacyclic intermediates, granting valuable insights into their reactivity. These findings served as the guiding principles for the design of my own project, which will build upon and continue the investigation of the reactivities of the nickellacyclic intermediates previously developed by our group.

1.4   Objectives and contents of the thesis

The selection of cyclonickelated aryl phosphinites as a model system for our project is grounded in recent investigations conducted within our research group as presented in the previous section. Thus, our group has established that aryl phosphinites derived from substituted phenols and naphthols readily undergo C−H nickelation, resulting in the formation of stable and isolable cyclometalated complexes. The choice of this phosphinite substrate is motivated by its simplicity, accessibility, and its close resemblance to real-world examples. Furthermore, the incorporation of phosphorus nuclei renders this model system amenable to facile monitoring through ^{31}P NMR spectroscopy. Additionally, the rarity and chemical stability of the isolated nickelacyclic species make these ideal candidates or model systems for probing its reactivity with a secondary coupling partner.

A limited number of results from our previous studies also established that functionalization of the aryl moiety in the above-mentioned model systems is also feasible based on C–C and C–P coupling reactions. However, these reactions have not been optimized or expanded. Therefore, expanding the range of C–X coupling reactions is the main objective of my Ph. D. project. The main strategy adopted in my studies rests on an analogy with the type of C–X bond coupling that was achieved in our group, namely: C–Br bond activation of benzyl bromide[41] and P–Cl/Br bond activation in halophosphines[44] as shown below:

Scheme 1. 51. Formation of C-P bond
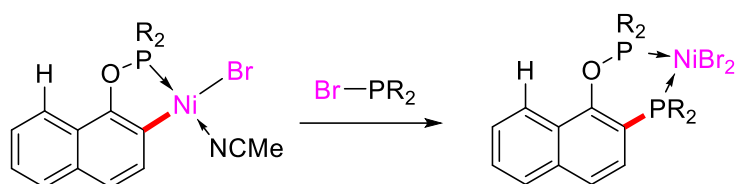
Scheme 1. 52. Proposed scheme to form C-N bond

NR$_2$OH is similarly polar to PR$_2$Br
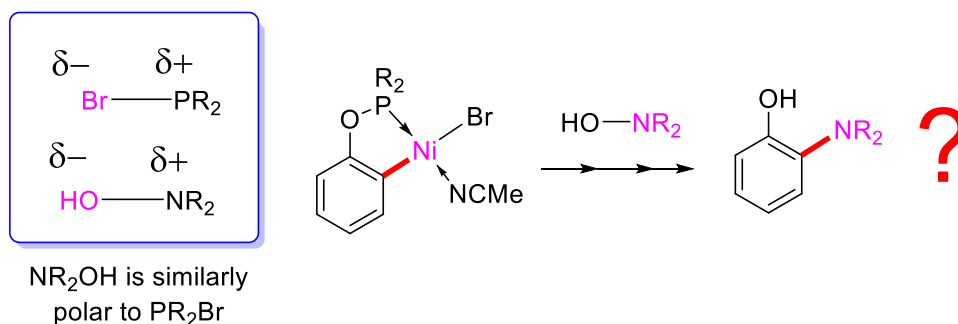
Therefore, we set out with the goal of testing the feasibility of activating some other labile bonds e.g., C−X, N−X or X–X bonds as shown in the scheme below (**Scheme 1. 53**).

Scheme 1. 53. Proposed reactivity study of nickelacyclic intermediate
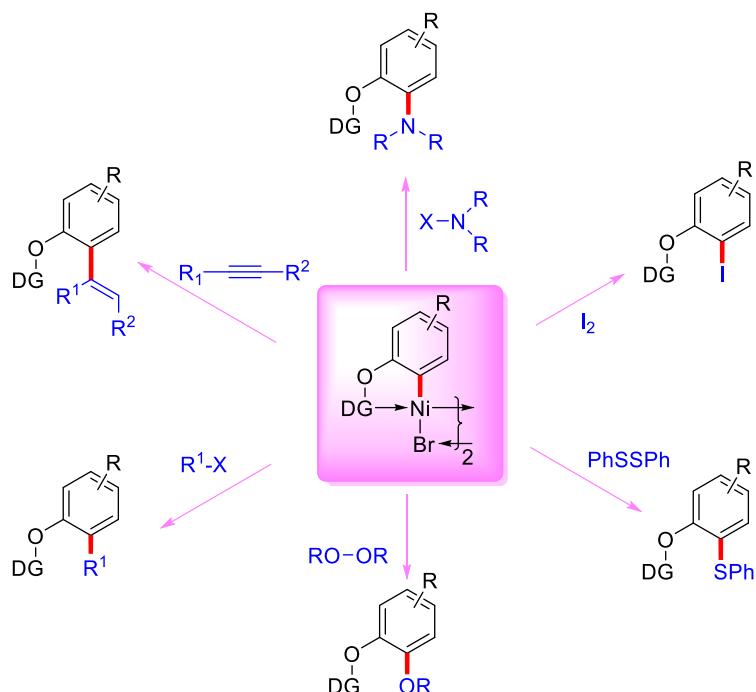
We selected hydroxylamines, R_2NOH, and the 1,2,4-traizile shown above as substrates possessing potentially labile N–O and N–N bonds, respectively. The results of these investigations are described in **Chapters 2** to **4** which are separate articles, each exploring different parts of the topic as detailed below. **Chapter 5** wraps up everything with some conclusions and a few suggestions for future work.

Chapter -2 delves into the interactions between hydroxylamines and four ortho-nickelated compounds derived from aryl phosphinites $3-R'-C_6H_4OPR_2$ (R = i-Pr; R' = H, Cl, OMe, NMe$_2$). The main objective of this study was to ascertain whether nickellacyclic complexes derived from phosphinites could react with hydroxylamines to enable C–N functionalization of the aryl group through the rupture of their labile O–N bonds followed by reductive elimination. This process draws parallels to the C–P coupling observed with chlorophosphines. While the anticipated C–N coupling outcome did not come to fruition, our investigations have yielded intriguing insights into the interactions of Ni complexes with hydroxylamines. Notably, we have uncovered a straightforward pathway for the dehydration of these substrates to imines.

Scheme 1. 54. Reactivity of nickelacyclic complex with hydroxyl amine

Chapter 3, on the other hand, explored the potential for C–N coupling using reagents that contain N–N single bonds. This report outlines the outcomes of our investigations into the reactions between our ortho-nickelated complexes and 4-amino-4H-1,2,4-triazole. While this approach similarly did not yield the intended C–N coupling, we have successfully isolated novel mononuclear and dinuclear adducts. Notably, these adducts exhibit intriguing solution exchange dynamics, a subject elaborated upon in this report.

Scheme 1. 55. Reactivity of nickelacyclic complex with and 4-amino-4H-1,2,4-triazole
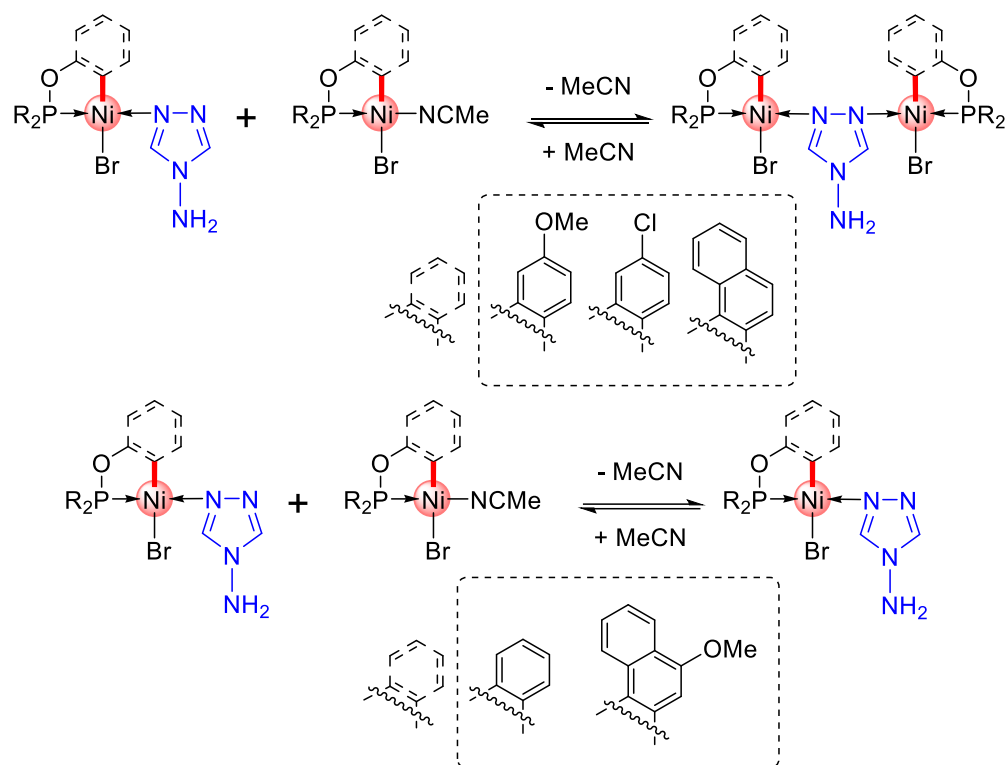
In both **Chapter 2** and **Chapter 3**, we explored the viability of achieving C–O/C–N functionalization within these complexes by subjecting them to reagents characterized by weak element-element bonds, specifically hydroxylamines and 4-amino-4H-1,2,4-triazole. Building upon the investigations mentioned earlier, **Chapter - 4** turns our attention to the reactivity of hydroxylamines in the presence of oxidants like TEMPO. These studies have yielded the creation of unusual Ni-TEMPOH complexes. These newly discovered compounds have allowed us to investigate the coordination chemistry displayed by them when they interact with different nucleophiles. The details of these investigations are elaborated upon in this report.

Scheme 1. 56. Formation of Ni(II)-TEMPOH complexes
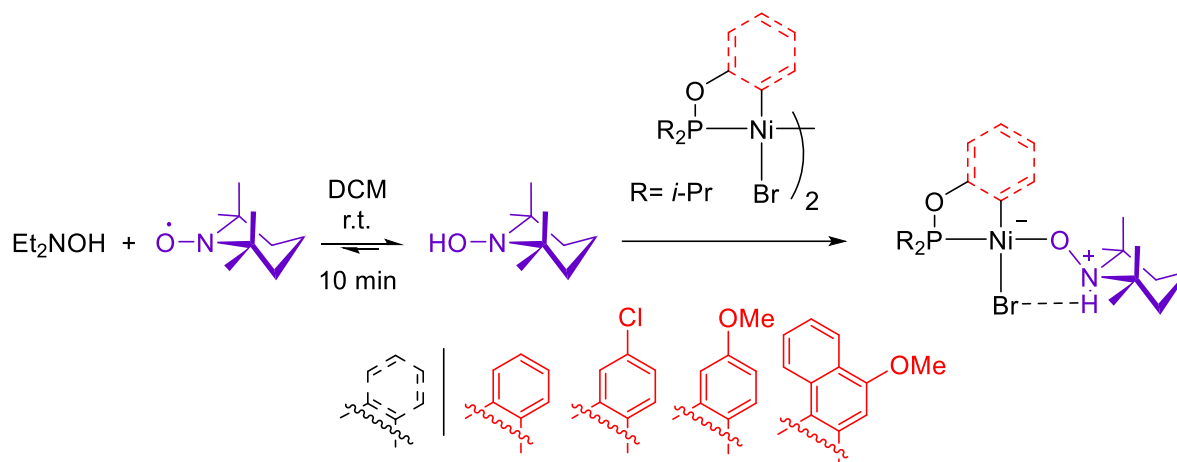
Scheme 1. 57. Reactivities of Ni(II)-TEMPOH complexes with nucleophiles
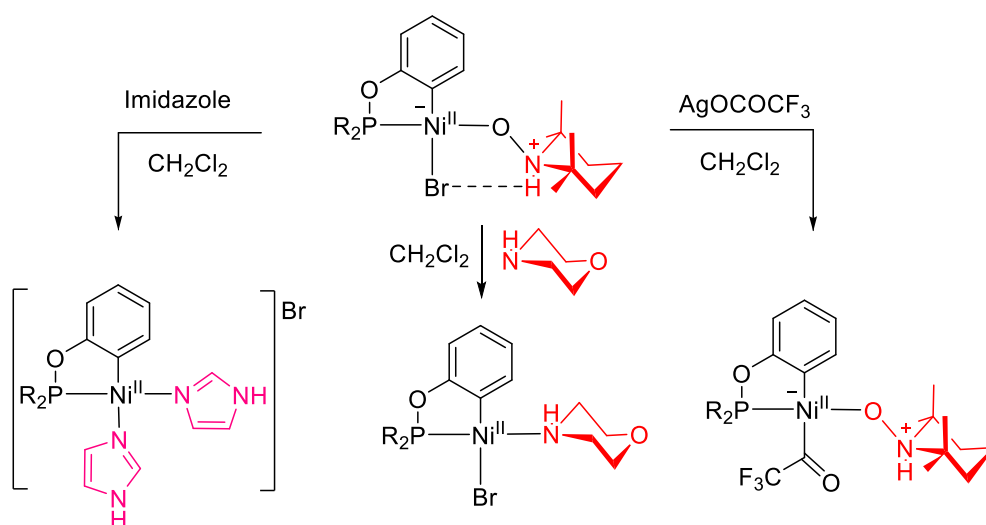
1.5   References

(1)   Ujwaldev, S. M.; Harry, N. A.; Divakar, M. A.; Anilkumar, G. Cobalt-Catalyzed C-H Activation: Recent Progress in Heterocyclic Chemistry. *Catalysis Science and Technology*. Royal Society of Chemistry 2018, pp 5983–6018. https://doi.org/10.1039/c8cy01418c.

(2)   Chen, X.; Engle, K. M.; Wang, D. H.; Jin-Quan, Y. Palladium(II)-CataIyzed C-H Activation/C-C Cross-Coupling Reactions: Versatility and Practicality. *Angewandte Chemie - International Edition* **2009**, *48* (28), 5094–5115. https://doi.org/10.1002/anie.200806273.

(3)   Bryan, M. C.; Dillon, B.; Hamann, L. G.; Hughes, G. J.; Kopach, M. E.; Peterson, E. A.; Pourashraf, M.; Raheem, I.; Richardson, P.; Richter, D.; Sneddon, H. F. Sustainable Practices in Medicinal Chemistry: Current State and Future Directions. *Journal of Medicinal Chemistry*. August 8, 2013, pp 6007–6021. https://doi.org/10.1021/jm400250p.

(4)   Gandeepan, P.; Ackermann, L. Transient Directing Groups for Transformative C–H Activation by Synergistic Metal Catalysis. *Chem*. Elsevier Inc February 8, 2018, pp 199–222. https://doi.org/10.1016/j.chempr.2017.11.002.

(5)   Ackermann, L. Robust Ruthenium(II)-Catalyzed C-H Arylations: Carboxylate Assistance for the Efficient Synthesis of Angiotensin-II-Receptor Blockers. *Organic Process Research and Development*. American Chemical Society January 16, 2015, pp 260–269. https://doi.org/10.1021/op500330g.

(6)   Seki, M. A New Catalytic System for Ru-Catalyzed C-H Arylation Reactions and Its Application in the Practical Syntheses of Pharmaceutical Agents. *Organic Process Research and Development*. American Chemical Society May 20, 2016, pp 867–877. https://doi.org/10.1021/acs.oprd.6b00116.

(7)   Zhang, J.; Kang, L. J.; Parker, T. C.; Blakey, S. B.; Luscombe, C. K.; Marder, S. R. Recent Developments in C–H Activation for Materials Science in the Center for Selective C–H Activation. *Molecules* **2018**, *23* (4), 1–13. https://doi.org/10.3390/molecules23040922.

(8)   Wax, M. J.; Stryker, J. M.; Buchanan, J. M.; Kovac, C. A.; Bergman, R. G. Reversible C-H Insertion/Reductive Elimination in (H5-Pentamethylcyclopentadienyl)(Trimethylphosphine)-Iridium Complexes. Use in Determining Relative Metal-Carbon Bond Energies and Thermally

Activating Methane. *J Am Chem Soc* **1984**, *106* (4), 1121–1122. https://doi.org/10.1021/ja00316a054.

(9)   Lu, Q.; Glorius, F. Radical Enantioselective C(sp3)−H Functionalization. *Angewandte Chemie - International Edition* **2017**, *56* (1), 49–51. https://doi.org/10.1002/anie.201609105.

(10)   Waterman, R. σ-Bond Metathesis: A 30-Year Retrospective. *Organometallics* **2013**, *32* (24), 7249–7263. https://doi.org/10.1021/om400760k.

(11)   Boutadla, Y.; Davies, D. L.; Macgregor, S. A.; Poblador-Bahamonde, A. I. Mechanisms of C–H Bond Activation: Rich Synergy between Computation and Experiment. *Journal of the Chemical Society. Dalton Transactions*. July 21, 2009, pp 5820–5831. https://doi.org/10.1039/b904967c.

(12)   Desai, L. V.; Stowers, K. J.; Sanford, M. S. Insights into Directing Group Ability in Palladium-Catalyzed C-H Bond Functionalization. *J Am Chem Soc* **2008**, *130* (40), 13285–13293. https://doi.org/10.1021/ja8045519.

(13)   Guihaumé, J.; Halbert, S.; Eisenstein, O.; Perutz, R. N. Hydrofluoroarylation of Alkynes with Ni Catalysts. C-H Activation via Ligand-to-Ligand Hydrogen Transfer, an Alternative to Oxidative Addition. *Organometallics* **2012**, *31* (4), 1300–1314. https://doi.org/10.1021/om2005673.

(14)   Kleiman, J. P.; Dubeck, M. The Preparation of Cyclopentadienyl [o-(Phenylazo)Phenyl] Nickel. *Journal of the American Chemical Society*. May 1, 1963, pp 1544–1545. https://doi.org/10.1021/ja00893a040.

(15)   Aihara, Y.; Chatani, N. Nickel-Catalyzed Direct Alkylation of C-H Bonds in Benzamides and Acrylamides with Functionalized Alkyl Halides via Bidentate-Chelation Assistance. *J Am Chem Soc* **2013**, *135* (14), 5308–5311. https://doi.org/10.1021/ja401344e.

(16)   Soni, V.; Jagtap, R. A.; Gonnade, R. G.; Punji, B. Unified Strategy for Nickel-Catalyzed C-2 Alkylation of Indoles through Chelation Assistance. *ACS Catal* **2016**, *6* (9), 5666–5672. https://doi.org/10.1021/acscatal.6b02003.

(17)   Di, N. S. C. H. B.; Chen, H.; Li, P.; Wang, M.; Wang, L. Nickel-Catalyzed Site-Selective C − H Bond Di Fl Uoroalkylation of 8 - Aminoquinolines on the C5-Position. **2016**, 8–11. https://doi.org/10.1021/acs.orglett.6b02166.

(18)   Wu, X.; Zhao, Y.; Ge, H. Nickel-Catalyzed Site-Selective Alkylation of Unactivated C(sp3)-H Bonds. *J Am Chem Soc* **2014**, *136* (5), 1789–1792. https://doi.org/10.1021/ja413131m.

(19)   Honeycutt, A. P.; Hoover, J. M. Nickel-Catalyzed Oxidative Decarboxylative (Hetero)Arylation of Unactivated C-H Bonds: Ni and Ag Synergy. *ACS Catal* **2017**, *7* (7), 4597–4601. https://doi.org/10.1021/acscatal.7b01683.

(20)   Gooßen, L. J.; Linder, C.; Rodríguez, N.; Lange, P. P.; Fromm, A. Silver-Catalysed Protodecarboxylation of Carboxylic Acids. *Chemical Communications* **2009**, No. 46, 7173–7175. https://doi.org/10.1039/b912509d.

(21)   Xue, L.; Su, W.; Lin, Z. Mechanism of Silver- and Copper-Catalyzed Decarboxylation Reactions of Aryl Carboxylic Acids. *Dalton Transactions* **2011**, *40* (44), 11926–11936. https://doi.org/10.1039/c1dt10771b.

(22)   Shih, W. C.; Chen, W. C.; Lai, Y. C.; Yu, M. S.; Ho, J. J.; Yap, G. P. A.; Ong, T. G. The Regioselective Switch for Amino-NHC Mediated C-H Activation of Benzimidazole via Ni-Al Synergistic Catalysis. *Org Lett* **2012**, *14* (8), 2046–2049. https://doi.org/10.1021/ol300570f.

(23)   Wang, X.; Xie, P.; Qiu, R.; Zhu, L.; Liu, T.; Li, Y.; Iwasaki, T.; Au, C. T.; Xu, X.; Xia, Y.; Yin, S. F.; Kambe, N. Nickel-Catalyzed Direct Alkylation of Thiophenes via Double C(sp3)-H/C(sp2)-H Bond Cleavage: The Importance of KH_2PO_4. *Chemical Communications* **2017**, *53* (59), 8316–8319. https://doi.org/10.1039/c7cc04252c.

(24)   Luo, F. X.; Cao, Z. C.; Zhao, H. W.; Wang, D.; Zhang, Y. F.; Xu, X.; Shi, Z. J. Nickel-Catalyzed Oxidative Coupling of Unactivated C(sp3)-H Bonds in Aliphatic Amides with Terminal Alkynes. *Organometallics* **2017**, *36* (1), 18–21. https://doi.org/10.1021/acs.organomet.6b00529.

(25)   Liu, Y. J.; Liu, Y. H.; Yan, S. Y.; Shi, B. F. A Sustainable and Simple Catalytic System for Direct Alkynylation of C(sp2)-H Bonds with Low Nickel Loadings. *Chemical Communications* **2015**, *51* (29), 6388–6391. https://doi.org/10.1039/c5cc01163a.

(26)   Khake, S. M.; Soni, V.; Gonnade, R. G.; Punji, B. A General Nickel-Catalyzed Method for C−H Bond Alkynylation of Heteroarenes Through Chelation Assistance. *Chemistry - A European Journal* **2017**, *23* (12), 2907–2914. https://doi.org/10.1002/chem.201605306.

(27) Lin, C.; Chen, Z.; Liu, Z.; Zhang, Y. Nickel-Catalyzed Stereoselective Alkenylation of C(Sp3)-H Bonds with Terminal Alkynes. *Org Lett* **2017**, *19* (4), 850–853. https://doi.org/10.1021/acs.orglett.6b03856.

(28) Mukai, T.; Hirano, K.; Satoh, T.; Miura, M. Nickel-Catalyzed C-H Alkenylation and Alkylation of 1,3,4-Oxadiazoles with Alkynes and Styrenes. *Journal of Organic Chemistry* **2009**, *74* (16), 6410–6413. https://doi.org/10.1021/jo901350j.

(29) Liu, Y. J.; Zhang, Z. Z.; Yan, S. Y.; Liu, Y. H.; Shi, B. F. Ni(II)/BINOL-Catalyzed Alkenylation of Unactivated C(sp3)-H Bonds. *Chemical Communications* **2015**, *51* (37), 7899–7902. https://doi.org/10.1039/c5cc02254a.

(30) Aihara, Y.; Chatani, N. Nickel-Catalyzed Reaction of C-H Bonds in Amides with I_2: Ortho-Iodination via the Cleavage of C(sp2)-H Bonds and Oxidative Cyclization to β-Lactams via the Cleavage of C(sp3)-H Bonds. *ACS Catal* **2016**, *6* (7), 4323–4329. https://doi.org/10.1021/acscatal.6b00964.

(31) Müller, T.; Ackermann, L. Nickel-Catalyzed C−H Chalcogenation of Anilines. *Chemistry - A European Journal* **2016**, *22* (40), 14151–14154. https://doi.org/10.1002/chem.201603092.

(32) Reddy, V. P.; Qiu, R.; Iwasaki, T.; Kambe, N. Nickel-Catalyzed Synthesis of Diarylsulfides and Sulfones via C-H Bond Functionalization of Arylamides. *Org Biomol Chem* **2015**, *13* (24), 6803–6813. https://doi.org/10.1039/c5ob00149h.

(33) Yan, Q.; Chen, Z.; Yu, W.; Yin, H.; Liu, Z.; Zhang, Y. Nickel-Catalyzed Direct Amination of Arenes with Alkylamines. *Org Lett* **2015**, *17* (10), 2482–2485. https://doi.org/10.1021/acs.orglett.5b00990.

(34) Deb, A.; Bag, S.; Kancherla, R.; Maiti, D. Palladium-Catalyzed Aryl C-H Olefination with Unactivated, Aliphatic Alkenes. *J Am Chem Soc* **2014**, *136* (39), 13602–13605. https://doi.org/10.1021/ja5082734.

(35) Deb, A.; Hazra, A.; Peng, Q.; Paton, R. S.; Maiti, D. Detailed Mechanistic Studies on Palladium-Catalyzed Selective C–H Olefination with Aliphatic Alkenes: A Significant Influence of Proton Shuttling. *J Am Chem Soc* **2017**, *139* (2), 763–775. https://doi.org/10.1021/jacs.6b10309.

(36) Park, H.; Verma, P.; Hong, K.; Yu, J. Q. Controlling Pd(IV) Reductive Elimination Pathways Enables Pd(II)-Catalysed Enantioselective C(sp3)-H Fluorination. *Nat Chem* **2018**, *10* (7), 755–762. https://doi.org/10.1038/s41557-018-0048-1.

(37) Antermite, D.; Affron, D. P.; Bull, J. A. Regio- and Stereoselective Palladium-Catalyzed C(sp3)-H Arylation of Pyrrolidines and Piperidines with C(3) Directing Groups. *Org Lett* **2018**, *20* (13), 3948–3952. https://doi.org/10.1021/acs.orglett.8b01521.

(38) Antermite, D.; White, A. J. P.; Casarrubios, L.; Bull, J. A. On the Mechanism and Selectivity of Palladium-Catalyzed C(sp3)-H Arylation of Pyrrolidines and Piperidines at Unactivated C4 Positions: Discovery of an Improved Dimethylaminoquinoline Amide Directing Group. *ACS Catal* **2023**, *13* (14), 9597–9615. https://doi.org/10.1021/acscatal.3c01980.

(39) Roy, P.; Bour, J. R.; Kampf, J. W.; Sanford, M. S. Catalytically Relevant Intermediates in the Ni-Catalyzed C(sp2)-H and C(sp3)-H Functionalization of Aminoquinoline Substrates. *J Am Chem Soc* **2019**, *141* (43), 17382–17387. https://doi.org/10.1021/jacs.9b09109.

(40) Beattie, D. D.; Grunwald, A. C.; Perse, T.; Schafer, L. L.; Love, J. A. Understanding Ni(II)-Mediated C(sp3)-H Activation: Tertiary Ureas as Model Substrates. *J Am Chem Soc* **2018**, *140* (39), 12602–12610. https://doi.org/10.1021/jacs.8b07708.

(41) Vabre, B.; Deschamps, F.; Zargarian, D. Ortho Derivatization of Phenols through C-H Nickelation: Synthesis, Characterization, and Reactivities of Ortho-Nickelated Phosphinite Complexes. *Organometallics* **2014**, *33* (22), 6623–6632. https://doi.org/10.1021/om500938u.

(42) Mangin, L. P.; Zargarian, D. C-H Nickellation of Phenol-Derived Phosphinites: Regioselectivity and Structures of Cyclonickellated Complexes. *Dalton Transactions* **2017**, *46* (46), 16159–16170. https://doi.org/10.1039/c7dt03403b.

(43) Mangin, L. P.; Zargarian, D. C-H Nickelation of Aryl Phosphinites: Mechanistic Aspects. *Organometallics* **2019**, *38* (7), 1479–1492. https://doi.org/10.1021/acs.organomet.8b00899.

(44) Mangin, L. P.; Zargarian, D. C-H Nickelation of Naphthyl Phosphinites: Electronic and Steric Limitations, Regioselectivity, and Tandem C-P Functionalization. *Organometallics* **2019**, *38* (24), 4687–4700. https://doi.org/10.1021/acs.organomet.9b00660.

2.1 Chapter −2− Reactivities of Cyclonickellated Complexes with Hydroxylamines: Formation of κ^O-Hydroxylamine and κ^N-Imine Adducts and a κ^O, κ^N-Aminoxide Derivative

Rajib K. Sarker, Loïc P. Mangin, and Davit Zargarian*

Département de chimie, Université de Montréal, Montréal (Québec), Canada H3C 3J7.

2.2   Abstract

This report discusses the reactivities of hydroxylamines with a family of nickellacyclic complexes prepared by C—H nickelation of aryl phosphinites. Treating the dimeric complexes κ^C,κ^P-{2-OPR$_2$,4-R'-C$_6$H$_4$}$_2$Ni$_2$(μ-Br)$_2$ (R = i-Pr; R' = H, Cl, OMe, NMe$_2$) or their monomeric acetonitrile adducts κ^C,κ^P-{2-OPR$_2$,4-R'-C$_6$H$_4$}Ni(Br)(NCMe) with hydroxylamines showed three types of reactivities depending on the Ni complex, the reaction solvent, and the substrate used: (1) the benzyl-protected substrate PhCH$_2$ONH$_2$ gave simple N-bound adducts with all Ni complexes; (2) the parent Ni dimer (R' = H) reacted with Et$_2$NOH and (PhCH$_2$)$_2$NOH in CH$_2$Cl$_2$ to give, respectively, the zwitterionic amine oxide κ^C,κ^P-{2-OPR$_2$-C$_6$H$_5$}Ni(κ^O-ONHEt$_2$)Br and the bidentate aminoxide (i-R$_2$POPh)Ni{κ^O,κ^N -ON(CH$_2$Ph)$_2$}Br; (3) the analogous reaction of substituted Ni complexes (R' = Cl, OMe, NMe$_2$) with hydroxylamines in acetonitrile gave adducts of imines derived from dehydration of Et$_2$NOH and (PhCH$_2$)$_2$NOH. The latter reactivity proceeds optimally in acetonitrile, but it also occurs to a lesser extent in C$_6$D$_6$ if the reaction is allowed to go for more than 24 h. Different mechanistic scenarios have been considered to rationalize the observed hydroxylamine→imine transformation.

2.3   Introduction

Synthetic methodologies based on C—H functionalization using base-metal precursors have grown in prominence over the past two decades, to the point where such methodologies are now a central part of the global drive to develop sustainable chemical processes.[1,2] The most common approach to metal-catalyzed C—H functionalization requires the presence in substrates of directing groups that bind the metal atom to facilitate its interaction with the target C—H moiety.[3–5] Such chelation-assisted strategies generate metallacyclic intermediates that can then react with co-substrates to give the final products of the functionalization process. From a practical point of view, it is advantageous to ensure that such multi-step functionalization processes proceed directly to the end products in a "one-pot" manner. On the other hand, intercepting key intermediates and studying their stabilities and reactivities can provide valuable mechanistic insight that can help optimize the functionalization process.[6,7]

In this context, our group has shown that simple Ni(II) precursors can promote C—H metallation of phosphinites derived from phenol and naphthol, thus giving access to a rare family

of stable and isolable nickellacyclic complexes (**Scheme 2.1**).[8,9] We have also reported on the factors that affect the C—H nickellation step,[10] and briefly described the C—C and C—P functionalization reactivities observed with some of the isolated nickellacyclic complexes (**Scheme 2.1**).

Scheme 2. 1. Previously reported C—H nickellation and functionalization of aryl- and naphthyl-phosphinites.
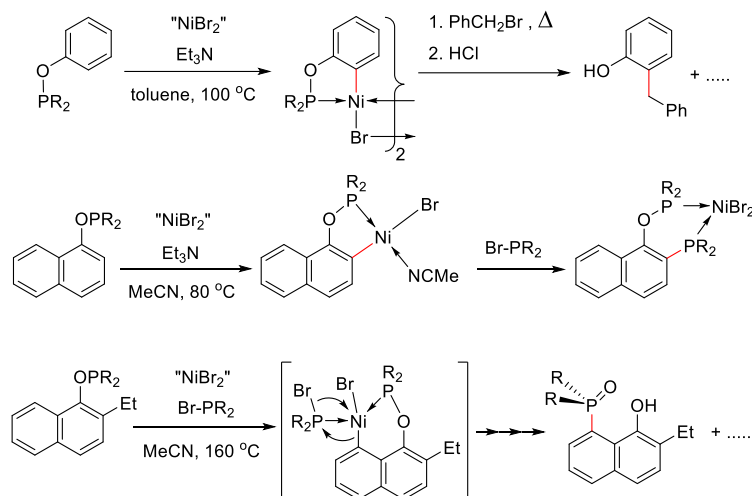
As a follow-up to our investigations on the theme of C—H functionalization, we set out to determine if our phosphinite-based nickellacyclic complexes might react with hydroxylamines to allow C—N functionalization of the aryl moiety, analogously to the C—P coupling observed with halophosphines (**Scheme 2.1**). The present report discusses the reactivities of hydroxylamines with four orthonickellated compounds derived from the aryl phosphinites 3-R'-$C_6H_4OPR_2$ (R = *i*-Pr; R' = H, Cl, OMe, NMe₂). Although the hoped-for C—N coupling did not materialize, we have made interesting observations on the reactivities of Ni complexes with hydroxylamines, including a facile process for dehydration of these substrates to imines, as described herein.

2.4   Results and discussion

2.3.1   Synthesis of the nickellacyclic complexes.

The methodology employed for preparation of the precursors required for our study is shown in **Scheme 2.2**. This methodology gave easy access to the previously reported dimeric complexes **1-**

3,[11–13] and the identity of each complex was established based on its characteristic $^{31}P\{^1H\}$ singlet resonance (C_6D_6, ppm): 199.0 (**1**), 200.7 (**2**), and 198.2 (**3**).

Scheme 2. 2. Synthesis of dimeric precursors **1-3.**

R'	Yield (%)
H (**1**)	92
Cl (**2**)	59
OMe (**3**)	63
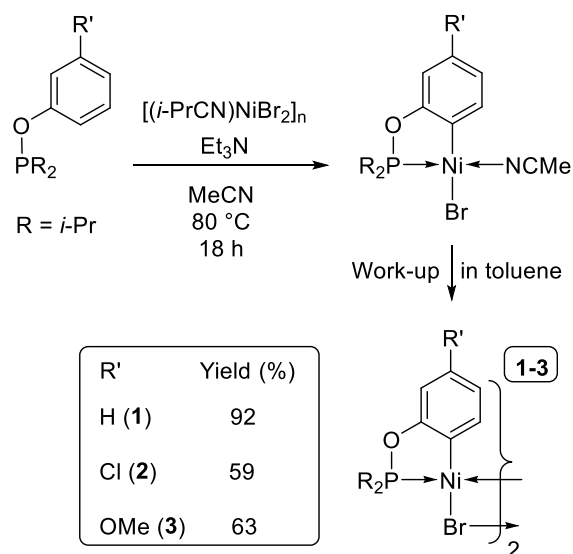
Having obtained the known dimers **1-3**, we set out to prepare the fourth (unreported) dimeric precursor **4** (R' = NMe$_2$). The pro-ligand 3-Me$_2$N-C$_6$H$_4$OP(*i*-Pr)$_2$ required for the synthesis of this precursor was prepared by treating 3-Me$_2$N-C$_6$H$_4$OH with ClP(*i*-Pr)$_2$ in the presence of Et$_3$N, and it was then used for the preparation of **4** according to the above procedure. Analysis of the final reaction mixture by $^{31}P\{^1H\}$ NMR showed a new singlet at 195.8 ppm, confirming the successful formation of **4-NCMe**, the acetonitrile adduct of the target cyclonickellated dimer **4**. Indeed, the pro-ligand 3-NMe$_2$-C$_6$H$_4$OP(*i*-Pr)$_2$ underwent C—H nickellation more readily than its previously studied analogues (R' = H, Cl, OMe) such that the heating shown in **Scheme 2. 2** was unnecessary in this case. This finding was consistent with our previous observation that C—H nickellation of aryl phosphinites is more facile for substrates bearing electron-releasing substituents.[14]

Unfortunately, however, complications arose during the second stage of the synthesis as we noted that the standard toluene work-up procedure used successfully to isolate the dimers **1-3** does not give pure samples of the target dimer **4**. Indeed, $^{31}P\{^1H\}$ NMR analysis of the solid obtained from the toluene work-up showed two sets of signals with a 3:1 integration ratio, a singlet at ca. 196.7 ppm attributed to the target dimer **4** along with AB doublets at ca. 182.5 and 150.2

ppm ($^2J_{PP}$= 327 Hz) attributed to complex **4'**, the phosphinite adduct of the target cyclometallated dimer **4** (**Scheme 2.3**).

Scheme 2. 3. Preparation of complex **4.**
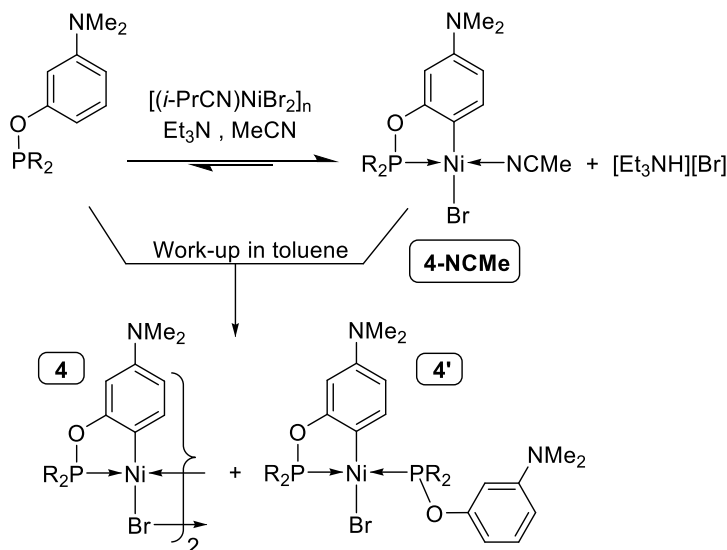
The formation of **4'** can be ascribed to side reactions that take place during the toluene work-up phase: the Et$_3$N·HBr generated in the C—H nickellation step of the synthesis of **4** partially protonates the newly formed Ni-aryl moiety, thereby giving back some NiBr$_2$ and re-forming the pro-ligand;[15] the latter then reacts with **4** to give the stable phosphinite adduct **4'** (**Scheme2. 3**).

The identity of **4'** was established unequivocally thanks to X-ray diffraction studies carried out on single crystals obtained from the recrystallization of the reaction mixture. (The solid-state structures of this and all other new compounds presented in this report will be discussed later.) Unfortunately, however, the target dimer **4** could not be isolated in pure form even though it is the major component of the mixture. Therefore, the reactivity studies of **4** were conducted using in-situ generated **4-NCMe**.

Reactivities of the dimeric precursors with hydroxylamines. With the required cyclonickellated precursors in hand, we proceeded to examine their reactivities with the hydroxylamines BnONH$_2$ (Bn = PhCH$_2$), Et$_2$NOH, and Bn$_2$NOH. These substrates were selected to probe the three different types of reactivities we anticipated: (1) likely formation of simple *N*- or *O*-bound adducts, (2) possible protonation of the Ni-Ar moiety in the dimers by the relatively acidic proton R$_2$NO*H* to

give aminoxide derivatives (Ni—ONR$_2$), and (3) possible homolytic cleavage of the hydroxylamine N—O bond to give Ni-aminyl or Ni-amide derivatives. Thus, the benzyl-protected substrate BnONH$_2$ would suppress the protonation pathway and let us assess the relative nucleophilicities of the *N*- and *O*-lone pairs, whereas Et$_2$NOH and Bn$_2$NOH would reveal the impact of steric/electronic factors on the reactivities. The results of these studies are described below.

Room temperature treatment of the parent dimer **1** with BnONH$_2$ (supplied as its HCl salt and neutralized in-situ with Et$_3$N) gave two new species that turned out to be the Ni-chloro and Ni-bromo derivatives of the monomeric *N*-bound adduct **5a** shown in **Scheme 2. 4**. The chloro derivative forms as a result of the facile exchange of Ni-Br with Cl$^-$ ions generated in-situ from pre-treatment of BnONH$_2$·HCl with Et$_3$N.

Scheme 2. 4. Preparation of adducts **5a-5c.**
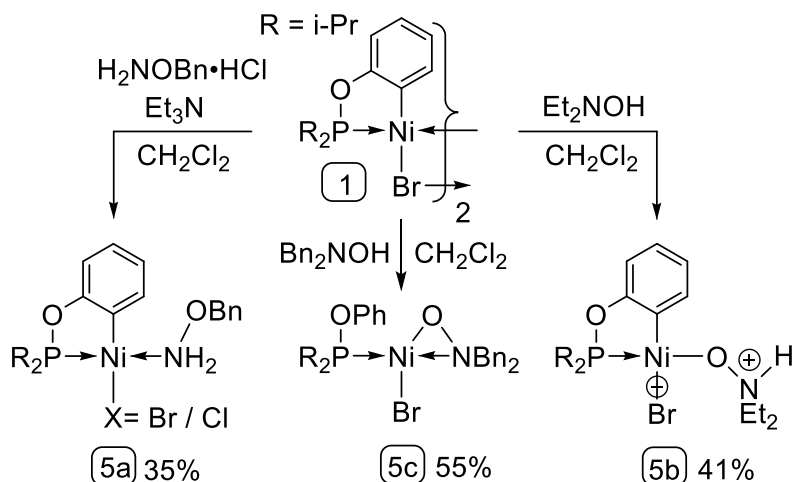
The low isolated yield of **5a** is related to the difficulties encountered in the work-up of the sticky solid left after evaporation of the reaction solvent, and does not imply the formation of multiple products. Indeed, the two derivatives of **5a** are the only species observed in the ^{31}P{^{1}H} NMR spectrum of the crude reaction mixture (**Fig. S126**).

Next, we tested the reactions of precursor **1** with the two unprotected hydroxylamine substrates. These gave two different outcomes: the reaction with Et$_2$NOH gave **5b**, which can be described as a zwitterionic adduct or a κ^O-amine oxide, whereas the reaction with Bn$_2$NOH gave the {κ^O,κ^N-aminoxide species **5c** by protonation of the Ni-aryl moiety in **1** (**Scheme 2. 4**). ^{31}P

NMR monitoring of these reactions showed that the Et$_2$NOH reaction was fairly clean, the crude mixture showing only one major and one minor species in ca. 93:7 ratio (**Fig. S2. 127**), but the corresponding spectrum for the Bn$_2$NOH reaction mixture showed 4 new resonances with the major one accounting for ca. 60% of the combined signal intensities (**Fig. S2. 129**). Yet, the work-up process led to isolation of a lower yield of **5b** than **5c** (**Scheme 2. 4**).

The ^{31}P{^{1}H} NMR spectra (C$_6$D$_6$) displayed the following characteristic singlet resonances: δ 195.2 for **5a-Cl** and 198.3 for **5a-Br** (ratio of 86:14); 201.5 for **5b**; 173.3 for **5c**. The ^{1}H NMR spectra were also diagnostic. For example, the ONHEt$_2$ proton in **5b** gave a broad and downfield signal at ca. 9 ppm, whereas no such signal was detected in the spectrum of **5c** consistent with the absence of an NH or OH moiety in this compound. Moreover, the diastereotopic benzylic protons in **5c** displayed two ABX-type doublets of doublets as a result of coupling with the P nucleus ($^4J_{HP}$ = 2 and 6 Hz), whereas the OCH_2Ph protons in **5a** display broad singlets. Compounds **5a-5c** were also studied by single-crystal X-ray diffraction studies to unequivocally confirm the assigned structures (vide infra).

One common aspect of the reactions shown in **Scheme 2. 4** is the impact of solvent on reactivity outcomes. For instance, **5a** forms most readily in CH$_2$Cl$_2$ and toluene, whereas its formation is less favored in acetonitrile; this is presumably because the in-situ formed acetonitrile adduct **1-NCMe** is fairly stable toward substitution by BnONH$_2$. Similarly, using acetonitrile instead of CH$_2$Cl$_2$ hampered the reactions of **1** with Et$_2$NOH and Bn$_2$NOH. For instance, running the reaction of **1** with Et$_2$NOH in acetonitrile gave a 2:1 mixture of **5b** and the acetonitrile adduct **1-NCMe** (**Fig. S2. 128**), implying that competitive acetonitrile binding reduces the extent of hydroxylamine coordination, thereby hindering the formation of **5b**. Indeed, re-dissolving pure **5b** in acetonitrile gives a 2:1 mixture of **5b** and **1-NCMe**. In the case of the analogous acetonitrile reaction with Bn$_2$NOH, the formation of **5c** was suppressed completely as we obtained a 1:1 mixture of the acetonitrile adduct **1-NCMe** and a new species believed to be a simple Bn$_2$NOH adduct (**Fig. S2. 130**). In this case, however, **5c** is stable in acetonitrile, because the protonation of the Ni-Ar moiety cannot be reversed.

Next, we probed the reactivities of the Cl- and MeO-substituted dimers **2** and **3** with the three hydroxylamine substrates. The reactions with BnONH$_2$ proceeded similarly to the reaction with **1** to give the chloro- and bromo-derivatives of the simple *N*-bound adduct **6a** and **7a** (**Scheme**

2. 5). In contrast, very different ^{reactivities} were observed with Et$_2$NOH and Bn$_2$NOH, giving the Ni-imine products **6b**/**7b** and **6c**/**7c**, respectively.

Scheme 2. 5. Preparation of adducts **6a-6c** and **7a-7c**.
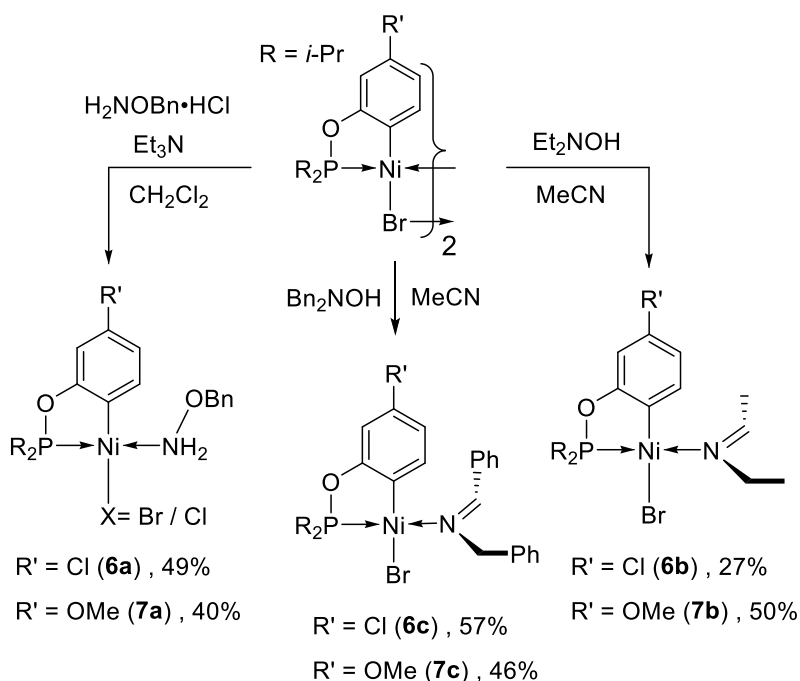
We emphasize again that these reactions appear fairly clean by NMR, and so the generally low isolated yields of the products do not imply major side-reactions, relating instead to their difficult recrystallizations. For instance, the ^{31}P{^{1}H} NMR spectrum recorded for the crude mixture of the reaction of **2** with Et$_2$NOH showed that the resonances for **6b** and the acetonitrile adduct **2-NCMe** account for nearly 90% of the combined signal intensities (**Fig. S2. 131**); similarly, in the corresponding spectrum for the reaction of **3** with Et$_2$NOH the resonance assigned to the imine adduct **7b** accounted for more than 90% of the combined intensities (**Fig. S2. 132**).

Single crystals were obtained for the new complexes **6a-c**, **7b**, and **7c**, allowing us to confirm their solid-state structures.[16] In the case of **7a**, we were unable to grow single crystals suitable for accurate X-ray diffraction studies, but the identity of this compound was established reliably based on NMR spectra.

The ^{31}P{^{1}H} NMR spectra (C$_6$D$_6$) of the new compounds showed these characteristic singlets: δ 199.0 for **6a-Br** and 195.6 for **6a-Cl** (ratio 57:43); 195.5 for **6b**; 196.3 for **6c**; 197.1 for **7a-Br** and 193.8 for **7a-Cl** (ratio 30:70); 193.8 for **7b**; and 194.9 for **7c**. For the imine adducts, the

^{13}C NMR spectra showed the NC$_{sp2}$HR signals (R = CH$_3$ and Ph) ατ δ 166, and the ^{1}H NMR spectra showed the expected signals for the vinylic protons NC(H)R at δ 6.49-6.55 (m, **6b**), 6.63-6.67 (m, **7b**), 7.80 (d, $^4J_{HP}$ ≈ 8.7 Hz, **6c**), and 7.86 (d, $^4J_{HP}$ ≈ 8.6 Hz, **7c**), respectively, as well as the anticipated ABX-type doublets of doublets for the diastereotopic NCH_2R protons in **7b** and **7c**.

Another noteworthy feature of the ^{1}H NMR spectra for **6c** and **7c** is the unusually downfield signals for the ortho protons of the (benzyl) Ph rings, at δ 8.82 and 8.93, respectively. We examined the solid-state structures of these complexes to see if any unexpected H·····element close contacts present in the crystal lattice might provide a rationale for these observations. Although some close Ni·····H contacts were, indeed, located in the examined structures, these appear to be a common feature of these imine adducts. Thus, the available data does not allow us to pinpoint a specific bonding phenomenon (e.g., agostic or similar interactions involving orbital overlap) that might explain the observed downfield chemical shifts. A summary of the structural analyses conducted to investigate this question is provided in the supporting information.

The reactivities of the Me$_2$N-substituted precursor was studied next using in-situ generated **4-NCMe**. Reactions with BnONH$_2$ and Et$_2$NOH followed pathways similar to those observed with the analogous dimers **2** and **3**, i.e., giving the simple *N*-bound adduct **8a** and the imine adduct **8b**, respectively (**Scheme 2. 6**). On the other hand, the reaction with Bn$_2$NOH gave no tractable products which could be isolated in a pure form and characterized.

Scheme 2. 6. Preparation of adducts **8a** and **8b**.
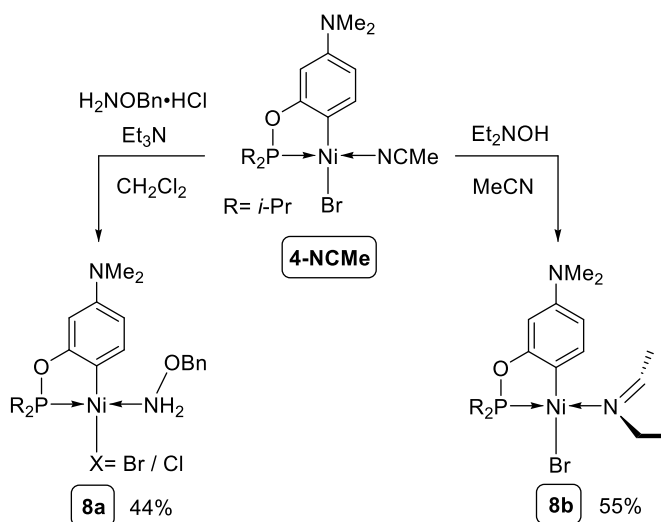
The $^{31}P\{^1H\}$ NMR spectra (C$_6$D$_6$) of the new BnONH$_2$ adducts showed characteristic singlets at δ 196.1 for **8a-Br** and 192.8 for **8a-Cl** (ratio 77:33), whereas the corresponding signal for the new imine adduct **8b** appeared at 192.9 ppm. The ^1H NMR spectra of the benzyl-protected hydroxylamine adduct **8a** and the imine adduct **8b** were consistent with the absence of a plane of symmetry in these molecules. Complex **8a** also showed two broad signals at 5.47 and 5.25 ppm for the N*H*$_2$ and OC*H*$_2$ protons.

Synthesis of a simple amine adduct. In addition to the new complexes presented above, we also prepared a simple amine adduct for the purpose of comparing its spectral features and solid-state structure to those of the imine and hydroxylamine adducts under discussion. Thus, treating the dimer **3** with Et$_2$NH generated adduct **7d** (**Scheme 2. 7**), which was fully characterized by NMR and single crystals X-ray diffraction studies.

Scheme 2. 7. Preparation of the Et$_2$NH adduct **7d.**
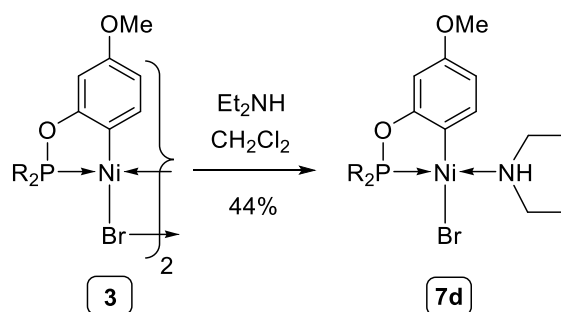
The $^{31}P\{^1H\}$ NMR spectrum of **7d** showed the anticipated singlet resonance at 192.6 ppm, whereas the ^1H NMR spectral features were fully consistent with the presence of an effective plane of symmetry in the coordination plane resulting in the pairwise equivalence of the symmetry-related NC*H*$_2$C*H*$_3$ and PC*H*C*H*$_3$ groups above and below this plan.[17] Moreover, one of the multiplets for the 4 diastereotopic NC*H*$_2$ protons (resonating at 2.1 ppm) integrates for 3 protons, leading us to suspect that it overlaps with the signal for the N*H* proton.

2.3.2 On the mechanism(s) for the conversion of hydroxylamines into imines.

The unanticipated observation of the hydroxylamine-to-imine conversions promoted by three of our cyclonickelated complexes prompted us to study the mechanism of this transformation. A

literature search revealed that two different mechanistic proposals have been put forth for hydroxylamine-to-imine conversions. Murahashi's group was the first to report a $TiCl_3$-promoted conversion of hydroxylamines $R^1CH_2N(R^2)OH$ into imines,[18–20] and this group has proposed a radical pathway consisting of three distinct stages:[21] (1) initial homolysis of the N—O bond in the substrate generates $TiCl_3(OH)$ and the aminyl intermediate $R^1CH_2N(^{\bullet})R^2$; (2) a 1,2-hydrogen shift converts the aminyl into the α-aminoalkyl radical $R^1CH(^{\bullet})N(H)R^2$; (3) electron-transfer from the latter to $TiCl_3(OH)$ regenerates $TiCl_3$ and produces the imine product and an equivalent of water.

The second mechanistic proposal for hydroxylamine-to-imine conversions (or hydroxylamine dehydration) is a non-radical pathway promoted by late transition metal systems. This alternative proposal is, in fact, based on the generally accepted mechanism for hydration of nitriles, a transformation that is promoted by a variety of transition metal compounds.[22] A recent report has adapted such a non-radical mechanism to rationalize the Pt(II)-promoted dehydration of hydroxylamines into imines via a nucleophilic attack by hydroxylamines on coordinated cyanamides.[23]

Both of the above mechanistic scenarios have some appeal for the system under discussion here. Murahashi's radical pathway is in accord with our original expectation that the N—O bond in hydroxylamines might be prone to a homolytic cleavage. However, such a process is much more likely to occur with an open-shell precursor such as $TiCl_3$ rather than with our closed-shell Ni(II) precursors. Indeed, divalent nickel centers are usually electrophilic and tend to bind unsaturated substrates such as nitriles, thereby activating them to varying degrees towards nucleophilic attacks. For instance, our dimeric precursors readily form acetonitrile adducts.

Moreover, closely related Ni complexes bearing phosphinite-based pincer ligands are known to catalyze nucleophilic attacks by amines and alcohols on RCN (R = $CHCH_2$,[24] $CHCHPh$,[25] Me,[26,27] Ph[28]).[29] For these reasons, a non-radical pathway involving nucleophilic attack on coordinated nitriles seemed *a priori* more plausible for the mechanism of the hydroxylamine-to-imine conversions observed in our system. Nevertheless, we undertook experiments to assess the respective merits of the two mechanistic postulates, as described below.

Our initial mechanistic investigations were focused primarily on the acetonitrile reaction of dimer **3** with two equivalents of Et_2NOH, because this system gives fairly clean outcomes. Analysis of the final reaction mixture confirmed the formation of the imine adduct **7b** as the anticipated main product (see **Scheme 2. 5**) in addition to a small crop of colorless crystals, which

were isolated and identified by XRD analysis as acetamide. This fortuitous observation provided an important clue regarding the mechanism of imine formation: the conversion of hydroxylamine to imine occurs concomitantly to the hydration of acetonitrile. This scenario would be consistent with the nucleophilic attack mechanism depicted in **Scheme 2. 8**, as well as the radical pathway inspired by Murahashi's proposal for the TiCl₃ system and shown in **Scheme 2. 9**.

Scheme 2. 8. Nucleophilic attack mechanism for Ni(II)-promoted dehydration of hydroxylamines**.**
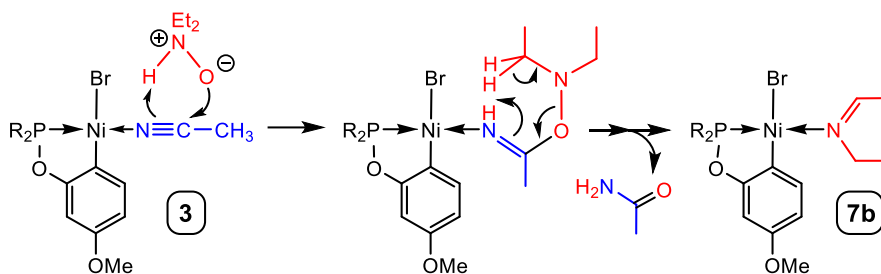
Scheme 2. 9. Radical pathway mechanism for Ni(II)-promoted dehydration of hydroxylamines.
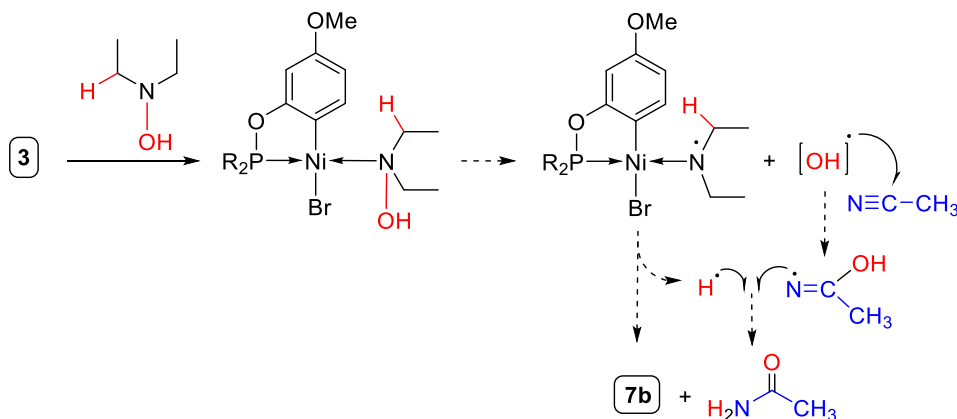
Since the nucleophilic attack scenario (**Scheme 2. 8**) is entirely predicated on the coordination of acetonitrile to Ni(II), its validity can be determined by conducting the reaction of **3** with Et₂NOH in a solvent other than MeCN to see if imine formation can be suppressed altogether. This idea was tested by treating **3** with two equiv of Et₂NOH in CH₂Cl₂ and monitoring the reaction progress by ^{31}P NMR spectroscopy. In contrast to the fairly clean formation of the imine derivative **7b** in acetonitrile, the analogous reaction in CH₂Cl₂ gave a much more complex

mixture with multiple ^{31}P resonances in the chemical shift region 205-120 ppm (**Figure S2. 133**). Most of these are minor, but the two major resonances accounting for >80% of the combined signal intensities are believed to be analogues of complexes **5b** and **5c** (see **Scheme 2. 4**). This assertion is based on the similarities of the chemical shifts of **5b** and **5c** to those of the major resonances generated in the CH$_2$Cl$_2$ reaction (201.5 vs. 201.5 ppm and 173.3 vs 171.3 ppm).

It is not clear whether the CH$_2$Cl$_2$ reaction generated the anticipated imine adduct **7b**, but two minor ^{31}P resonances appear in the chemical shift region associated with this product (194.7 and 193.5 ppm vs. 193.8 ppm for **7b** in C$_6$D$_6$). Significantly, the intensities of these resonances are about 6% and 3%, respectively, implying that even if one of these could be attributed to **7b**, imine formation is a minor side-reaction in CH$_2$Cl$_2$. Testing the reaction of **3** with Et$_2$NOH in toluene gave an outcome similar to the CH$_2$Cl$_2$ reaction (**Figure S2.134**): we obtained a complex mixture in which the minor ^{31}P resonances appearing in the chemical shift region of **7b** accounted for only 2% of the combined peak intensities.

We conclude from the above tests that the reaction of **3** with Et$_2$NOH follows different pathways depending on the reaction solvent: formation of the imine adduct **7b** is the main observed reactivity in acetonitrile, but it is at best a minor side-reaction in CH$_2$Cl$_2$ and toluene. This also implies that the acetonitrile reaction likely proceeds according to the non-radical pathway shown in **Scheme 2. 8**. To further support this possibility, we conducted the acetonitrile reactions of **3** with Et$_2$NOH in the presence of reagents such as the stable radical TEMPO (TEMPO = 2,2,6,6-(tetramethylpiperidin-1-yl)oxyl) or styrene that might intercept any radical intermediates, and compared the results to the reactions in the absence of these reagents. These tests showed nearly complete conversion of **3** to the anticipated imine adduct **7b**, thus establishing that this transformation is not hindered in the presence of substrates susceptible to trapping radical intermediates.

Finally, we examined the acetonitrile and C$_6$D$_6$ reactions of **3** with 2 equiv of Et$_2$NOH over 1-2 days to compare the time profiles of these reactions and possibly detect any intermediates involved in the process. The results of these tests are summarized by the time profiles shown in **Figure 2. 1**. It is worth noting that the starting dimer **3** is rapidly converted to new species in both reactions, but the evolution of the initially formed species throughout the reaction time-span was quite different in each case. Thus, the first ^{31}P NMR spectrum recorded 10 min after the acetonitrile

reaction was launched showed the formation of multiple resonances (**Figure S2. 138**). Of these resonances, the
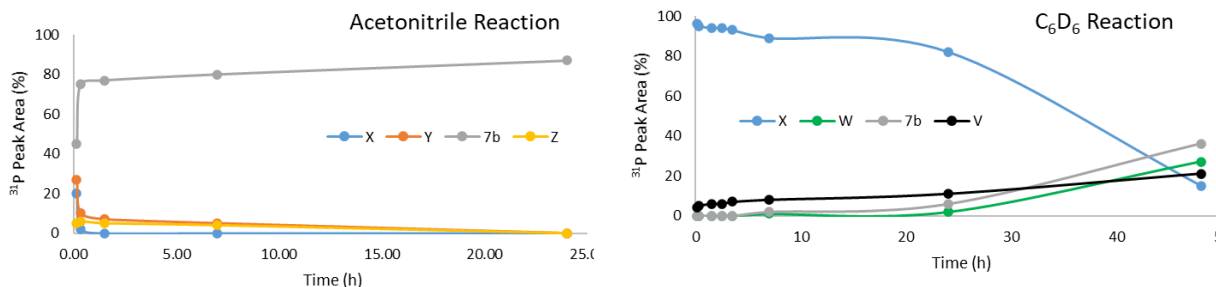
Figure 2. 1. Time plots for the reactions of **3** with **2** equiv of Et$_2$NOH in acetonitrile (left) and C$_6$D$_6$ (right). See ESI for experimental details and NMR spectra of the reaction mixtures.

ones appearing at around 90-80 ppm are thought to represent oxidized species that remained present and fairly constant in the reaction mixture throughout the reaction. In contrast, the more downfield resonances (210-170 ppm) showed significant variation over the reaction time-span; these latter resonances likely represent Ni derivatives of interest to the reaction mechanism. Of these, the four accounting for >80% of the combined signal intensities have been attributed to the following species: the 195.5 ppm resonance is the anticipated imine adduct **7b** (represented by the gray trace in the top plot); the 196.8 ppm is the acetonitrile adduct (represented by the Y trace in the top plot); the 201.1 and 172.0 ppm resonances are hydroxylamine adducts (represented by the X and Z traces in the top plot). Evolution of these four resonances over time led to the dominance of the imine adduct **7b**, which accounted for >80% and ca. 90% of the mixture after 7 and 24 h, respectively.

In contrast to what was observed for the acetonitrile reaction, we detected one main product during the first several hours of the C$_6$D$_6$ reaction; this species is represented by the blue trace for species X in the bottom plot. We believe that this species is the analogue of the zwitterionic adduct **5b** (**Scheme 2. 4**) based on the similarity of the ^{31}P chemical shift for these two species (see **Figs S2. 143** and **S2. 144**). Monitoring this reaction beyond 24 h showed that this species is gradually converted to the imine adduct **7b** (gray trace) and two unknown products (represented by the W

and V trace in the bottom plot). It is important to emphasize that the imine adduct **7b** remains a minor product in this reaction after 48 h.

The time profile plots shown in **Figure 2. 1** allow us to show that the imine adduct **7b** is the predominant product of the acetonitrile reaction after only a few minutes, whereas it is only a minor product in C_6D_6 (<20%) even after 48 h. Such a major discrepancy in the outcomes of these two reactions underlines the crucial role played by the solvent, and it supports the contention that the conversion of hydroxylamines to imines in acetonitrile proceeds via the nucleophilic attack mechanism depicted in **Scheme 2. 8**. On the other hand, we cannot rule out the involvement of a radical pathway in the formation of minor quantities of imine adducts in solvents other than acetonitrile.

To shed further light on the mechanistic debate outlined above, we undertook DFT calculations to model the hydroxylamine-to-imine transformations observed in our system. Interestingly, these computational studies provided strong support for the proposed mechanism that involves concomitant hydroxylamine dehydration and acetonitrile hydration (**Scheme 2. 8**). The radical pathway was also explored, as were two other scenarios, but all of these involve unrealistically high energy barriers (>50 kcal/mol), which leads us to rule them out in favor of the nucleophilic attack pathway supported by the NMR data discussed above. (See ESI for a summary of our DFT results.)

2.3.3   Solid-state structures of the new products.

During the course of this investigation, we isolated 13 new Ni complexes and conducted single crystal X-ray diffraction studies on 12 of them. The crystals obtained for adducts **5a** and **8a** showed telltale signs for co-crystallization of the Ni-Cl and Ni-Br derivatives in the asymmetric unit resulting in double-occupancy of the halide atom in these structures. This was successfully modelled as a substitutional disorder. There were also some indications that a similar Cl/Br disorder might exist in the structure of **6a**, but in this case we ignored the potential substitutional disorder because the isolated crystals were twinned and of bad quality.

The electronic supporting information attached to this report provides crystal data and structure refinement details (**Tables S2. 1-S2. 5**), as well as lists of the most noteworthy bond distances (**Table S2. 6**) and angles (**Table S2. 7**) for all new complexes. Molecular diagrams for some of the more pertinent structures are included below (**Figure 2. 2**), and all of the diagrams are also provided in the ESI section (**Figure S2. 143-S2. 154**). One common feature in all of the

structures presented in this study is the fairly planar coordination geometry around the central Ni atom. Thus, the Ni centre in all the complexes is only slightly out of the mean plane defined by the 4 ligating atoms, this distance being <0.04 Å in all complexes except **6c** and **7c** in which it is about 0.08 Å. In the case of complexes featuring a central cyclonickelated aromatic moiety (i.e., all except **5c**), the mean plane of this ring is twisted with respect to the mean coordination plane by 1-12° in all complexes except **4'**. In the latter complex, this twist angle is 17°, presumably to minimize the repulsions between the two bulky phosphinite ligands.

Most of the complexes analyzed by XRD studies also show fairly minor angular distortions and deviations from the ideal values of 90° and 180° for cis and trans bond angles, respectively. For example, in all complexes except **5c** the cis angles range from 82° to 101°, whereas the trans angles are 166-180°. In contrast, complex **5c** exhibits major deviations from ideal values in the 4 bond angles involving the central Ni atom (43°, 102°, 107°, and 108°). Similarly, significant deviation from the ideal value was found for one of the 4 angles around the sp3-hybridized N atom of the the aminoxide ligand ($\angle$O-N-Ni = 66°).
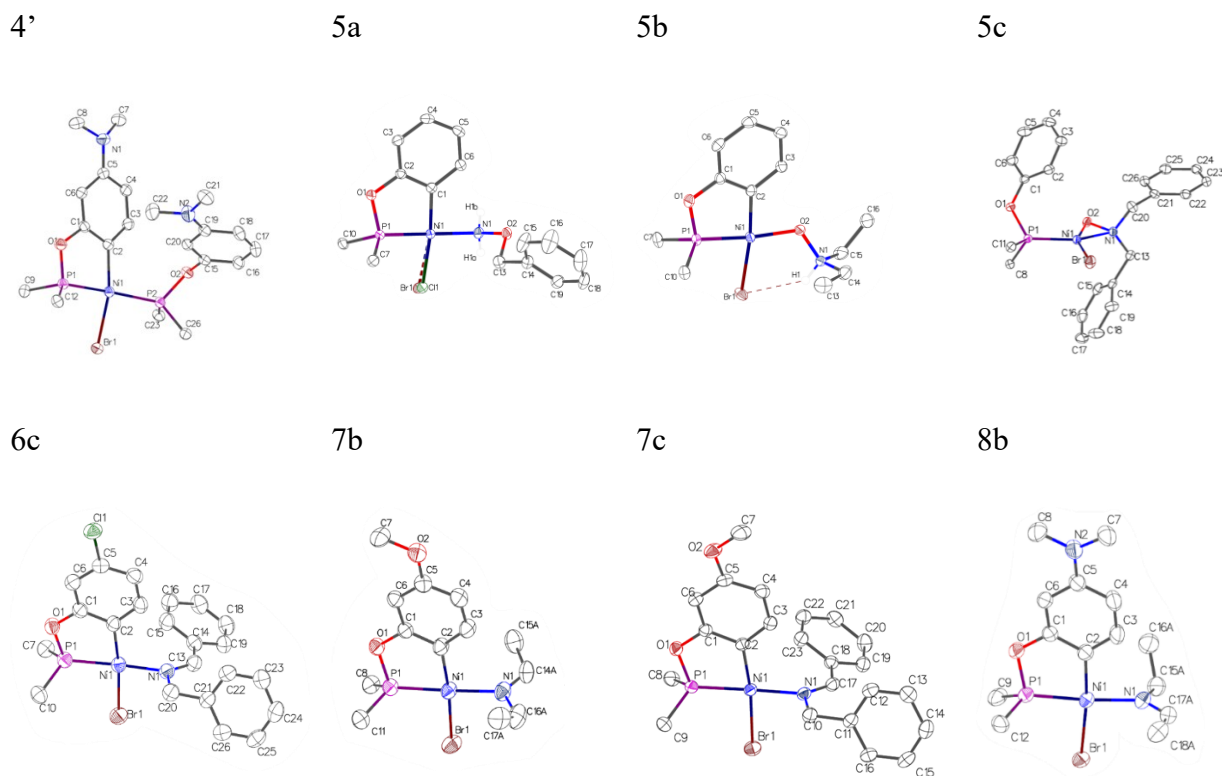
Figure 2. 2. Molecular diagrams of some of the new complexes presented in this report. Thermal ellipsoids are shown at the 50% probability level. Hydrogen atoms the Me groups of the i-Pr substituents have been omitted for clarity.

Among the new complexes presented in this study, the most unique coordination geometry is presented by complex **5c**. Indeed, what makes this a fairly uncommon compound is its unusual 3-membered Ni-O-N ring. To be sure, metallacyclic complexes analogous to **5c** are known for a few transition metals,[30–36] but to our knowledge there are only three previously reported Ni(II) complexes of this type, all of which are based on (κ^O,κ^N–TEMPO).[37–39] These compounds display solid state parameters fairly similar to those found in **5c**. Also reported in the literature is a similar, but not analogous, complex featuring a 3-membered nickellacyclic moiety based on a "side-bound" η^2–nitrobenzene ligand coordinated to Ni(0).[40]

All Ni-ligand distances in the new complexes under discussion are within the expected range for structurally similar Ni(II) complexes (see **Table 2. 1**);[41–44] nevertheless, a number of comparisons are given here to provide useful insights. For instance, the unequal P1—Ni and P2—Ni distances in complex **4'** (2.14 vs 2.25 Å) reflect the stabilizing effect of the 5-membered metallacycle (chelate effect). In complex **5c**, the Ni—O bond distance is shorter than the Ni—N

bond distance (1.84 vs 1.90 Å), as found for other Ni(II)–(κ^O,κ^N-TEMPO) complexes. Likewise (and unsurprisingly), the Ni—O distance in **5b** is also significantly shorter than the Ni—N distances in **5a** (ca. 1.92 vs 1.97 Å), whereas the Ni—P distances in these complexes are essentially equivalent (ca. 2.10 Å); this implies that the O- and N-bound ligands exert comparable trans influences. On the other hand, complexes **5a** and **8a** display essentially equivalent Ni—N distances (1.97 Å), yet the Ni—P distance is somewhat shorter in **5a** (2.10 vs 2.12 Å).

A number of interesting structural features are also present in the imine adducts and the Et$_2$NH adduct, and a few remarks and comparisons on these features are warranted. For example, all imine moieties are clearly planar (the sum of the three angles involving the imine-*N* atoms are 359-360°) and oriented nearly perpendicularly to the coordination plane of the complex: 83° in **6b**; 90° in **7b** and **8b**; 87° in **6c** and 89° in **7c**. Interestingly, the plane defined by the non-hydrogen atoms of the Et$_2$NH moiety in **7d** (C-C-N-C-C) is also oriented nearly perpendicularly (89°) with respect to the coordination plane. The Ni—N bond distance is significantly longer in **7d** vs **7b** (2.00 vs 1.95 Å), consistent with the generally greater nucleophilicity of imines vs amines. On the other hand, the much shorter Ni—P bond distances in the imine adducts relative to the corresponding distance in complex **4'** (2.10-2011 vs. 2.14 Å) indicate that imine moieties possess a much weaker trans influence relative to the phosphinite ligand. Finally, among the imine moieties, the Ni—N bond distances are somewhat longer for the CH$_3$C(H)=NEt imine moieties in **6b** (**Figure S2. 147**), **7b** (**Figure 2. 2**), and in **8b** (**Figure 2. 2**) relative to the presumably bulkier imine moieties PhC(H)=NBn in **6c** and **7c** (**Figure 2. 2**; 1.95 vs. 1.93-1.94 Å).

2.5   Summary & conclusion

The main goal of this study was to probe the potential of hydroxylamines for inducing C—N functionalization with our phosphinite-based nickellacyclic complexes. In analogy to the known reactivity of our nickellacyclic complexes with halophosphines, we had anticipated that homolysis of the relatively labile N—O bond in hydroxylamines would generate reactive Ni-amido or aminyl intermediates that would lead to C—N coupling. Instead, we observed a range of reactivities depending on (a) whether or not the hydroxylamine substrate was protected at its OH moiety, (b) whether the aryl moiety of the cyclonickellated complex had a non-H substituent, and also (c) the type of *N*-substituent. These reactivities are represented in **Scheme 2. 10**.

Scheme 2. 10. Summary of observed reactivities with hydroxylamines
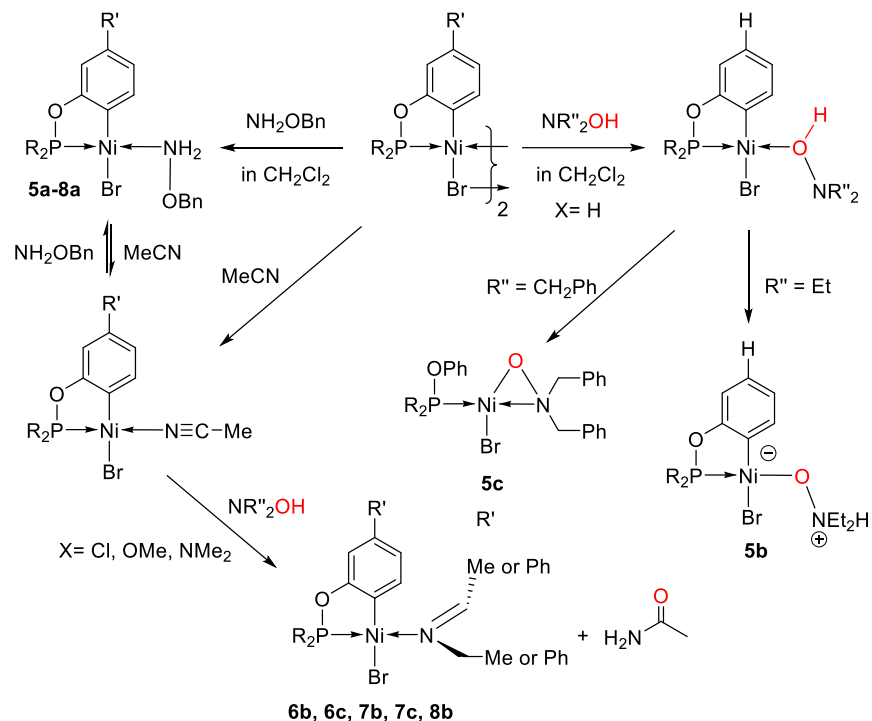
The most consistent reactivity observed for all four cyclonickellated precursors was formation of the $(BnO)H_2N{\rightarrow}Ni$ adducts **5a-8a**. These were obtained readily when our precursors were treated with $BnONH_2$ in CH_2Cl_2 regardless of the nature of the substituent on the aryl moiety of the precursor, but partial solvolysis occurs in acetonitrile to give the acetonitrile adducts.

In contrast to the uniform reactivity seen with $BnONH_2$, the reactivities with unprotected hydroxylamines depended strongly on the Ni precursor as well as on the reaction solvent. In CH_2Cl_2, the unsubstituted precursor **1** formed *O*-bound adducts initially that reacted further to give two different products depending on the *N*-substituent of the substrate, the zwitterionic hydroxylamine oxide **5b** with R'' = Et, and the κ^O,κ^N- aminoxide **5c** with R'' = CH_2Ph. A third type of reactivity observed in our study was the formation of the imine adducts **6b-8b**, **6c**, and **7c** from the acetonitrile reaction of hydroxylamines with the Ni precursors possessing a non-H substituent on their aryl moieties.

A number of literature precedents and experimental observations have allowed us to rationalize the transformation of hydroxylamines into imines via a nucleophilic attack on the in-situ generated acetonitrile adduct. A DFT analysis of a model reaction has also provided support

for this scenario. It should be noted, however, that an alternative radical pathway cannot be ruled out for the formation of the imine adduct **7b** as a minor side-product (2-20%) when precursor **3** was treated with Et_2NOH in CH_2Cl_2, toluene, or C_6D_6.

Other aspects of the observed reactivities with hydroxylamines that still remain obscure include (a) the decisive impact of the aryl substituent in our Ni precursors controlling the formation of **5b/5c** vs. the imine adducts, and (b) the strong influence of the hydroxylamine substituent R'' favoring the formation of **5b** vs **5c**. Future studies will aim to improve our understanding of the reactivities of hydroxylamines with our cyclonickelated precursors.

2.6   Associated content

Supporting Information. Synthetic procedures, NMR Spectra, single crystal structure data and additional figures, PXRD diffraction diagrams, a summary of the structural analyses to rationalize the unusually downfield chemical shits observed in the ^{1}H NMR spectra of complexes **6c** and **7c**, and a summary of the DFT analysis.

2.7   Author information

1. **Corresponding Author**

* E-mail: zargarian.davit@umontreal.ca

CONFLICTS OF INTERES

The authors declare no conflict of interest

2.8   Acknowledgement

Chapter −2− Supporting Information

S2.1 General experimental considerations

All manipulations were carried out under a nitrogen atmosphere using standard Schlenk techniques and an inert-atmosphere box. Solvents were dried by passage over a column of activated alumina, collected under nitrogen, and stored over 3 Å molecular sieves inside transfer/storage flasks equipped with high vacuum valves (Straus flasks). Et_3N was dried over CaH_2. The Ni^{II} precursor $[(i\text{-PrCN})NiBr_2]_n$ used throughout this study was prepared as reported previously.[12,13] The dimeric precursors **1-3** were prepared using a published procedure.[11] Other reagents were purchased from Sigma-Aldrich or FisherSci and used without further purification.

The NMR spectra were recorded at 400 MHz (^1H), 125.72 MHz (^{13}C), and 202.4 MHz (^{31}P). Chemical shift values are reported in ppm (δ) and referenced internally to the residual solvent signals (^1H and ^{13}C: 1.94 and 118.26 ppm for CD_3CN; 7.26 and 77.16 for $CDCl_3$; 7.16 and 128.06 for C_6D_6) or externally (^{31}P: H_3PO_4 in D_2O, $\delta = 0$). The minimal precision of the NMR spectra was found to be 0.3 Hz for ^1H, 0.7 Hz for ^{13}C and 2 Hz for ^{31}P.

Single crystals of all the structurally characterized complexes were grown from Et_2O solutions cooled to -35 °C. The crystallographic data for all structures were collected on either a Bruker Microsource (Cu radiation) or a Bruker Venture Metaljet (Ga radiation) via the Bruker APEX II or APEX III[45] software packages. Cell refinement and data reduction were performed using SAINT.[46] An empirical absorption correction, based on multiple measurements of equivalent reflections, was applied using the program SADABS or TWINABS.[47] The space group was confirmed by the XPREP[48] routine in APEX. The structures were solved in OLEX[49] using the SHELX[50] suite and refined by full-matrix least squares with SHEXL.[51] All non-hydrogen atoms were refined with anisotropic displacement parameters, whereas hydrogen atoms were set in calculated positions and refined via the riding model, with thermal parameters being 1.5 times that of the carbon bearing the H in question. All Thermal ellipsoid plots were drawn using OLEX.

S2.2 Procedures for the synthesis of the new phosphinite ligand and the Ni complexes

3-NMe$_2$-C$_6$H$_4$OP(*i*-Pr)$_2$. A 100 mL Schlenk flask was charged with Et$_3$N (1.252 mL, 8.975 mmol, 1.2 equiv) and 3-NMe$_2$-C$_6$H$_4$OH (1.026 mL, 7.479 mmol, 1 equiv) dissolved in 35 mL THF. Dropwise addition of ClP(*i*-Pr)$_2$ (1.190 mL, 7.479 mmol, 1 equiv) to this solution led to salt precipitation. The resulting mixture was stirred under inert atmosphere for 2 h at room temperature, followed by solvent evaporation and extraction of the residues with 3 × 25 mL Et$_2$O. Evaporation of the extracts afforded the target ligand as a dark oil (1.689 g, 6.667 mmol, 89 %). ^{1}H NMR (400 MHz, 20 °C, C$_6$D$_6$): δ 1.03 (dd, 6H, CH(C*H$_3$*), $^3J_{HH}$ = 7.2, $^3J_{HP}$ = 15.7), 1.20 (dd, 6H, CH(C*H$_3$*), $^3J_{HH}$ = 7.0, $^3J_{HP}$ = 10.4), 1.82 (dsept, 2H, C*H*(CH$_3$)$_2$, $^3J_{HH}$ = 7.1, $^2J_{HP}$ = 2.7), 2.52 (s, 6H, N(C*H$_3$*), 6.30 (m, 1H, C$_{Ar}$-*H*, $^3J_{HH}$ = 8.3, $^4J_{HP}$ = 2.5, $^4J_{HH}$ = 0.5), 6.76 (psq, 1H, C$_{Ar}$-*H*, $^4J_{HH}$ = 2.3), 6.87 (psdtd, 1H, C4$_{Ar}$-H, $^3J_{HH}$ = 8.1, J = 2.3, J = 0.8), 7.15 (t, 1H, C$_{Ar}$-*H*, $^3J_{HH}$ = 8.1). ^{13}C{^{1}H} NMR (125.72 MHz, 20 °C, C$_6$D$_6$): δ 17.26 (d, $^2J_{PC}$ = 8.7, *C*H$_3$), 17.99 (d, $^2J_{PC}$ = 20.7, *C*H$_3$), 28.65 (d, J_{PC} = 18.4, *C*H), 40.21 (s, N*C*H$_3$), 103.48 (d, J_{PC} = 10.3, C$_{Ar}$), 106.85 (d, J_{PC} = 0.8, C$_{Ar}$), 107.15 (d, J_{PC} = 12.0, C$_{Ar}$), 130.03 (s, C$_{Ar}$), 152.38 (s, C$_{Ar}$), 161.01 (d, $^2J_{PC}$ = 8.8, C1$_{Ar}$). ^{31}P{^{1}H} NMR (202.4 MHz, 20 °C, CDCl$_3$): 143.87 (s, 1P).

[{κ^P,κ^C-(*i*-Pr)$_2$PO-(5-NMe$_2$-C$_6$H$_3$)}Ni(μ-Br)]$_2$ (4'). A 100 mL Schlenk flask was charged with a solution of the ligand 3-NMe$_2$-C$_6$H$_4$OP(*i*-Pr)$_2$ (984 mg, 3.882 mmol, 1.00 equiv) in 40 mL MeCN, {(*i*-PrCN)NiBr$_2$}$_n$ (1.340 g, 4.658 mmol, 1.2 equiv), and Et$_3$N (471 mg, 4.658 mmol, 1.2 equiv). The mixture was stirred at room temperature overnight. Evaporation of the solvent, followed by extraction with toluene (3 × 20 mL) and evaporation of the volatiles gave a viscous material. This was dissolved in minimum amount of Et$_2$O and then hexane was added to precipitate the desired dimer. Cannula filtration of the mixture and subsequent evaporation of the filtrate gave a solid residue (0.937 mg). NMR analysis of this solid showed that it contained both the desired dimer, **4**, and the new complex **4'**, the product of reprotonation at the aryl-Ni moiety. The ^{31}P{^{1}H} NMR (C$_6$D$_6$) spectrum showed a singlet at 196.7 assigned to **4** and two doublets at ca. 150 (d, 1P, J_{PP} = 323.0), 182 (d, 1P, J_{PP} = 323.1) assigned to **4'**. Based on the weight of the solid residue obtained from the reaction and the integration values of these signals, we estimate yields of 38% for **4** and 20% for **4'**. Several attempts at purification of this mixture by recrystallization resulted in the isolation of a small crop of crystals for complex **4'**, but we did not succeed in isolating pure samples of the desired dimer **4**. For this reason, the crude mixture generated from the reaction of {(*i*-PrCN)NiBr$_2$}$_n$ with the ligand was used for reactivity studies with hydroxy amines. The NMR

spectra of [{κ^P,κ^C-(i-Pr)$_2$PO-(5-NMe$_2$-C$_6$H$_3$)}{κ^P-(i-Pr)$_2$PO-(5-NMe$_2$-C$_6$H$_4$)}NiBr] (**4'**) are provided here. [^1]H NMR (400 MHz, 20 °C, CDCl$_3$): δ 1.38 (dd, 12H, CHCH_3, $^3J_{HH}$ = 7.2, $^3J_{HP}$ = 13.4), 1.46-1.54 (m, 12H), 2.59 (sextd, 2H, CH(CH$_3$)(CH$_3$), $^3J_{HP}$ = 7.1, $^3J_{HH}$ = 2.1), 2.78 (s, 6H, NCH_3), 2.79 (s, 6H, NCH_3), 2.80 (m, 2H, CH(CH$_3$)(CH$_3$)), 5.95 (dd, 1H, o-C$_6$H$_5$, $^3J_{HH}$ = 8.7, $^5J_{HH}$ = 2.4), 6.15 (d, 1H, o-C$_6$H$_5$, $^5J_{HH}$ = 2.8), 6.30 (dd, 1H, $^3J_{HH}$ = 8.2, $^5J_{HH}$ = 2.1), 6.78 (dt, 1H, p- or m-C$_6$H$_5$), 6.86 (ps q, 1H, C$_6$H$_5$), 7.01(t, 1H, p-C$_6$H$_5$, $^3J_{HH}$ = 8.1), 7.17 (dd, 1H, o-C$_6$H$_5$, $^3J_{HH}$ = 8.7, $^5J_{HH}$ = 0.7), 7.36 (s, 1H). ^{13}C{^{1}H} NMR (125.72 MHz, 20 °C, CDCl$_3$): δ 17.28 (s, CH$_3$), 18.02 (s, CH$_3$), 19.01(d, CH$_3$, J_{CP} = 3.7), 20.47 (d, CH$_3$, J_{CP} = 4.7), 28.58 (d, PCH, J_{CP} = 2.7), 28.82 (d, PCH, J_{CP} = 2.7), 29.76 (d, PCH, J_{CP} = 3.1), 29.93 (d, PCH, J_{CP} = 3.1), 40.63(d, J_{CP} = 12.7), 95.72 (d, J_{CP} = 14.1), 105.23 (d, C_{Ar}, J_{CP} = 6.4), 106.36, 107.08, 108.73 (d, C_{Ar}, J_{CP} = 5.2) 128.49, 129.26, 142.80 (d, J_{CP} = 12.3, C_{Ar}), 150.38, 151.59, 155.80 (d, J_{CP} = 5.2, C_{Ar}), 169.38, 169.56. ^{31}P{^{1}H} NMR (202.4 MHz, 20 °C, CDCl$_3$): 150.27 (d, 1P, J_{PP} = 323.0), 182.46 (d, 1P, J_{PP} = 323.1).

[{κ^P,κ^C-(i-Pr)$_2$PO-C$_6$H$_4$}{NH$_2$OBn}Ni(Cl/Br)] (**5a-Cl** and **5a-Br;** Bn= CH$_2$Ph). A 50 mL Schlenk flask containing 10 mL MeCN was charged with O-benzylhydroxylamine hydrochloride (76 mg, 0.476 mmol, 4 equiv) and Et$_3$N (48 mg, 0.476 mmol, 4 equiv). The resulting mixture was stirred for 45 min under inert atmosphere and at room temperature. To this mixture was added the dimer [{κ^P,κ^C-(i-Pr)$_2$PO-C$_6$H$_4$}Ni(μ-Br)]$_2$ (**1**, 83 mg, 0.119 mmol, 1 equiv) and the stirring was continued overnight under the same condition. Removal of volatiles under vacuum left a sticky, brown residue, which was treated with ca. 1 mL of Et$_2$O, filtered and the filtrate kept at -35 °C overnight. Brown crystals were separated and washed with cold hexane. (Yield: 37 mg, 0.086 mmol 35 %). ^{1}H NMR (400 MHz, 20 °C, CDCl$_3$): δ 1.36 (dd, 6H, CHCH_3, $^3J_{HH}$ = 7.0, $^3J_{HP}$ = 14.7), 1.52 (dd, 6H, CHCH_3, $^3J_{HH}$ = 7.2, $^3J_{HP}$ = 17.7), 2.36 (psoct, 2H, CHCH$_3$, $^3J_{HH}$ ≈ $^3J_{HP}$ = 7.1), 5.35 (br s, 2H, OCH_2), 6.06 (br s, 2H, NH_2), 6.68 (d, 1H, C3/6-H, $^3J_{HH}$ = 7.8), 6.73 (t, 1H, C4/5-H, $^3J_{HH}$ = 7.3), 7.02 (t, 1H, C4/5-H, $^3J_{HH}$ = 7.4), 7.10 (d, 1H, C3/6-H, $^3J_{HH}$ = 7.6). ^{13}C{^{1}H} NMR (125.72 MHz, 20 °C, CDCl$_3$): δ 17.00 (s, CH$_3$), 18.14 (d, $^2J_{PC}$ = 3.7, CH$_3$), 28.14 (s, P-CH), 28.40 (s, P-CH), 78.74 (s, CH$_2$), 110.70 (d, $^2J_{PC}$ =13, 1C, $C$2), 121.21 (d, J_{PC} = 2.05, 1C, $C$4/5), 127.20 (s, 1C, $C$4/5), 128.94 (s, 2C, C_{Ar}), 129.21 (s, 1C, C_{Ar}), 129.45 (s, 2C, C_{Ar}), 134.63 (s, 1C, C_{Ar}), 136.25 (br, 1C, $C$3/6), 167.91 (d, J_{PC} = 11.5, 1C, C1$_{Ar}$) . The spectrum does not display the anticipated signals for two quaternary aromatic carbons. ^{31}P{^{1}H} NMR (202.4 MHz, 20 °C, CDCl$_3$): 195.19 (**5a-Cl,** 87%), 198.25 (**5a-Br,** 13%).

[{κ^P,κ^C-(i-Pr)₂PO-C₆H₄}{κ^N-Et₂NOH}NiBr] (5b). A 50 mL Schlenk flask containing 5 mL of CH₂Cl₂ was charged with the parent dimer [{κ^P,κ^C-(i-Pr)₂PO-C₆H₄}Ni(μ-Br)]₂ (**1**, 100 mg, 0.134 mmol, 1.00 equiv) and Et₂NOH (0.024 mg, 0.268 mmol, 2.00 equiv). The solution was stirred overnight at room temperature and under inert atmosphere. Removal of volatiles under vacuum left a sticky, brown residue, which was treated with ca. 1 mL of Et₂O, filtered and the filtrate kept at -35 °C overnight. Brown crystals were separated and washed with cold hexane. (Yield: 0.049 mg, 41 %). ¹H NMR (400 MHz, 20 °C, C₆D₆): δ 1.05 (t, 6H, NCH₂CH_3, $^3J_{HH}$ = 7.2), 1.24 (dd, 6H, CHCH_3, $^3J_{HH}$ = 7.0, $^3J_{HP}$ = 14.2), 1.55 (dd, 6H, CHCH_3, $^3J_{HH}$ = 7.2, $^3J_{HP}$ = 17.0), 2.15-2.27 (m, 4H, overlap of NCH_2 and PCH), 2.31-2.41 (m, 2H, NCH_2), 6.89 (dd, 1H, C3/6$_{Ar}$-H, $^3J_{HH}$ = 7.7, $^4J_{HH}$ = 1.4), 6.99 (tdd, 1H, C4/5$_{Ar}$-H, $^3J_{HH}$ = 7.5, $^4J_{HH}$ = 1.7, $^5J_{HP}$ = 1.3), 7.08 (tdd, 1H, C4/5$_{Ar}$-H, $^3J_{HH}$ = 7.4, $^4J_{HH}$ = 2.0, $^6J_{HP}$ = 1.6), 7.85 (dt, 1H, C3/6$_{Ar}$-H, $^3J_{HH}$ = 7.7, $^4J_{HP} \approx$ $^4J_{HH}$ = 1.8), 9.02 (s, 1H, OH). ¹³C{¹H} NMR (125.72 MHz, 20 °C, C₆D₆): δ 9.24 (s, NCH₂CH₃), 17.12 (d, $^2J_{PC}$ = 1.6, PCHCH₃), 18.63 (d, $^2J_{PC}$ = 3.9, PCHCH₃), 28.80 (d, J_{PC} = 26.3, PCH), 53.99 (s, NCH₂), 110.01 (d, J_{PC} = 13.09), 120.39 (d, J = 2.3), 126.71 (s), 134.01 (d, J = 36.3), 135.02 (d, J = 3.9), 167.60 (d, $^2J_{PC}$ = 13.3, $C$1). ³¹P{¹H} NMR (202.4 MHz, 20 °C, C₆D₆): 201.52 (s, 1P).

[{PhOP(i-Pr)₂}{κ^O,κ^N-ON(Bn)₂}NiBr] (5c). A 50 mL Schlenk flask containing 5 mL of CH₂Cl₂ was charged with the parent dimer [{κ^P,κ^C-(i-Pr)₂PO-C₆H₄}Ni(μ-Br)]₂ (**1**, 100 mg, 0.144 mmol, 1.00 equiv) and *N,N*-dibenzylhydroxylamine (61 mg, 0.287 mmol, 2.00 equiv). The solution was stirred overnight at room temperature and under inert atmosphere. Removal of volatiles under vacuum left a sticky, red residue, which was treated with ca. 1 mL of Et₂O, filtered and the filtrate kept at -35 °C overnight. Dark red crystals were separated and washed with cold hexane. (Yield: 77 mg, 0.138 mmol 55 %). ¹H NMR (400 MHz, 20 °C, C₆D₆): δ 1.02 (dd, 6H, CHCH_3, $^3J_{HH}$ = 7.1, $^3J_{HP}$ = 14.6), 1.19 (dd, 6H, CHCH_3, $^3J_{HH}$ = 17.1, $^3J_{HP}$ = 7.1), 2.00 (psoct, 2H, PCH, $^3J_{HH}$ = 7.1), 3.43 (dd, 2H, NCH_2, $^2J_{HH}$ = 13.2, $^4J_{HP}$ = 6.3), 4.07 (dd, 2H, NCH_2, $^2J_{HH}$ = 13.0, $^4J_{HP}$ = 1.9), 6.90 (t, 1H, *p*-C$_{Ar}H$, $^3J_{HH}$ = 7.3), 7.20-7.10 (m, 8H, C$_{Ar}$-H), 7.42 (d, 2H, *o*- C$_{Ar}H$, $^3J_{HH}$ = 8.4), 7.47 (d, 4H, *o*-C$_{Ar}H$, $^3J_{HH}$ = 7.0). ¹³C{¹H} NMR (125.72 MHz, 20 °C, C₆D₆): δ 16.78 (s, 2C, CH₃), 17.62 (d, 2C, $^2J_{PC}$ = 5.5, CH₃), 28.79 (s, C, PCH), 29.02 (s, C, PCH), 63.40 (s, 2C, NCH₂), 121.21 (d, 2C, J = 4.9, C_{Ar}), 123.67 (s, 1C, C_{Ar}), 128.54 (s, 4C, C_{Ar}), 128.68 (s, 2C, C_{Ar}), 129.52 (s, 2C, C_{Ar}), 132.41 (s, 4C, C_{Ar}), 132.92 (s, 2C, C_{Ar}), 156.34 (d, $^2J_{PC}$ = 3.7, $C$1). ³¹P{¹H} NMR (202.4 MHz, 20 °C, C₆D₆): δ 173.31 (s, 1P).

[{κ^P,κ^C-(*i*-Pr)$_2$PO-(5-Cl-C$_6$H$_3$)}{κ^N-NH$_2$OBn}Ni(Cl/Br)] (6a-Cl and **6a-Br).** A 50 mL Schlenk flask containing 10 mL of CH$_2$Cl$_2$ was charged with O-benzylhydroxylamine hydrochloride (100 mg, 0.143 mmol, 1.0 equiv) and Et$_3$N (58 mg, 0.572 mmol, 4 equiv). The resulting mixture was stirred for 45 min under inert atmosphere at room temperature. To this mixture was added the dimer [{κ^P,κ^C-(*i*-Pr)$_2$PO-(5-Cl-C$_6$H$_3$)}Ni(μ-Br)]$_2$ (**2**, 91 mg, 0.119 mmol, 1 equiv) and was stirred overnight under same condition. Removal of volatiles under vacuum left a sticky, yellow residue, which was treated with ca. 1 mL of Et$_2$O, filtered and the filtrate kept at -35 °C overnight. Needle shaped yellow crystals were separated and washed with cold hexane. (Yield: 66 mg, 0.137 mmol, 49 %). ^{1}H and ^{13}C NMR data are provided for the bromo derivative only. ^{1}H NMR (400 MHz, 20 °C, C$_6$D$_6$): δ 1.12 (dd, 6H, CHCH_3, $^3J_{HH}$ = 6.9, $^3J_{HP}$ = 14.8), 1.43 (dd, 6H, CHCH_3, $^3J_{HH}$ = 7.1, $^3J_{HP}$ = 17.8), 2.17 (sept, 2H, CH(CH$_3$)(CH$_3$), $^3J_{HH}$ = 7.0), 4.94 (s, 2H, OCH_2), 5.19 (s, 2H, NH_2), 6.86 (d, 1H, C3-H, $^3J_{HH}$ = 7.7), 6.9 (br s, 2H, C$_{Ar}$-H), 7.07-7.02 (m, 3H, *p*- and *m*-C$_6$H$_5$), 7.12 (d, 1H, *o*-C$_6$H$_5$, $^3J_{HH}$ = 7.3). ^{13}C{^{1}H} NMR (125.72 MHz, 20 °C, C$_6$D$_6$): δ 16.77 (s, CH$_3$), 17.99 (s, CH$_3$), 18.37 (s, CH$_3$), 28.22 (s, PCH), 28.47 (s, PCH), 78.38, 111.43 (d, J_{CP} = 13.4, C_{Ar}), 121.30 28.23 (s, C_{Ar}), 128.59 (s, C_{Ar}), 128.86 (s, C_{Ar}), 129.05 (s, C_{Ar}), 129.44 (s, C_{Ar}), 132.73(s, C_{Ar}), 135.01(s, C_{Ar}), 137.45(s, C_{Ar}), 137.78 (br s, C_{Ar}). ^{31}P{^{1}H} NMR (202.4 MHz, 20 °C, C$_6$D$_6$): 195.59 (**6a-Cl**, 57%), 198.97 (**6a-Br**, 43%).

[{κ^P,κ^C-(*i*-Pr)$_2$PO-(5-Cl-C$_6$H$_3$)}{κ^N-(CH$_3$CH$_2$-)(CH$_3$CH=)N}Ni(Br)] (6b). A 50 mL Schlenk flask containing 10 mL MeCN was charged with the dimer [{κ^P,κ^C-(*i*-Pr)$_2$PO-(5-Cl-C$_6$H$_3$)}Ni(μ-Br)]$_2$ (**2**, 153 mg, 0.20 mmol, 1.00 equiv) and Et$_2$NOH (36 mg, 0.40 mmol, 2.00 equiv). The solution was stirred overnight at room temperature and under inert atmosphere. Removal of volatiles under vacuum left a sticky, brown residue, which was treated with ca. 1 mL of Et$_2$O, filtered and the filtrate kept at -35 °C overnight. Brown crystals were separated and washed with cold hexane. (Yield: 49 mg, 0.11 mmol, 27 %). ^{1}H NMR (400 MHz, 20 °C, C$_6$D$_6$): δ 1.12 (dd, 3H, $^3J_{HH}$ =7.0, $^3J_{HP}$ = 14, CHCH_3), 1.19 (dd, 3H, $^3J_{HH}$ =7.0, $^3J_{HP}$ = 14, CHCH_3), 1.40 (t, 3H, $^3J_{HH}$ = 7.4, NCH$_2$CH_3), 1.47 (dd, 3H, CHCH_3, $^3J_{HH}$ = 7.2, $^3J_{HP}$= 17.0), 1.51 (dd, 3H, CHCH_3, $^3J_{HH}$ = 7.2, $^3J_{HP}$= 17.0), 2.19 (d, 3H, NCHCH_3, $^3J_{HH}$= 5.1), 2.28 (psoct, 2H, CHCH$_3$, $^3J_{HH}$ = 7.1), 3.14 (sext, 1H, NCH_2, $^3J_{HH}$ = 6.9), 3.75 (sextd, 1H, NCH_2, $^3J_{HH}$ =7.5, $^4J_{Hp}$ = 1.5), 6.18 (dd, 1H, C3-H, $^3J_{HH}$ = 8.1, J_{HP} = 0.7), 6.49-6.55 (m, 1H, NCH), 6.80 (ddd, 1H, C4-H, $^3J_{HH}$ =8.2, $^4J_{HH}$ = 2.0, $^6J_{HP}$ =0.9), 6.92 (d, 1H, C6-H, $^4J_{HH}$ =2.1). ^{13}C{^{1}H} NMR (125.72 MHz, 20 °C, C$_6$D$_6$): δ 15.72 (s, 1C, NCH$_2$$CH_3$), 16.80 (d, 1C, $^2J_{PC}$ = 2.4, PCHCH$_3$), 17.00 (d, 1C, $^2J_{PC}$ = 1.8, PCHCH$_3$), 18.56 (d, 1C,

$^2J_{PC}$ = 1.4, PCHCH_3), 18.60 (d, 1C, $^2J_{PC}$ = 1.5, PCHCH_3) , 23.47 (s, 1C, NCHCH_3), 28.62 (d, 1C, $^1J_{PC}$ = 12.4, PCH), 28.89 (d, 1C, $^1J_{PC}$ = 11.7, PCH), 56.43 (s, 1C, NCH_2), 111.45 (d, 1C, $^2J_{PC}$ = 13.2, $C$2), 121.00 (d, J_{PC} = 2.2, C_{Ar}), 127.55 (s, C_{Ar}), 138.07 (d, 1C, J_{PC} = 2.6, C_{Ar}), 166.34 (s, 1C, NCH) . ^{31}P{^{1}H} NMR (202.4 MHz, 20 °C, C_6D_6): δ 195.50 (s, 1P).

[{κ^P,κ^C-(i-Pr)$_2$PO-(5-Cl-C$_6$H$_3$)}{κ^N-(PhCH$_2$-)(PhCH=)N}Ni(Br)] (6c). A 50 mL Schlenk flask containing 10 mL MeCN was charged with dimer [{κ^P,κ^C-(i-Pr)$_2$PO-(5-Cl-C$_6$H$_3$)}Ni(μ-Br)]$_2$ (153 mg, 0.20 mmol, 1.00 equiv) and Bn$_2$NOH (85 mg, 0.40 mmol, 2.00 equiv). The solution was stirred overnight at room temperature and under inert atmosphere. Removal of volatiles under vacuum left a sticky, yellow residue, which was treated with ca. 1 mL of Et$_2$O, filtered and the filtrate kept at -35 °C overnight. Yellow crystals were separated and washed with cold hexane. (Yield: 133 mg, 0.27 mmol, 57 %). ^{1}H NMR (400 MHz, 20 °C, C$_6$D$_6$): δ 1.20 (dd, 3H, $^3J_{HH}$ = 7.0, $^3J_{HP}$ = 14.4, CHCH_3), 1.24 (dd, 3H, $^3J_{HH}$ = 7.0, $^3J_{HP}$ = 15.2, CHCH_3), 1.50 (dd, 3H, CHCH_3, $^3J_{HH}$ = 7.2, $^3J_{HP}$ = 17.0), 1.62 (dd, 3H, CHCH_3, $^3J_{HH}$ = 7.2, $^3J_{HP}$ = 17.5), 2.24 (psoct, 1H, CHCH$_3$, $^3J_{HH}$ = $^3J_{HP}$ =7.0), 2.45 (psoct, 1H, CHCH$_3$, $^3J_{HH}$ = $^3J_{HP}$ =7.0), 5.30 (dd, 1H, NCH_2, $^2J_{HH}$ = 15.6, $^4J_{HP}$ =1.5), 5.75 (d, 1H, NCH_2, $^2J_{HH}$ = 15.7), 6.37 (dd, 1H, C3-H, $^3J_{HH}$ = 8.2, J_{HP} = 0.8), 6.60 (ddd, 1H, C4-H, $^3J_{HH}$ = 8.2, $^4J_{HH}$ = 2.1 ,J_{HP} =0.9), 6.61 (d, 1H, C6-H, $^4J_{HH}$ = 2.1), 7.10-7.1 (m, 6H, (p- and m-Ph)$_2$), 7.21-7.24 (m, 2H, Ph), 7.80 (d, 1H, NCH, $^4J_{HP}$ = 8.7), 8.82 (d, 2H, CH-$ortho$-Ph, $^3J_{HH}$ = 7.1). ^{13}C{^{1}H} NMR (125.72 MHz, 20 °C, C$_6$D$_6$): δ 16.79 (d, 1C, $^2J_{CP}$ = 2.5, PCHCH_3), 17.12 (s, 1C, PCHCH_3), 18.42 (d, 1C, $^2J_{CP}$ = 3.3, PCHCH_3), 18.94 (d, 1C, $^2J_{CP}$ = 3.0, PCHCH_3), 28.55 (d, 1C, J_{CP} = 20.6, PCH), 28.82 (d, 1C, J_{CP} = 23.2, PCH), 63.46 (s, 1C, NCH_2), 111.42 (d, 1C, $^2J_{PC}$ = 13.2, $C$2), 121.44 (d, 1C, J_{PC} = 2.0, C_{Ar}), 128.43 (s, 2C, Ph), 128.69 (s, 1C, Ph), 129.18 (s, 2C, Ph), 131.27 (s, 2C, Ph), 131.75 (s, 2C, Ph), 131.8 (s, 1C, Ph), 132.11 (s, 1C, Ph), 132.21 (s, 1C, C_{Ar} or Ph), 133.81 (d, 1C, J_{PC} = 1.5, C_{Ar}), 134.73 (s, 1C, C_{Ar} or Ph), 137.75 (d, 1C, J_{PC} = 2.5, C_{Ar}), 166.52 (s, 1C, NCH), 168.03 (d, $^2J_{CP}$ = 14.1, 1C, $C$1). ^{31}P{^{1}H} NMR (202.4 MHz, 20 °C, C$_6$D$_6$): δ 196.32 (s, 1P).

[{κ^P,κ^C-(i-Pr)$_2$PO-(5-OMe-C$_6$H$_3$)}{κ^N-NH$_2$OBn}Ni(Cl/Br)] (7a-Cl and **7a-Br):** A 50 mL Schlenk flask containing 10 mL CH$_2$Cl$_2$ was charged with O-benzylhydroxylamine hydrochloride (55 mg, 0.344 mmol, 2.5 equiv) and Et$_3$N (35 mg, 0.344 mmol, 2.5 equiv). The resulting mixture was stirred for 45 min under inert atmosphere at room temperature. To this mixture was added the dimer [**3**, {κ^P,κ^C-(i-Pr)$_2$PO-(5-OMe-C$_6$H$_3$)}Ni(μ-Br)]$_2$ (104 mg, 0.138 mmol, 1.0 equiv) and was stirred overnight under same condition. Removal of volatiles under vacuum left a sticky, brown

residue, which was treated with ca. 1 mL of Et$_2$O, filtered and the filtrate kept at -35 $^\circ$C overnight. Very fine brown crystals were separated and washed with cold hexane. (Yield: 52 mg, 0.11 mmol, 40%). ^{1}H and ^{13}C NMR data are provided for the chloro derivative only. ^{1}H NMR (400 MHz, 20 $^\circ$C, C$_6$D$_6$): δ 1.22 (dd, 6H, CHCH_3, $^3J_{HH}$ = 7.0, $^3J_{HP}$ = 14.5), 1.52 (dd, 6H, CHCH_3, $^3J_{HH}$ = 7.2, $^3J_{HP}$ = 17.6), 2.20-2.23 (m, 2H, CHCH$_3$), 3.35 (s, 3H, OCH_3), 5.16 (br s, 2H, OCH_2), 5.46 (br s, 2H, NH_2), 6.56 (dd, 1H, C3-H, $^3J_{HH}$ = 7.8, $^4J_{HP}$ = 1.9), 6.62 (br s, 1H, C6-H), 7.01-7.09 (m, 4H, C$_{Ar}$-H), 7.22 (d, 2H, O-C$_{Ar}$-H, $^3J_{HH}$ = 7.8). ^{13}C{^{1}H} NMR (125.72 MHz, 20 $^\circ$C, C$_6$D$_6$): δ 16.89 (s, CH$_3$), 18.12 (d, $^2J_{PC}$ = 2.7, CH$_3$), 28.17 (s, P-CH), 28.43 (s, P-CH), 54.81 (s, OCH$_3$), 78.38 (s, CH$_2$), 97.84 (d, $^2J_{PC}$ =14.2, 1C, $C$6), 107.72 (d, J_{PC} = 2.05, 1C, $C$3), 128.59 (s, 1C, C_{Ar}), 128.79 (s, 2C, C_{Ar}), 128.88 (s, 1C, C_{Ar}), 129.51 (s, 2C, C_{Ar}), 135.40 (s, 1C, C_{Ar}), 160.74 (s, 1C, C_{Ar}). ^{31}P{^{1}H} NMR (202.4 MHz, 20 $^\circ$C, C$_6$D$_6$): δ 193. 59 (**7a-Cl**, 70%), 197.12 59 (**7a-Br**, 30%).

[{κ^P,κ^C-(i-Pr)$_2$PO-(5-OMe-C$_6$H$_3$)}{κ^N-(CH$_3$CH$_2$-)(CH$_3$CH=)N}Ni(Br)] (7b). A 50 mL Schlenk flask containing 10 mL MeCN was charged with the dimer [{κ^P,κ^C-(i-Pr)$_2$PO-(5-OMe-C$_6$H$_3$)}Ni(μ-Br)]$_2$ (**3**, 204 mg, 0.269 mmol, 1.00 equiv) and Et$_2$NOH (48 mg, 0.54 mmol, 2.00 equiv). The solution was stirred overnight at room temperature and under inert atmosphere. Removal of volatiles under vacuum left a sticky, brown residue, which was treated with ca. 1 mL of Et$_2$O, filtered and the filtrate kept at -35 $^\circ$C overnight. Brown crystals were separated and washed with cold hexane. (Yield: 124 mg, 50 %). ^{1}H NMR (400 MHz, 20 $^\circ$C, C$_6$D$_6$): δ 1.23 (dd, 3H, CHCH_3, $^3J_{HH}$ = 7.0, $^3J_{HH}$ = 14.6), 1. 29 (dd, 3H, CHCH_3, $^3J_{HH}$ = 7.0, $^3J_{HH}$ = 14.6), 1. 49 (t, 3H, CH$_2$CH_3, $^3J_{HH}$ = 7.4), 1. 56 (dd, 3H, CHCH_3, $^3J_{HH}$ = 7.2, $^3J_{HH}$ = 15.4), 1. 60 (dd, 3H, CHCH_3, $^3J_{HH}$ = 7.2, $^3J_{HH}$ = 15.4), 2.31 (d, 3H, NCHCH_3, $^3J_{HH}$ = 4.9), 2.33-2.43 (m, 2H, PCHCH$_3$), 3.23-3.30 (m, 1H, NCH_2), 3.35 (s, 3H, OCH_3), 3.80-3.90 (m, 1H, NCH_2), 6.28 (dd, 1H, C3$_{Ar}$-H, $^3J_{HH}$ = 8.4, $^4J_{HP}$ = 0.8), 6.5 (ddd, 1H,C4$_{Ar}$-H, $^3J_{HH}$ = 8.4, $^3J_{HH}$ = 2.6, $^3J_{HH}$ = 0.9), 6.61 (d, 1H, C6$_{Ar}$-H, $^4J_{HP}$ = 2.2 $\approx$ $^4J_{HH}$ =2.2), 6.63-6.67 (m, 1H, NCH). ^{13}C{^{1}H} NMR (125.72 MHz, 20 $^\circ$C, C$_6$D$_6$): δ 15.83 (s, 1C, NCH$_2$$CH_3$), 16.95 (d, 1C, $^2J_{PC}$ = 1.8, PCHCH$_3$), 17.14 (d, 1C, $^2J_{PC}$ = 1.2, PCHCH$_3$), 18.71 (d, 1C, $^2J_{PC}$ = 1.5, PCHCH$_3$), 18.74 (d, 1C, $^2J_{PC}$ = 1.8, PCHCH$_3$) , 23.61 (s, 1C, NCHCH$_3$), 28.56 (d, 1C, $^1J_{PC}$ = 12.7, PCH), 28.83 (d, 1C, $^1J_{PC}$ = 12.0, PCH), 54.80 (s, 1C, OCH$_3$), 56.56 (s, 1C, NCH$_2$), 97.55 (d, 1C, $^3J_{PC}$ = 13.9, $C$6), 107.68 (d, 1C, $^4J_{PC}$ = 2.0, $C$4), 122.79 (d, 1C, J_{PC} = 33.6, C_{Ar}), 137.47 (d, 1C, $^3J_{PC}$ = 2.7, C3$_{Ar}$), 160.33 (s, 1C, C_{Ar}), 165.95 (s, 1C, NCH), 168.55 (d, 1C, J_{PC} = 14.9, $C$1). ^{31}P{^{1}H} NMR (202.4 MHz, 20 $^\circ$C, C$_6$D$_6$): δ 193.84 (s, 1P).

[{κ^P,κ^C-(i-Pr)₂PO-(5-OMe-C₆H₃)}{κ^N-(PhCH₂-)(PhCH=)N}Ni(Br)] (7c). A 50 mL Schlenk flask containing 10 mL MeCN was charged with the dimer [{κ^P,κ^C-(i-Pr)₂PO-(5-OMe-C₆H₃)}Ni(μ-Br)]₂ (**3**, 200 mg, 0.265 mmol, 1.00 equiv) and Bn₂NOH (113 mg, 0.529 mmol, 2.00 equiv). The solution was stirred overnight at room temperature and under inert atmosphere. Removal of volatiles under vacuum left a sticky, yellow residue, which was treated with ca. 1 mL of Et₂O, filtered and the filtrate kept at -35 °C overnight. Yellow crystals were separated and washed with cold hexane. (Yield: 144 mg, 0.25 mmol, 46 %). ^{1}H NMR (400 MHz, 20 °C, C₆D₆): δ 1.30 (dd, 3H, CHCH_3, $^3J_{HH}$ = 7.0 ,$^3J_{HP}$ = 14.3), 1.34 (dd, 3H, CHCH_3, $^3J_{HH}$ = 7.0 ,$^3J_{HP}$ = 14.9) 1.58 (dd, 3H, CHCH_3, $^3J_{HH}$ = 7.2, $^3J_{HP}$ = 16.9), 1.71 (dd, 3H, CHCH_3, $^3J_{HH}$ = 7.2, $^3J_{HP}$ = 17.3), 2.34 (psoct, 1H, PCH, $^3J_{HH}$ = 7.2), 2.53 (oct, 1H, PCH, $^3J_{HH}$ = 6.9), 3.27 (s, 3H, OCH_3), 5.41 (d, 1H, NCH_2, $^2J_{HH}$ = 15.8), 5.93 (d, 1H, NCH_2, $^2J_{HH}$ = 15.8), 6.30 (dd, 1H, C3$_{Ar}$-H, $^3J_{HH}$ = 8.4, $^4J_{HP}$ = 2.0), 6.48 (d, 1H, C4$_{Ar}$-H, $^3J_{HH}$ = 8.4), 6.61 (d, 1H, C6$_{Ar}$-H, $^4J_{HP}$ = 2.5 ≈ $^4J_{HH}$ = 2.5), 7.10-7.13 (m, 6H, (p- and m-Ph)₂), 7.28 (d, 2H, o-Ph, J_{HH} = 8.0), 7.86 (d, 1H, NCH, $^4J_{HP}$ = 8.6), 8.93 (d, 2H, o-Ph, $^3J_{HH}$ = 8.1). ^{13}C{^{1}H} NMR (125.72 MHz, 20 °C, C₆D₆): δ 16.92 (d, 1C, $^2J_{CP}$ = 2.5, PCHCH_3), 17.24 (s, 1C, PCHCH_3), 18.55 (d, 1C, $^2J_{CP}$ = 3.5, PCHCH_3), 19.07 (d, 1C, $^2J_{CP}$ = 3.2, PCHCH_3), 28.50 (d, 1C, J_{CP} = 17.2, PCH), 28.77 (d, 1C, J_{CP} = 19.8, PCH), 54.72 (s, 1C, OCH_3), 63.37 (s, 1C, NCH_2), 96.81 (d, 1C, $^3J_{PC}$ = 13.8, $C$6), 107.87 (d, 1C, $^3J_{PC}$ = 1.2, $C$3), 122.77 (d, 1C, J_{PC} = 33.2, C_{Ar}), 128.39 (s, 2C, Ph), 128.59 (s, 1C, Ph), 129.17 (s, 2C, Ph), 131.36 (s, 2C, Ph), 131.88 (s, 2C, C_{Ar}), 131.93 (s, 1C, C_{Ar}), 137.05 (d, 1C, J_{PC} = 2.7, C4$_{Ar}$), 160.31 (s, 1C, C_{Ar}), 166.12 (s, 1C, NCH), 168.38 (d, 1C, J_{PC} = 14.4, C_{Ar}). ^{31}P{^{1}H} NMR (202.4 MHz, 20 °C, C₆D₆): δ 194.94 (s, 1P).

[{κ^P, κ^C-(i-Pr)₂PO-(5-OMe-C₆H₄}{κ^N-Et₂NH}NiBr] (7d). A 50 mL Schlenk flask containing 10 mL toluene was charged with the dimer [{κ^P,κ^C-(i-Pr)₂PO-(OMe-C₆H₃}Ni(μ-Br)]₂ (**1**, 100 mg, 0.132 mmol, 1 equiv) and Et₂NH (0.019 mg, 0.264 mmol, 2 equiv). The solution was stirred overnight at room temperature and under inert atmosphere. Removal of volatiles under vacuum left a sticky, brown residue, which was treated with ca. 1 mL of Et₂O, filtered and the filtrate kept at -35 °C overnight. Brown crystals were separated and washed with cold hexane. (Yield: 53 mg, 44 %). ^{1}H NMR (400 MHz, 20 °C, C₆D₆): δ 1.22 (dd, 6H, CHCH_3, $^3J_{HP}$ = 14.5, $^3J_{HH}$ = 7.0), 1.43(t, 6H, CH₂CH_3, $^3J_{HH}$ = 6.7), 1.54 (dd, 6H, CHCH_3, $^3J_{HP}$ = 17.0, $^3J_{HH}$ = 7.2), 2.13 (br s, 3H, overlap of NCH_2 and NH), 2.34 (psoct, 2H, PCH), 3.22 (br s, CH_2), 3.36 (s, OCH_3), 6.38 (d, 1H,C3$_{Ar}$-H, $^3J_{HH}$ = 7.7), 6.55 (d, 1H, C4$_{Ar}$-H, $^3J_{HH}$ = 8.0), 6.60 (d, 1H, C6$_{Ar}$-H, $^3J_{HH}$ = 2.5). ^{13}C{^{1}H} NMR (125.72 MHz, 20 °C, C₆D₆): δ 15.30 (s, 2C, NCH₂CH_3), 17.07 (d, 2C, $^2J_{PC}$ = 1.7, PCHCH_3), 18.78

(d, 2C, $^2J_{PC}$ = 3.2, PCHCH_3), 28.85 (s, 1C, PCH), 29.12 (s, 1C, PCH), 46.57 (d, 2C, $^2J_{PC}$ = 1.4, NCH_2), 54.75 (s, 1C, OCH_3), 97.80 (d, 1C, $^3J_{PC}$ = 13.6, $C$6), 107.52 (d, 1C, $^4J_{PC}$ = 2.1, $C$4), 122.21 (d, 1C, $^2J_{PC}$ = 34.5, $C$2/1), 134.60 (d, 1C, $^2J_{PC}$ = 3.1, $C$3), 160.26 (d, 1C, $^2J_{PC}$ =1.0, C_{Ar}), 168.55 (d, 1C, $^2J_{PC}$ = 14.9, $C$1). ^{31}P{^{1}H} NMR (202.4 MHz, 20 °C, C_6D_6): 192.64 (s, 1P).

[{κ^P,κ^C-(*i*-Pr)$_2$PO-(5-NMe$_2$-C$_6$H$_3$)}(κ^N-H$_2$NOBn)Ni(Cl/Br)] (**8a-Cl** and **8a-Br**). A 50 mL Schlenk flask containing 25 mL MeCN was charged with a solution of the proligand 3-NMe$_2$-C$_6$H$_4$OP(*i*-Pr)$_2$ (157 mg, 0.619 mmol, 1.00 equiv), {(*i*-PrCN)NiBr$_2$}$_n$ (214 mg, 0.744 mmol, 1.2 equiv), and Et$_3$N (75 mg, 0.744 mmol, 2 equiv). The mixture was stirred at room temperature overnight. In a separate 8 mL vial, O-benzylhydroxylamine hydrochloride (198 mg, 1.239 mmol, 2 equiv) and Et$_3$N (125 mg, 1.239 mmol, 2 equiv) were dissolved in 5 ml of MeCN, stirred for 45 min and then added to the 50 mL flask. The resulting mixture was again stirred overnight at room temperature. Removal of volatiles under vacuum left a sticky, brown residue, which was treated with ca. 2 mL of Et$_2$O, filtered and the filtrate kept at -35 °C overnight. Brown crystals were separated and washed with cold hexane. (Yield: 164 mg, 0.349 mmol, 55 %). ^{1}H and ^{13}C NMR data are provided for the chloro derivative only. ^{1}H NMR (400 MHz, 20 °C, C_6D_6): δ 1.27 (dd, 6H, CHCH_3, $^3J_{HH}$ = 6.1, $^3J_{HP}$ = 14.1), 1.56 (dd, 6H, CHCH_3, $^3J_{HH}$ = 6.5, $^3J_{HP}$ = 17.2), 2.27 (br s, 2H, PCH), 2.55 (s, 6H, N(CH_3)$_2$), 5.25 (br s, 2H, OCH_2), 5.47 (br s, 2H, NH_2), 6.35 (broad s, 1H, C3$_{Ar}$-H), 6.45 (s, 1H, C4$_{Ar}$-H), 7.01-7.09 (m, 4H, p, m-C$_{Ar}$-H), 7.28 (d, 2H, o-C$_{Ar}$-H). ^{13}C{^{1}H} NMR (125.72 MHz, 20 °C, C_6D_6): δ 15.96 (d, $^2J_{CP}$ = 1.2, CH_3) 17.20 (d, $^2J_{CP}$ = 2.7, CH_3), 27.17 (s, P-CH), 27.43 (s, P-CH), 39.40 (s, N-CH_3), 77.38 (s, O-CH_2), 95.81(s, 1C, $C$4), 106.09(s, 1C, $C$3), 127.59 (s, 1C, C_{Ar}), 127.74 (s, 2C, C_{Ar}), 128.52 (s, 2C, C_{Ar}), 134.74 (s, 1C, C_{Ar}), 135.70 (s, 1C, C_{Ar}), 135.74 (s, 1C, C_{Ar}), 150.56 (s, 1C, C_{Ar}). ^{31}P{^{1}H} NMR (202.4 MHz, 20 °C, C_6D_6): 192.78 59 (**8a-Cl**, 77%), 196.11 59 (**8a-Br**, 23%).

[{κ^P,κ^C-(*i*-Pr)$_2$PO-(5-NMe$_2$-C$_6$H$_3$)}{κ^N-(CH$_3$CH$_2$-)(CH$_3$CH=)N}Ni(Br)] (**8b**). A 100 mL Schlenk flask containing 25 mL MeCN was charged with the proligand 3-NMe$_2$-C$_6$H$_4$OP (375 mg, 1.48 mmol, 1.00 equiv), the nickel precursor {(*i*-PrCN)NiBr$_2$}$_n$ (511 mg, 1.78 mmol, 1.20 equiv), and Et$_3$N (248.30 µL, 1.78 mmol, 1.20 equiv). The resulting mixture was stirred at room temperature overnight followed by reduction of volume to 5 mL under vacuum. Next, excess Et$_2$O was added to the mixture and placed in the fridge for 45 min to precipitate the impurities. After 45 min the solution was filtered through cotton. To the filtrate was added Et$_2$NOH (149.0 µL, 1.48

mmol, 1.00 equiv) and stirred overnight at room temperature maintaining inert atmosphere. Removal of the volatiles under vacuum left a sticky, brown residue, which was treated with ca. 2 mL of Et_2O, filtered and the filtrate kept at -35 $^\circ$C overnight. Brown crystals were separated and washed with cold hexane. (Yield: 128 mg, 0.10 mmol, 18 %). ^{1}H NMR (400 MHz, 20 °C, C_6D_6): δ 1.27 (dd, 3H, CHCH_3, $^3J_{HH}$ = 6.9, $^3J_{HP}$ = 14.5), 1.33 (dd, 3H, CHCH_3, $^3J_{HH}$ = 6.9, $^3J_{HP}$ = 14.7), 1.53 (t, 3H, NCH$_2$CH_3, $^3J_{HH}$ = 7.3), 1.60 (dd, 3H, CHCH_3, $^3J_{HH}$ = 7.3, $^3J_{HP}$ = 15.8), 1.64 (dd, 3H, CHCH_3, $^3J_{HH}$ = 7.2, $^3J_{HP}$ = 15.6), 2.38 (d, 3H, NCHCH_3, $^3J_{HH}$ = 4.5), 2.41-2.49 (m, 2H, PCH), 2.55 (s, 6H, N(CH_3)$_2$, 3.34 (pssext, 1H, NCH_2, $^3J_{HH}$ = 6.6), 3.91 (pssext, 1H, NCH_2, $^3J_{HH}$ = 7.0), 6.26 (d, 1H, C4$_{Ar}$-H, $^3J_{HH}$ = 7.6), 6.33 (d, 1H, C3$_{Ar}$-H, $^3J_{HH}$ = 8.3), 6.45 (d, 1H, C6$_{Ar}$-H, $^4J_{HH}$ = 2.5 ≈ $^4J_{HP}$ = 2.5), 6.71 (br s, 1H, NCH). ^{13}C{^{1}H} NMR (125.72 MHz, 20 °C, C_6D_6): δ 15.90 (s, 1C, NCH$_2$$CH_3$), 17.03 (d, 1C, $^2J_{PC}$ = 2.0, PCHCH$_3$), 17.22 (d, 1C, $^2J_{PC}$ = 1.1, PCHCH$_3$), 18.81 (d, 1C, $^2J_{PC}$ = 3.6, PCHCH$_3$), 23.66 (s, 1C, PCHCH$_3$) , 28.55 (d, 1C, $^1J_{PC}$ = 12.5, PCH), 28.81 (d, 1C, $^1J_{PC}$ = 11.6, PCH), 40.53 (s, 2C, NCH$_3$), 56.67 (s, 1C, NCHCH$_3$), 65.91 (s, 1C, NCH$_2$), 96.92 (d, 1C, $^5J_{PC}$ = 14, C_{Ar}), 106.82 (d, 1C, $^4J_{PC}$ = 2.0, C_{Ar}), 118.39 (d, 1C, J_{PC} = 34.8, C_{Ar}), 137.50 (d, 1C, J_{PC} = 2.6, C_{Ar}), 151.21 (s, 1C, C_{Ar}), 165.66 (s, 1C, NCH), 169.16 (d, 1C, J_{PC} = 15.0, C1). ^{31}P{^{1}H} NMR (202.4 MHz, 20 °C, C_6D_6): δ 192.89 (s, 1P).

S2.3 NMR spectra of new compounds

Ligand **3-NMe₂-C₆H₄OP(*i*-Pr)₂**
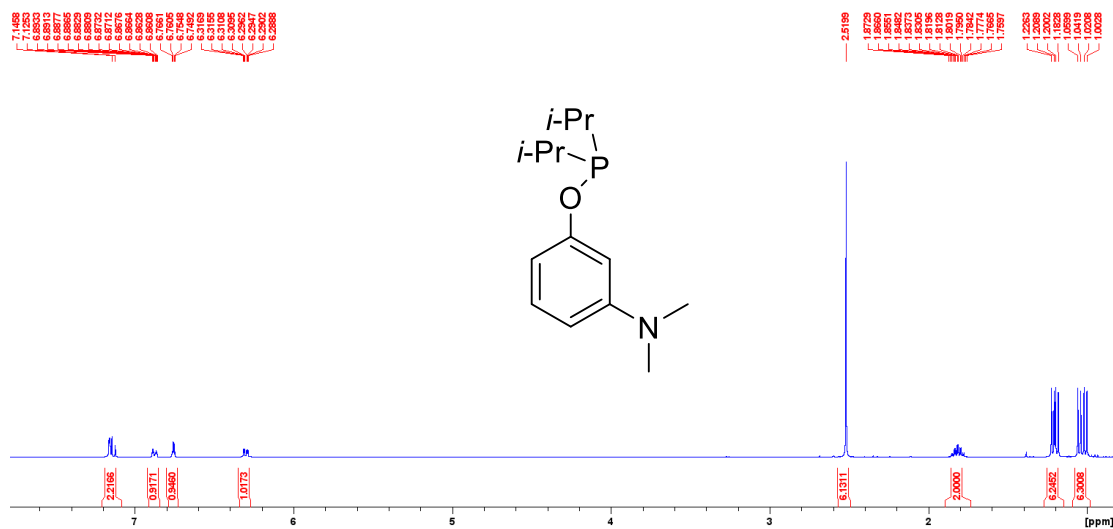
Figure S2. 1. Full ¹H NMR spectrum of 3-NMe₂-C₆H₄OP(i-Pr)₂ in C₆D₆.
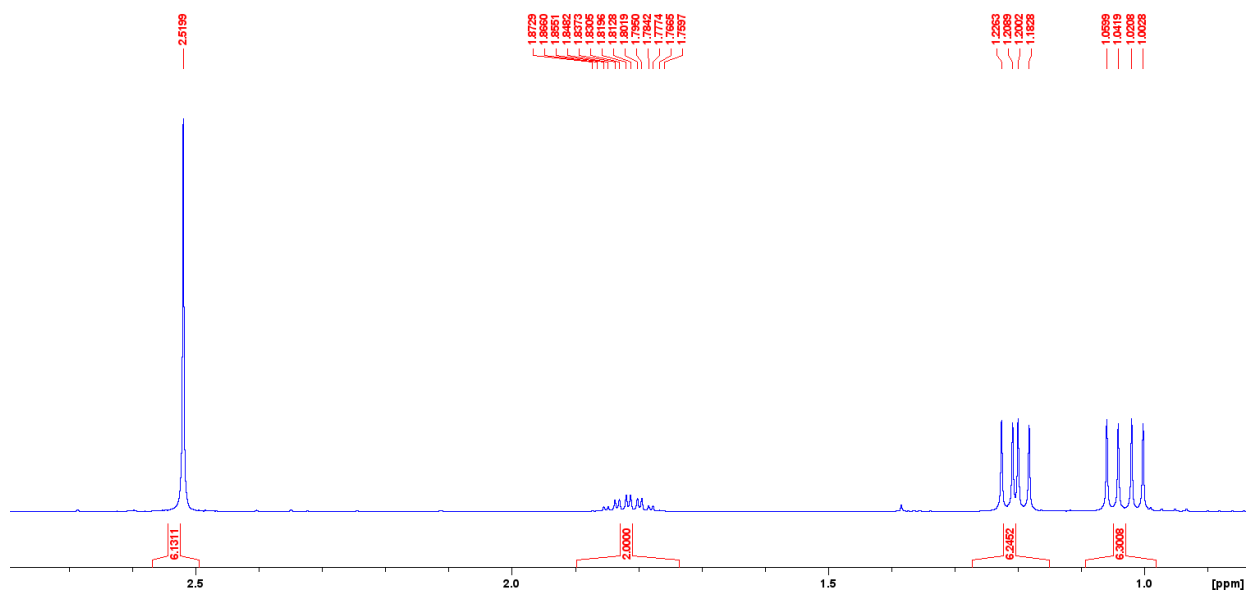
Figure S2. 2. The aliphatic region of the ¹H NMR spectrum of 3-NMe₂-C₆H₄OP(*i*-Pr)₂ in C₆D₆.

Figure S2. 3. The aromatic region of the ^{1}H NMR spectrum of 3-NMe$_2$-C$_6$H$_4$OP(i-Pr)$_2$ in C$_6$D$_6$.

Figure S2. 4. Full ^{13}C{^{1}H} NMR spectrum of 3-NMe$_2$-C$_6$H$_4$OP(i-Pr)$_2$ in C$_6$D$_6$.
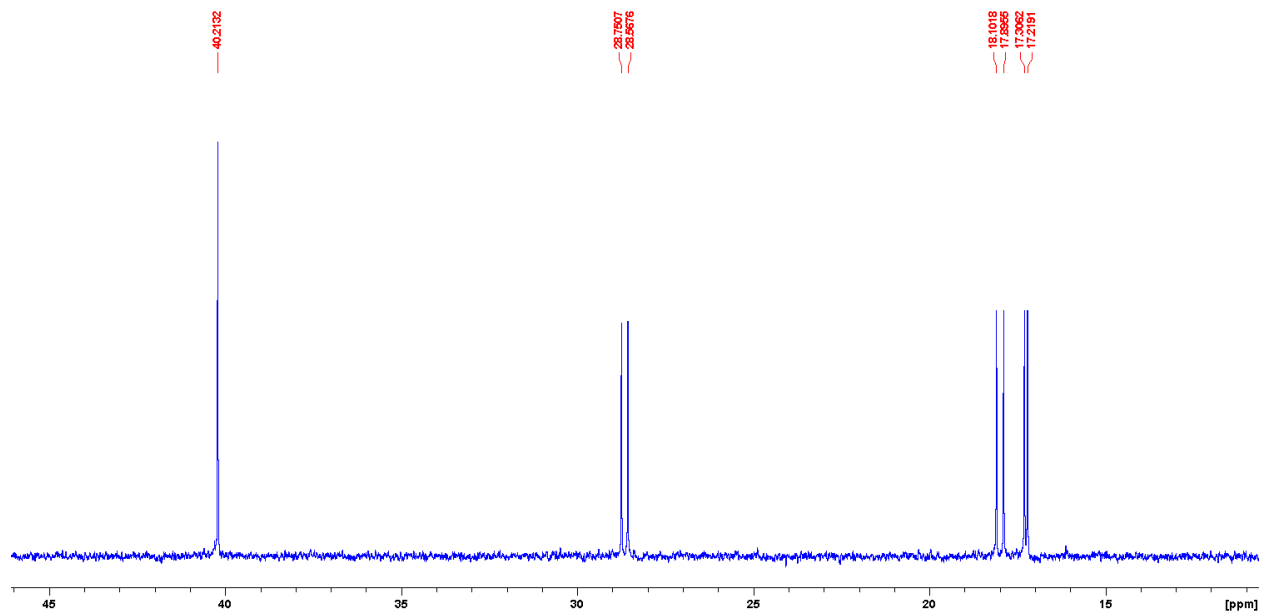
Figure S2. 5. The aliphatic region of the $^{13}C\{^{1}H\}$ NMR spectrum of 3-NMe$_2$-C$_6$H$_4$OP(i-Pr)$_2$ in C$_6$D$_6$.
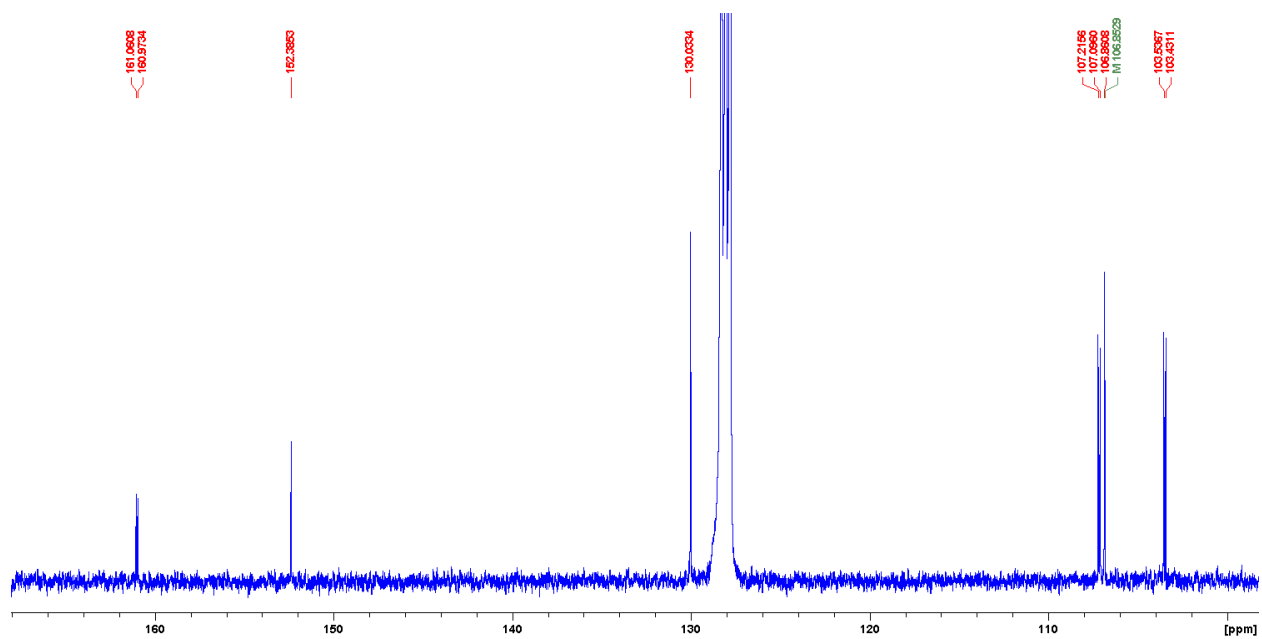
Figure S2. 6. The aromatic region of the $^{13}C\{^{1}H\}$ NMR spectrum of 3-NMe$_2$-C$_6$H$_4$OP(i-Pr)$_2$ in C$_6$D$_6$.
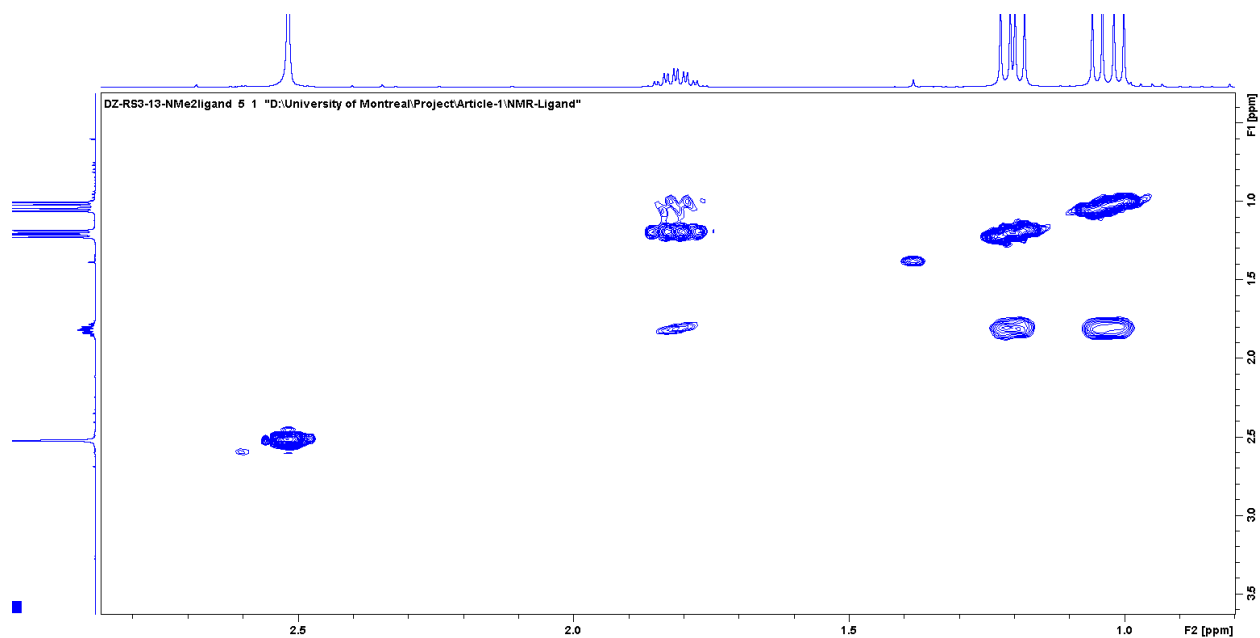
Figure S2. 7. The aliphatic region of the COSY NMR spectrum of 3-NMe$_2$-C$_6$H$_4$OP(i-Pr)$_2$ in C$_6$D$_6$.
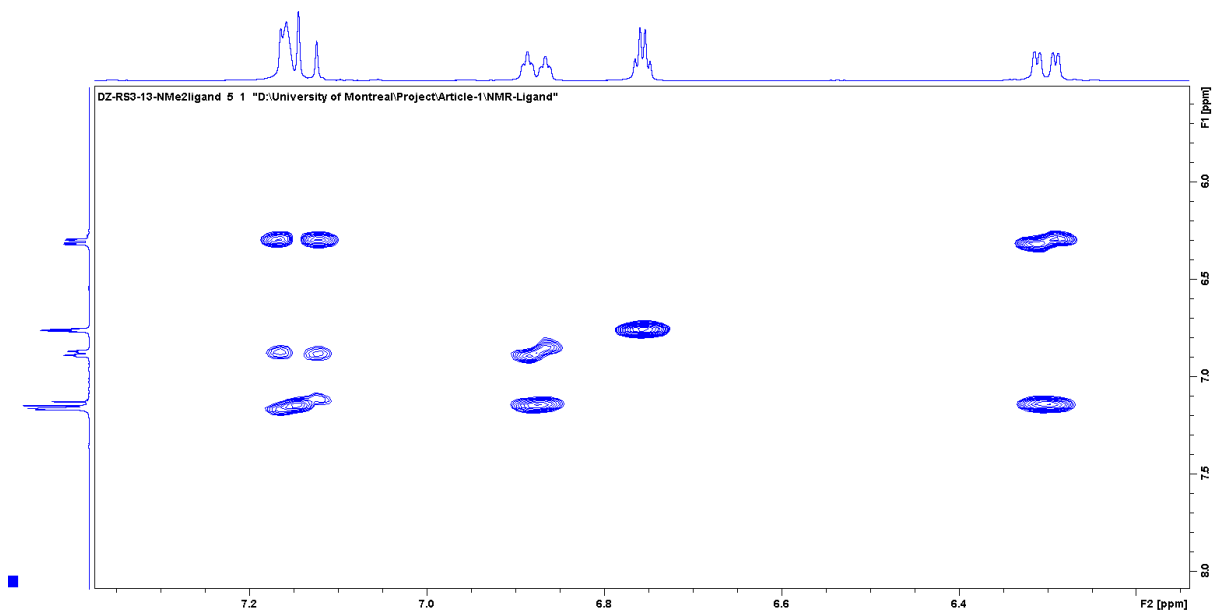
Figure S2. 8. The aromatic region of the COSY NMR spectrum of 3-NMe$_2$-C$_6$H$_4$OP(i-Pr)$_2$ in C$_6$D$_6$.
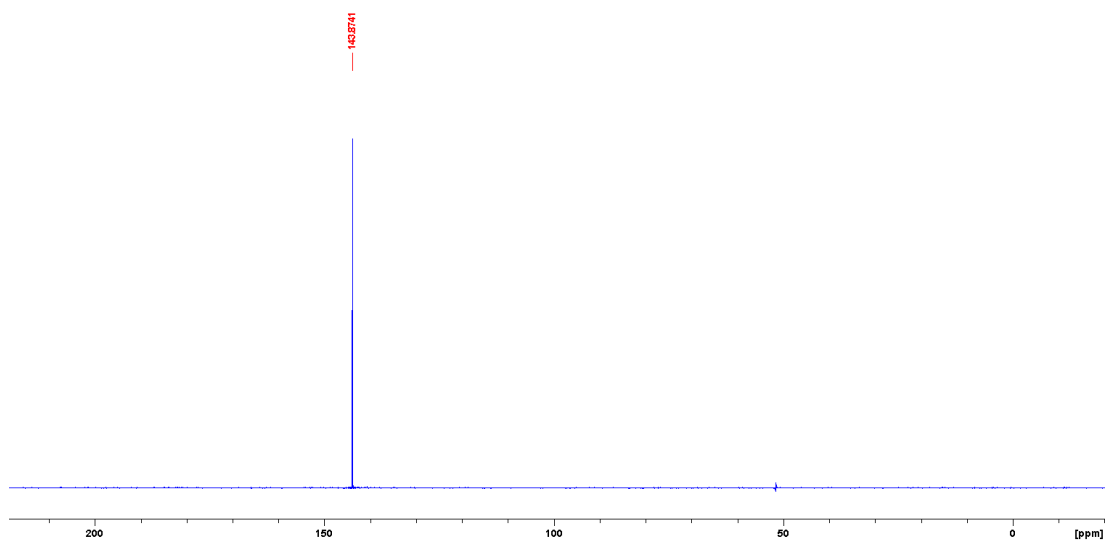
Figure S2. 9. $^{31}P\{^{1}H\}$ NMR spectrum of 3-NMe$_2$-C$_6$H$_4$OP(i-Pr)$_2$ in C$_6$D$_6$.

NMR spectra of Complex **4'**:
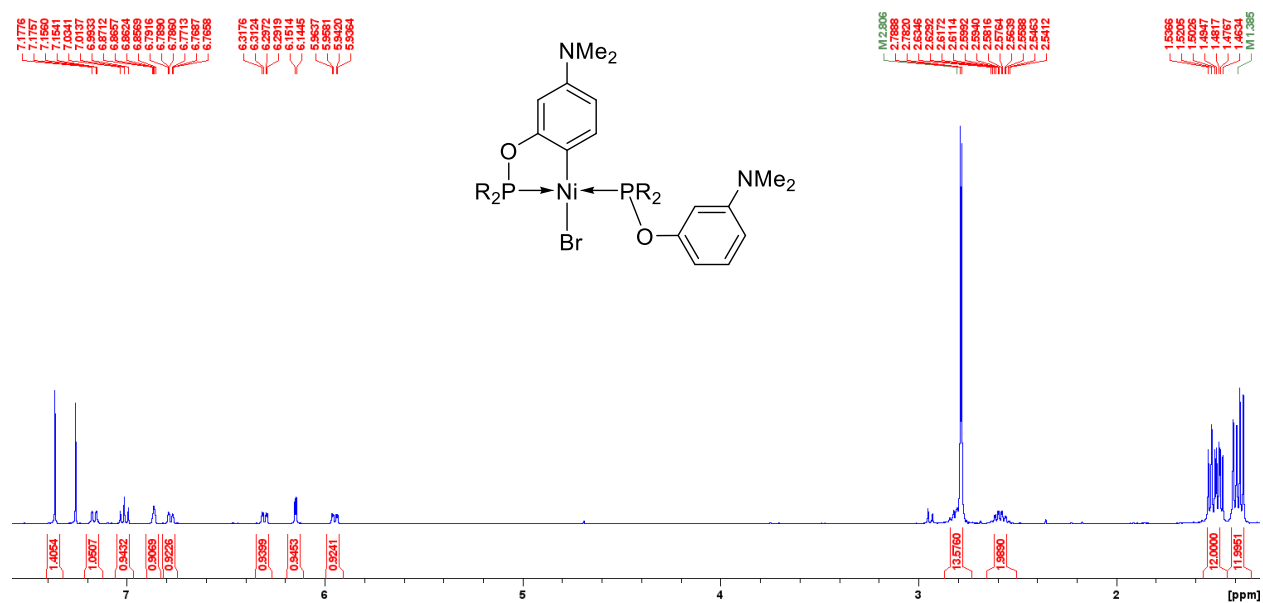
Figure S2. 10. Full ^{1}H NMR spectrum of **4'** in CDCl$_3$
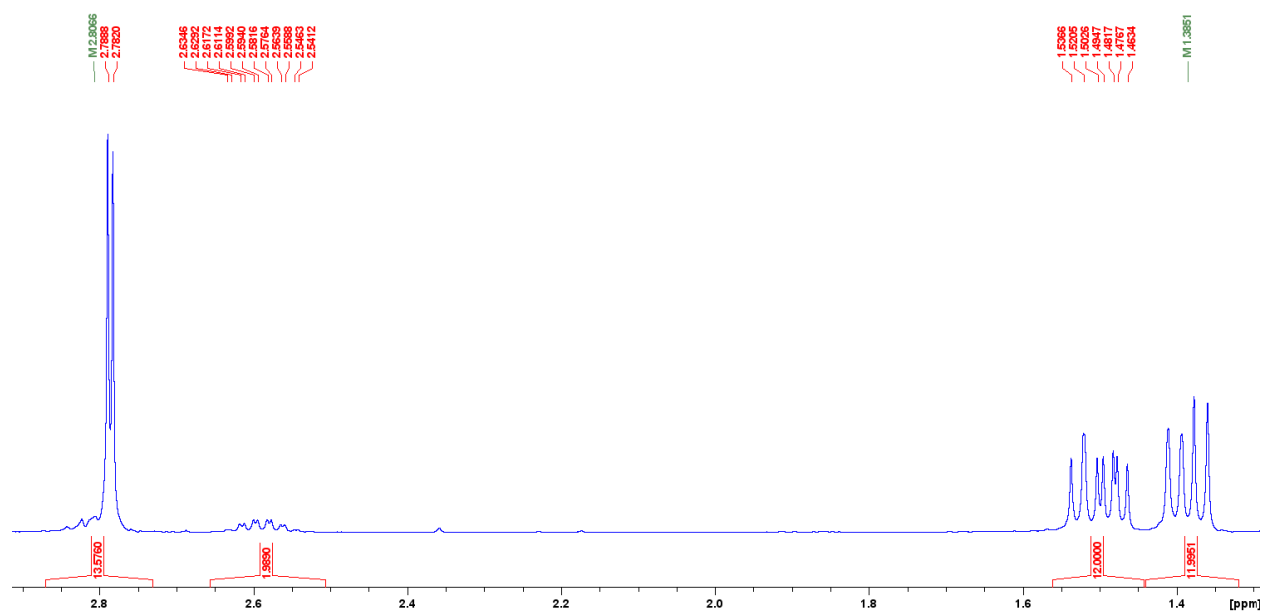
Figure S2. 11. The aliphatic region of the ^{1}H NMR spectrum of **4'** in CDCl$_3$.
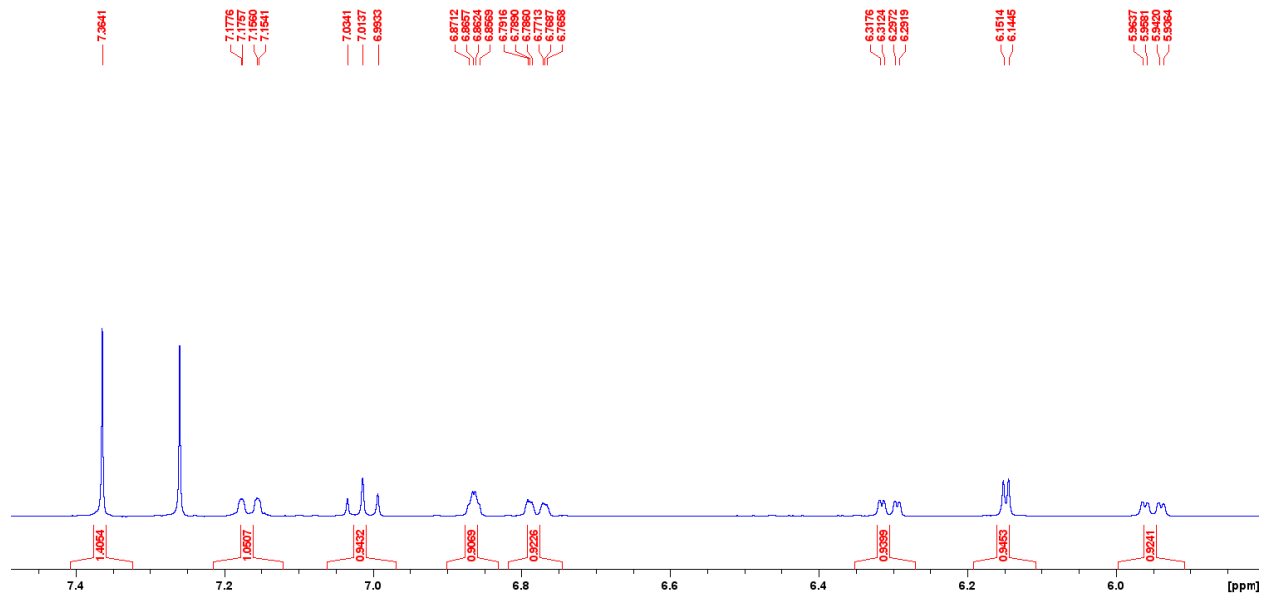
Figure S2. 12. The aromatic region of the ^{1}H NMR spectrum of **4'** in CDCl$_3$.
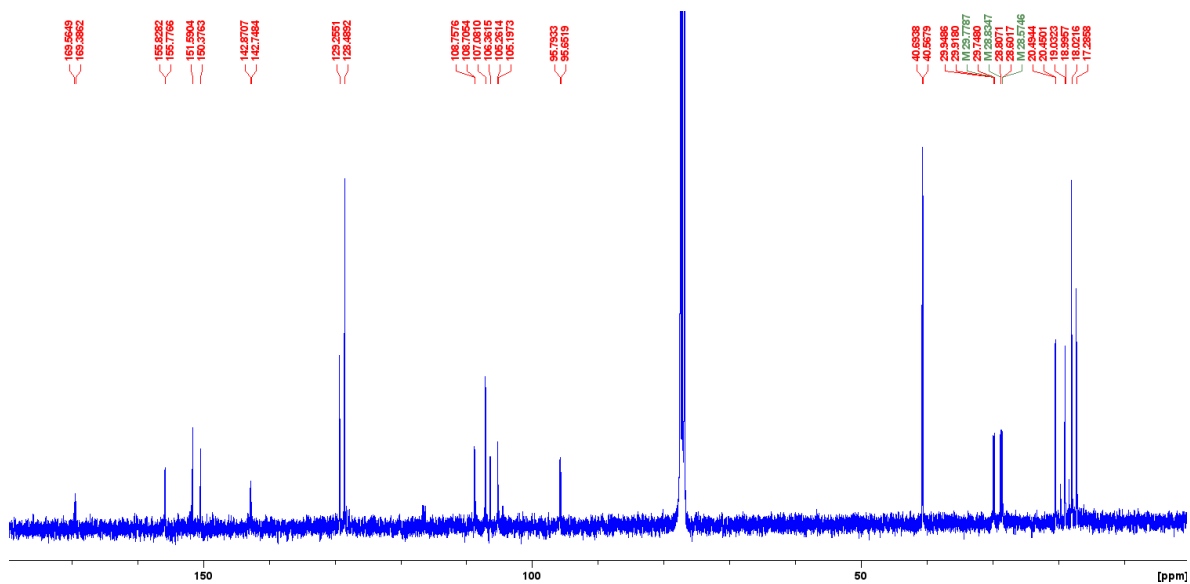
Figure S2. 13. Full ^{13}C{^{1}H} NMR spectrum of **4'** in CDCl$_3$.
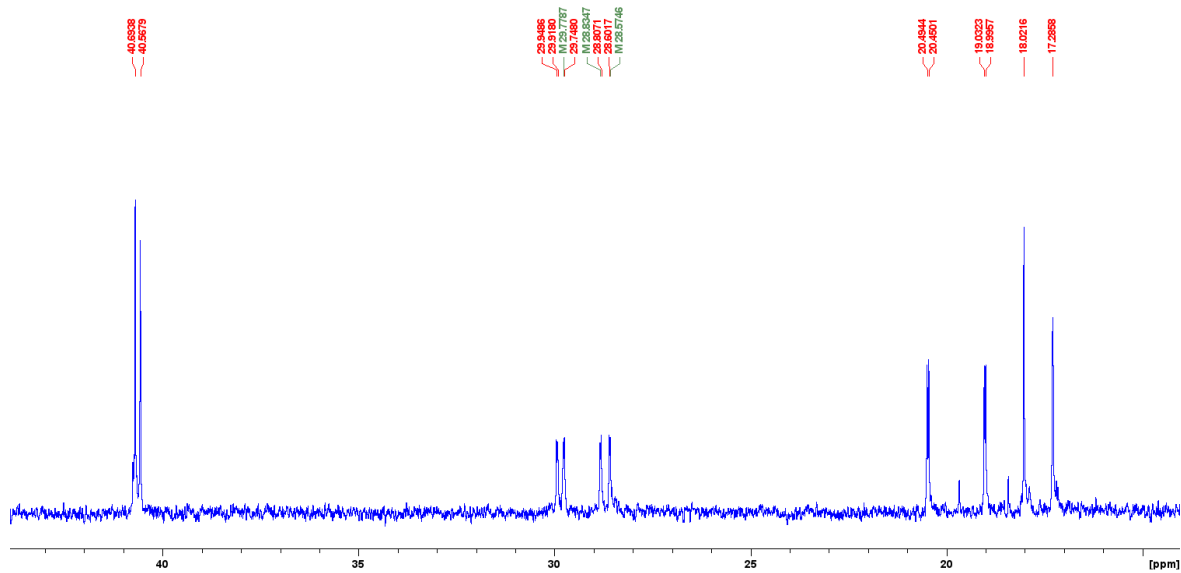
Figure S2. 14. The aliphatic region of the $^{13}C\{^1H\}$ NMR spectrum of **4'** in CDCl$_3$.
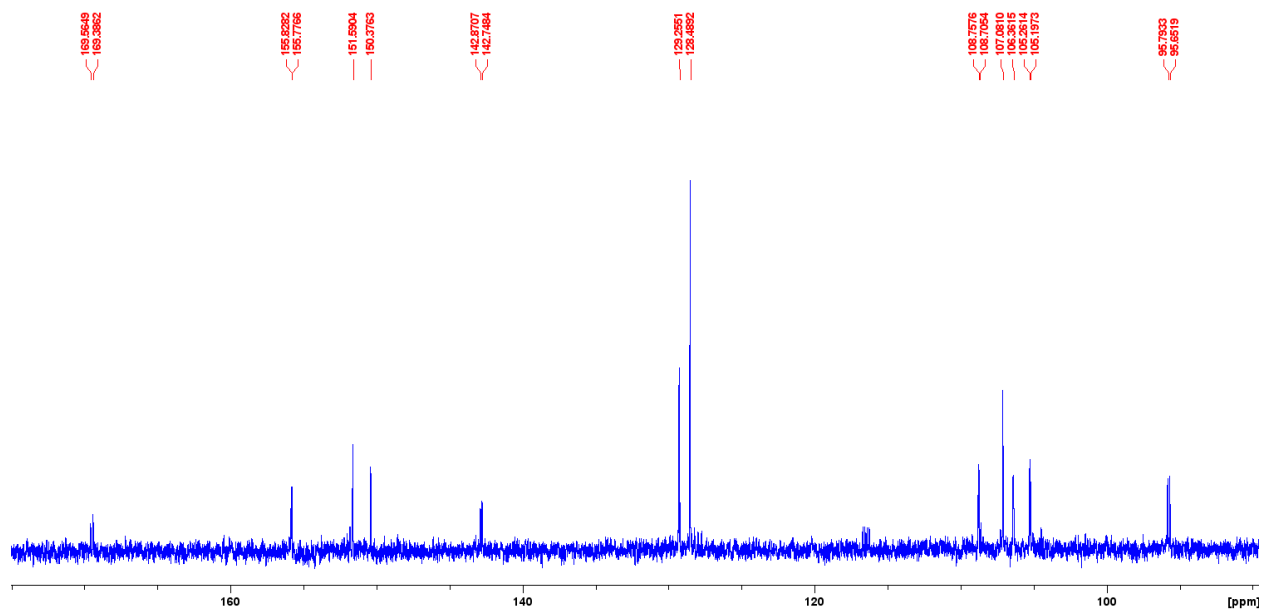
Figure S2. 15. The aromatic region of the $^{13}C\{^1H\}$ NMR spectrum of **4'** in CDCl$_3$.
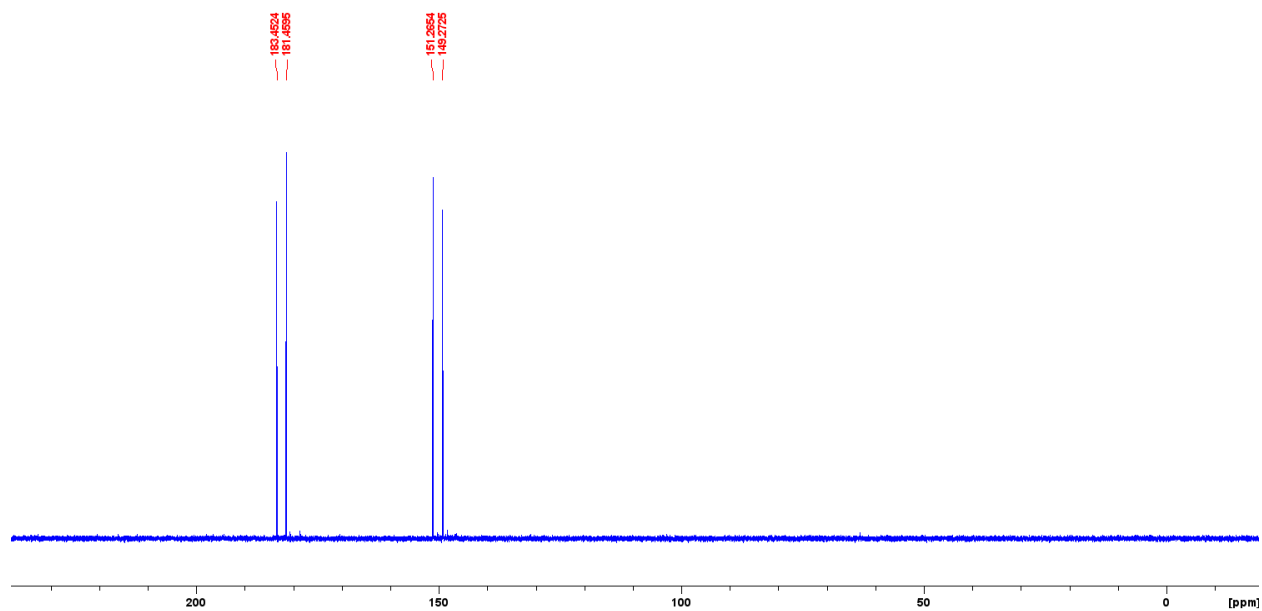
Figure S2. 16. Full ^{31}P NMR spectrum of **4'** in CDCl$_3$.

NMR spectra of complex **5a**

Figure S2. 17. Full ^{1}H NMR spectrum of **5a** in CDCl$_3$.

Figure S2. 18. The aliphatic region of the ^{1}H NMR spectrum of **5a** in CDCl$_3$.
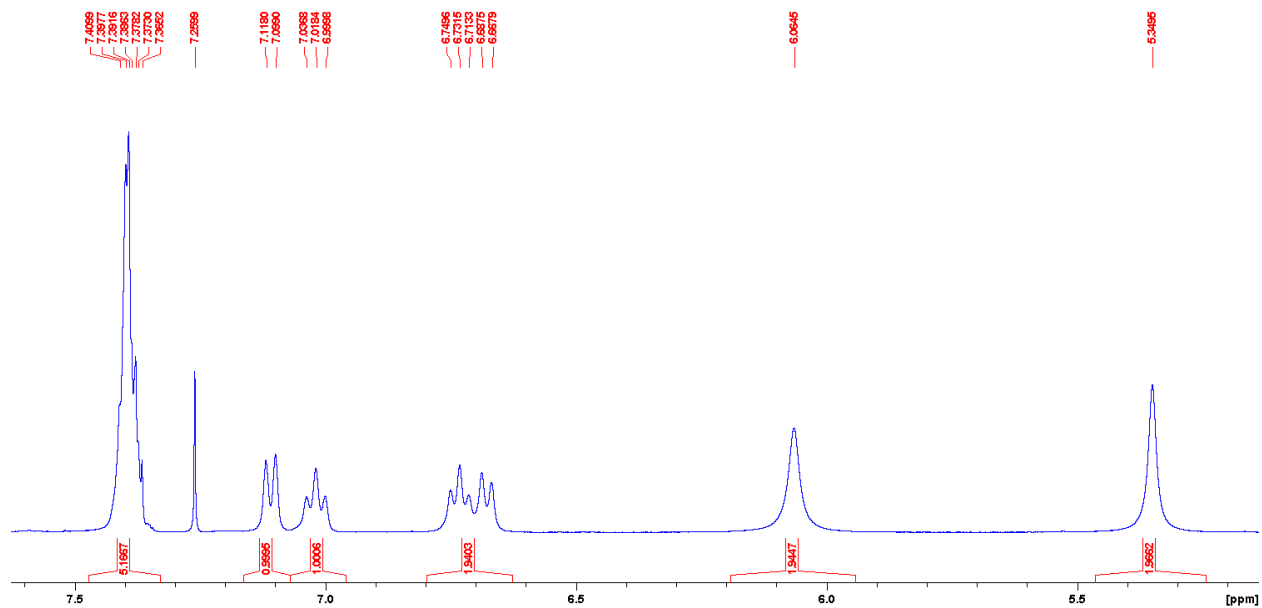
Figure S2. 19. The aromatic region of the ^{1}H NMR spectrum of **5a** in CDCl$_3$.
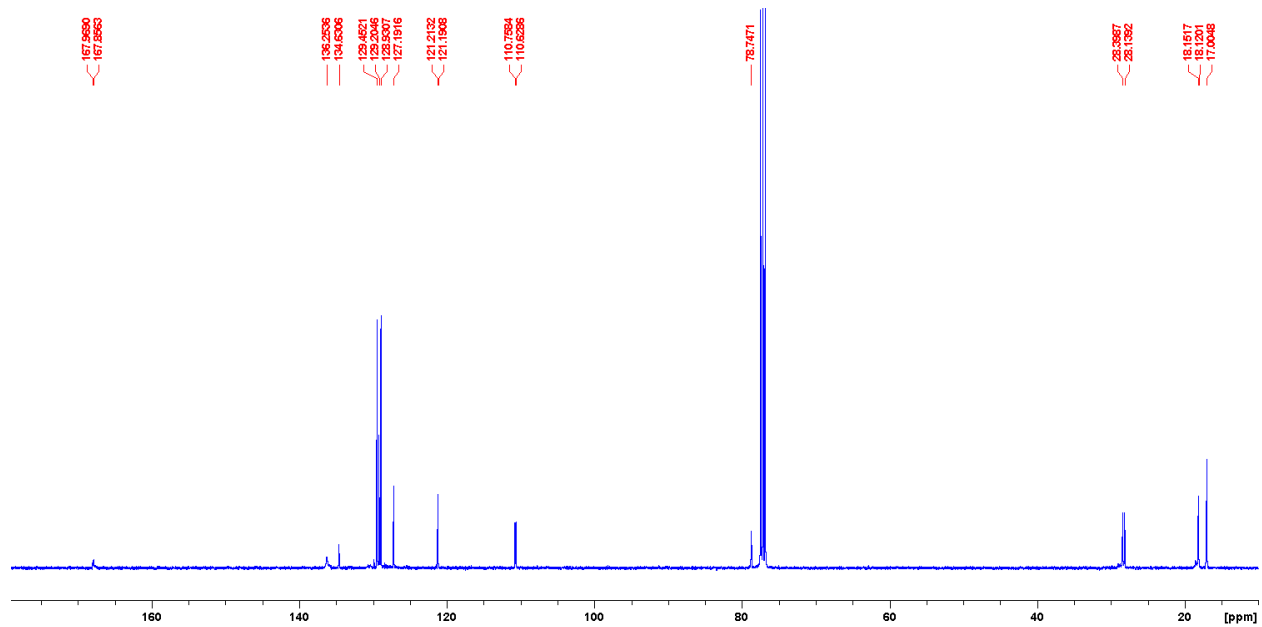
Figure S2. 20. Full ^{13}C{^{1}H} NMR spectrum of **5a** in CDCl$_3$.
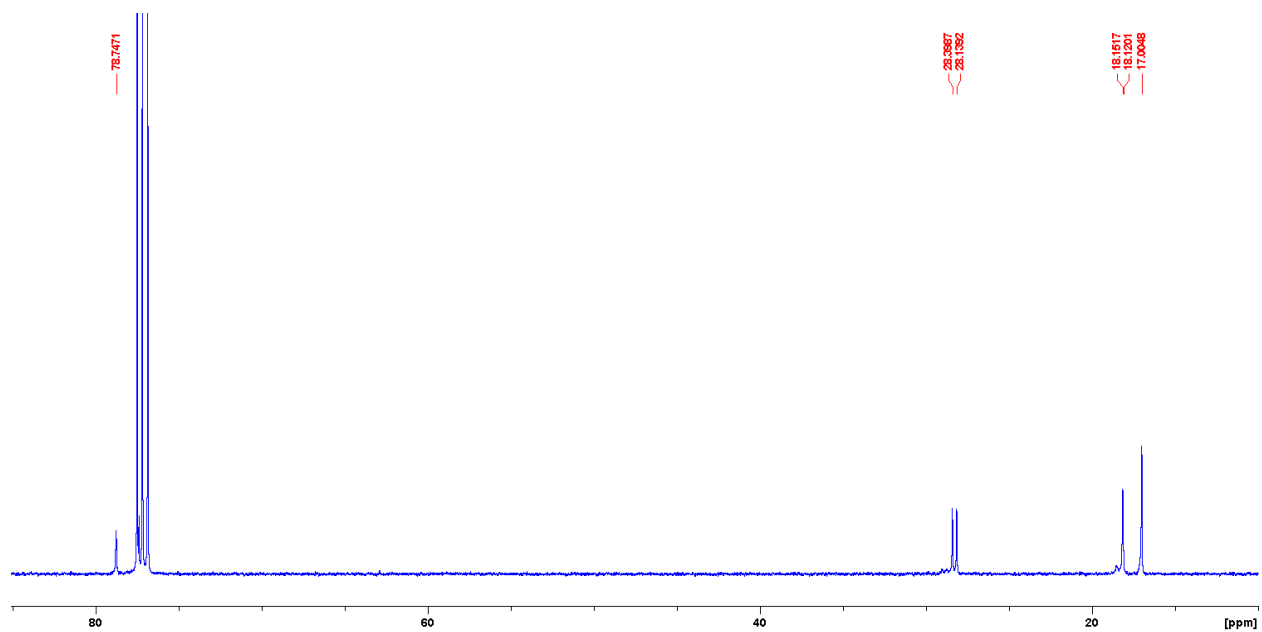
Figure S2. 21. The aliphatic region of the $^{13}C\{^1H\}$ NMR spectrum of **5a** in CDCl$_3$.
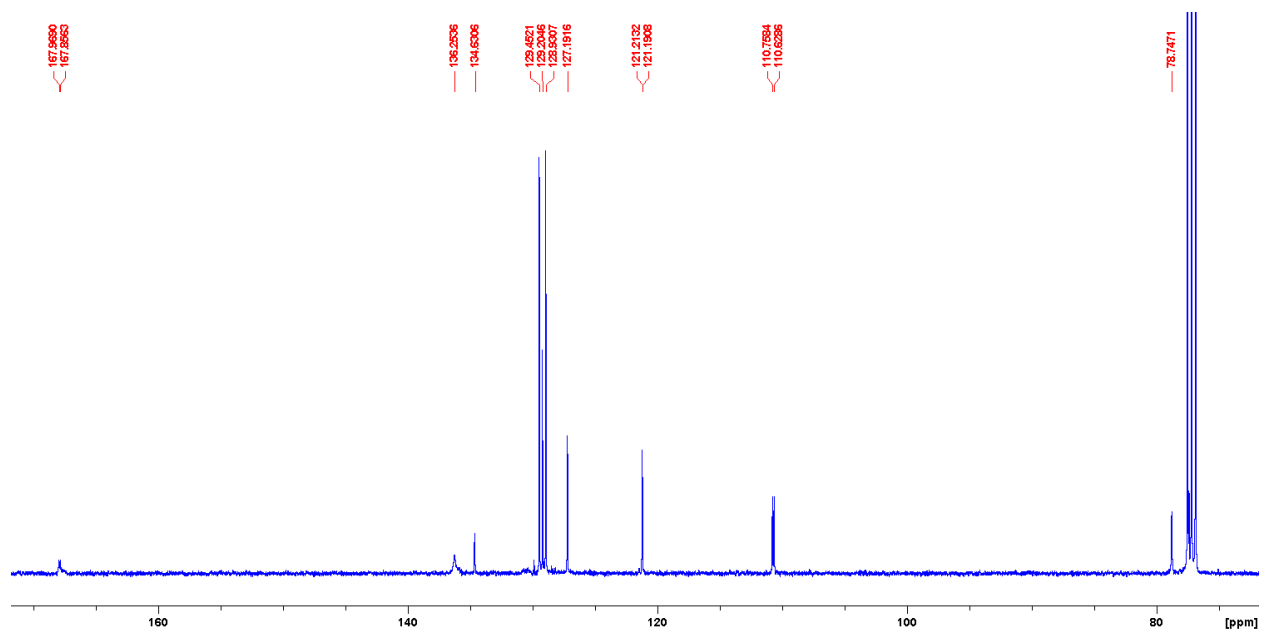
Figure S2. 22. The aromatic region of the $^{13}C\{^1H\}$ NMR spectrum of **5a** in CDCl$_3$.
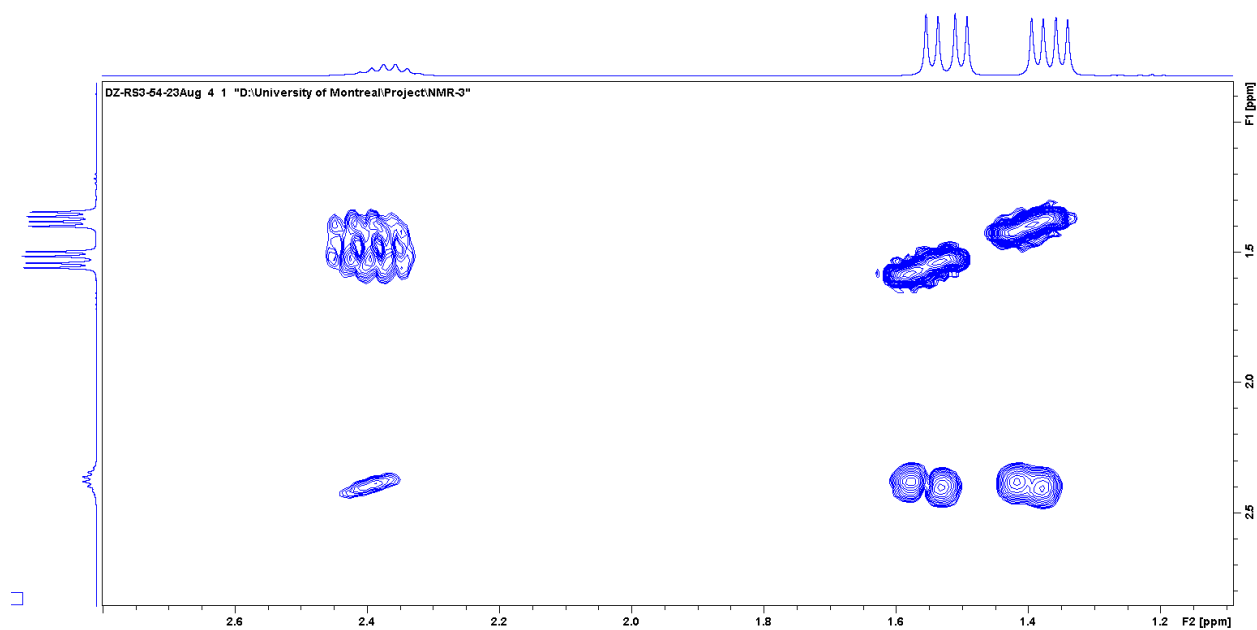
Figure S2. 23. The aliphatic region of the COSY NMR spectrum of **5a** in CDCl₃.
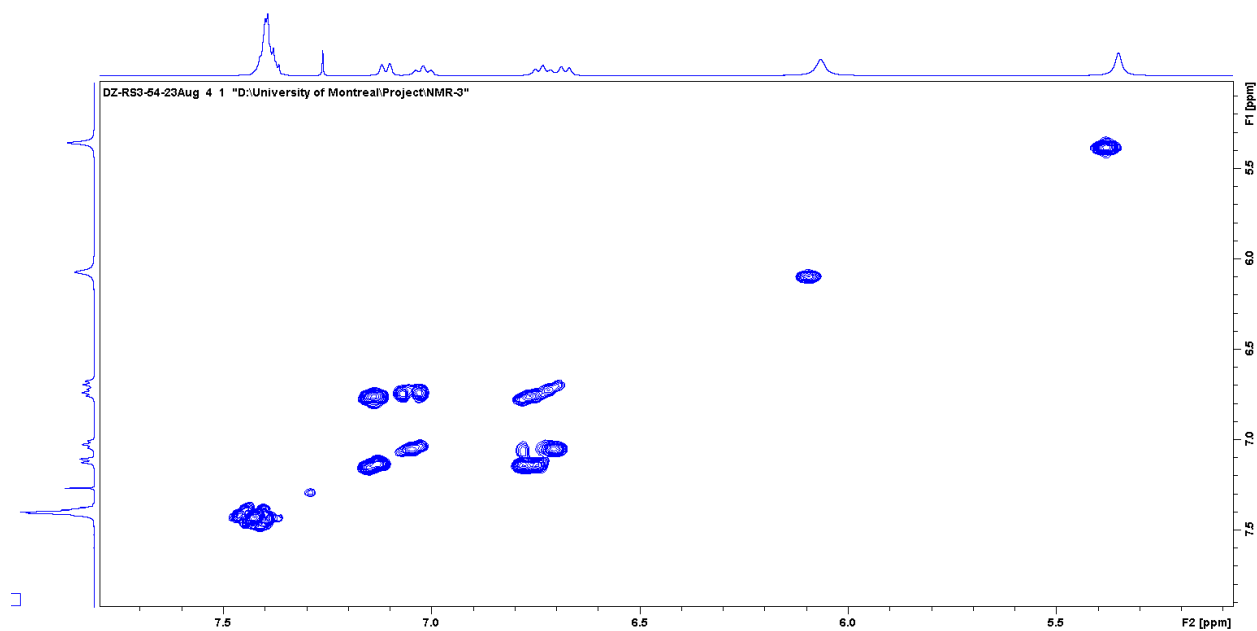
Figure S2. 24. The aromatic region of the COSY NMR spectrum of **5a** in CDCl₃.
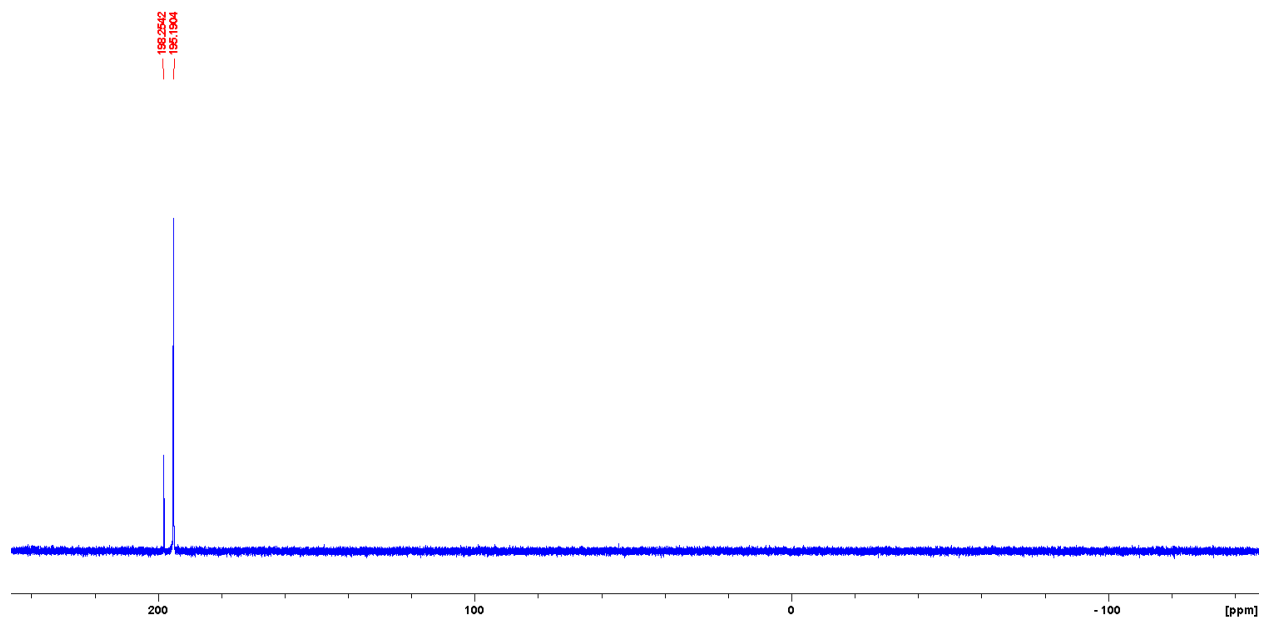
Figure S2. 25. ^{31}P{^{1}H} NMR spectrum of **5a** in CDCl$_3$.

NMR spectra of complex **5b**
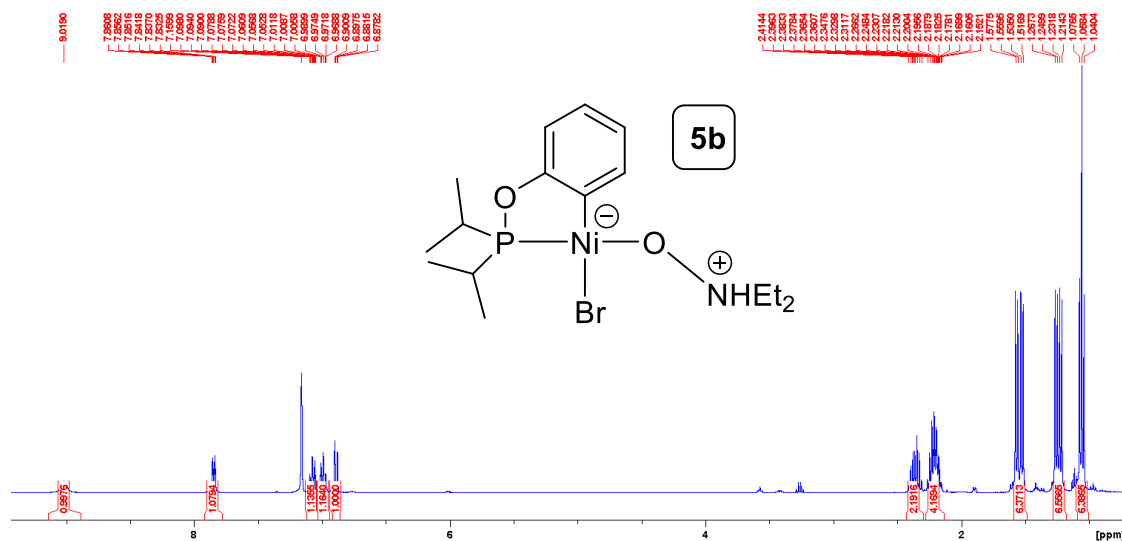
Figure S2. 26. Full ^{1}H NMR spectrum of **5b** in C$_6$D$_6$.
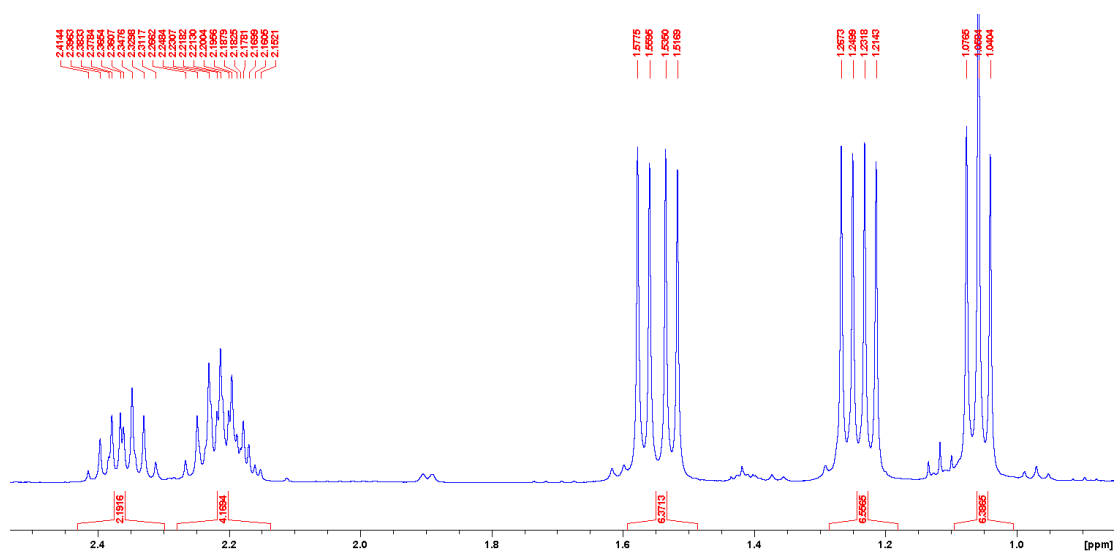
Figure S2. 27. The aliphatic region of the ^{1}H NMR spectrum of **5b** in C$_6$D$_6$.

Figure S2. 28. The aromatic region of the ^{1}H NMR spectrum of **5b** in C_6D_6.

Figure S2. 29. Full ^{13}C NMR spectrum of **5b** in C_6D_6.
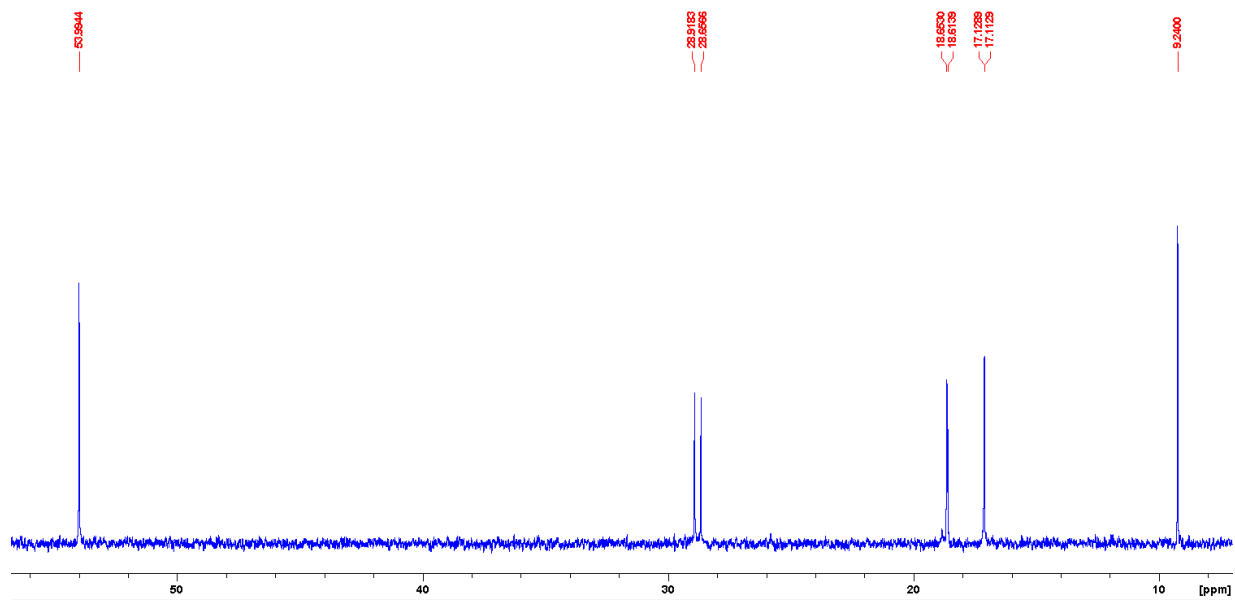
Figure S2. 30. The aliphatic region of the ^{13}C NMR spectrum of **5b** in C_6D_6.
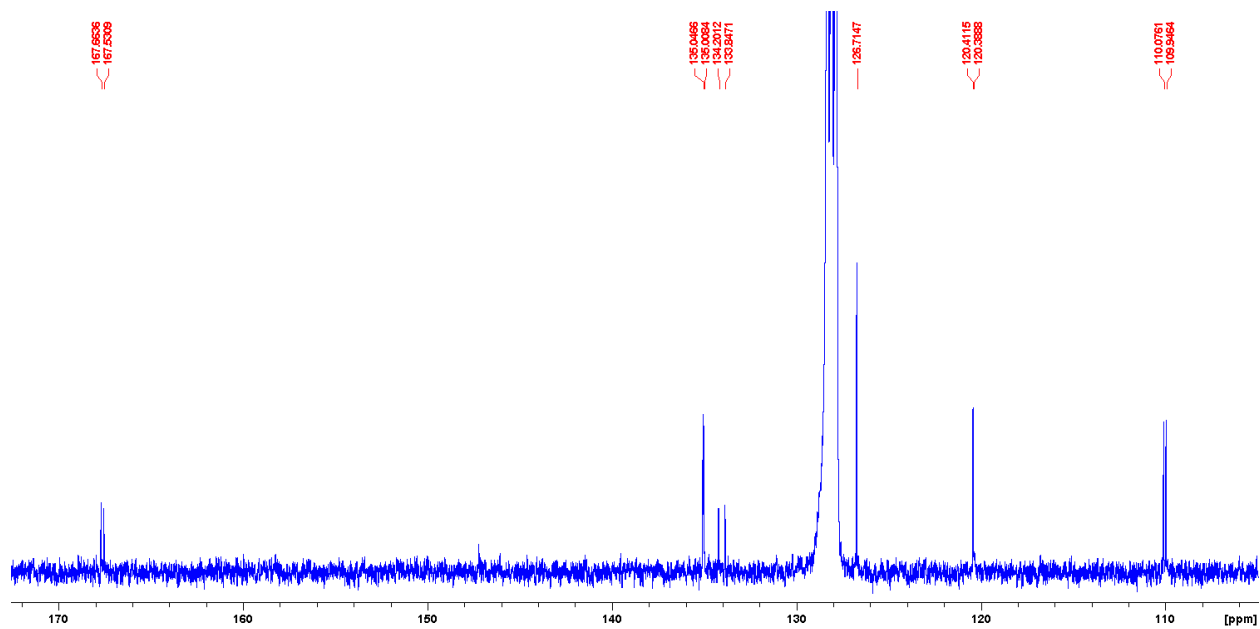
Figure S2. 31. The aromatic region of the ^{13}C NMR spectrum of **5b** in C_6D_6.
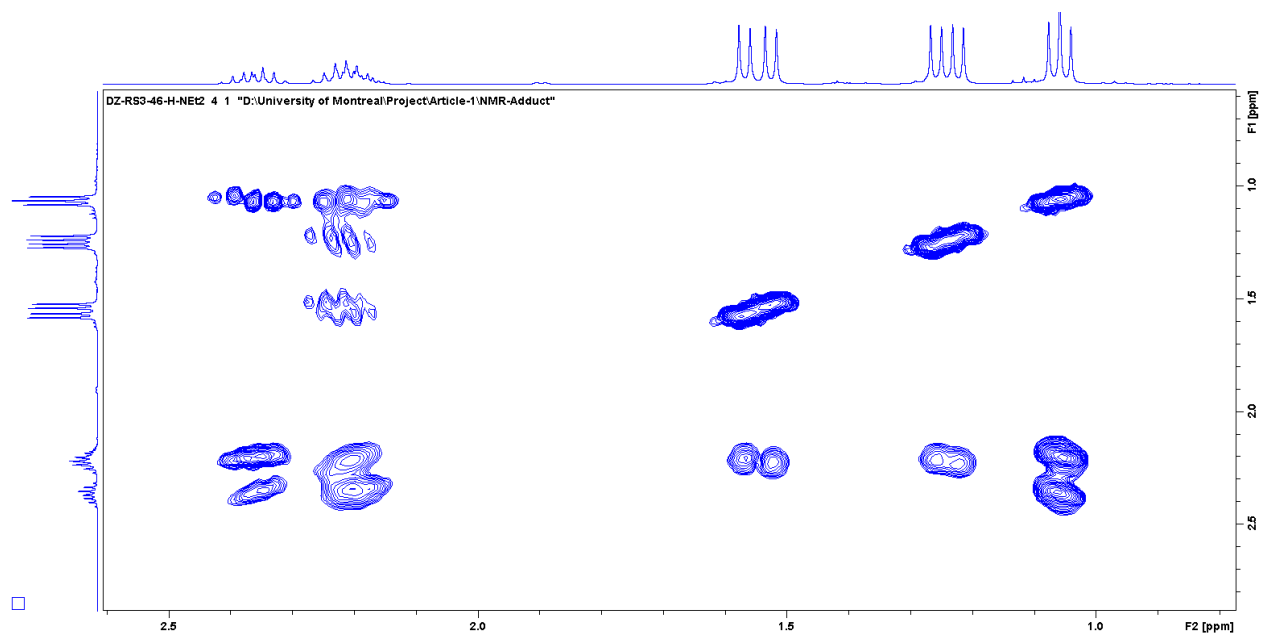
Figure S2. 32. The aliphatic region of the COSY NMR spectrum of **5b** in C_6D_6.
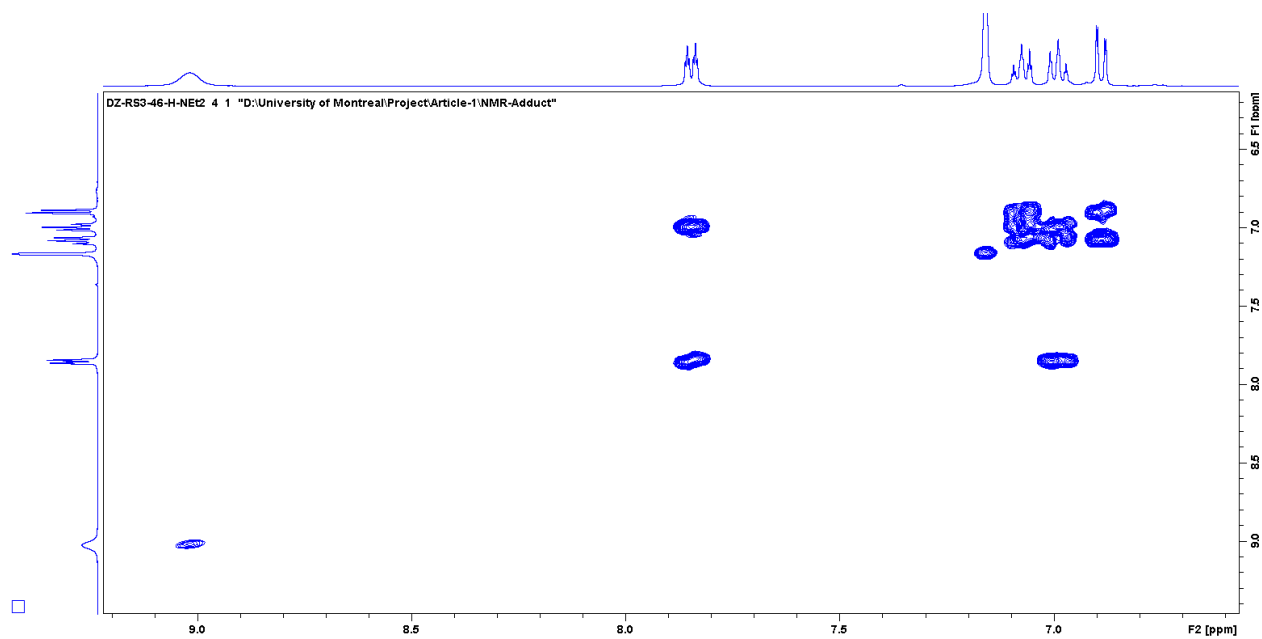
Figure S2. 33. The aromatic region of the COSY NMR spectrum of **5b** in C_6D_6.

201.5168
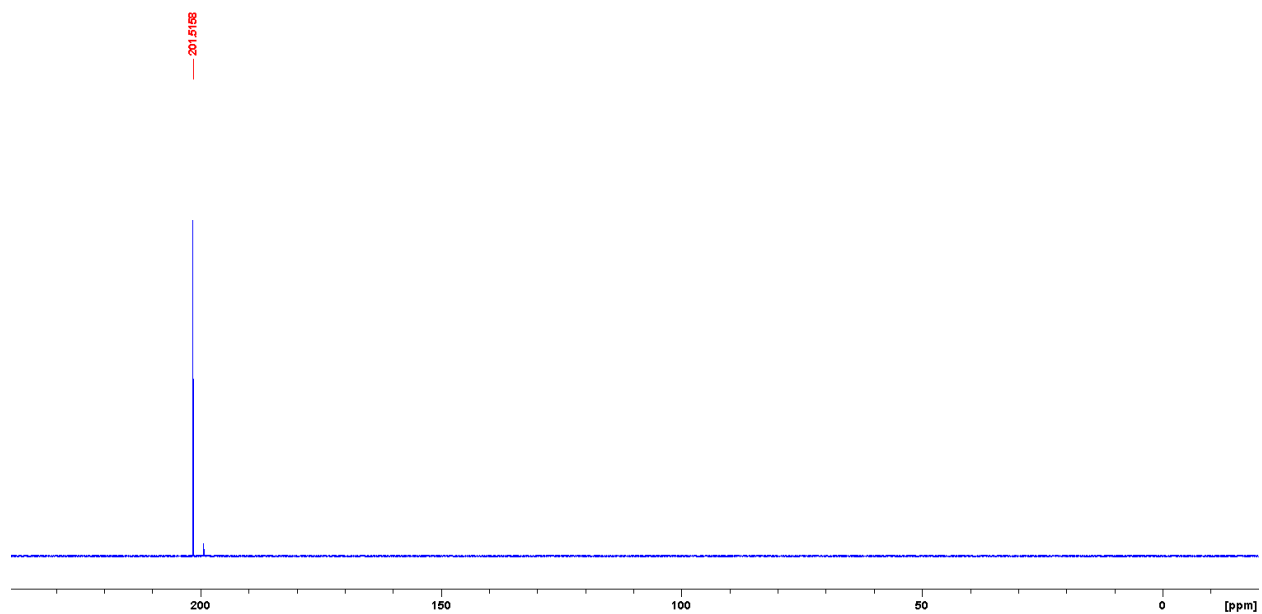
Figure S2. 34. Full $^{31}P\{^1H\}$ NMR spectrum of **5b** in C_6D_6.

NMR spectra of complex **5c**
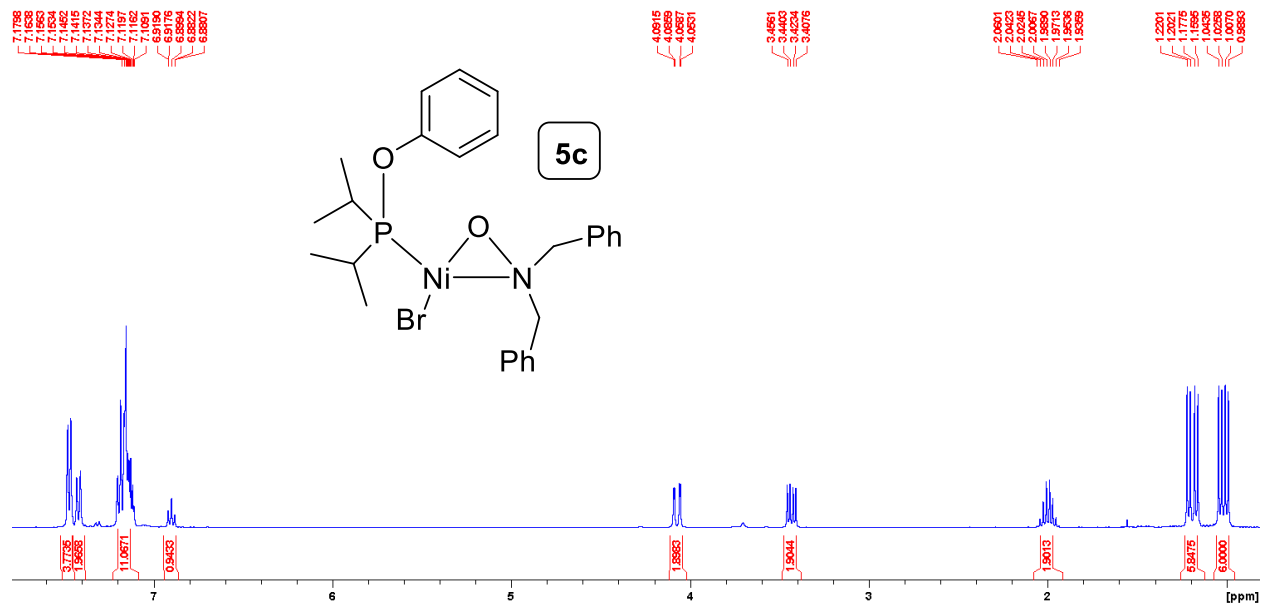
Figure S2. 35. Full ^{1}H NMR spectrum of **5c** in C$_6$D$_6$.
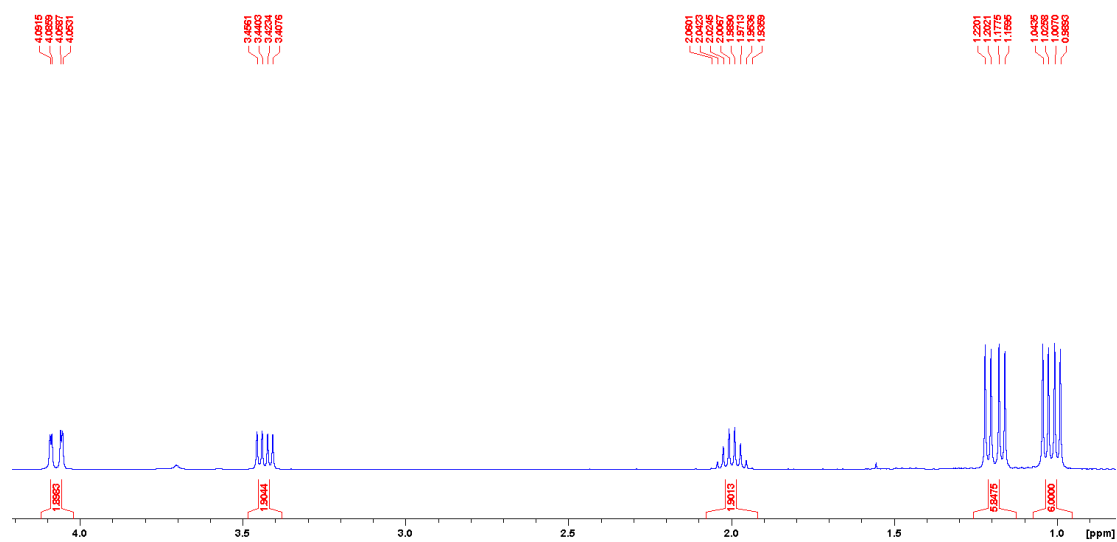
Figure S2. 36. The aliphatic region of the ^{1}H NMR spectrum of **5c** in C$_6$D$_6$.
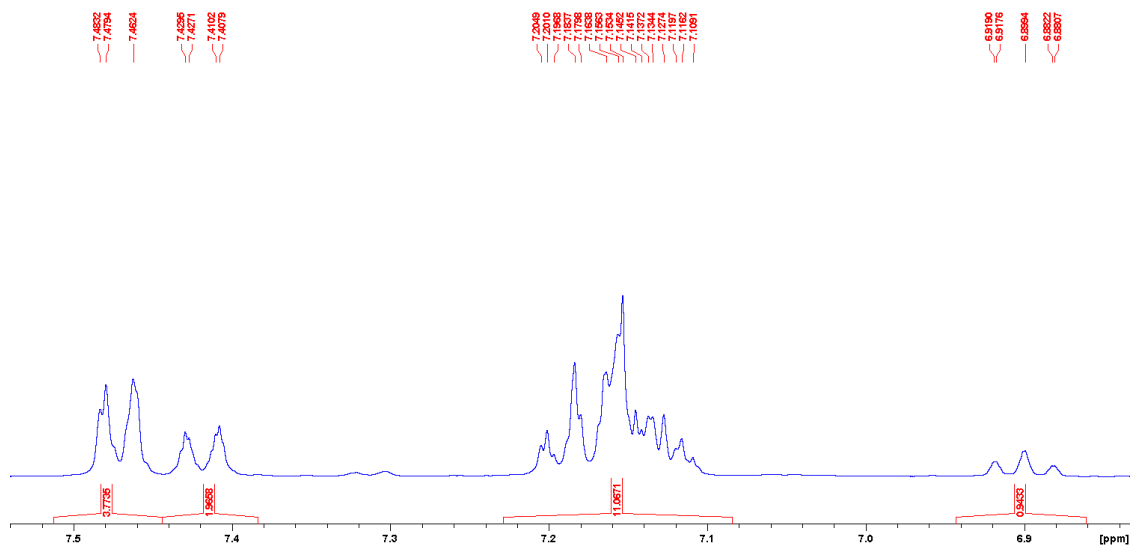
Figure S2. 37. The aromatic region of the ^{1}H NMR spectrum of **5c** in C$_6$D$_6$.
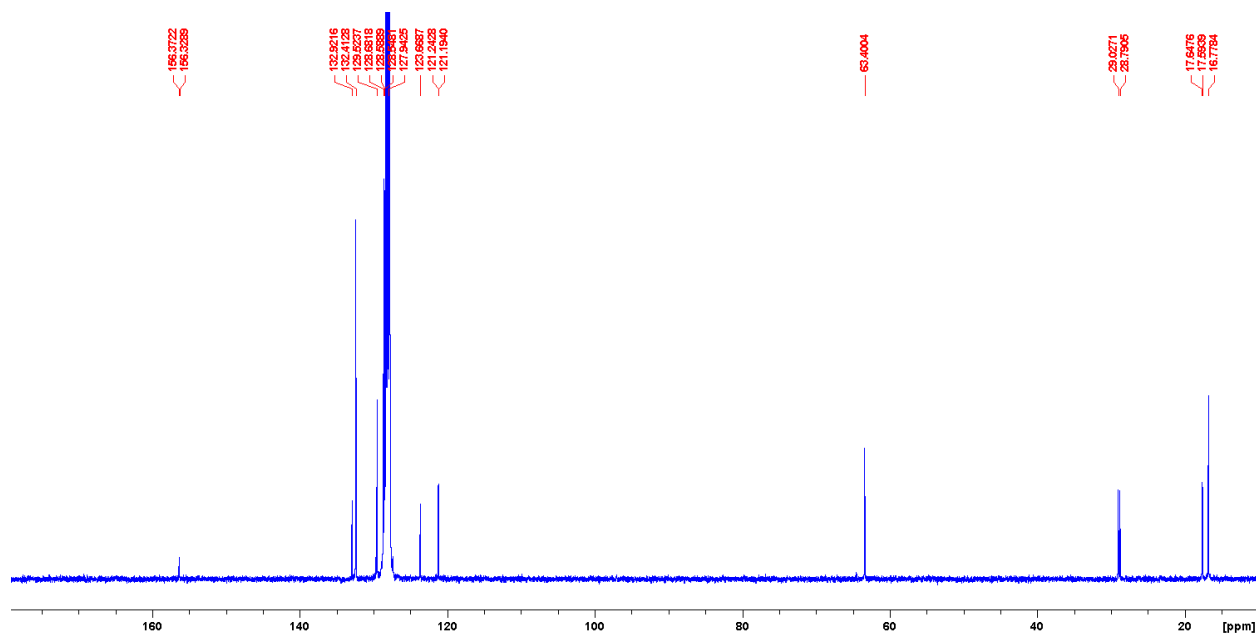
Figure S2. 38. Full ^{13}C NMR spectrum of **5c** in C$_6$D$_6$.
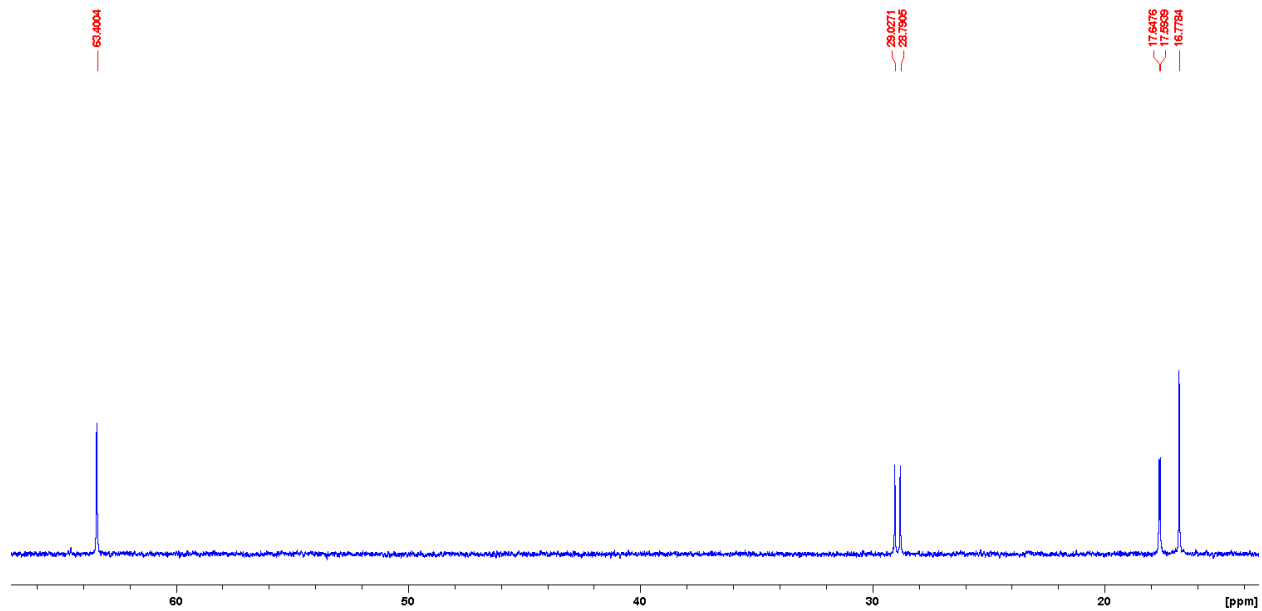
Figure S2. 39. The aliphatic region of the ^{13}C NMR spectrum of **5c** in C_6D_6.
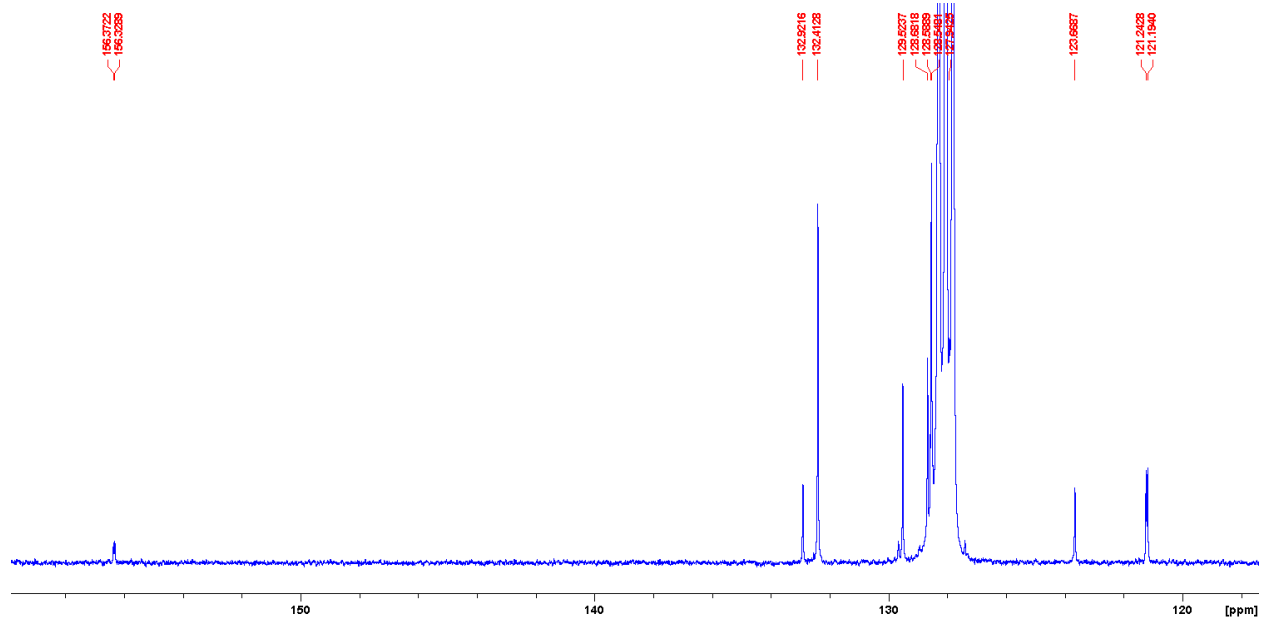
Figure S2. 40. The aromatic region of the ^{13}C NMR spectrum of **5c** in C_6D_6.
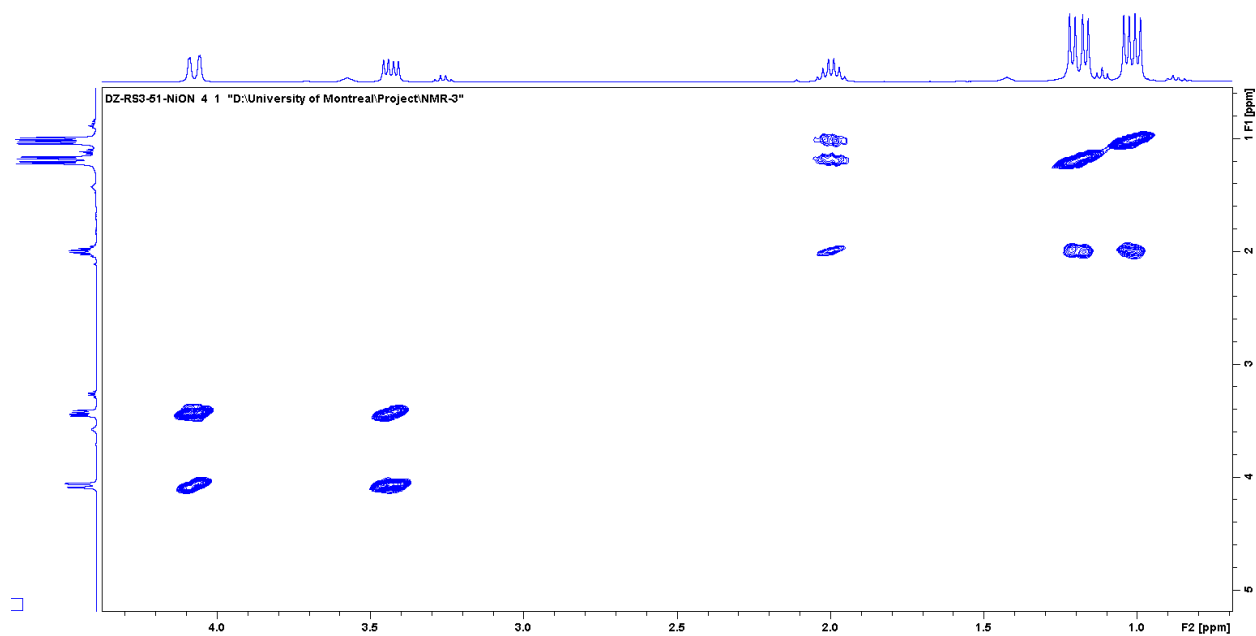
Figure S2. 41. The aliphatic region of the COSY NMR spectrum of **5c** in C$_6$D$_6$.
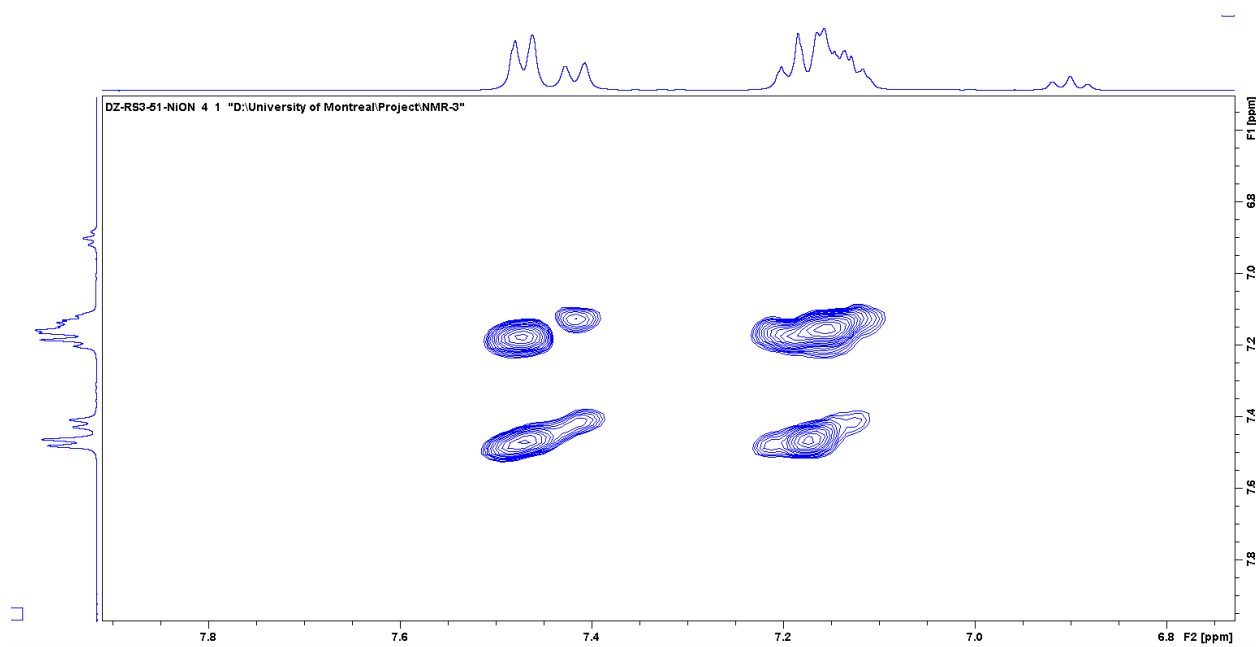
Figure S2. 42. The aromatic region of the COSY NMR spectrum of **5c** in C$_6$D$_6$.
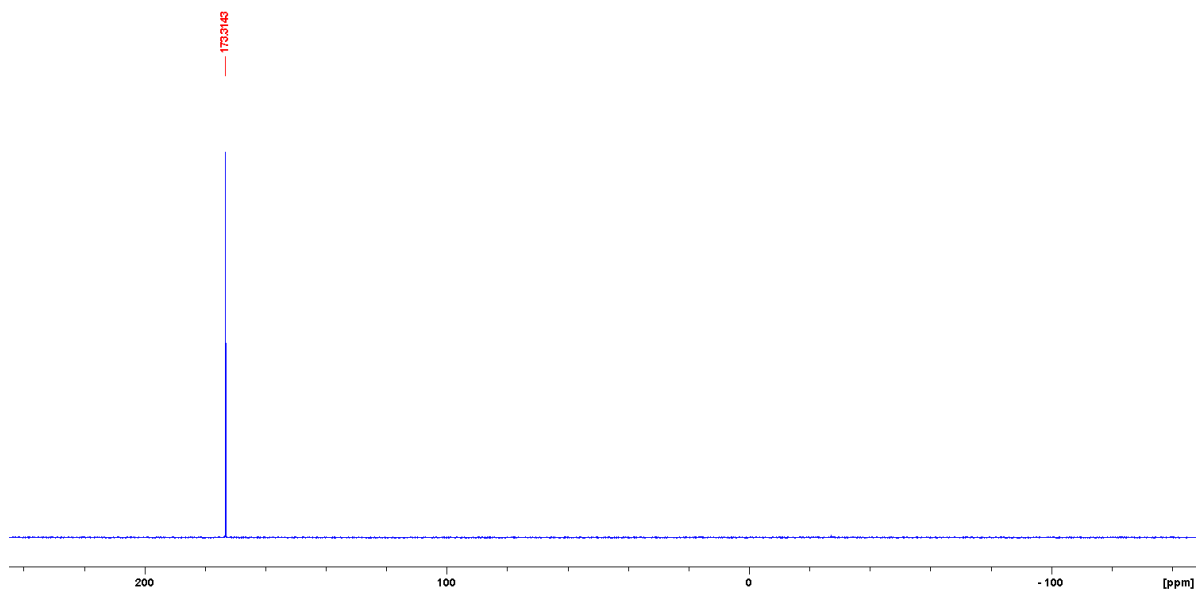
Figure S2. 43. Full ^{31}P{^{1}H} NMR spectrum of **5c** in C_6D_6.

NMR spectra of complex **6a**
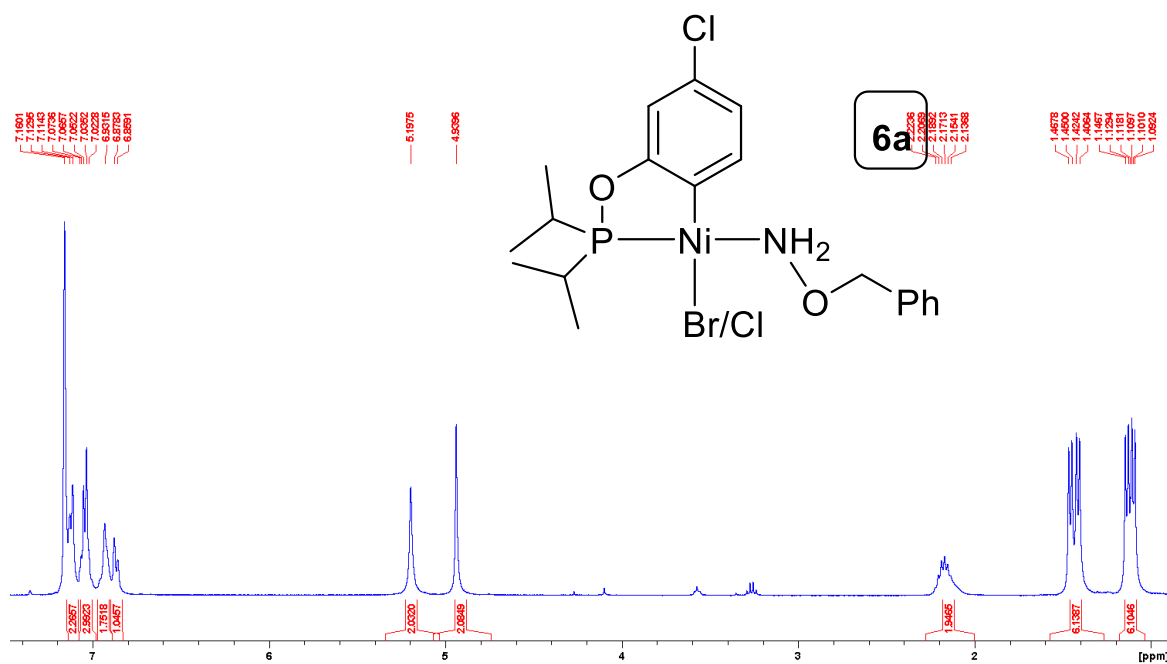
Figure S2. 44. Full ^{1}H NMR spectrum of **6a** in C$_6$D$_6$.
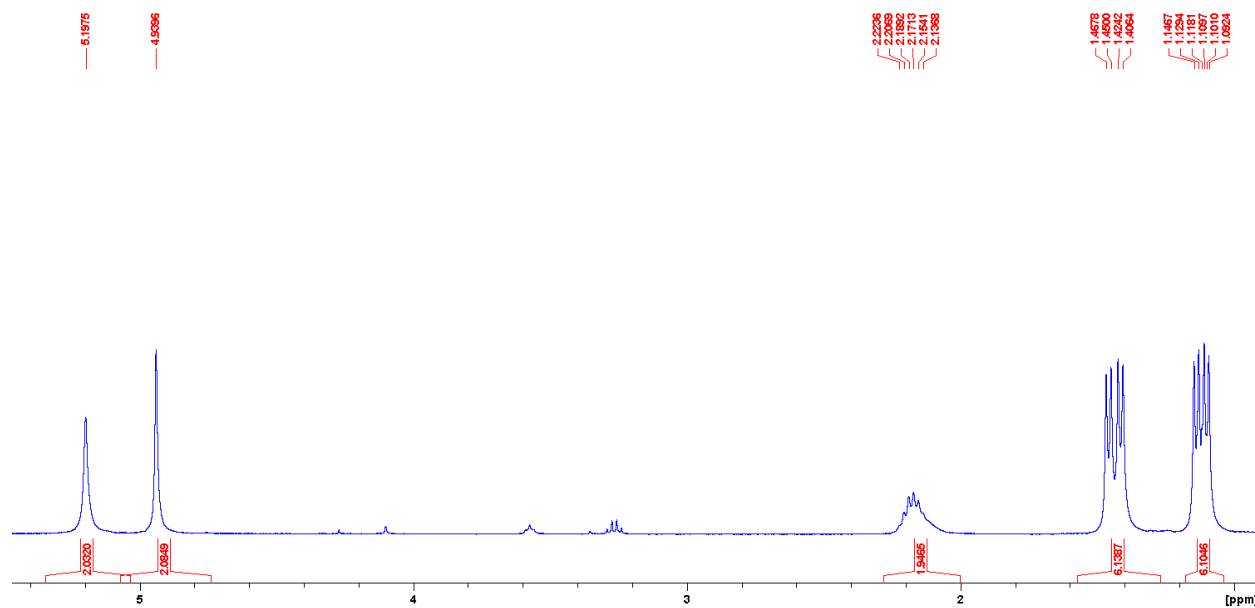
Figure S2. 45. The aliphatic region of the ^{1}H NMR spectrum of **6a** in C$_6$D$_6$.
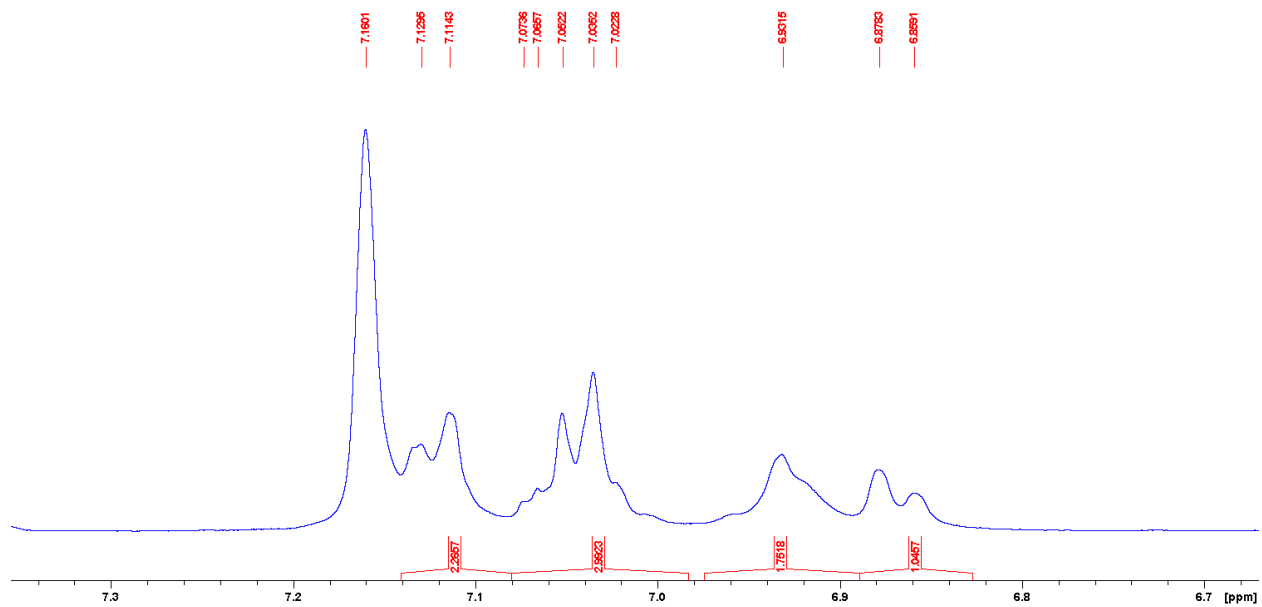
Figure S2. 46. The aromatic region of the ^{1}H NMR spectrum of **6a** in C$_6$D$_6$.
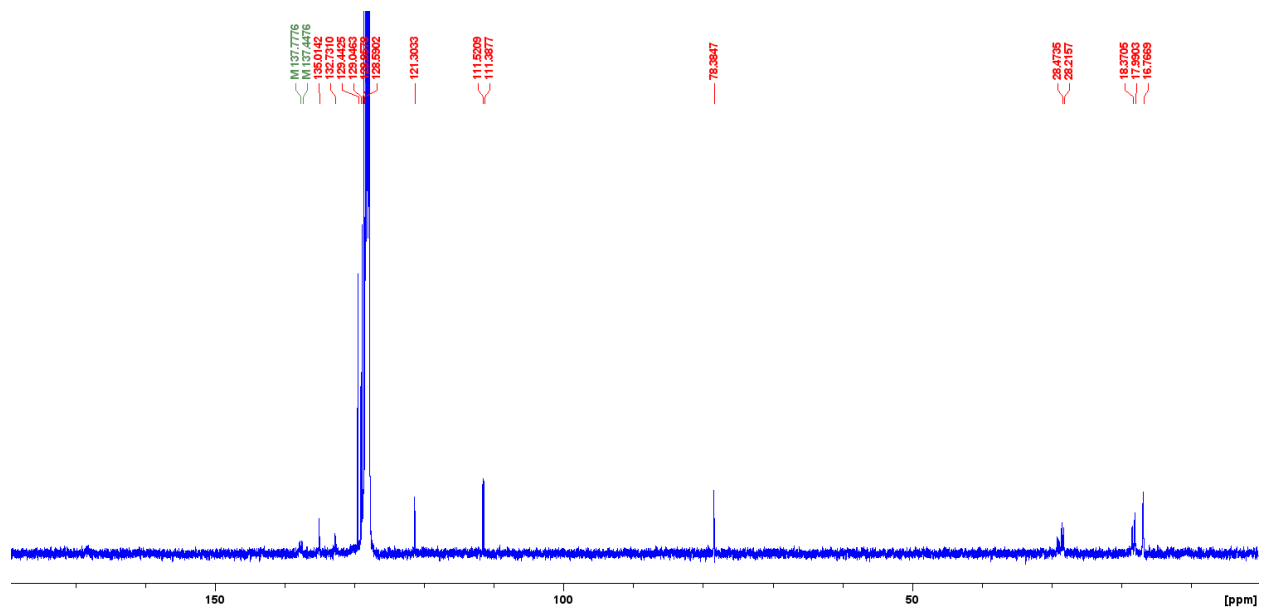
Figure S2. 47. Full ^{13}C NMR spectrum of **6a** in C$_6$D$_6$.
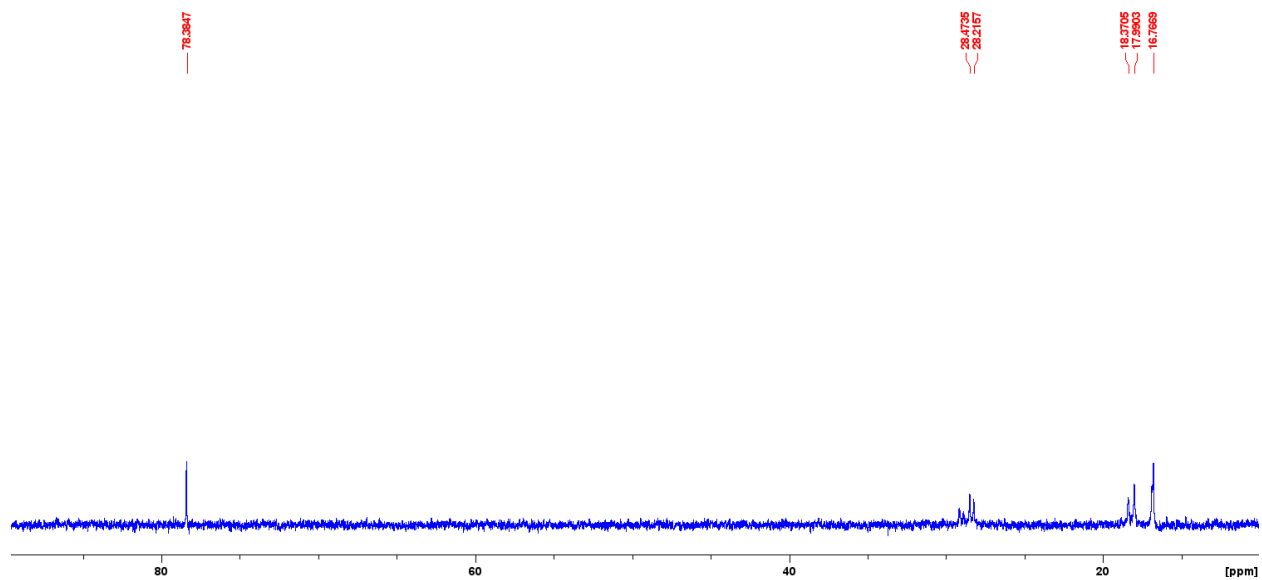
Figure S2. 48. The aliphatic region of the ^{13}C NMR spectrum of **6a** in C$_6$D$_6$.
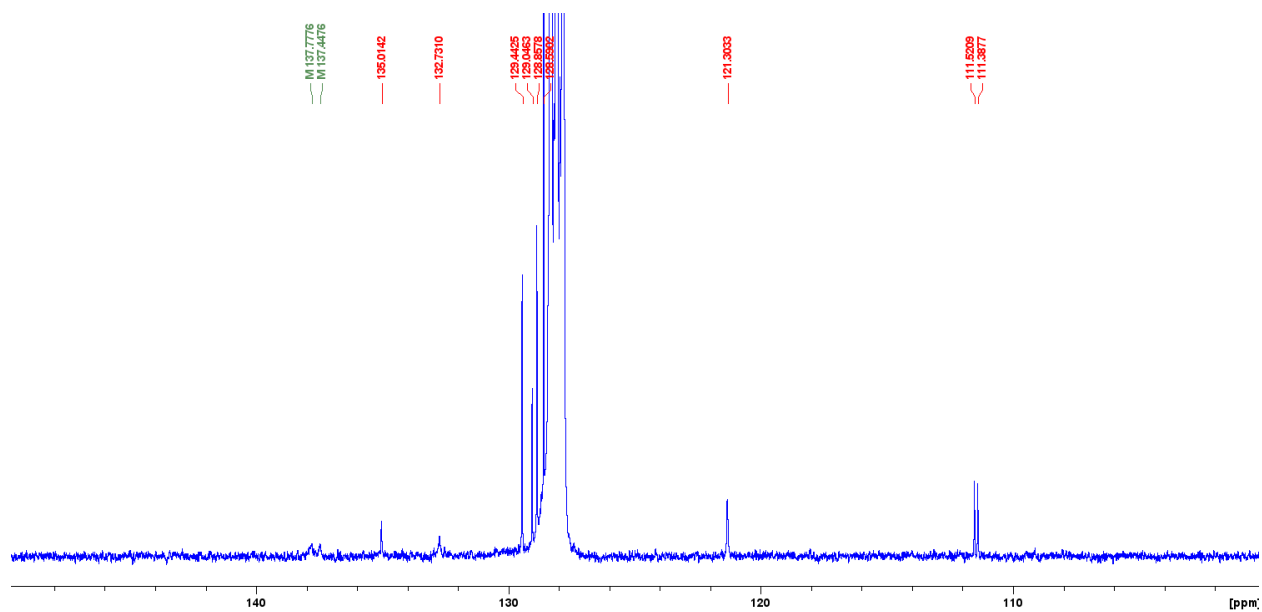
Figure S2. 49. The aromatic region of the ^{13}C NMR spectrum of **6a** in C$_6$D$_6$.
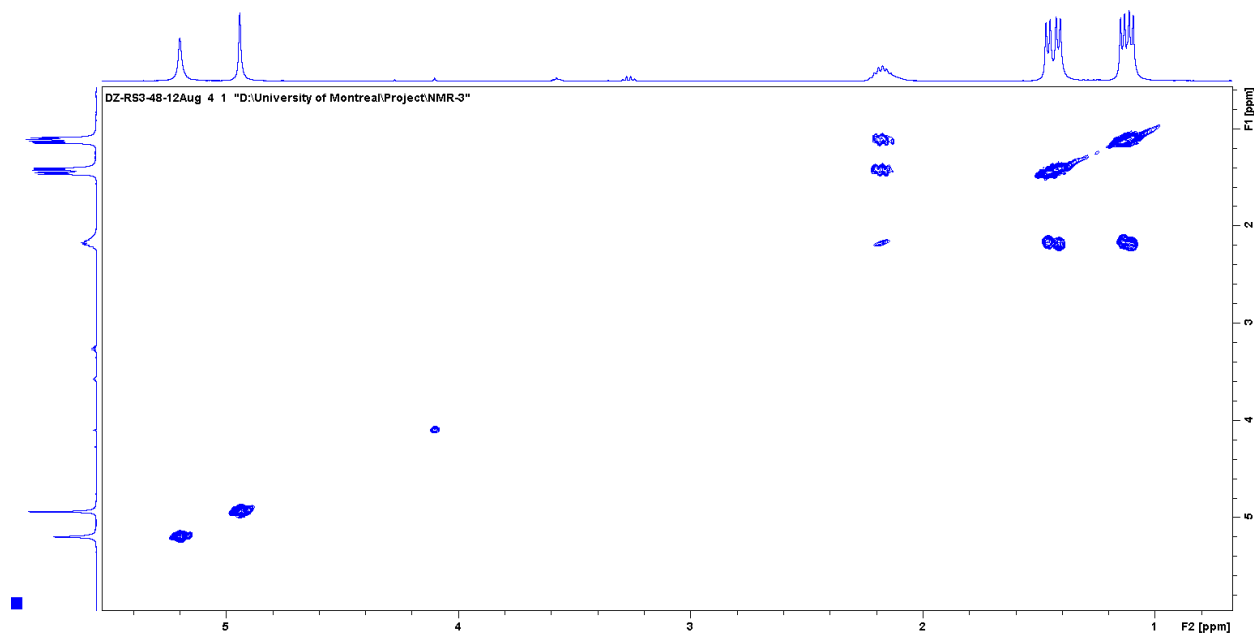
Figure S2. 50. The aliphatic region of the COSY NMR spectrum of **6a** in C_6D_6.
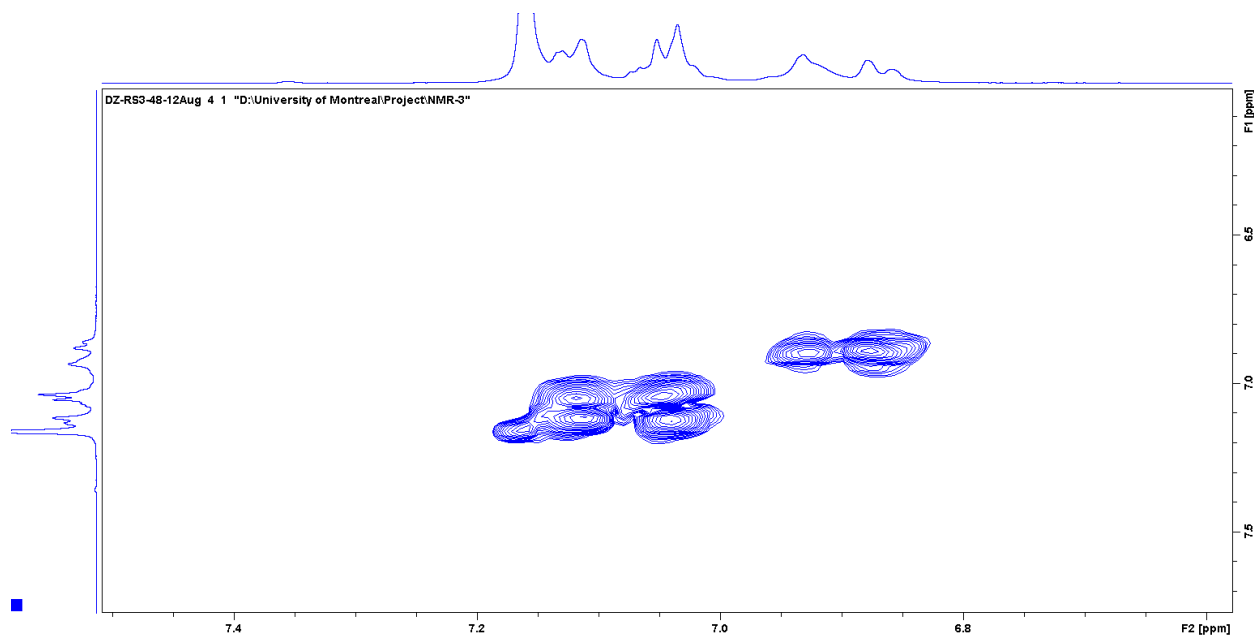
Figure S2. 51. The aromatic region of the COSY NMR spectrum of **6a** in C_6D_6.
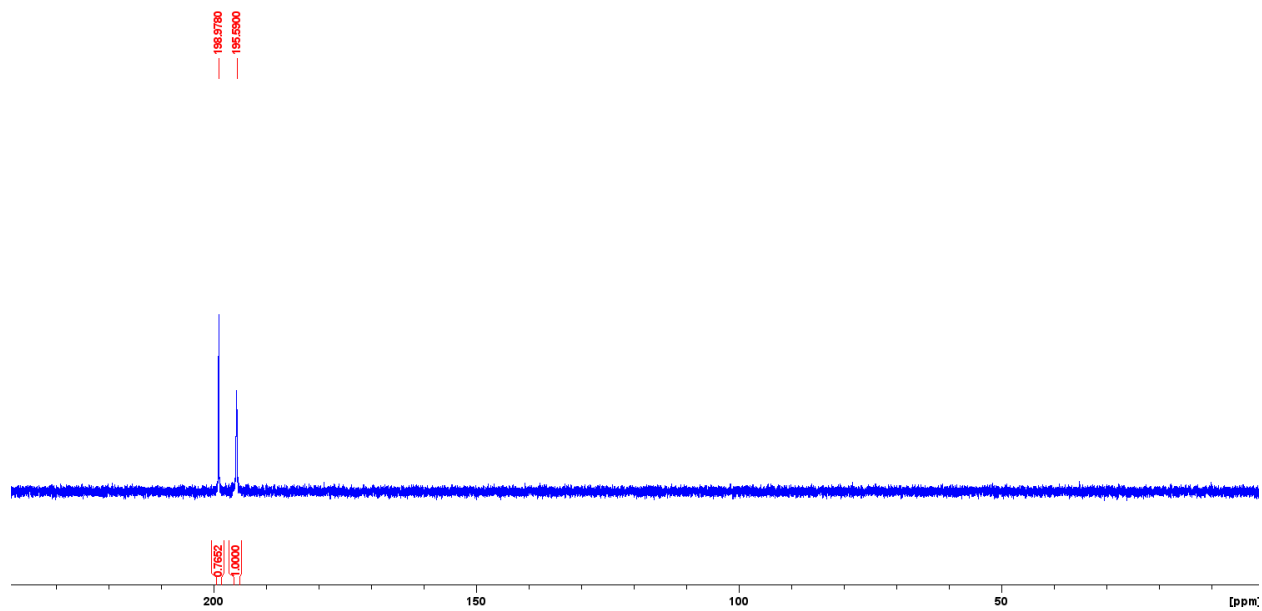
Figure S2. 52. $^{31}P\{^1H\}$ NMR spectrum of **6a** in C_6D_6.

NMR spectra of complex **6b**

Figure S2. 53. Full ^{1}H NMR spectrum of **6b** in C$_6$D$_6$.

Figure S2. 54. The aliphatic region of the ^{1}H NMR spectrum of **6b** in C$_6$D$_6$.
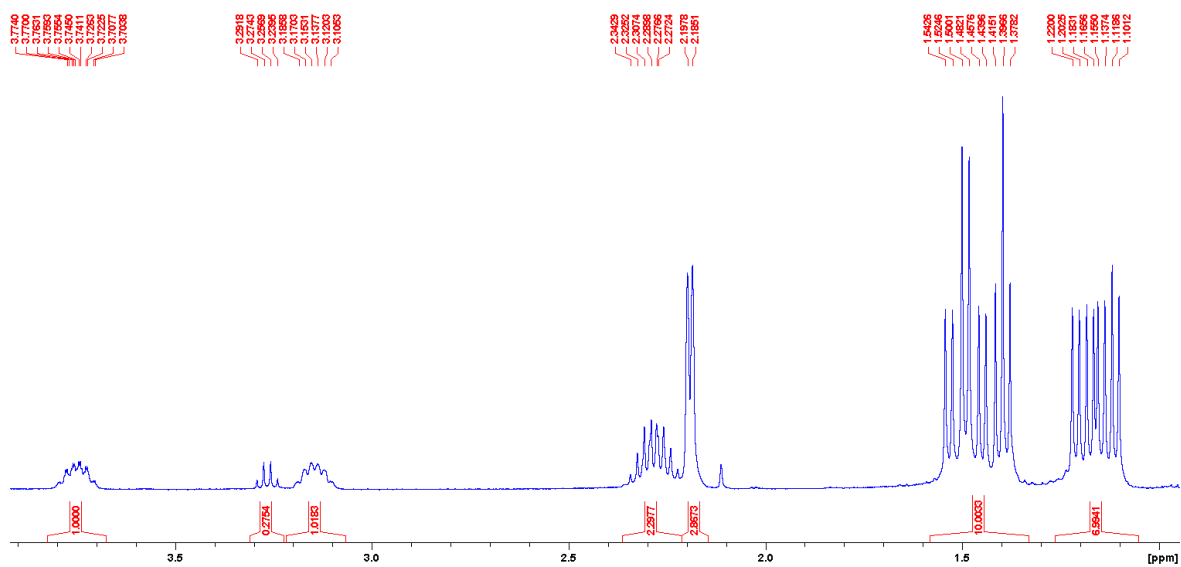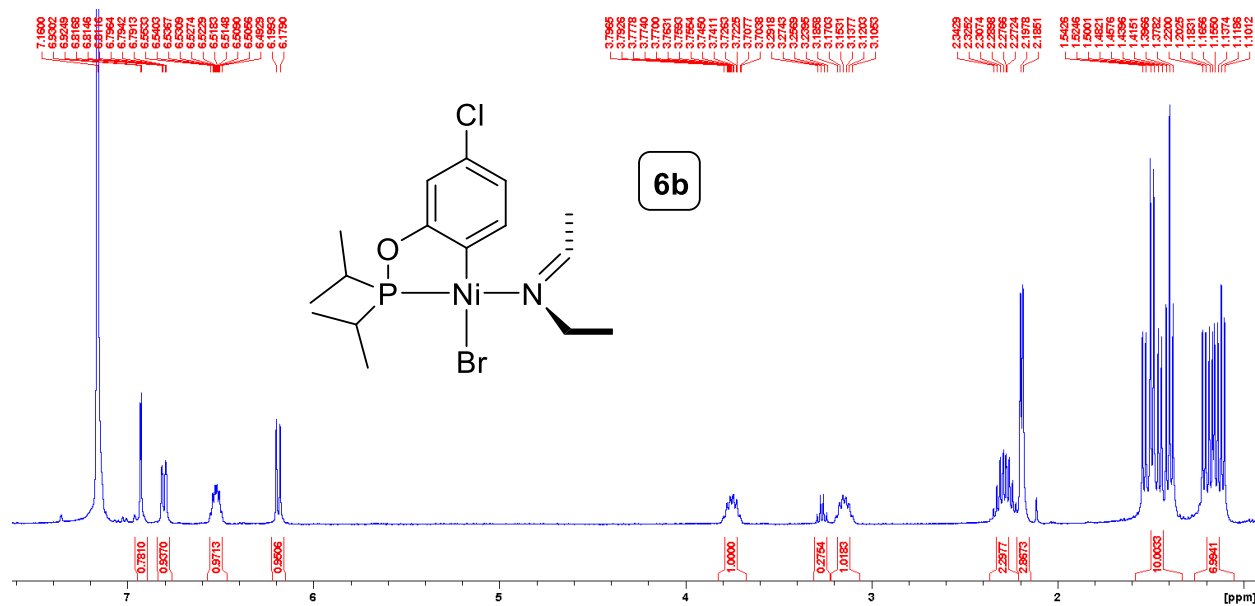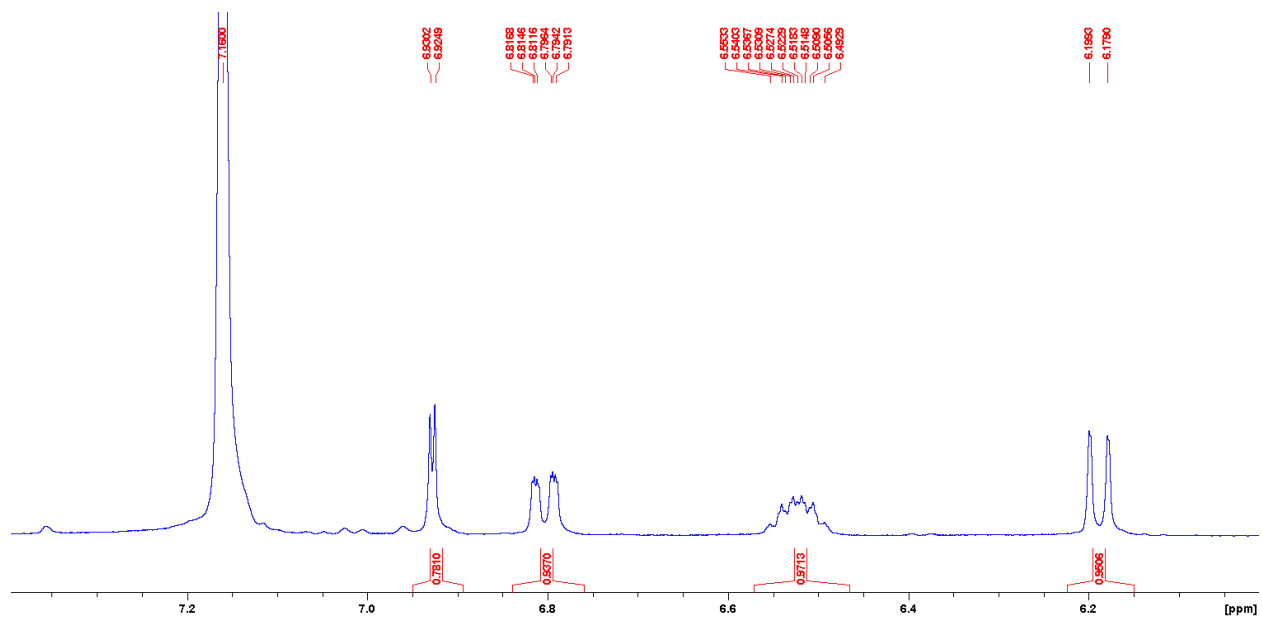
Figure S2. 55. The aromatic region of the ^{1}H NMR spectrum of **6b** in C_6D_6.
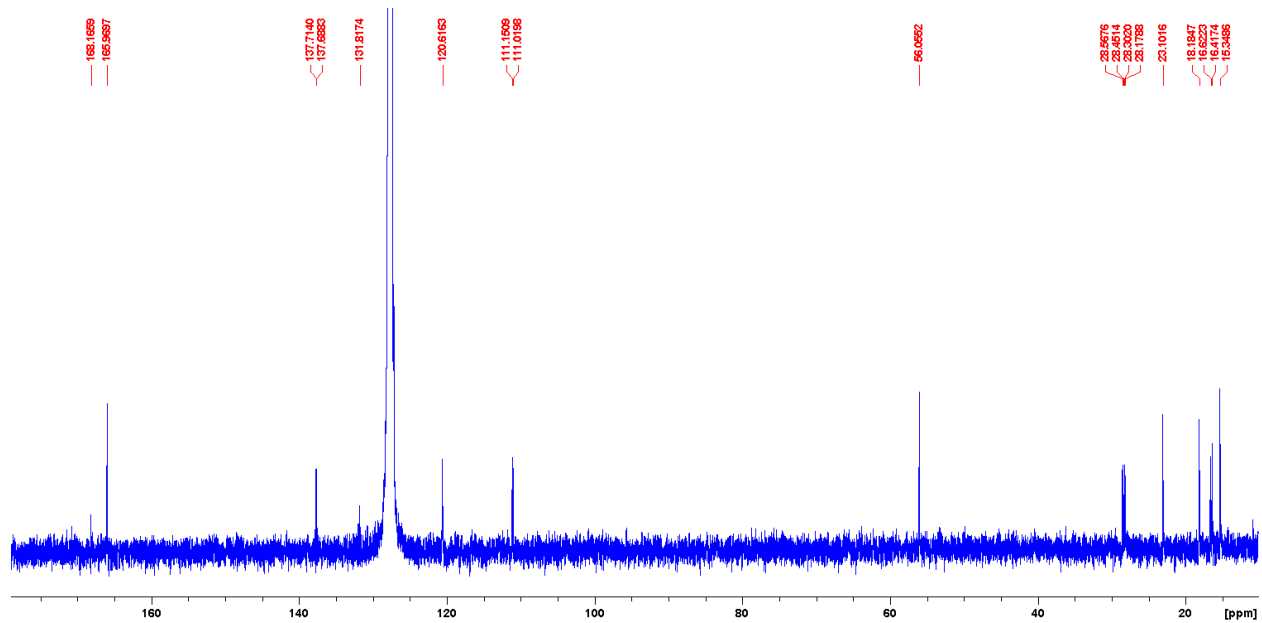
Figure S2. 56. Full ^{13}C NMR spectrum of **6b** in C_6D_6.
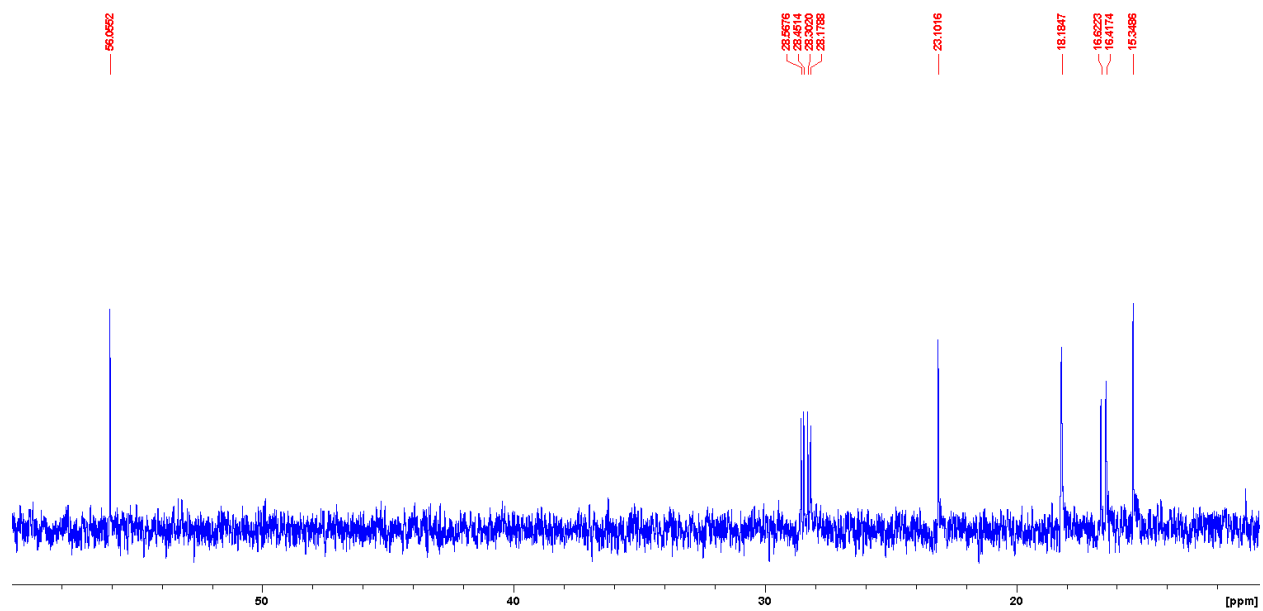
Figure S2. 57. The aliphatic region of the ^{13}C NMR spectrum of **6b** in C_6D_6.
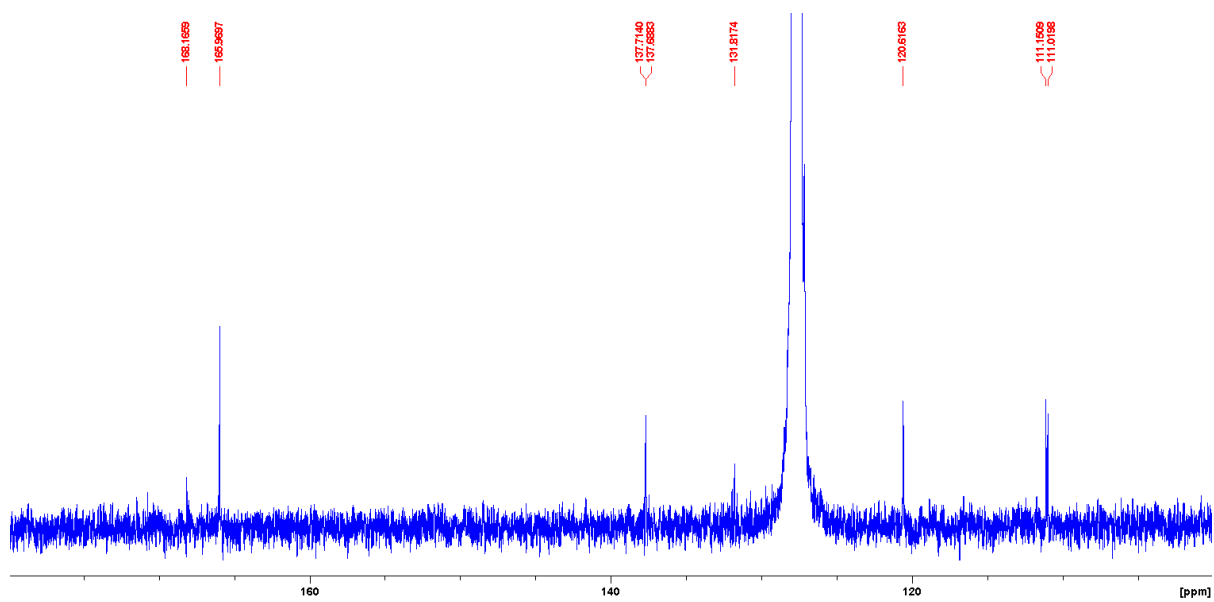
Figure S2. 58. The aromatic region of the ^{13}C NMR spectrum of **6b** in C_6D_6.
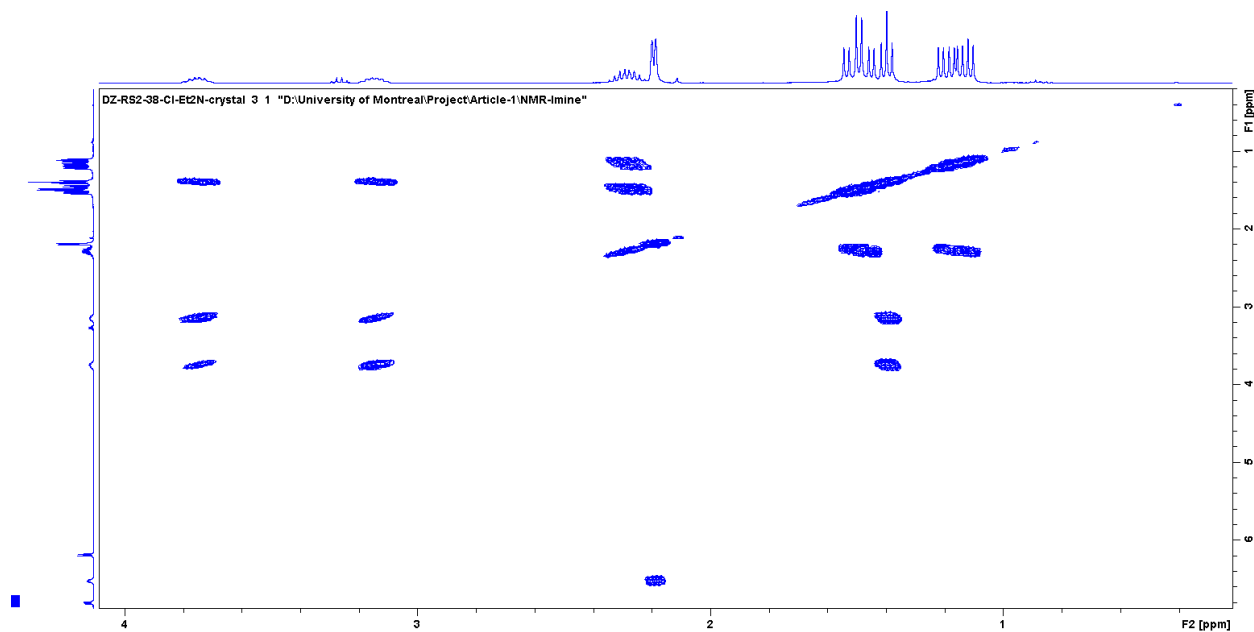
Figure S2. 59. The aliphatic region of the COSY NMR spectrum of **6b** in C_6D_6.
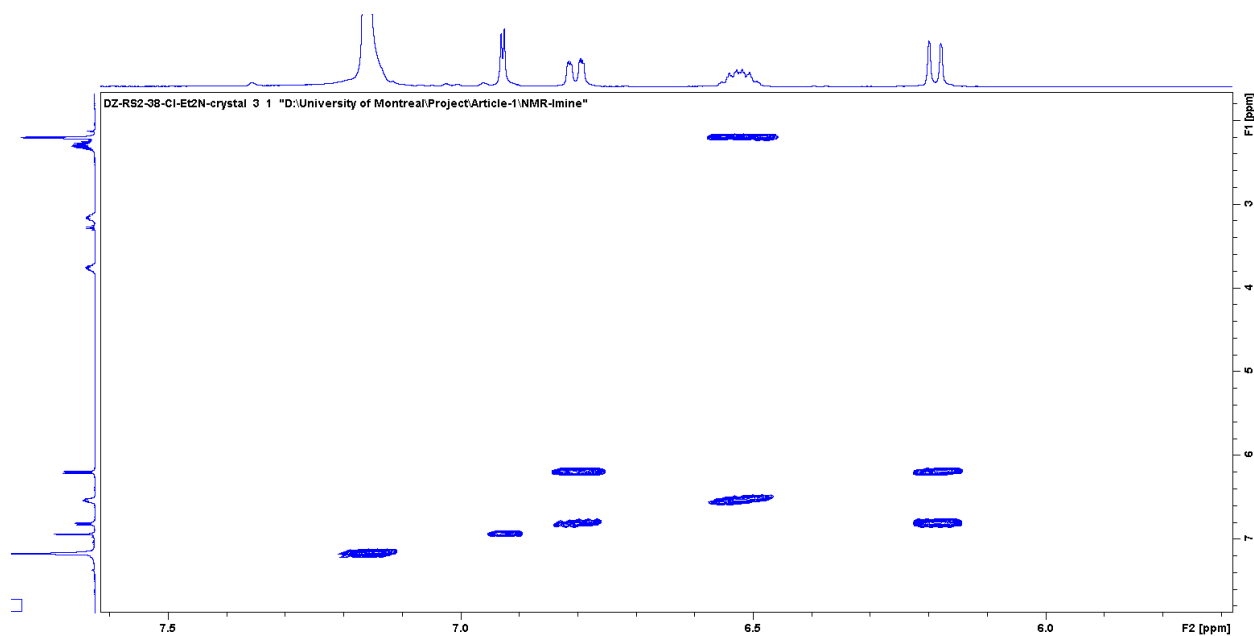
Figure S2. 60. The aromatic region of the COSY NMR spectrum of **6b** in C_6D_6.
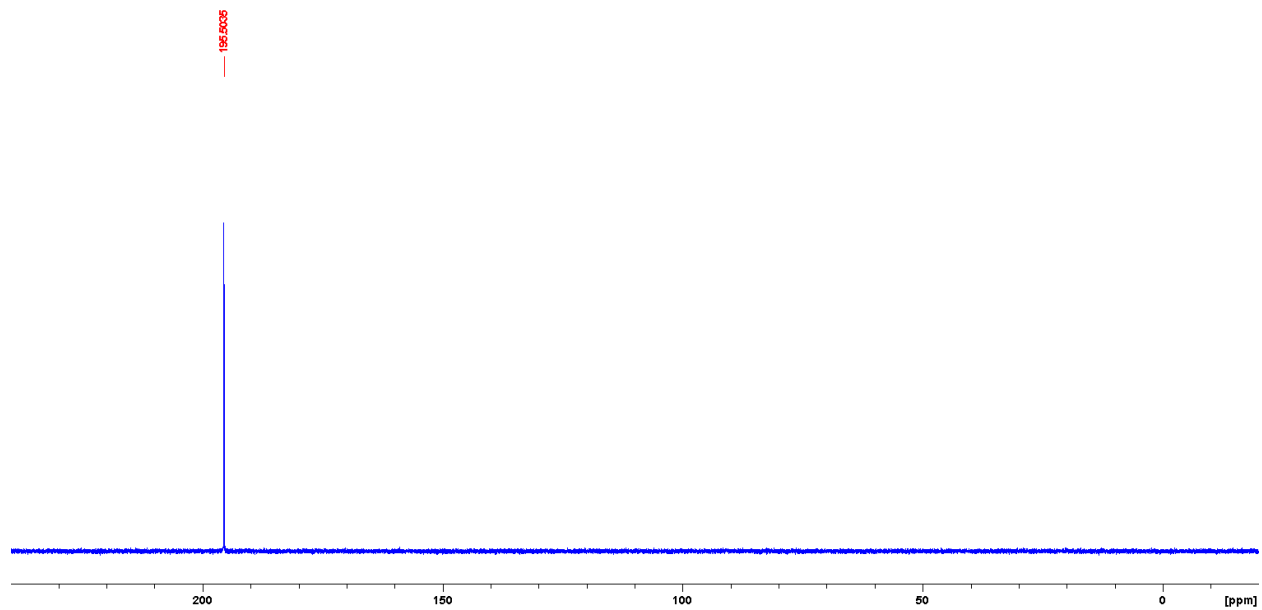
Figure S2. 61. Full $^{31}P\{^1H\}$ NMR spectrum of **6b** in C_6D_6.

NMR spectra of complex **6c**
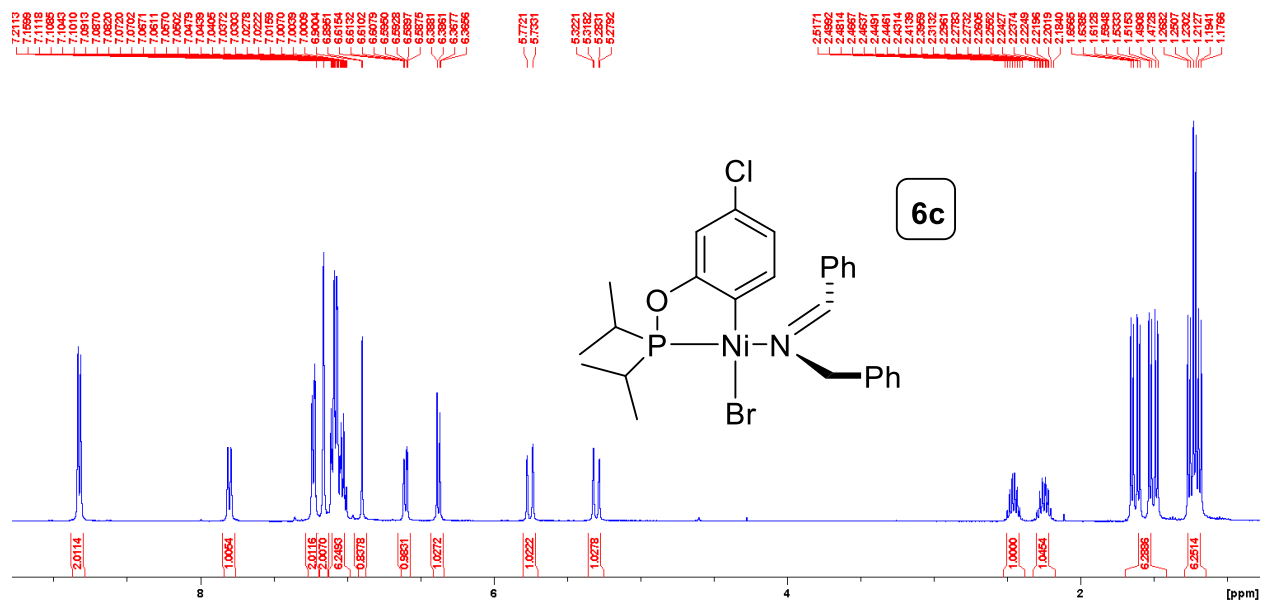
Figure S2. 62. Full ^{1}H NMR spectrum of **6c** in C$_6$D$_6$.
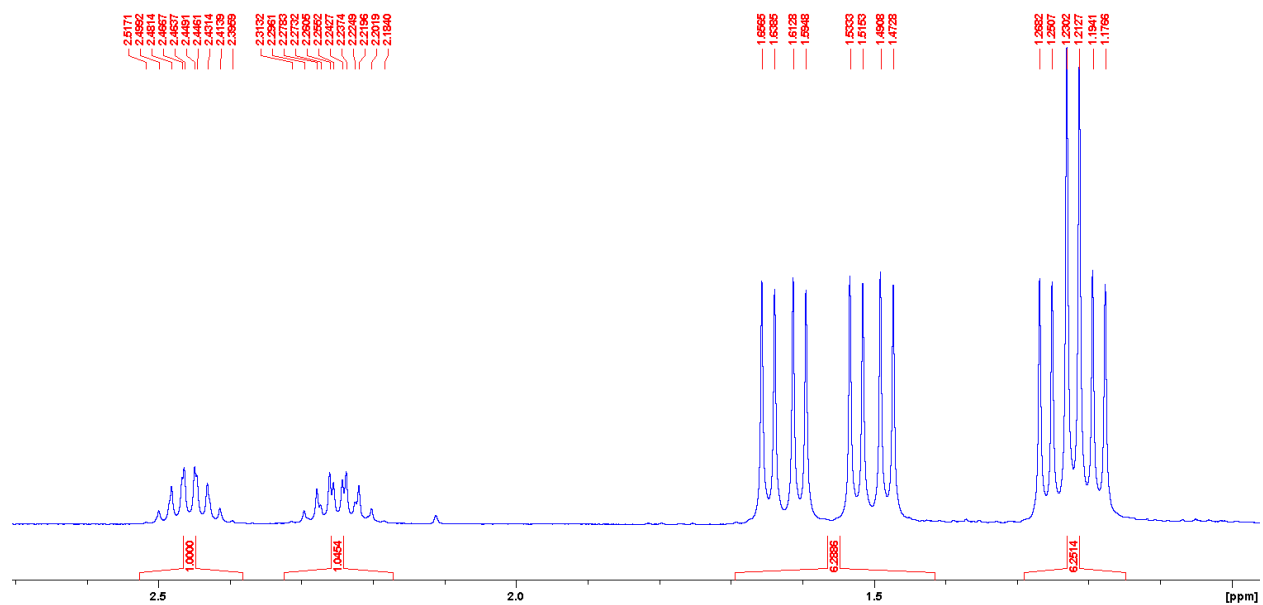
Figure S2. 63. The aliphatic region of the ^{1}H NMR spectrum of **6c** in C$_6$D$_6$.
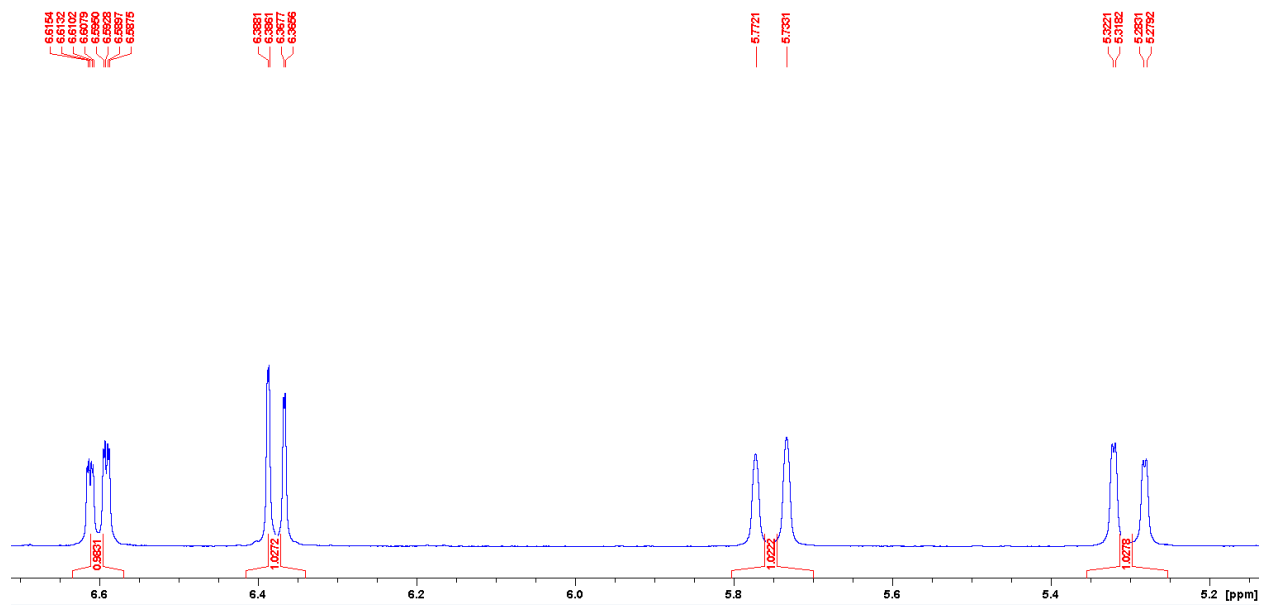
Figure S2. 64. The olefinic region of the ^{1}H NMR spectrum of **6c** in C$_6$D$_6$.
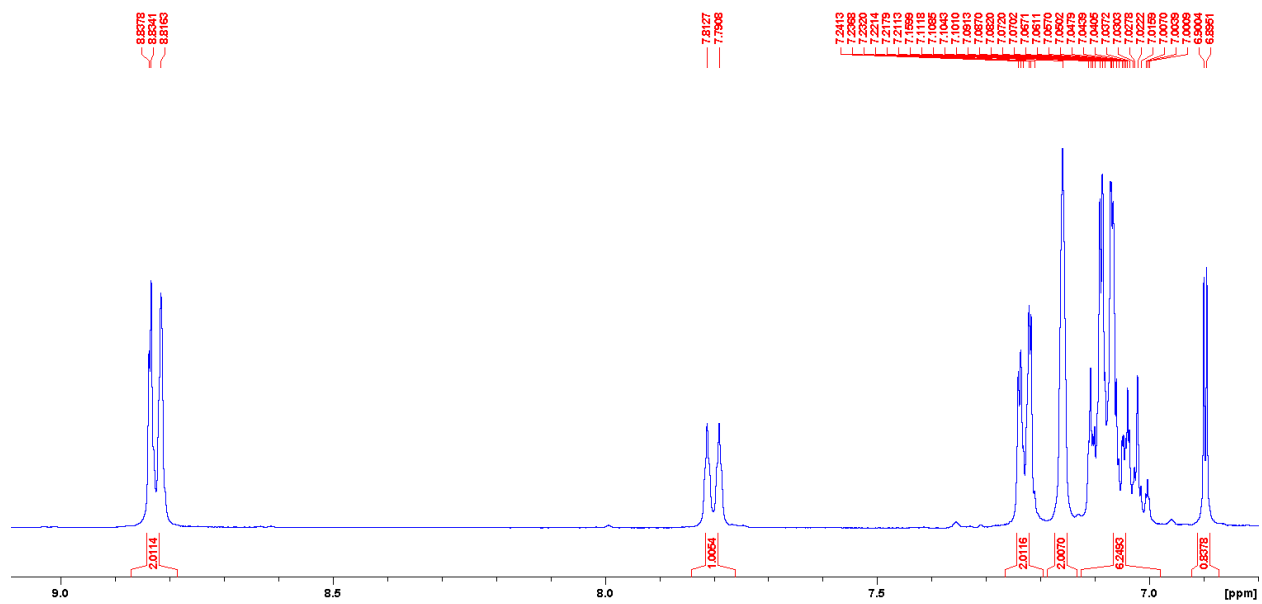
Figure S2. 65. The aromatic region of the ^{1}H NMR spectrum of **6c** in C$_6$D$_6$.
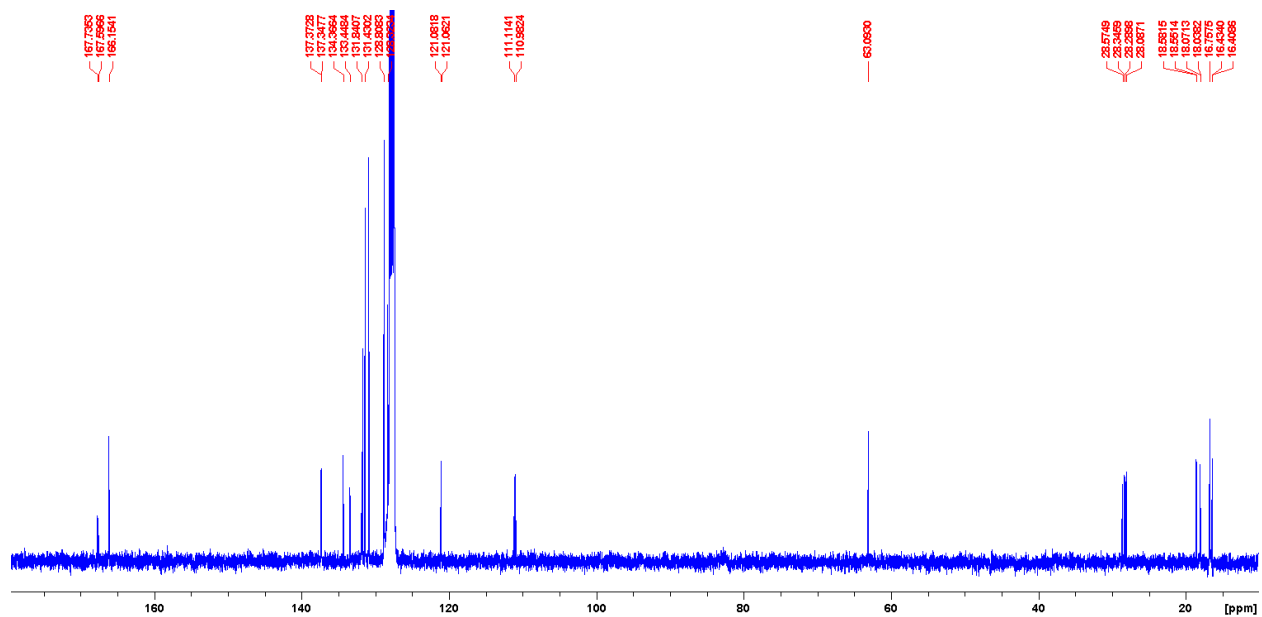
Figure S2. 66. Full ^{13}C NMR spectrum of **6c** in C$_6$D$_6$.
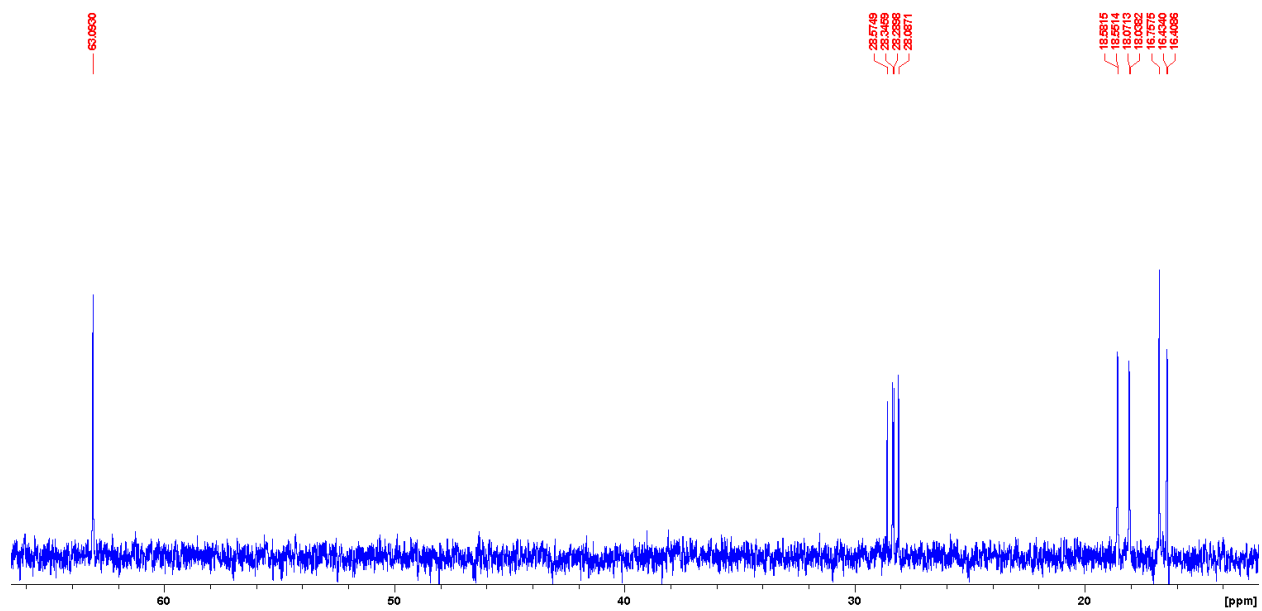
Figure S2. 67. The aliphatic region of the ^{13}C NMR spectrum of **6c** in C$_6$D$_6$.
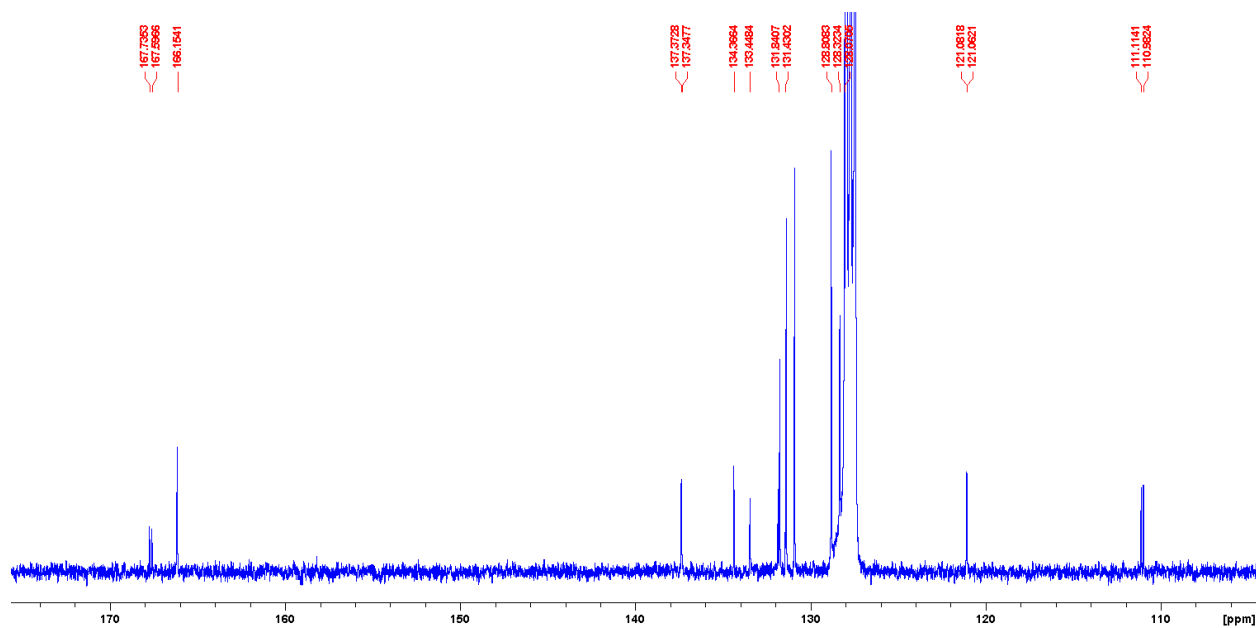
Figure S2. 68. The aromatic region of the ^{13}C NMR spectrum of **6c** in C_6D_6.
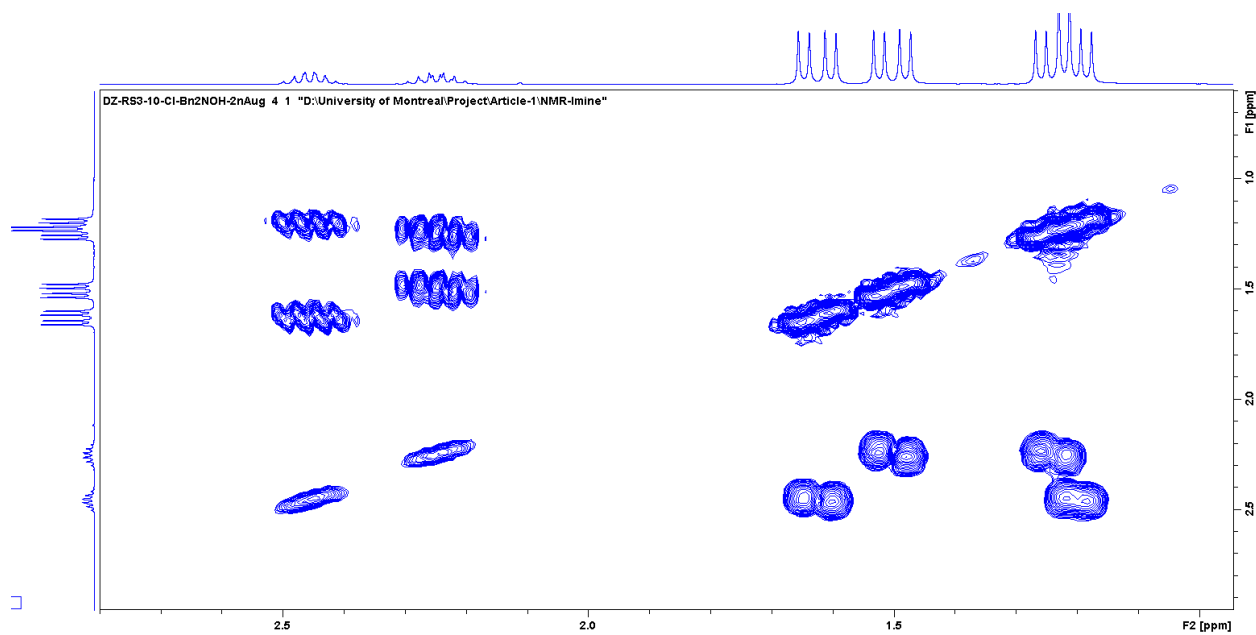
Figure S2. 69. The aliphatic region of the COSY NMR spectrum of **6c** in C_6D_6.
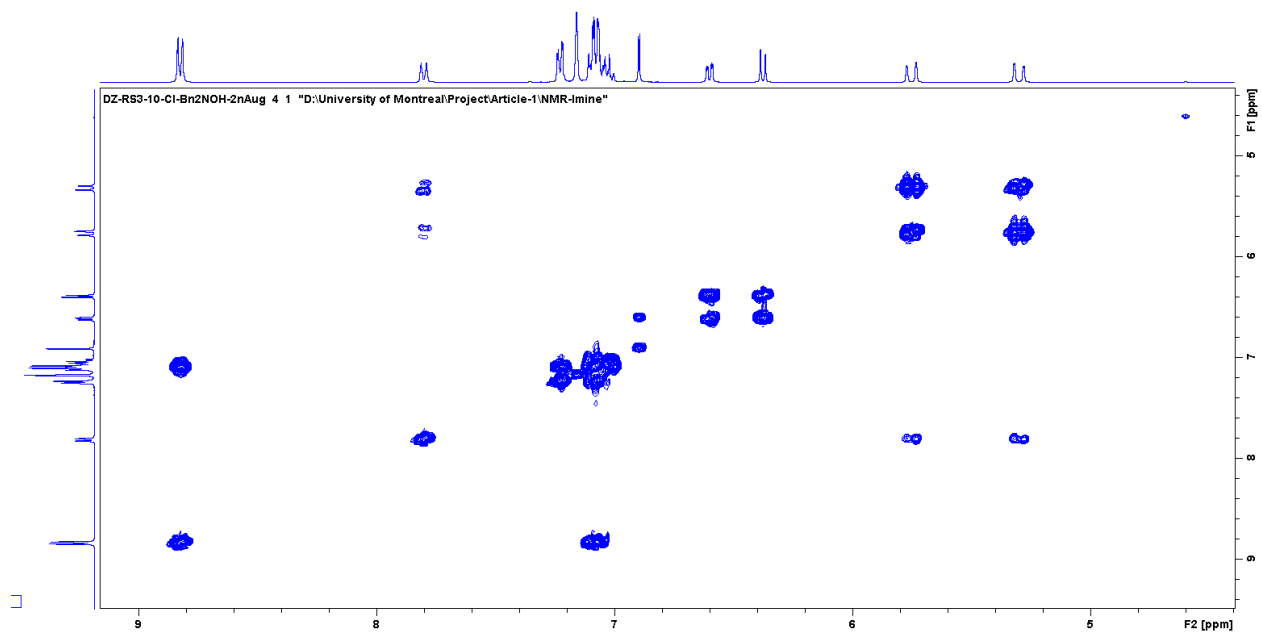
Figure S2. 70. The aromatic region of the COSY NMR spectrum of **6c** in C_6D_6.
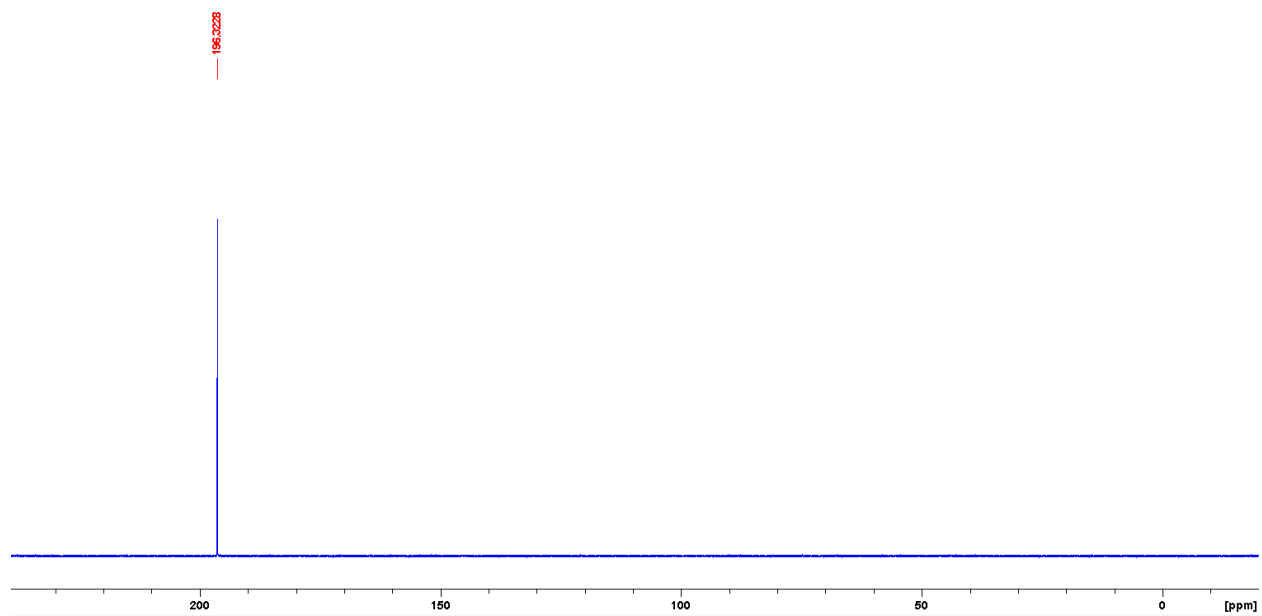
Figure S2. 71. $^{31}P\{^1H\}$ NMR spectrum of **6c** in C_6D_6.

NMR spectra of complex **7a**
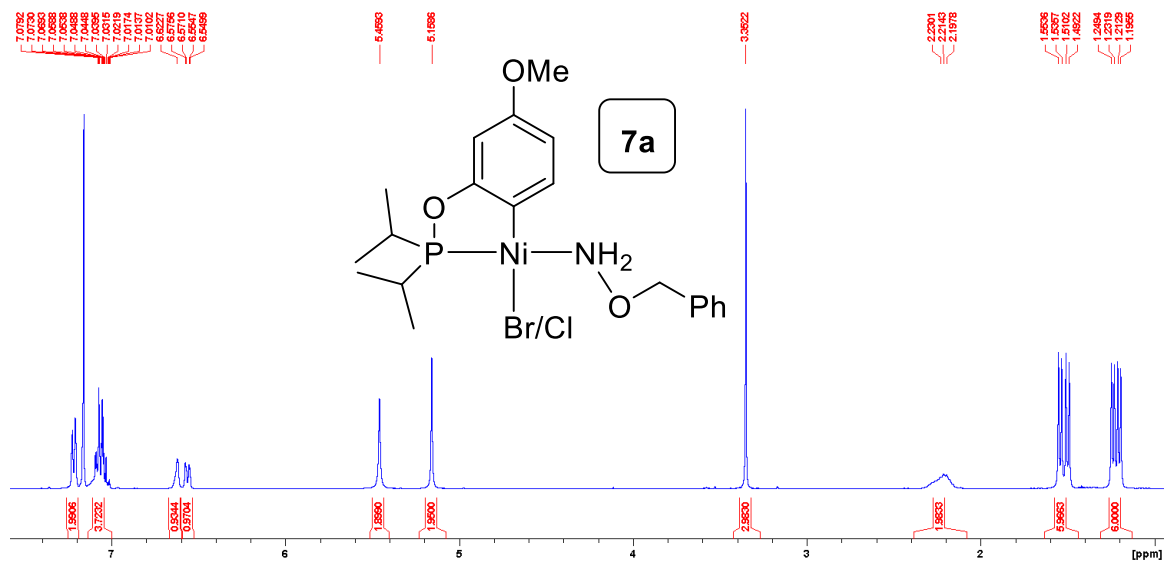
Figure S2. 72. Full ^{1}H NMR spectrum of **7a** in C$_6$D$_6$.
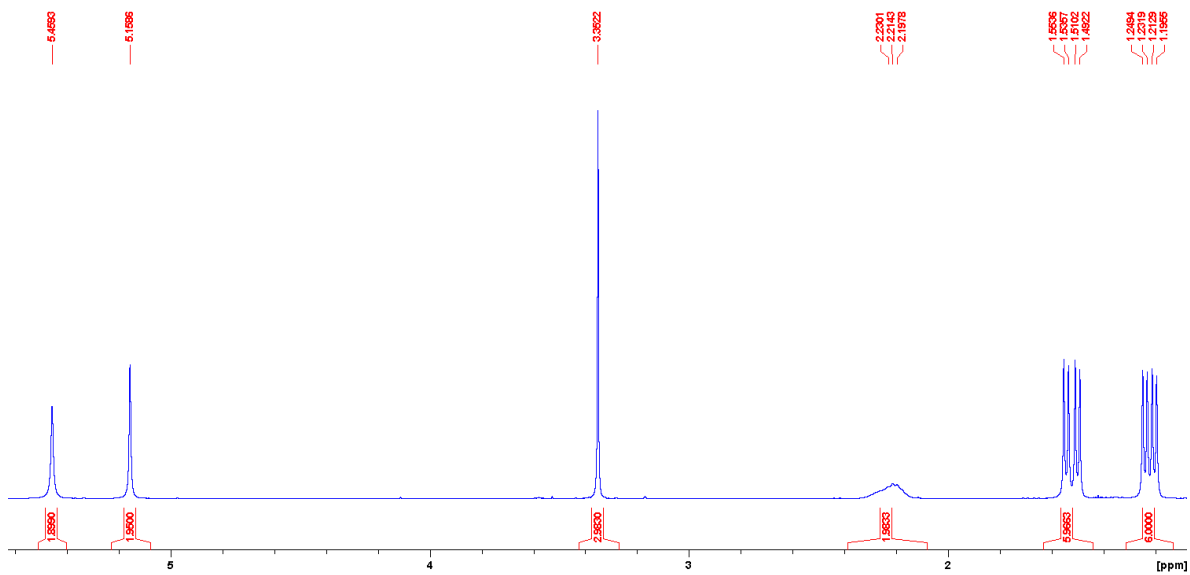
Figure S2. 73. The aliphatic region of the ^{1}H NMR spectrum of **7a** in C$_6$D$_6$.
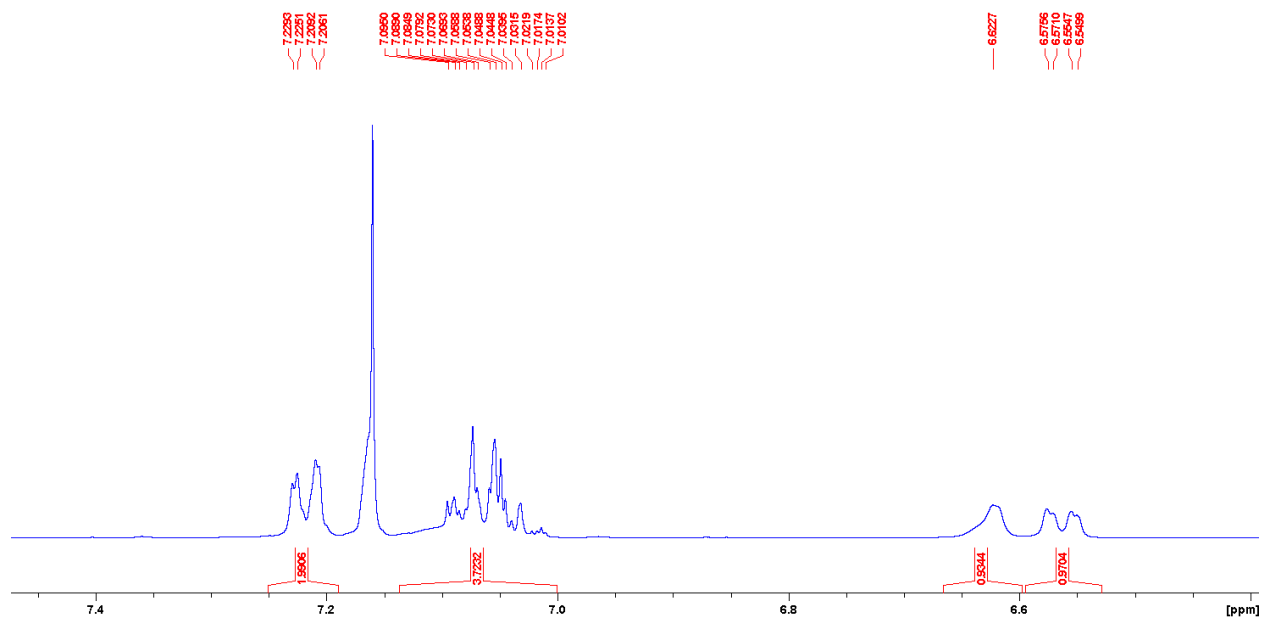
Figure S2. 74. The aromatic region of the ^{1}H NMR spectrum of **7a** in C$_6$D$_6$.
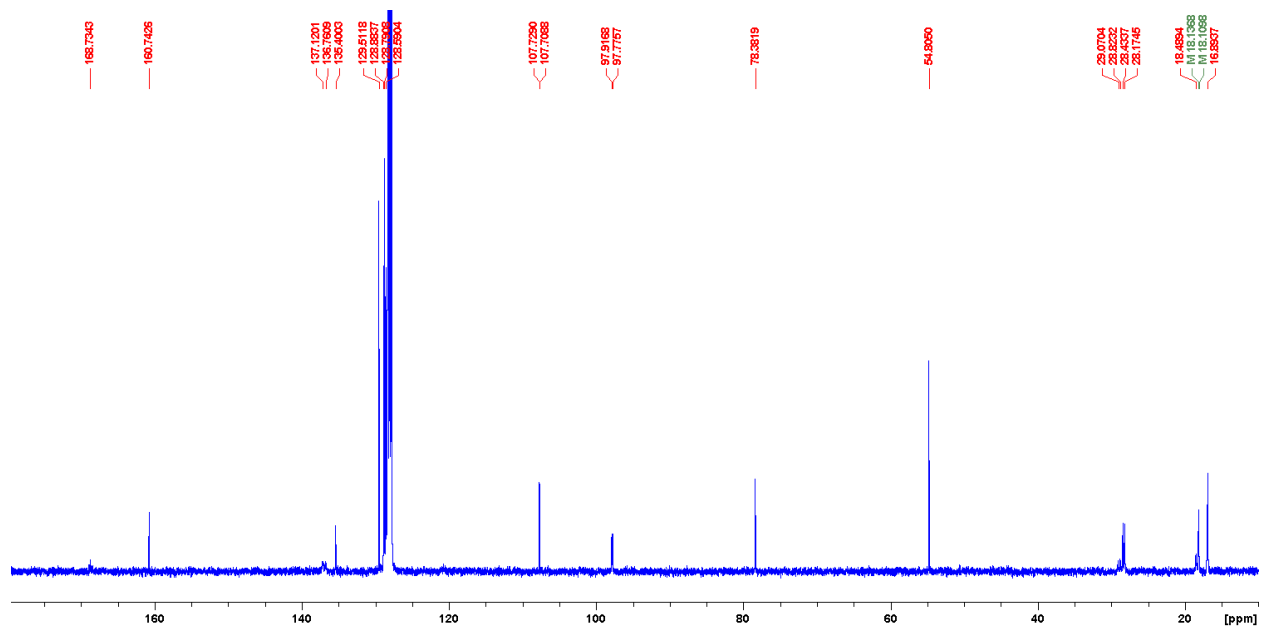
Figure S2. 75. Full ^{13}C NMR spectrum of **7a** in C$_6$D$_6$.
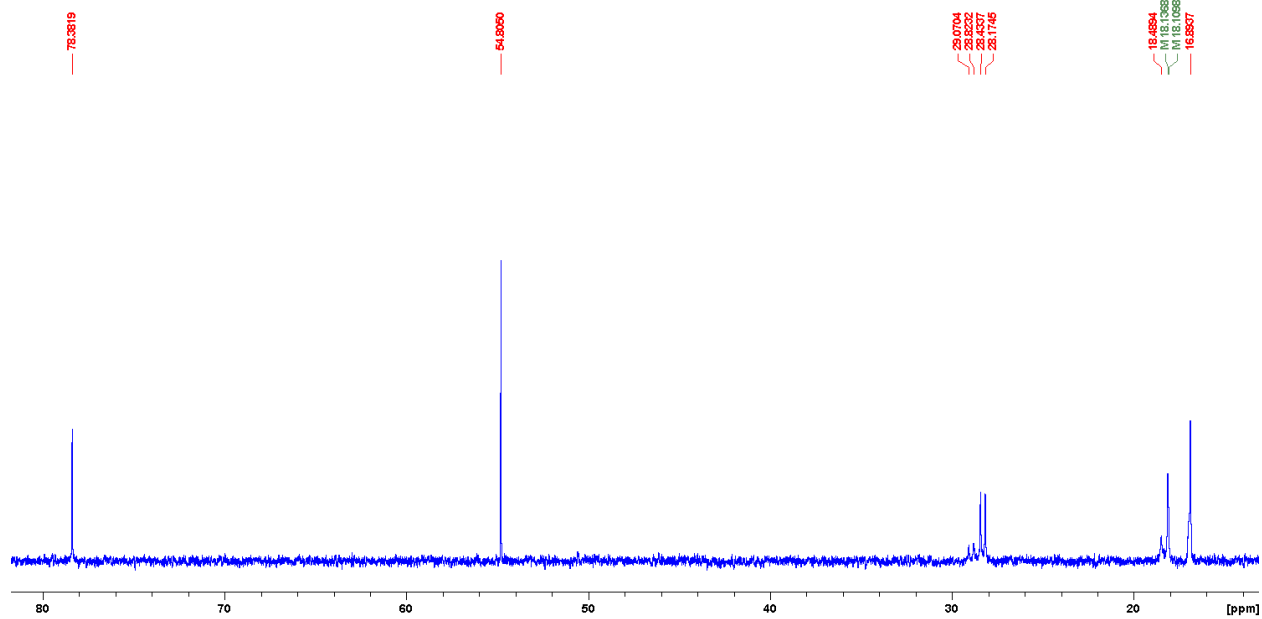
Figure S2. 76. The aliphatic region of the ^{13}C NMR spectrum of **7a** in C_6D_6.
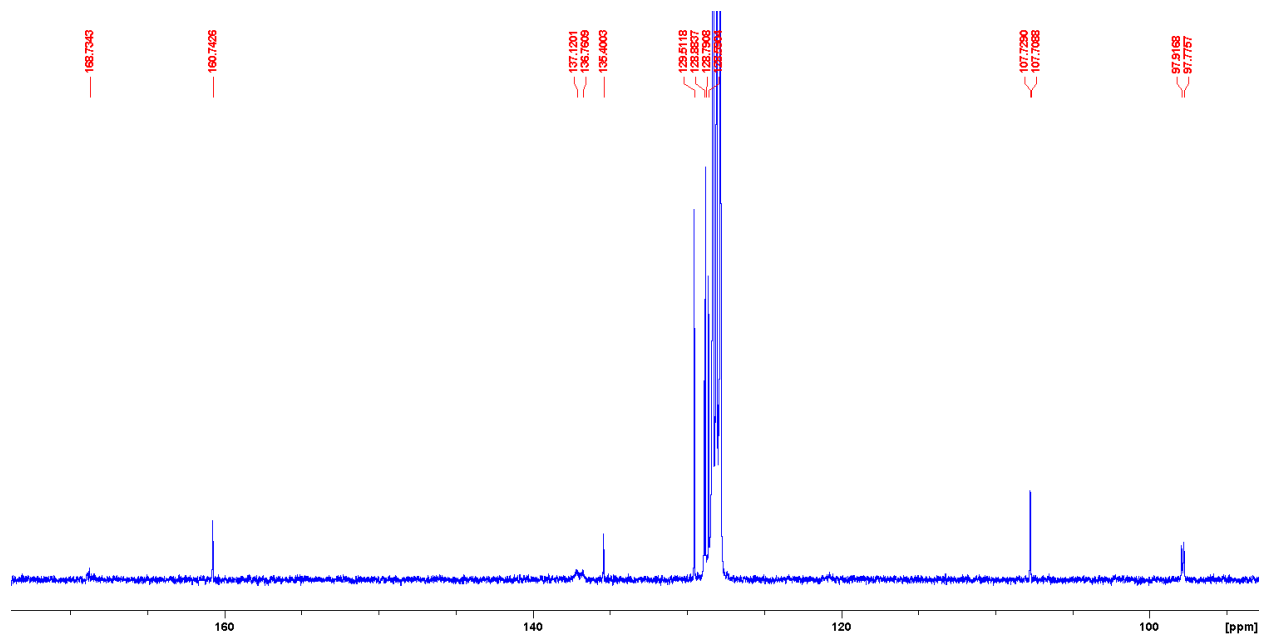
Figure S2. 77. The aromatic region of the ^{13}C NMR spectrum of **7a** in C_6D_6.
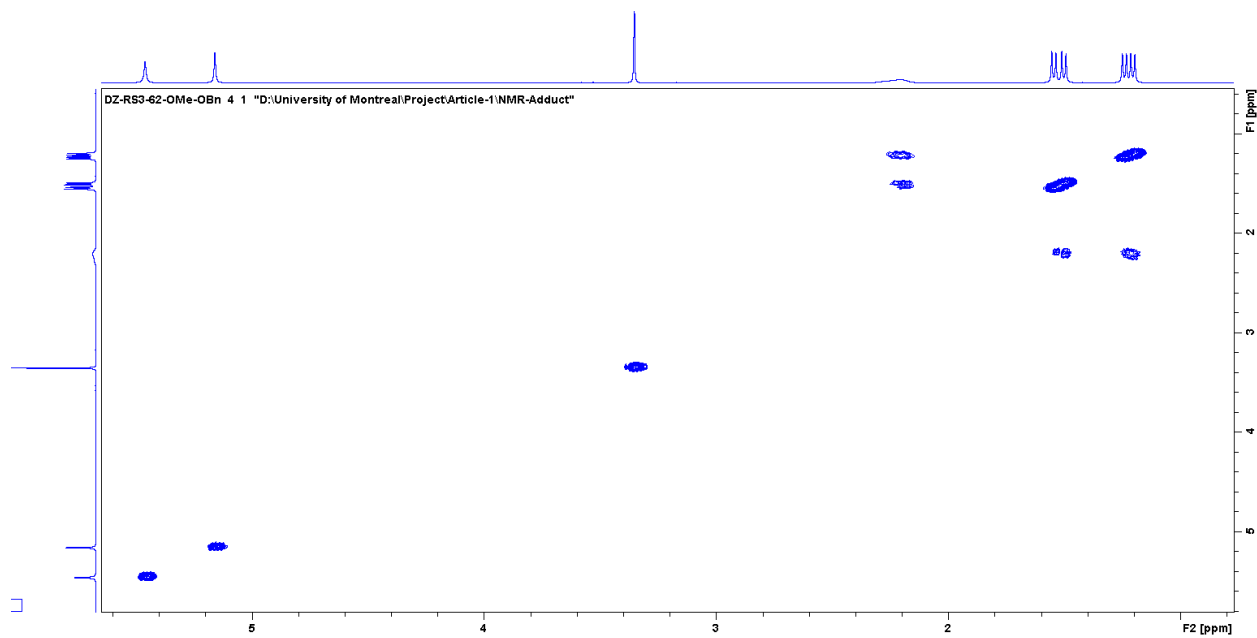
Figure S2. 78. The aliphatic region of the COSY NMR spectrum of **7a** in C_6D_6.
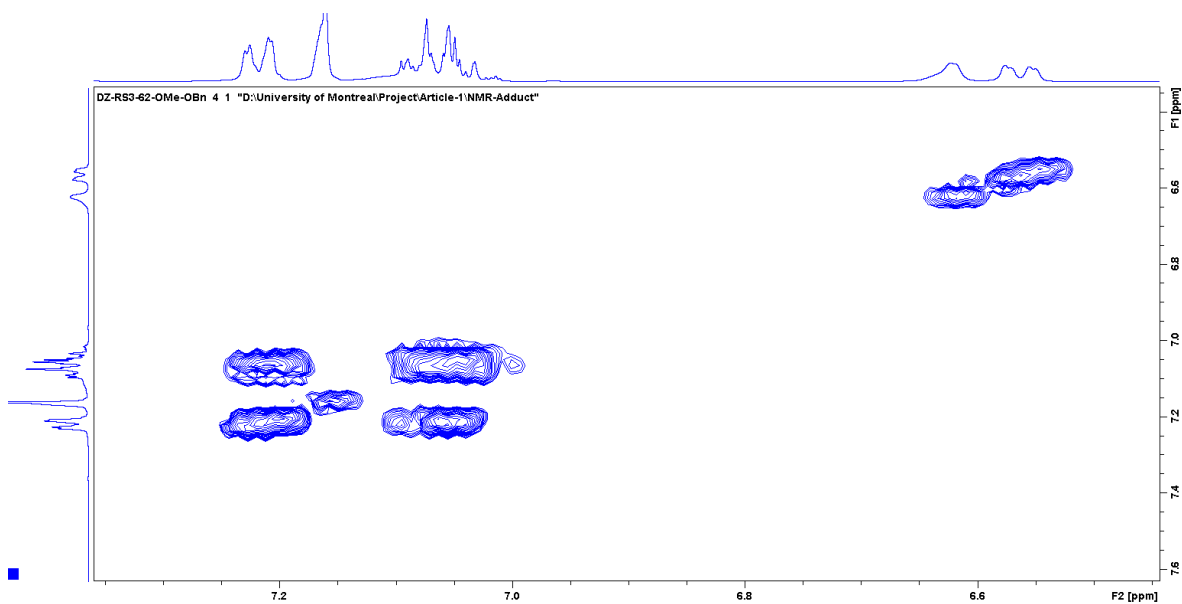
Figure S2. 79. The aromatic region of the COSY NMR spectrum of **7a** in C_6D_6.
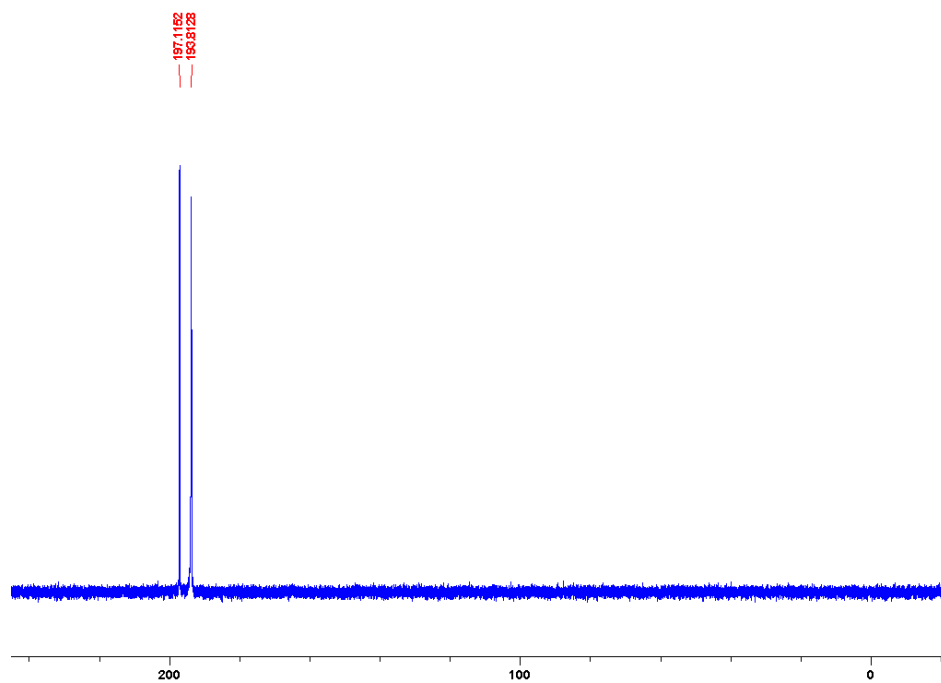
Figure S2. 80. $^{31}P\{^{1}H\}$ NMR spectrum of **7a** in C_6D_6.

NMR spectra of complex **7b**
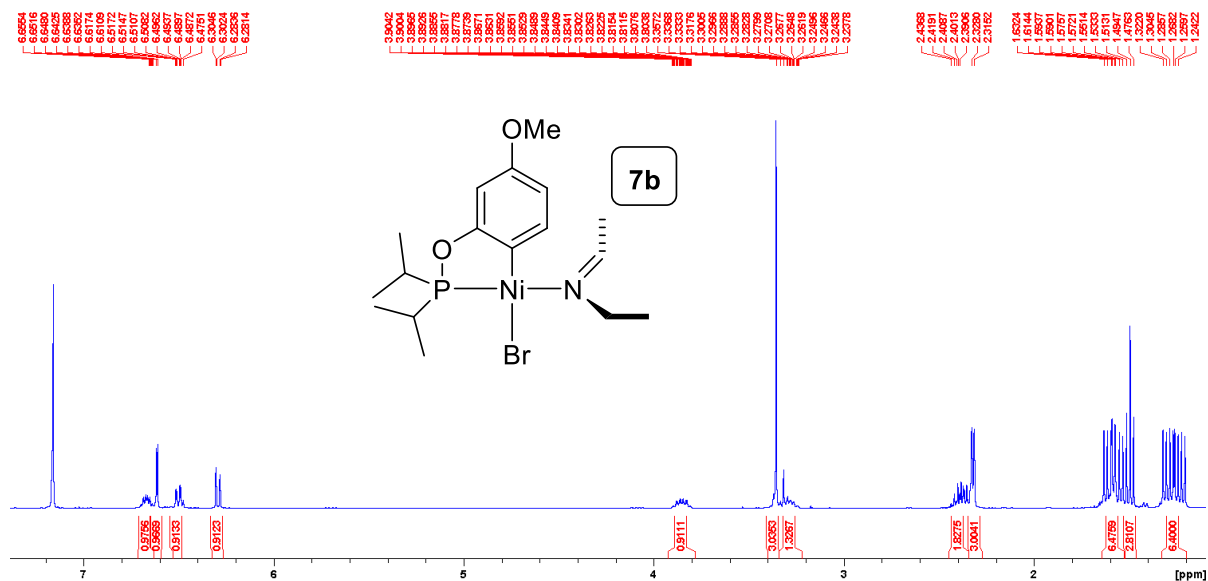
Figure S2. 81. Full ^{1}H NMR spectrum of **7b** in C$_6$D$_6$.
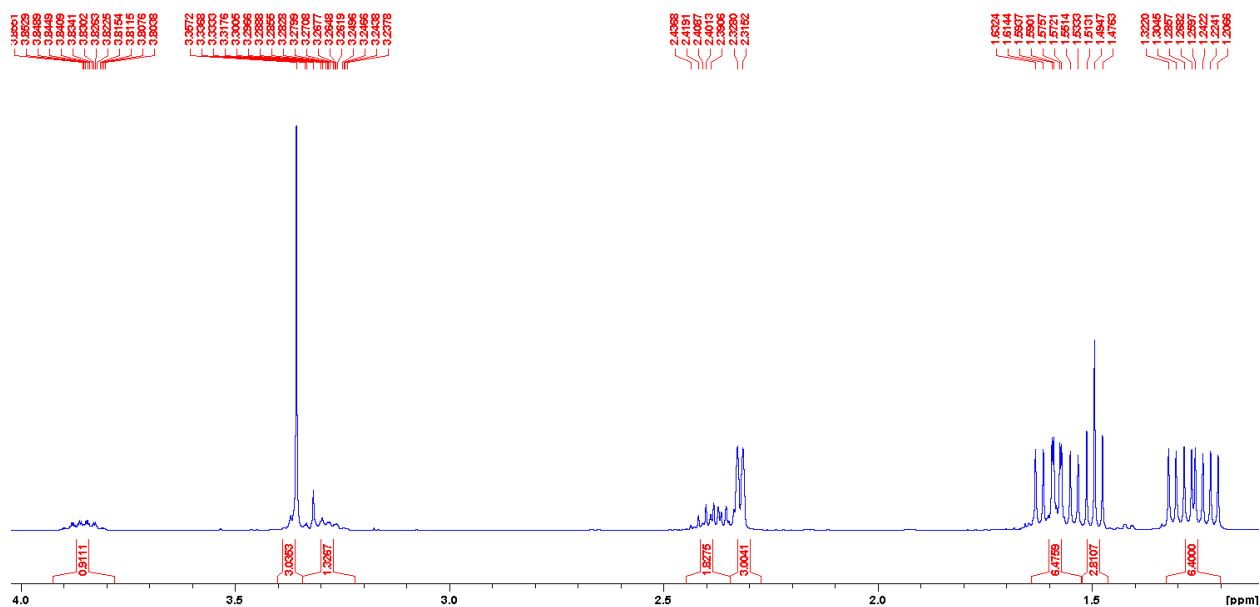
Figure S2. 82. The aliphatic region of the ^{1}H NMR spectrum of **7b** in C$_6$D$_6$.
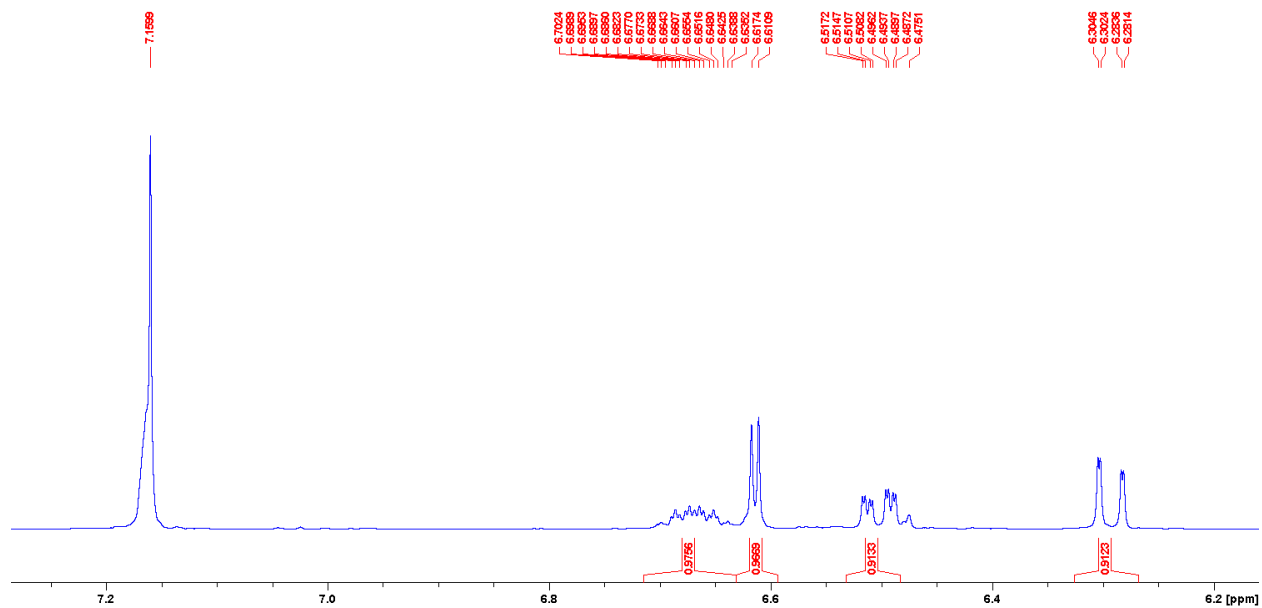
Figure S2. 83. The aromatic region of the ^{1}H NMR spectrum of **7b** in C$_6$D$_6$.
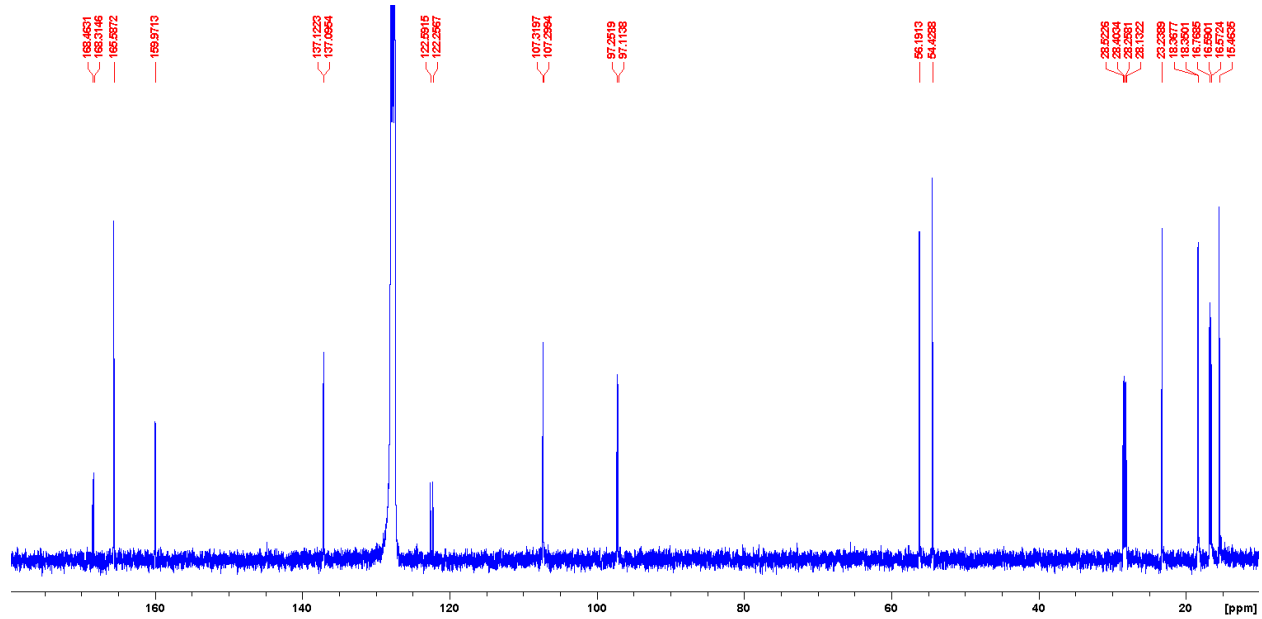
Figure S2. 84. Full ^{13}C NMR spectrum of **7b** in C$_6$D$_6$.
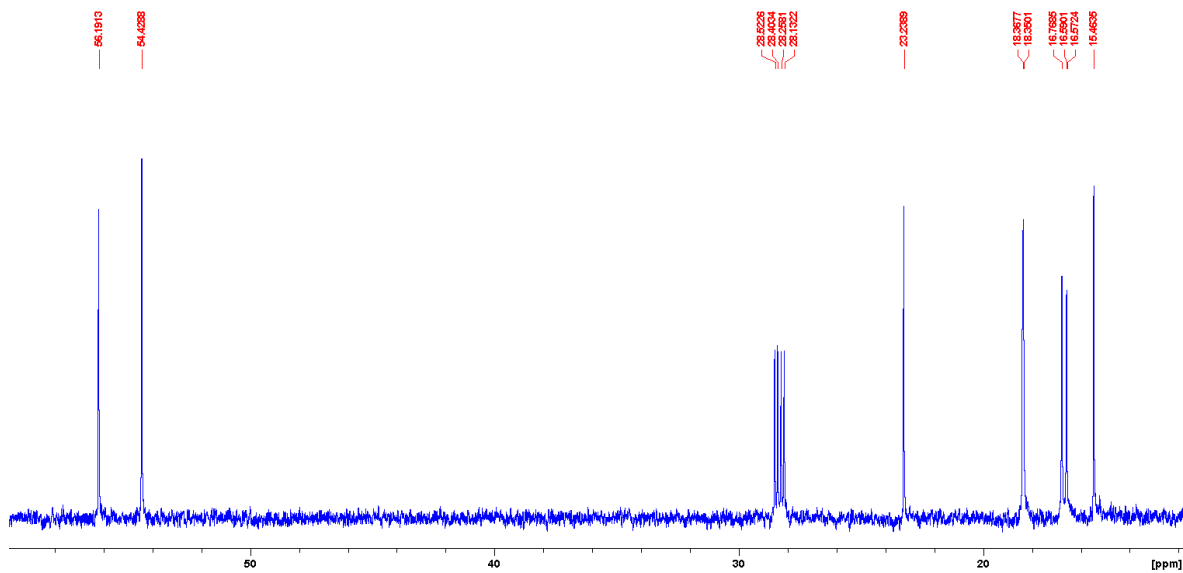
Figure S2. 85. The aliphatic region of the ^{13}C NMR spectrum of **7b** in C_6D_6.
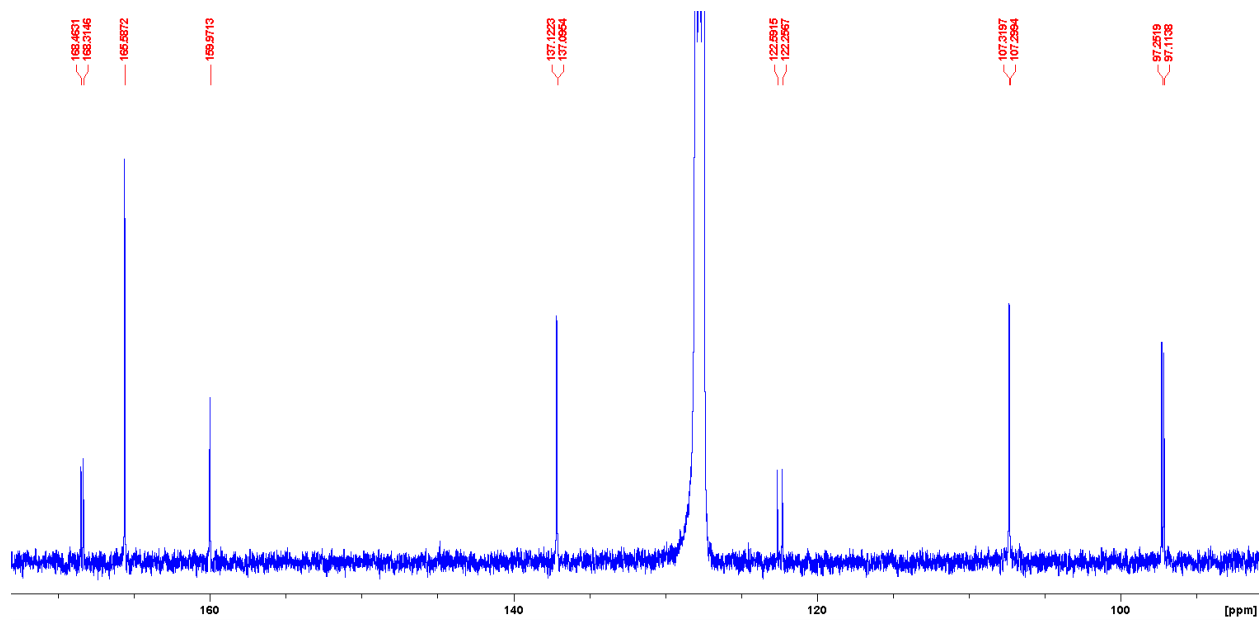
Figure S2. 86. The aromatic region of the ^{13}C NMR spectrum of **7b** in C_6D_6.
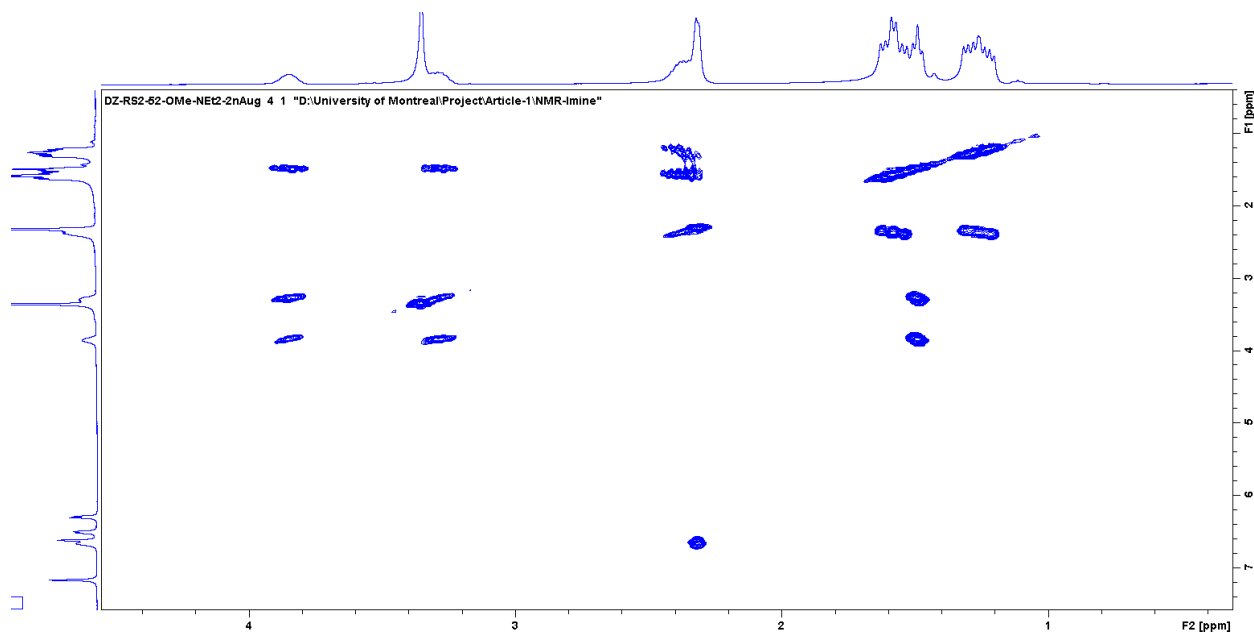
Figure S2. 87. The aliphatic region of the COSY NMR spectrum of **7b** in C_6D_6.
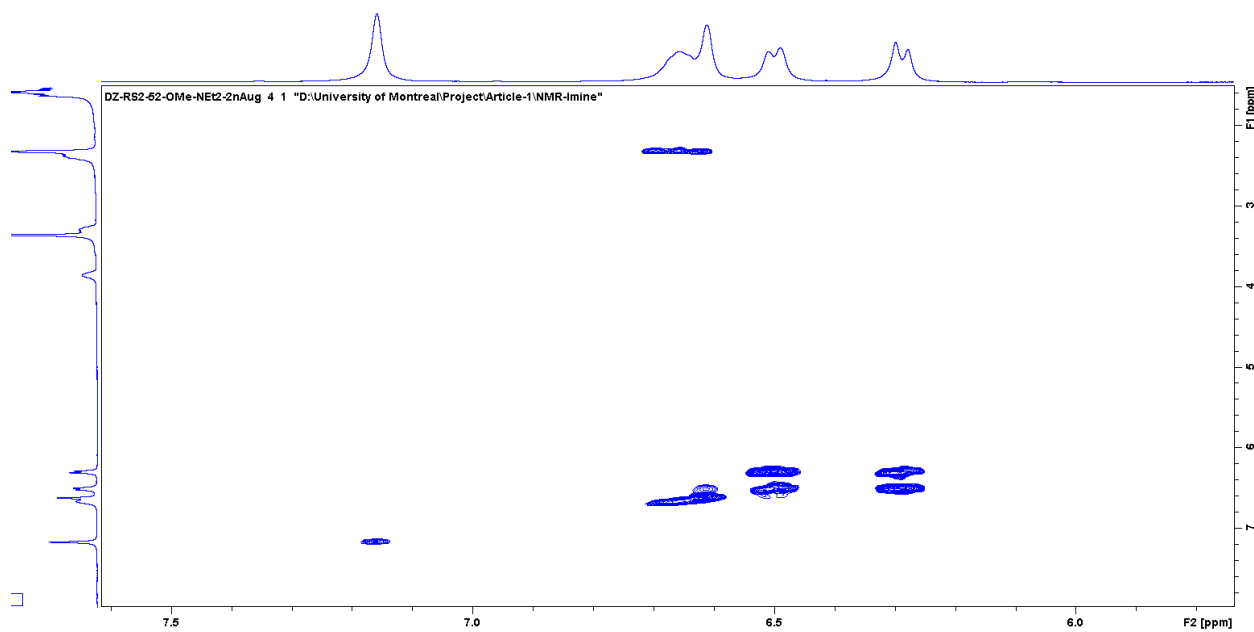
Figure S2. 88. The aromatic region of the COSY NMR spectrum of **7b** in C_6D_6.
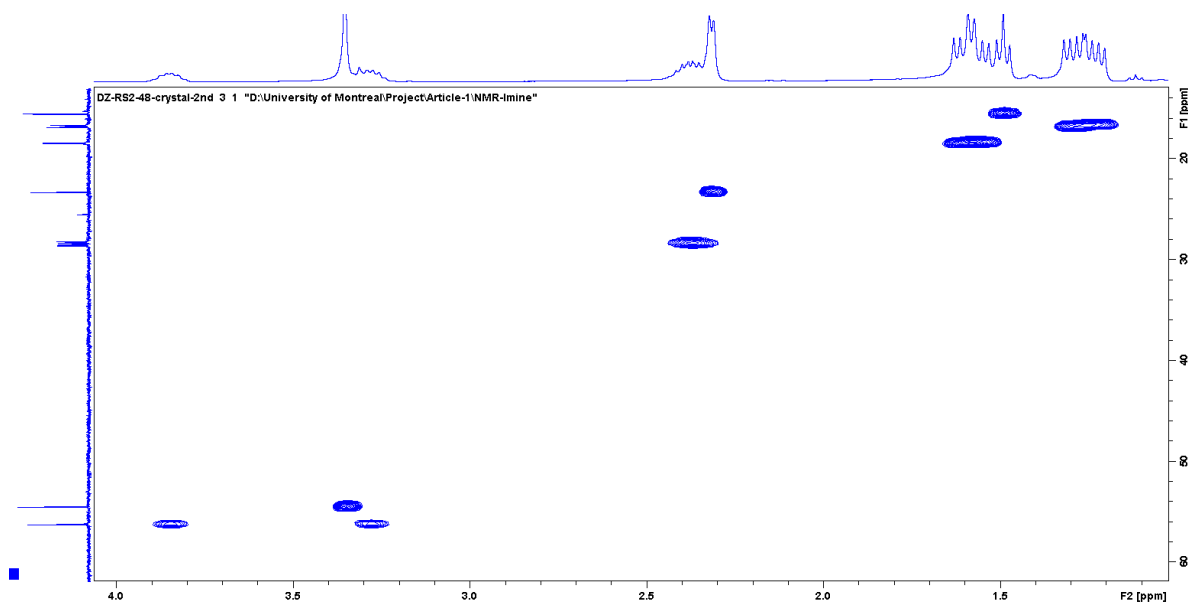
Figure S2. 89. The aliphatic region of the HSQC NMR spectrum of **7b** in C_6D_6.
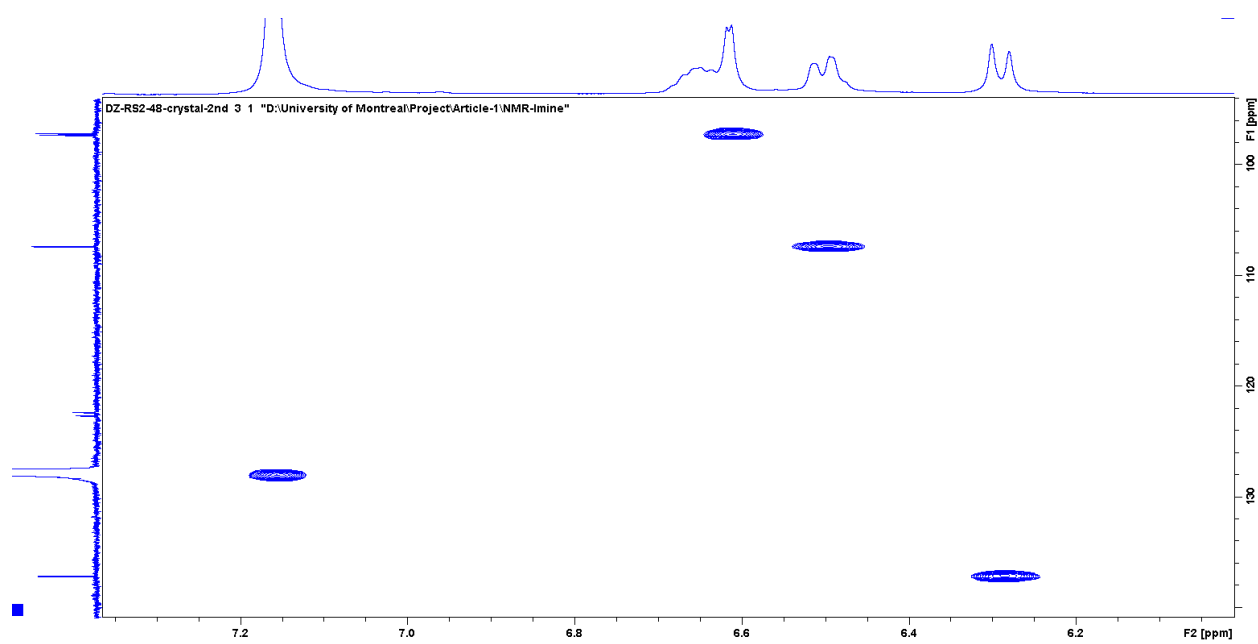
Figure S2. 90. The aromatic region of the HSQC NMR spectrum of **7b** in C_6D_6.
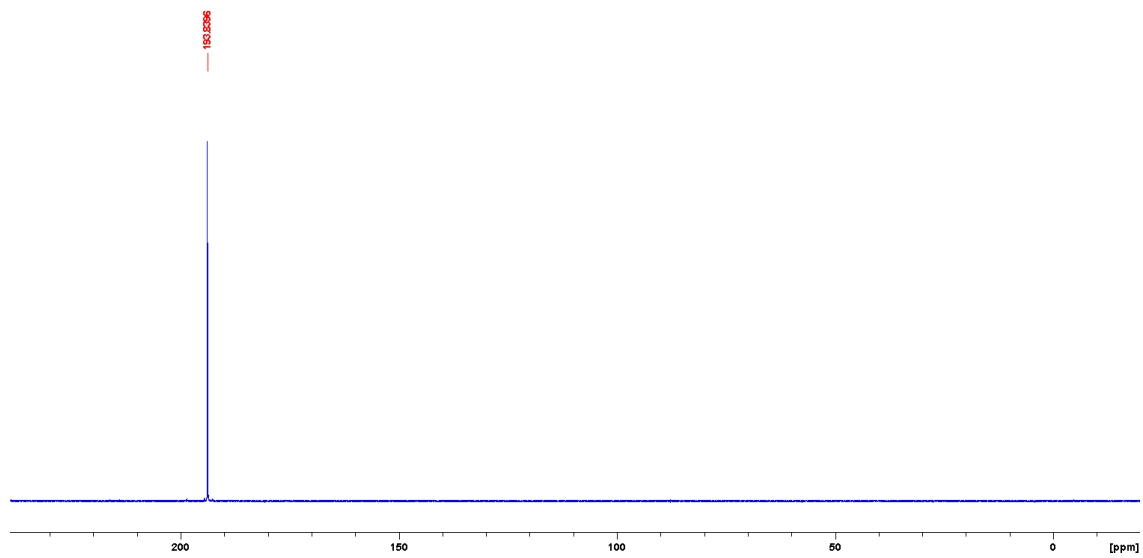
Figure S2. 91. $^{31}P\{^{1}H\}$ NMR spectrum of **7b** in C_6D_6.

NMR spectra of complex **7c**
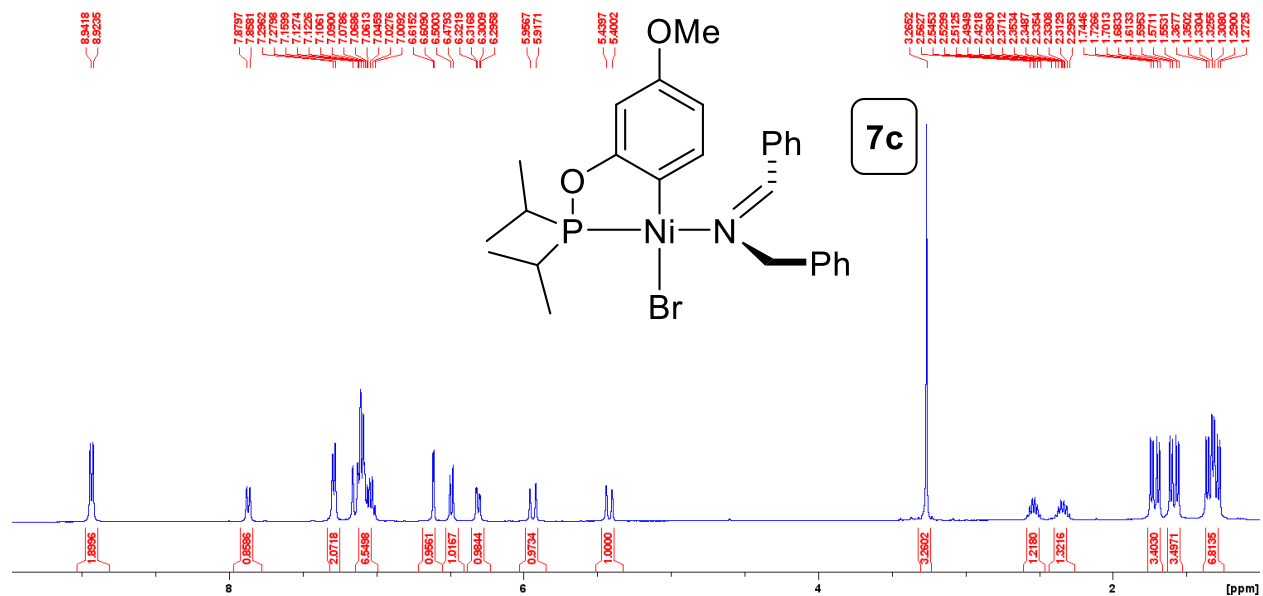
Figure S2. 92. Full ^{1}H NMR spectrum of **7c** in C$_6$D$_6$.
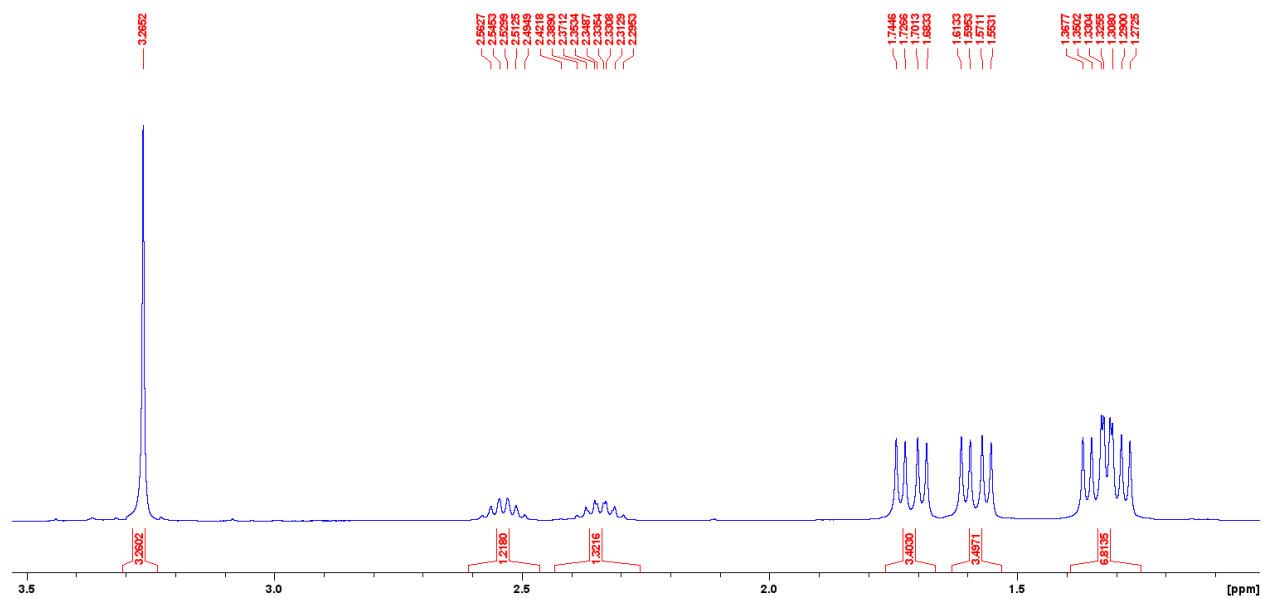
Figure S2. 93. The aliphatic region of the ^{1}H NMR spectrum of **7c** in C$_6$D$_6$.
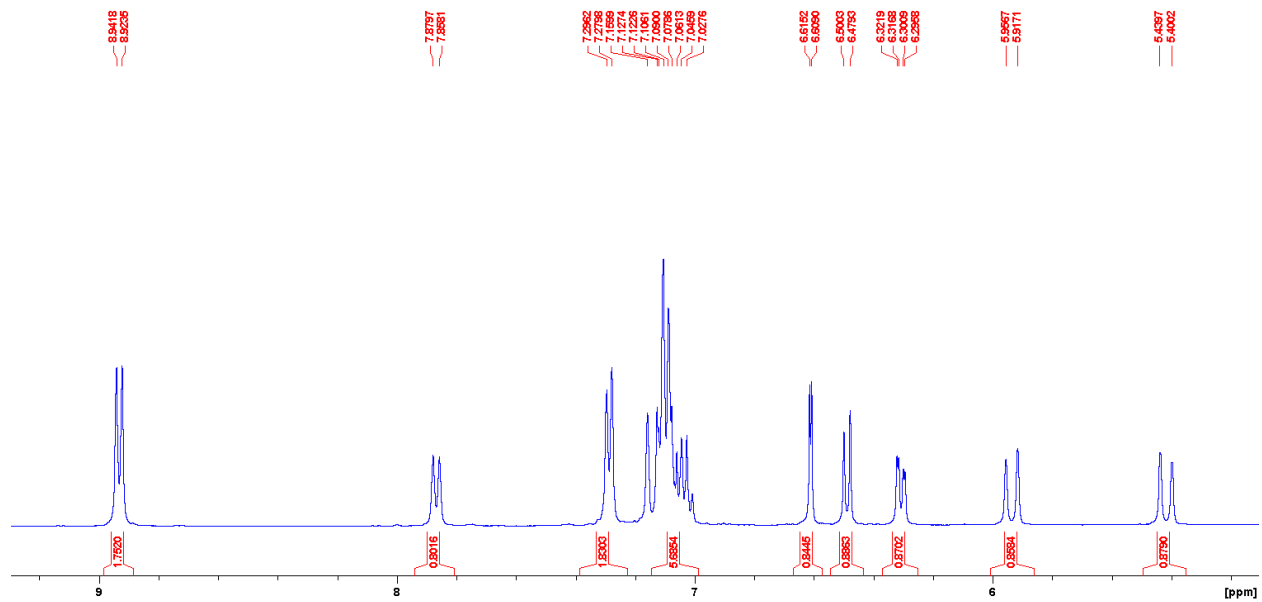
Figure S2. 94. The aromatic region of the ^{1}H NMR spectrum of **7c** in C$_6$D$_6$.
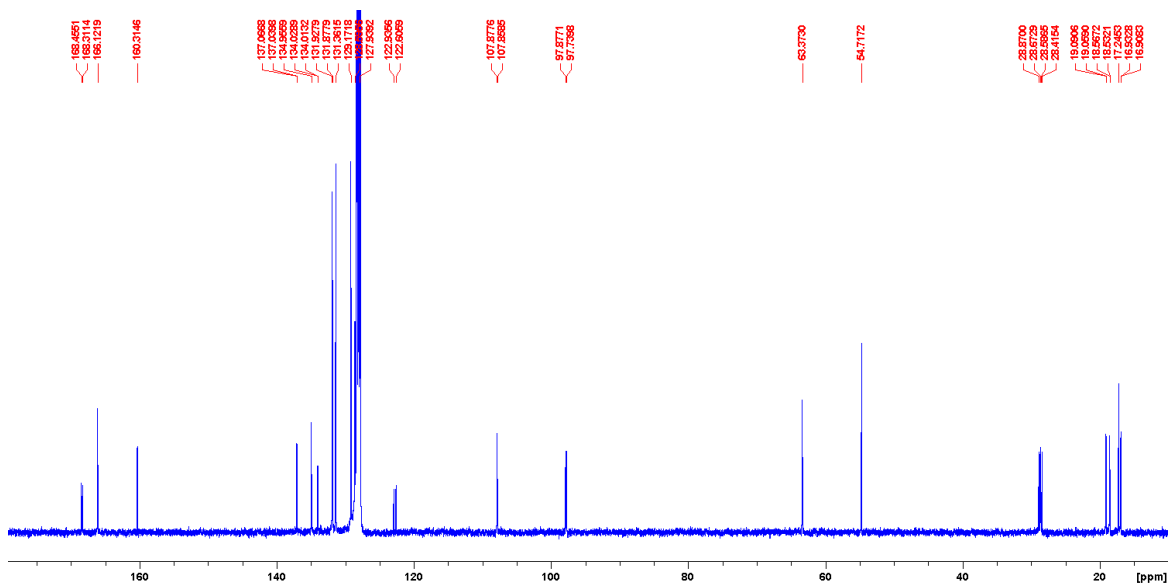
Figure S2. 95. Full ^{13}C NMR spectrum of **7c** in C$_6$D$_6$.
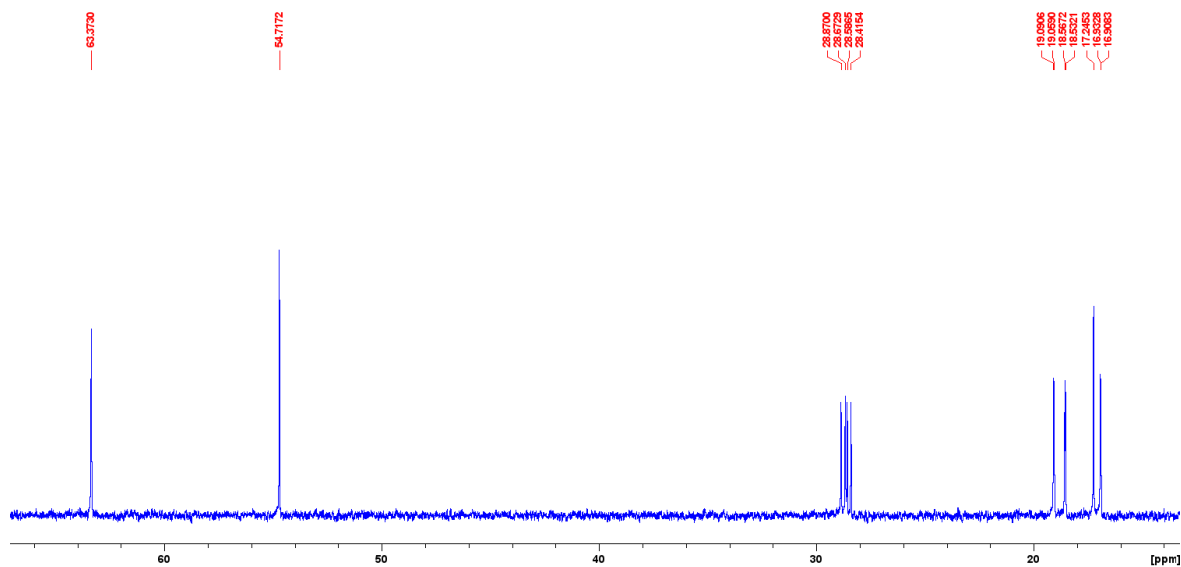
Figure S2. 96. The aliphatic region of the ^{13}C NMR spectrum of **7c** in C_6D_6.
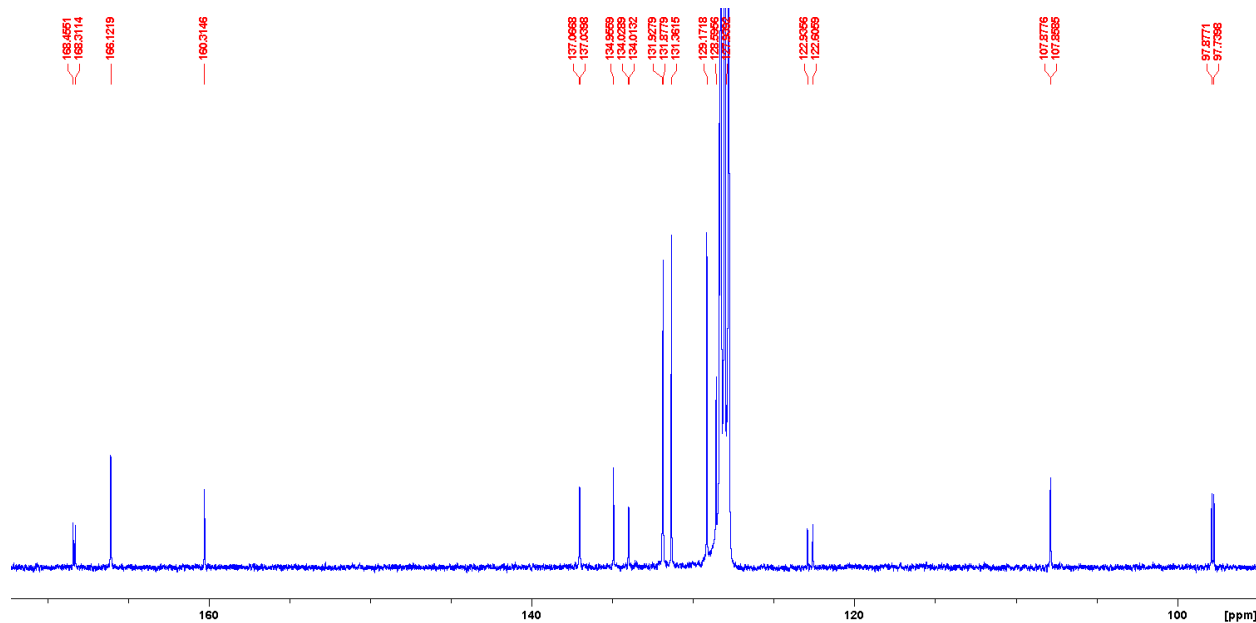
Figure S2. 97. The aromatic region of the ^{13}C NMR spectrum of **7c** in C_6D_6.

161

Figure S2. 98. The aliphatic region of the COSY NMR spectrum of **7c** in C_6D_6.

Figure S2. 99. The aromatic region of the COSY NMR spectrum of **7c** in C_6D_6.
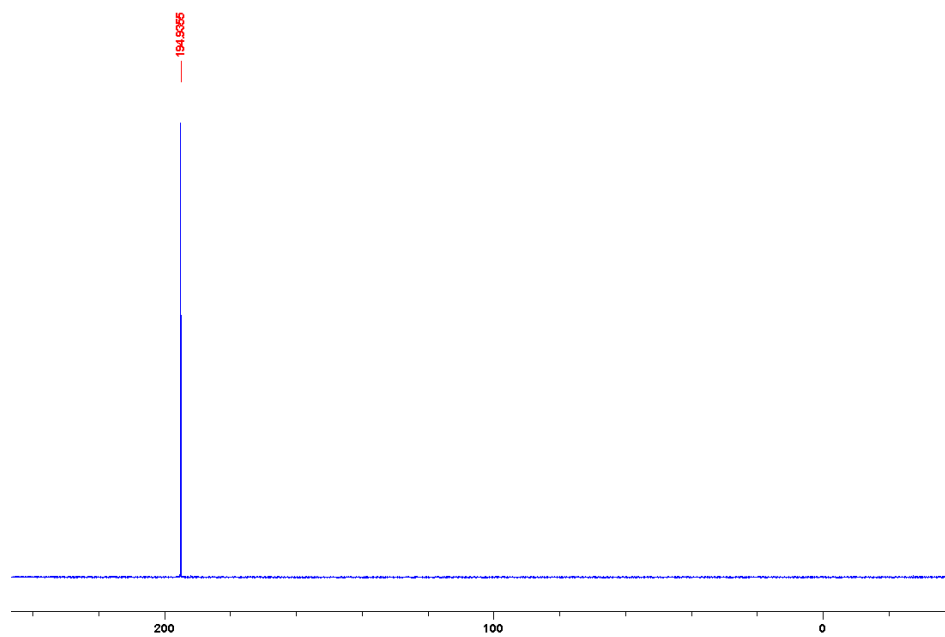
Figure S2. 100. $^{31}P\{^{1}H\}$ NMR spectrum of **7c** in C_6D_6.

NMR spectra of complex **7d**
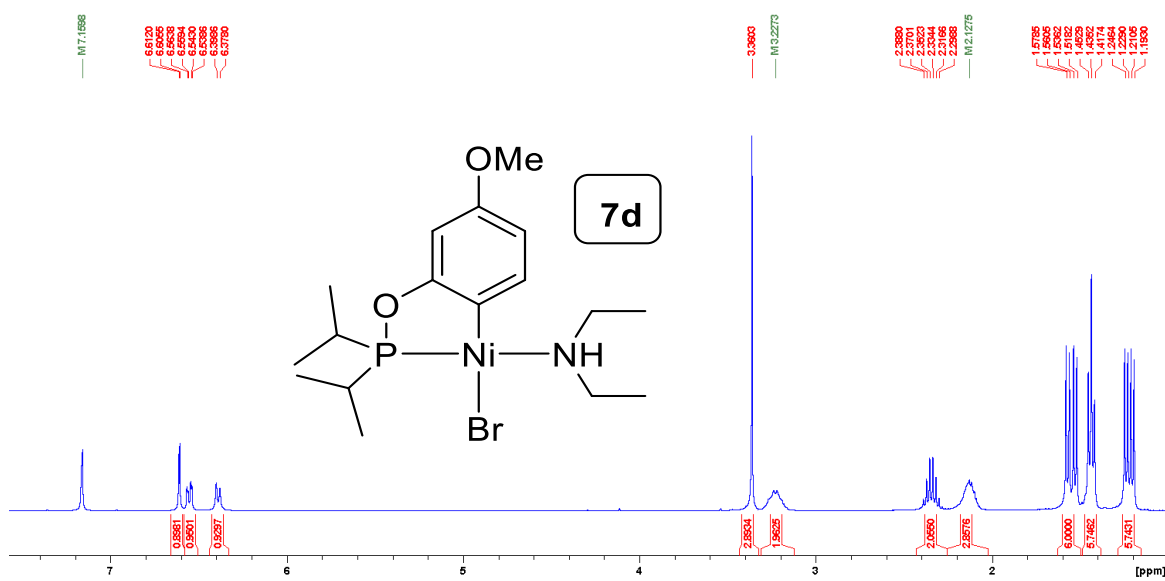
Figure S2. 101. Full ^{1}H NMR spectrum of **7d** in C_6D_6.
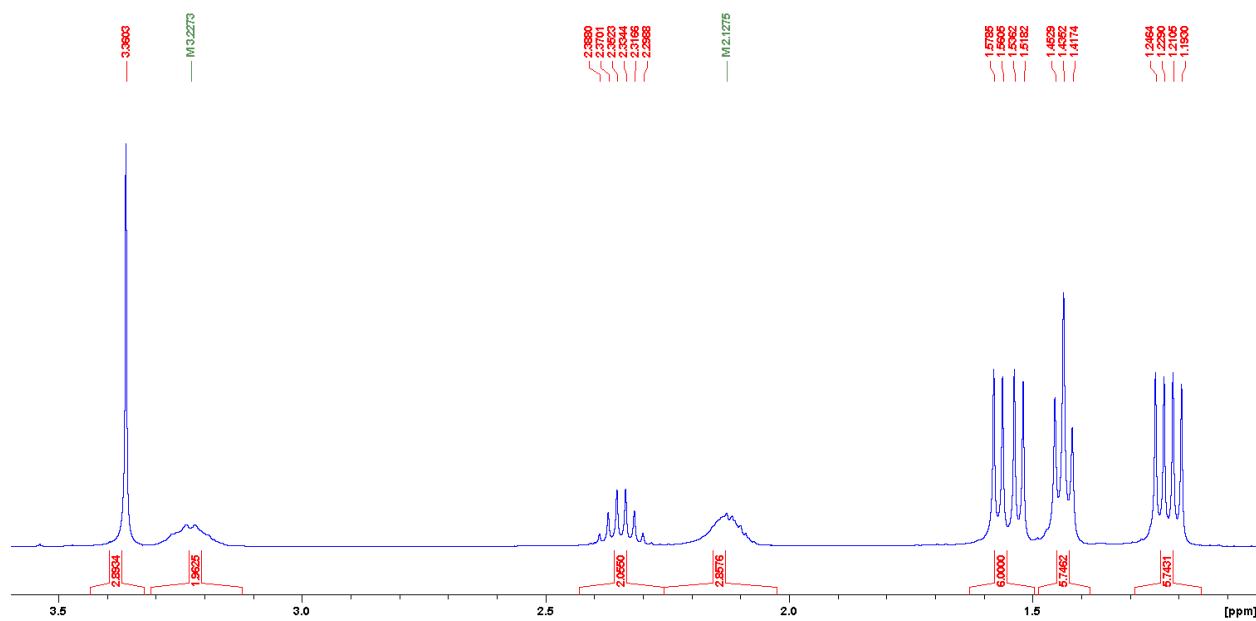
Figure S2. 102. The aliphatic region of the ^{1}H NMR spectrum of **7d** in C_6D_6.
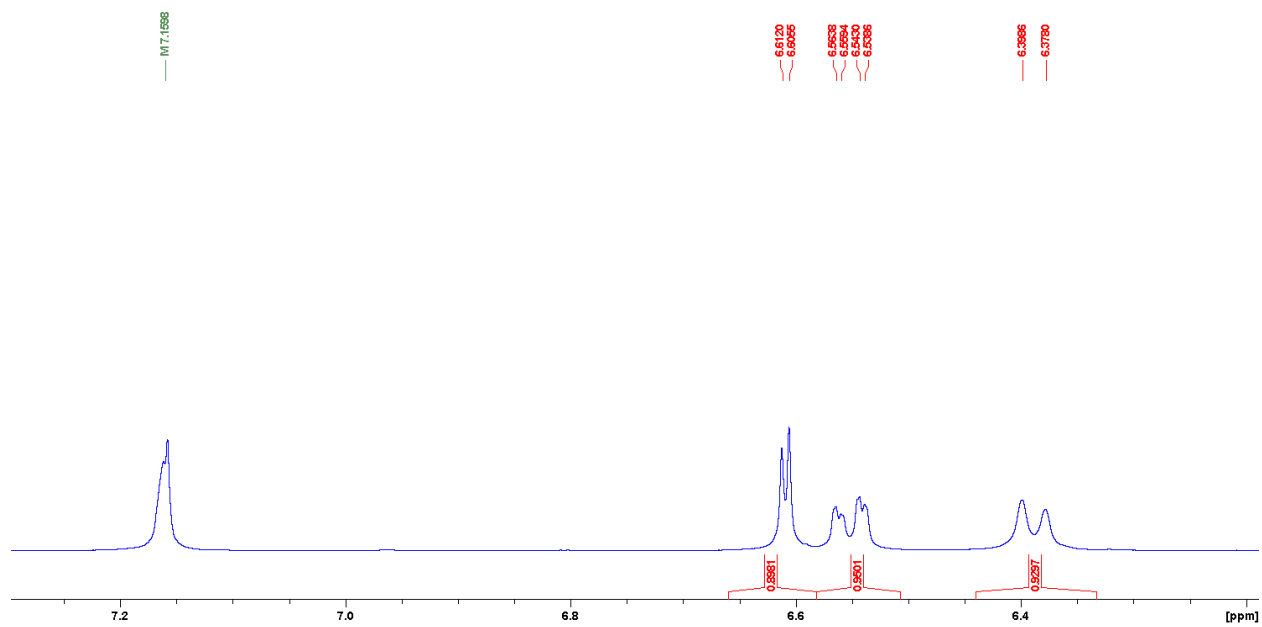
Figure S2. 103. The aromatic region of the ^{1}H NMR spectrum of **7d** in C_6D_6.
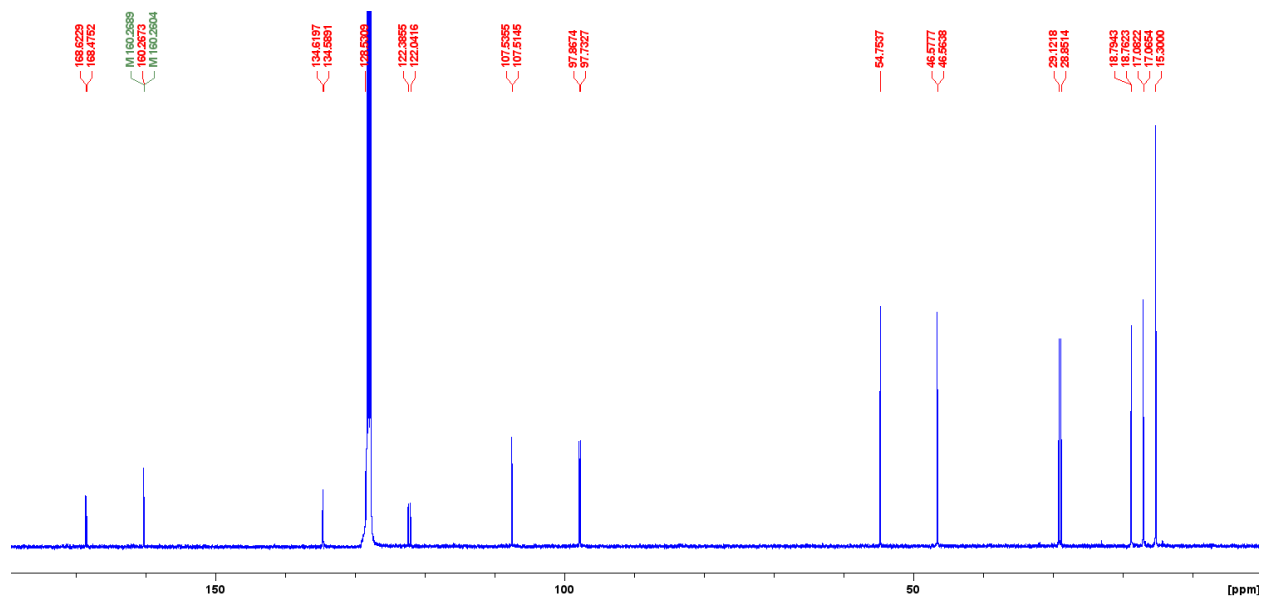
Figure S2. 104. Full ^{13}C NMR spectrum of **7d** in C_6D_6.
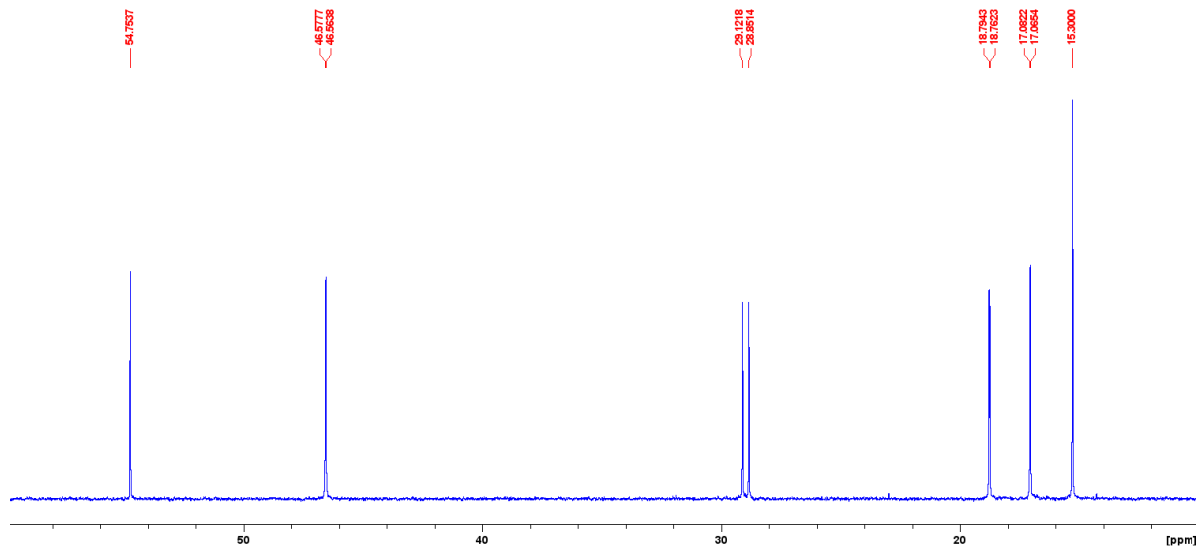
Figure S2. 105. The aliphatic region of the ^{13}C NMR spectrum of **7d** in C_6D_6.
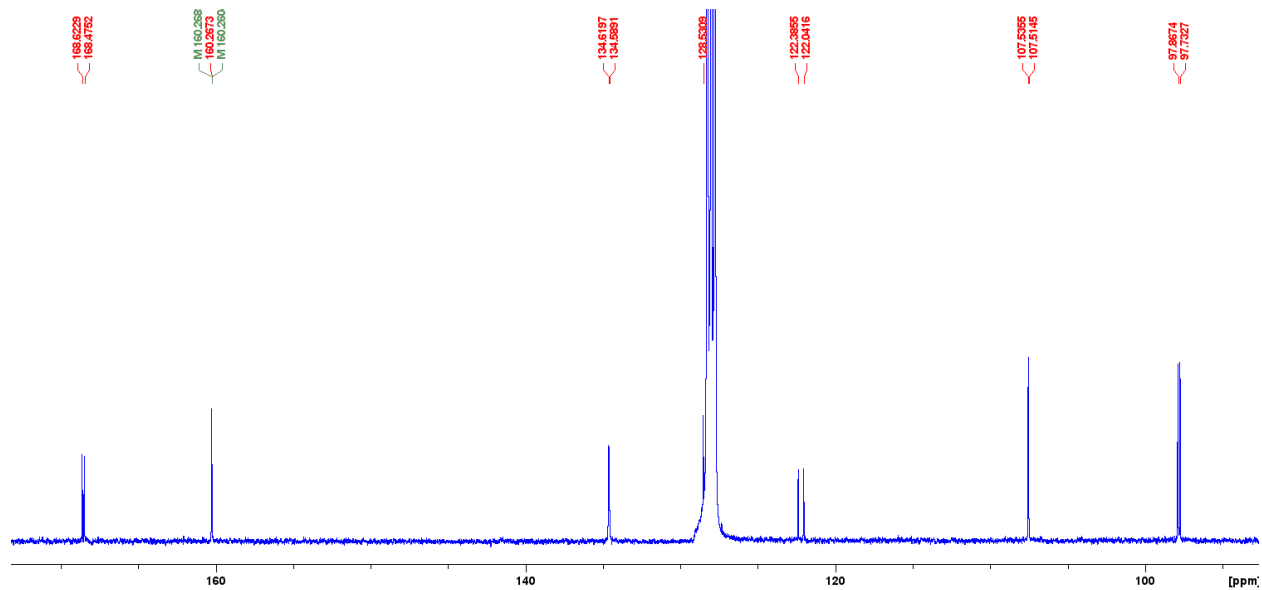
Figure S2. 106. The aromatic region of the ^{13}C NMR spectrum of **7d** in C_6D_6.
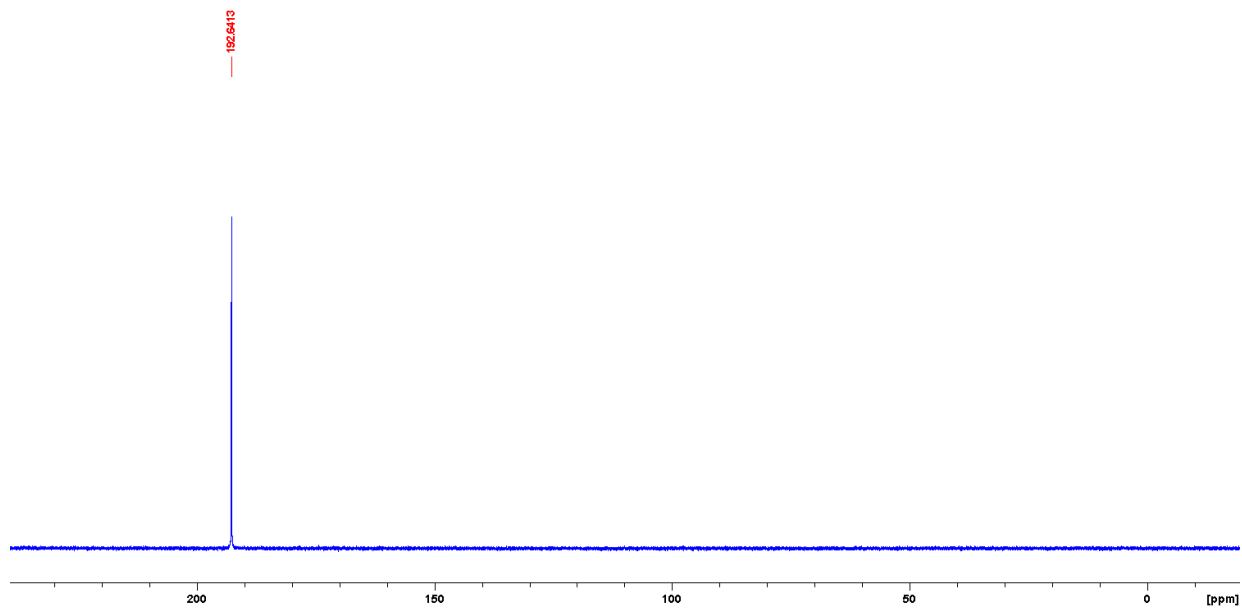
Figure S2. 107. $^{31}P\{^1H\}$ NMR spectrum of **7d** in C_6D_6.

NMR spectra of complexes **8a**
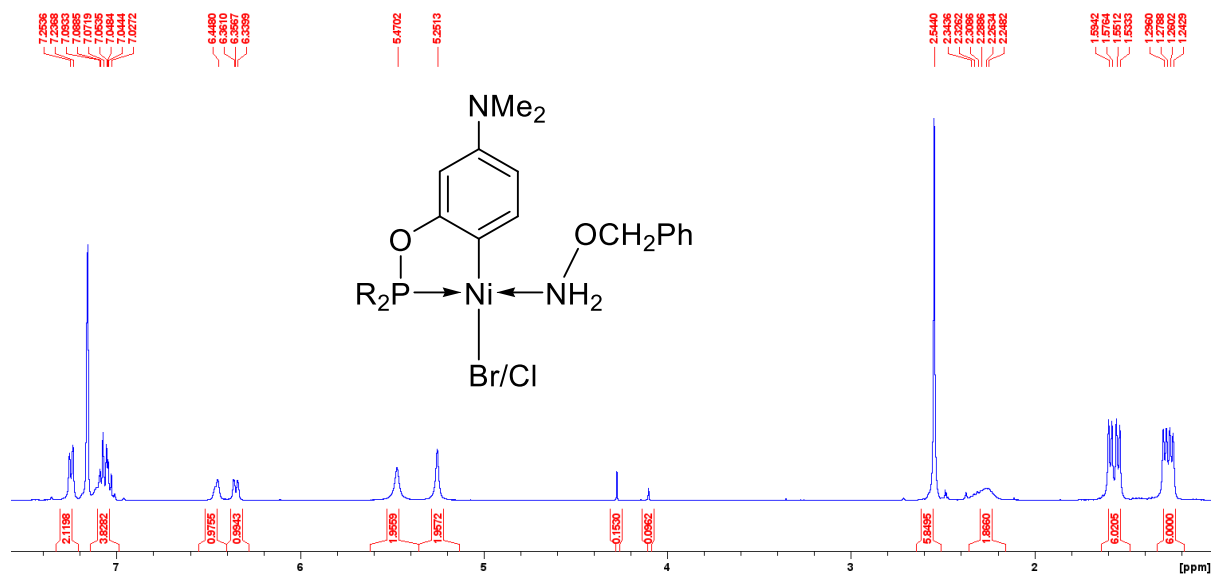
Figure S2. 108. ^{1}H NMR spectrum of **8a** in C_6D_6.
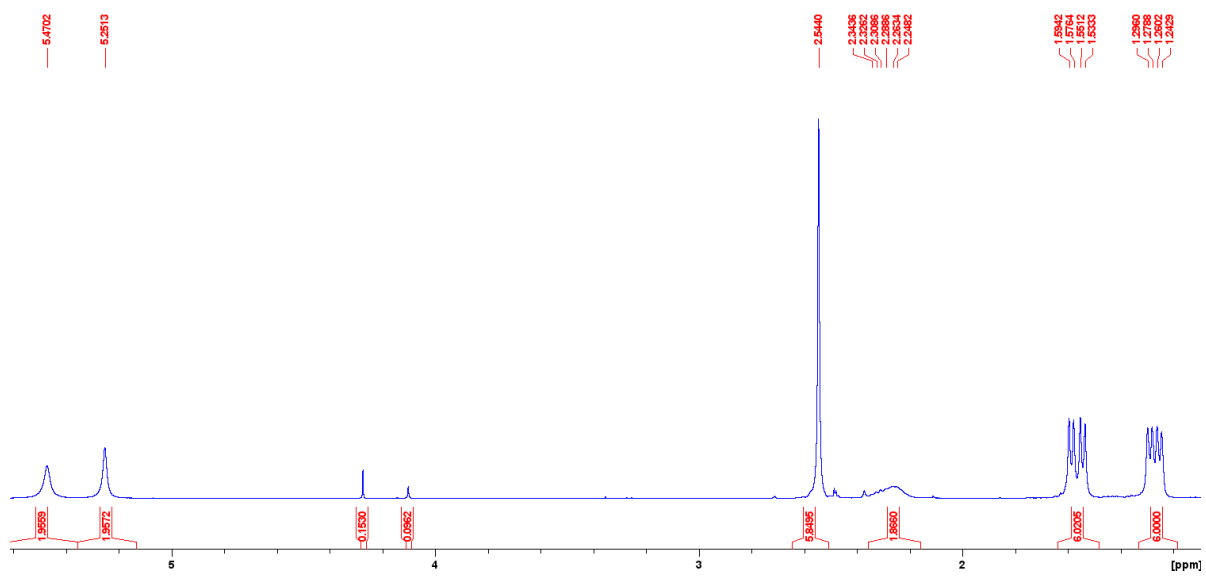
Figure S2. 109. The aliphatic region of the ^{1}H NMR spectrum of **8a** in C_6D_6.
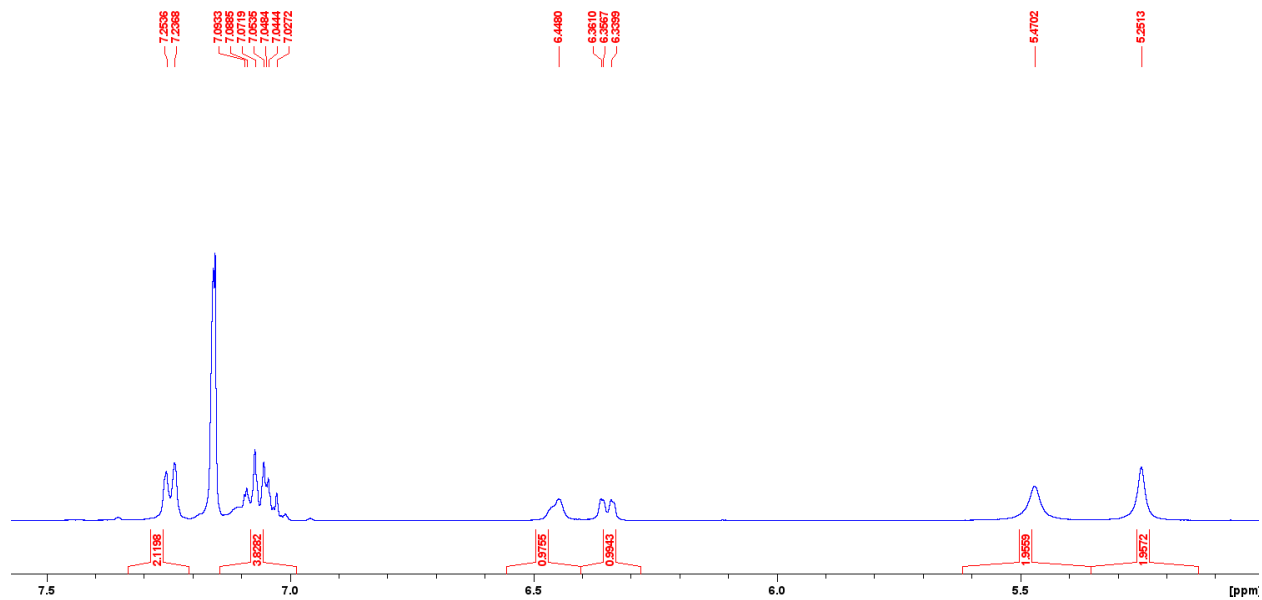
Figure S2. 110. The aromatic region of the ^{1}H NMR spectrum of **8a** in C_6D_6.
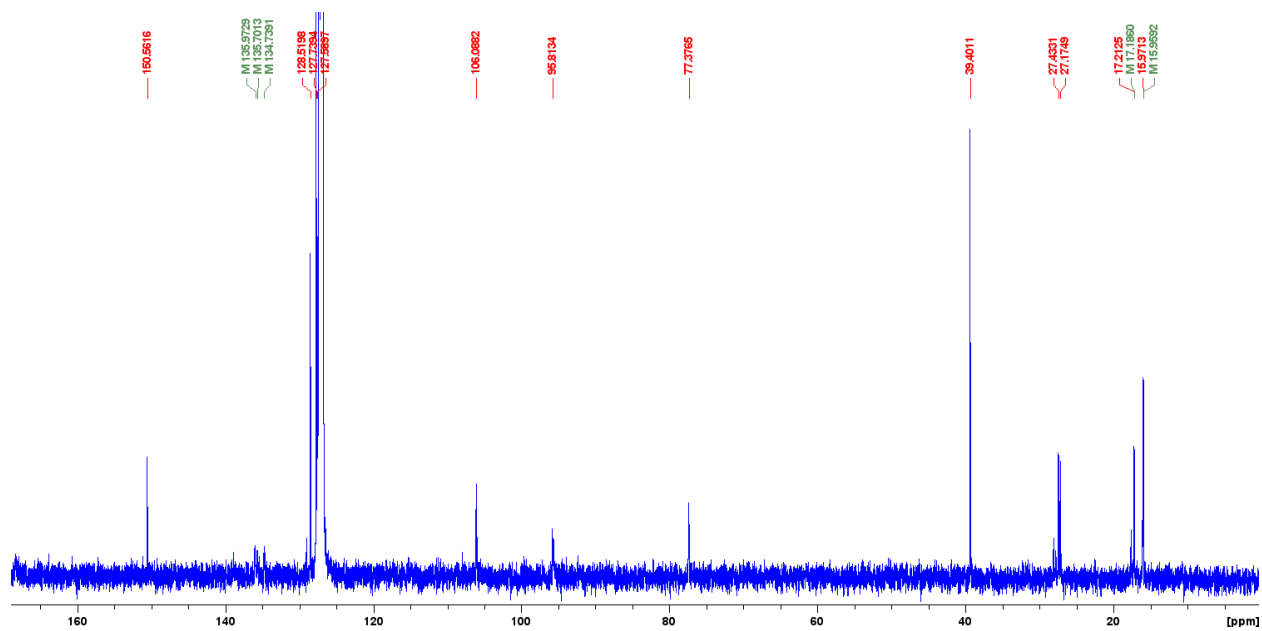
Figure S2. 111. Full ^{13}C NMR spectrum of **8a** in C_6D_6.
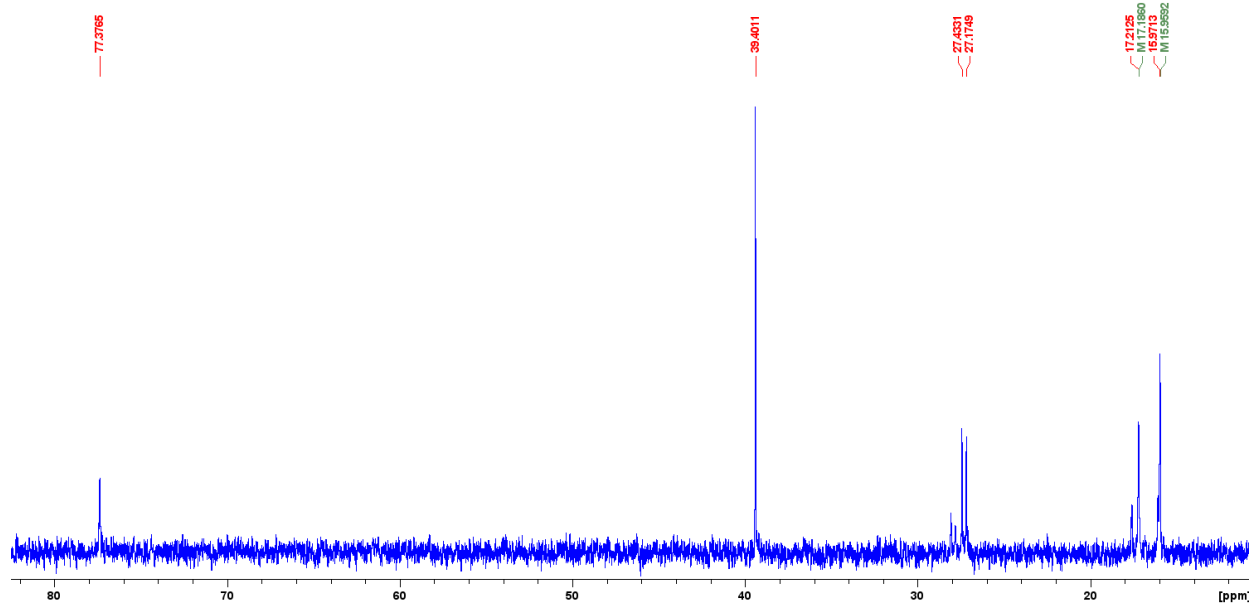
Figure S2. 112. The aliphatic region of the ^{13}C NMR spectrum of **8a** in C$_6$D$_6$.
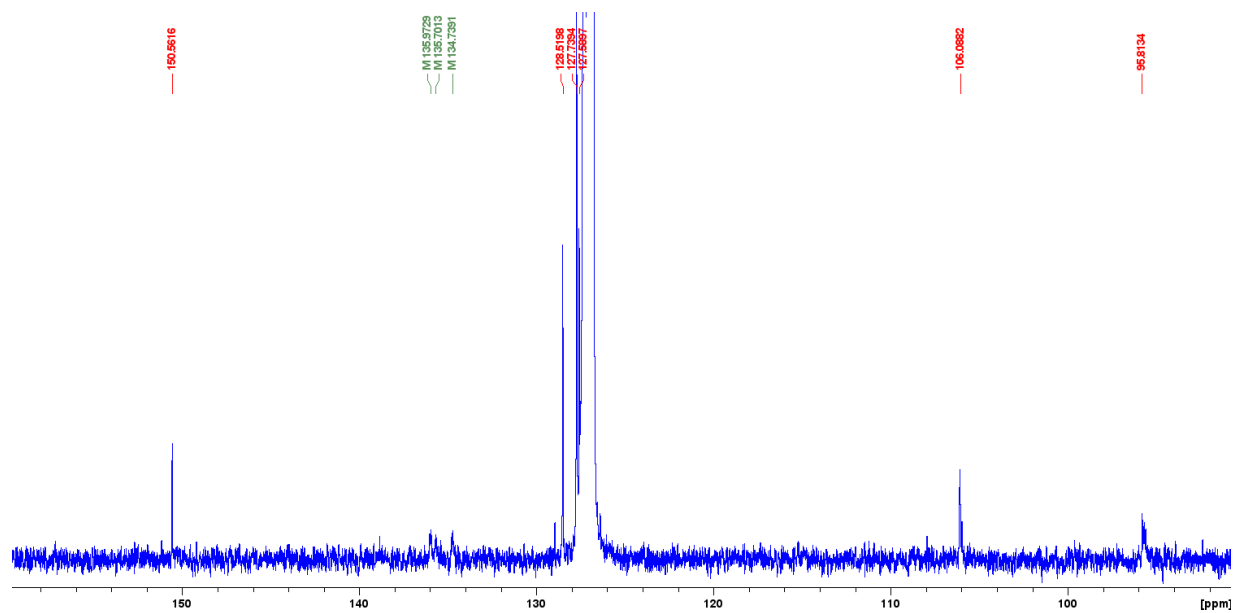
Figure S2. 113. The aromatic region of the ^{13}C NMR spectrum of **8a** in C$_6$D$_6$.

170
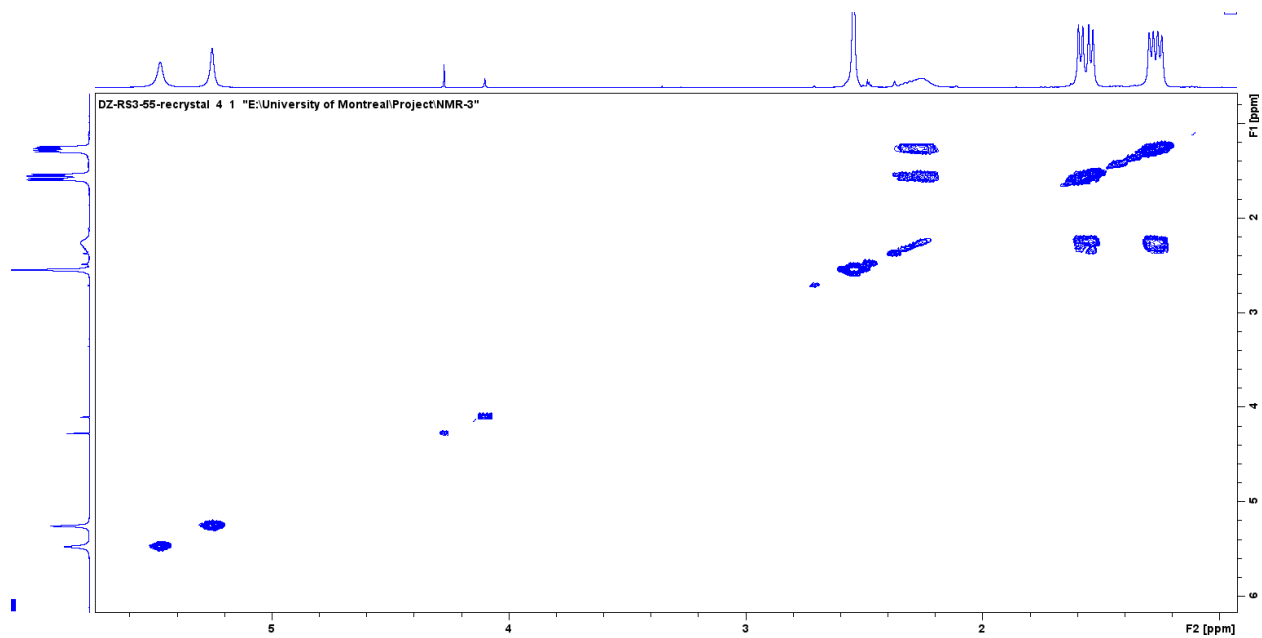
Figure S2. 114. The aliphatic region of the COSY NMR spectrum of **8a** in C_6D_6.
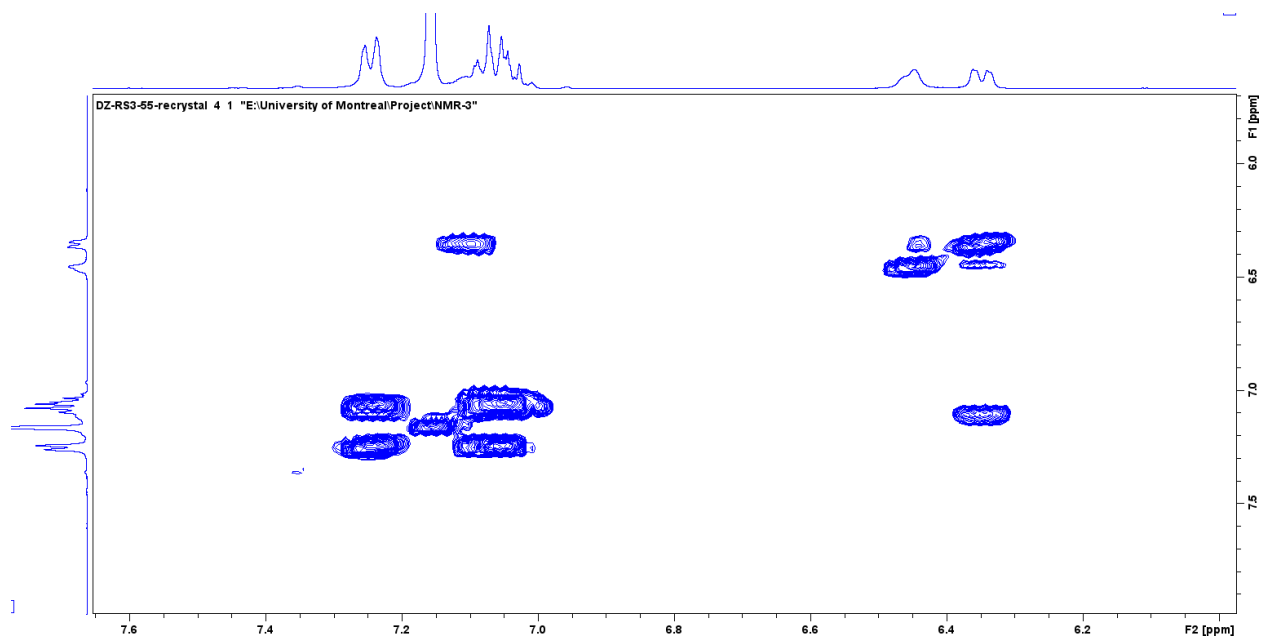
Figure S2. 115. The aromatic region of the COSY NMR spectrum of **8a** in C_6D_6.

171
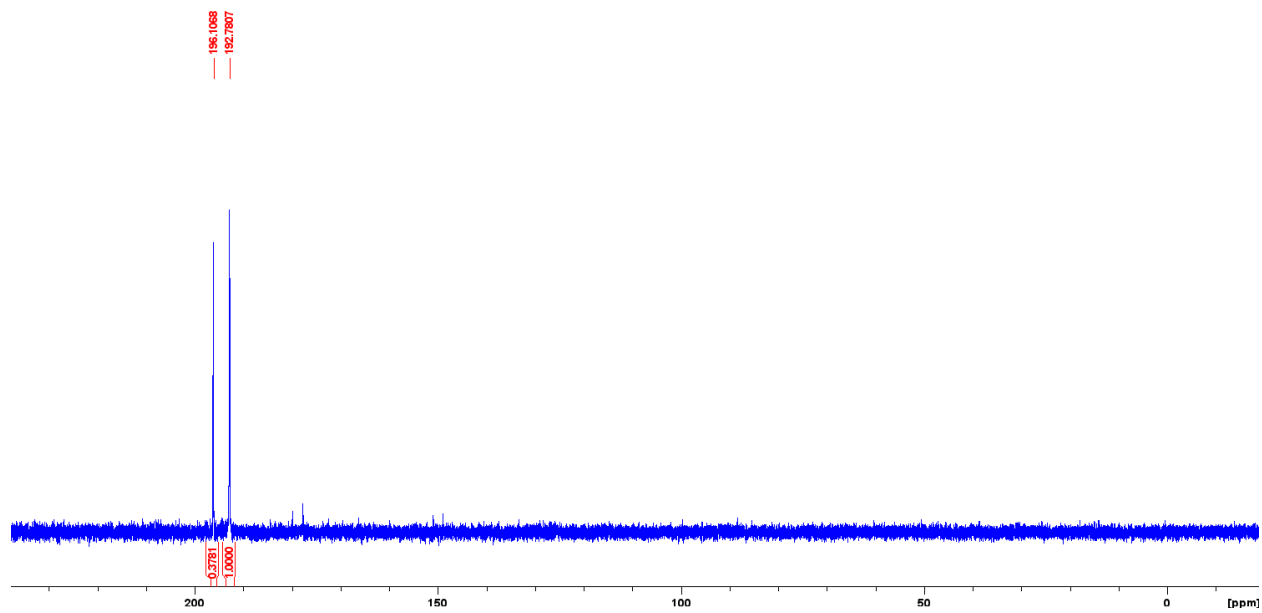
Figure S2. 116. $^{31}P\{^1H\}$ NMR spectrum of **8a** in C_6D_6.

NMR spectra of complexes **8b**

Figure S2. 117. Full ^{1}H NMR spectrum of **8b** in C$_6$D$_6$.

Figure S2. 118. The aliphatic region of the ^{1}H NMR spectrum of **8b** in C$_6$D$_6$.
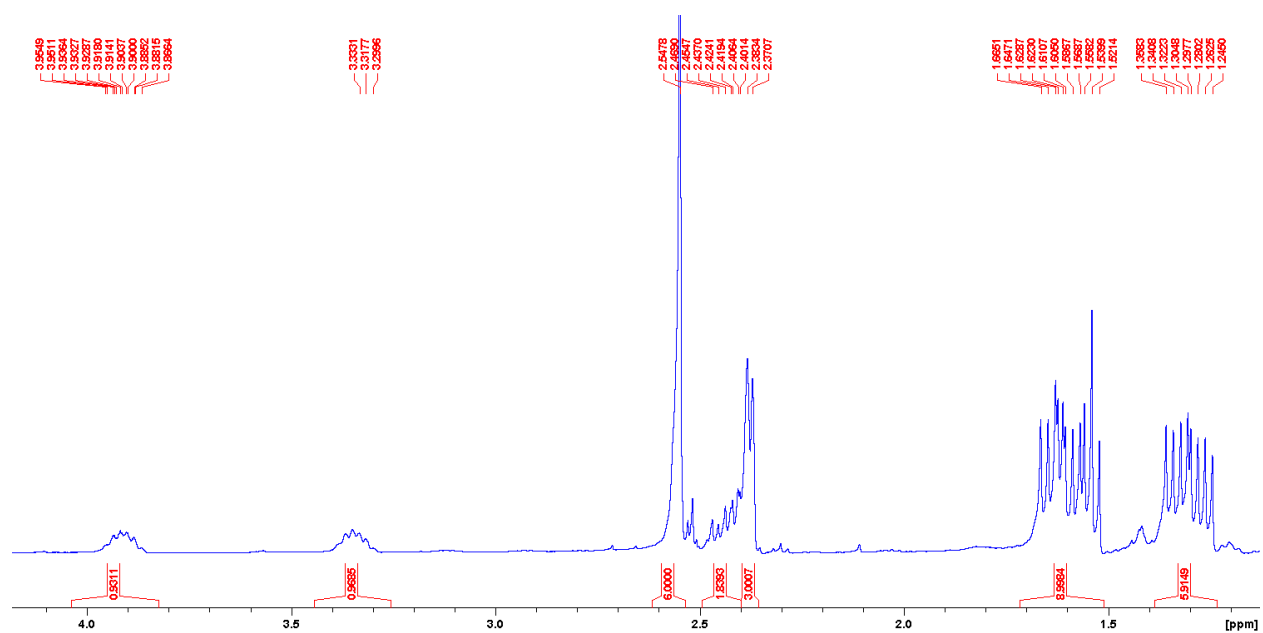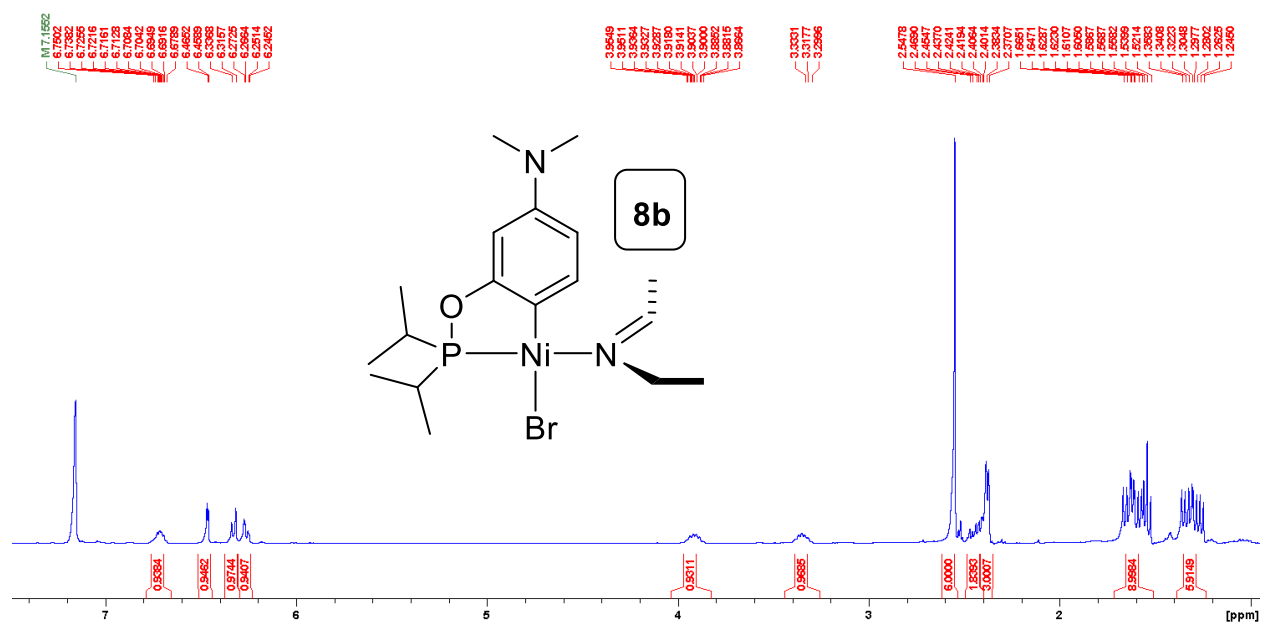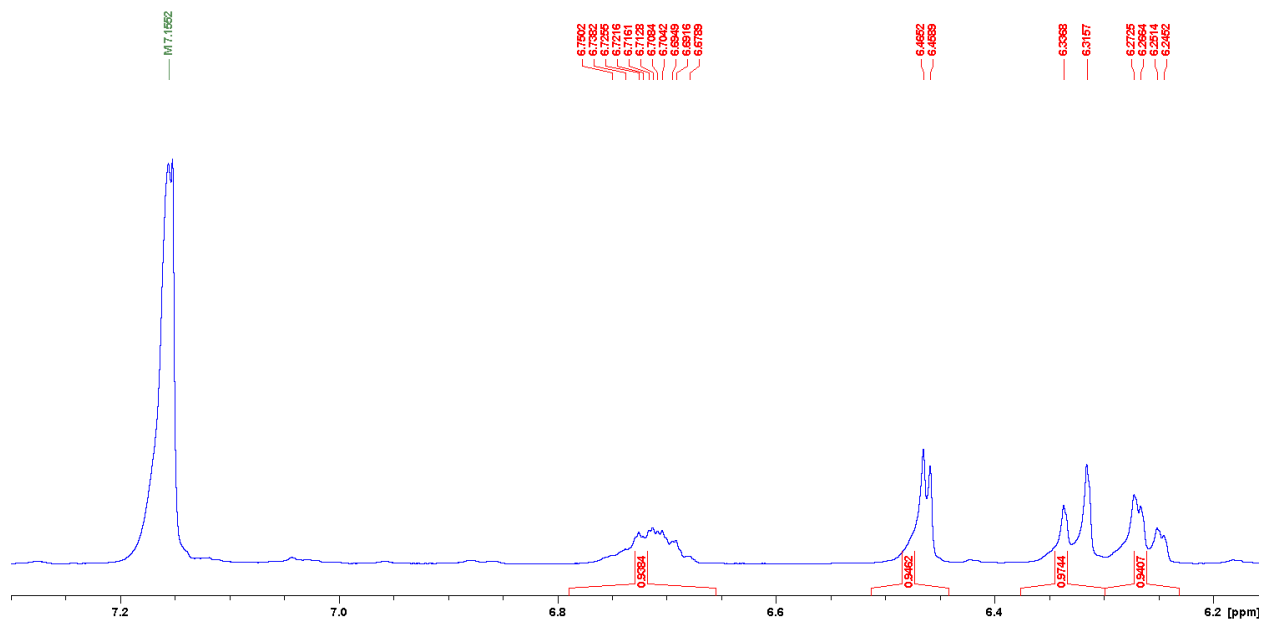
Figure S2. 119. The aromatic region of the ^{1}H NMR spectrum of **8b** in C_6D_6.
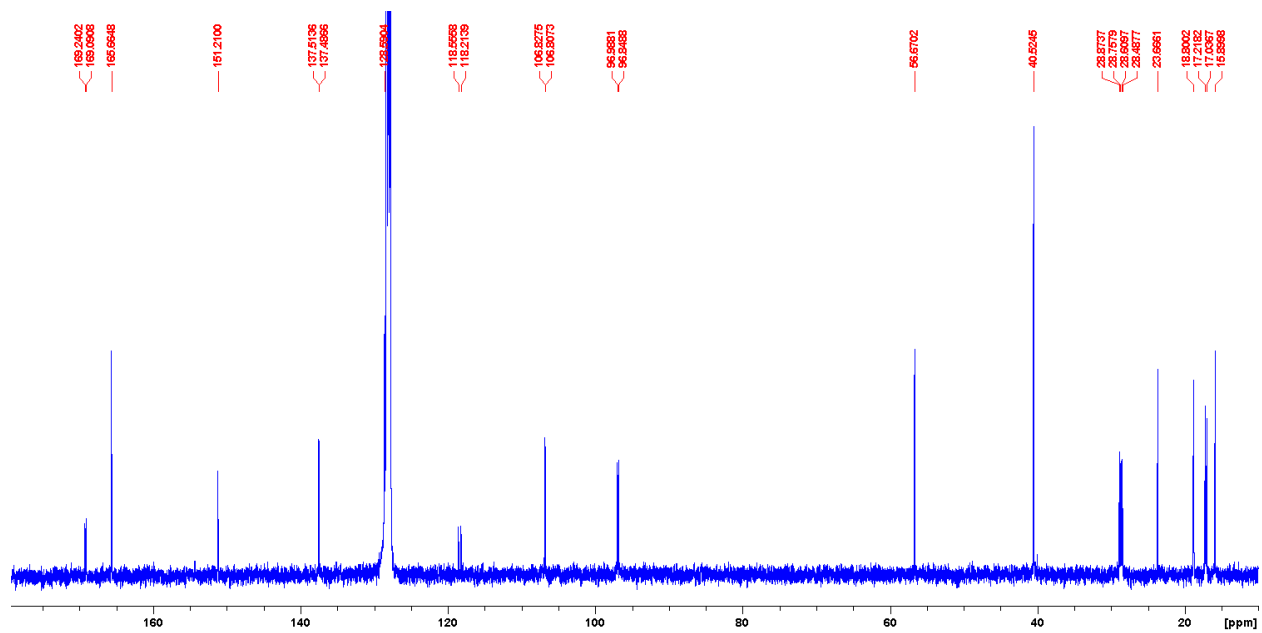
Figure S2. 120. Full ^{13}C NMR spectrum of **8b** in C_6D_6.
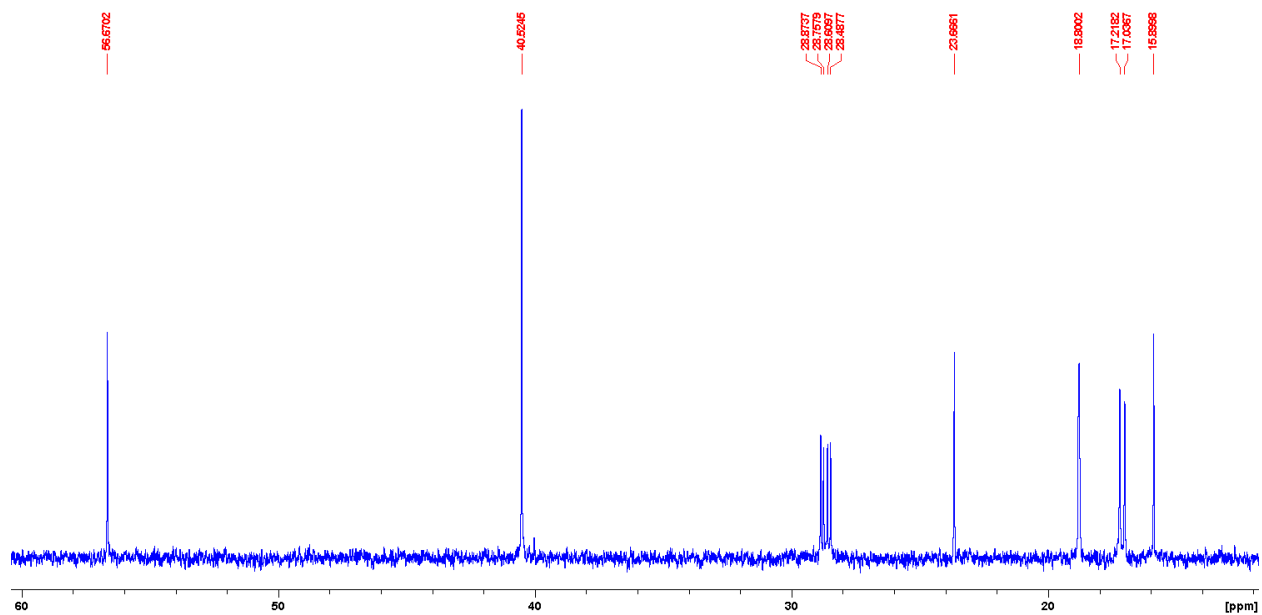
Figure S2. 121. The aliphatic region of the ^{13}C NMR spectrum of **8b** in C_6D_6.
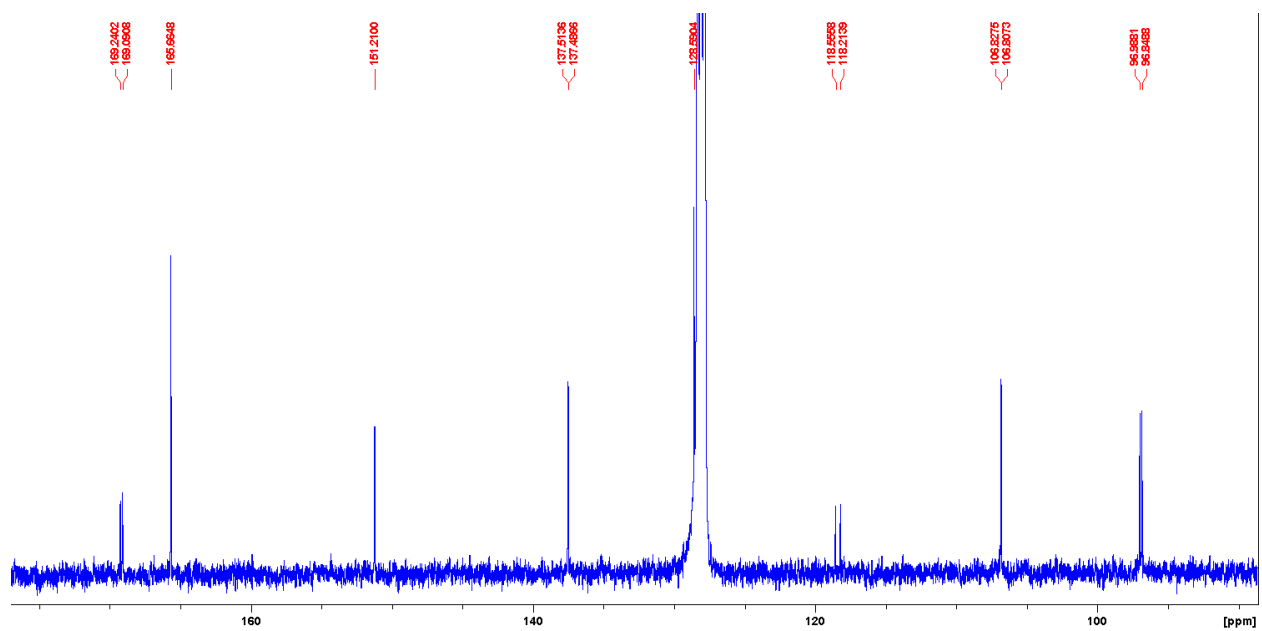
Figure S2. 122. The aromatic region of the ^{13}C NMR spectrum of **8b** in C_6D_6.
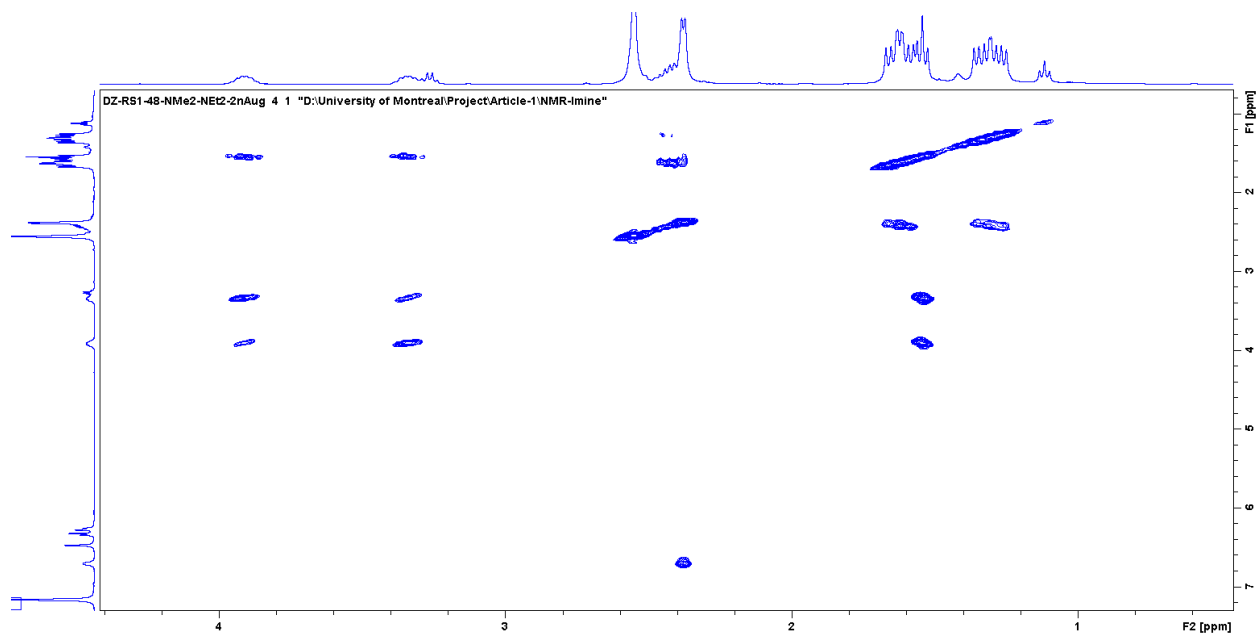
Figure S2. 123. The aliphatic region of the COSY NMR spectrum of **8b** in C_6D_6.
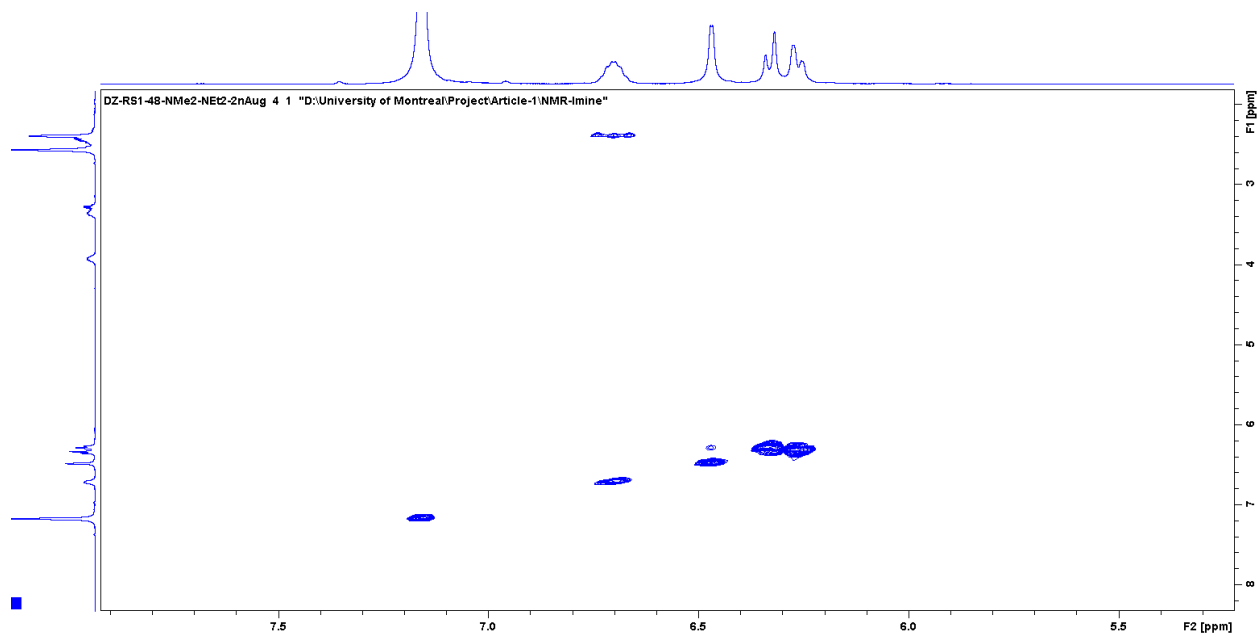
Figure S2. 124. The aromatic region of the COSY NMR spectrum of **8b** in C_6D_6.
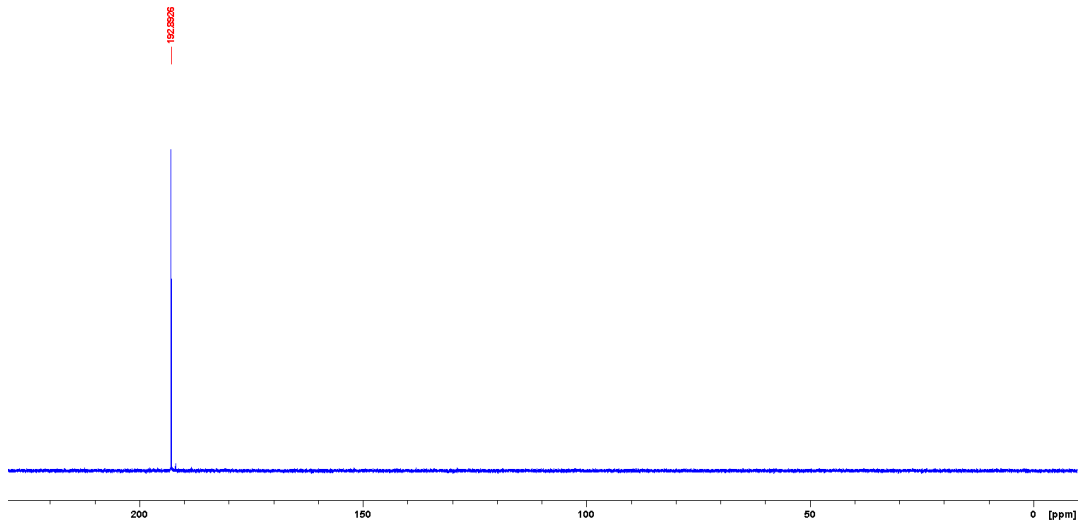
Figure S2. 125. $^{31}P\{^1H\}$ NMR spectrum of **8b** in C_6D_6.

S2.4 ^{31}P NMR spectra of some crude reaction mixtures
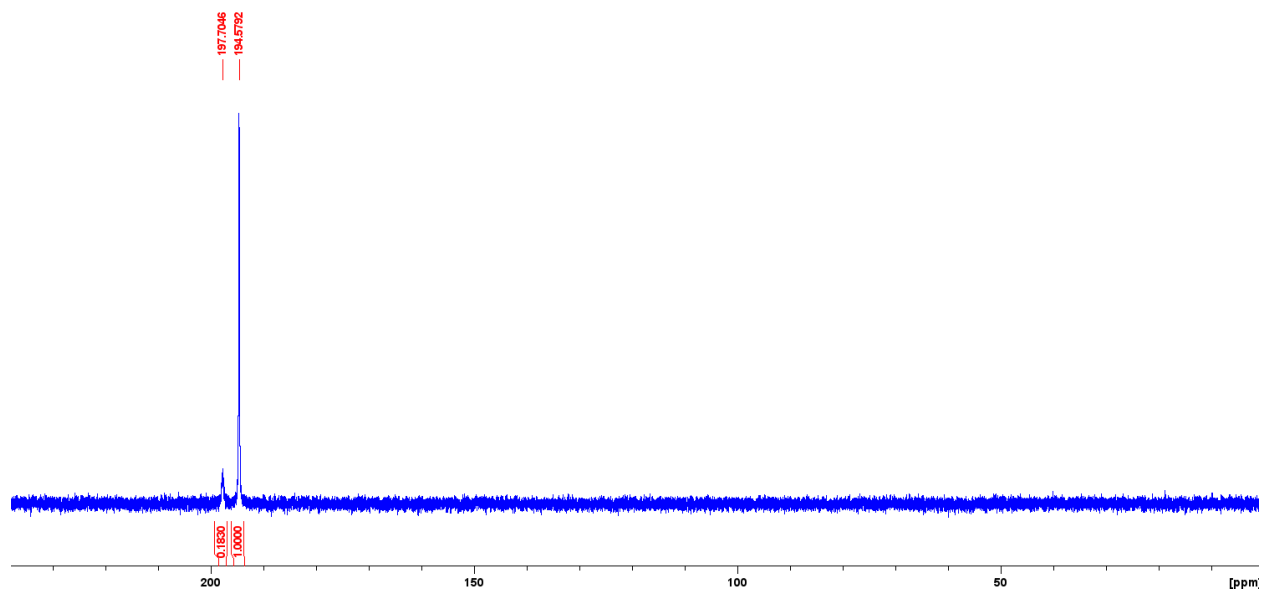
Figure S2. 126. ^{31}P{^{1}H} NMR spectrum of the crude mixture for the reaction **1** + BnONH$_2$ in CH$_2$Cl$_2$.
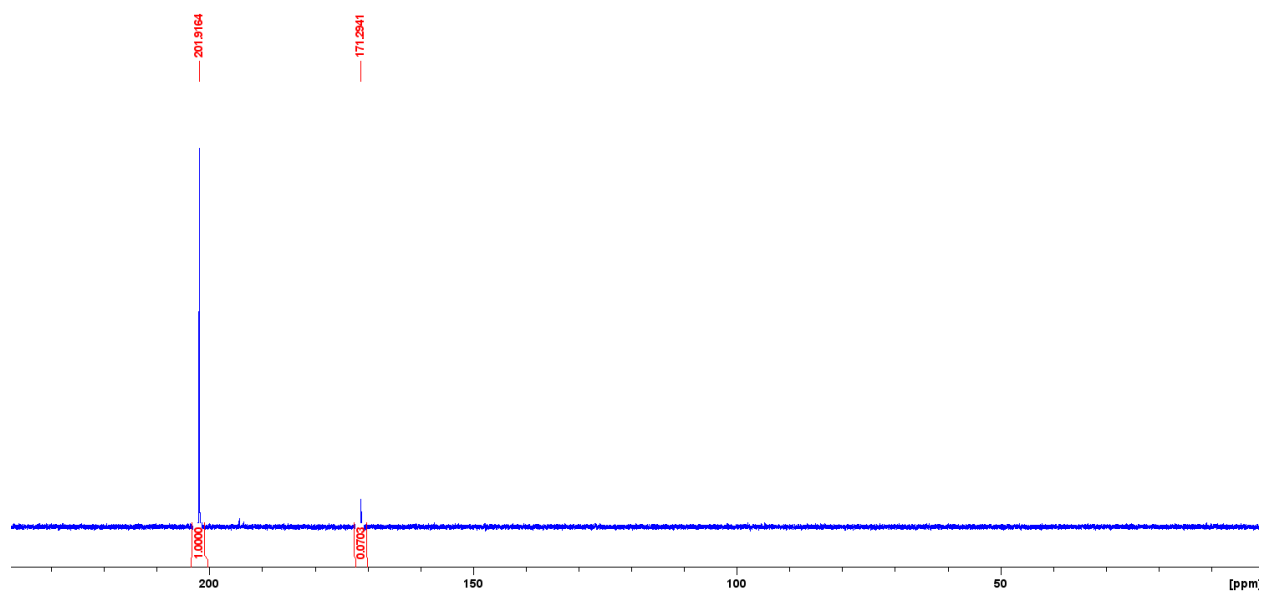
Figure S2. 127. ^{31}P{^{1}H} NMR spectrum of the crude mixture for the reaction **1** + Et$_2$NOH in CH$_2$Cl$_2$.

178
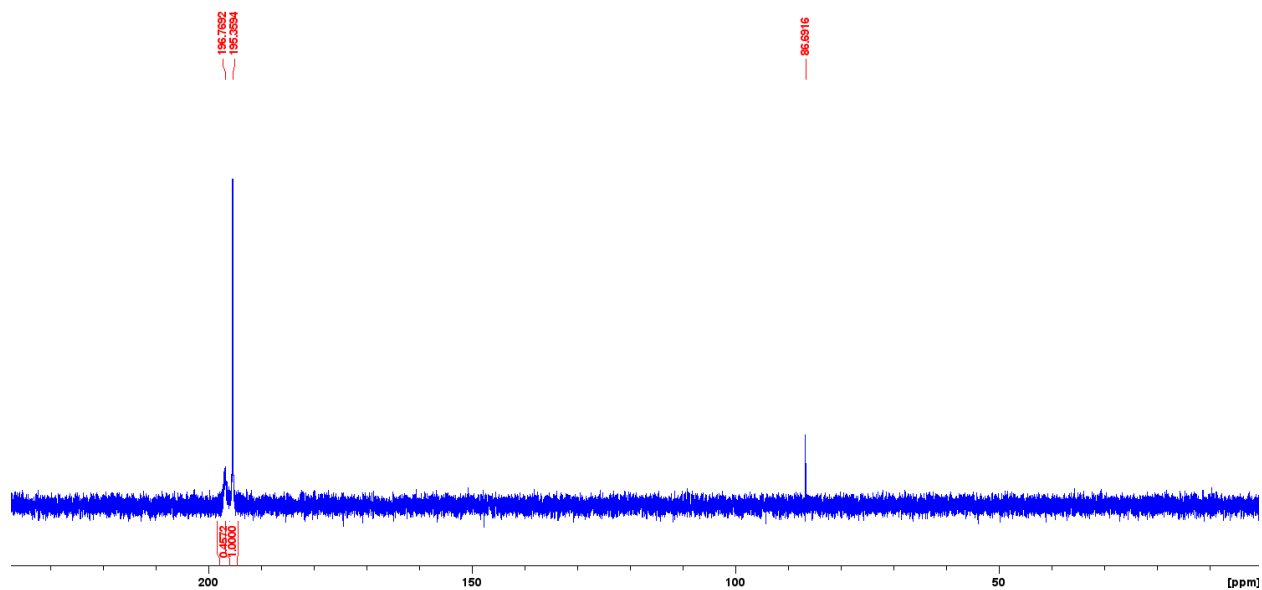
Figure S2. 128. ^{31}P{^{1}H} NMR spectrum of the crude mixture for the reaction **1-NCMe** + Et$_2$NOH in acetonitrile.
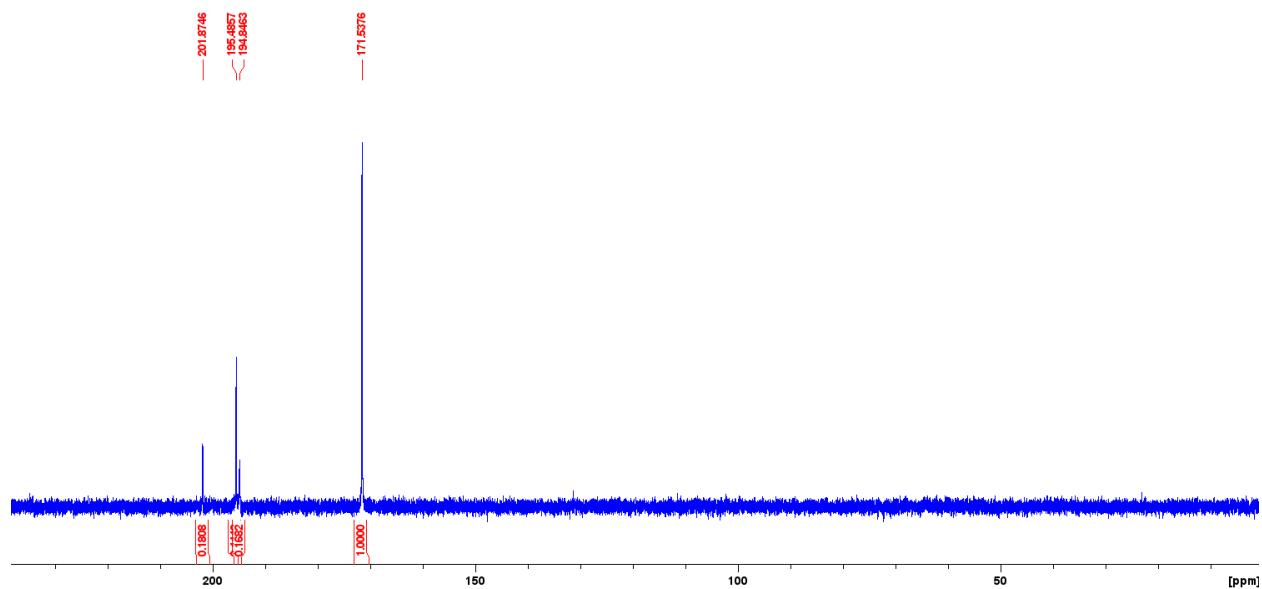
Figure S2. 129. ^{31}P{^{1}H} NMR spectrum of the crude mixture for the reaction **1** + Bn$_2$NOH in CH$_2$Cl$_2$.
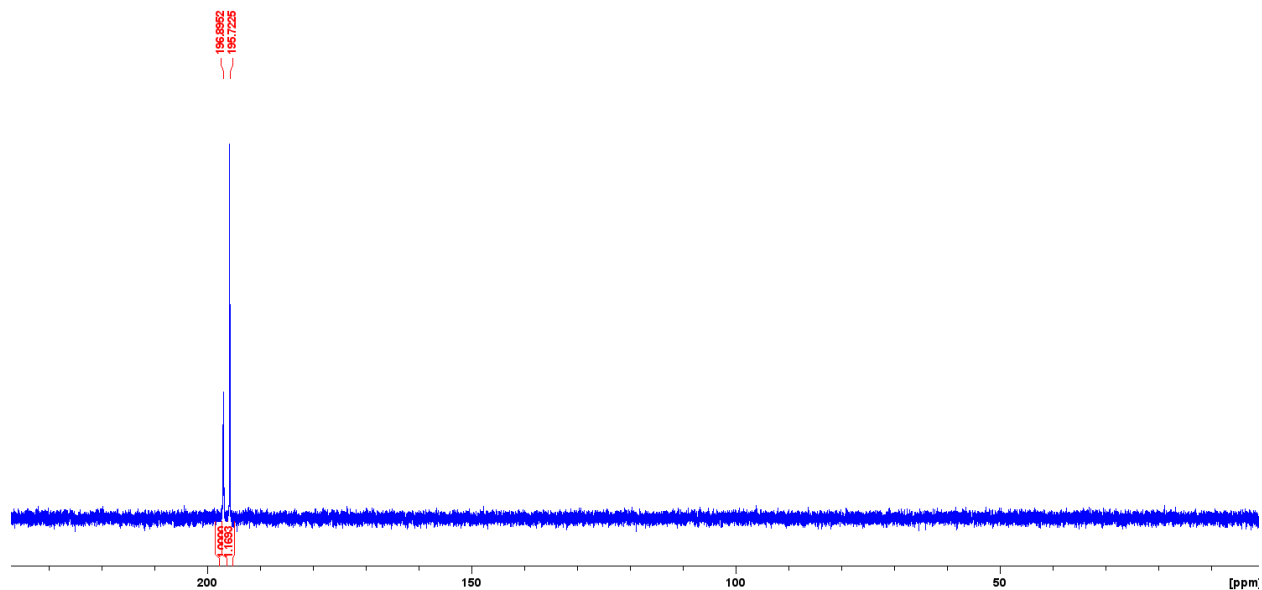
Figure S2. 130. $^{31}P\{^1H\}$ NMR spectrum of the crude mixture for the reaction **1** + Bn$_2$NOH in acetonitrile.
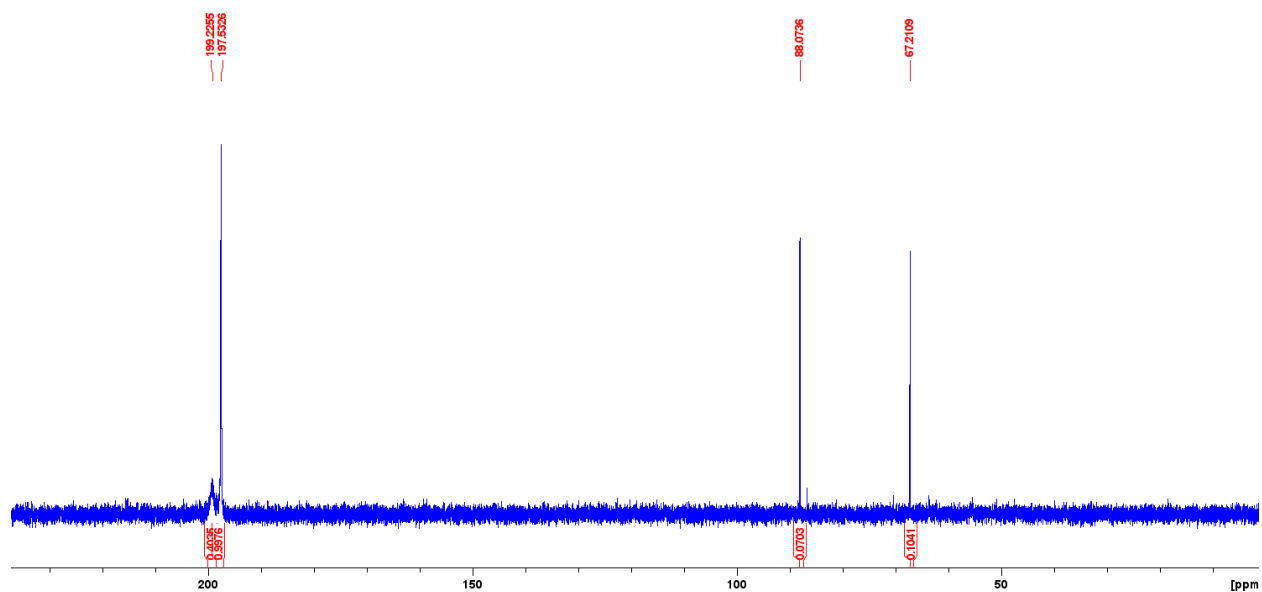
Figure S2. 131. $^{31}P\{^1H\}$ NMR spectrum of the crude mixture for the reaction **2** + Et$_2$NOH in acetonitrile.
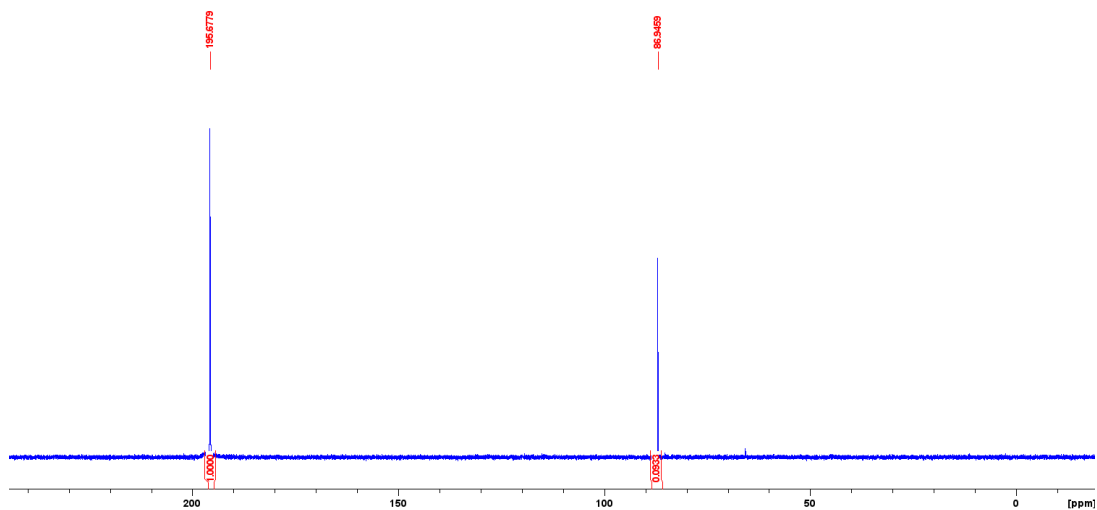
Figure S2. 132. $^{31}P\{^1H\}$ NMR spectrum of the crude mixture for the reaction **3** + Et$_2$NOH in acetonitrile.
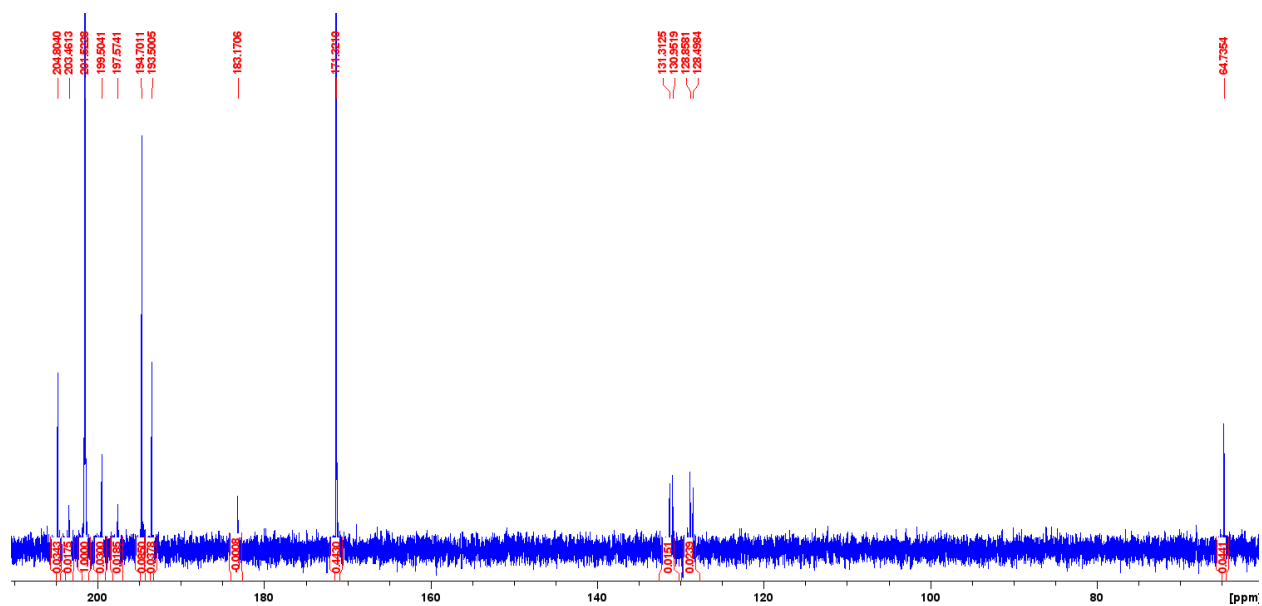
Figure S2. 133. $^{31}P\{^1H\}$ NMR spectrum of the crude mixture for the reaction **3** + Et$_2$NOH in CH$_2$Cl$_2$.
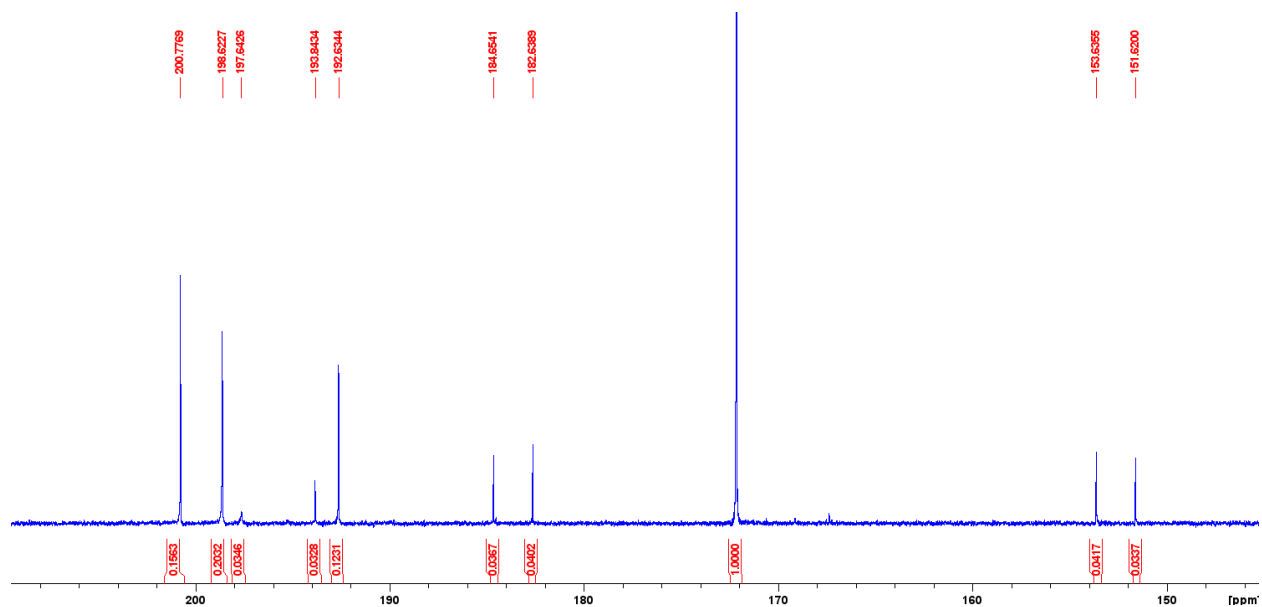
Figure S2. 134. $^{31}P\{^1H\}$ NMR spectrum of the crude mixture for the reaction **3** + Et$_2$NOH in toluene.
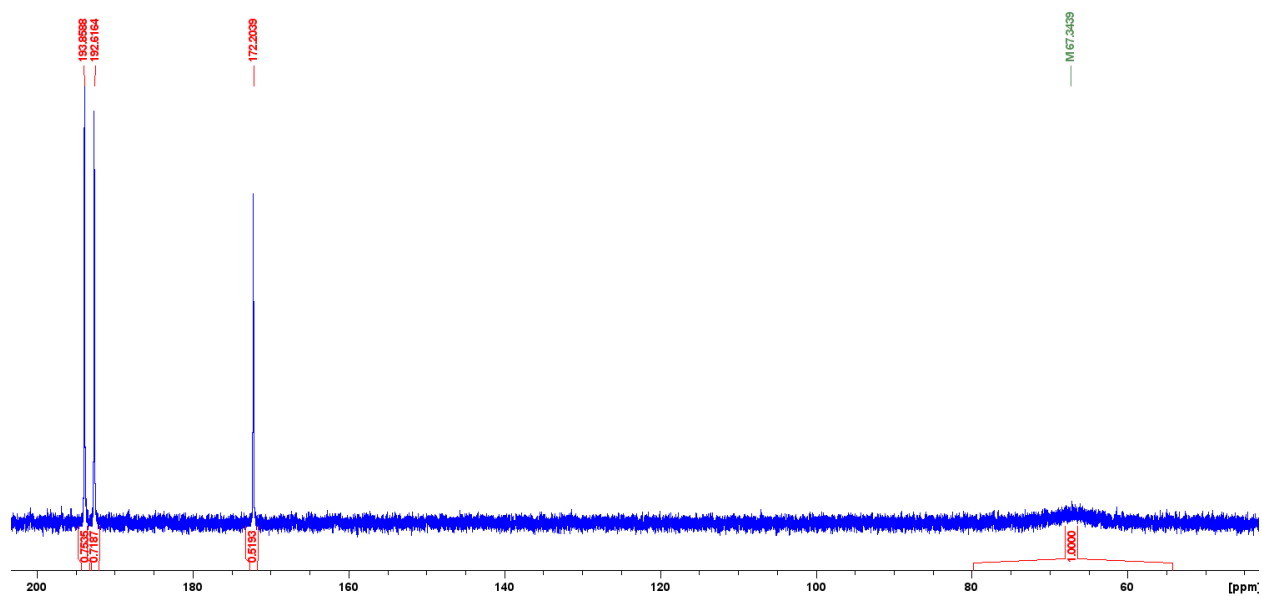
Figure S2. 135. $^{31}P\{^1H\}$ NMR spectrum of the crude mixture for the reaction **3** + Et$_2$NOH in C$_6$D$_6$.
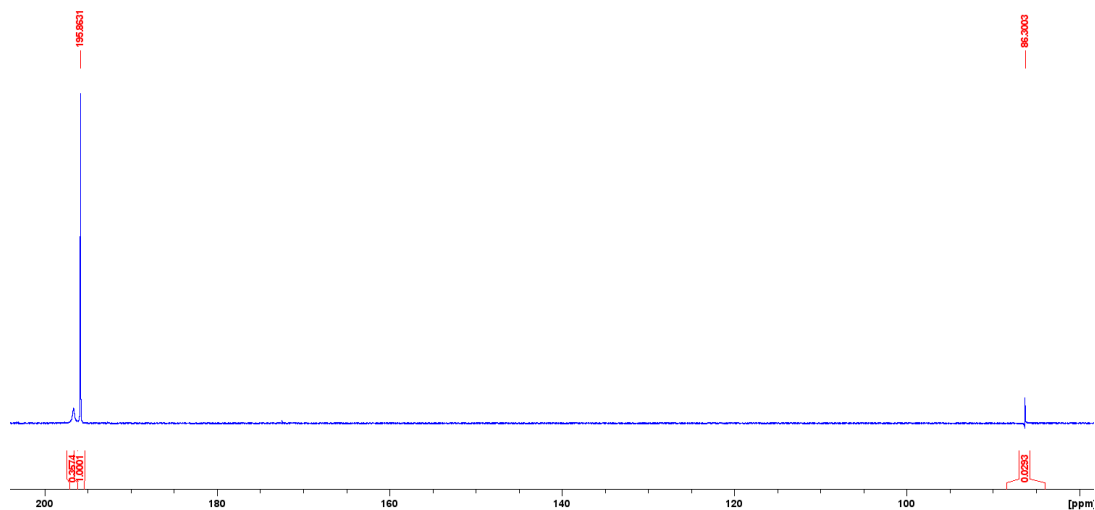
Figure S2. 136. $^{31}P\{^1H\}$ NMR spectrum of the crude mixture for the reaction **3** + Bn$_2$NOH in acetonitrile.
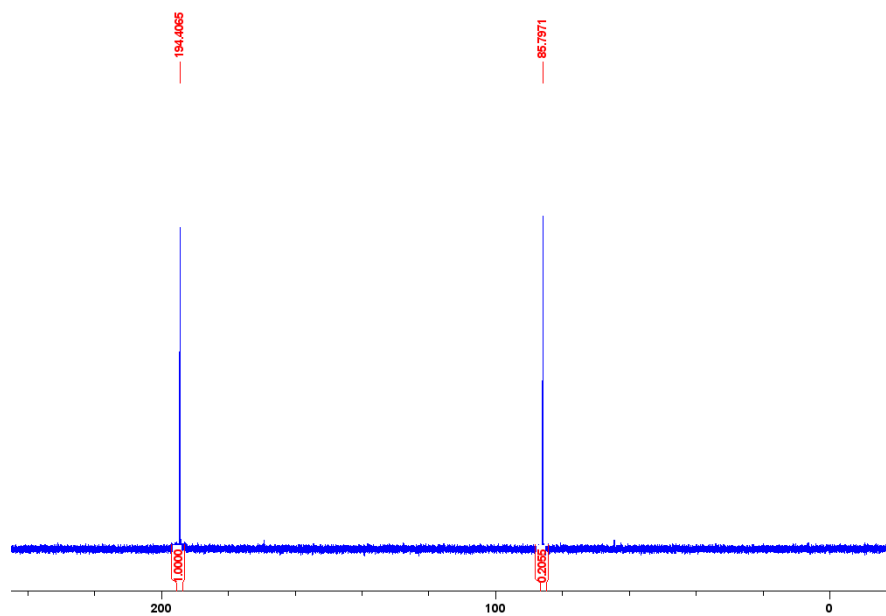
Figure S2. 137. $^{31}P\{^1H\}$ NMR spectrum of the crude mixture for the reaction **4-NCMe** + Et$_2$NOH in acetonitrile.

S2.5 Procedure and ^{31}P NMR spectra of the time profile experiments.

A stock solution was prepared by dissolving 30 mg of dimer **3**, [{κ^P,κ^C-(i-Pr)$_2$PO-(5-OMe-C$_6$H$_3$)}Ni(μ-Br)]$_2$, (0.040 mmol) and 7 mg of Et$_2$NOH (0.079 mmol) in 6 mL MeCN or C$_6$D$_6$. This was stirred at room temperature and under inert atmosphere for about 1-2 min to ensure homogeneity, and then a small portion of it ($\approx$ 1mL) was withdrawn to prepare an NMR sample to be used for recording the ^{31}P NMR spectra of the reaction mixture over the reaction time interval (20 h for the acetonitrile reaction, 48 h for the C$_6$D$_6$ reaction). The concentrations of the major products/intermediates detected in this reaction were estimated from the integration values for the 4 most intense signals appearing in the chemical shift region 210-170 ppm. These were plotted as % of the combined integration values against elapsed time to generate the time profile for this reaction.
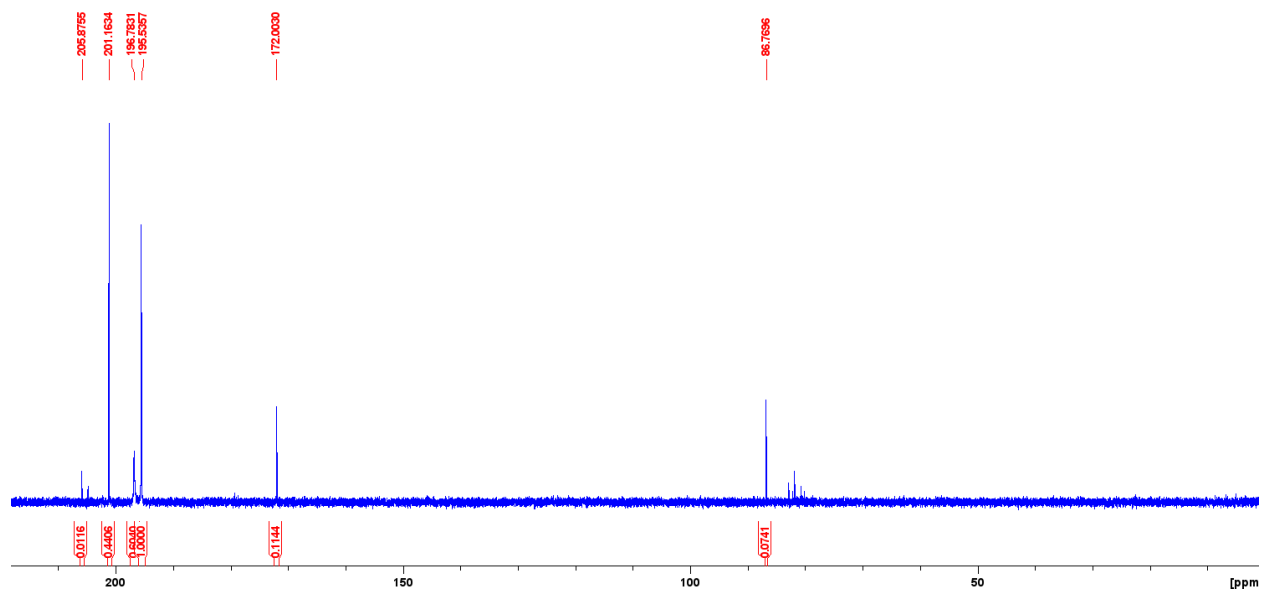
Figure S2. 138. ^{31}P{^{1}H} NMR spectrum of the crude mixture for the reaction **3** + Et$_2$NOH in acetonitrile (t= 10 min).
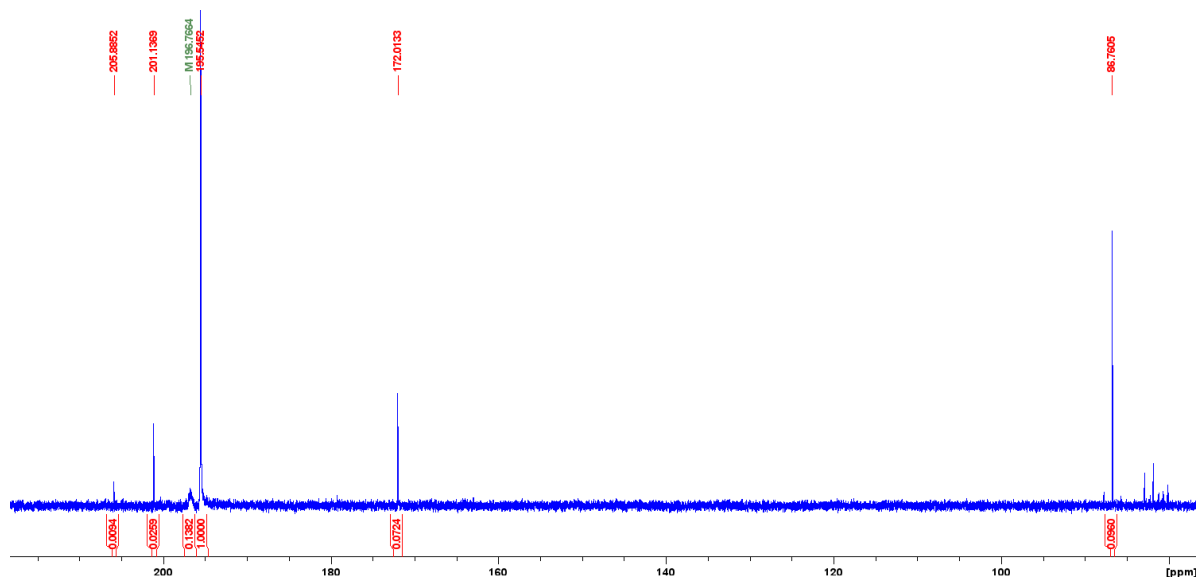
Figure S2. 139. $^{31}P\{^1H\}$ NMR spectrum of the crude mixture for the reaction **3** + Et$_2$NOH in acetonitrile (t= 20 min).
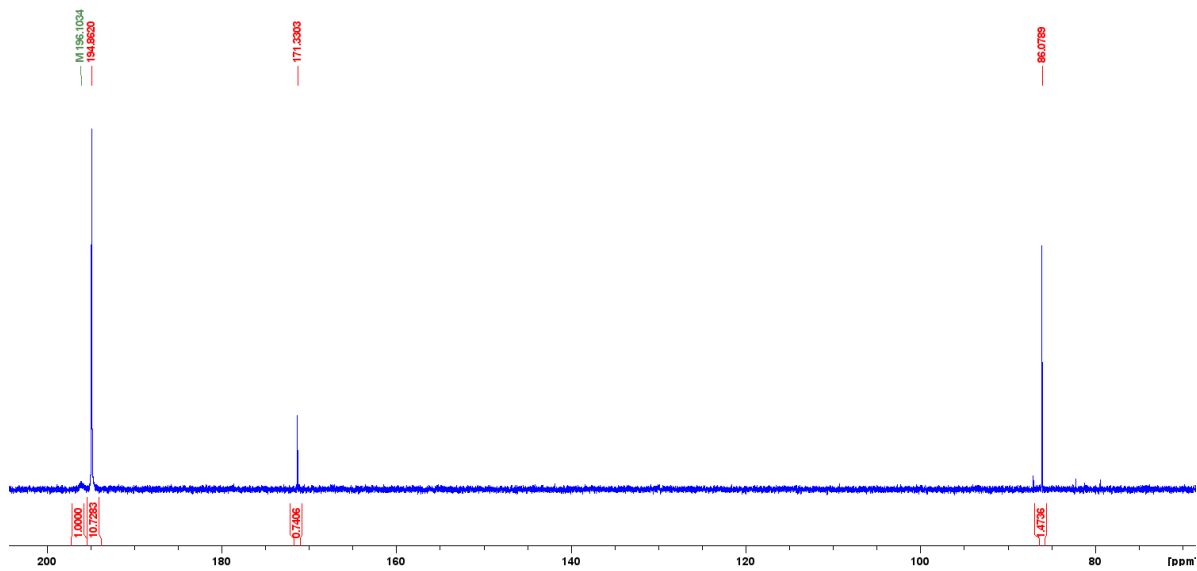
Figure S2. 140. $^{31}P\{^1H\}$ NMR spectrum of the crude mixture for the reaction **3** + Et$_2$NOH in acetonitrile (t= 90 min).
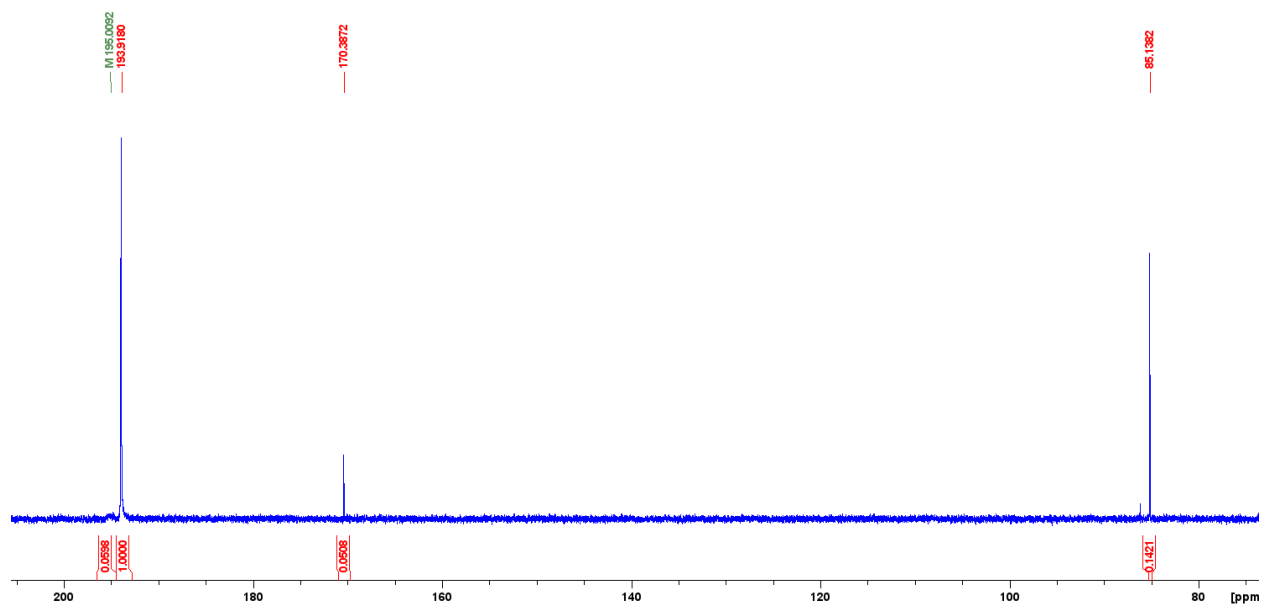
Figure S2. 141. $^{31}P\{^1H\}$ NMR spectrum of the crude mixture for the reaction **3** + Et$_2$NOH in acetonitrile (t= 7 h).
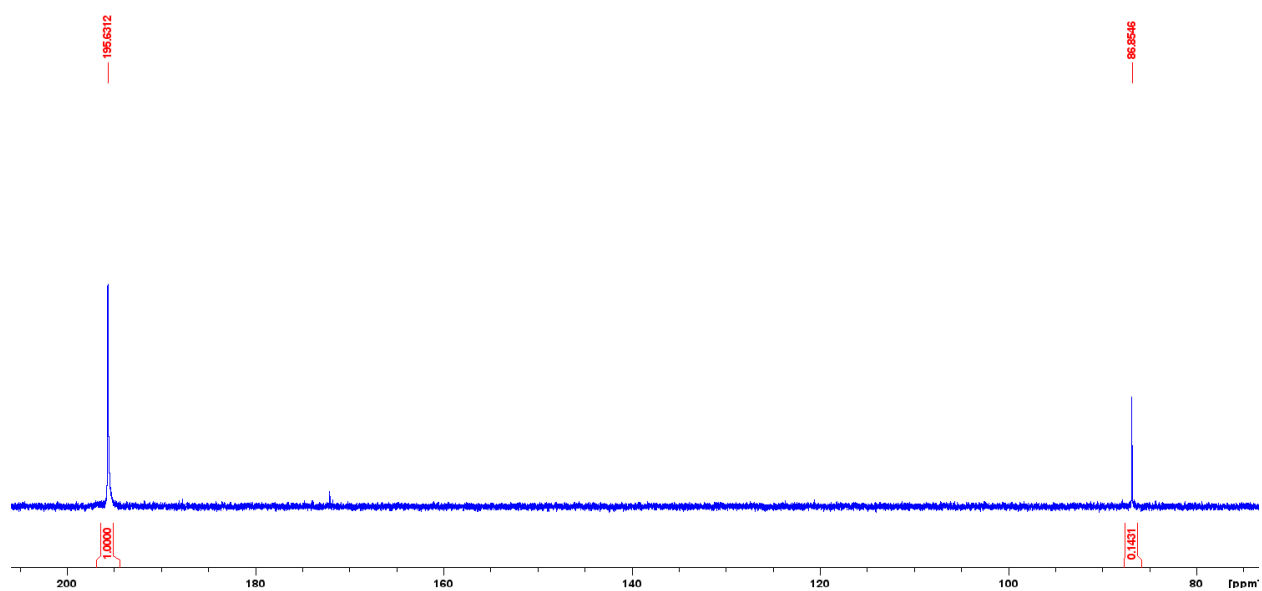
Figure S2. 142. $^{31}P\{^1H\}$ NMR spectrum of the crude mixture for the reaction **3** + Et$_2$NOH in acetonitrile (t= 20 h).
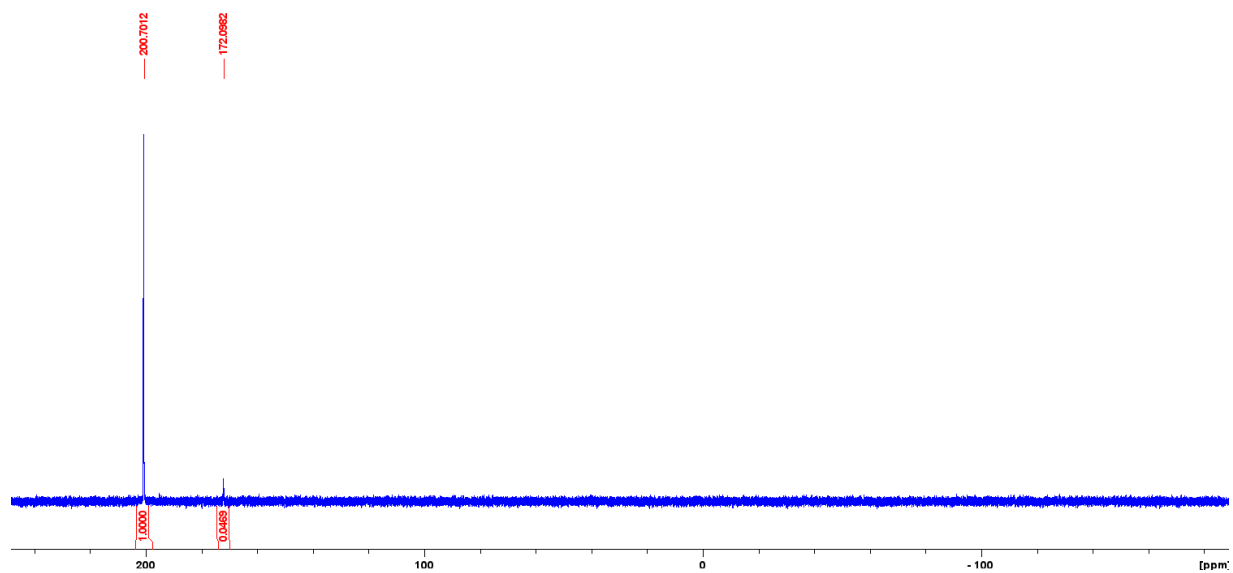
Figure S2. 143. $^{31}P\{^1H\}$ NMR spectrum of the crude mixture for the reaction **3** + Et$_2$NOH in C$_6$D$_6$ (t= 10 min).
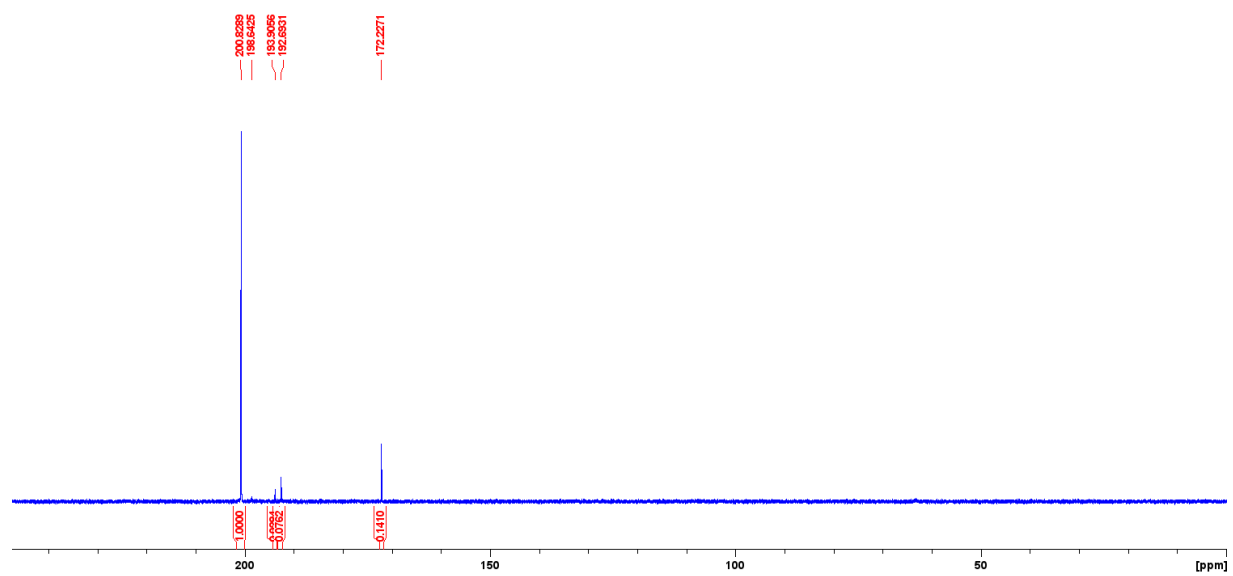
Figure S2. 144. $^{31}P\{^1H\}$ NMR spectrum of the crude mixture for the reaction **3** + Et$_2$NOH in C$_6$D$_6$ (t= 24 h).
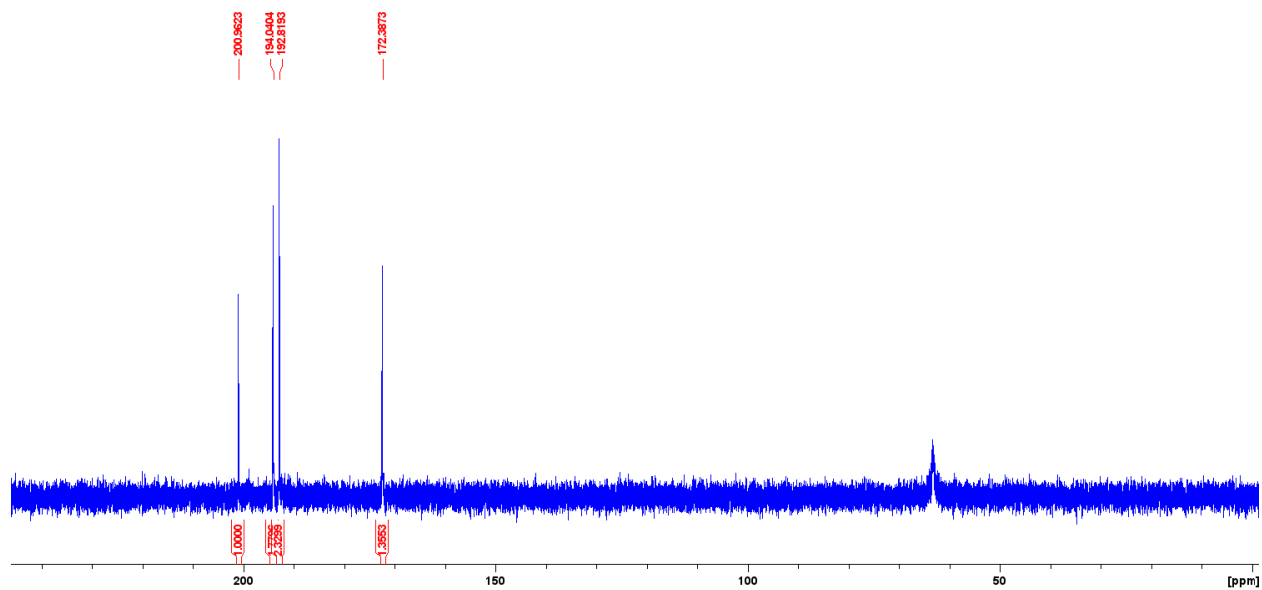
Figure S2. 145. $^{31}P\{^{1}H\}$ NMR spectrum of the crude mixture for the reaction **3** + Et$_2$NOH in C$_6$D$_6$ (t= 48 h).

S2.6 PXRD diffractogram of selected complexes

Powder X-ray diffraction data were collected for 10 powder samples to establish bulk purity. The data collection mode and instrumental details are given below, and the diffraction patterns and the Rietveld fits are shown in the following pages.

Mode organic standard 10 min"

Instrument: Malvern PanAlytical Empyrean 3

Geometry: Bragg Brentano θ - θ

Radiation: CuKα, λ = 1.54178 Å (45 kV, 40 mA)

Detector: PIXcel^{3D}

       mode 1D continuous scan (255 channels)

       Pulse height distribution (PHD): 25%-70%

Optics Incident side: iCore module:

       Bragg-Brentano HD Cu X-ray mirror;

       automatic divergence slit set to irradiated length of 10 mm;

       0.03 rad Soller slit;

       14 mm primary mask, 6 mm secondary mask.

Optics diffracted side: dCore module:

       automatic anti-scatter slit set to irradiated length of 10 mm;

       0.04 rad Soller slit.

Scan: 2θ range: 4 to 40°;

       Step size: 0.0131°;

       Counting time 45.6 s;

       Total time: 10 min.
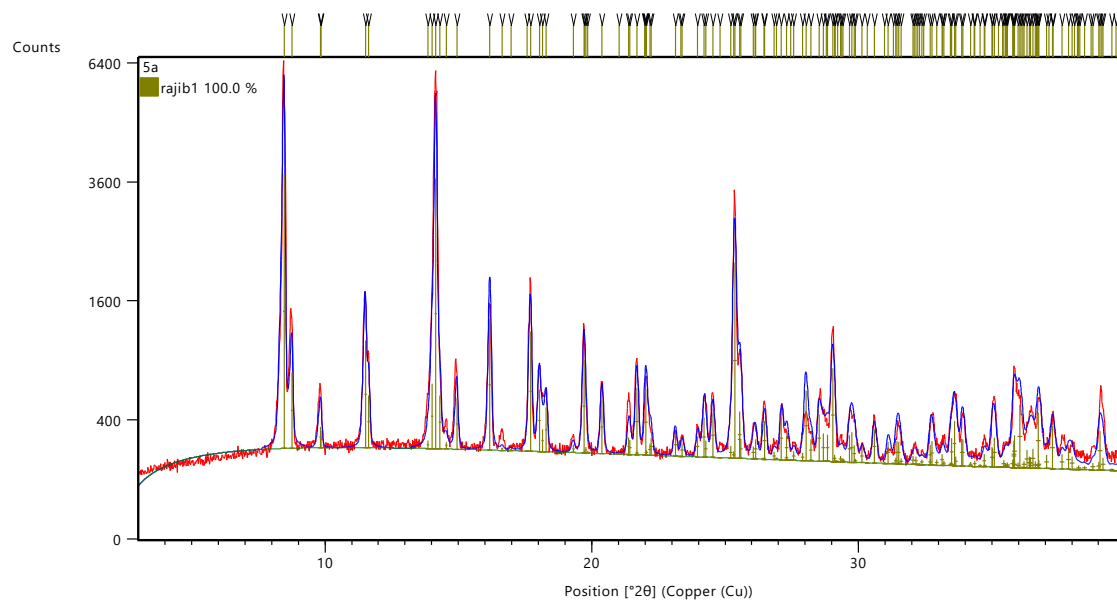
Figure S2. 146. PXRD pattern obtained experimentally for complex **5a** (red trace) and the simulated pattern (blue trace) obtained by a Rietveld fit based on the unit cell parameters of complex **5a**.
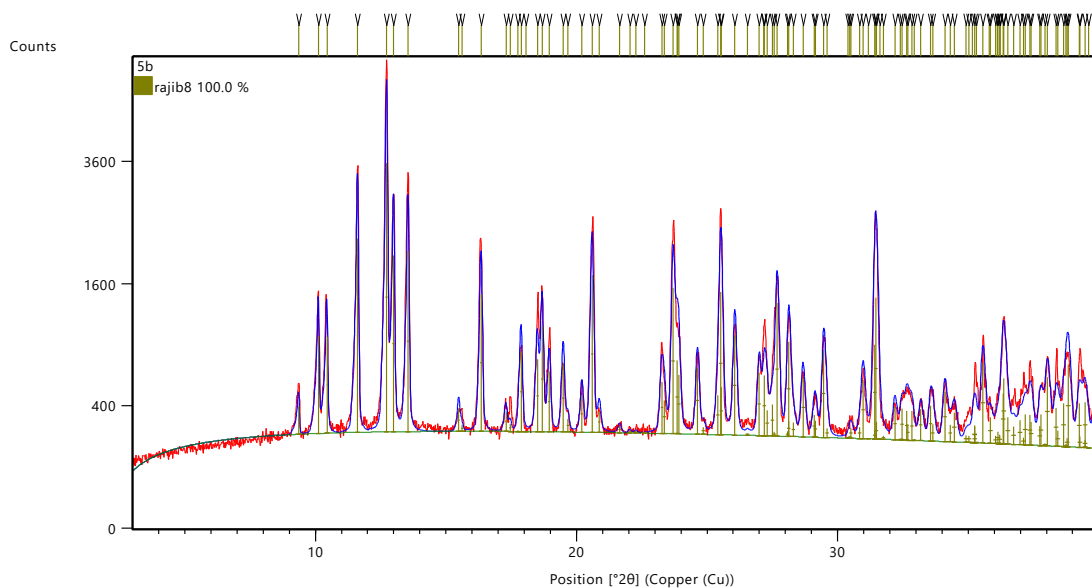
Figure S2. 147. PXRD pattern obtained experimentally for complex **5b** (red trace) and the simulated pattern (blue trace) obtained by a Rietveld fit based on the unit cell parameters of complex **5b**.
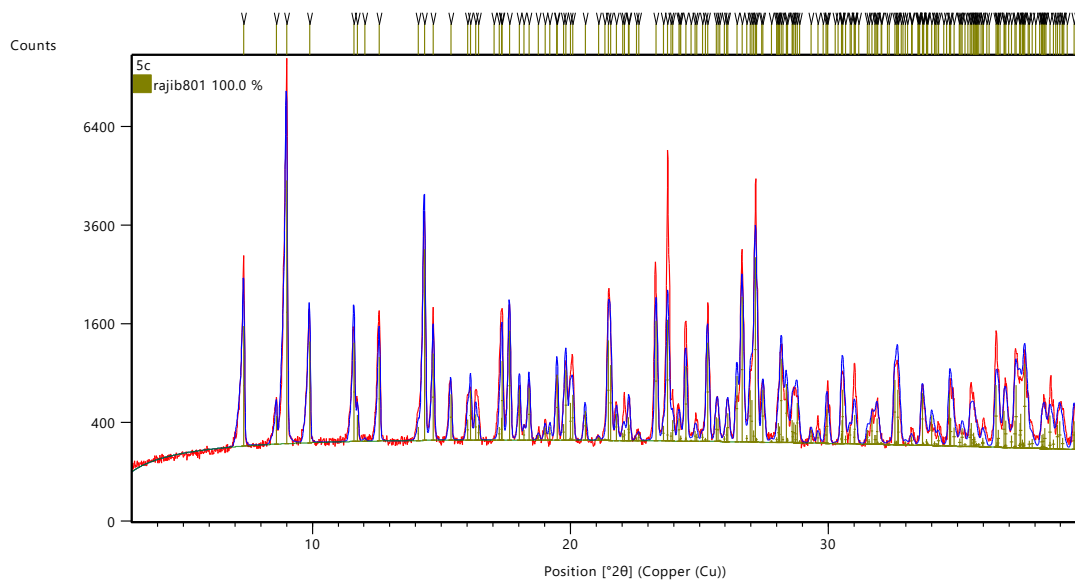
Figure S2. 148. PXRD pattern obtained experimentally for complex **5c** (red trace) and the simulated pattern (blue trace) obtained by on a Rietveld fit based on the unit cell parameters of complex **5c**.
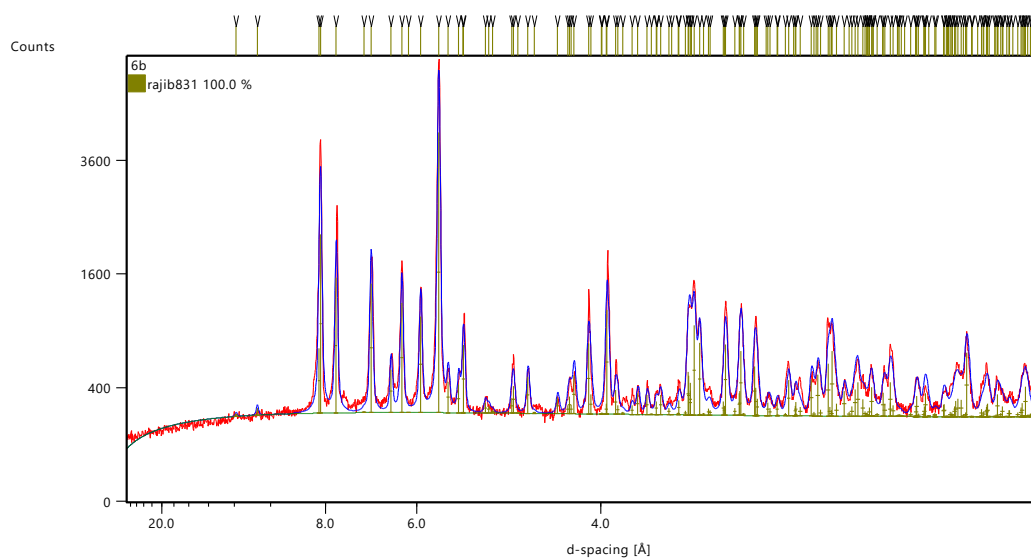
Figure S2. 149. PXRD pattern obtained experimentally for complex **6b** (red trace) and the simulated pattern (blue trace) obtained by a Rietveld fit based on the unit cell parameters of complex **6b**.
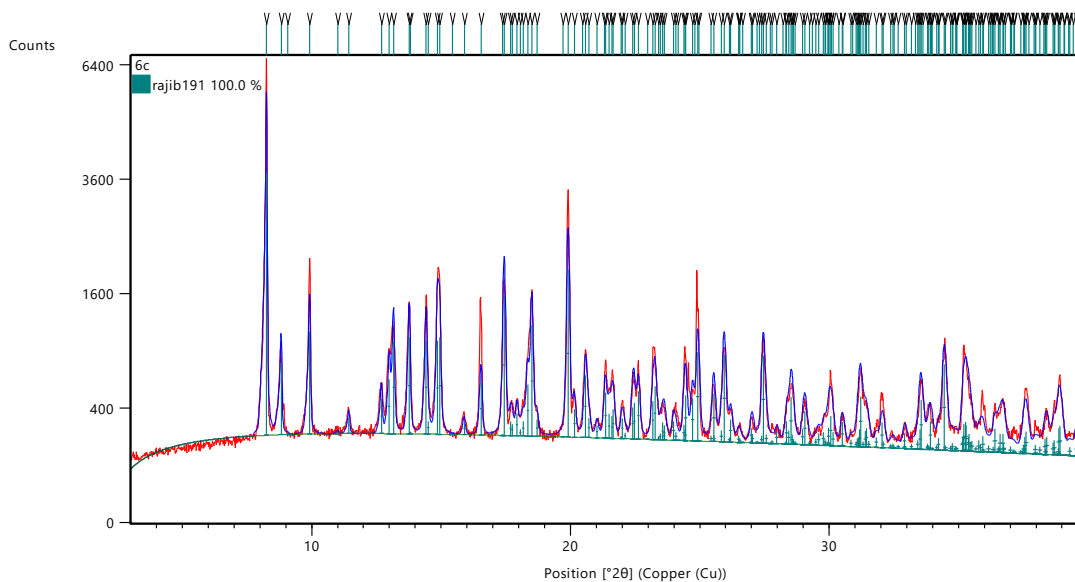
Figure S2. 150. PXRD pattern obtained experimentally for complex **6c** (red trace) and the simulated pattern (blue trace) obtained by a Rietveld fit based on the unit cell parameters of complex **6c**.
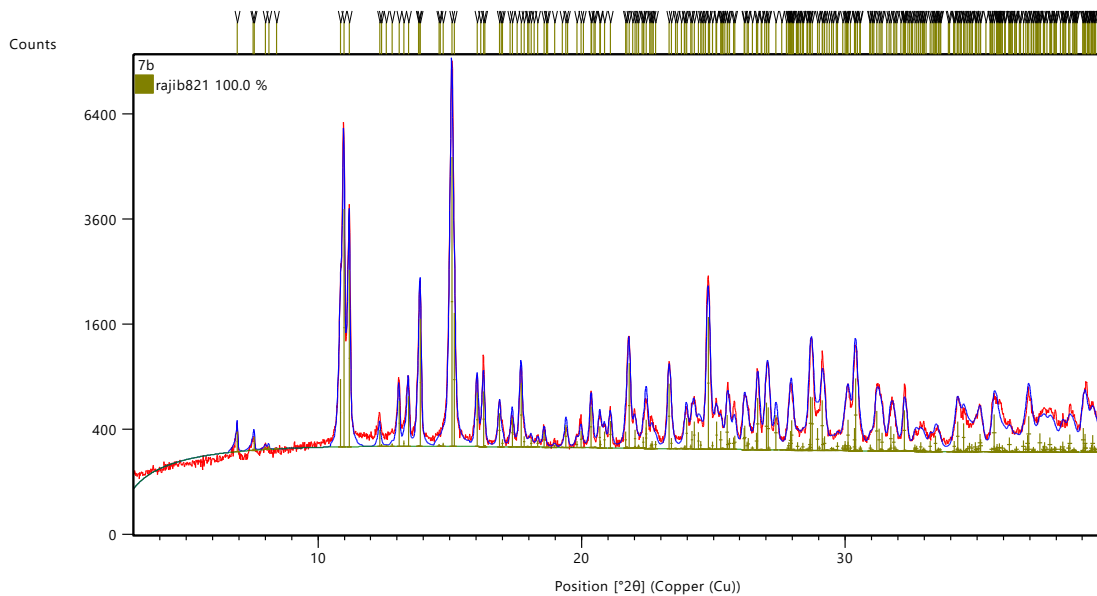
Figure S2. 151. PXRD pattern obtained experimentally for complex **7b** (red trace) and the simulated pattern (blue trace) obtained by a Rietveld fit based on the unit cell parameters of complex **7b**.
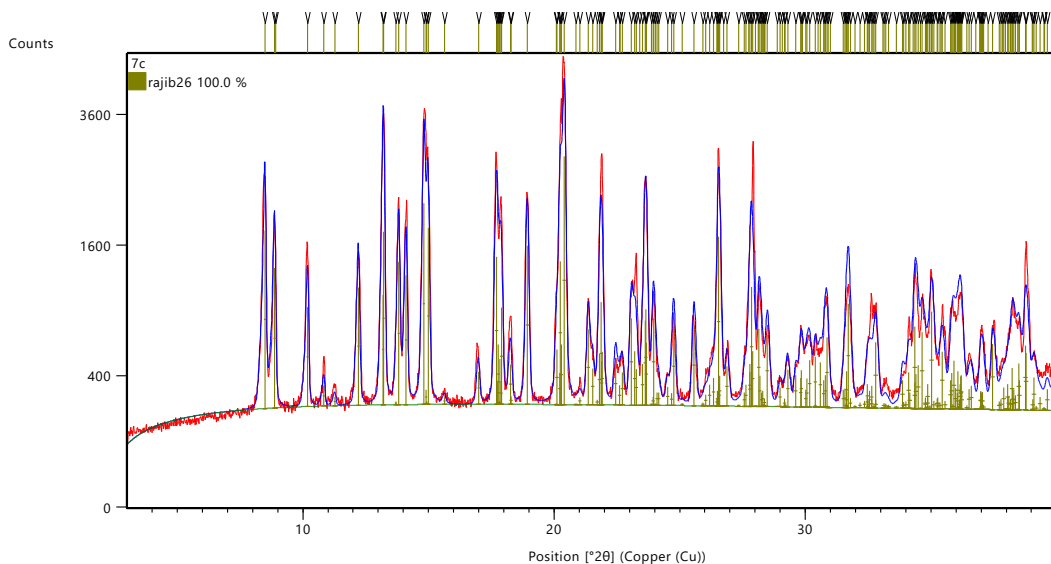
Figure S2. 152. PXRD pattern obtained experimentally for complex **7c** (red trace) and the simulated pattern (blue trace) obtained by a Rietveld fit based on the unit cell parameters of complex **7c**.
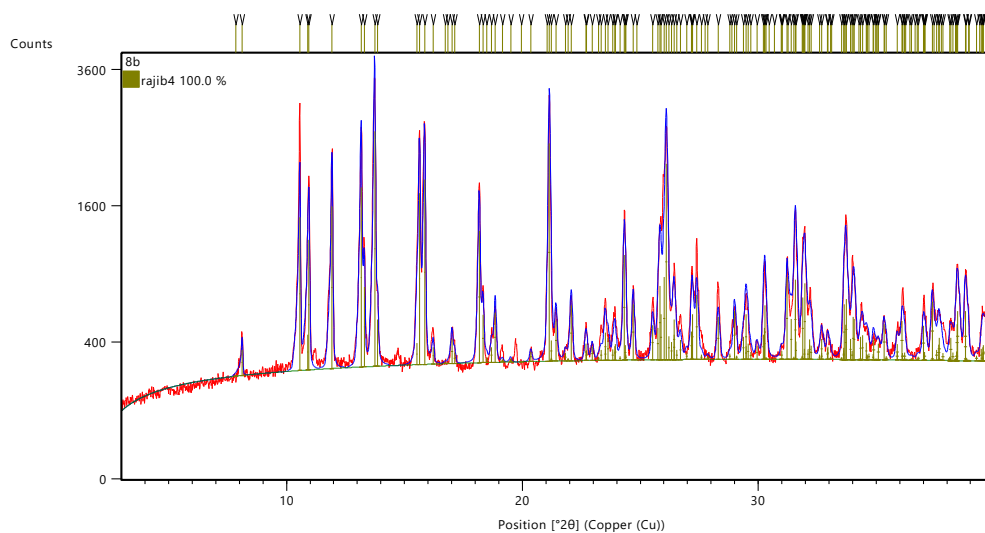
Figure S2. 153. PXRD pattern obtained experimentally for complex **8b** (red trace) and the simulated pattern (blue trace) obtained by a Rietveld fit based on the unit cell parameters of complex 8b.

S2.7 Crystallographic data

Table S2. 1: Crystal description and refinement indicators for complex **4'**

	4'
chemical formula	$C_{28}H_{47}BrN_2NiO_2P_2$
crystal colour	orange
crystal size (mm)	$0.07 \times 0.08 \times 0.065$
index ranges	$-11 \leq h \leq 11$ $-14 \leq k \leq 14$ $-21 \leq l \leq 21$
_Fw_; _F_(000)	644.23; 676.0
_T_ (K)	150
wavelength (Å)	1.34139
space group	P-1
_a_ (Å)	8.6766(3)
_b_ (Å)	10.8198(4)
_c_ (Å)	16.2208(6)
α (deg)	91.2360(10)
β (deg)	93.385(2)
γ (deg)	90.311(2)
_Z_	2
_V_ (Å³)	1519.75(10)
ρ_{calcd} (g·cm⁻³)	1.408
μ (mm⁻¹)	5.295
θ range (deg); completeness	4.748 - 121.456; 0.998
collected reflections; R_σ	36465; 0.0250
unique reflections; R_{int}	6953; 0.0363
R1[a]; wR2[b] [I > 2σ(I)]	0.0255; 0.0695
R1; wR2 [all data]	0.0269; 0.0706
GOOF	1.046
largest diff peak and hole	0.75 and -0.47

[a] $R_1 = \Sigma(||F_o|-|F_c||)/\Sigma|F_o|$

[b] $wR_2 = \{\Sigma[w(F_o{}^2-F_c{}^2)^2]/\Sigma[w(F_o{}^2)^2]\}^{1/2}$

Table S2. 2: Crystal description and refinement indicators for compounds **5a-5c**

	5a	5b	5c
chemical formula	$C_{19}H_{27}Br_{0.3}Cl_{0.7}NNiO_2P$	$C_{16}H_{29}BrNNiO_2P$	$C_{26}H_{33}BrNNiO_2P$
crystal colour	yellow	brown	red
crystal size (mm)	$0.1 \times 0.224 \times 0.065$	$0.101 \times 0.129 \times 0.130$	$0.075 \times 0.145 \times 0.200$
index ranges	$-10 \leq h \leq 11$	$-12 \leq h \leq 12$	$-39 \leq h \leq 39$
	$-13 \leq k \leq 13$	$-13 \leq k \leq 12$	$-11 \leq k \leq 11$
	$-13 \leq l \leq 13$	$-20 \leq l \leq 20$	$-26 \leq l \leq 26$
Fw; *F*(000)	438.33; 458.0	436.99; 904	561.12; 2320.0
T (K)	100	100	100
wavelength (Å)	1.54178	1.54178	1.54178
space group	P-1	$P2_12_12_1$	C2/c
a (Å)	9.2167(3)	10.312(3)	32.2326(6)
b (Å)	10.7893(3)	11.182(3)	9.4013(2)
c (Å)	11.1469(3)	16.878(5)	21.8275(4)
α (deg)	108.3090(10)	90	90
β (deg)	99.2590(10)	90	128.5790(10)
γ (deg)	99.2440(10)	90	90
Z	2	4	8
V (Å³)	1011.92(5)	1946.1(9)	5170.76(18)
ρ_{calcd} (g·cm⁻³)	1.439	1.491	1.442
μ (mm⁻¹)	3.728	4.661	3.648
θ range (deg); completeness	4.977- 72.028; 0.974	4.744− 72.212; 0.995	3.508– 71.960; 1.000
collected reflections; R_σ	41853; 0.0089	40151; 0.0143	34847; 0.0156
unique reflections; R_{int}	3861; 0.0217	3813; 0.0293	5060; 0.0275
R1[a]; wR2[b] [I > 2σ(I)]	0.0237; 0.0640	0.0168; 0.0436	0.0267; 0.0711
R1; wR2 [all data]	0.0238; 0.0640	0.0168; 0.0436	0.0278; 0.0720
GOOF	1.063	1.094	1.047
largest diff peak and hole	0.39 and -0.20	0.57 and -0.26	0.86 and -0.55

[a] $R_1 = \Sigma(||F_o|-|F_c||)/\Sigma|F_o|$

[b] $wR_2 = \{\Sigma[w(F_o^2 - F_c^2)^2]/\Sigma[w(F_o^2)^2]\}^{\frac{1}{2}}$

Table S2. 3: Crystal description and refinement indicators for compounds **6b** and **6c**.

	6b	**6c**
chemical formula	$C_{16}H_{26}BrClNNiOP$	$C_{26}H_{30}BrClNNiOP$
crystal colour	brown	yellow
crystal size (mm)	$0.09 \times 0.09 \times 0.14$	$0.07 \times 0.07 \times 0.17$
index ranges	$-9 \leq h \leq 10$ $-12 \leq k \leq 13$ $-0 \leq l \leq 14$	$-15 \leq h \leq 15$ $-19 \leq k \leq 19$ $-16 \leq l \leq 15$
Fw; *F(000)*	453.42, 464.0	577.55; 1184.0
T (K)	100	150
wavelength (Å)	1.54178	1.34139
space group	P-1	$P2_1/n$
a (Å)	8.1691(4)	12.9011(5)
b (Å)	10.6197(5)	15.7816(6)
c (Å)	11.5954(5)	13.2557(5)
α (deg)	85.083(2)	90
β (deg)	83.391(3)	107.169(2)
γ (deg)	89.300(3)	90
Z	2	4
V (Å³)	995.58(8)	2578.93(17)
ρ_{calcd} (g·cm⁻³)	1.513	1.488
μ (mm⁻¹)	5.748	6.422
θ range (deg); completeness	3.851 – 72.221; 0.981	3.655 – 55.022; 1.000
collected reflections; R_σ	26093; 0.0348	34837; 0.0410
unique reflections; R_{int}	3767; 0.1273	4899; 0.0691
R1[a]; wR2[b] [I > 2σ(I)]	0.0535; 0.1480	0.0374; 0.0868
R1; wR2 [all data]	0.0578; 0.1519	0.0518; 0.0935
GOOF	1.132	1.050
largest diff peak and hole	1.33 and -0.56	0.35 and -0.50

[a] $R_1 = \Sigma(||F_o|-|F_c||)/\Sigma|F_o|$

[b] $wR_2 = \{\Sigma[w(F_o^2-F_c^2)^2]/\Sigma[w(F_o^2)^2]\}^{\frac{1}{2}}$

Table S2. 4: Crystal description and refinement indicators for compounds **7b-7d**.

	7b	7c	7d
chemical formula	$C_{17}H_{29}BrNNiO_2P$	$C_{27}H_{33}BrNNiO_2P$	$C_{17}H_{31}BrNNiO_2P$
crystal colour	yellow	yellow	yellow
crystal size (mm)	$0.08 \times 0.11 \times 0.13$	$0.15 \times 0.16 \times 0.26$	$0.07 \times 0.13 \times 0.15$
index ranges	$-11 \leq h \leq 11$ $-13 \leq k \leq 13$ $-29 \leq l \leq 29$	$-17 \leq h \leq 16$ $-20 \leq k \leq 20$ $-17 \leq l \leq 17$	$-14 \leq h \leq 14$ $-15 \leq k \leq 15$ $-20 \leq l \leq 20$
Fw; *F*(000)	449; 928.0	573.13; 1184.0	451.02; 936.0
T (K)	150	150	150
wavelength (Å)	1.34139	1.34139	1.34139
space group	P-1	$P2_1/n$	$P2_1/c$
a (Å)	8.7051(4)	13.1430(3)	11.3886(4)
b (Å)	10.5840(5)	15.5918(4)	11.7955(4)
c (Å)	22.8298(11)	13.1678(3)	15.5240(5)
α (deg)	87.918(2)	90	90
β (deg)	86.659(2)	103.5710(10)	92.048(2)
γ (deg)	74.060(2)	90	90
Z	4	4	4
V (Å³)	2018.65(17)	2623.05(11)	2084.07(12)
ρ_{calcd} (g·cm⁻³)	1.477	1.451	1.437
μ (mm⁻¹)	7.316	5.718	7.087
θ range (deg); completeness	3.375 – 60.836; 0.994	3.892 – 60.656; 0.977	3.378 – 60.641; 0.993
collected reflections; R_σ	41903; 0.0593	38929; 0.0313	31567; 0.0372
unique reflections; R_{int}	9162; 0.0701	5913; 0.0435	4759; 0.0533
R1[a]; wR2[b] [I > 2σ(I)]	0.0733; 0.2153	0.0272; 0.0706	0.0516; 0.1664
R1; wR2 [all data]	0.0835; 0.2304	0.0276; 0.0709	0.0526; 0.1684
GOOF	1.067	1.102	1.115
largest diff peak and hole	1.60 and -1.43	0.30 and -0.37	0.95 and -1.19

[a] $R_1 = \Sigma(||F_o|-|F_c||)/\Sigma|F_o|$

[b] $wR_2 = \{\Sigma[w(F_o^2-F_c^2)^2]/\Sigma[w(F_o^2)^2]\}^{1/2}$

Table S2. 5: Crystal description and refinement indicators for compounds **8a** and **8b**

	8a	8b
chemical formula	$C_{21}H_{32}Br_{0.7}Cl_{0.3}N_2NiO_2P$	$C_{18}H_{32}BrN_2NiOP$
crystal colour	yellow	brown
crystal size (mm)	$0.065 \times 0.081 \times 0.143$	$0.08 \times 0.10 \times 0.13$
index ranges	$0 \le h \le 25$ $-12 \le k \le 0$ $-13 \le l \le 13$	$-36 \le h \le 36$ $-8 \le k \le 10$ $-26 \le l \le 26$
Fw; *F*(000)	500.74; 1042.0	462.04; 1920.0
T (K)	100	100
wavelength (Å)	1.54178	1.54178
space group	Pc	C2/c
a (Å)	20.5518(11)	29.6233(12)
b (Å)	10.3023(5)	8.5715(4)
c (Å)	10.8188(7)	21.7605(15)
α (deg)	90	90
β (deg)	97.918(3)	130.3570(10)
γ (deg)	90	90
Z	4	8
V (Å³)	2268.8(2)	4210.4(4)
ρ_{calcd} (g·cm⁻³)	1.466	1.458
μ (mm⁻¹)	3.814	4.319
θ range (deg); completeness	2.170- 72.555; 0.983	3.916 – 70.098; 0.991
collected reflections; R_σ	14082; 0.0401	41086; 0.0232
unique reflections; R_{int}	4343; 0.0746	3962; 0.0450
R1[a]; wR2[b] [I > 2σ(I)]	0.0516; 0.1452	0.0299; 0.0841
R1; wR2 [all data]	0.0538; 0.1484	0.0301; 0.0843
GOOF	1.047	1.081
largest diff peak and hole	0.98 and -0.79	0.50 and -0.35

[a] $R_1 = \Sigma(||F_o|-|F_c||)/\Sigma|F_o|$
[b] $wR_2 = \{\Sigma[w(F_o^2 - F_c^2)^2]/\Sigma[w(F_o^2)^2]\}^{1/2}$

S2.8 Additional Thermal ellipsoid plots
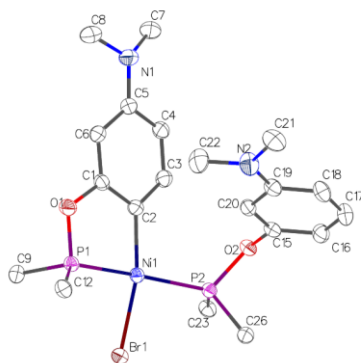
Figure S2. 154. Side view of the molecular diagram of compound **4'**. Thermal ellipsoids are shown at the 50% probability level; hydrogen atoms are refined via riding model.
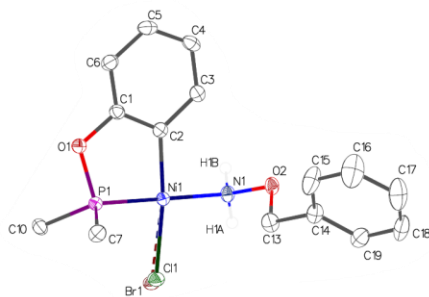
Figure S2. 155. Side view of the molecular diagram of compound **5a**. Thermal ellipsoids are shown at the 50% probability level; hydrogen atoms are refined via riding model.
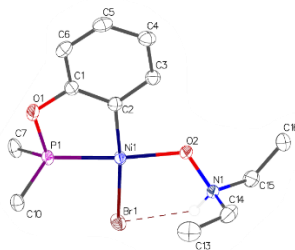
Figure S2. 156. Side view of the molecular diagram of compound **5b**. Thermal ellipsoids are shown at the 50% probability level; hydrogen atoms are refined via riding model.
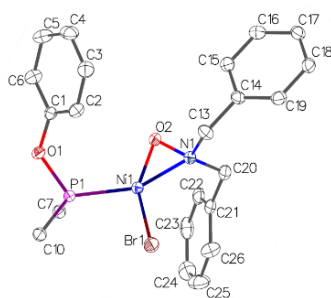
Figure S2. 157. Side view of the molecular diagram of compound **5c**. Thermal ellipsoids are shown at the 50% probability level; hydrogen atoms are refined via riding model.
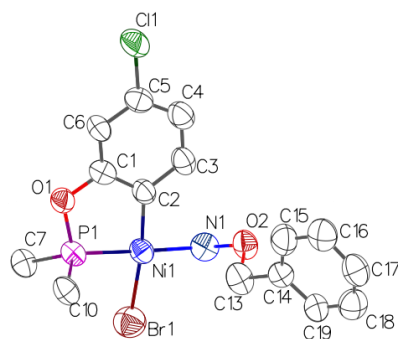
Figure S2. 158. Side view of the molecular diagram of compound **6a**. Thermal ellipsoids are shown at the 50% probability level; hydrogen atoms are refined via riding model.
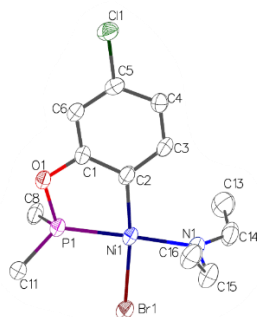
Figure S2. 159. Side view of the molecular diagram of compound **6b**. Thermal ellipsoids are shown at the 50% probability level; hydrogen atoms are refined via riding model.
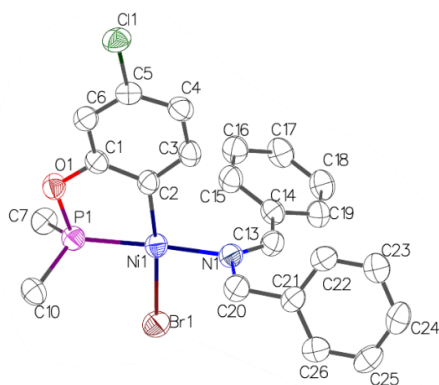
Figure S2. 160. Side view of the molecular diagram of compound **6c**. Thermal ellipsoids are shown at the 50% probability level; hydrogen atoms are refined via riding model.
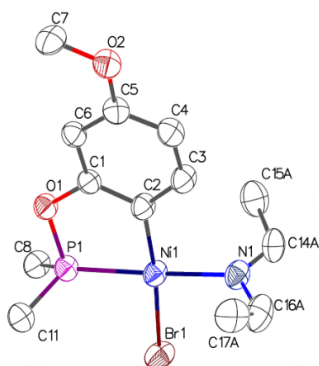
Figure S2. 161. Side view of the molecular diagram of compound **7b**. Thermal ellipsoids are shown at the 50% probability level; hydrogen atoms are refined via riding model.
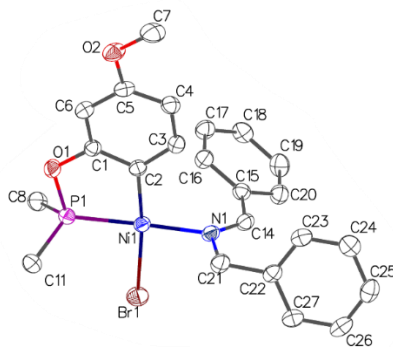
Figure S2. 162. Side view of the molecular diagram of compound **7c**. Thermal ellipsoids are shown at the 50% probability level; hydrogen atoms are refined via riding model.
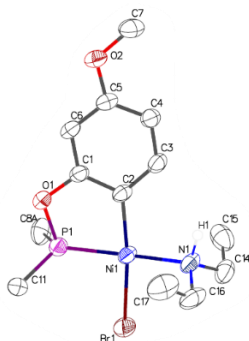
Figure S2. 163. Side view of the molecular diagram of compound **7d**. Thermal ellipsoids are shown at the 50% probability level; hydrogen atoms are refined via riding model.
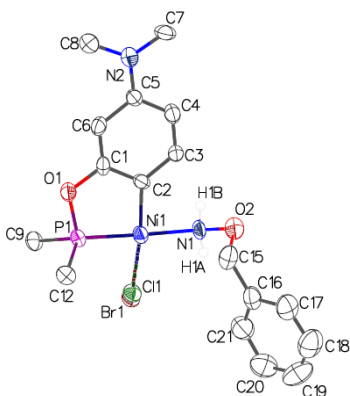
Figure S2. 164. Side view of the molecular diagram of compound **8a**. Thermal ellipsoids are shown at the 50% probability level; hydrogen atoms are refined via riding model.
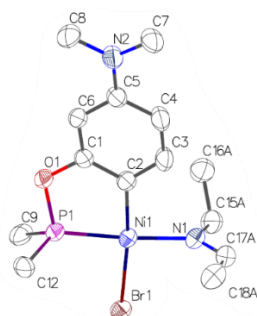
Figure S2. 165. Side view of the molecular diagram of compound **8b**. Thermal ellipsoids are shown at the 50% probability level; hydrogen atoms are refined via riding model.

Table S2. 6: Selected bond distances (Å) for all new complexes.

	Ni–C2	Ni–P1	Ni–Cl/Br	Ni–N/Ni-O	N–O	N–C$_{sp2}$	N–C$_{sp3}$
4'	1.9310(15)	2.1364(4)	2.3576(3)				
5a	1.9091(13)	2.1024(4)	2.250(8)/ 2.320(9)	1.9762(11)	1.4533(13)		
5b	1.911(2)	2.1007(8)	2.3749(6)	1.9173(17)	1.405(3)		
5c		2.1568(5)	2.3055(3)	1.8956(13)/ 1.8378(11)	1.3768(17)		
6b	1.909(4)	2.1058(11)	2.3506(8)	1.945(3)		1.289(6)	1.456(6)
6c	1.907(4)	2.1031(11)	2.3500(7)	1.934(3)		1.277(5)	1.505(5)
7b	1.916(4)	2.1047(11)	2.3664(7)	1.942(3)		1.265(18)	1.513(16)
7c	1.911(3)	2.1054(7)	2.3581(5)	1.943(2)		1.273(3)	1.489(3)
7d	1.918(2)	2.1041(7)	2.3699(4)	1.999(2)			1.492(4)
8a	1.911(14)	2.120(4)	2.12(2)/ 2.350(4)	1.973(11)	1.446(15)		
8b	1.912(2)	2.1047(7)	2.3711(4)	1.950(2)		1.295(4)	1.416(4)

Table S2. 7: Selected bond angles (°) for all new complexes.

	C–Ni–Cl/Br	N/O–Ni–P1	C–Ni–P1	C–Ni–N/O	P1–Ni–Cl/Br	N/O–Ni–Cl/Br	Ni–N–C$_{sp2}$
4'	166.20(4)		81.95(4)		88.605(12)		
5a	173.5(2)/ 169.7(2)	177.93(3)	83.28(4)	95.96(5)	90.8(2)/ 88.0(3)	90.0(2)/ 93.0(3)	
5b	173.12(7)	172.97(6)	83.26(8)	89.79(9)	91.05(3)	95.96(5)	
5c							
6b	172.79(12)	176.25(11)	83.39(12)	96.57(16)	89.54(4)	90.58(10)	124.9(3)
6c	173.82(12)	172.75(10)	83.67(12)	94.64(15)	90.27(4)	91.22(10)	128.8(3)
7b	173.75(11)	177.53(11)	83.24(12)	94.33(15)	90.54(3)	91.88(11)	126.7(7)
7c	172.58(8)	175.00(7)	83.41(8)	95.06(10)	90.32(2)	90.85(7)	128.34(19)
7d	169.71(7)	171.84(8)	82.78(8)	95.2(1)	89.04(2)	93.75(7)	
8a	175.6(9)/ 171.2(4)	178.5(4)	83.2(4)	95.9(5)	92.5(7)/ 90.86(14)	88.4(8)/ 90.1(4)	
8b	173.74(4)	174.86(7)	82.43(7)	95.26(9)	91.52(2)	90.89(6)	124.4(2)

S2.9 Regarding the unusually downfield signals in the ^{1}H NMR spectra of 6c and 7c.

Recall that the ^{1}H NMR spectra for **6c** and **7c** displayed unusually downfield signals at δ 8.93 and 8.82, respectively, which were assigned to the ortho protons belonging to one of the Ph rings in the imine moiety PhCH$_2$NCHPh. In search of some rationale for these observations, we examined the solid-state structures of these complexes to see if any unexpected H---element close contacts might be present in the crystal lattice. Indeed, we found that one of the ortho protons in the <u>Ph</u>C(H)N moiety of these complexes does lie fairly close to the Ni atom (Ni---H$_{ortho}$ ≈ 2.44 in **6c** and 2.49 Å in **7c**). Assuming (a) that the orientation observed in the solid-state of these complexes is maintained in solution, and (b) that there is free and rapid rotation around the Ph-C(H)N bond, it seemed conceivable that the unusually downfield signals for the ortho protons in **6c** and **7c** might be related to such close contacts.

The question arises whether the observed Ni---H$_{ortho}$ distances reflect orbital interactions, or whether they are caused by the specific orientation of the Ph ring, which might, in turn, be dictated by some other factor. To be sure, agostic Ni----(H-C) interactions should not be favored in the 16-electron d^8 complexes under discussion here because they are perceived to be functionally saturated. Nevertheless, we examined the solid-state parameters for **6c** and **7c** in search of clues that might rationalize the particular orientation of the Ph ring in question. We found that the vinylic proton in the imine moiety NCHPh is orientated toward and fairly close to the Ph ring of the NCH2Ph moiety (H---C$_{ipso}$. ≈ 2.35 and 2.34 Å, respectively).

Therefore, it seemed plausible that the short Ni---H$_{ortho}$ distances in **6c** and **7c** might be due to secondary structural constraints such as this observed H---C$_{ipso}$ close contact. If it were true that the unusual Ni---H interactions are related to the particular orientation of Ph groups, then such interactions must not be present in those structures that lack Ph moieties in the imine ligand. Yet, when we inspected the solid-state structures of the analogous complexes **6b** and **7b** that feature a NCH(CH$_3$) moiety but no Ph substituents, we found that both CH$_3$ groups in these complexes were pointing toward the Ni centre and the Ni---H$_{CH3}$ distances were almost as short as for the *ortho* protons in **6c** and **7c** (ca. 2.55-2.87 Å vs 2.44 and 2.49 Å). In other words, the absence of Ph moieties in **6b** and **7b** does not appear to eliminate close Ni---H contacts. What is more, this phenomenon appears to be quite general as both CH$_3$ groups in the amine and imine adducts **7d**

and **8b** also point toward the Ni centre, and the Ni---H$_{CH3}$ contacts found in these complexes are almost as short: 2.75-2.80 Å in **7d** and 2.70-2.86 Å in **8b**.

To conclude from the above findings, the close Ni---H contacts in question appear to be a common feature of the imine and amine adducts discussed here, but the data at hand do not allow us to pinpoint a specific phenomenon that might rationalize our observations. We hope to probe this phenomenon in future investigations.

S2.10 DFT Computational studies.

<u>Experimental</u>

All DFT calculations were performed using Gaussian 16 revision C01 package on Graham cluster, access to which was granted by CalculCanada/ComputeCanada . Geometry optimizations were carried out in standard conditions (namely equimolar amounts of the MeCN adduct and Et2NOH) using Pople's 6-311+g** basis set[52–56] for all light atoms (C, H, O, P, N) and Karlsruhe triple zeta def2TZVP basis set for Ni and Br.[57] The M06 functional[58] was exploited in implicit acetonitrile solvent using the SMD model.[59] Local minima were assessed by default convergence criteria and the absence of imaginary frequencies in the frequency calculations. Transition states were assessed by the existence of a single imaginary frequency along the expected reaction coordinate and have been linked to intermediates by the intrinsic reaction coordinates (irc) routine using the local quadratic approximation (lqa),[60,61] followed by re-optimization. The energies displayed on the schemes and figures are ΔG0 and the values in parenthesis are ΔH0, and include the solvation energies. For the transition state TS31, the thermal parameters induced a lower energy than its closely related intermediate int21, and so the local barrier of 0.6 kcal/mol was determined by their difference in electronic energies only (in other words, the same thermal correction was applied for both geometries). The transition states TS81 and TS82 for the OH radical transfer were found by a fragment guess (open shell singlet) followed by an SCF calculation and test of the wavefunction's stability. Further optimization of a transition state using the same guess generated broken symmetry transition states, for which the wavefunction was shown to be stable under the perturbations considered by Gaussian. Molecular diagrams of the relevant intermediates and transition states were generated by CYLview20.[62] The geometry of all presented stationary points are available in the .xyz file provided with the ESI.

<u>Discussion</u>

The DFT studies summarized here were undertaken to shed light on the mechanism of hydroxylamines dehydration promoted by the cyclonickelated dimeric complexes κ^C,κ^P-{2-OP(i-Pr)$_2$,4-X-C$_6$H$_4$}$_2$Ni$_2$(μ-Br)$_2$ (X = H, Cl, OMe, NMe$_2$). The reaction energy profile was calculated at the M06/6-311+g**/def2TZVP(Ni,Br) level of theory in implicit MeCN solvent using the SMD model.[63] The energies discussed and displayed on the figures are Gibbs free energies, and are referenced to the acetonitrile adduct int10-NCMe (**Figure S2. 166**). It should also be noted that the monomeric acetonitrile adduct of the parent dimeric Ni complex (X = H) has been used as a realistic model for the precursor complex, because such adducts are known to form readily in MeCN solutions. Moreover, the *i*-Pr substituents of the phosphinite moiety in the title complexes were replaced with Me groups for simplicity and to avoid making the
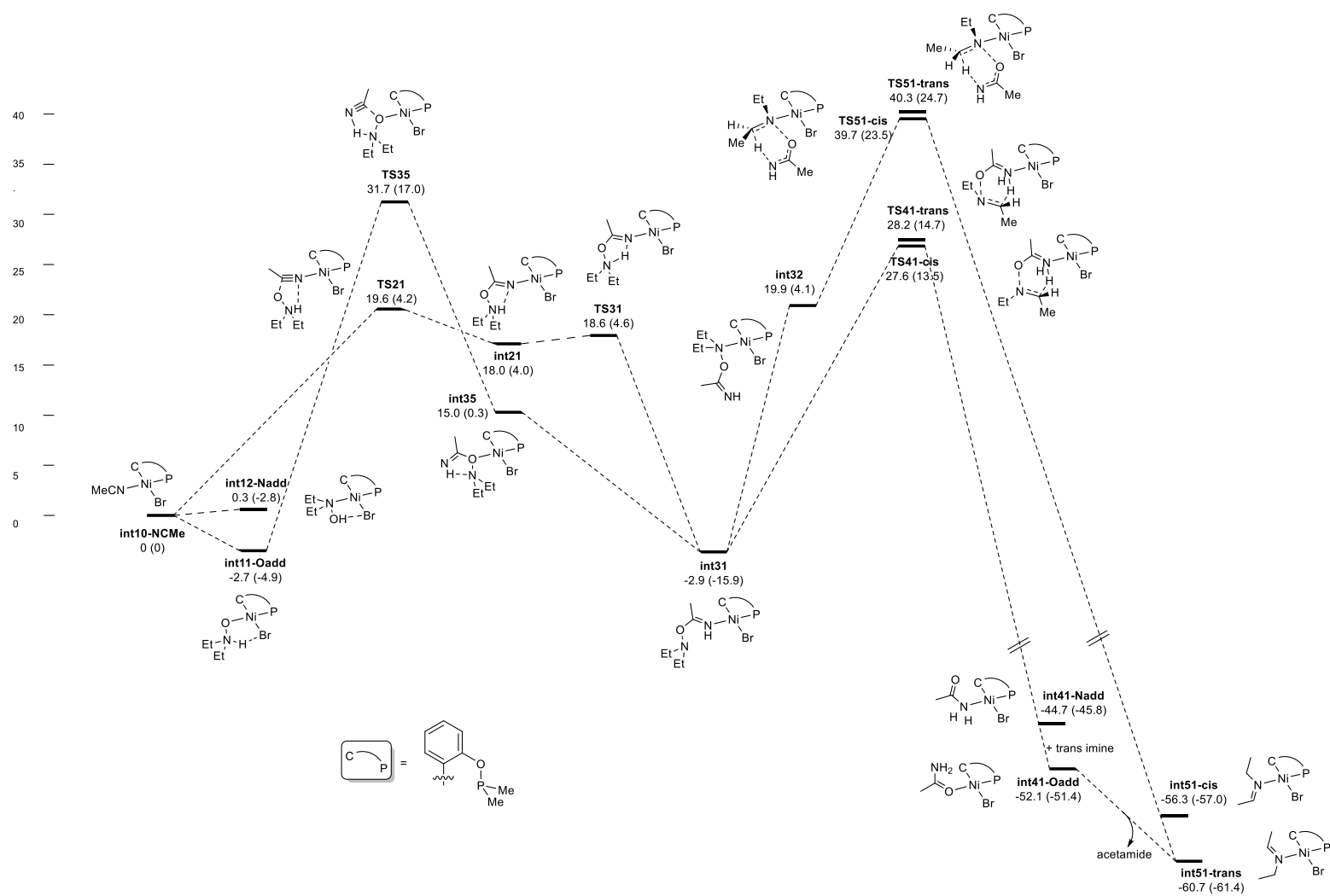
Figure S2. 166. *Proposed potential energy surface for the dehydration of hydroxylamines via a nucleophilic attack pathway*

computational work more cumbersome due to the various possible conformations of the *i*-Pr groups. Thus, the model complex κ^C,κ^P-{2-OPMe$_2$-C$_6$H$_4$}Ni(Br)(NCMe) has served as the starting point of our calculations.

As a first step, we studied the thermodynamics of substrate coordination to the nickel center. It was found that the replacement of MeCN by the canonical form of the hydroxylamine substrate, Et$_2$NOH, was not favored. In contrast, the substitution reaction becomes nearly thermoneutral (+0.3 kcal/mol) when the OH group in the substrate is allowed to form a hydrogen-bond with the Br ligand (**int12-Nadd**), whereas using the zwitterionic form Et$_2$N(H)$^+$O$^-$ made the substitution fully exergonic (by 2.7 kcal/mol). The latter reaction leads to **int11-Oadd**. This observation is in accordance with the following experimental observations: (1) the closely related adduct **5b** was isolated from the reaction of dimer **1** with Et$_2$NOH in CH$_2$Cl$_2$, and (2) re-dissolving crystals of **5b** in MeCN led to partial reformation of the acetonitrile adduct, implying the viability of the proposed equilibrium κ^C,κ^P-{2-OPMe$_2$-C$_6$H$_4$}Ni(Br)(NCMe) $\leftrightarrows$ **int11-Oadd**.

The second step on the postulated pathway for dehydration of hydroxylamine (i.e., a closed shell nucleophilic addition by the hydroxylamine substrate on Ni-coordinated MeCN) is the attack of the substrate on the nitrile carbon. The lower transition state for this step (**Figure S2. 167**) was found to be the addition of the zwitterionic hydroxylamine, the process being aided by hydrogen bonding between the NH moiety of the substrate and the N atom of the MeCN ligand. The barrier for this process is 19.6 kcal/mol (**TS21**), and leads to an intermediate containing the zwitterionic ligand Et$_2$N$^+$(H)-O-C(Me)(=N$^-$), **int21**, with only a slightly lower energy of 18.0 kcal/mol.

TS21 19.6 (4.2)	TS35 31.7 (17.0)	TS22 33.3 (19.7)	TS25 58.4 (44.0)
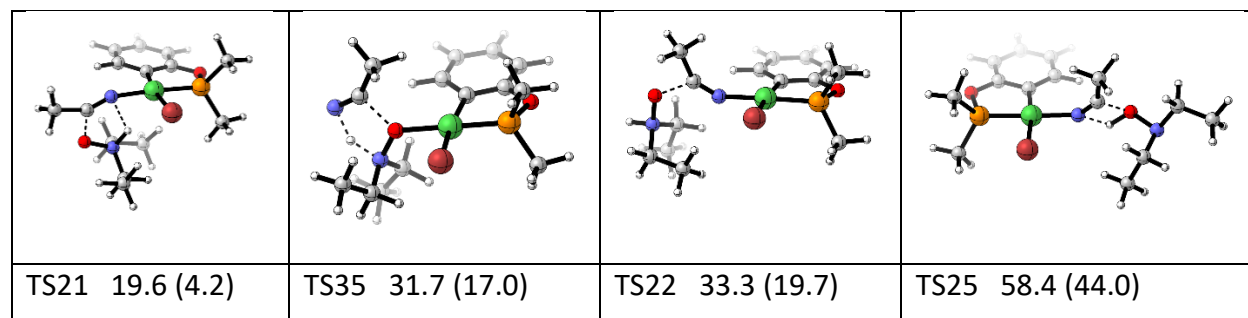
Figure S2. 167. Molecular diagrams of various transition states for the nucleophilic attach of the zwitterionic hydroxylamine on MeCN

It is worth emphasizing that the nucleophilic attack is significantly less favorable without the assistance of a hydrogen bonding (**TS22**, 33.3 kcal/mol) or via a concerted O-H addition on the nitrile involving the canonical form of the hydroxylamine (**TS25**, 58.4 kcal/mol). In addition, the attack from the Ni-bound zwitterionic hydroxylamine adduct **int11-Oadd** to an external MeCN molecule (**TS35**) also has a higher barrier of 31.7 kcal/mol; this approach leads to the more energetic **int35**, which, although being stabilized by internal H-bonding, should quickly convert to **int31**. Subsequent to the nucleophilic attack described above, the N—*H* proton is then transferred in a somewhat barrierless manner to generate the much more stable tautomer **int31** (by -2.9 kcal/mol). We speculate that the course of this reaction can probably be observed. Indeed, the ^{31}P monitoring of the reaction of dimer **3** with Et_2NOH in acetonitrile revealed a number of unidentified peaks that might well represent such intermediates.

The dehydration products must form from this key intermediate **int31** through a cyclic proton transfer whereby H^+ jumps from the α-carbon of the $N(C\underline{H}_2CH_3)_2$ moiety to the imine nitrogen atom coordinated to Ni. This process, that leads to either a trans- or a cis-imine, can pass through four possible transition states, all in a very narrow range of energies. In addition, the two lower energy transition states leading to the cis imine (**TS41-cis**) or the trans-imine (**TS41-trans**) showed very similar $\Delta G^{\ddagger}$ values, 27.6 and 28.2 kcal/mol, respectively (**Figure S2. 168**). These transition states lead to a free imine and a Ni-acetamide complex, which is first bound via the NH2 (**int41-Nadd**) but later converts to the O-bound isomer (**int41-Oadd**). With these two products being as low as -44.7 and -52.1 kcal/mol, respectively, this is the most exergonic step of the process, and the one that renders the overall transformation irreversible. The acetamide is then exchanged by the free imine, where the trans-imine complex **int51-trans** (-60.7 kcal/mol) is significatively lower in energy than its cis counterpart **int51-cis** (-56.3 kcal/mol). This implies that, although there is little or no kinetic E/Z selectivity in the system, the Ni center must promote the isomerization to the more stable trans-imine Ni-complex since this is the only isolated product (as observed in the crystal structures). Further substitution of the Ni-bound imine by a MeCN ligand is disfavored by 7.6 kcal/mol, consistent with the observed isolation of the imine adducts. It should be noted that the (unobserved) re-formation of the acetonitrile adduct would increase the overall barrier in the event of a Ni-catalyzed dehydration of hydroxylamines coupled to nitrile hydration.
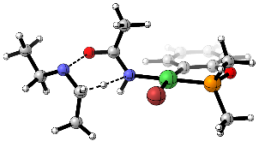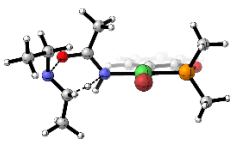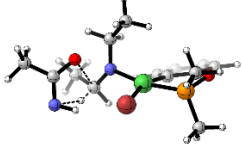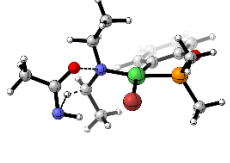
TS41-cis 27.6 (13.5)	TS41-trans 28.2 (14.7)	TS51-cis 39.7 (23.5)	TS51-trans 40.3 (24.7)

Figure S2. 168. Molecular diagrams of transition states for the cyclic intramolecular proton transfer leading to breakage of the N-O bond.

Another pathway starts from **int35**, a coordination isomer of the more stable **int31** wherein the N α to the O is bound to the nickel center during the cyclic proton transfer, and leads directly to free acetamide and **int51-cis/trans**. Again, the four possible transition states were found in a very narrow range, with little to no cis/trans selectivity, but these transition sates (**TS51-cis** and **TS51-trans**) were found as high as 39.7 and 40.3 respectively. Finally, another pathway from the zwitterionic intermediate **int21**, which was confirmed to be a local minimum, leads to a Ni-bound deprotonated acetamide and cis/trans iminium (**Figure S169**). Although this step is also found to be largely exergonic (-33.2 and -36.9 kcal/mol), the located barriers are much higher: **TS45-cis** with ΔG‡ of 57.2 kcal/mol and **TS45-trans**, with 57.0 kcal/mol.
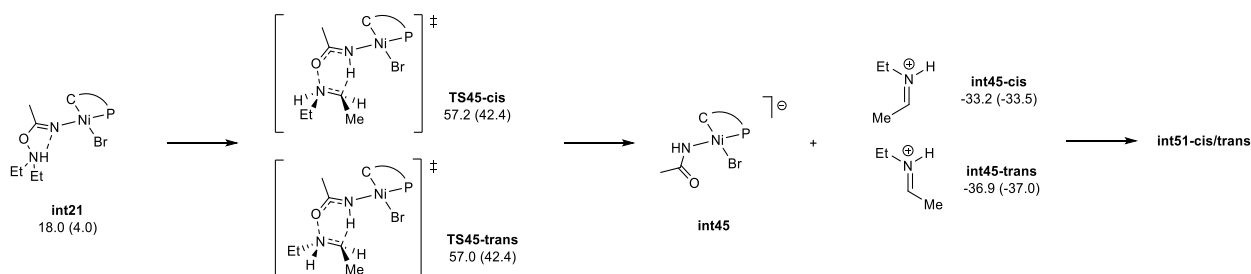
Figure S2. 169. Proposed energy profile for the direct proton transfer from **int21**. Energies presented are ΔG^0 (ΔH^0) and are expressed in kcal/mol.

Finally, two additional pathways were probed: one going through Ni(IV) intermediates, and one going through radical species (**Figure S2. 170)**. The first one implies the N-O oxidative addition from the canonical hydroxylamine bound to the metal center (either through the O atom, **int12-Oadd** at 7.5 kcal/mol, or the N atom, **int12-Nadd** at 0.3 kcal/mol) and leading to 5-coordinate Ni(IV) intermediates featuring apical positions occupied by the NEt$_2$ fragment (**int71** at 29.5 kcal/mol) or the OH fragment (**int72** at 32.3 kcal/mol). However, the transition states to

access these intermediates, **TS71** and **TS72**, are > 10 kcal/mol higher in energy than the more favored Ni(II) pathway, with $\Delta G^{\ddagger}$ of 39.8 and 43.8 kcal/mol. In addition, coordination of MeCN, which we believe is necessary to form acetamide, gives 6-coordinate intermediates as high as 37.5 and 36.5 kcal/mol for **int71-NCMe** and **int72-NCMe**, respectively, making this pathway improbable.
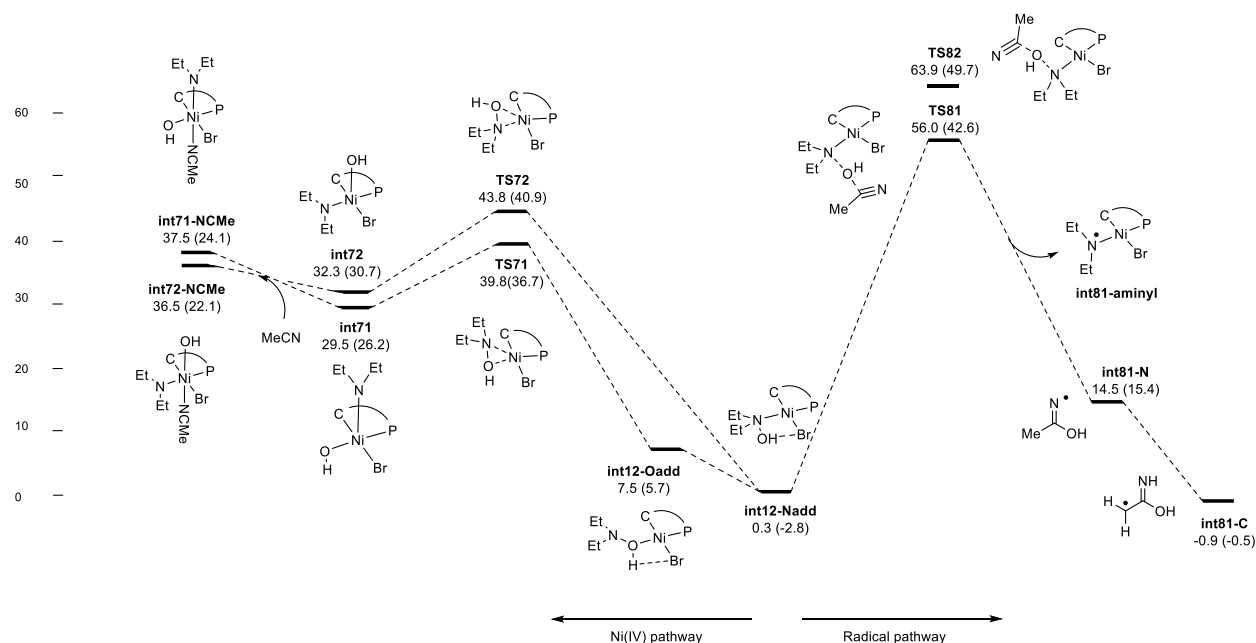
Figure S2. 170. Proposed potential energy surface for the Ni(IV) and radical pathways at the M06/6-311+g**/def2TZVP level of theory. Energies presented are ΔG^0 (ΔH^0) and are expressed in kcal/mol.

The second additional pathway involves a formal OH·radical transfer from the N-bound canonical hydroxylamine to an external molecule of MeCN, leading to the acetamide radical, primarily centered on the nitrogen (**int81-N** at 14.5 kcal/mol) which should tautomerize to its more stable form with the radical centered on the carbon atom (**int81-C** at -0.9 kcal/mol, **Figure S171**). This step also generates a radical Ni-NEt₂ complex, **int81**, which has been shown to be a Ni(II) species bearing an aminyl ligand, with most of the spin density located on the nitrogen. Although this step is nearly thermoneutral, the transition states located for this radical transfer, **TS81** and **TS82**, were found highly energetic with $\Delta G^{\ddagger}$ of 56.0 and 63.9 kcal/mol, indicating that this pathway is the least probable.

TS81　56.0 (42.6)　　　　TS82　63.9 (49.7)
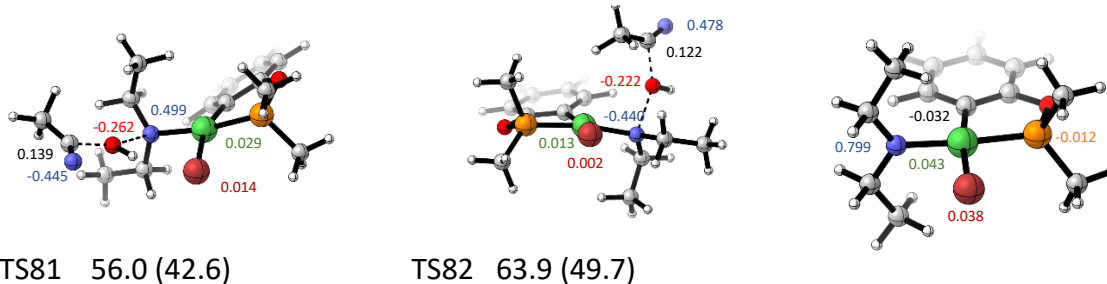
Figure S2. 171. Molecular diagrams for the transition states and the Ni-aminyl intermediate on the radical transfer pathway. The numbers on the diagram represent Mulliken spin populations at the M06/6-311+g**/def2TZVP level of theory.

The above results allow us to conclude that, overall, the most probable pathway involves the attack of the zwitterionic hydroxylamine on the C≡N bond of a Ni-coordinated acetonitrile ligand, in an asynchronous manner, to give the stable ligand (Et$_2$NO)(Me)C=NH bound to Ni. The latter breaks apart into an imine and a molecule of acetamide through a concerted cyclic proton transfer/O-N bond breaking, on a closed shell surface. Although at this level of theory the overall barrier (from **int11-Oadd**) of 30.3 kcal/mol is too high to compare with the actual observed rate of reaction, this seems to us the most probable pathway and is in accordance with the mechanistic experiments described in the main manuscript. Adding a correction for the huge excess of MeCN in the actual reaction conditions only lowers the overall barrier by 4.3 kcal/mol only. In addition, the results of DFT calculations conducted on a Ni-free reaction show that the thermodynamics are similar (-53.0 kcal/mol). However, the barriers on the potential energy surface are higher, and indicate that the nickel complex facilitates the nucleophilic attack (this time in a synchronous fashion) by 7.7 kcal/mol, and the formation of the products by 8.5 kcal/mol.

2.9　References

(1)　Castro, L. C. M.; Chatani, N.; Sortais, J.-B. Highlight Review Nickel Catalysts/N,N′-Bidentate Directing Groups: An Excellent Partnership in Directed CH Activation Reactions. *Chem. Lett* **2015**, *44*, 410–421. https://doi.org/10.1246/cl.150024.

(2)　Gandeepan, P.; Müller, T.; Zell, D.; Cera, G.; Warratz, S.; Ackermann, L. 3d Transition Metals for C−H Activation. *Chem Rev* **2019**, *119* (4), 2192–2452. https://doi.org/10.1021/acs.chemrev.8b00507.

(3)　Colby, D. A.; Bergman, R. G.; Ellman, J. A. Rhodium-Catalyzed C-C Bond Formation via Heteroatom-Directed C−H Bond Activation. *Chem Rev* **2010**, *110* (2), 624–655. https://doi.org/10.1021/cr900005n.

(4)　Rouquet, G.; Chatani, N. Catalytic Functionalization of C(sp2)-H and C(sp3)-H Bonds by Using Bidentate Directing Groups. *Angewandte Chemie - International Edition* **2013**, *52* (45), 11726–11743. https://doi.org/10.1002/anie.201301451.

(5)　Arockiam, P. B.; Bruneau, C.; Dixneuf, P. H. Ruthenium(II)-Catalyzed C−H Bond Activation and Functionalization. *Chem Rev* **2012**, *112* (11), 5879–5918. https://doi.org/10.1021/cr300153j.

(6)　Roy, P.; Bour, J. R.; Kampf, J. W.; Sanford, M. S. Catalytically Relevant Intermediates in the Ni-Catalyzed C(sp2)-H and C(sp3)-H Functionalization of Aminoquinoline Substrates. *J Am Chem Soc* **2019**, *141* (43), 17382–17387. https://doi.org/10.1021/jacs.9b09109.

(7)　Beattie, D. D.; Grunwald, A. C.; Perse, T.; Schafer, L. L.; Love, J. A. Understanding Ni(II)-Mediated C(sp3)-H Activation: Tertiary Ureas as Model Substrates. *J Am Chem Soc* **2018**, *140* (39), 12602–12610. https://doi.org/10.1021/jacs.8b07708.

(8)　Vabre, B.; Deschamps, F.; Zargarian, D. Ortho Derivatization of Phenols through C−H Nickelation: Synthesis, Characterization, and Reactivities of Ortho-Nickelated Phosphinite Complexes. *Organometallics* **2014**, *33* (22), 6623–6632. https://doi.org/10.1021/om500938u.

(9)   Mangin, L. P.; Zargarian, D. C−H Nickelation of Naphthyl Phosphinites: Electronic and Steric Limitations, Regioselectivity, and Tandem C-P Functionalization. *Organometallics* **2019**, *38* (24), 4687–4700. https://doi.org/10.1021/acs.organomet.9b00660.

(10)   Mangin, L. P.; Zargarian, D. C−H Nickelation of Aryl Phosphinites: Mechanistic Aspects. *Organometallics* **2019**, *38* (7), 1479–1492. https://doi.org/10.1021/acs.organomet.8b00899.

(11)   Mangin, L. P.; Zargarian, D. C−H Nickellation of Phenol-Derived Phosphinites: Regioselectivity and Structures of Cyclonickellated Complexes. *Dalton Transactions* **2017**, *46* (46), 16159–16170. https://doi.org/10.1039/c7dt03403b.

(12)   Vabre, B.; Spasyuk, D. M.; Zargarian, D. Impact of Backbone Substituents on POCOP-Ni Pincer Complexes: A Structural, Spectroscopic, and Electrochemical Study. *Organometallics* **2012**, *31* (24), 8561–8570. https://doi.org/10.1021/om3009475.

(13)   Vabre, B.; Lindeperg, F.; Zargarian, D. Direct, One-Pot Synthesis of POCOP-Type Pincer Complexes from Metallic Nickel. *Green Chemistry* **2013**, *15* (11), 3188–3194. https://doi.org/10.1039/c3gc40968f.

(14)   We Have Shown Previously That the C−H Nickellation Step in Our System Proceeds More Readily When the Phosphinite Aromatic Ring Bears Electron-Donating Substituents. (See Ref. 10.). **2023**.

(15)   It Should Be Emphasized That the C−H Nickellation Reaction Is, in Principle, Reversible as We Have Shown Previously. (See Ref. 10.) Of Course, the Equilibrium in Question Is Nearly Completely Driven Forward for Most Substrates, Especially When It Is Conducted in Acetonitrile; This Is Because the in-Situ Generated HBr Is Quenched by the Added Base.

(16)   In the Case of 6a, the Crystals Obtained Were Twinned and of Insufficient Quality for Establishing Accurate Structural Parameters; Nevertheless, the Data Obtained Allowed Us to Confirm Atom Connectivity.

(17)   For Instance, We Observed: 2 Signals for the 4 Phosphinite Me Groups; One Signal for the Two PCH Protons; One Signal for the Two Amine Me Groups; and Two Poorly Resolved Multiplets for the 4 Diastereotopic NCH$_2$ Protons.

(18)   Murahashi, S.-I.; Kodera, Y. Titanium (III) Induced Transformations of N,N-Disubstituted Hydroxylamines to Imines and Secondary Amines. *Tetrahedron Lett* **1985**, *26* (38), 4633–4636.

(19)   O'Dowd, H.; Lewis, J. G.; Gordeev, M. F. Novel 6-Position Modified 1-Thioalkyl-Lincosamines. *Tetrahedron Lett* **2008**, *49* (18), 2979–2981. https://doi.org/10.1016/j.tetlet.2008.02.167.

(20)   Otero, J. M.; Soengas, R. G.; Estévez, J. C.; Estévez, R. J.; Watkin, D. J.; Evinson, E. L.; Nash, R. J.; Fleet, G. W. J. Preliminary Studies on the Transformation of Nitrosugars into Branched Chain Iminosugars: Synthesis of 1,4-Dideoxy-4-C-Hydroxymethyl-1,4-Imino-Pentanols. *Org Lett* **2007**, *9* (4), 623–626. https://doi.org/10.1021/ol062887v.

(21)   Kodera, Y.; Watanabe Shoji; Imada Yasushi; Murahashi Shun-Ichi. Titanium(III)-Induced Transformation of Hydroxylamines to Imines or Secondary Amines. *The Chemical Society of Japan* **1994**, *67*, 2542–2549.

(22)   Ahmed, T. J.; Knapp, S. M. M.; Tyler, D. R. Frontiers in Catalytic Nitrile Hydration: Nitrile and Cyanohydrin Hydration Catalyzed by Homogeneous Organometallic Complexes. *Coordination Chemistry Reviews*. April 2011, pp 949–974. https://doi.org/10.1016/j.ccr.2010.08.018.

(23)   Anisimova, T. B.; Bokach, N. A.; Dolgushin, F. M.; Kukushkin, V. Y. Dialkylcyanamides Are More Reactive Substrates toward Metal-Mediated Nucleophilic Addition than Alkylcyanides. *Dalton Transactions* **2013**, *42* (34), 12460–12467. https://doi.org/10.1039/c3dt51137e.

(24)   Castonguay, A.; Spasyuk, D. M.; Madern, N.; Beauchamp, A. L.; Zargarian, D. Regioselective Hydroamination of Acrylonitrile Catalyzed by Cationic Pincer Complexes of Nickel(II). *Organometallics* **2009**, *28* (7), 2134–2141. https://doi.org/10.1021/om800840u.

(25)   Lefvre, X.; Durieux, G.; Lesturgez, S.; Zargarian, D. Addition of Amines and Phenols to Acrylonitrile Derivatives Catalyzed by the POCOP-Type Pincer Complex [{κ^P, κ^C, κ^P -2,6-

(i-Pr$_2$PO)$_2$C$_6$H$_3$}Ni(NCMe)][OSO$_2$CF$_3$]. *J Mol Catal A Chem* **2011**, *335* (1–2), 1–7. https://doi.org/10.1016/j.molcata.2010.11.010.

(26)   Lapointe, S.; Zargarian, D. On the Mechanism of Ni(II)-Promoted Michael-Type Hydroamination of Acrylonitrile and Its Substituted Derivatives. *Dalton Transactions* **2016**, *45* (40), 15800–15810. https://doi.org/10.1039/c6dt02105k.

(27)   Pandarus, V.; Zargarian, D. New Pincer-Type Diphosphinito (POCOP) Complexes of Nickel. *Organometallics* **2007**, *26* (17), 4321–4334. https://doi.org/10.1021/om700400x.

(28)   Vabre, B.; Canac, Y.; Lepetit, C.; Duhayon, C.; Chauvin, R.; Zargarian, D. Charge Effects in PCP Pincer Complexes of Ni^{II} Bearing Phosphinite and Imidazol(I)Ophosphine Coordinating Jaws: From Synthesis to Catalysis through Bonding Analysis. *Chemistry - A European Journal* **2015**, *21* (48), 17403–17414. https://doi.org/10.1002/chem.201502491.

(29)   Salah, A. B.; Offenstein, C.; Zargarian, D. Hydroamination and Alcoholysis of Acrylonitrile Promoted by the Pincer Complex {κ^P, κ^C, κ^P -2,6- (Ph$_2$PO)$_2$C$_6$H$_3$}Ni(OSO$_2$CF$_3$). *Organometallics* **2011**, *30* (20), 5352–5364. https://doi.org/10.1021/om200549p.

(30)   Peter Jaitner; Wolfgang Huber. Syntheses and Characterization of the Electron-Deficient Complex (TMPO)V(CO)$_3$. *Inorganica Chim Acta* **1987**, *129*, L45–L46.

(31)   P. Jaitner; W. Huber; G. Hunter; O. Scheidsteger. Synthesis and X-Ray Structure of (2,2,6,6-Tetramethyl-Piperidinyl-1-Oxo-O,N)Tricarbonylmanganese(0); "Side-on" Coordination of the Nitroxyl Radical to Manganese. *J Organomet Chem* **1983**, *259*, C1–C5.

(32)   Jaitner, P.; Huber, W.; Gieren, A.; Bet, H. (TMPO)Co(CO)$_2$: Synthese Und Röntgenstrukturanalyse Eines Planar Koordinierten Cobalt(I)-Komplexes. *J Organomet Chem* **1986**, *311*, 379–385.

(33)   Beck, W.; Schmidtner, K. Palladiumhalogenid-Komplexe Mit Dem Di-tert.-butylstickstoffoxid-Radikal [XPdON(C(CH$_3$)$_3$)$_2$]$_2$ (X = Cl, Br). *Chem Ber* **1967**, *100* (10), 3363–3367. https://doi.org/10.1002/cber.19671001026.

(34)   Okunaka Masaaki; Matsubayashi Gen-etsu; Tanaka Toshio. Palladium(II) Complexes of 2,2,6,6-Tetramethylpiperidine N-Oxyl Radical. *Bull Chem Soc Jpn* **1977**, *50* (4), 907–909.

(35)   Dickman, M. H.; Doedens, R. J. Structure of Chloro(2,2,4,4-Tetramethylpiperidiny 1-1-Oxo-O,N)(Triphenylphosphine)Palladium(II), a Metal Complex of a Reduced Nitroxyl Radical. *Inorg Chem* **1982**, *21* (2), 682–684.

(36)   Laughier, J.; Latour, J.-M.; Caneschi, A.; Rey, P. Structural and Redox Properties of the Tempo Adducts of Copper(II) Halides. *Inorg. Chem.* **1991**, *30*, 4474–4477.

(37)   Mindiola, D. J.; Waterman, R.; Jenkins, D. M.; Hillhouse, G. L. Synthesis of 1,2-Bis(Di-Tert-Butylphosphino)Ethane (Dtbpe) Complexes of Nickel: Radical Coupling and Reduction Reactions Promoted by the Nickel(I) Dimer [(Dtbpe)NiCl]₂. *Inorganica Chim Acta* **2003**, *345*, 299–308.

(38)   Ito, M.; Matsumoto, T.; Tatsumi, K. Synthesis and Reactions of Mono- and Dinuclear Ni(I) Thiolate Complexes. *Inorg Chem* **2009**, *48* (5), 2215–2223. https://doi.org/10.1021/ic802276w.

(39)   Chakraborty, U.; Urban, F.; Mühldorf, B.; Rebreyend, C.; De Bruin, B.; Van Velzen, N.; Harder, S.; Wolf, R. Accessing the CpArNi(I) Synthon: Reactions with N-Heterocyclic Carbenes, TEMPO, Sulfur, and Selenium. *Organometallics* **2016**, *35* (11), 1624–1631. https://doi.org/10.1021/acs.organomet.6b00084.

(40)   Otsuka, S.; Aotani, Y.; Tatsuno, Y.; Yoshida, T. And References Therein. (19) L. Vaska. *Inorg Chem* **1976**, *15* (3), 656–660.

(41)   Lefèvre, X.; Spasyuk, D. M.; Zargarian, D. New POCOP-Type Pincer Complexes of Nickel(II). *J Organomet Chem* **2011**, *696* (4), 864–870. https://doi.org/10.1016/j.jorganchem.2010.10.019.

(42)   Hao, J.; Vabre, B.; Zargarian, D. POCOP-Ligated Nickel Siloxide Complexes: Syntheses, Characterization, and Reactivities. *Organometallics* **2014**, *33* (22), 6568–6576. https://doi.org/10.1021/om500916d.

(43)   Lapointe, S.; Vabre, B.; Zargarian, D. POCOP-Type Pincer Complexes of Nickel: Synthesis, Characterization, and Ligand Exchange Reactivities of New Cationic Acetonitrile Adducts. *Organometallics* **2015**, *34* (14), 3520–3531. https://doi.org/10.1021/acs.organomet.5b00272.

(44) Hao, J.; Vabre, B.; Zargarian, D. Reactions of Phenylhydrosilanes with Pincer-Nickel Complexes: Evidence for New Si-O and Si-C Bond Formation Pathways. *J Am Chem Soc* **2015**, *137* (48), 15287–15298. https://doi.org/10.1021/jacs.5b10066.

(45) Bruker (2012). APEX2 / Bruker (2016) APEX3, Bruker AXS Inc., Madison, WI, USA.

(46) Bruker (2012). "SAINT Integration Software for Single Crystal Data", Bruker AXS Inc., Madison, WI, USA. (a).

(47) (A) G. M. Sheldrick (1996). SADABS/TWINABS. University of Göttingen, Germany. (b) Bruker (2001). SADABS/TWINABS. Bruker AXS Inc., Madison, Wisconsin, USA. Bruker (2012). Data Preparation and Reciprocal Space Exploration Program, Bruker AXS Inc., Madi-Son, WI, USA.

(48) Bruker (2012). Data Preparation and Reciprocal Space Exploration Program, Bruker AXS Inc., Madison, WI, USA.

(49) A: O. V. Dolomanov, L. J. Bourhis, R. J. Gildea, J. A. K. Howard and H. Puschmann. "OLEX2: A Com-Plete Structure Solution, Refinement and Analysis Program". J. Appl. Cryst., 2009, 42, 339-341. https://doi.org/10.1021/acs.inorgchem.3c01236.

(50) Sheldrick, G. M. SHELXT - Integrated Space-Group and Crystal-Structure Determination. *Acta Crystallogr A* **2015**, *71* (1), 3–8. https://doi.org/10.1107/S2053273314026370.

(51) Sheldrick, G. M. Crystal Structure Refinement with SHELXL. *Acta Crystallogr C Struct Chem* **2015**, *71*, 3–8. https://doi.org/10.1107/S2053229614024218.

(52) Krishnan, R.; Binkley, J. S.; Seeger, R.; Pople, J. A. Self-Consistent Molecular Orbital Methods. XX. A Basis Set for Correlated Wave Functions. *J Chem Phys* **1980**, *72* (1), 650–654. https://doi.org/10.1063/1.438955.

(53) Clark, T.; Chandrasekhar, J.; Spitznagel, G. W.; Schleyer, P. V. R. Efficient Diffuse Function-augmented Basis Sets for Anion Calculations. III. The 3-21+G Basis Set for First-row Elements, Li–F. *J Comput Chem* **1983**, *4* (3), 294–301. https://doi.org/10.1002/jcc.540040303.

(54)　McLean, A. D.; Chandler, G. S. Contracted Gaussian Basis Sets for Molecular Calculations. I. Second Row Atoms, Z=11-18. *J Chem Phys* **1980**, *72* (10), 5639–5648. https://doi.org/10.1063/1.438980.

(55)　Francl, M. M.; Pietro, W. J.; Hehre, W. J.; Binkley, J. S.; Gordon, M. S.; DeFrees, D. J.; Pople, J. A. Self-Consistent Molecular Orbital Methods. XXIII. A Polarization-Type Basis Set for Second-Row Elements. *J Chem Phys* **1982**, *77* (7), 3654–3665. https://doi.org/10.1063/1.444267.

(56)　Spitznagel, G. W.; Clark, T.; von Ragué Schleyer, P.; Hehre, W. J. An Evaluation of the Performance of Diffuse Function-augmented Basis Sets for Second Row Elements, Na-Cl. *J Comput Chem* **1987**, *8* (8), 1109–1116. https://doi.org/10.1002/jcc.540080807.

(57)　Weigend, F.; Ahlrichs, R. Balanced Basis Sets of Split Valence, Triple Zeta Valence and Quadruple Zeta Valence Quality for H to Rn: Design and Assessment of Accuracy. *Physical Chemistry Chemical Physics* **2005**, *7* (18), 3297–3305. https://doi.org/10.1039/b508541a.

(58)　Zhao, Y.; Truhlar, D. G. The M06 Suite of Density Functionals for Main Group Thermochemistry, Thermochemical Kinetics, Noncovalent Interactions, Excited States, and Transition Elements: Two New Functionals and Systematic Testing of Four M06-Class Functionals and 12 Other Functionals. *Theor Chem Acc* **2008**, *120* (1–3), 215–241. https://doi.org/10.1007/s00214-007-0310-x.

(59)　Marenich, A. V.; Cramer, C. J.; Truhlar, D. G. Universal Solvation Model Based on Solute Electron Density and on a Continuum Model of the Solvent Defined by the Bulk Dielectric Constant and Atomic Surface Tensions. *Journal of Physical Chemistry B* **2009**, *113* (18), 6378–6396. https://doi.org/10.1021/jp810292n.

(60)　Page, M.; McIver, J. W. On Evaluating the Reaction Path Hamiltonian. *J Chem Phys* **1988**, *88* (2), 922–935. https://doi.org/10.1063/1.454172.

(61)　Page, M.; Doubleday, C.; McIver, J. W. Following Steepest Descent Reaction Paths. The Use of Higher Energy Derivatives with Ab Initio Electronic Structure Methods. *J Chem Phys* **1990**, *93* (8), 5634–5642. https://doi.org/10.1063/1.459634.

(62)　CYLview20; Legault, C. Y. Université de Sherbrooke, 2020 (Http://Www.Cylview.Org).

(63)   Note That the Cyclonickelation Reaction Leading to the Title Complexes Has Been Modelled Using the Same Computational Procedures Used in the Present Study. We Have Shown That This Approach Generated Data That Were Very Close to the Experimentally Obtained Results: L. P. Mangin, D. Zargarian, Organometallics, 2019, 38, Organometallics 2019, 38, 1479-1492.

3.1 Chapter −3− Cyclonickelated Complexes Featuring a Terminal or Bridging Triazole

Rajib K. Sarker and Davit Zargarian*

Département de chimie, Université de Montréal, Montréal (Québec), Canada H3C 3J7.

Full Paper

3.2 Abstract:

Cyclometallated complexes can serve as models for studying mechanistic details of C–H functionalization processes. In this context, we have shown that the cyclonickelated complexes $\{\kappa^P,\kappa^C\text{-}(\text{i-Pr})_2\text{PO-Ar}\}\text{Ni(Br)(NCMe)}$ can be isolated from C–H nickelation of aryl phosphinites, and they react with various substrates to furnish functionalized products. A recent investigation showed that treating these complexes with hydroxylamines $\text{HO–N(CH}_2\text{R)}_2$ results in the hoped-for rupture of the N–O bond; unfortunately, however, this reactivity gave the imine adducts $\{\kappa^P,\kappa^C\text{-}(\text{i-Pr})_2\text{PO-Ar}\}\text{Ni(Br)}(\kappa^N\text{-N(CH}_2\text{R)CH=CHR})$ arising from net dehydration of the hydroxylamine substrate instead of the desired C–N functionalization. In continuation of our previous studies, we have explored the reactivities of the said cyclonickelated complexes with 4-Amino-4H-1,2,4-triazole featuring a potentially labile N–N bond. Even though we have observed signs of a decomposition pathway which might involve N–N bond rupture, this turned out to be a minor component of the overall reactivity, the major pathway leading to the formation of simple triazole adducts. Thus, we have isolated the mononuclear adducts $\{\kappa^P,\kappa^C\text{-}(\text{i-Pr})_2\text{PO-Ar}\}\text{Ni(Br)}(\kappa^N\text{-4-amino-4H-1,2,4-triazole})$ **2a** and **2e**, as well as the triazole-bridged dinuclear adducts $[\{\kappa^P,\kappa^C\text{-}(\text{i-Pr})_2\text{PO-Ar}\}\text{Ni(Br)}\}_2(\mu,\kappa^N,\kappa^{N'}\text{-4-amino-4H-1,2,4-triazole})$ **3b**, **3c**, and **3d**. Variable temperature NMR monitoring of the reactions between the Ni precursors and the triazole substrate indicated that the new triazole adducts were involved in a dynamic exchange process. Analyses of the NMR data pointed to the mono- and dinuclear adducts of triazole being involved in dynamic equilibria with their corresponding acetonitrile adducts. Interestingly, in all cases the species that crystallizes out of the solution is either the mononuclear or the dinuclear triazole adduct, never both. Moreover, the choice of which adduct is favored for crystallization seems to depend on the specific precursor used, **1a** and **1e** giving the mononuclear products exclusively, whereas **1b**, **1c** and **1d** gave only the dinuclear products.
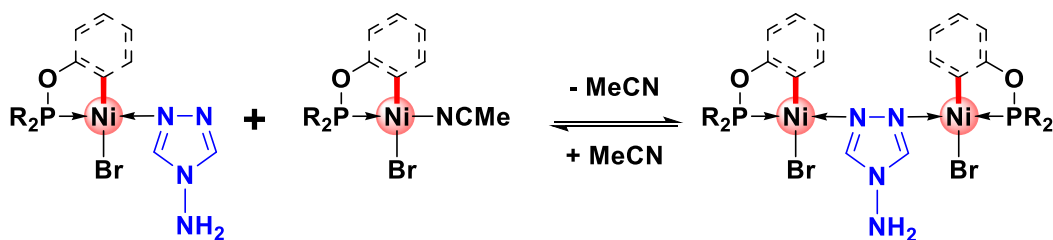
3.3   Introduction

Sustainable production of valuable fine chemicals will likely rely on a multitude of versatile synthetic approaches, one of which is the so-called chelation-assisted C—H functionalization using base-metal precursors.[1–5] In the most practical variant of this methodology, the multi-step functionalization process is conducted in a "one-pot" manner, leading directly to the end products. On the other hand, the development of evermore attractive versions of this methodology can benefit from a different approach, one consisting of distinct studies focused on the various steps of the C—H functionalization process. Indeed, such one-by-one analysis of different stages of the process allows for the interception of key intermediates and detailed examination of their reactivities with co-substrates, thus providing valuable mechanistic insight that can help optimize the functionalization process. Recent examples of this approach have been reported by the groups of Schaefer and Love,[6] and Sanford.[7]

In this context, our group has reported on the reactivities of pincer complexes prepared via C_{sp2}—H and C_{sp3}—H nickellation of resorcinol and 1,3-propandiol derivatives, and investigated the C_{sp2}—H nickellation of phosphinites derived from phenol.[8–16] We have shown, for instance, that in the case of substrates derived from phenol the nickellation step is often reversible, and have identified some of the reaction conditions that favor the nickellation step.[17,18] Moreover, isolation of thermally stable orthonickelated complexes arising from the C_{sp2}—H nickellation of phosphinites derived from phenol and naphthol has allowed us to examine their reactivities in the context of C—C and C—P functionalization reactions (**Scheme 3. 1**).

Scheme 3. 1. Previously reported C—H nickelation and functionalization of aryl- and naphthyl-phosphinites
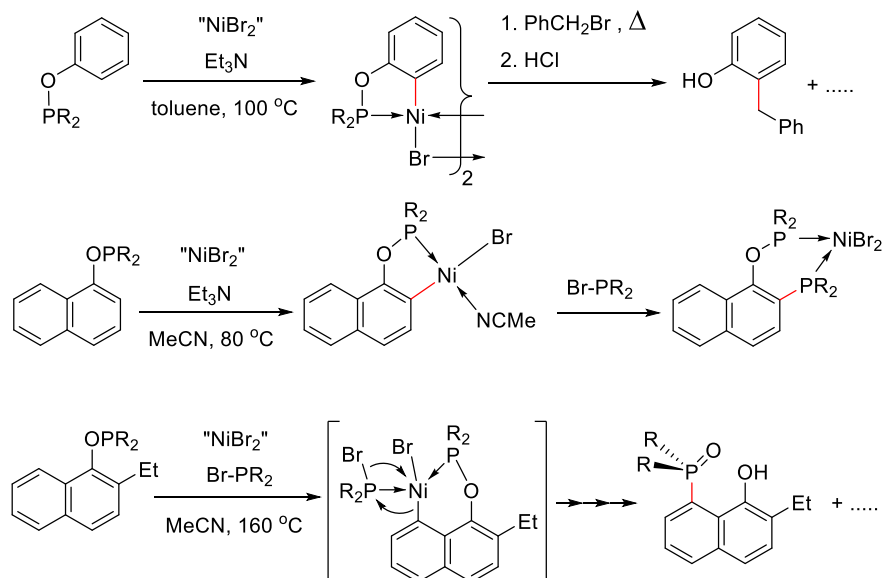
As a follow-up to the reactivities of the nickellacyclic complexes illustrated in **Scheme 3. 1**, we have turned our attention to assessing the potential for C—N functionalization. Recently, we probed the reactivities of these complexes with the hydroxylamines $R_2N\text{-OH}$, anticipating that their relatively labile N—O bond might facilitate C—N coupling. Unfortunately, this approach led mostly to the formation of simple hydroxylamine adducts, one aminoxide derivative, and adducts of imines arising from dehydration of the hydroxylamine substrates (**Scheme 3. 2**).[19]

Scheme 3. 2. Previously reported reactivities of orthonickelated complexes with hydroxylamines
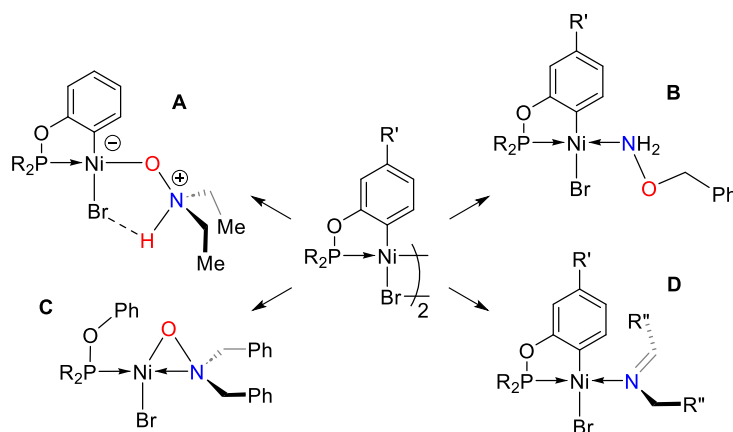
In continuation of these investigations, we have examined the C—N coupling potential of reagents featuring N—N single bonds. The present report describes the reactivities of our orthonickelated complexes with 4-amino-4H-1,2,4-triazole. Although this approach also failed to induce the hoped-for C—N coupling (**Scheme 3. 3**, path **A**), we have isolated new mononuclear and dinuclear adducts that display interesting solution exchange dynamics reported herein (**Scheme 3. 3**, path **B**).

Scheme 3. 3. Proposed and observed reactivities of orthonickelated complexes with triazole
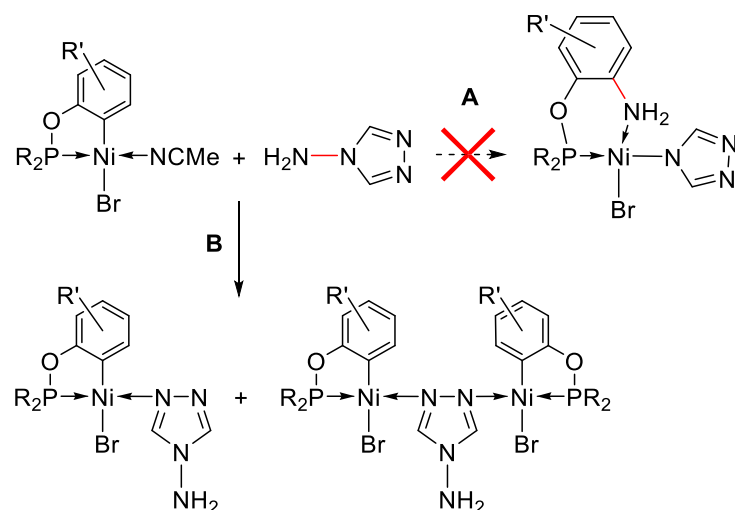
3.4   Results and discussion

3.3.1   Reactivities of the parent dimeric precursor 1a with 4-amino-4H-1,2,4-triazole.

We began our reactivity studies by treating an acetonitrile solution of the dimeric precursor **1a** with two equivalents of the triazole substrate, thus ensuring a Ni : triazole ratio of 1:1. Before discussing the outcome of this reaction, it is worth noting that our previous studies have established that dissolving our dimeric precursors **1** in acetonitrile leads to the immediate formation of the corresponding acetonitrile adducts **1-NCMe**.[20] On the basis of the somewhat broad linewidths of the ^{31}P signals detected for the acetonitrile mixtures of **1**, we believe that the dimers and their corresponding acetonitrile adducts are in equilibrium. Thus, we believe that in the present case it is adduct **1a** that reacts with the added triazole, as shown in **Scheme 3. 4**.

Scheme 3. 4. Synthesis of complex 2a
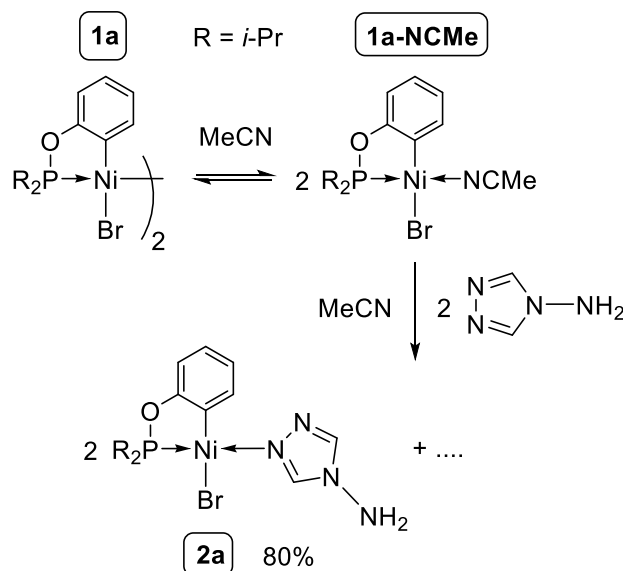
The reaction of the in-situ generated acetonitrile adduct **1a-NCMe** with triazole caused a color change from green to brown and resulted in the precipitation of a white solid. The $^{31}P\{^{1}H\}$ NMR spectrum of this mixture (**Figure S3. 2** in ESI) displayed a few low-intensity singlets in the 50-70 ppm region of the spectrum, which are normally associated with phosphine oxides, as well as a more intense singlet appearing at around the same chemical shift as the signal for the precursor (ca. 196 ppm).[21] Interestingly, the major signal in this spectrum is more than twice as broad as the original resonance for **1a-NCMe**, the corresponding values of full width at half maximum, FWHM, being ca. 22 vs. 10 Hz. These observations suggested that the reaction of **1a-NCMe** with the triazole substrate gives a simple triazole adduct as the major product (**Scheme 3. 4**), in addition to minor amounts of unidentified side-products likely arising from an oxidative decomposition process.

To confirm the identity of the products Shown in **Scheme 3. 4**, we worked-up the reaction mixture as follows: filtration of the reaction mixture separated the insoluble off-white solids, and evaporation of the red-brown filtrate gave a yellow solid, which was recrystallized from Et$_2$O to give a brown crystalline solid. XRD analysis of a single crystal selected from this batch revealed the simple adduct **2a** featuring a Ni←N dative bond with one of the imine nitrogen atoms of the

triazole. The molecular diagram for **2a** is shown in **Figure 3. 2**, and the solid-state parameters will be discussed later, along with the results of XRD analyses for all new products obtained during the course of this study (*vide infra*).

The off-white solid obtained from the filtration of the reaction mixture dissolved in D_2O to give a pale greenish-blue solution. However, the $^{31}P\{^1H\}$ and ^1H NMR spectra of this solution showed no signals, presumably because of the paramagnetic character of the species formed in D_2O. Unfortunately, we did not succeed in growing single crystals from this solution to allow a reliable identification of this product. Nevertheless, we can conclude that the reaction of **1a** with 4-amino-triazole follows two pathways, a major one that gives the simple adduct **2a**, and a minor decomposition pathway that gives a number of unidentified side-products.

The NMR characterization of **2a** not only supported the molecular structure revealed by our solid-state data, but also indicated that this compound was involved in a dynamic exchange process in solution. The first hint of this exchange process was the observation of a very broad singlet resonance in the room temperature $^{31}P\{^1H\}$ NMR spectrum of **2a** (FWHM~ 49 Hz; **Figure S3. 3**). This prompted us to examine the low-temperature spectrum, which showed that cooling a CD_3CN sample of **2a** to -40 °C caused the replacement of the ^{31}P singlet observed at 196 ppm in the ambient temperature spectrum by two new singlets appearing at ca. 197 and 200 ppm (**Figure S3. 4**). Integration of the new peaks gave a 1 : 0.28 ratio.

The dynamic exchange process implied by the above observations was also apparent from some features of the ^1H and ^{13}C NMR spectra of **2a**. For instance, the room temperature ^1H NMR spectrum of **2a** (**Figures S5-S7**) displayed three broad resonances for the following signals: one of the aryl protons (at ca. 6.4 ppm), the NH_2 protons (at ca. 5.5 ppm), and one set of P-CH_3 protons (at ca. 1.5 ppm). More significantly, whereas the solid-state structure of **2a** would suggest that there should be two distinct singlet resonances for the two symmetry-inequivalent triazole N=CH protons, what we observed instead was only one broad signal at ca. 8.4 ppm, integrating for two protons (**Figure S3.7**). The latter signal could be attributed to the imine carbon of the triazole ligand based on the $^{13}C\{^1H\}$ NMR and HSQC spectra of **2a** (**Figure S3. 10**), thus confirming that the two N=CH nuclei that are symmetry-inequivalent in the solid-state structure of **2a** become

equivalent in solution. In other words, the observed solid-state structure of **2a** is not maintained in solution, presumably because of the dynamic exchange process alluded to above.

To gain more insight on this exchange process, we recorded variable temperature NMR spectra for a CD_3CN solution of **2a**. The ^1H NMR spectra showed that warming the sample above 25 °C led to a sharpening of the broad signals seen in the ambient temperature spectrum, whereas cooling the samples led to further broadening of most of these signals. For instance, the broad peaks observed at ca. 6.4 and 5.5 ppm in the ambient temperature spectrum and attributed to the aryl C*H* and N*H*$_2$ protons broadened and new peaks emerged at ca. 6.1 and 5.8 ppm (**Figure S3.11**). In contrast, the broad resonance at ca. 1.5 ppm attributed to one set of PCH(C*H*$_3$)$_2$ protons sharpened considerably upon cooling and split into two multiplets. Moreover, the broad singlet appearing at ca. 8.4 ppm in the ambient temperature spectrum and attributed to the imine protons NC*H* shifted more downfield upon cooling, and eventually (at -40 °C) gave rise to two new broad resonances, one a singlet (ca. 8.6 ppm) and the other a doublet (8.2 ppm), with the integration ratio of ca. 1:0.3, respectively (**Figure S3.12**).

The dynamic exchange process revealed by the above NMR data can be rationalized by the two scenarios outlined in **Scheme 3. 5**, both of which would render the imine *CH* nuclei equivalent: (a) equilibrium interconversion (**2a⇄3a**) between the mononuclear adduct **2a** and the symmetrical dinuclear species **3a** featuring a bridging triazole, or (b) conversion of **2a** with a simple adduct featuring Ni←NH$_2$ coordination.

Scheme 3. 5. The equilibrium formation of **2a** and **3a**
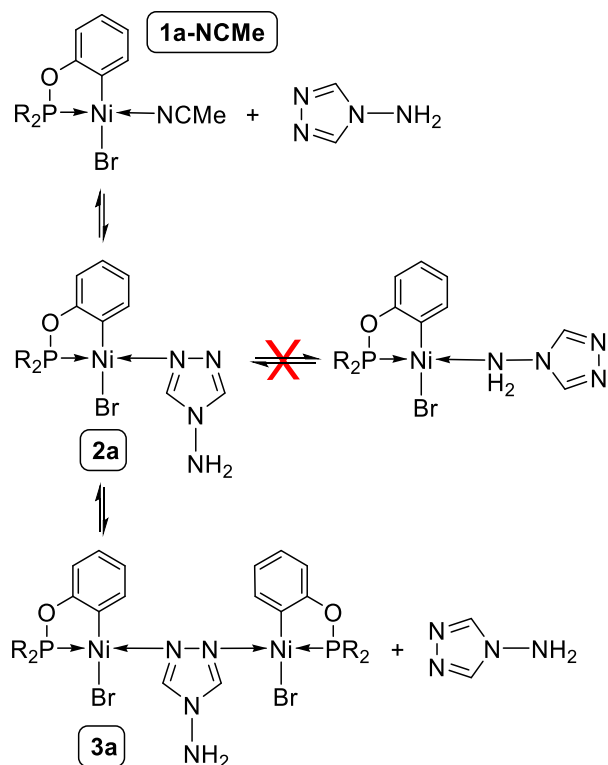
We reasoned that the two scenarios shown in **Scheme 3. 5** can be distinguished by studying the impact of excess triazole on the equilibrium position, since addition of triazole should affect the proposed **2a⇌3a** exchange, whereas the postulated equilibrium involving imine/amine modes of bonding should not be impacted by the number of triazole present. Therefore, we added 2, 4, 6, 8, and 10 additional equivalents of the triazole substrate to a CH_3CN solution of adduct **2a** and monitored the reaction by NMR. While little or no spectral change was observed with 2 equiv of triazole,[22] larger excess of this substrate resulted in the gradual replacement of the ambient temperature ^{31}P singlet at ca. 196 ppm by a singlet at ca. 200 ppm (**Figure 3. 1**). The latter was the dominant resonance in the presence of 10 equiv of triazole, indicating that it represents **2a**.
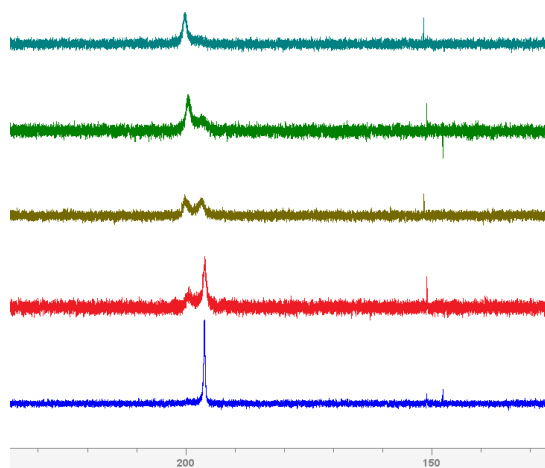
Figure 3. 1. $^{31}P\{^1H\}$ NMR spectra of 2a with various amounts of triazole (bottom to top): 2 equiv (blue trace); 4 equiv (red trace); 6 equiv (brown); 8 equiv (green trace); 10 equiv (blue-green trace).

The above results support the idea that in acetonitrile solutions the mononuclear triazole adduct **2a** is in equilibrium with both **1a-NCMe** and the dinuclear adduct **3a** (**Scheme 3. 5**). Interestingly, the data suggest that although the mononuclear species **2a** is the sole species obtained from crystallization, this species is in fact not the major species present in solution at ambient temperature.

3.3.2 Reactivities of 4-amino-4H-1,2,4-triazole with the dimeric precursors 1b-1e.

Next, we studied the reactions of the dimeric precursors **1b-1e**, which were obtained from the C−H nickellation of the corresponding substituted phenol and naphthol-based phosphinites with 4-amino-triazole.[20,23] The results of these studies hinted at a mononuclear-dinuclear equilibrium phenomenon similar to what was observed with **2a/3a**. However, the crystalline products obtained from three of these reactions turned out to be the dinuclear species **3b-3d**, whereas a mononuclear adduct was obtained only with **2e** (**Scheme 3. 6**).

Scheme 3. 6. Equilibrium formation of 2b-2e and 3b-3e
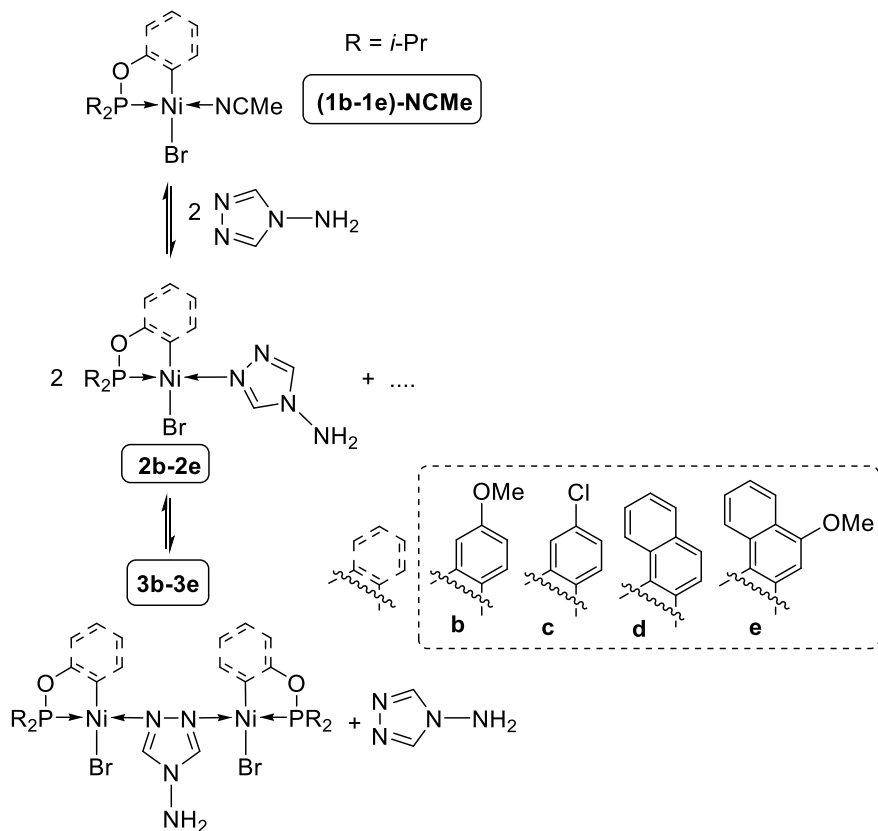
The $^{31}P\{^1H\}$ NMR spectra of **3b-3e** showed fairly broad singlet resonances at ca. 193-198 ppm, FWHM values (in Hz) being ca. 24 (**3b**), 19 (**3c**), 98 (**3d**), and 46 (**2e**). The broadness of these signals hinted at an exchange process that results in averaged signals. The ^1H NMR spectra were also consistent with this possibility, displaying signals of various broadness at ca. δ 8.5 (N=C*H*), 6.5 (aromatic H), 5.5 (N*H*$_2$), and 1.45 (PC*H*$_3$). (See the relevant ESI sections for the individual NMR spectra recorded for **3b-3e**.)

As in the case of the triazole adducts **2a/3a** discussed above, we noted that adding triazole to samples of the adducts derived from **1b-1e** showed signal broadening consistent with the dynamic exchange equilibrium depicted in **Scheme 3. 6**. For instance, the ^{31}P singlet for **1c-NCMe** (the acetonitrile adduct of the dimer **1c**) broadened significantly from FWHM ≈ 5 Hz to 26 and 56 Hz in the presence of 2 or 3 equiv of triazole, respectively (**Figure S3.32**).[24] Moreover, the original signal split into two very broad resonances in the presence of 10 equiv of triazole.

Finally, it is worth noting that we observed in mixtures of the precursors **1b-1e** and triazole a minor oxidative decomposition process similar to that observed in the analogous mixtures with **1a**. To estimate the extent of this decomposition, we examined the $^{31}P\{^1H\}$ NMR spectra of acetonitrile mixtures containing **1b** and precisely measured quantities of PPh$_3$ and triazole. These experiments allowed us to conclude that ca. 10% of the cyclonickelated complexes decompose when they come in contact with triazole. For more details on how these calibration experiments were carried out see ESI (section 4 and **Figure S3.56**.).

3.3.3   Structural characterization of the new complexes.

Single crystal diffraction analyses have been performed for the new triazole adducts **2a**, **3b**, **3c**, **3d**, and **2e**. The molecular diagrams of these compounds are shown in **Figure 3. 2**, and the most pertinent structural parameters for the solid-state structures are listed in **Table 1**. The crystal data are presented in the ESI, and the structures are briefly described below.

The coordination geometry around the Ni centre in all five of the new complexes is slightly distorted square planar, with minor angular deviations from ideal values observed for the cis and trans angles (83-98°; 167-178°). In all cases, the Ni centre is positioned off its coordination plane (defined by the ligating atoms C, P, Br, and N) by ca. 0.017-0.078 Å. The angle formed between the coordination planes in the mononuclear adducts and the plane of the terminal triazole is ca. 50° (**2a**) and 65° (**2e**), whereas the corresponding angles in the dinuclear complexes **3b-3d** are in the 59-63° range.

The Ni-Br, Ni-P, and Ni-C distances observed in the triazole complexes under discussion fall within the range of values reported for analogous adducts {κ^P,κ^C-(i-Pr)$_2$PO-Ar}Ni(Br)L: 1.894-1.932 Å for Ni-C, 2.087-2.136 Å for Ni-P, and 2.342-2.397 Å for Ni-Br.[8,17,19,20,25–28] As for the Ni-N$_{triazole}$ distances, it is interesting to note, first, that these are shorter by > 10 e.s.d. values in the mononuclear complexes **2a** and **2e** relative to their dinuclear analogues **3b-3d** wherein the triazole bridges two Ni centers. On the other hand, comparison of the Ni-N$_{triazole}$ distances observed in our complexes to analogous distances in previously reported complexes is less straight forward, as explained below.

To begin with, we have noted that the Ni-N$_{triazole}$ distances in the mononuclear adducts **2a** (1.944(3) Å) and **2e** (1.930(3) Å) are comparable to the Ni-N$_{imine}$ distances reported for {κ^P,κ^C-(i-Pr)$_2$PO-

Ar}Ni(Br)(imine) (1.934-1.950 Å).[19] However, direct comparisons to previously reported Ni(II)-triazole adducts is complicated because latter are exclusively coordination complexes featuring hexacoordinated Ni(II) centers ligated to heteroatoms (no Ni-C bond), a fact that would be expected to result in significantly longer Ni-$N_{traizole}$ distances.[29–38] Thus, nearly all Ni-$N_{triazole}$ distances reported previously exceed 2.00 Å, as exemplified by the following cases: 2.043(4)-2.016(5) Å reported for $[Ni_3(\mu\text{-triazole})_6(H_2O)_6](NO_3)_6$[39]; 2.053(3) and 2.059(3) Å reported for $[Ni_2Cl_2(\mu\text{-triazole})_2(OH_2)_4](ClO_4)_2$[39]; 2.107(3) Å reported for $[Ni_2(\mu\text{-triazole})_2(NCMe)_4](BF_4)_2$.[40] It should be emphasized that the latter Ni-$N_{triazole}$ distances are also significantly longer than the corresponding distances 1.962(2)-1.976(3) Å found in our dinuclear complexes **3b-3d**.

3.5 Conclusion

The present study has resulted in the synthesis of 5 new mono- and dinuclear adducts of Ni(II). Although this outcome diverged from the initial objectives of this investigation, the results obtained are potentially promising. Indeed, we have noted that complexes of 3d transition metals, including Ni(II), featuring multitopic and bridging triazole derivatives have attracted increasing interest over the past 2-3 decades for their potential applications. For example, Ni(II) complexes displaying bridging triazole moieties display variable ferromagnetic and anti-ferromagnetic characteristics and magneto-structural correlations,[38,40,41] and have been used for formulating new energetic materials[42] and MOF's[29] Moreover, owing to the close similarities between the electronics and coordination properties of triazole and imidazole derivatives, Ni-triazole compounds are under investigation as bioinorganic models for studying the mechanisms of enzymatic reactions and complex biological systems such as metalloenzymes.[35,40]

It is also worth noting that all previously reported Ni-triazole adducts are coordination complexes featuring only Ni-heteroatom linkages (Ni-O, Ni-O, Ni-Cl, etc.), thus making the triazole complexes isolated in the present study the first examples (to our knowledge) of organonickel adducts of triazole featuring Ni-C bonds. Moreover, **2a** and **2e** are rare examples of mononuclear complexes featuring terminal M-triazole moieties. Indeed, the impact of triazole: M molar ratio, solvent, and concentration on crystallization of mono- vs. multinuclear adducts is the subject of current research efforts, but remains poorly understood to date.[40] Future investigations will

address this topic, as well as pursuing insights into the decomposition reactivity observed between our Ni(II) precursors and 4-Amino-4H-1,2,4-triazole.

Table 3. 1. Selected bonds (Å) and angles (°) for Complexes **2a**, **2e**, and **3b-3d**.

	Ni–C2	Ni–P1	Ni–Br	Ni–N	C-Ni-Br	P1-Ni–N
2a	1.910(4)	2.1012(10)	2.3656(7)	1.944(3)	170.41(11)	177.77(10)
2e	1.909(3)	2.1046(9)	2.3546(5)	1.930(3)	172.73(9)	175.91(9)
3b	1.905(2)	2.1102(5)	2.3823(3)	1.966(1)	167.62(5)	176.01(4)
	1.908(2)	2.1121(5)	2.3794(3)	1.963(1)	168.97(5)	177.62(4)
3c	1.907(2)	2.1094(5)	2.3779(4)	1.962(2)	167.64(6)	176.49(5)
	1.908(2)	2.1136(5)	2.3670(4)	1.967(2)	168.39(6)	176.88(5)
3d	1.913(3)	2.1099(10)	2.3688(6)	1.976(3)	167.23(9)	175.64(8)
	1.914(3)	2.1129(10)	2.3843(6)	1.970(3)	168.06(9)	176.04(8)
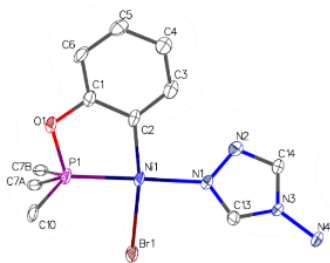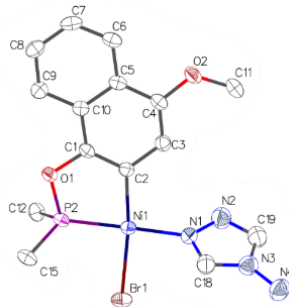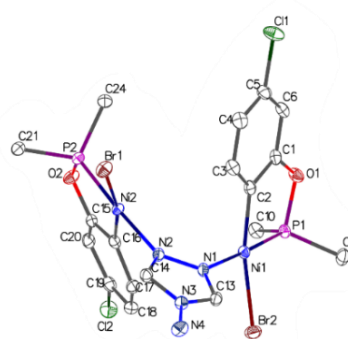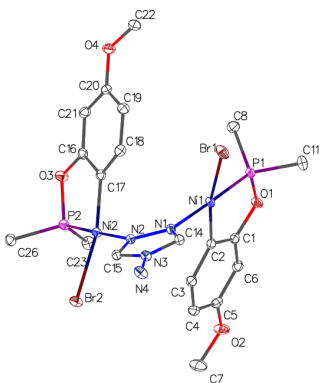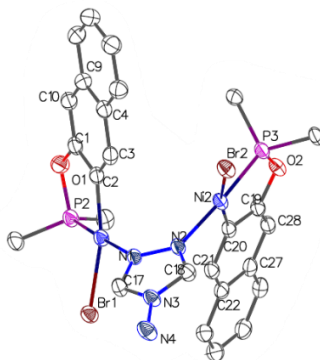
Figure 3. 2. Molecular diagram of the triazole adducts isolated in this study. Thermal ellipsoids are shown at the 50% probability level; hydrogen atoms are refined via riding model.

3.6 Associated content

Supporting Information. Electronic Supplementary Information (ESI) available: synthetic procedures, NMR spectra, single crystal structure data and additional figures. CCDC 2279934 (complex **2a**), 2279935 (complex **3b**), 2279936 (complex **3c**), 2279937 (complex **3d**), and 2279939 (complex **2e**). For ESI and crystallographic data in CIF or other electronic format see DOI: xxxxxxxx

3.7 Author information

Corresponding Author

* E-mail: zargarian.davit@umontreal.ca

3.8 Conflicts of interest

The authors declare no conflict of interest.

3.9 Acknowledgements

Chapter −3− Supporting information

S3.1 General experimental considerations

All manipulations were carried out under a nitrogen atmosphere using standard Schlenk techniques and an inert-atmosphere box. The transfer/addition of all liquid reagents/reactants was performed with BRAND Transfer pette® micropipettes (20-200 µL and 100-1000µL). Reported volumes should be considered to be within ±7 µL (for > 200 µL transfers) and ±3 µL (for < 200 µL transfers) of the measurements, with a >99% confidence level.[43] Solvents were dried by passage over a column of activated alumina, collected under nitrogen, and stored over 3 Å molecular sieves inside transfer/storage flasks equipped with high vacuum valves (Straus flasks). Et_3N was dried over CaH_2. The Ni^{II} precursor $[(i\text{-PrCN})NiBr_2]_n$ used throughout this study was prepared as reported previously.[26,27] Other reagents were purchased from Sigma-Aldrich or FisherSci and used without further purification.

Single crystals of the structurally characterized complexes were all grown at -35 °C under inert atmosphere using the following solutions: pure Et_2O solutions for **2a** and **3b**; Et_2O solution layered with hexane for **3c**; Et_2O solution layered with THF for **3d**; THF solution layered with Et_2O for **2e**. The crystallographic data for all structures were collected on either a Bruker Microsource (Cu radiation) or a Bruker Venture Metaljet (Ga radiation) via the Bruker APEX II or APEX III[44] software packages. Cell refinement and data reduction were performed using SAINT.[45] An empirical absorption correction, based on multiple measurements of equivalent reflections, was applied using the program SADABS or TWINABS.[46] The space group was confirmed by the XPREP[47] routine in APEX. The structures were solved in OLEX[48] using the SHELX[49] suite and refined by full-matrix least squares with SHEXL.[50] All non-hydrogen atoms were refined with anisotropic displacement parameters, whereas hydrogen atoms were set in calculated positions and refined via the riding model, with thermal parameters being 1.5 times that of the carbon bearing the H in question. All Thermal ellipsoid plots were drawn using OLEX.

S3.2 Procedures for the synthesis of new complexes

[{κ^P,κ^C-(i-Pr)₂PO-(C₆H₄)}Ni(Br)(4-amino-4H-1,2,4-triazole)], 2a. A 50 mL Schlenk flask containing 5 mL of MeCN was charged with the parent dimer [{$\kappa,^P\kappa^C$-(i-Pr)₂PO-C₆H₄}Ni(μ-Br)]₂ (**1a**, 70 mg, 0.101 mmol) and 4-amino-4H-1,2,4-triazole (17 mg, 0.201 mmol, 1.00 equiv). The solution was stirred overnight at room temperature and under inert atmosphere. Next, the reaction mixture was filtered to remove white precipitate, followed by removal of volatiles under vacuum. The resulting yellow residue was treated with ca. 1 mL of Et₂O, filtered, and the filtrate kept overnight at -35 °C. Brown crystals were separated and washed with cold hexane. (Yield: 100 mg, 0.232 mmol 80 %). ^{1}H NMR (400 MHz, 20 °C, CD₃CN): δ 1.33 (dd, 6H, CHCH_3, $^3J_{HP}$ = 14.9, $^3J_{HH}$ = 7.0), 1.47 (dd, 6H, CHCH_3, $^3J_{HP}$ = 17.2, $^3J_{HH}$ = 6.4), 2.44 (pseudo-oct, 2H, PCH, $^3J_{HH}$ = 7.1), 5.50 (br s, 2H, NH_2), 6.43 (br s, 1H, C$_{Ar}$-H), 6.54 (t, 1H, C4$_{Ar}$-H, $^3J_{HH}$ = 7.1), 6.69 (d, 1H, C6$_{Ar}$-H, $^3J_{HH}$ = 7.7), 6.93 (t, 1H, C5$_{Ar}$-H, $^3J_{HH}$ = 7.5), 8.44 (br s, 2H, N=CH). ^{13}C{^{1}H} NMR (125.72 MHz, 20 °C, CD₃CN): δ 17.25 (d, 2C, $^2J_{PC}$ = 1.5, CH₃), 18.86 (s, 2C, CH₃), 29.23 (d, 2C, $^2J_{PC}$ = 28.0, PCH), 110.67 (d, 1C, J_{PC} = 13.0, C$_{Ar}$), 121.50 (s, 1C, C$_{Ar}$), 127.55 (s, C, C$_{Ar}$), 139.40 (s, 1C, C$_{Ar}$), 146.15 (s, 2C, N=CH), 168.37 (d, $^2J_{PC}$ = 3.7, C1$_{Ar}$). ^{31}P{^{1}H} NMR (202.4 MHz, 20 °C, C₆D₆): δ 195.92 (s, 1P). Anal. calc. for C₁₄H₂₂BrN₄NiOP.Et₂O: C, 42.72; H, 6.37; N, 11.07. Found: C, 42.99; H, 6.16; N, 12.38.

[{κ^P,κ^C-(i-Pr)₂PO-(5-OMe-C₆H₃)}Ni(Br)}₂(μ,κ^N,$\kappa^{N'}$-4-amino-4H-1,2,4-triazole)], 3b. A 50 mL Schlenk flask containing 10 mL of MeCN was charged with the dimer [{κ^P,κ^C-(i-Pr)₂PO-(5-OMe-C₆H₃)}Ni(μ-Br)]₂ (**1b**, 70 mg, 0.092 mmol, 1.00 equiv) and 4-amino-4H-1,2,4-triazole (8 mg, 0.092 mmol, 1.00 equiv). The solution was stirred overnight at room temperature and under inert atmosphere. Next, the reaction mixture was filtered to remove white precipitate, followed by removal of volatiles under vacuum. The resulting yellow residue was treated with ca. 1 mL of Et₂O, filtered and the filtrate kept overnight at room temperature. Brown crystals were separated and washed with cold hexane. (Yield: 54 mg, 0.064 mmol, 70 %). ^{1}H NMR (400 MHz, 20 °C, CD₃CN): δ 1.32 (dd, 12H, CHCH_3, $^3J_{HH}$ = 7.0, $^3J_{HH}$ = 14.8), 1. 47 (dd, 12H, CHCH_3, $^3J_{HH}$ = 6.2, $^3J_{HH}$ = 17.0), 2.42 (ps oct, 4H, CH_2CH₃, $^3J_{HH}$ = 7.4), 3.67 (s, 6H, OCH_3), 5.49 (br s, 2H, NH_2), 6.21 (dd, 2H, C3$_{Ar}$-H, $^3J_{HP}$ = 8.9, $^3J_{HH}$ = 1.9), 6.26 (d, 2H, C4$_{Ar}$-H, $^3J_{HH}$ = 2.6), 6.47 (br s, 2H, C5$_{Ar}$-H), 8.46 (br s, 2H, N=CH). ^{13}C{^{1}H} NMR (125.72 MHz, 20 °C, CD₃CN): δ 17.22 (s, 1C, PCHCH₃), 18.84 (s, C, PCHCH₃), 29.20 (d, 4C, PCH, J_{PC} = 28.0), 55.76 (s, 1C, OCH₃), 97.63 (d, 1C, J_{PC} = 14.9, C$_{Ar}$), 107.42 (s, C$_{Ar}$), 139.32 (s, C$_{Ar}$), 146.17 (s, C$_{Ar}$), 160.75 (s, C$_{Ar}$), 168.64 (d,

1C, J_{PC} = 15.2, $C2$).^{31}P{^{1}H} NMR (202.4 MHz, 20 °C, CD$_3$CN): δ 195.83 (s, 1P). Anal. calc. for C$_{28}$H$_{44}$Br$_2$N$_4$Ni$_2$O$_4$P$_2$: C, 40.04; H, 5.28; Br, N, 6.67. Found: C, 39.67; H, 5.31; N, 6.55.

[{κ^P,κ^C-(i-Pr)$_2$PO-(5-Cl-C$_6$H$_3$)}Ni(Br)}$_2$($\mu,\kappa^N,\kappa^{N'}$-4-amino-4H-1,2,4-triazole)], 3c. A 50 mL Schlenk flask containing 10 mL of MeCN was charged with the dimer [{κ^P,κ^C-(i-Pr)$_2$PO-(5-Cl-C$_6$H$_3$)}Ni(μ-Br)]$_2$(**2**, 100 mg, 0.131 mmol, 1.00 equiv) and 4-amino-4H-1,2,4-triazole (11 mg, 0.131 mmol, 1.00 equiv). The solution was stirred overnight at room temperature and under inert atmosphere. Next, the reaction mixture was filtered to remove white precipitate, followed by removal of volatiles under vacuum. The resulting yellow residue was treated with ca. 1 mL of Et$_2$O and ca. 2mL of hexane, filtered and the filtrate kept overnight at -35 °C. Brown crystals were separated and washed with cold hexane. (Yield: 54 mg, 0.064 mmol, 48 %).^{1}H NMR (400 MHz, 20 °C, CD$_3$CN): δ 1.32 (dd, 12H, CHCH_3, $^3J_{HH}$ = 7.0, $^3J_{HP}$ = 14.8), 1.47 (dd, 12H, CH(CH_3), $^3J_{HH}$ = 7.1, $^3J_{HP}$ = 17.7), 2.45 (ps oct, 4H, CH(CH$_3$)$_2$, $^3J_{HH}$ = 7.2), 5.46 (br s, 2H, NH_2), 6.62 (ddd, 2H, C3$_{Ar}$-H, $^2J_{HH}$ = 8.3, $^3J_{HP}$ = 2.1,$^4J_{HH}$ = 1.0), 6.67 (d, 1H, C6$_{Ar}$-H, $^3J_{HH}$= 2.2), 6.71 (d, 1H, C4$_{Ar}$-H, $^3J_{HH}$= 7.9), 8.48 (br s, 1H, N=CH). ^{13}C{^{1}H} NMR (125.72 MHz, 20 °C, CD$_3$CN): δ 17.17 (d, $^2J_{PC}$ = 2.1, CH$_3$), 18.78 (d, $^2J_{PC}$ = 2.8, CH$_3$), 29.42 (d, J_{PC} = 28.3, PCH), 111.08 (d, J_{PC} = 13.4, C$_{Ar}$), 121.25 (d, J_{PC} = 2.0, C$_{Ar}$), 132.30 (s, C$_{Ar}$), 140.17 (s, C$_{Ar}$), 146.41 (s, C$_{Ar}$), 168.35 (d, $^2J_{PC}$ = 13.4, C1$_{Ar}$). ^{31}P{^{1}H} NMR (202.4 MHz, 20 °C, CD$_3$CN): δ 197.94 (s, 1P). Anal. calc. for C$_{26}$H$_{38}$Br$_2$Cl$_2$N$_4$Ni$_2$O$_2$P$_2$: C, 36.80; H, 4.51; N, 6.60. Found: C, 36.41; H, 4.51; N, 6.37.

[{κ^P,κ^C-(i-Pr)$_2$PO-(C$_{10}$H$_6$)}Ni(Br)}$_2$($\mu,\kappa^N,\kappa^{N'}$-4-amino-4H-1,2,4-triazole)], 3d. A 50 mL Schlenk flask containing 10 mL MeCN was charged with the dimer [{κ^P,κ^C-(i-Pr)$_2$PO-(C$_{10}$H$_6$)}Ni(μ-Br)]$_2$ (**5**, 100 mg, 0126 mmol, 1.00 equiv) and 4-amino-4H-1,2,4-triazole (11 mg, 0.126 mmol, 1.00 equiv). The solution was stirred overnight at room temperature and under inert atmosphere. Next, the reaction mixture was filtered to remove white precipitate, followed by removal of volatiles under vacuum. The resulting yellow residue was treated with ca. 1 mL of Et$_2$O and 1-3 drops of THF, filtered and the filtrate kept overnight at room temperature. Brown crystals were separated and washed with cold hexane. (Yield: 27 mg, 0.030 mmol, 24 %).^{1}H NMR (400 MHz, 20 °C, CD$_3$CN): δ 1.38 (dd, 3H,$^3J_{HH}$ =7.0, $^3J_{HP}$ =14.8, CHCH_3), 1.49 (ps d, 3H, CHCH_3), 2.52 (ps oct, 4H, $^3J_{HH}$ = 7.1, CHCH_3), 5.56 (s, 3H, NH_2), 6.72 (s, 3H, C$_{Ar}$-H), 7.0 (s, 2H, C$_{Ar}$-H), 7.17 (td, 1H, C$_{Ar}$-H, $^3J_{HH}$ = 7.4, $^4J_{HH}$ = 1.1), 7.28 (td, 1H, C$_{Ar}$-H,$^3J_{HH}$ =7.5, $^4J_{HP}$ = 1.2), 7.44 (d, 1H, C$_{Ar}$-H, $^3J_{HH}$ = 8.1), 7.59 (d, 1H, C$_{Ar}$-H, $^3J_{HH}$ = 8.2), 8.45 (s, 1H, N=CH). ^{13}C{^{1}H} NMR (125.72

MHz, 20 °C, CD$_3$CN): δ 17.26 (s, 2C, PCHCH$_3$), 18.80 (s, 2C, PCHCH$_3$), 29.27 (d, 4C, $^2J_{PC}$= 27.5, PCHCH$_3$), 104.79 (d, 1C, $^2J_{PC}$= 12.2, C_{Ar}), 124.00 (s, 1C, C_{Ar}), 125.97 (s, 1C, C_{Ar}), 126.98 (s, 1C, C_{Ar}), 127.63 (s, 1C, C_{Ar}), 130.25 (d, 1C, $^2J_{PC}$ =2.4, C_{Ar}), 134.50 (s, C_{Ar}), 139.07 (s, C_{Ar}), 146.17 (s, 1C, C_{Ar}), 167.29 (d, 1C, $^2J_{PC}$ =12.8, C2) .^{31}P{^{1}H} NMR (202.4 MHz, 20 °C, CD$_3$CN): δ 197.22 (s, 1P).

[{κ^P,κ^C-(i-Pr)$_2$PO-(4-MeO-C$_{10}$H$_5$)}Ni(Br)(4-amino-4H-1,2,4-triazole)], 2e. A 50 mL Schlenk flask containing 10 mL MeCN was charged with the dimer [{κ^P,κ^C-(i-Pr)$_2$PO-(4-MeO-C$_{10}$H$_5$)}Ni(μ-Br)]$_2$ (**1e**, 100 mg, 0.117 mmol, 1.00 equiv) and 4-amino-4H-1,2,4-triazole (0.020 mg, 0.234 mmol, 2 equiv). The solution was stirred overnight at room temperature and under inert atmosphere. Next, the reaction mixture was filtered to remove white precipitate, followed by removal of volatiles under vacuum. The resulting yellow residue was treated with ca. 1 mL of THF, filtered and layered with 0.3 mL of Et$_2$O, and allowed to stand overnight at room temperature. Brown crystals were separated and washed with cold hexane. (Yield: 58 mg, 0.113 mmol, 48 %).
^{1}H NMR (400 MHz, 20 °C, CD$_3$CN): δ 1.39 (dd, 3H, $^3J_{HH}$ =7.0, $^3J_{HP}$ = 14.7, CHCH_3), 1.51 (dd, 3H, $^3J_{HH}$ = 5.8, $^3J_{HP}$ = 16.6, CHCH_3), 2.52 (ps oct, 4H, $^3J_{HH}$ = 7.1, CHCH$_3$), 3.73 (s, 3H, OCH_3), 5.51 (s, 2H, NH_2), 6.05 (s, 1H, C$_{Ar}$-H), 7.37 (m, 2H, C$_{Ar}$-H), 7.82 (dd, 1H, C$_{Ar}$-H, $^3J_{HH}$ = 7.6, $^4J_{HH}$ = 1.3), 7.98 (td, 1H, C$_{Ar}$-H, $^3J_{HH}$ =7.9, $^4J_{HP}$ = 1.0), 8.48 (br s, 1H, N=CH). ^{13}C{^{1}H} NMR (125.72 MHz, 20 °C, CD$_3$CN): δ 17.33 (s, 2C, PCHCH$_3$), 18.96 (s, 2C, PCHCH$_3$), 29.40 (d, 2C, $^2J_{PC}$= 27.5, PCHCH$_3$), 56.12 (s, 1C, OMe), 113.90 (d, 1C, $^2J_{PC}$= 3.3, C_{Ar}), 121.95 (s, 1C, C_{Ar}), 122.07 (s, 1C, C_{Ar}), 122.54 (s, 1C, C_{Ar}), 122.90 (s, 1C, C_{Ar}), 125.25 (s, C_{Ar}), 125.77 (s, C_{Ar}), 126.57 (s, C_{Ar}), 146.31 (s, C_{Ar}), 148.70 (s, C_{Ar}). ^{31}P{^{1}H} NMR (202.4 MHz, 20 °C, CD$_3$CN): δ 193.26 (s, 1P). Anal. calc. for C$_{19}$H$_{26}$BrN$_4$NiO$_2$P: C, 44.57; H, 5.12; N, 10.94. Found: C, 44.25; H, 5.11; N, 11.43.

S3.3 Complete characterization of the new compounds

Complex **2a**
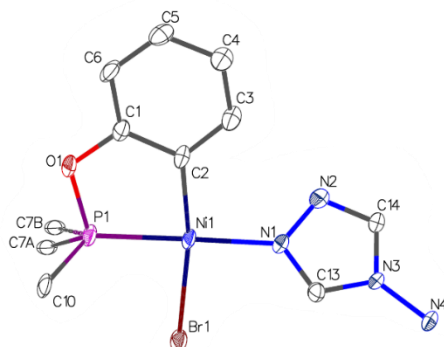
Figure S3. 1. Side view of the molecular diagram of compound **2a**. Thermal ellipsoids are shown at the 50% probability level; hydrogen atoms are refined via riding model.
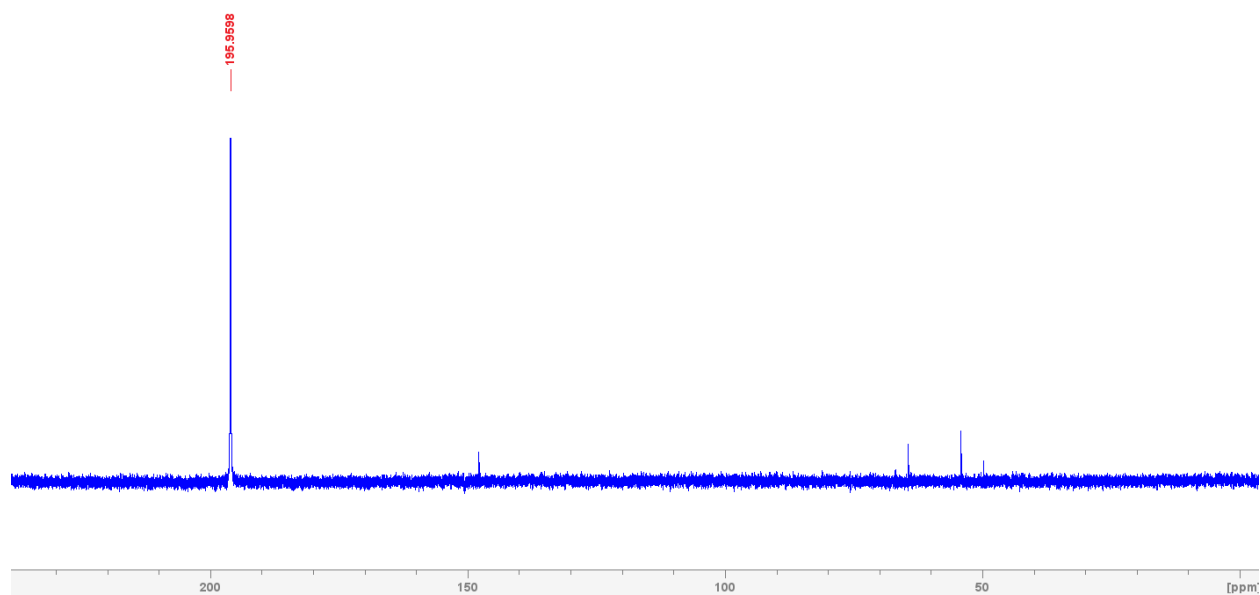
Figure S3. 2. The room temperature ^{31}P{^{1}H} NMR spectrum (CH$_3$CN) of the crude reaction mixture obtained upon treating the parent dimer **1a** with 1 equiv of triazole.
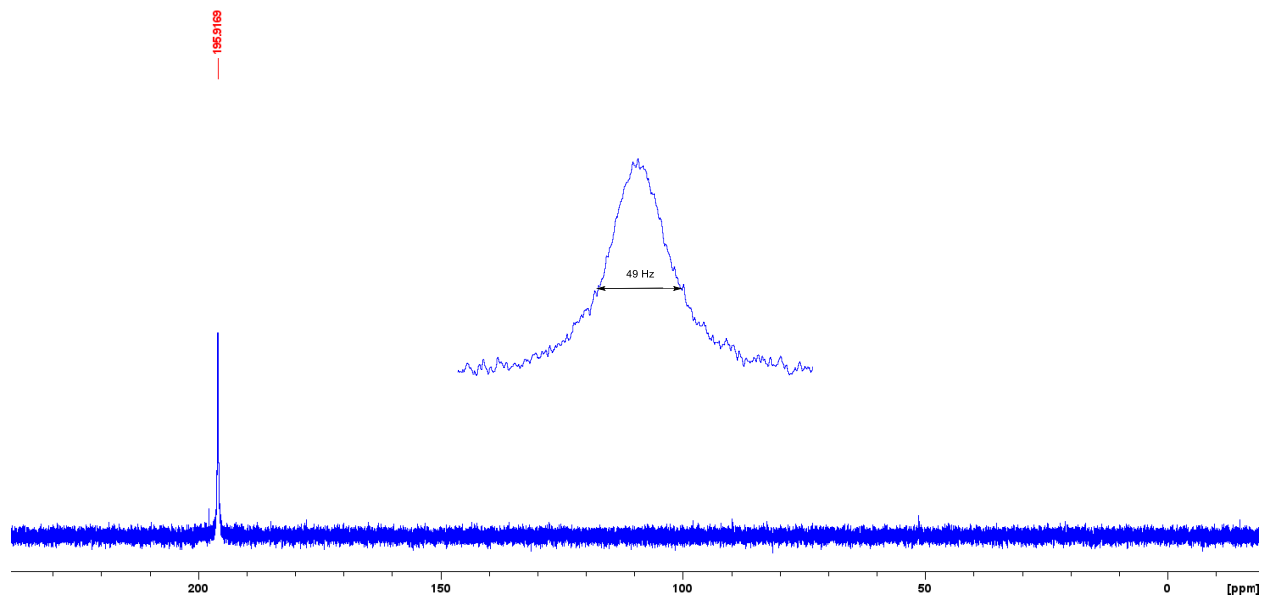
Figure S3. 3. $^{31}P\{^1H\}$ NMR spectrum (CD$_3$CN) of **2a**.
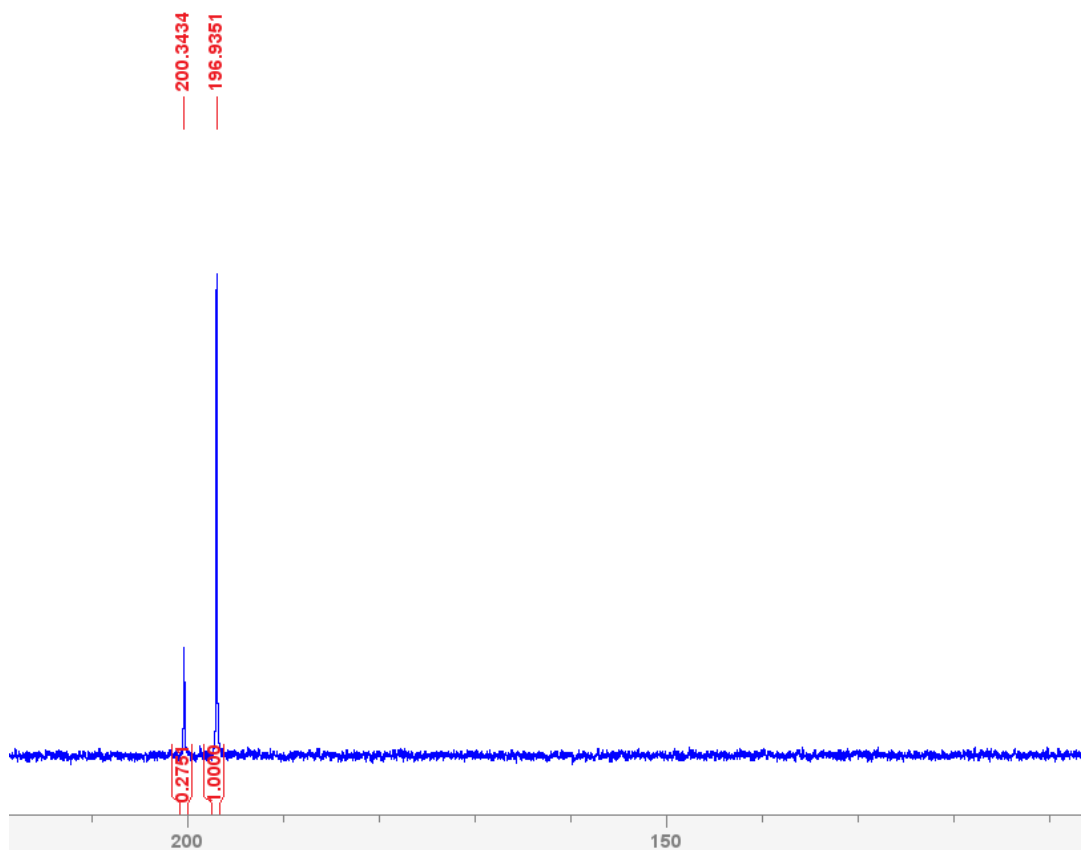
Figure S3. 4. $^{31}P\{^1H\}$ NMR spectrum (CD$_3$CN) of **2a** at – 40 ºC.

243
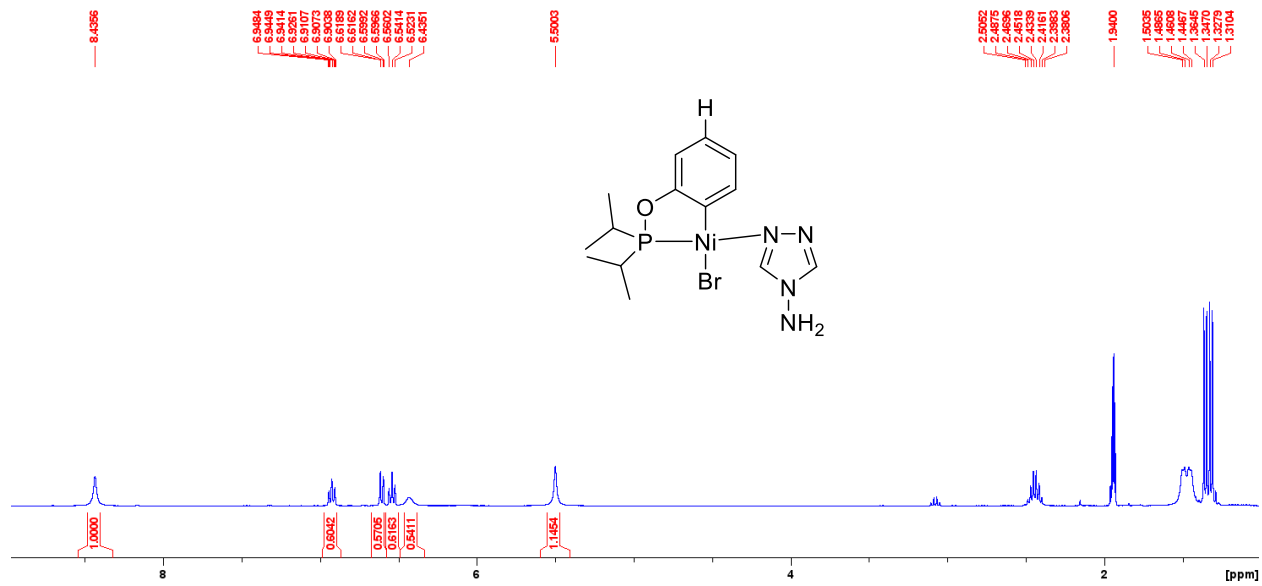
Figure S3. 5. Full ^{1}H NMR spectrum of **2a** in CD$_3$CN.
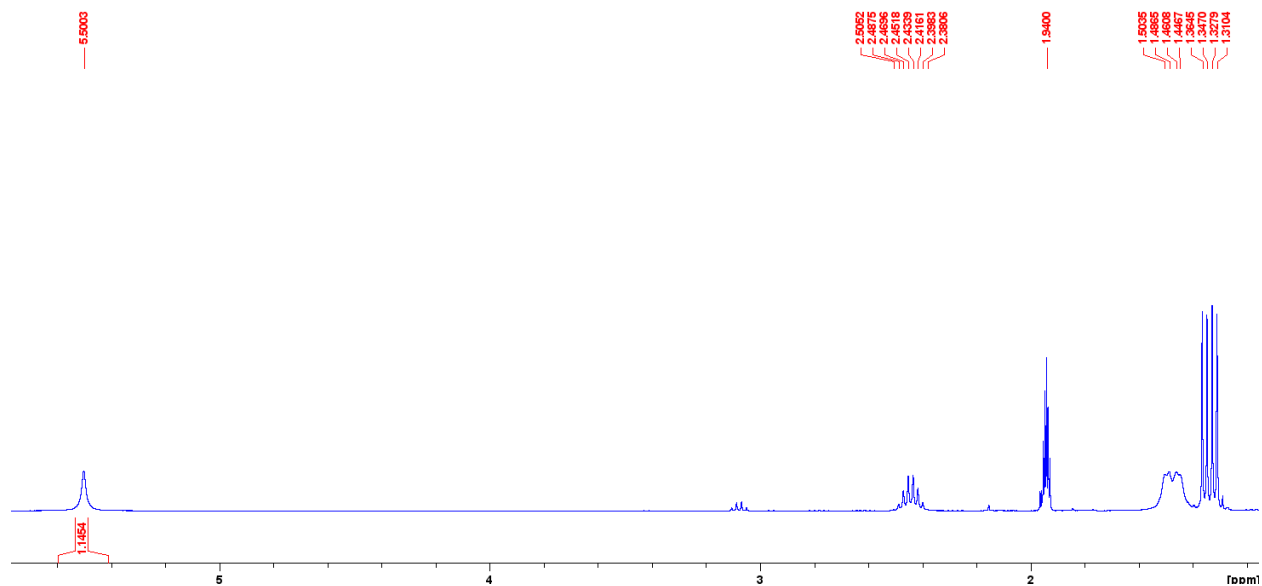
Figure S3. 6. The expanded aliphatic region of the ^{1}H NMR spectrum of **2a** in CD$_3$CN.
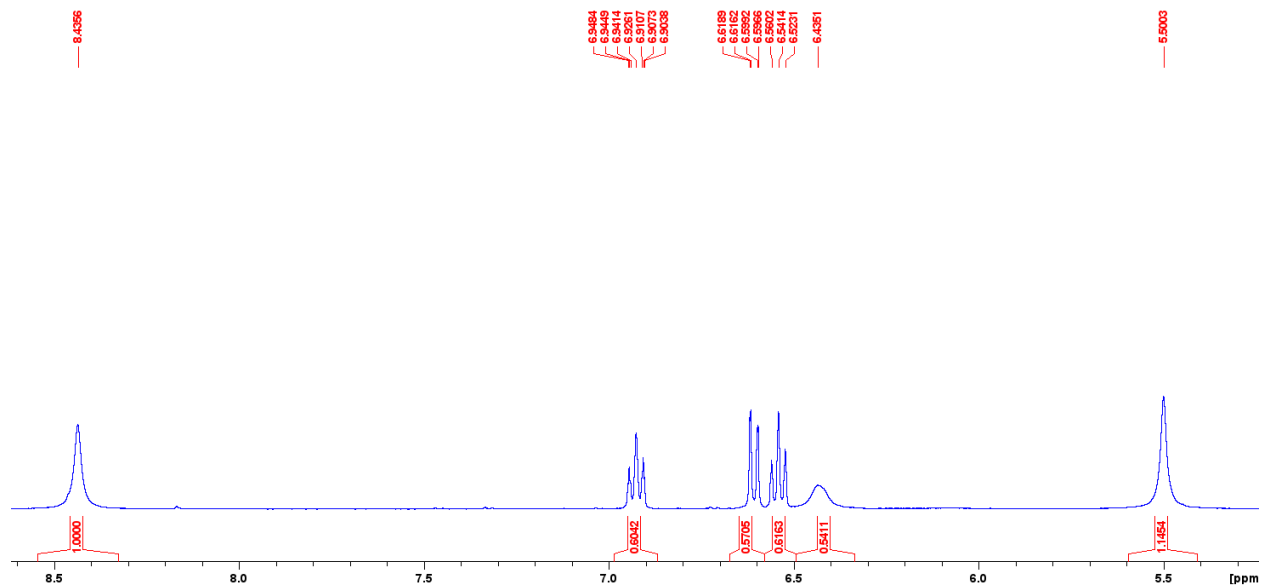
Figure S3. 7. The expanded aromatic region of the ^{1}H NMR spectrum of **2a** in CD$_3$CN.
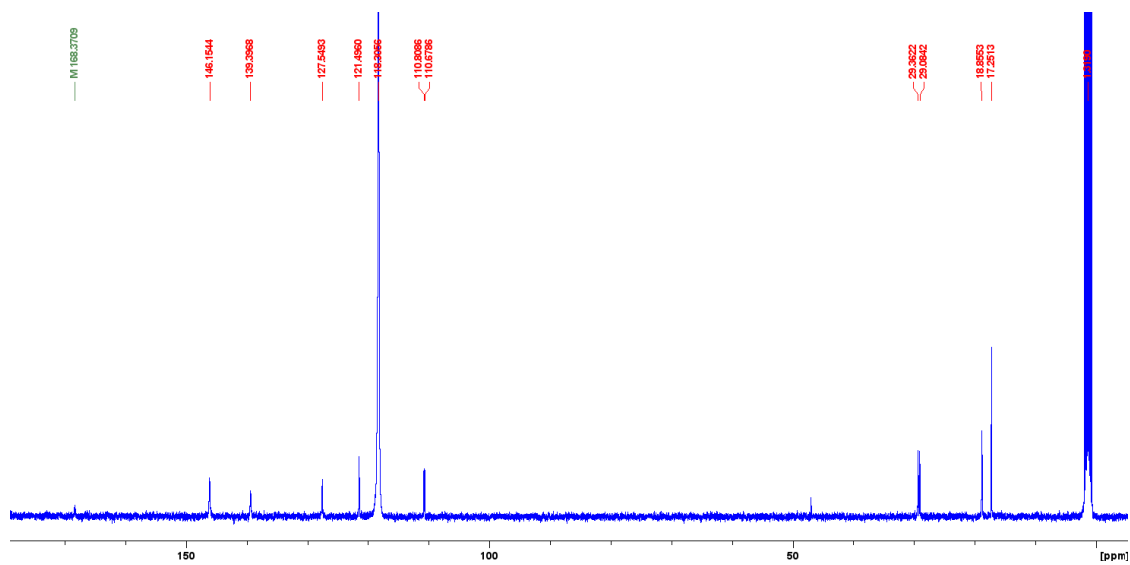
Figure S3. 8. Full ^{13}C NMR spectrum of **2a** in CD$_3$CN.
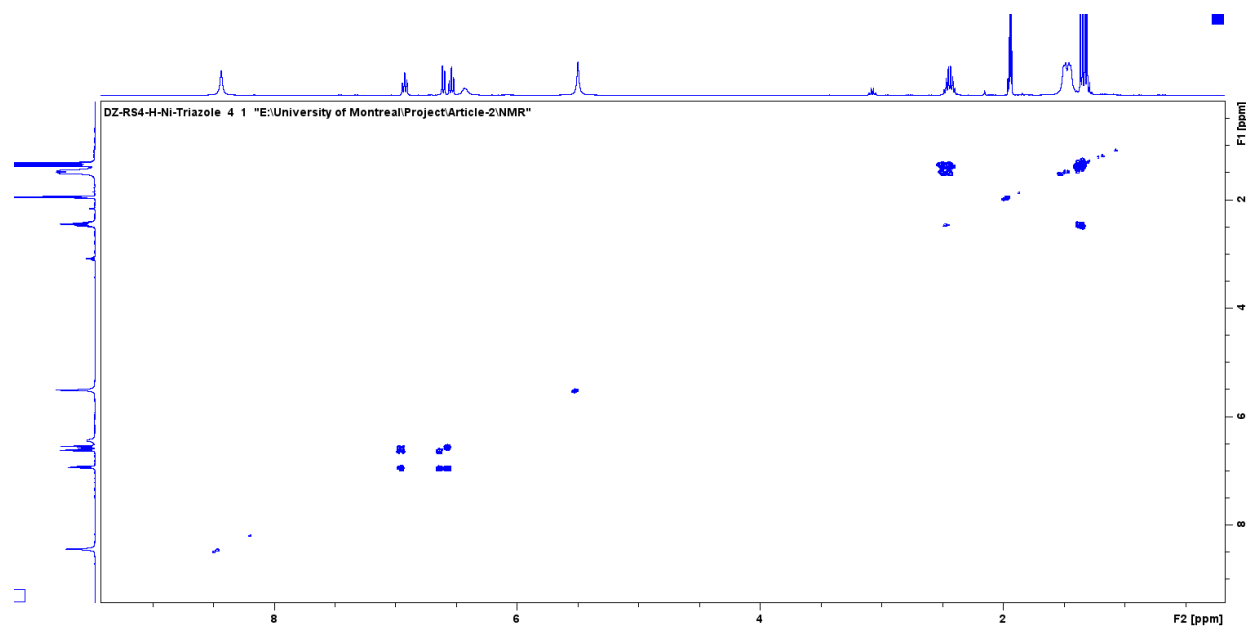
Figure S3. 9. Full ^{1}H-^{1}H COSY NMR spectrum of **2a** in CD$_3$CN.
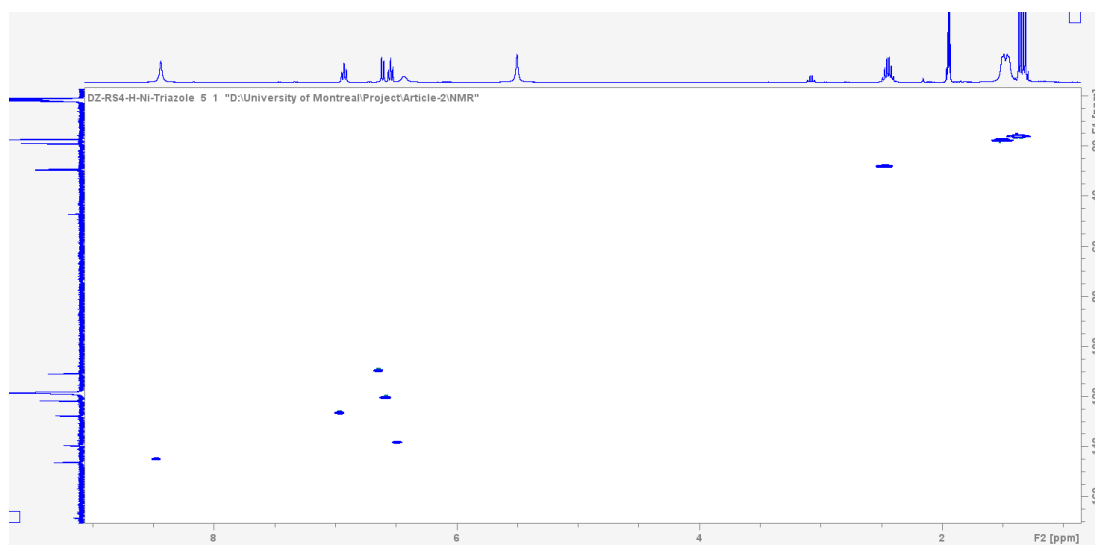
Figure S3. 10. Full HSQC-Edited NMR spectrum of **2a** in CD$_3$CN.
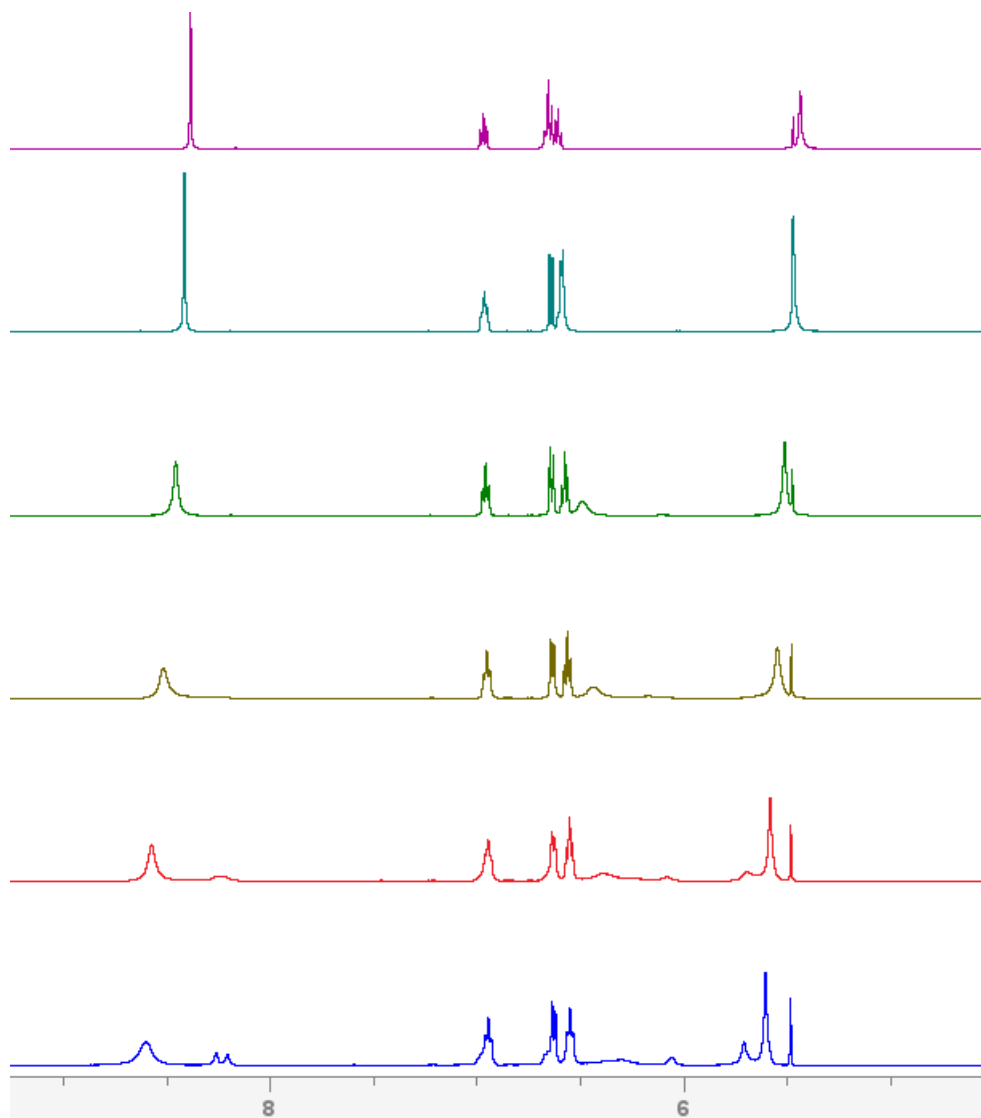
Figure S3. 11. Aromatic region of the VT ^{1}H NMR (CD$_3$CN) spectrum of **2a**. (Bottom to top: - 40, - 25, 0, 25, 50, and 70 °C).
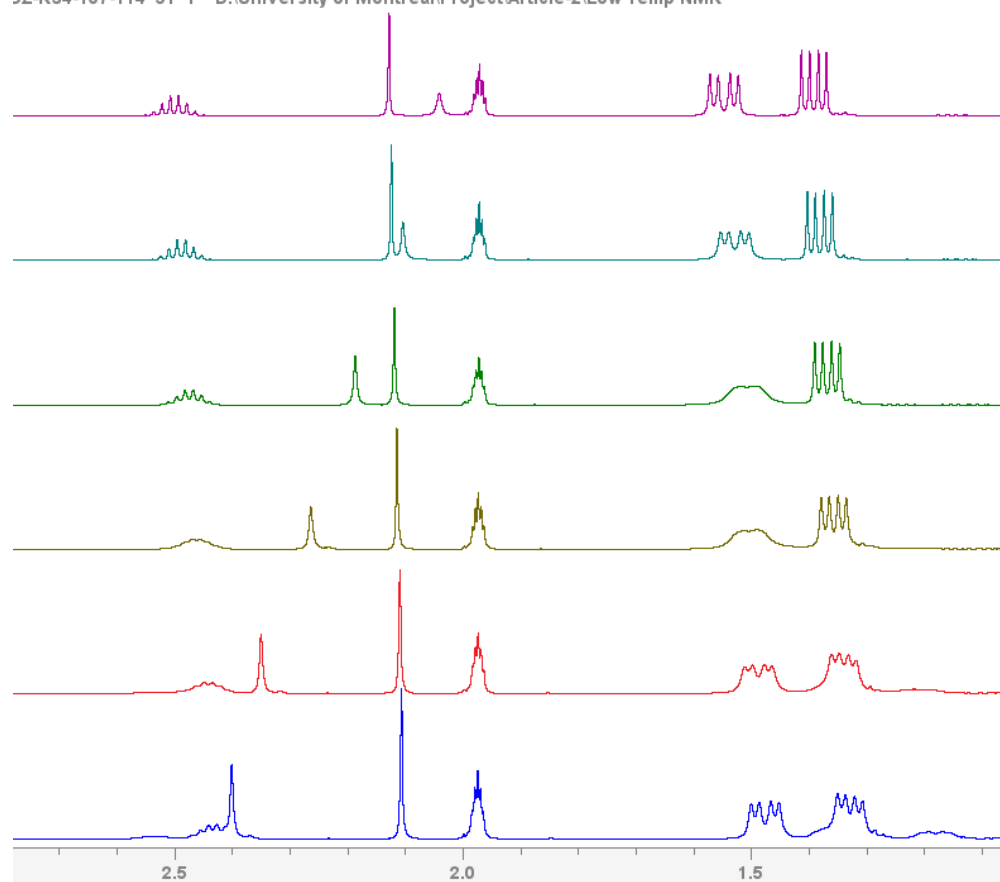
Figure S3. 12. Aliphatic region of the VT ^{1}H NMR (CD$_3$CN) spectrum of **2a**. (Bottom to top: -40, -25, 0, 25, 50, and 70 ^{o}C).
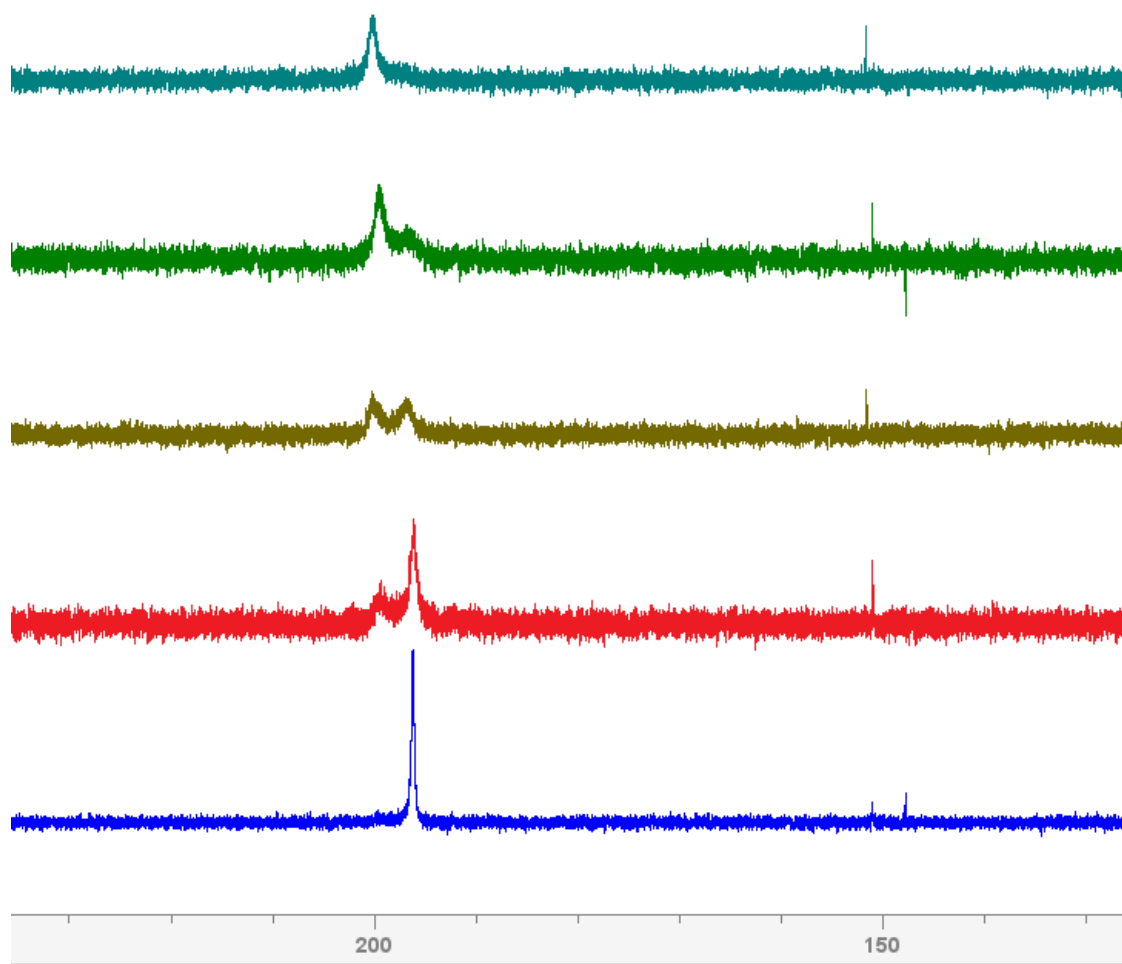
Figure S3. 13. $^{31}P\{^1H\}$ NMR spectra of **2a** with various amounts of triazole (bottom to top): 2 equiv (blue trace); 4 equiv (red trace); 6 equiv (brown); 8 equiv (green trace); 10 equiv (blue-green trace).

Complex **3b**
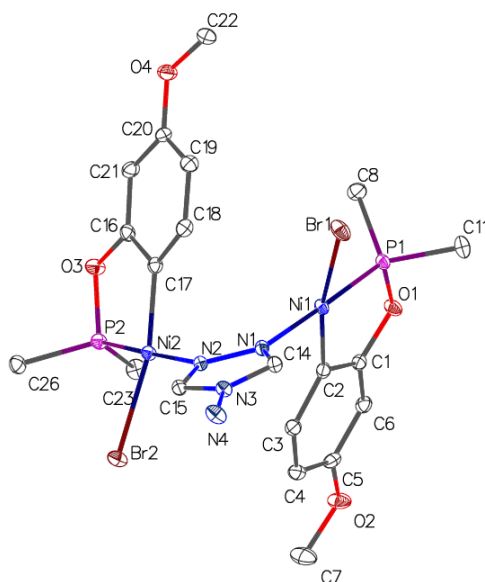
Figure S3. 14. Side view of the molecular diagram of compound **3b**. Thermal ellipsoids are shown at the 50% probability level; hydrogen atoms are refined using a riding model.
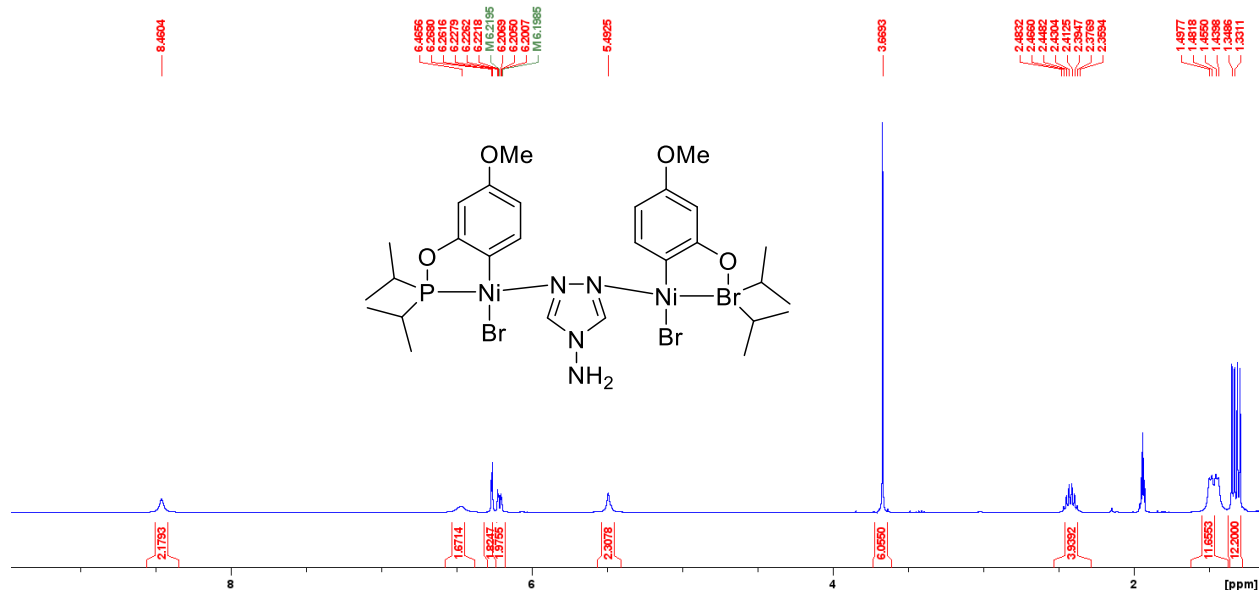
Figure S3. 15. Full ^{1}H NMR spectrum of .**3b**. in CD$_3$CN.
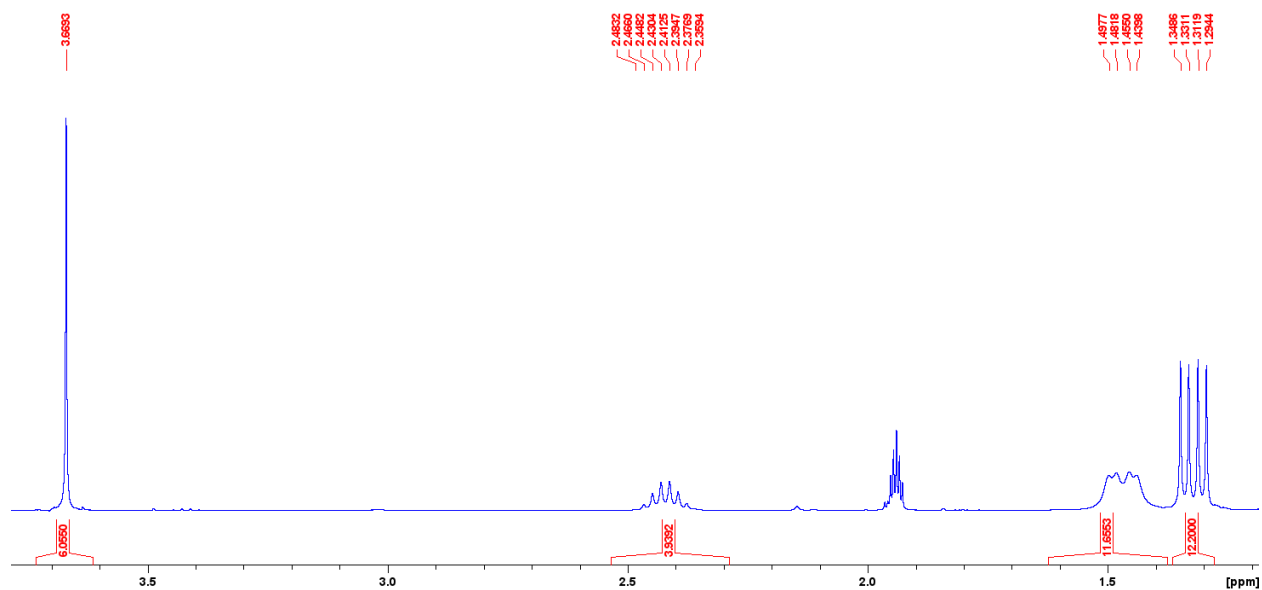
Figure S3. 16. The expanded aliphatic region of the ^{1}H NMR spectrum of **3b** in CD$_3$CN.
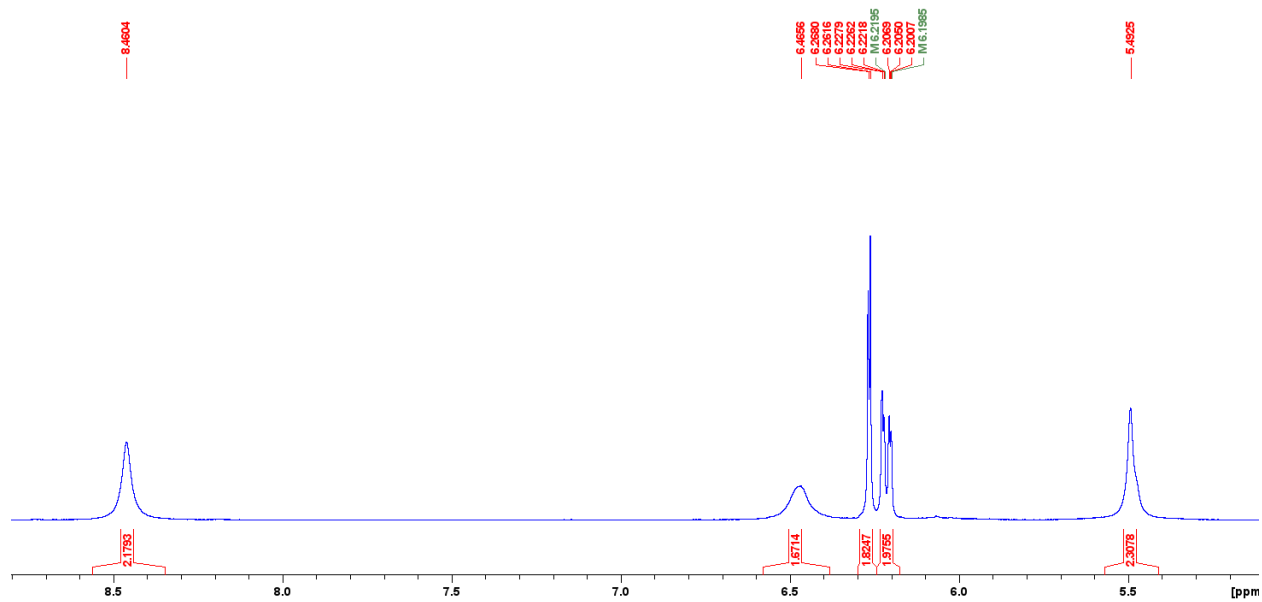
Figure S3. 17. The expanded aromatic region of the ^{1}H NMR spectrum of **3b** in CD$_3$CN.
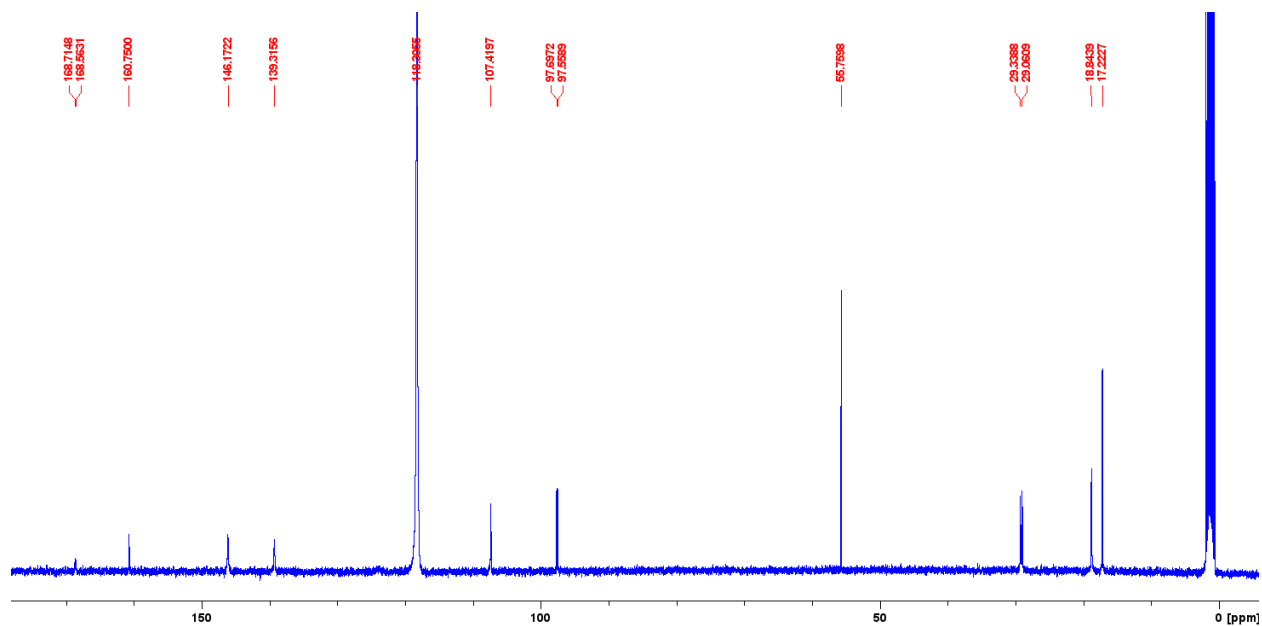
Figure S3. 18. Full ^{13}C NMR spectrum of **3b** in CD$_3$CN.
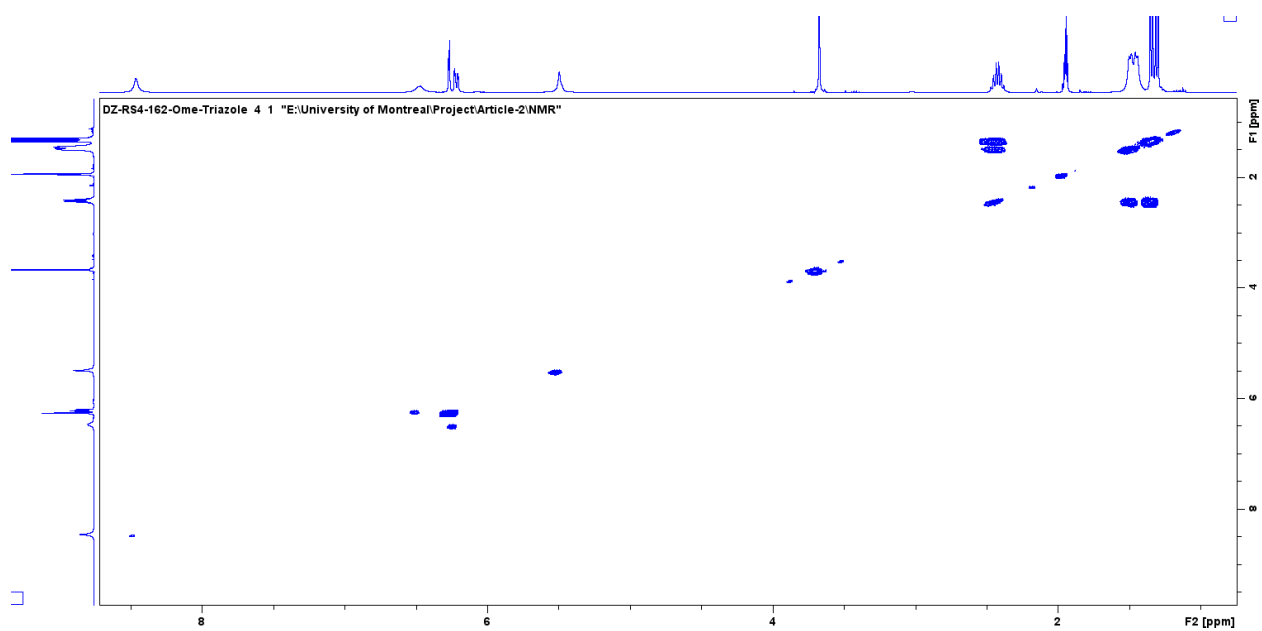
Figure S3. 19. Full ^{1}H-^{1}H COSY NMR spectrum of **3b** in CD$_3$CN.
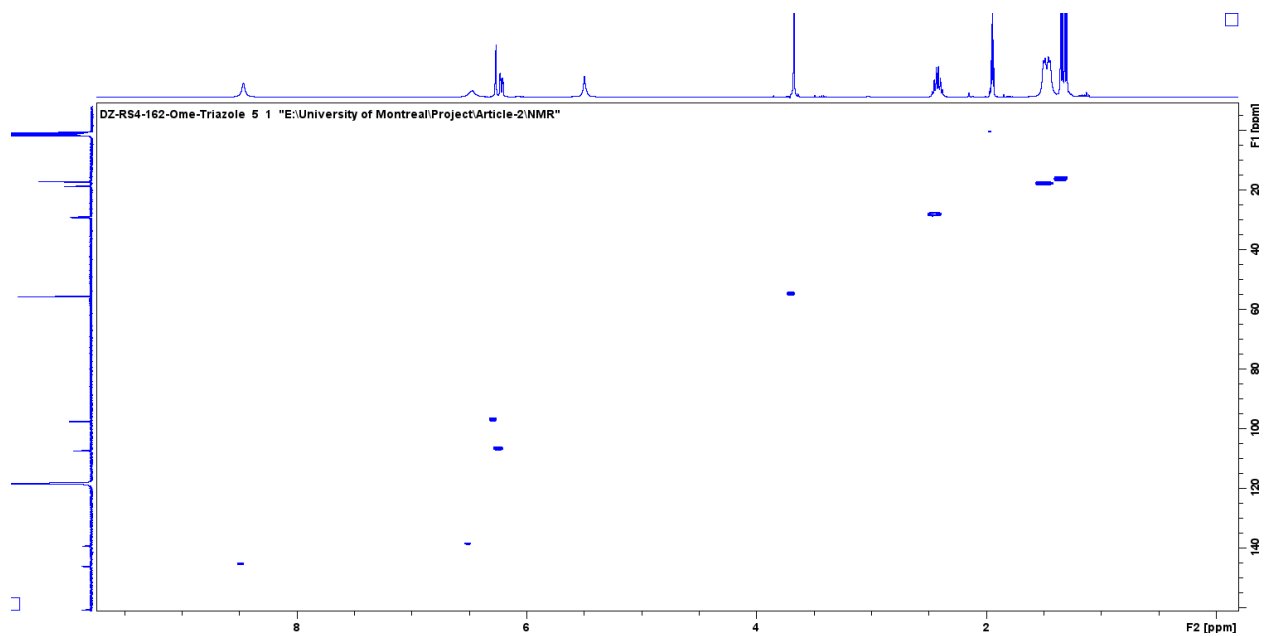
Figure S3. 20. Full HSQC-Edited NMR spectrum of **3b** in CD$_3$CN.
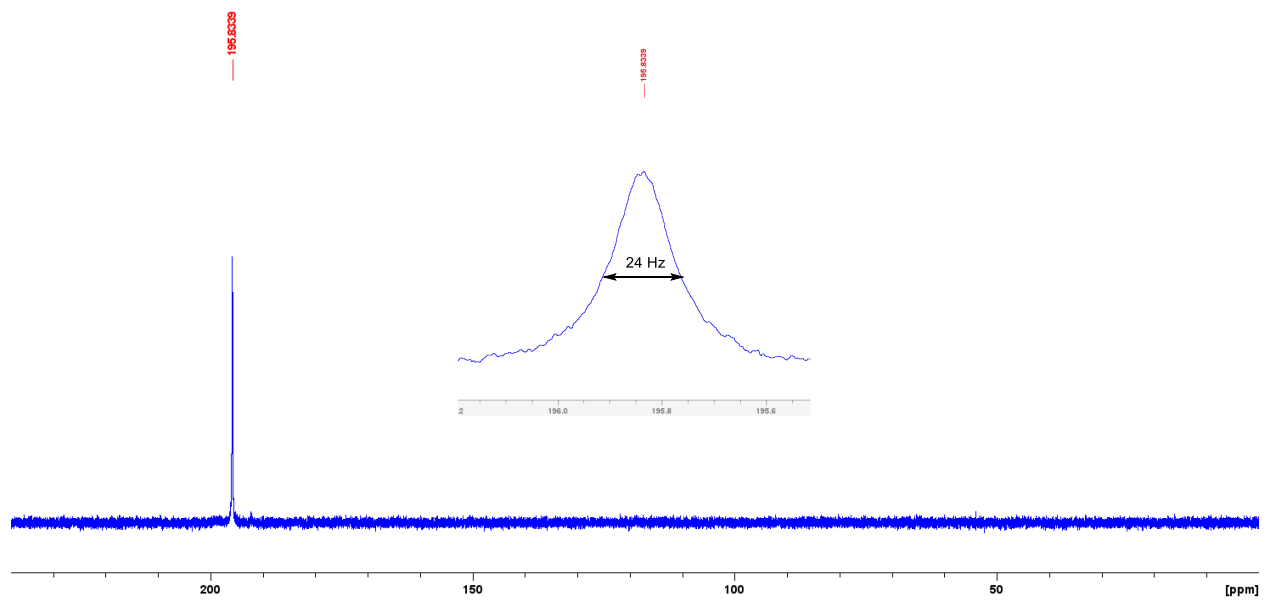
Figure S3. 21. ^{31}P{^{1}H} NMR spectrum of **3b** in CD$_3$CN.

Complex **3c**
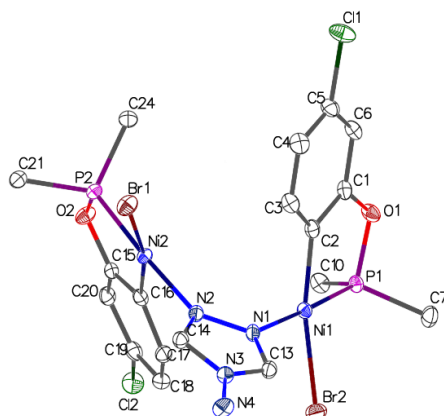
Figure S3. 22. Side view of the molecular diagram of compound **3c**. Thermal ellipsoids are shown at the 50 % probability level; hydrogen atoms are refined using a riding model.
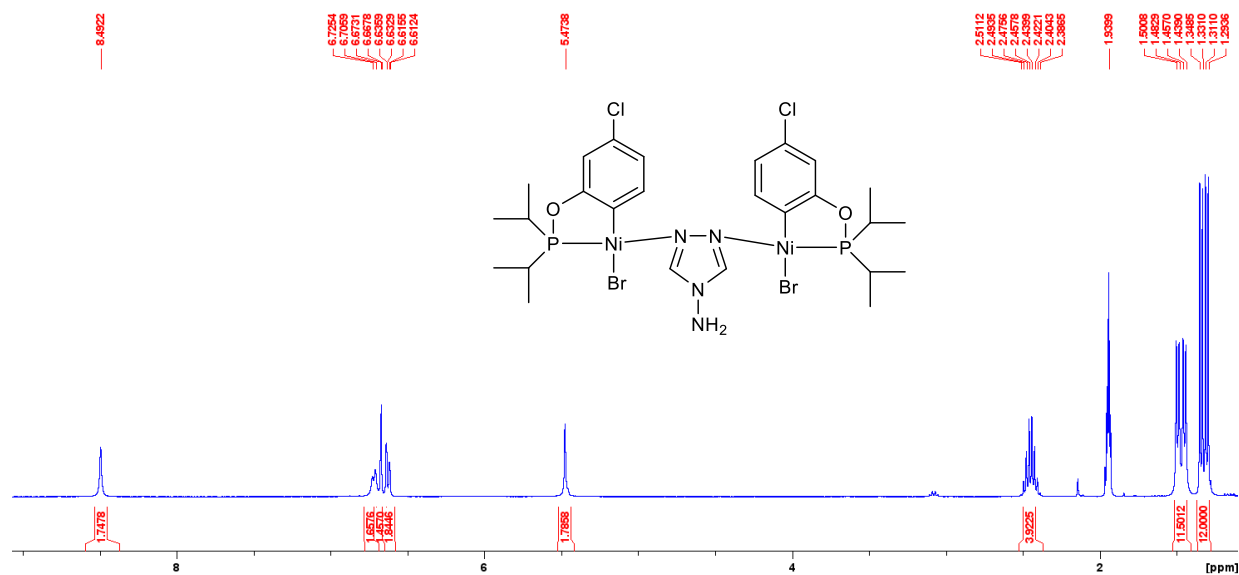
Figure S3. 23. Full ^{1}H NMR spectrum of **3c** in CD$_3$CN.

The Me protons show only two signals (each in the form of an AX doublet), suggesting that there is an axis of rotation along the N-NH$_2$ bond and bisecting the CH=N-N=CH bond. This axis renders the two Ni moieties equivalent. The existence of an axis of rotation would also explain why we have one set of ^{1}H signals for the two Ni moieties, and also one N=C-H. There is also a mirror plane that makes the two i-Pr groups (below and above the coordination plane) equivalent. The latter can only be the case if there is rapid, free rotation about the N-Ni bond.
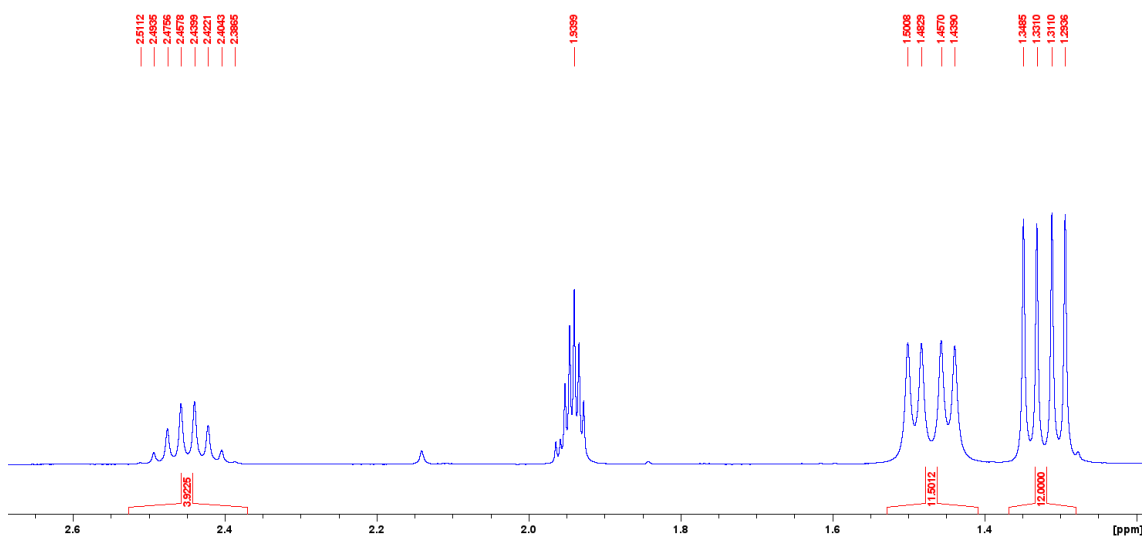
Figure S3. 24. The expanded aliphatic region of the ^{1}H NMR spectrum of **3c** in CD$_3$CN.
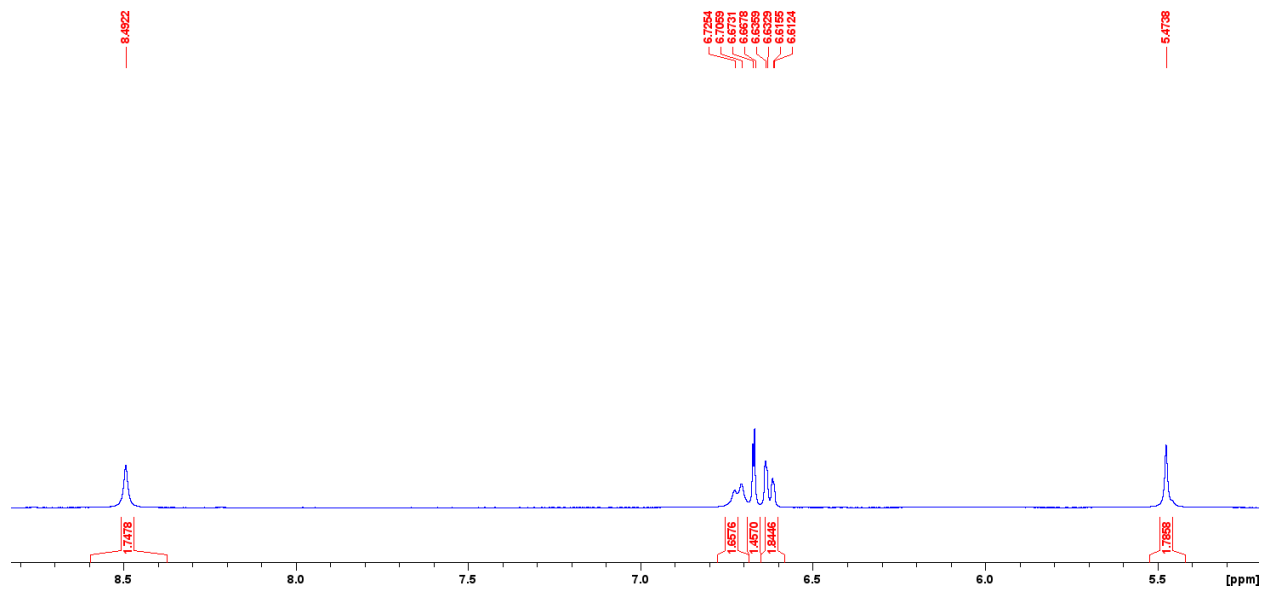
Figure S3. 25. The expanded aromatic region of the ^{1}H NMR spectrum of **3c** in CD$_3$CN.
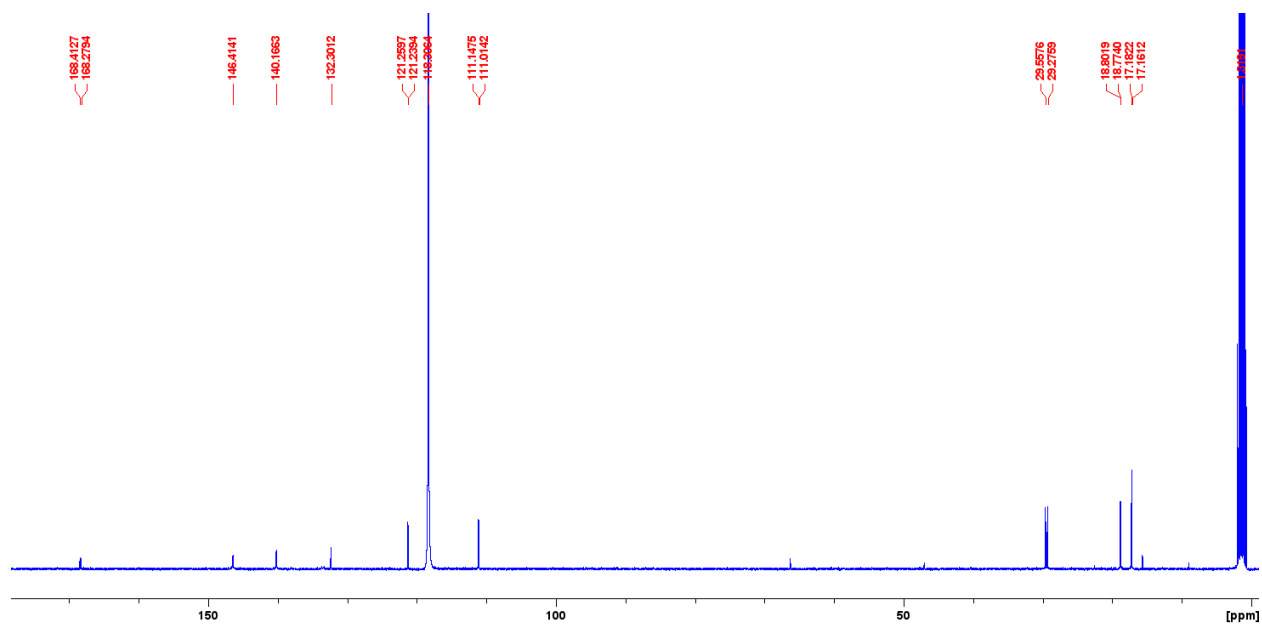
Figure S3. 26. Full ^{13}C NMR spectrum of **3c** in CD$_3$CN.
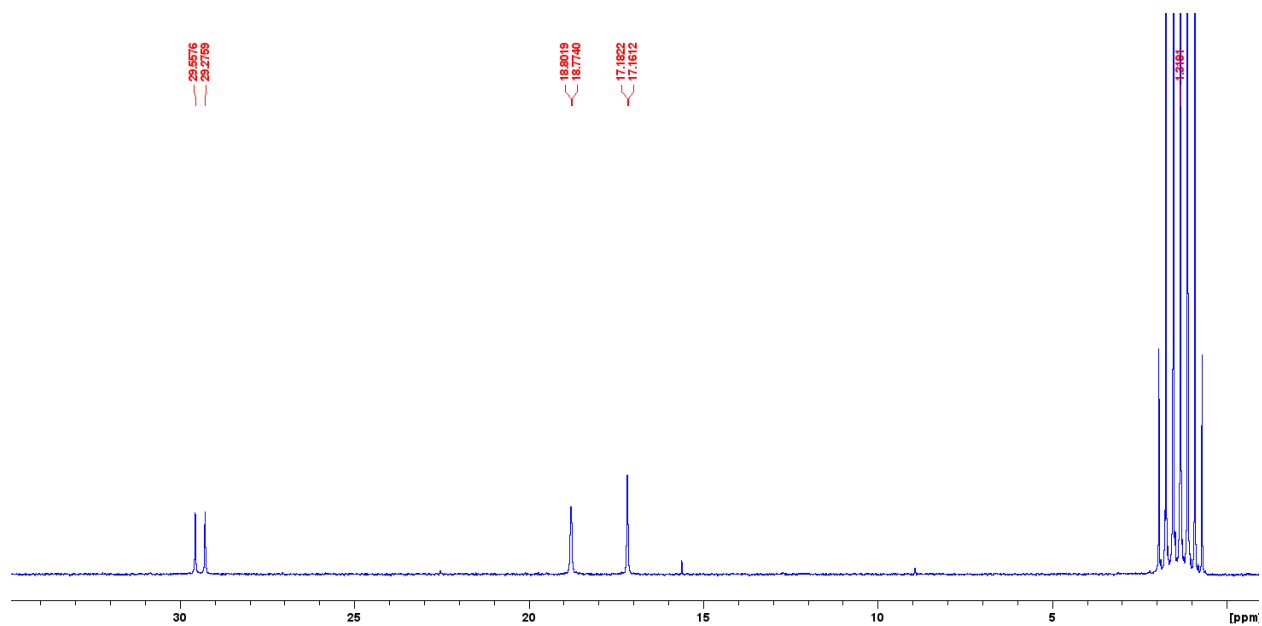
Figure S3. 27. The expanded aliphatic region of the ^{13}C NMR spectrum of **3c** in CD$_3$CN.
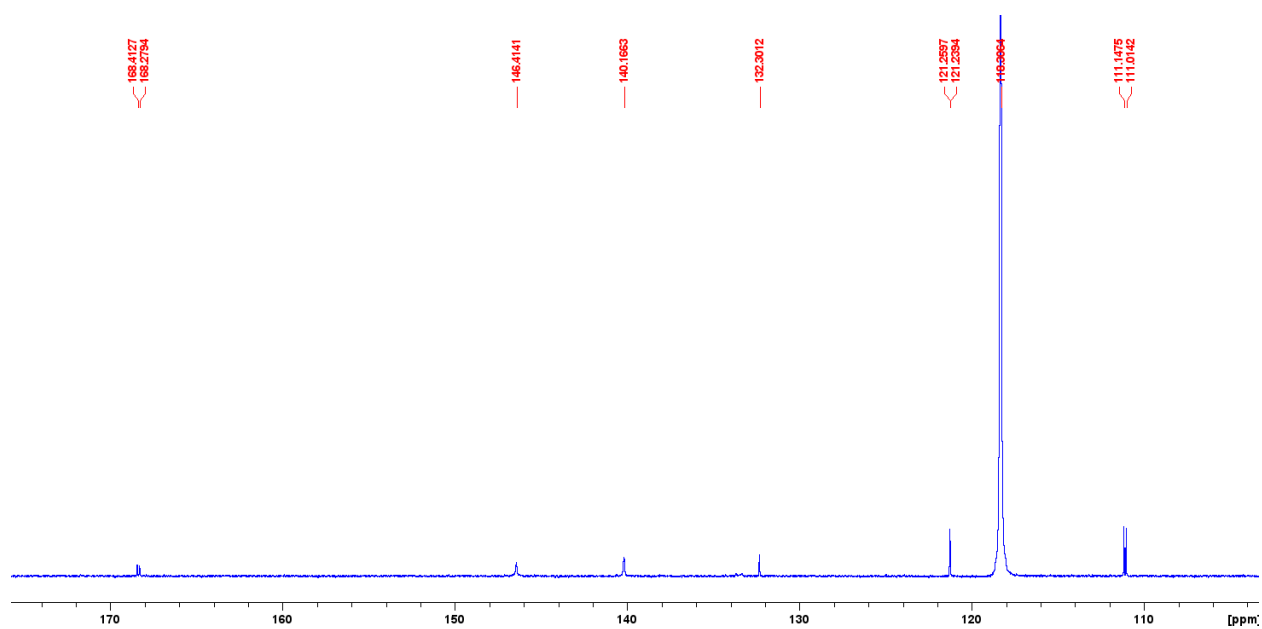
Figure S3. 28. The expanded aromatic region of the ^{13}C NMR spectrum of **3c** in CD$_3$CN.
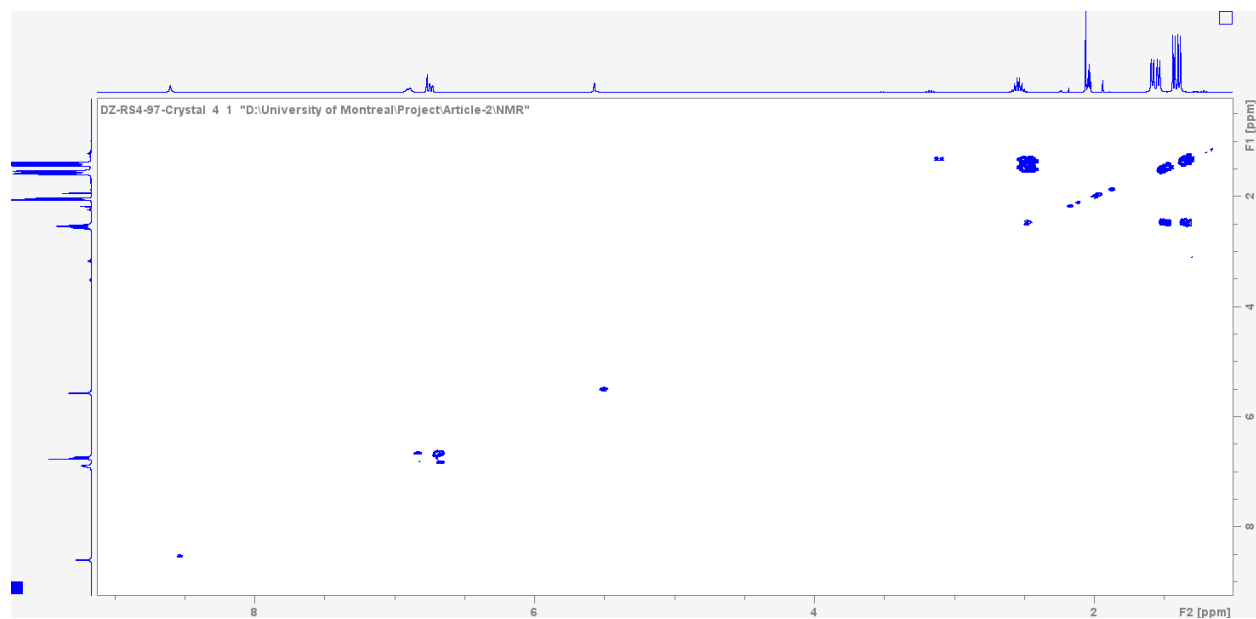
Figure S3. 29. Full ^{1}H-^{1}H COSY NMR spectrum of **3c** in C_6D_6.
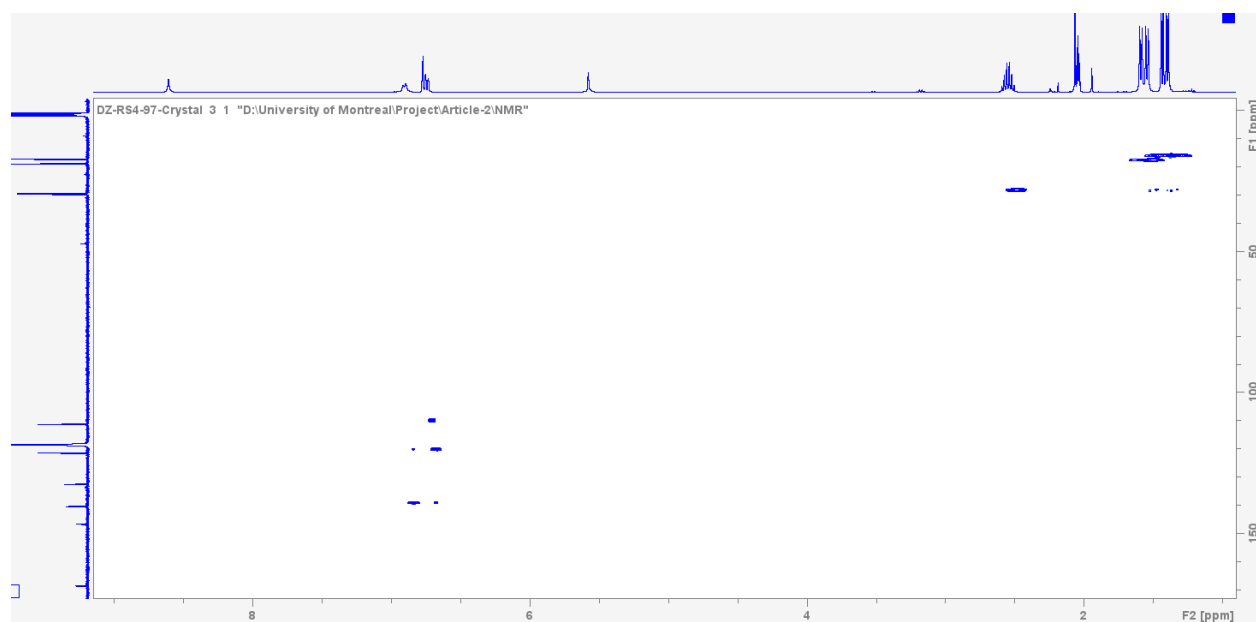
Figure S3. 30. Full HSQC - Edited NMR spectrum of **3c** in C_6D_6.
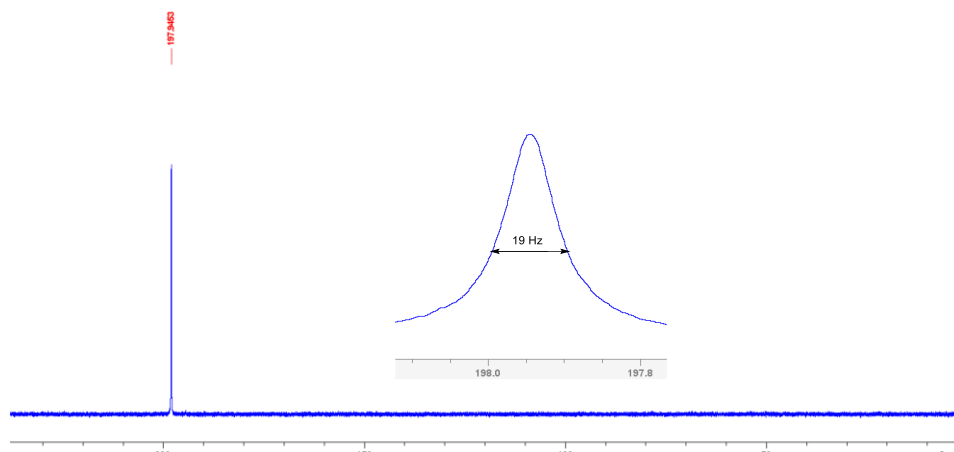
Figure S3. 31. $^{31}P\{^1H\}$ NMR spectrum of. **3c**. in CD$_3$CN.
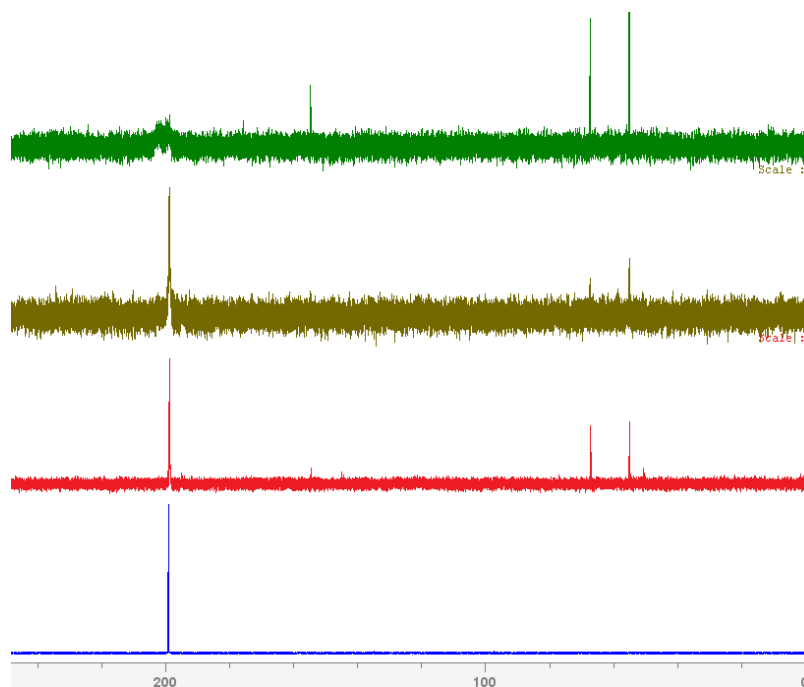
Figure S3. 32. $^{31}P\{^1H\}$ NMR spectra recorded for an acetonitrile sample of **1c** (0.15 M) to which were added successive quantities of triazole to measure the broadness (FWMH) of the resonance at ca. 199 ppm as a function of triazole amount, as follows: blue trace (0 equiv, or $\Delta_v^{1/2\eta} \approx 5$ Hz); red trace (2 equiv, $\Delta_v^{1/2\eta} \approx 26$ Hz); brown trace (3 equiv, $\Delta_v^{1/2\eta} \approx 56$ Hz); green trace (10 equiv).

Complex **3d**:
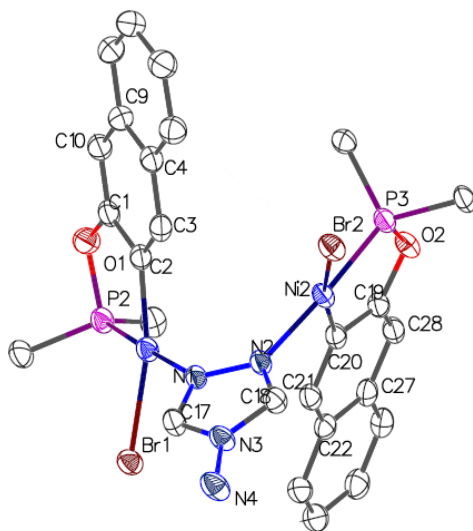
Figure S3. 33. Side view of the molecular diagram of compound **3d**. Thermal ellipsoids are shown at the 50% probability level; hydrogen atoms are refined via riding model.
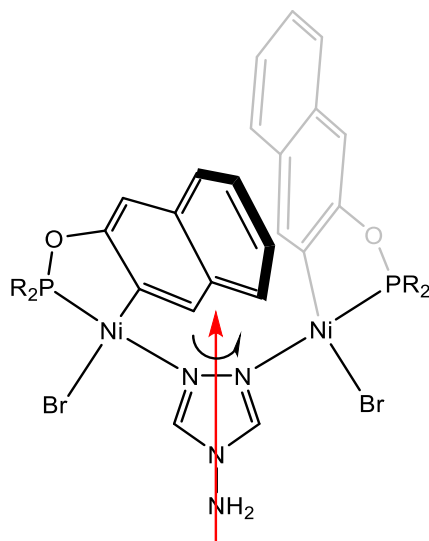
There appears to be a C_2 axis in this complex which is parallel with the N-NH$_2$ bond and bisects the CHN-NCH bond. The planes defined by Ni/P/O/C/C atoms and the naphthyl fragment are at 62° to each other.
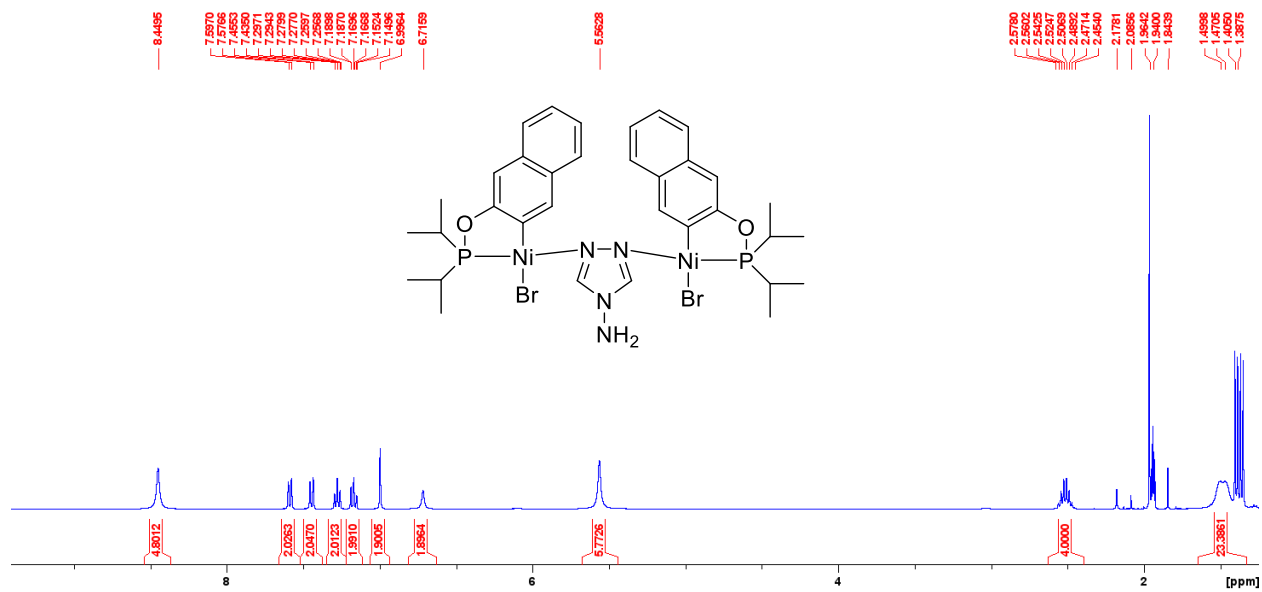
Figure S3. 34. Full ^{1}H NMR spectrum of **3d** in CD$_3$CN.
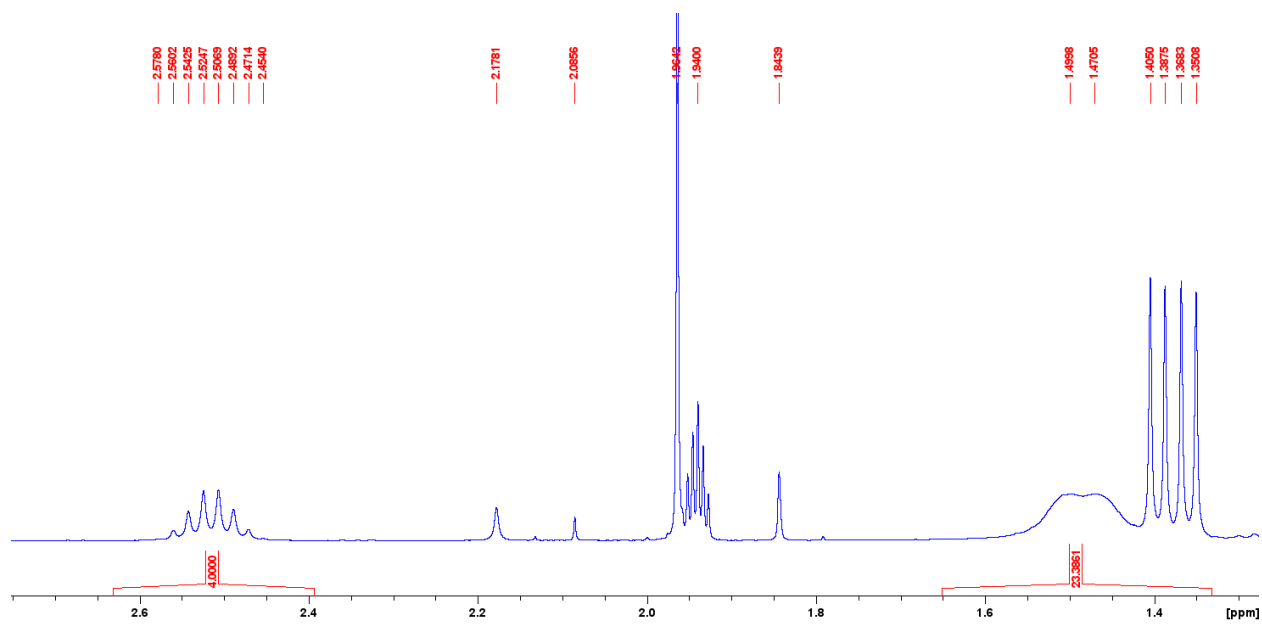
Figure S3. 35. The expanded aliphatic region of the ^{1}H NMR spectrum of **3d** in CD$_3$CN.
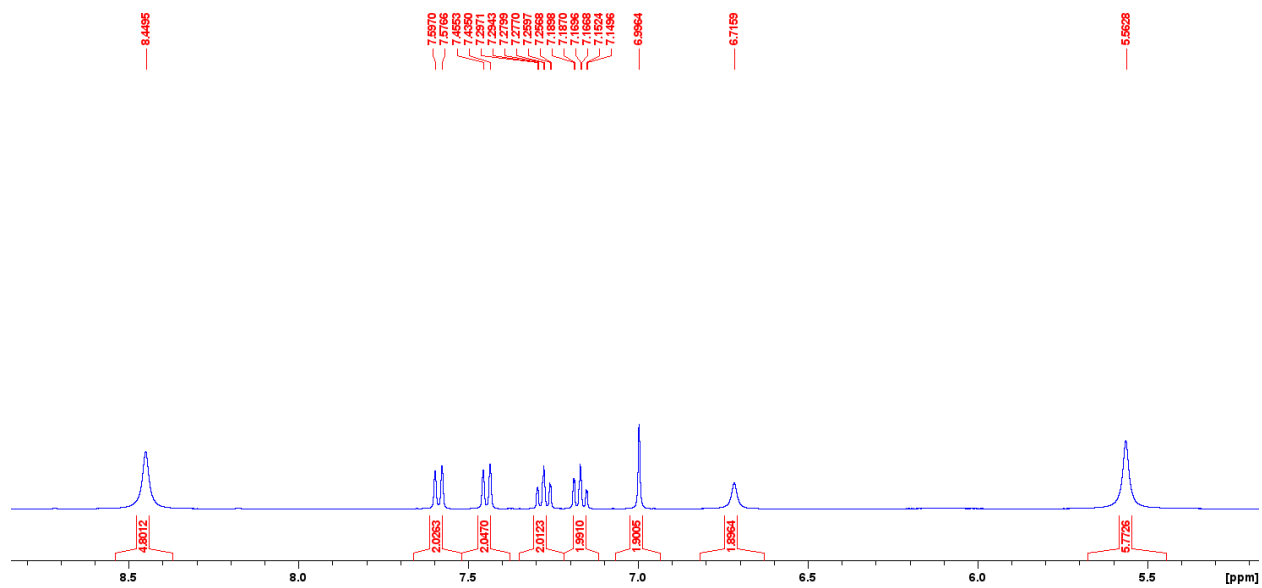
Figure S3. 36. The expanded aromatic region of the ^{1}H NMR spectrum of **3d** in CD$_3$CN.
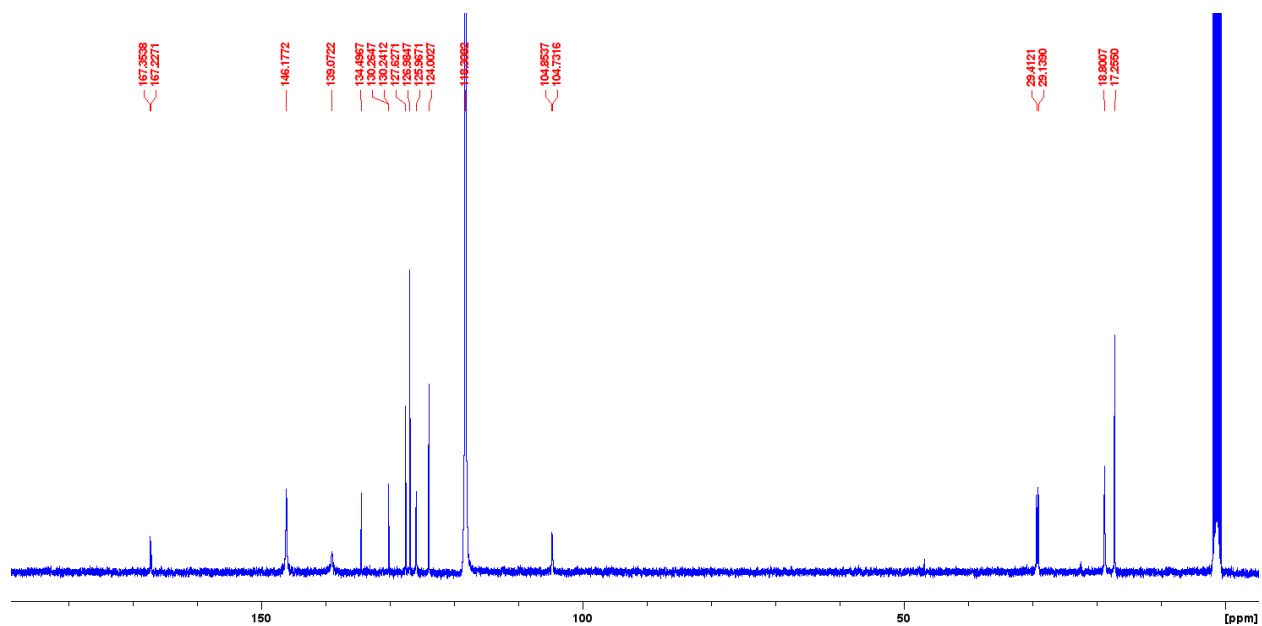
Figure S3. 37. Full ^{13}C NMR spectrum of **3d** in CD$_3$CN.
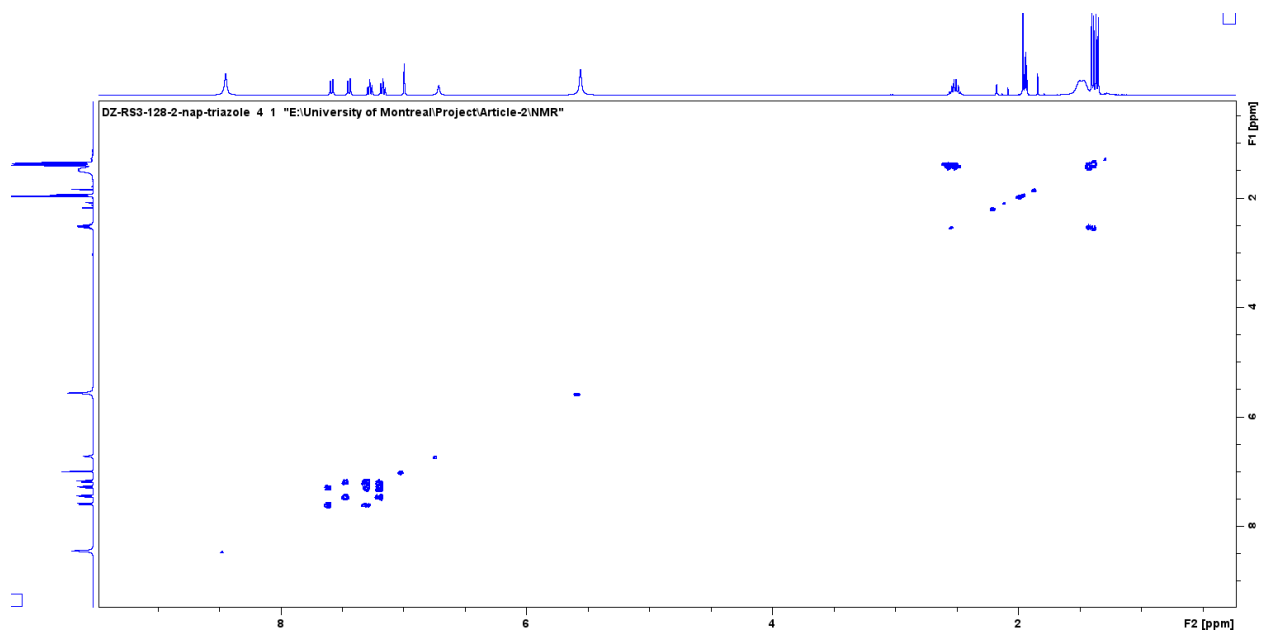
Figure S3. 38. Full ^1H-^1H COSY NMR spectrum of **3d** in CD$_3$CN.
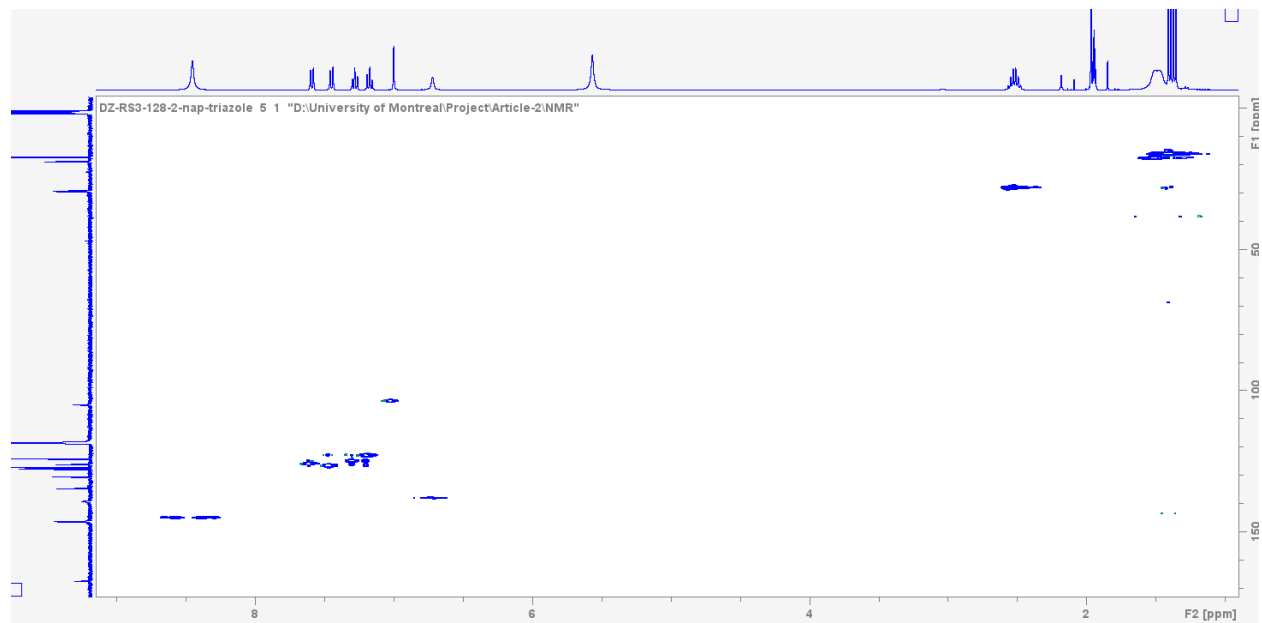
Figure S3. 39. Full HSQC-Edited NMR spectrum of **3d** in CD$_3$CN.
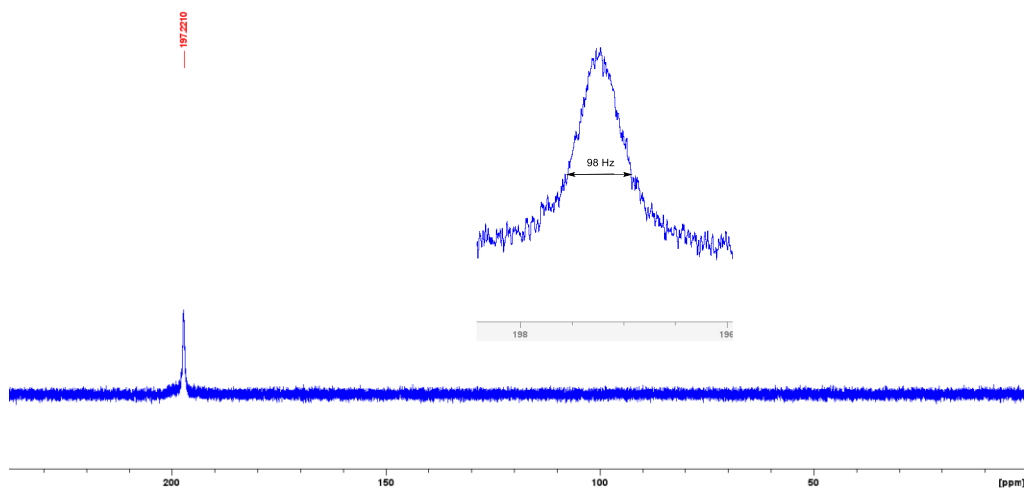
Figure S3. 40. $^{31}P\{^1H\}$ NMR spectrum of **3d** in CD$_3$CN.
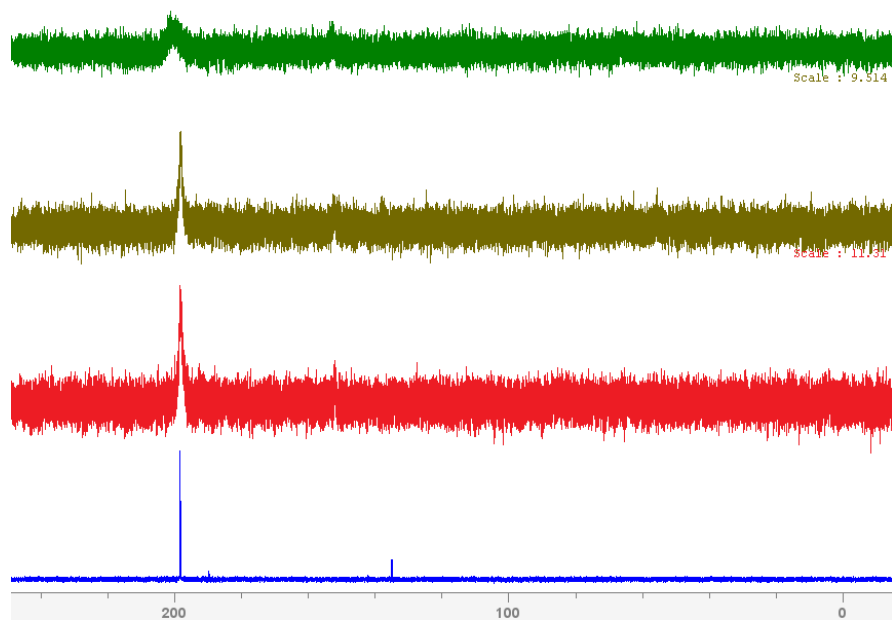
Figure S3. 41. $^{31}P\{^1H\}$ NMR spectra recorded for an acetonitrile sample of **1d** (0.15 M) to which were added successive quantities of triazole to measure the broadness (FWMH) of the resonance at ca. 198 ppm as a function of triazole amount, as follows: blue trace (0 equiv, or $\Delta_v^{1/2\eta} \approx 10$ Hz); red trace (2 equiv, $\Delta_v^{1/2\eta} \approx 200$ Hz); brown trace (3 equiv, $\Delta_v^{1/2\eta} \approx 228$ Hz); green trace (10 equiv, $\Delta_v^{1/2\eta} \approx 1000$ Hz).

Complex **2e**
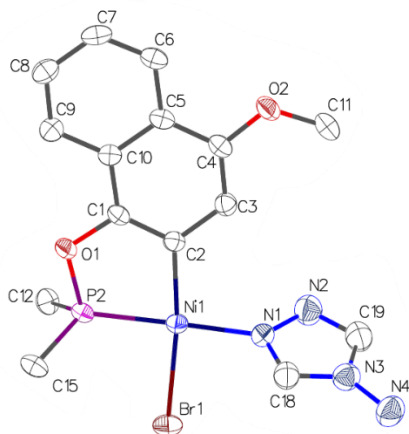
Figure S3. 42. Side view of the molecular diagram of compound **2e**. Thermal ellipsoids are shown at the 50% probability level; hydrogen atoms are refined via riding model.
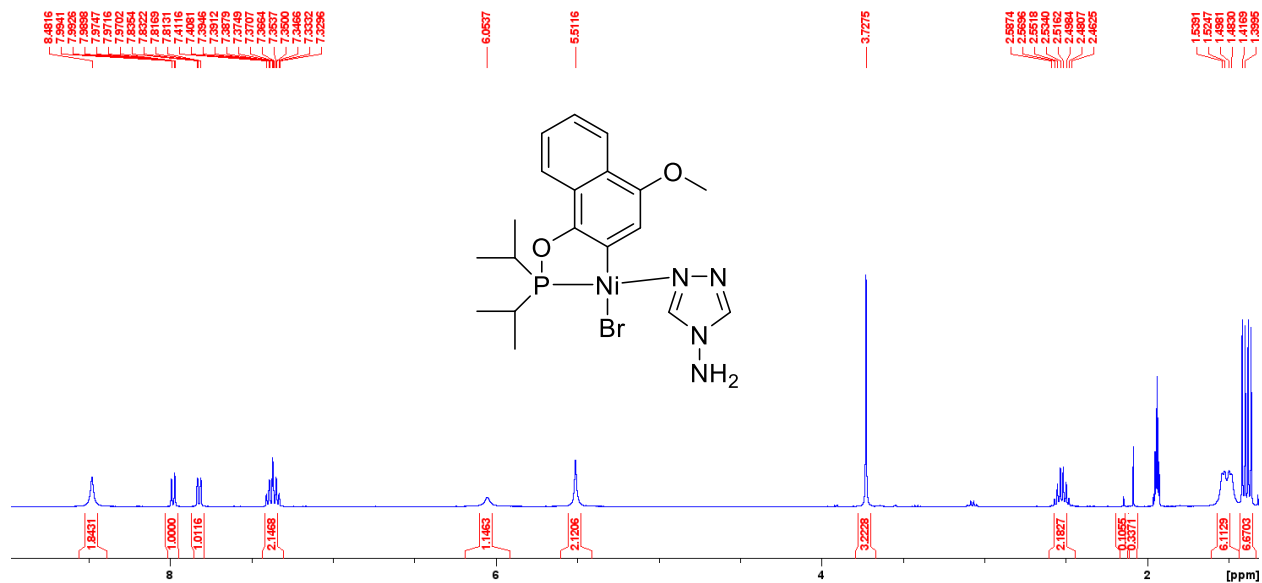
Figure S3. 43. Full ^{1}H NMR spectrum of **2e** in CD_3CN.
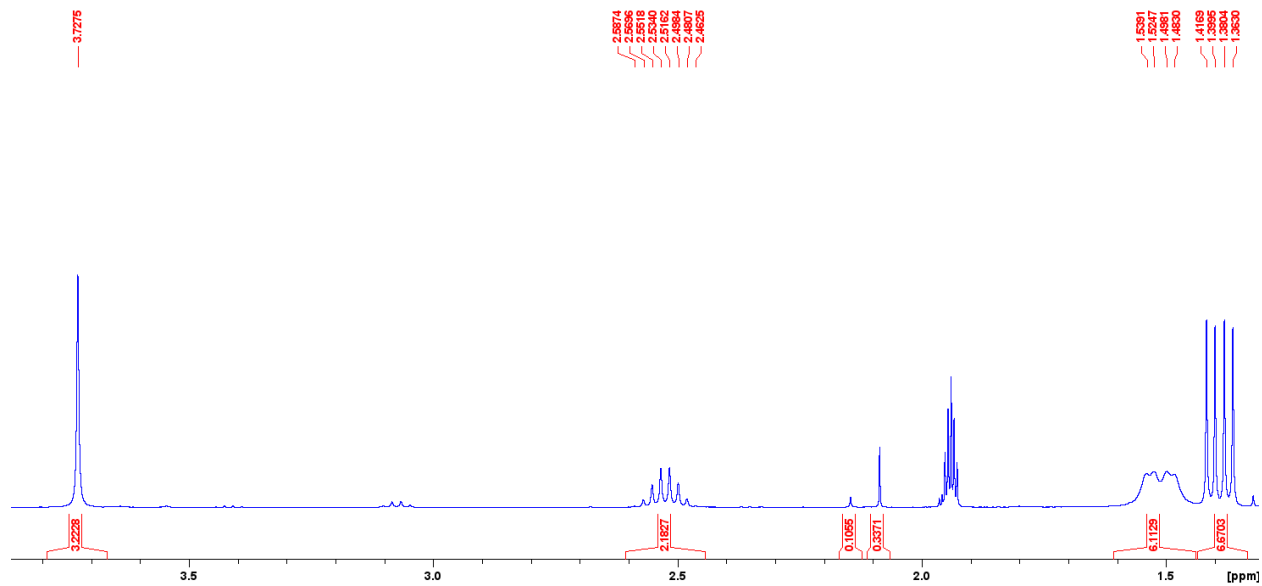
Figure S3. 44. The expanded aliphatic region of the ^{1}H NMR spectrum of **2e** in CD$_3$CN.
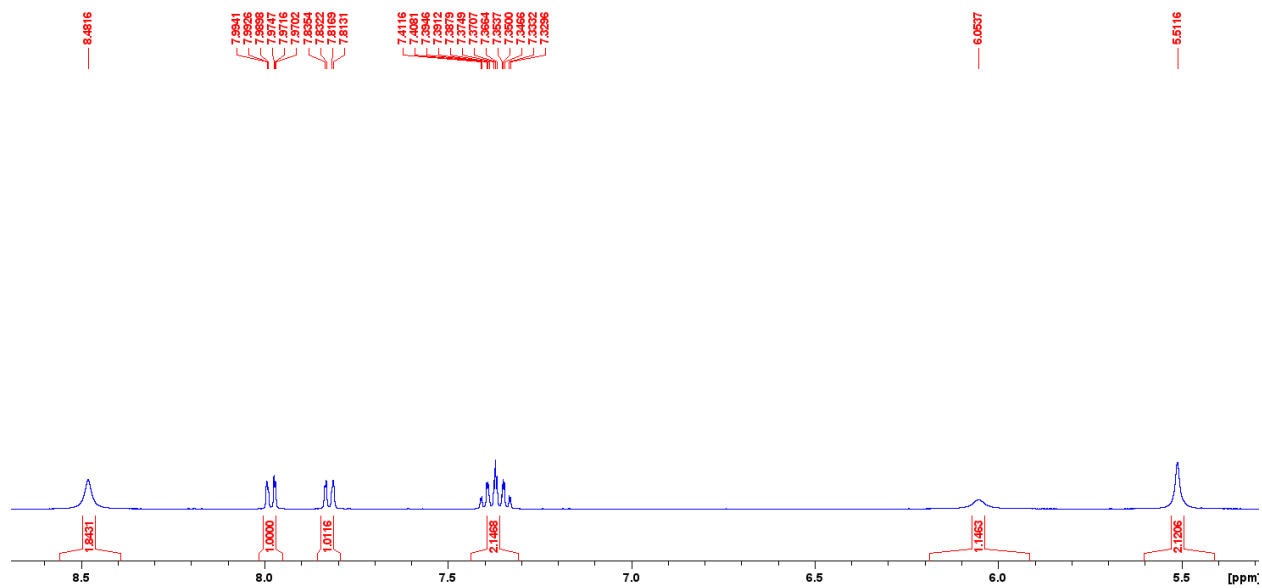
Figure S3. 45. The expanded aromatic region of the ^{1}H NMR spectrum of **2e** in CD$_3$CN.
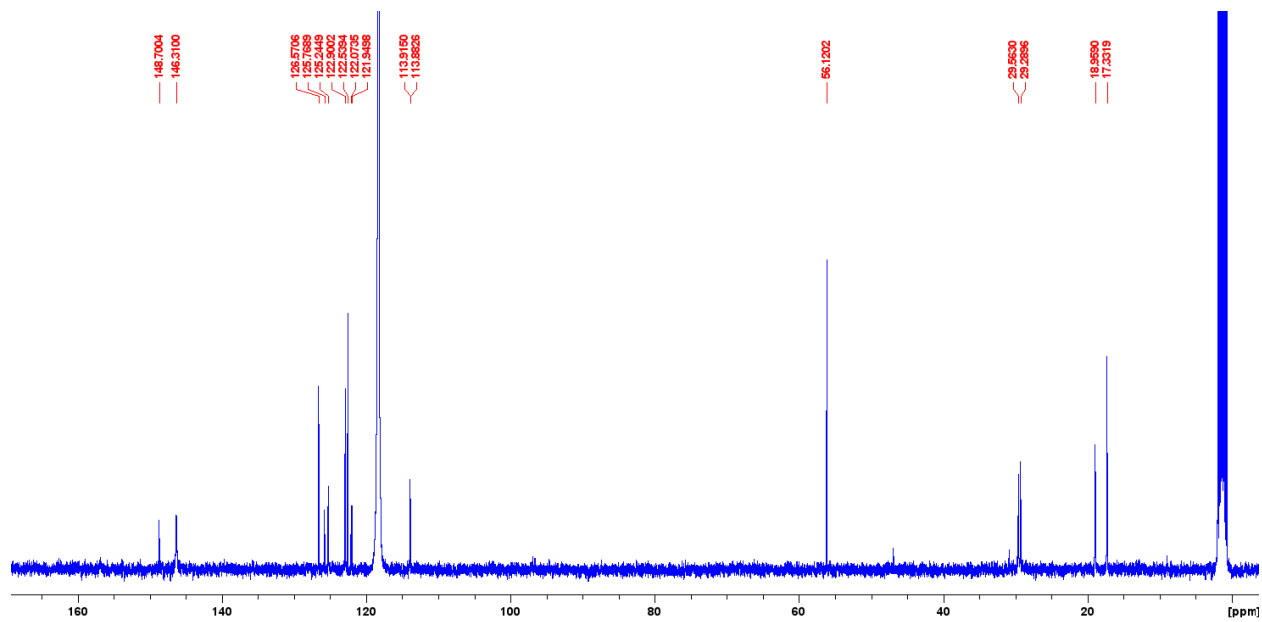
Figure S3. 46. Full ^{13}C NMR spectrum of **2e** in CD$_3$CN.
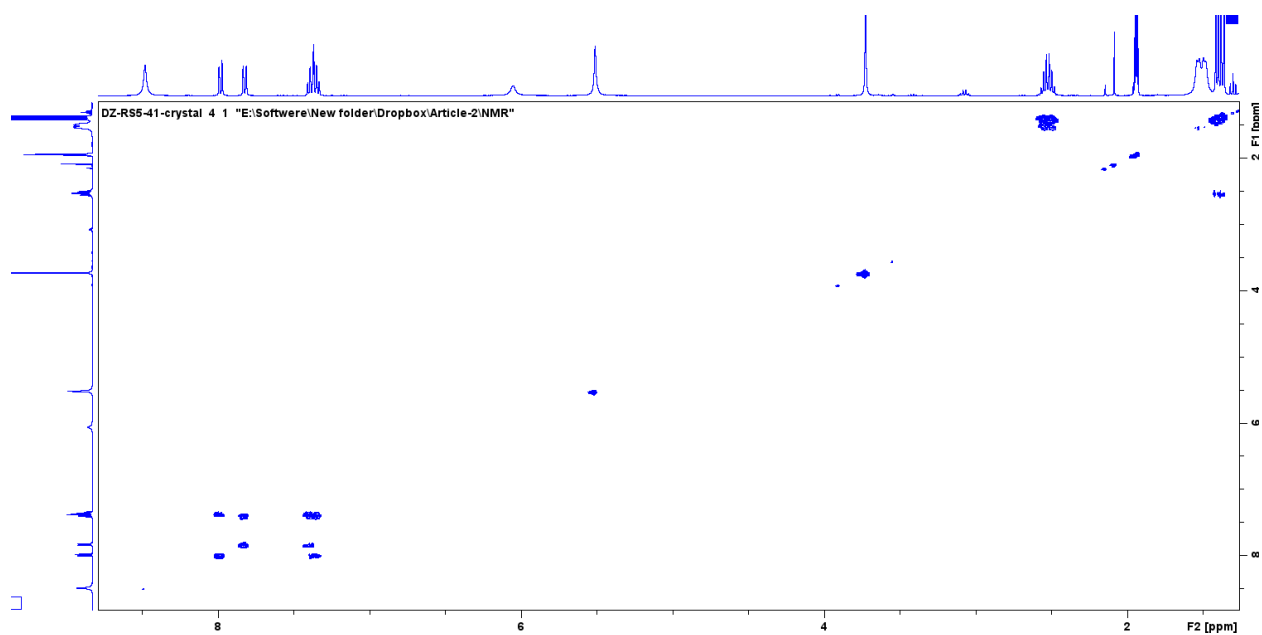
Figure S3. 47. Full COSY NMR spectrum of **2e** in CD$_3$CN.
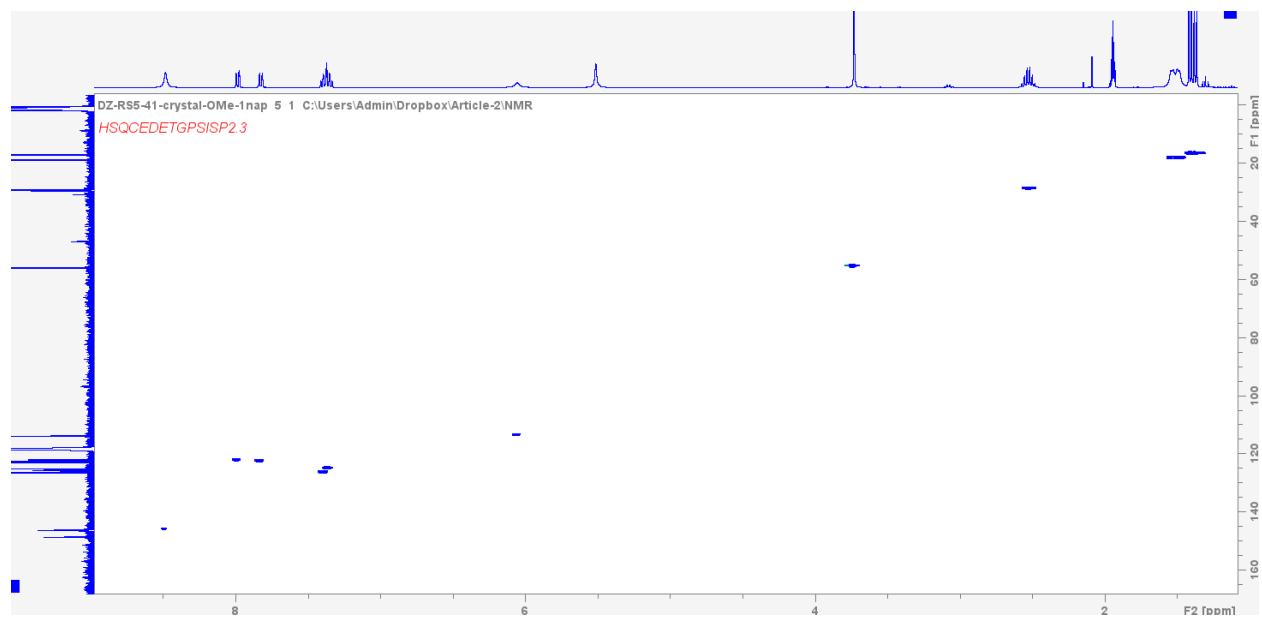
Figure S3. 48. Full HSQC-Edited NMR spectrum of **2e** in CD$_3$CN.
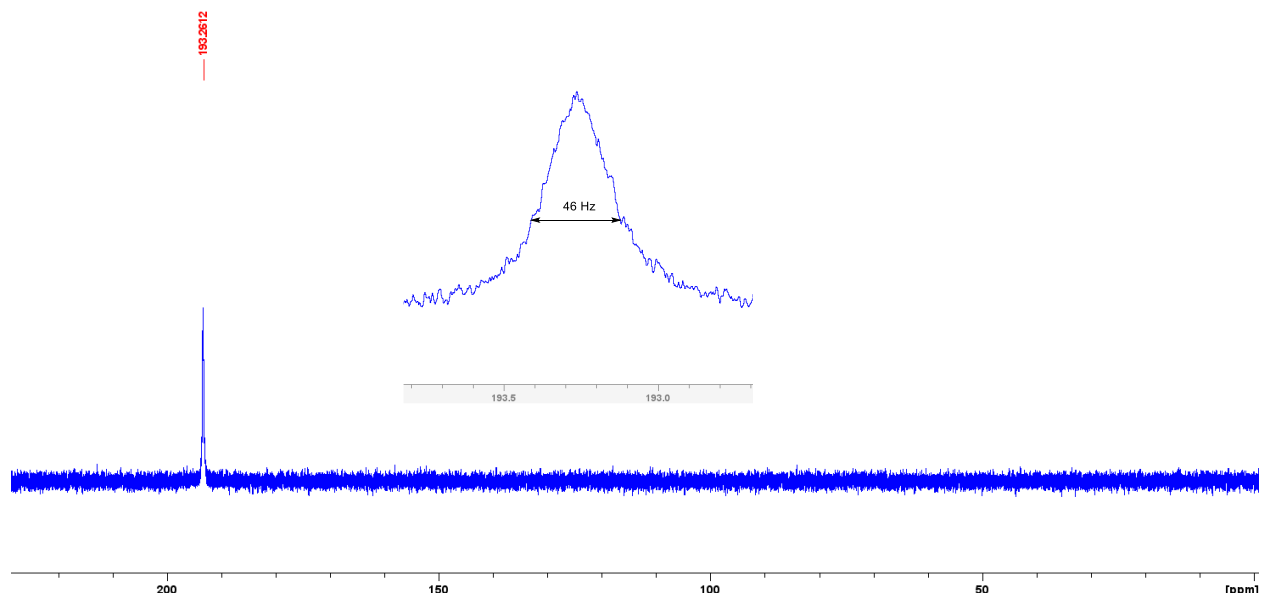
Figure S3. 49. ^{31}P$\{^1$H$\}$ NMR spectrum of **2e** in CD$_3$CN.
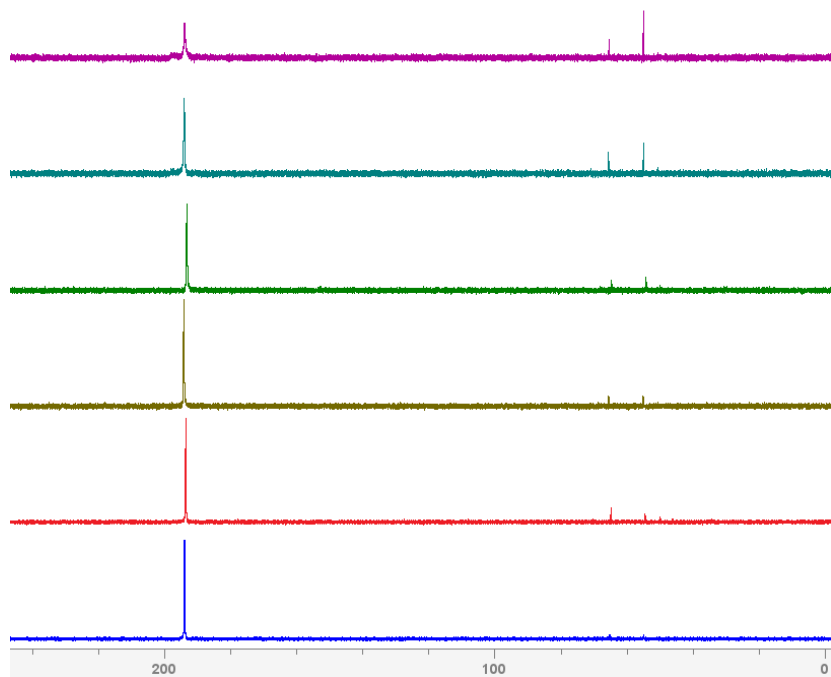
Figure S3. 50. $^{31}P\{^1H\}$ NMR spectrum of **2e** with various amounts of triazole added as follows (bottom to top): 0 equiv (blue trace); 0.25 equiv (red trace); 0.5 equiv (brown trace); 1.0 equiv (green trace); 1.5 equiv (equiv (blue-green trace); 3 equiv (purple trace), 2 eq, 1.5 eq, 0.5 eq,). The line-broadening values ($\Delta_v^{1/2\eta}$, in Hz) were measured to be ca. 20 (blue trace), 28 (red trace), and 100 (purple trace).

S3.4 Other relevant spectra and calibration procedure
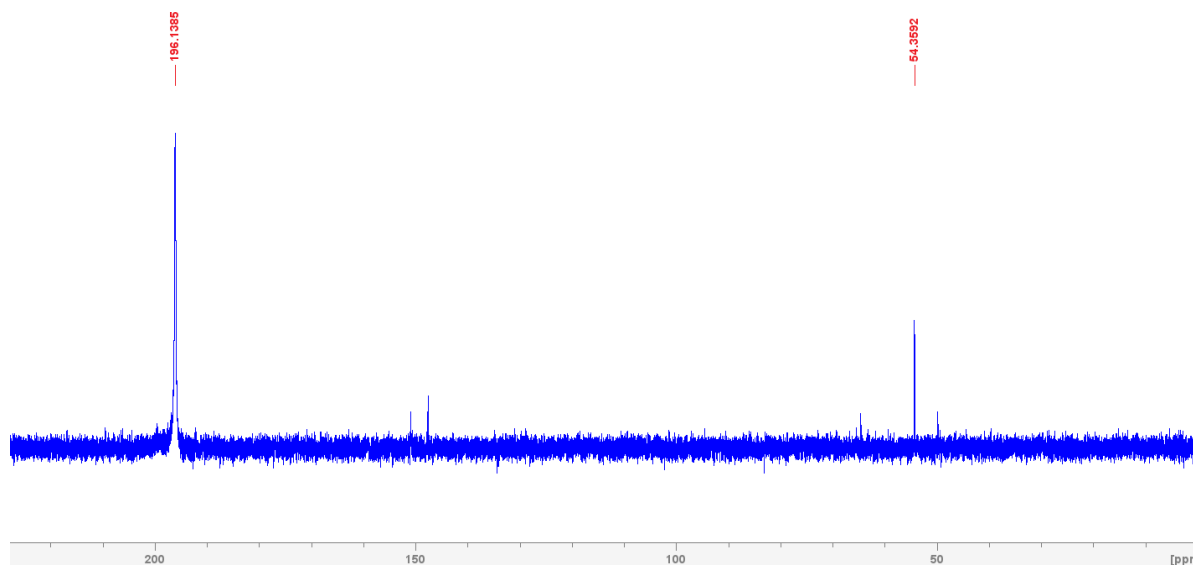
Figure S3. 51. ^{31}P NMR spectrum of the reaction mixture containing the dimer **1a** and 0.5 equiv of triazole (Ni : triazole ratio of 2:1).
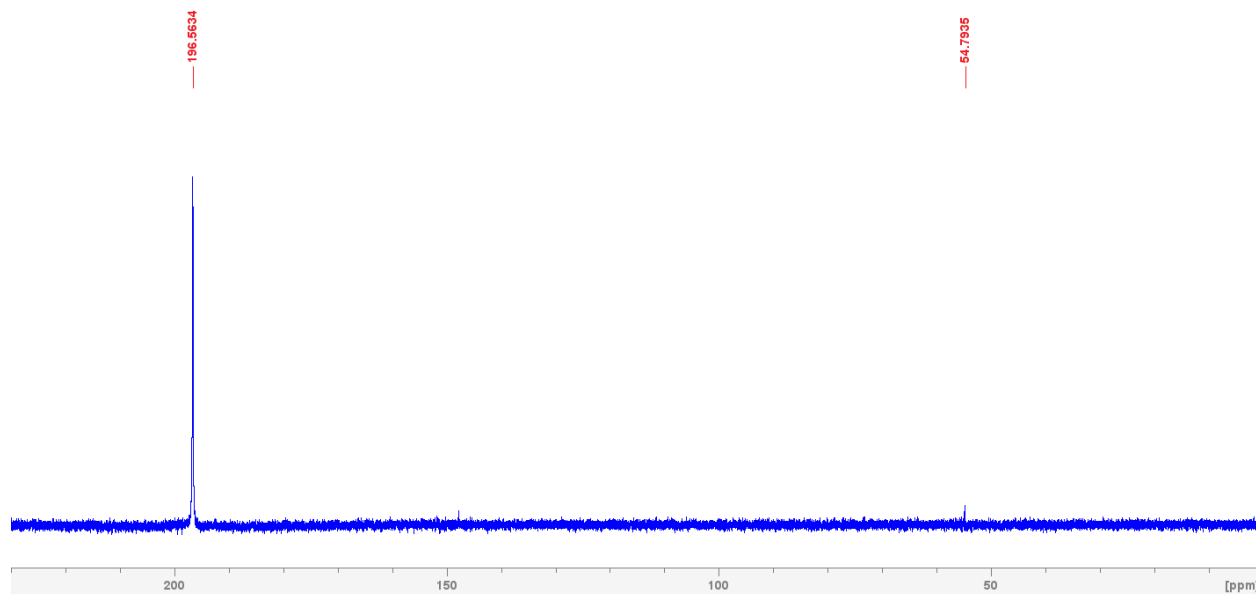
Figure S3. 52. ^{31}P NMR spectrum of the reaction mixture containing the dimer **1b** and 0.5 equiv of triazole (Ni : triazole ratio of 2:1).
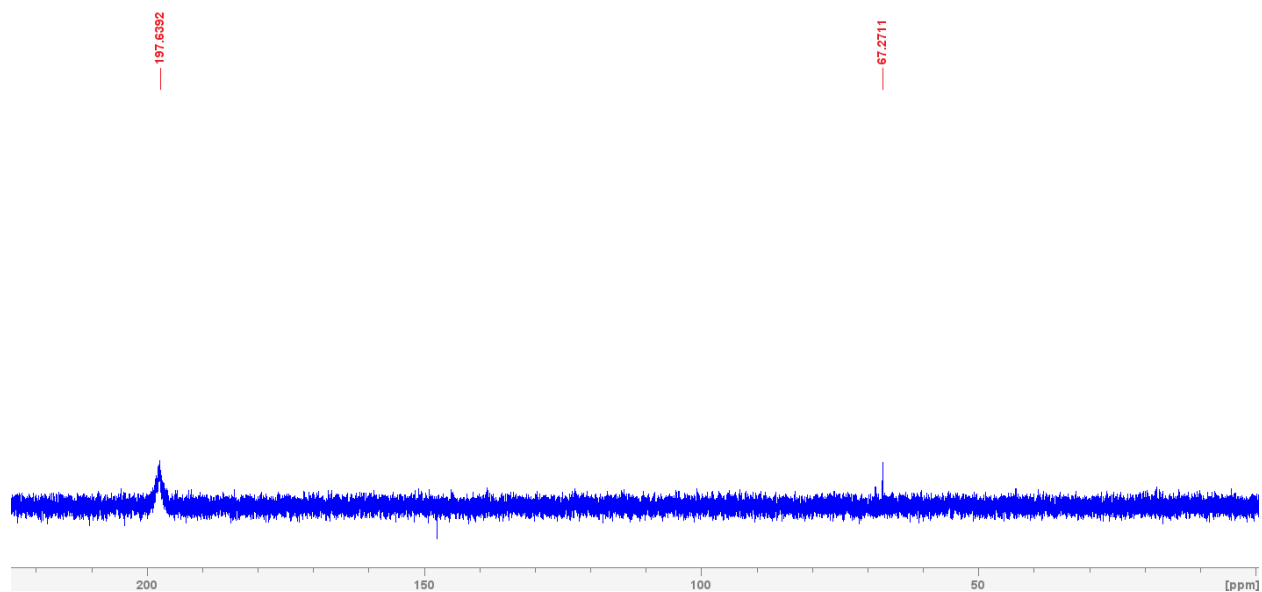
Figure S3. 53. ^{31}P NMR spectrum of the reaction mixture containing the dimer **1c** and 0.5 equiv of triazole (Ni : triazole ratio of 2:1).
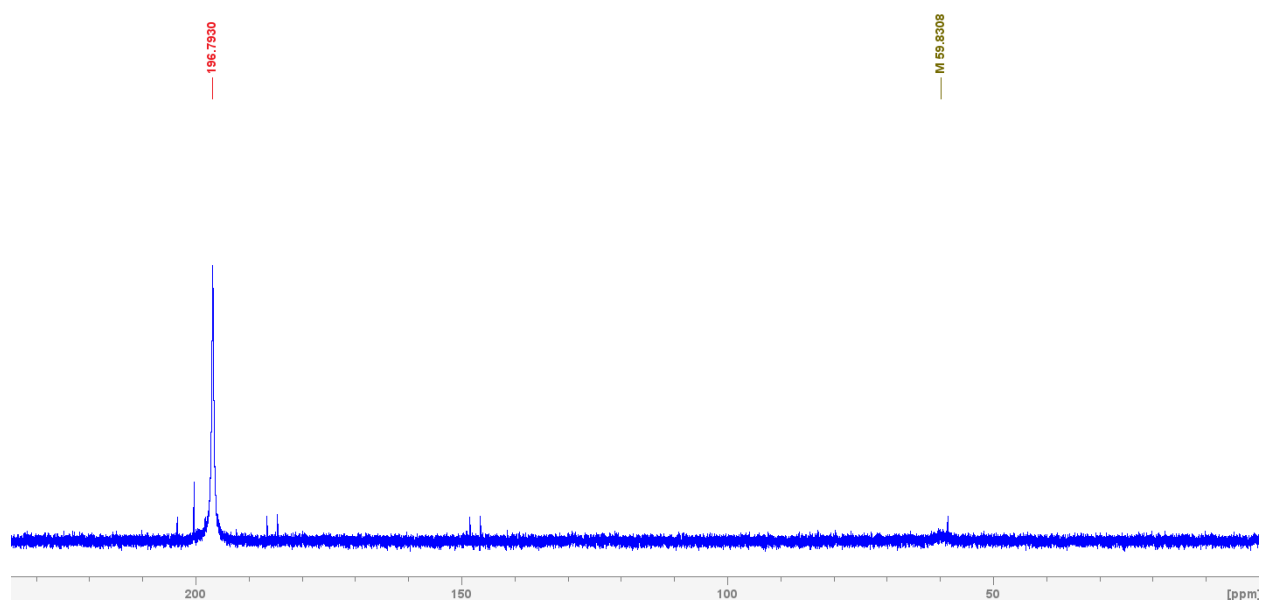
Figure S3. 54. ^{31}P NMR spectrum of the reaction mixture containing the dimer **1d** and 0.5 equiv of triazole (Ni: triazole ratio of 2:1).

271
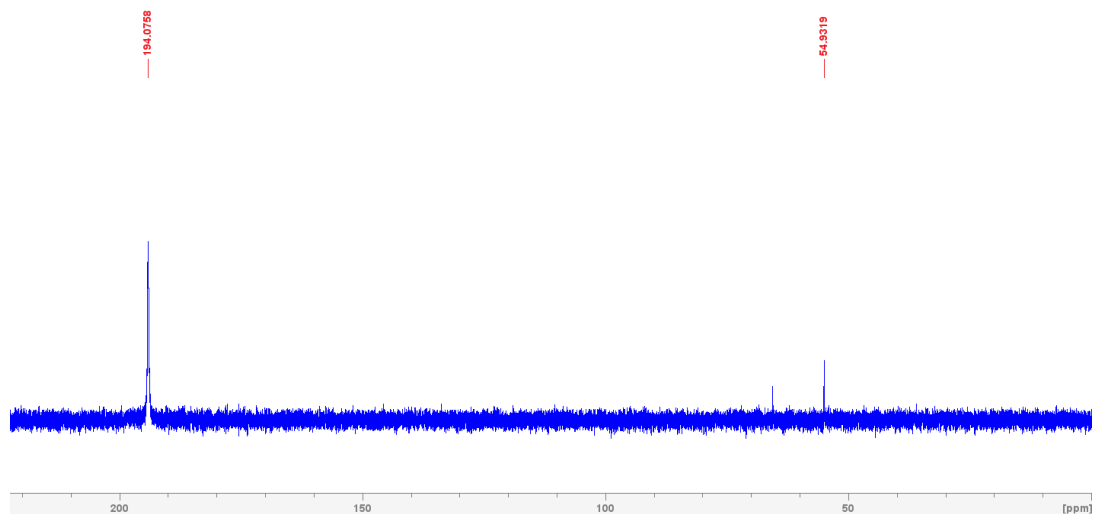
Figure S3. 55. ^{31}P NMR spectrum of the reaction mixture containing the dimer **1e** and 0.5 equiv of triazole (Ni: triazole ratio of 2:1).

<u>Procedure for estimating extent of decomposition.</u> To estimate the extent of decomposition taking place when our cyclonickellated complexes are treated with 4-Amino-4H-1,2,4-triazole, we conducted the following calibration experiments. Acetonitrile solutions of the dimeric precursors **1** were treated with 2-4 equiv of PPh$_3$ and the mixtures analyzed by ^{31}P{^{1}H} NMR spectroscopy. The spectra displayed a very broad signal at ca. – 1.6 ppm, implying a dynamic exchange process. Addition of two equivalents of the triazole substrate to these mixtures caused a color change and resulted in the precipitation of a white solid. NMR analysis of this mixture showed the emergence of two ^{31}P singlets, one for the triazole adduct in question and the other for free PPh$_3$ (ca. -4 ppm). Integration values for the two signals indicated ca. 10% signal loss, which we attribute to the decomposition product.
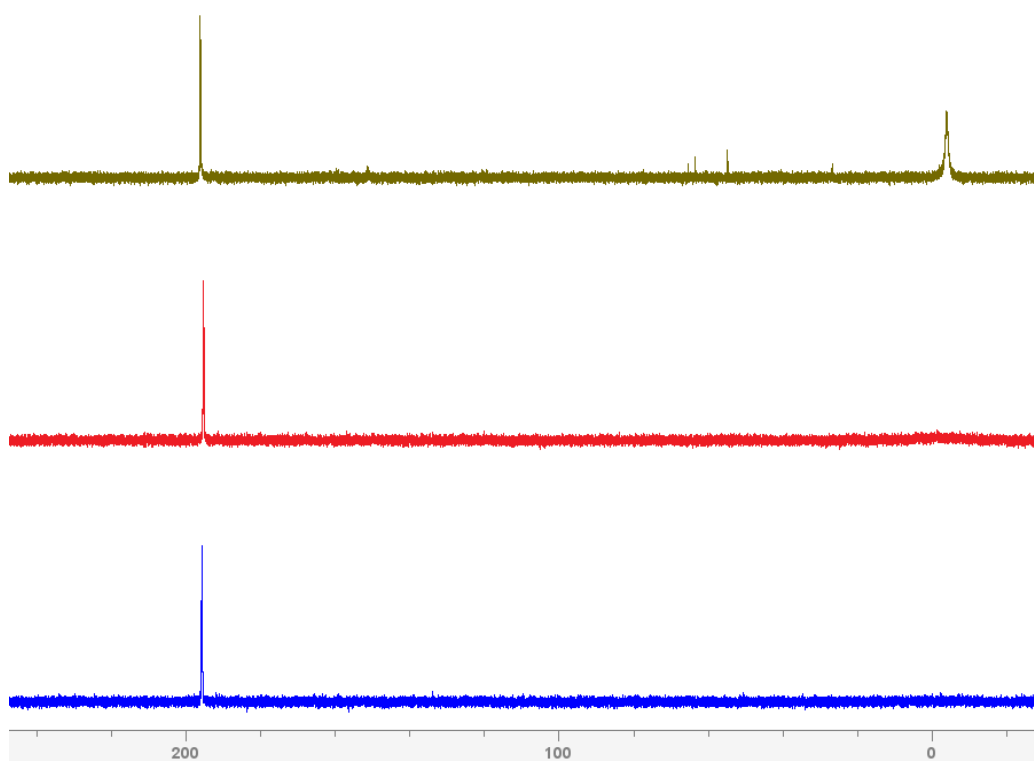
Figure S3. 56. ^{31}P NMR spectrum of the reaction mixture containing the dimer 1b in MeCN (blue trace), with 4 equiv of PPh$_3$ (red trace), and 1 equiv of triazole.

S3.5 Crystallographic data tables

Table S3. 1: Crystal description and refinement indicators for compounds **2a**, **3b**, and **3c**

	2a	2e
chemical formula	$C_{18}H_{32}BrN_4NiO_2P$	$C_{19}H_{26}BrN_4NiO_2P$
crystal colour	brown	brown
crystal size (mm)	$0.07 \times 0.09 \times 0.11$	$0.101 \times 0.147 \times 0.157$
index ranges	$-22 \le h \le 22$ $-12 \le k \le 12$ $-15 \le l \le 15$	$-10 \le h \le 11$ $-9 \le k \le 9$ $-33 \le l \le 34$
Fw; $F(000)$	506.06; 1048.0	512.03; 1048.0
T (K)	100	150
wavelength (Å)	1.54178	1.34139
space group	$P2_1/c$	$P2_1/c$
a (Å)	18.1212(7)	9.5653(3)
b (Å)	10.4717(4)	8.0558(3)
c (Å)	12.7679(5)	28.0138(10)
α (deg)	90	90
β (deg)	109.572(2)	96.011(2)
γ (deg)	90	90
Z	4	4
V (Å^3)	2282.84(16)	2146.77(13)
ρ_{calcd} (g·cm^{-3})	1.472	1.584
μ (mm^{-1})	4.096	6.962
θ range (deg); completeness	2.588–70.245; 0.985	5.519–54.901; 0.983
collected reflections; R_σ	42874; 0.0375	19434; 0.0310
unique reflections; R_{int}	4278; 0.0779	3986; 0.0378
R1[a]; wR2[b] [I > 2σ(I)]	0.0519; 0.1296	0.0363; 0.0948
R1; wR2 [all data]	0.0619; 0.1375	0.0389; 0.0962
GOOF	1.031	1.104
largest diff peak and hole	0.84 and -1.17	0.70 and -0.59

[a] $R_1 = \Sigma(||F_o|-|F_c||)/\Sigma|F_o|$

[b] $wR_2 = \{\Sigma[w(F_o^2-F_c^2)^2]/\Sigma[w(F_o^2)^2]\}^{1/2}$

Table S3. 2: Crystal description and refinement indicators for compounds **3d** and **2e**.

	3b	3c	3d
chemical formula	$C_{28}H_{44}Br_2N_4Ni_2O_4P_2$	$C_{26}H_{38}N_4O_2P_2Cl_2Ni_2Br_2$	$C_{34}H_{44}Br_2N_4Ni_2O_2P_2 \cdot Et_2O$
crystal colour	brown	brown	brown
crystal size (mm)	0.073× 0.110 × 0.141	0.10× 0.11 × 0.27	0.150 × 0.158 × 0.182
index ranges	$-13 \leq h \leq 13$	$-13 \leq h \leq 13$	$-12 \leq h \leq 12$
	$-14 \leq k \leq 14$	$-14 \leq k \leq 14$	$-14 \leq k \leq 14$
	$-18 \leq l \leq 18$	$-18 \leq l \leq 18$	$-21 \leq l \leq 21$
Fw; *F*(000)	839.85; 856.0	848.68; 856.0	954.03; 980.0
T (K)	100	100	100
wavelength (Å)	1.54178	1.54178	1.54178
space group	P-1	P-1	P-1
a (Å)	11.19470(10)	11.0941(2)	10.5964(2)
b (Å)	12.2617(2)	11.5657(2)	11.9969(3
c (Å)	15.0084(2)	15.4224(3)	17.6986(4)
α (deg)	107.6910(10)	107.5790(10)	76.0080(10)
β (deg)	94.8850(10)	93.8320(10)	73.1910(10)
γ (deg)	116.4600(10)	113.3940(10)	80.5220(10)
Z	2	2	2
V (Å^3)	1697.35(4)	1691.48(6)	2078.98(8)
ρ_{calcd} (g·cm^{-3})	1.643	1.666	1.524
μ (mm^{-1})	5.342	6.742	4.419
θ range (deg); completeness	3.199–70.098; 0.979	3.077–70.3; 0.978	2.665–70.096; 0.978
collected reflections; R_σ	46865; 0.0140	46337; 0.0170	57071; 0.0311
unique reflections; R_{int}	6291; 0.0268	6255; 0.0323	7675; 0.0559
R1[a]; wR2[b] [I > 2σ(I)]	0.0205; 0.0511	0.0229; 0.0565	0.0430; 0.1107
R1; wR2 [all data]	0.0215; 0.0517	0.0244; 0.0573	0.0519; 0.1177
GOOF	1.066	1.087	1.034
largest diff peak and hole	0.50 and -0.33	0.47 and -0.43	1.28 and -0.54

[a] $R_1 = \Sigma(||F_o|-|F_c||)/\Sigma|F_o|$

[b] $wR_2 = \{\Sigma[w(F_o^2-F_c^2)^2]/\Sigma[w(F_o^2)^2]\}^{1/2}$

3.10 References

[1]   D.A. Colby, R.G. Bergman, J.A. Ellman, Rhodium-catalyzed C-C bond formation via Heteroatom-directed C−H bond activation, Chem Rev. 110 (2010) 624–655. https://doi.org/10.1021/cr900005n.

[2]   P.B. Arockiam, C. Bruneau, P.H. Dixneuf, Ruthenium(II)-catalyzed C−H bond activation and functionalization, Chem Rev. 112 (2012) 5879–5918. https://doi.org/10.1021/cr300153j.

[3]   G. Rouquet, N. Chatani, Catalytic functionalization of C(sp2)-H and C(sp3)-H bonds by using bidentate directing groups, Angewandte Chemie - International Edition. 52 (2013) 11726–11743. https://doi.org/10.1002/anie.201301451.

[4]   L.C.M. Castro, N. Chatani, J.-B. Sortais, Highlight Review Nickel Catalysts/N,N′-Bidentate Directing Groups: An Excellent Partnership in Directed CH Activation Reactions, Chem. Lett. 44 (2015) 410–421. https://doi.org/10.1246/cl.150024.

[5]   P. Gandeepan, T. Müller, D. Zell, G. Cera, S. Warratz, L. Ackermann, 3d Transition Metals for C−H Activation, Chem Rev. 119 (2019) 2192–2452. https://doi.org/10.1021/acs.chemrev.8b00507.

[6]   D.D. Beattie, A.C. Grunwald, T. Perse, L.L. Schafer, J.A. Love, Understanding Ni(II)-Mediated C(sp3)-H Activation: Tertiary Ureas as Model Substrates, J Am Chem Soc. 140 (2018) 12602–12610. https://doi.org/10.1021/jacs.8b07708.

[7]   P. Roy, J.R. Bour, J.W. Kampf, M.S. Sanford, Catalytically Relevant Intermediates in the Ni-Catalyzed C(sp2)-H and C(sp3)-H Functionalization of Aminoquinoline Substrates, J Am Chem Soc. 141 (2019) 17382–17387. https://doi.org/10.1021/jacs.9b09109.

[8]   B. Vabre, F. Deschamps, D. Zargarian, Ortho derivatization of phenols through C−H nickelation: Synthesis, characterization, and reactivities of ortho-nickelated phosphinite complexes, Organometallics. 33 (2014) 6623–6632. https://doi.org/10.1021/om500938u.

[9]   J. Hao, B. Vabre, B. Mougang-Soumé, D. Zargarian, Small Molecule Activation by POCsp3OP-Nickel Complexes, Chemistry - A European Journal. 20 (2014) 12544–12552. https://doi.org/10.1002/chem.201402933.

[10]   J. Hao, B. Mougang-Soumé, B. Vabre, D. Zargarian, On the stability of a $POC_{sp3}OP$-type pincer ligand in nickel(II) complexes, Angewandte Chemie - International Edition. 53 (2014) 3218–3222. https://doi.org/10.1002/anie.201310386.

[11]   J. Hao, B. Vabre, D. Zargarian, Reactions of Phenylhydrosilanes with Pincer-Nickel Complexes: Evidence for New Si-O and Si-C Bond Formation Pathways, J Am Chem Soc. 137 (2015) 15287–15298. https://doi.org/10.1021/jacs.5b10066.

[12]   J. Hao, B. Vabre, D. Zargarian, POCOP-ligated nickel siloxide complexes: Syntheses, characterization, and reactivities, Organometallics. 33 (2014) 6568–6576. https://doi.org/10.1021/om500916d.

[13]   S. Lapointe, B. Vabre, D. Zargarian, POCOP-Type Pincer Complexes of Nickel: Synthesis, Characterization, and Ligand Exchange Reactivities of New Cationic Acetonitrile Adducts, Organometallics. 34 (2015) 3520–3531. https://doi.org/10.1021/acs.organomet.5b00272.

[14]   B. Mougang-Soumé, F. Belanger-Gariépy, D. Zargarian, Synthesis, characterization, and oxidation of new $POCN_{imine}$-type pincer complexes of nickel, Organometallics. 33 (2014) 5990–6002. https://doi.org/10.1021/om500529e.

[15]   N. Rahimi, D. Zargarian, Cationic tetra-and pentacoordinate complexes of nickel based on POCN-and POCOP-Type pincer ligands: Synthesis, characterization, and ligand exchange studies, New Journal of Chemistry. 45 (2021) 15063–15073. https://doi.org/10.1039/d1nj01355f.

[16]   V. Pandarus, A. Castonguay, D. Zargarian, Ni(II) complexes featuring non-metallated pincer-type ligands, Dalton Transactions. (2008) 4756–4761. https://doi.org/10.1039/b802222d.

[17]   L.P. Mangin, D. Zargarian, C−H Nickelation of Aryl Phosphinites: Mechanistic Aspects, Organometallics. 38 (2019) 1479–1492. https://doi.org/10.1021/acs.organomet.8b00899.

[18] B. Vabre, M.L. Lambert, A. Petit, D.H. Ess, D. Zargarian, Nickelation of PCP- and POCOP-type pincer ligands: Kinetics and mechanism, Organometallics. 31 (2012) 6041–6053. https://doi.org/10.1021/om3003784.

[19] R.K. Sarker, L.P. Mangin, D. Zargarian, Reactivities of cyclonickellated complexes with hydroxylamines: formation of κ^O-hydroxylamine and κ^N-imine adducts and a κ^O, κ^N-aminoxide derivative, Dalton Transactions. 52 (2023) 366–375. https://doi.org/10.1039/d2dt02979k.

[20] L.P. Mangin, D. Zargarian, C−H nickellation of phenol-derived phosphinites: Regioselectivity and structures of cyclonickellated complexes, Dalton Transactions. 46 (2017) 16159–16170. https://doi.org/10.1039/c7dt03403b.

[21] Based on the integration values of the multiple signals detected in the ^{31}P NMR spectrum for the reaction mixture (Fig. S2), we estimate that the major signal constitutes ca. 95% of the overall signal intensity, (n.d.).

[22] It should be noted, however, that addition of triazole to the solutions of 2a seems to lead to some decomposition that causes the initially clear sample to become somewhat cloudy. Filtration of these cloudy samples gave traces of a white solid that proved intractable., (n.d.).

[23] L.P. Mangin, D. Zargarian, C−H Nickelation of Naphthyl Phosphinites: Electronic and Steric Limitations, Regioselectivity, and Tandem C-P Functionalization, Organometallics. 38 (2019) 4687–4700. https://doi.org/10.1021/acs.organomet.9b00660.

[24] It should be added that the same decomposition process suspected to be occurring in the mixtures of triazole and 2a were also observed here as we observed the initially clear solutions of 3b-3e becoming cloudy upon addition of the triazole., (n.d.).

[25] L.P. Mangin, D. Zargarian, C−H Nickelation of Aryl Phosphinites: Mechanistic Aspects, Organometallics. 38 (2019) 1479–1492. https://doi.org/10.1021/acs.organomet.8b00899.

[26] B. Vabre, F. Lindeperg, D. Zargarian, Direct, one-pot synthesis of POCOP-type pincer complexes from metallic nickel, Green Chemistry. 15 (2013) 3188–3194. https://doi.org/10.1039/c3gc40968f.

[27] B. Vabre, D.M. Spasyuk, D. Zargarian, Impact of backbone substituents on POCOP-Ni pincer complexes: A structural, spectroscopic, and electrochemical study, Organometallics. 31 (2012) 8561–8570. https://doi.org/10.1021/om3009475.

[28] B. Vabre, Y. Canac, C. Lepetit, C. Duhayon, R. Chauvin, D. Zargarian, Charge Effects in PCP Pincer Complexes of Ni^{II} bearing Phosphinite and Imidazol(I)ophosphine Coordinating Jaws: From Synthesis to Catalysis through Bonding Analysis, Chemistry - A European Journal. 21 (2015) 17403–17414. https://doi.org/10.1002/chem.201502491.

[29] X.N. Wang, P. Zhang, A. Kirchon, J.L. Li, W.M. Chen, Y.M. Zhao, B. Li, H.C. Zhou, Crystallographic Visualization of Postsynthetic Nickel Clusters into Metal-Organic Framework, J Am Chem Soc. 141 (2019) 13654–13663. https://doi.org/10.1021/jacs.9b06711.

[30] X.L. Wang, C.H. Gong, J.W. Zhang, L.L. Hou, J. Luan, G.C. Liu, Substituent position-induced diverse architectures of polyoxovanadate-based hybrid materials constructed from a linear trinuclear transition metal complex and a hexanuclear $[V_6O_{18}]^{6-}$ cluster, CrystEngComm. 16 (2014) 7745–7752. https://doi.org/10.1039/c4ce00988f.

[31] S. Poornima, S. Anbu, R. Ravishankaran, S. Sundaramoorthy, K.N. Vennila, A.A. Karande, D. Velmurugan, M. Kandaswamy, DNA and protein targeting 1,2,4-triazole based water soluble dinickel(II) complexes enhances antiproliferation and lactate dehydrogenase inhibition, Polyhedron. 62 (2013) 26–36. https://doi.org/10.1016/j.poly.2013.06.017.

[32] J. Li, C. Wei, Y. Han, Y. Mei, X. Cheng, X. Huang, C. Hu, Triazole-directed fabrication of polyoxovanadate-based metal-organic frameworks as efficient multifunctional heterogeneous catalysts for the Knoevenagel condensation and oxidation of alcohols, Dalton Transactions. 50 (2021) 10082–10091. https://doi.org/10.1039/d1dt01413g.

[33] M.H. Klingele, B. Moubaraki, K.S. Murray, S. Brooker, Synthesis and some first-row transition-metal complexes of the 1,2,4-triazole-based bis(terdentate) ligands TsPMAT and PMAT, in: Chemistry - A European Journal, 2005: pp. 6962–6973. https://doi.org/10.1002/chem.200500387.

[34]   Y.Z. Tong, Q.L. Wang, M. Si, J. Qi, S.P. Yan, G.M. Yang, P. Cheng, D.Z. Liao, Crystal structure, spectroscopy and magnetism of trinuclear nickel(II), cobalt(II) complexes and their solid solution, in: Polyhedron, 2011: pp. 3151–3157. https://doi.org/10.1016/j.poly.2011.03.024.

[35]   P. Ren, B. Ding, W. Shi, Y. Wang, T. Lu, P. Cheng, 2D and 3D sulfate-water supramolecular networks templated via triazole-nickel(II) complexes, Inorganica Chim Acta. 359 (2006) 3824–3830. https://doi.org/10.1016/j.ica.2006.04.024.

[36]   M.H. Klingele, P.D.W. Boyd, B. Moubaraki, K.S. Murray, S. Brooker, Probing the dinucleating behaviour of a bis-bidentate ligand: Synthesis and characterisation of some di- and mononuclear cobalt(II), nickel(II), copper(II) and zinc(II) complexes of 3,5-di(2-pyridyl)-4-(1H-pyrrol-1-yl)-4H-1,2,4- triazole, Eur J Inorg Chem. (2006) 573–589. https://doi.org/10.1002/ejic.200500972.

[37]   O. Roubeau, P. Gamez, S.J. Teat, Dinuclear complexes with a triple N1,N2-triazole bridge that exhibit partial spin crossover and weak antiferromagnetic interactions, Eur J Inorg Chem. (2013) 934–942. https://doi.org/10.1002/ejic.201201126.

[38]   Q. Zhao, H. Li, Z. Chen, R. Fang, Synthesis, crystal structures and magnetic properties of $[Co_3(NCS)_6(admtrz)_6]\cdot CH_3OH\cdot H_2O$ and $[Ni_3(NCS)_6(admtrz)_6]\cdot 1.5H_2O$ (admtrz=4-amino-3,5-dimethyl-1,2,4-triazole), Inorganica Chim Acta. 336 (2002) 142–146. https://doi.org/10.1016/S0020-1693(02)00909-X.

[39]   C. Xu, J. Zhang, X. Yin, Z. Cheng, Structural Diversity and Properties of M(II) Coordination Compounds Constructed by 3-Hydrazino-4-amino-1,2,4-triazole Dihydrochloride as Starting Material, Inorg Chem. 55 (2016) 322–329. https://doi.org/10.1021/acs.inorgchem.5b02434.

[40]   J. Olguín, M. Kalisz, R. Clérac, S. Brooker, Di- and tetra-nuclear copper(II), nickel(II), and cobalt(II) complexes of four bis-tetradentate triazole-based ligands: Synthesis, structure, and magnetic properties, Inorg Chem. 51 (2012) 5058–5069. https://doi.org/10.1021/ic202537c.

[41] H.S. Yoo, J.H. Lim, J.S. Kang, E.K. Koh, C.S. Hong, Triazole-bridged magnetic M(II) assemblies (M = Co, Ni) capped with the end-on terephthalate dianion involving multi-intermolecular contacts, Polyhedron. 26 (2007) 4383–4388. https://doi.org/10.1016/j.poly.2007.05.051.

[42] C. Xu, J. Zhang, X. Yin, Z. Cheng, Structural Diversity and Properties of M(II) Coordination Compounds Constructed by 3-Hydrazino-4-amino-1,2,4-triazole Dihydrochloride as Starting Material, Inorg Chem. 55 (2016) 322–329. https://doi.org/10.1021/acs.inorgchem.5b02434.

[43] Calibration of the 100-1000 µL micropipette with 20 ∈ 500 µL aliquots of deionized H2O re-vealed that we must allow an accuracy (systematic error) of +4 µL and a precision of ±3 µL for our measurements, with > 99% confidence. The 20-200 µL micropipette was calibrated by the same procedure, with 150 µL aliquots, and revealed an accuracy of +0.3 µL and a precision of ±3 µL for our measurements, with > 99% confidence., (n.d.).

[44] Bruker (2012). APEX2 / Bruker (2016) APEX3, Bruker AXS Inc., Madison, WI, USA., (n.d.).

[45] Bruker (2012). "SAINT Integration Software for Single Crystal Data", Bruker AXS Inc., Madison, WI, USA. (a), (n.d.).

[46] (a) G. M. Sheldrick (1996). SADABS/TWINABS. University of Göttingen, Germany. (b) Bruker (2001). SADABS/TWINABS. Bruker AXS Inc., Madison, Wisconsin, USA. Bruker (2012). Data Preparation and Reciprocal Space Exploration Program, Bruker AXS Inc., Madi-son, WI, USA., (n.d.).

[47] Bruker (2012). Data Preparation and Reciprocal Space Exploration Program, Bruker AXS Inc., Madison, WI, USA., (n.d.).

[48] A: O. V. Dolomanov, L. J. Bourhis, R. J. Gildea, J. A. K. Howard and H. Puschmann. "OLEX2: a com-plete structure solution, refinement and analysis program". J. Appl. Cryst., 2009, 42, 339-341., (n.d.). https://doi.org/10.1021/acs.inorgchem.3c01236.

[49] G.M. Sheldrick, SHELXT - Integrated space-group and crystal-structure determination, Acta Crystallogr A. 71 (2015) 3–8. https://doi.org/10.1107/S2053273314026370.

[50]   G.M. Sheldrick, Crystal structure refinement with SHELXL, Acta Crystallogr C Struct Chem. 71 (2015) 3–8. https://doi.org/10.1107/S2053229614024218.

4. 1. Reactions of cyclonickelated complexes with hydroxylamines and TEMPO˙: isolation of new TEMPOH adducts of Ni(II) and their reactivities with nucleophiles and oxidants

Rajib K. Sarker and Davit Zargarian*

Département de chimie, Université de Montréal, Montréal (Québec), Canada H3C 3J7.

ABSTRACT: C–H functionalization processes are commonly believed to involve two main stages, the initial C–H metallation step giving a cyclometallated intermediate and the subsequent reactivities of this intermediate with various substrates to give the target functionalized product. Mechanistic studies focused on these two stages of reactivity can improve our understanding of the overall process. In this context, we have investigated the reactivities of a model system based on the precursors {i-Pr$_2$P(OAr)}$_2$NiBr$_2$ with the aim of identifying the conditions favoring the cyclonickelation and C–C/C–heteroatom coupling reactions. This contribution describes a study on the reactivities of the model complexes [{$\kappa P,\kappa C$-(i-Pr)$_2$PO-Ar}Ni(μ–Br)]$_2$, **1a-d** (Ar: C$_6$H$_4$, **a**; 3-Cl–C$_6$H$_3$, **b**; 3-OMe-C$_6$H$_3$, **c**; 4-OMe-napthalenyl, **d**), with hydroxylamines in the presence of TEMPO˙ (TEMPO˙ = (2,2,6,6-tetramethylpiperidinyl-1-yl)oxyl). The results of this study showed that treating **1a-d** with a mixture of Et$_2$NOH and TEMPO˙ did not afford the desired oxidation-induced functionalization of the Ni-aryl moiety in **1a-d**, giving instead the corresponding κ^O-TEMPOH adducts {$\kappa P,\kappa C$-(i-Pr)$_2$PO-Ar}Ni(Br)(κ^O-TEMPOH), **3a-d** (TEMPOH = N-hydroxy-2,2,6,6-tetramethylpiperidine). The TEMPOH moiety in these zwitterionic compounds **3** can be displaced by a large excess of acetonitrile, 10 equiv of morpholine, or 1-2 equivalents of imidazole. Although these reactions have given the authenticated products {$\kappa P,\kappa C$-(i-Pr)$_2$PO-C$_6$H$_4$}Ni(Br)(NCMe), **4a**, {$\kappa P,\kappa C$-(i-Pr)$_2$PO-C$_6$H$_4$}Ni(Br)(morpholine), **5a**, and [{$\kappa P,\kappa C$-(i-Pr)$_2$PO-C$_6$H$_4$}Ni(imidazole)$_2$][Br], **6a**, a few other products were also detected by NMR, indicating that the observed reactivities are far more complex than simple substitution of the TEMPOH moiety. Similarly, treating **3a** with AgOC(O)CF$_3$ results in the isolation of {$\kappa P,\kappa C$-(i-Pr)$_2$PO-C$_6$H$_4$}Ni{OC(O)CF$_3$}(κ^O-TEMPOH), **7a**, arising from the substitution of the bromo ligand, whereas spectroscopic evidence suggests further reactivity, possibly including displacement of TEMPOH and oxidative decomposition. Complexes **3** undergo irreversible electrochemical oxidation and failed to give tractable oxidation products when treated with oxidants such as CuBr$_2$, NBS, and ferrocenium salts known to induce single-electron oxidation of Ni(II) species.

1a

TEMPOH (or Et$_2$NOH + TEMPO$^•$)

morpholine

5a

3a

AgOC(O)CF$_3$

7a

imidazole

Br$^⊖$

6a
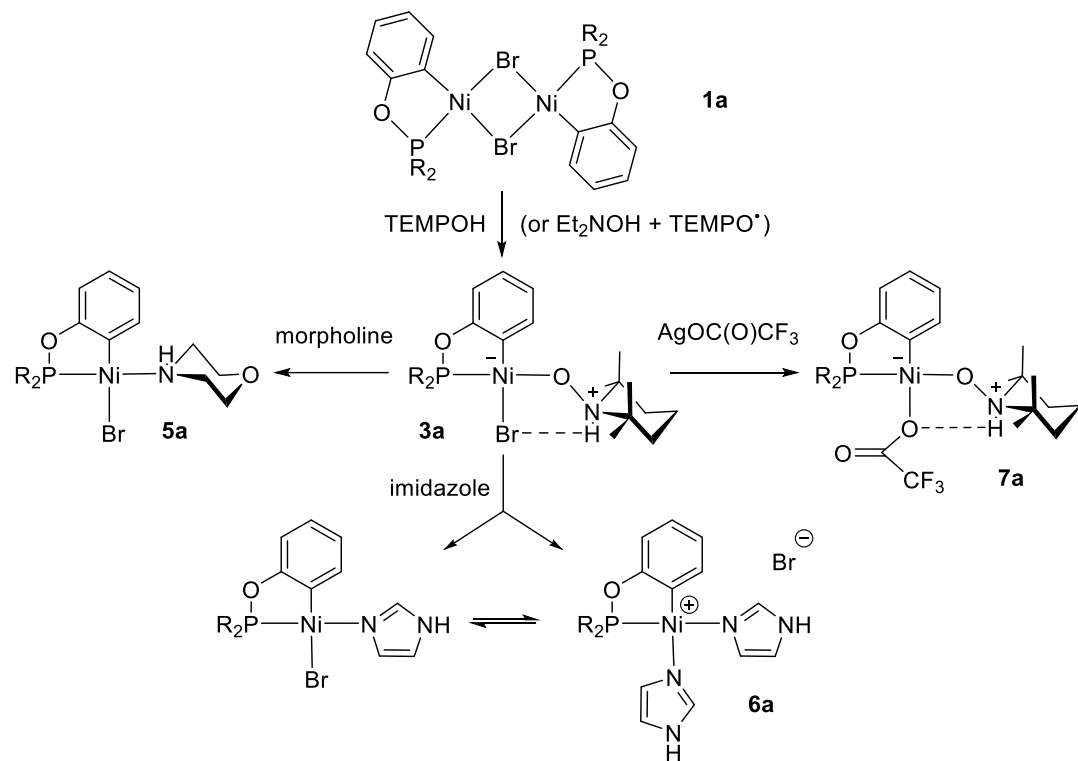
4. 2. Introduction

Transition-metal mediated direct C–H functionalization of organic compounds to form C–C or C–heteroatom has evolved into an attractive alternative to traditional cross-coupling reactions.[1–5] More specifically, the use of various functional groups in the target substrates for directing the site of C–H functionalization has proven to be a powerful methodology in this field.[6,7] The use of such directing groups also helps facilitate the difficult initial C–H metalation step, presumably by reducing the barrier for C–H binding and activation. A large number of C–H bond functionalization reactions exploiting this strategy have been reported lately, including arylation,[8] alkylation,[9] alkenylation,[10] amination,[11] borylation,[12] and halogenation.[13] Another development that has increased the appeal and practicality of chelation-directed C–H functionalization is the use of pre-catalysts based on earth-abundant 3d transition metals. Thus, many efficient C–H functionalization processes have been successfully implemented using Fe,[14–16] Co,[17–19] and Ni[20–25] complexes.

In contrast to the significant progress registered in developing practical protocols for 3d metal-catalyzed functionalization of non-activated C−H bonds, our understanding of how these processes work has not advanced as much. As a result, the intimate details of how catalytic cycles operate are largely lacking. The main reason for this paucity of mechanistic knowledge is that to date bulk of research studies have focused on the development of one-pot protocols that encompass the multiple steps of chelation, metalation, and functionalization steps. Of course, such a one-pot approach is attractive from a practical point of view, but it bypasses the detection and isolation of reaction intermediates and foregoes the chance to improve our understanding of reaction mechanisms. In the absence of clearly identified reaction intermediates, it is difficult to establish how they might promote the various functionalization steps as a function of variables such as temperature, base, solvents, ligands, oxidants etc. Therefore, to expedite the progress on the mechanism front requires greater efforts toward interception of the envisaged intermediates and examination of their stabilities and reactivities. Indeed, such efforts have begun already and recent reports by the groups of Schaefer and Love,[26,27] and Sanford[28] have provided valuable mechanistic insights on Ni-based systems.

The above considerations and our group's longstanding interest in organonickel chemistry in general,[29–33] and the synthesis of pincer complexes via C–H nickellation in particular,[34–36] motivated us to study the reactivities of simple Ni(II) precursors in C–H functionalization. Our approach in this endeavor consists of preparing thermally stable orthonickellated complexes by C–H nickellation and using them as model systems for probing the feasibility of C–C and C–heteroatom coupling. In previous reports, we

presented an optimized synthetic strategy for the preparation of cyclonickelated complexes from phenol- and arenol-derived ligands,[37,38] studied the impact of reaction conditions on the C–H nickelation step,[39] and provided proof of concept for C–C and C–P[40] functionalization of the cyclonickelated complexes when treated with various electrophiles (**Scheme 4. 1**).

Scheme 4. 1. C—H nickelation of aryl- and naphthyl-phosphinites and their C–C/C–P functionalization
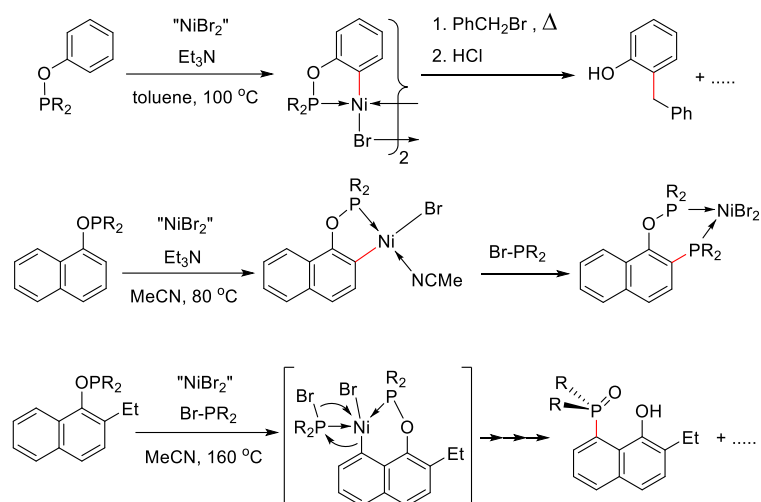
Subsequent studies tested the feasibility of C–O/C–N functionalization of these cyclonickelated complexes when treated with reagents featuring weak element-element bonds such as hydroxylamines[41] and 4-amino-4H-1,2,4-triazole.[42] The latter reagents failed to induce the desired C–O/C–N functionalization, giving instead novel zwitterionic and charge-neutral adducts of hydroxylamines (**A** and **B** in **Chart 1**), aminoxide (**C**), imine (**D**), and triazole (**E** and **F**).

Chart 1. Reactivities of orthonickelated complexes with hydroxylamines and 1,2,4-triazole
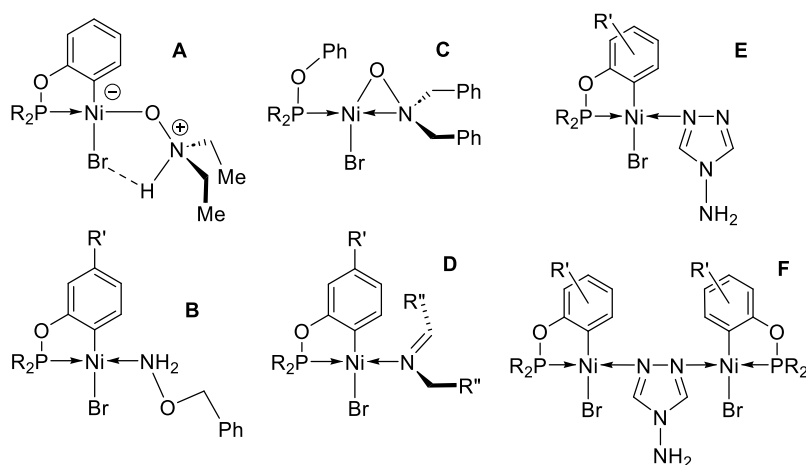
As a follow-up to the above studies, we have examined the reactivities of our cyclonickelated complexes with hydroxylamines in the presence of oxidants such as TEMPO• (TEMPO• = 2,2,6,6-

tetramethyl-1- piperidinyl-N-oxyl).[43,44] As described herein, these reactions did not lead to the desired C–heteroatom functionalization chemistry, generating instead a family of unusual Ni-TEMPOH complexes (TEMPOH = 2,2,6,6-tetramethyl-1- piperidinyl-N-hydroxy) that have afforded us an opportunity to probe the coordination chemistry and oxidation of these interesting compounds.

4. 3. Results and discussion

4. 3. 1.　　　　Synthesis of a new Ni(II)-κO-TEMPOH complex

A previous study showed that treating a DCM (DCM= CH_2Cl_2) solution of the parent dimer [{κP,κC-(i-Pr)$_2$PO-(C$_6$H$_4$)}Ni(μ-Br)]$_2$, **1a**, with Et$_2$NOH gives the zwitterionic adduct **2a** (**Scheme 4. 2**). We wondered if this compound might promote C–X functionalization of the Ni-aryl moiety via oxidation-induced reductive elimination. To test this idea, **2a** was treated with the aminoxyl radical TEMPO• in hopes of directly oxidizing **2a** or oxidatively displacing the Et$_2$NOH ligand, as shown in **Scheme 4. 2**.

Scheme 4. 2. Synthesis of Ni(II)-κO-TEMPOH complex **3a**
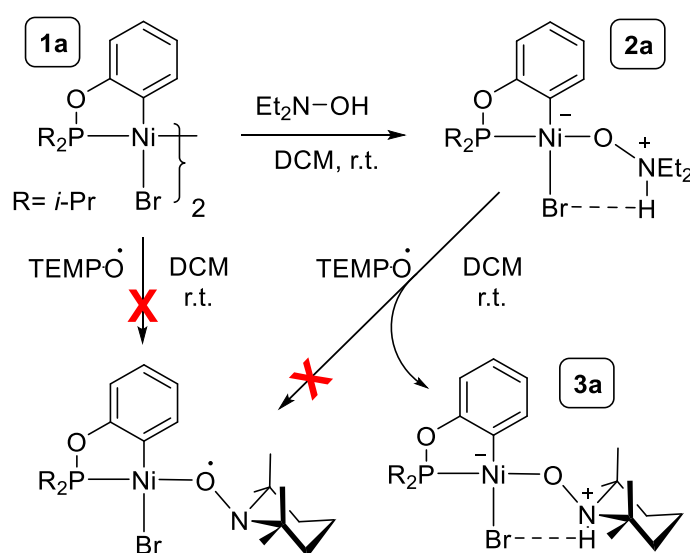
Monitoring the reaction progress by NMR spectroscopy showed a clean conversion of **2a** in the presence of TEMPO•, as reflected in the replacement of the ^{31}P signal for the starting material by a new signal. The closeness of the ^{31}P chemical shifts for the starting material and the product (201.5 vs 202.0 ppm) implied similar structures for the two species. Moreover, formation of a diamagnetic, NMR active species also implied that the hoped-for oxidation had not taken place. Standard work-up of the **2a**/TEMPO• reaction mixture resulted in isolation of a dark brown solid that was identified by single crystal diffraction studies as the Ni(II)-κO-TEMPOH complex **3a** (**Scheme 4. 2**).

A search of the literature has revealed that κO-TEMPOH (or η^1-TEMPOH) complexes such as **3a** are quite rare. Indeed, to our knowledge, the only precedents for such complexes are the Ni derivatives reported by Captain's group (**A** in **Chart 2**),[45,46] the Fe- and Al-TEMPOH derivatives reported by Hayton's group (**B**[47] and **C**[48]), and one Ir(III)-TEMPOH complex reported by Bas de Bruin's group.[49] In contrast, there are many more compounds featuring TEMPO moieties, [44,50] as opposed to TEMPOH.

Chart 2. Precedents for κ^O- or η^1-TEMPOH complexes
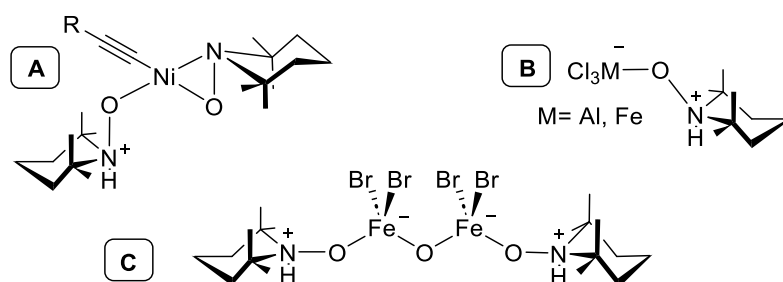
In a second attempt to access the postulated TEMPO$^\bullet$–Ni complex shown in **Scheme 4. 2**, we treated the dimeric precursor **1a** directly with 2 equiv of TEMPO$^\bullet$ (Ni:TEMPO$^\bullet$ = 1:1), but this approach also proved unsuccessful as we obtained only intractable black solids. Similarly, treating the TEMPOH complex **3a** with 1 equiv of TEMPO$^\bullet$ failed to induce the desired oxidation. We conclude that the target TEMPO$^\bullet$–Ni complex is thermally unstable, presumably because of O–C reductive elimination or oxidation of the fragile O–P moiety.

4. 3. 2.   Synthesis of the substituted Ni(II)-κ^O-TEMPOH complexes 3b-3d

The facile access to **3a** prompted us to prepare analogous Ni(II)-κ^O-TEMPOH complexes to allow an examination of the structures and reactivities of these compounds as a function of different aryl moieties. Unfortunately, however, applying the procedure outlined in **Scheme 4. 2** to the substituted derivatives of the dimeric precursor **1a** proved unsuccessful, giving instead the previously reported imine adducts shown in **Scheme 4. 3**.[41]

Scheme 4. 3. Alternative synthesis of Ni(II)-κ^O-TEMPOH complexes 3b-3d
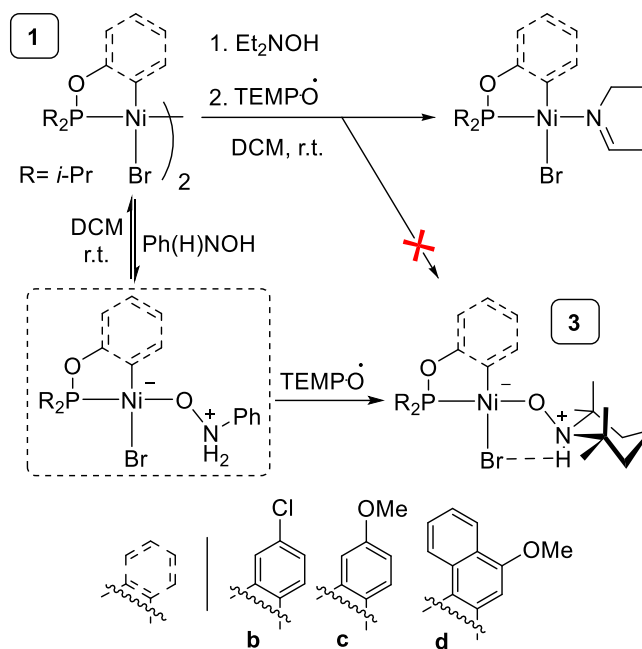
We reasoned that formation of the imine adducts instead of the target Ni(II)-κO-TEMPOH derivatives must be related to the more facile dehydration of Et$_2$NOH relative to the abstraction of a proton by TEMPO$^{\bullet}$. If this were the case, then circumventing this side reaction (for example, by using hydroxylamines lacking an α-CH moiety) should favor the formation of the target TEMPOH complexes. This hypothesis was tested by using Ph(H)NOH instead of Et$_2$NOH, with the following observations. Treating DCM solutions of **1b-d** with Ph(H)NOH led to gradual disappearance of the ^{31}P signals for the precursors and the emergence of new broad signals. Unfortunately, we failed to grow single crystals of the presumed zwitterionic products of these reactions, which are drawn inside the dashed rectangle in **Scheme 4. 3**. Nevertheless, the closeness of the ^{31}P chemical shifts for the mixtures of **1** and Ph(H)NOH to the corresponding signal for **2a** (198 vs 201.5 ppm) supports our belief that the anticipated zwitterionic adducts have formed. Therefore, we proceeded with the plan of treating **1b-d**/Ph(H)NOH mixtures with 1 equiv of TEMPO$^{\bullet}$ to see if they would be converted to the target TEMPOH products. The crude reaction mixtures showed sharp new ^{31}P singlets in the 200-203 ppm region, consistent with the conversion of the putative zwitterionic intermediates to the target κO-TEMPOH derivatives **3b-3d** (**Scheme 4. 3**). Fortunately, this time we were able to grow single crystals of these new products, thus allowing us to confirm their identities. The solid-state structures of the new TEMPOH complexes **3a-3d** will be discussed later.

The successful syntheses of the TEMPOH adducts from the **1b-1d**/Ph(H)NOH mixtures validated the importance of blocking the alternative pathway that leads to the corresponding imine adducts via dehydration of the hydroxylamine moiety. It occurred to us that this undesired dehydration might also be circumvented in another way, by ensuring that the H$^{\bullet}$ transfer from the hydroxylamine to TEMPO$^{\bullet}$ occurs prior to formation of the zwitterionic adducts shown inside the dashed rectangle in **Scheme 4. 3**. If such an approach were feasible, it would have the added advantage of working with all hydroxylamines, even those such as Et$_2$NOH that possess an α-CH moiety. Tests validated this hunch, thus allowing us to develop the generalized, two-step protocol shown in **Scheme 4. 4** for the synthesis of all four Ni-TEMPOH complexes.

Scheme 4. 4. Generalized synthesis of Ni-TEMPOH complexes 3a-3d
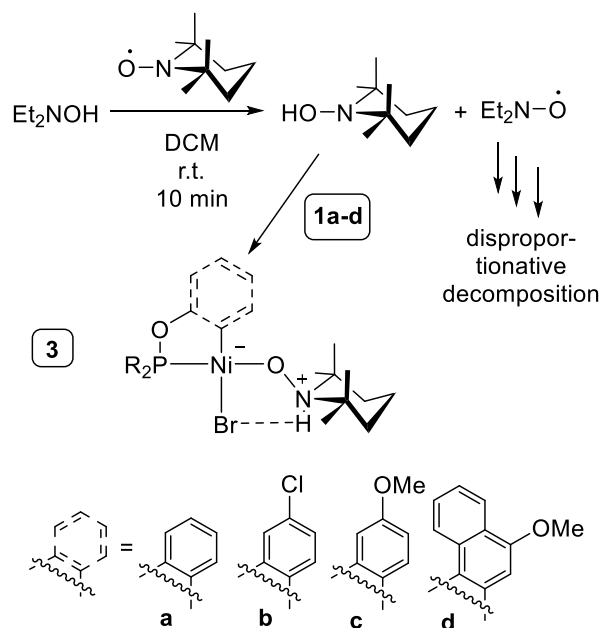
The syntheses of **3a-d** following the above protocol revealed two distinct color changes. In the first step of the process, the orange-colored TEMPO$^{\bullet}$/DCM solutions turned colorless relatively fast upon pre-mixing with Et$_2$NOH. This discoloration must result from the exchange of H$^{\bullet}$ between the starting materials to generate TEMPOH and the *N*-oxyl radical Et$_2$NO$^{\bullet}$. The latter is known to be thermally unstable[51] and undergo disproportionative decomposition to various side-products[52] (**Scheme 4. 4**). The second color change occurred during the second step of the protocol when addition of the dimeric Ni(II) precursors **1a-d** to the colorless mixtures containing TEMPOH gave dark-brown mixtures from which the TEMPOH adducts **3a-3d** were obtained in 43-77% yields.

4. 3. 3. Reactivities of Ni-TEMPOH complexes

Having developed a relatively facile access to rare η^1–TEMPOH complexes of Ni motivated us to learn more about the Ni–O bonding interaction in these species and to examine how easily the Ni-TEMPOH

moiety can be displaced.[50] We were also interested in establishing if the Ni center in these complexes could be oxidized to induce C–O coupling. The following sections describe the results of these reactivity studies.

Substitution reactions. Some of the observations made during the attempted synthesis of Ni TEMPOH complexes had indicated that acetonitrile is not an ideal solvent for the preparation of these species, hinting that the TEMPOH moiety might be susceptible to nucleophilic displacement. This was confirmed when we recorded the ^{31}P{^{1}H} NMR spectra of an acetonitrile solution of **1a** containing 1 or two equiv of TEMPOH. These spectra (**Figure S4. 10**) showed two main species, the major one identified as the known acetonitrile adduct [{$\kappa P,\kappa C$-(i-Pr)$_2$PO-(C$_6$H$_4$)}Ni(Br)(NCMe)]$_2$, **4a**, represented by a broad resonance at ca. 195 ppm, whereas the minor product represented by a sharp singlet at ca. 202 ppm was identified as the η^1-TEMPOH complex **3a**. The approximate integration ratios of the ^{31}P singlets representing **3a** and **4a** were 10:90 and 17:83 with Ni:TEMPOH ratios of 1:1 and 1:2, respectively. These observations indicate that **4a** and **3a** are involved in the ligand exchange equilibrium shown in **Scheme 4.5**.

Scheme 4. 5. Nucleophilic displacement of the TEMPOH moiety in 3a
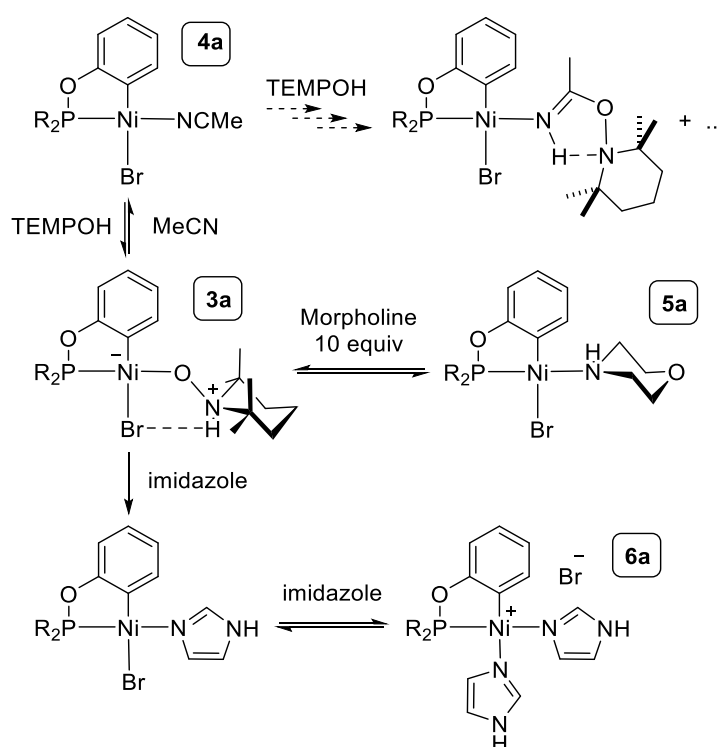
The ligand exchange equilibrium alluded to above was further supported by our observations from the following complementary NMR experiments. When excess MeCN was added to a DCM solution of **3a** featuring a Ni:TEMPOH:NCMe molar ratio of 1:1:300, the ^{31}P{^{1}H} NMR spectrum of the sample showed the new broad resonance representing **4a** (**Figure S4. 11**). The integration ratio for the ^{31}P resonances

representing **3a** and **4a** was initially 14:86, changing to 19:81 when one more equiv of TEMPOH was added.

Additional insight into the MeCN/TEMPOH substitution reactions was obtained from other NMR experiments using samples containing larger Ni:TEMPOH ratios. Thus, adding MeCN to a DCM solution of **3a** featuring a Ni:TEMPOH:NCMe molar ratio of 1:5:300 and recording the $^{31}P\{^1H\}$ NMR spectrum of this sample showed not only the anticipated resonances for **3a** and **4a**, but also a minor new peak at ca. 201 ppm (**Figure S4. 12**). Interestingly, successive additions of 1 and 2 additional equiv of TEMPOH to this sample (new Ni:TEMPOH:NCMe molar ratios of 1:6:300 and 1:8:300) resulted in incremental increases in the integration values of the peaks representing **3a** and the new peak at 201 ppm. Furthermore, another minor peak appeared as a shoulder on the broad resonance representing the MeCN adduct **4a**, as well as a peak in the spectral region associated with oxidative decomposition of the phosphinite ligand (60-80 ppm). The latter signal grew in intensity when the sample was allowed to stand over days.

To recap, the above observations point to an equilibrium exchange between the TEMPOH adduct **3a** and the MeCN adduct **4a**. We propose that **4a** undergoes slow and irreversible reactions with excess TEMPOH to give two new products, one of which is the postulated new Ni-imine product shown in **Scheme 4. 5** that arises from a nucleophilic addition by TEMPOH to the activated nitrile moiety in **4a**. This proposal is inspired by a previous observation of closely related Ni-imine derivatives formed via nucleophilic addition of hydroxylamines to **4a** (see species **D** in **Chart 1**),[41] as well as another literature precedent involving the reaction shown in equation 1.[53] Although the bis(imino) Re(IV) species shown below is thermally stable indefinitely, the putative Ni(II)-imino species shown in **Scheme 4. 5** appears to decompose over time.

$$ReCl_4(NCMe)_2 \xrightarrow[\text{r.t., 15 min}]{2\ Ar_2NOH} Cl_4Re\left(N\overset{}{\underset{H- -NAr_2}{\diagdown}}\overset{}{\diagup}O\right)_2 \qquad \text{(eq. 1)}$$
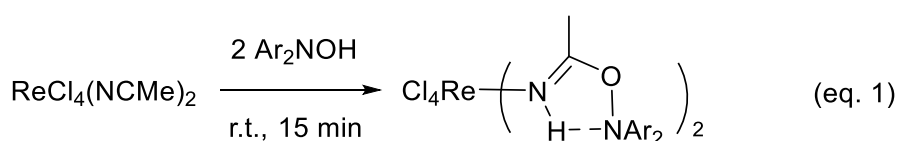
Next, we probed the displacement of TEMPOH in **3a** with morpholine, which proved more facile by comparison to the acetonitrile reaction discussed above. Nevertheless, 10 equiv of morpholine were required for a complete conversion (**Scheme 4. 5**). Tests also showed that the morpholine adduct **5a** can be prepared directly (and more conveniently) by treating the bromo precursor **1a** with 2 equiv of morpholine.[54] The spectroscopic and solid-state characterization of this new adduct will be presented later.

The reaction of **3a** with imidazole also hinted at a dynamic ligand exchange equilibrium, but in this case, we were surprised to find that addition of only one equiv of imidazole gave a ^{31}P NMR spectrum

displaying multiple new signals in the δ 191-195, as well as minor signals in the up-field region characteristic of oxidized phosphinites (**Figure S4. 58**). Addition of one more equiv of substrate led to disappearance of the ^{31}P signal for **3a**, and most of the other sharp peaks merged into a broad signal resonating at δ 192-194 (FWHM~ 10 and 50 Hz, respectively) that seemed to be composed of 2-3 overlapping signals; in addition, one of the upfield signals grew more intense, suggesting oxidative decomposition. Probing the ligand exchange reaction starting with the mono(imidazole) adduct showed a clearer picture (**Figure S4. 59**): when one equiv of TEMPOH was added to the mixture of dimer **1a** and imidazole to give a Ni:imidazole:TEMPOH ration of 1:1:1, we noted a 0.38:1.00 ratio for the integration values of the TEMPOH adduct **3a** and the compound we believe to be the charge-neutral (mono)imidazole adduct.

The above observations indicate that imidazole displaces TEMPOH in **3a** to give the corresponding imidazole adduct, this system also shows evidence for one or more side reactions, possibly including the displacement of Br as well, as illustrated in **Scheme 4. 5**. Work-up of this mixture containing **3a** and excess imidazole led to isolation of brown crystals that were identified as the cationic bis-imidazole adduct **6a**. As was noted for the morpholine adduct **5a**, compound **6a** was also accessible directly via the reaction of **1a** with 4 equiv of imidazole. The spectroscopic and solid-state characterization of **6a** will be presented below.

Finally, it should be noted that substitution of TEMPOH was unsuccessful with norbornene and DMSO, and even with one equiv of PPh$_3$. The failure to displace TEMPOH by PPh$_3$was particularly surprising given the silver affinity of Ni(II) precursors for this ligand.

Attempted oxidation of Ni(II)-TEMPOH complexes. Our long-standing interest in the synthesis and reactivities of high valent Ni complexes[55–58] prompted us to investigate the redox potential of the cyclometallated complexes under discussion. Cyclic voltammetry (CV) measurements of the η^1-TEMPOH adducts prepared in the course of the study indicated that none supported reversible electrochemical oxidation: we observed in every case essentially irreversible redox phenomena, presumably because of the decomposition of the oxidized/reduced intermediates. Next, we tested the chemical oxidation of some of the TEMPOH complexes by treating them with the oxidants CuBr$_2$, NBS, and ferrocenium salts that had proven effective for the oxidation of closely related POCN- and NCN-type pincer complexes of Ni(II).[59,60] Unfortunately, all of these attempts proved unsuccessful as we observed the decomposition of the TEMPOH adducts.

The above results prompted us to test the effectiveness of oxidants such as simple salts of Ag(I) that are less likely to engender oxidative decompositions. We selected AgOC(O)CF$_3$ for our tests based on a

recent report[61] that showed the effectiveness of this reagent for one-electron oxidation of (POCOP)Ir^{III}(H)(Cl), a pincer compound featuring phosphinite donor moieties. Thus, we treated a DCM solution of **3a** (generated in-situ by adding the dimeric precursor **1a** to the mixture of Et$_2$NOH and TEMPOH) with one equiv of AgOC(O)CF$_3$ and stirred for 2 h at ambient temperature. The ^{31}P{^{1}H} NMR spectrum of an aliquot of this reaction mixture showed incomplete conversion of **3a** to two new products represented by prominent singlets at ca. 204 and 200 ppm. Evaporation of the reaction mixture, followed by extraction of the solid residues with Et$_2$O and cooling the filtrate to -30 °C gave a crystalline solid that turned out to be the product represented by the ^{31}P singlet appearing at ca. 200 ppm. XRD analysis of a single crystal from this batch allowed us to identify this solid as the new derivative **7a** formed by substitution of the Br in **3a** by trifluoroacetate (**Scheme 4. 6**).

Scheme 4. 6. Reaction of 3a with AgOC(O)CF$_3$.
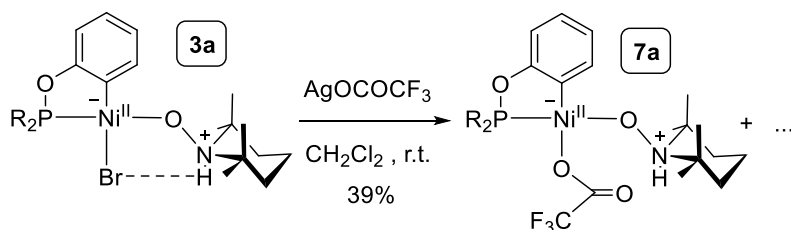
That one of the two major products formed from the reaction of **3a** with AgOC(O)CF$_3$ arises from displacement of the bromo ligand suggested that the other product might result from the substitution of TEMPOH. To test this possibility and also to explore whether one-electron oxidation might come about in the presence of excess Ag$^+$, we probed the impact of excess quantities of AgOC(O)CF$_3$ to samples of **3a**. **Figure S4. 70** shows the ^{31}P{^{1}H} NMR spectra recorded for a DCM sample of **3a** containing 1, 3, or 4 equiv of AgOC(O)CF$_3$, as follows. The first sample was prepared by combining **3a** and a stoichiometric amount of the silver salt and filtering the off-white solid that precipitated immediately. The spectrum recorded for this sample was very similar to what was described above for the mixture of **1a**/TEMPOH/AgOC(O)CF$_3$: it showed three main species, the unreacted precursor **3a** (singlet at ca. 202 ppm), complex **7a** (ca. 200.4 ppm), and an unidentified new product represented by a singlet at ca. 204 ppm; a less intense and broader signal was also observed at ca. 198 ppm. Integration ratios for these 4 signals indicated an approximately 87% conversion of **3a** (**Figures S4. 70 and S4. 71**).

Next, we added 2 additional equiv of AgOC(O)CF$_3$ to the above sample to give a 1:3 ratio of Ni:CF$_3$COO, and the resulting new sample was agitated periodically over one hour at ambient temperature before recording its NMR spectrum, which showed that the species present in the previous sample had been converted to a final product (or multiple species exchanging with one another) represented by one broad

resonance at 198 ppm (**Figure S4. 70b**, FWHM ~ 24 Hz). The $^{19}F\{^1H\}$ NMR spectrum of this sample showed a very broad new peak in the 160-200 ppm region in addition to a singlet at ca. -78 ppm (**Figure S4. 73**). Although there was no indication of oxidation in this spectrum, when the sample was allowed to stand for 24 h at ambient temperature and under nitrogen its spectrum showed the emergence of a new broad signal at ca. 163 ppm, as well as a few less intense signals appearing in 60-80 ppm region associated with oxidized phosphinites (**Figure S4. 70c**). It is interesting to note that a very similar spectrum was obtained from a sample containing only the dimeric precursor **1a** and 6 equiv of AgOC(O)CF$_3$ (to give a Ni:Ag ratio of 1:3), confirming that the species represented in these spectra do not contain any TEMPOH ligand (see **Figure S4. 74**). Finally, adding a 4-th equiv of AgOC(O)CF$_3$ to the sample increased the intensity of the broad new peak at ca. 163 ppm (**Figure S4. 70d**, FWHM ~ 156 Hz) and more signals appeared in the upfield region of the spectrum.

The above observations suggest that the trifluoroacetate anion can displace both the bromide and TEMPOH ligands in **3a**, as per the multi-step ligand substitution processes illustrated in **Scheme 4. 7**. It is worth emphasizing that to date the only Ni-derivative isolated and authenticated is complex **7a**. Therefore, the reactivities proposed in **Scheme 4. 7** must be treated as very tentative at this stage. The only other authenticated side-product formed in these reactions was piperidinium trifluoroacetate, presumably formed via deoxygenation of TEMPOH.[62]

Scheme 4. 7. Proposed reactivity of 3a with AgOC(O)CF₃.
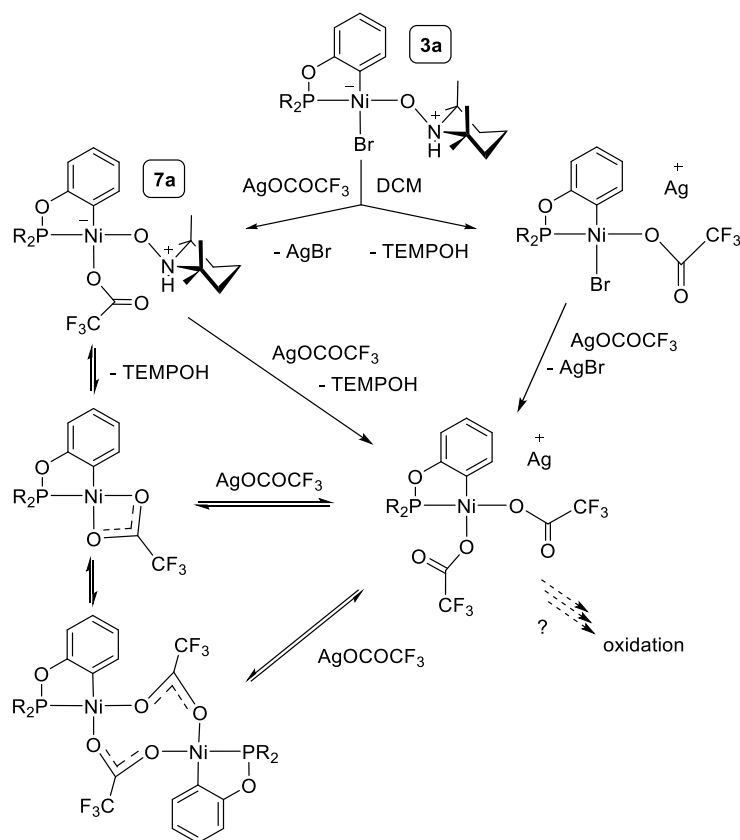
4. 3. 4. Characterization of the κ^O-TEMPOH complexes 3a-3d

These complexes were isolated as brown single crystals by employing standard work-up protocols on the reaction mixtures obtained during their syntheses. The compositional purity of the new products was established by elemental analysis, whereas their solution and solid-state structures were confirmed by ^{1}H, ^{31}P, and ^{13}C NMR spectroscopy and XRD studies, as described below.

The ^{31}P{^{1}H} NMR spectra recorded for C₆D₆ samples of the η^1-TEMPOH complexes displayed singlet resonances at δ 201.5 (**3a**), 203.0 (**3b**), 200.8 (**3c**), and 199.4 (**3d**), whereas the corresponding spectra recorded for DCM samples showed singlets that appeared more downfield by 02.-0.7 ppm. The ^{1}H and ^{13}C{^{1}H} NMR spectra (C₆D₆) of **3a-d** were also distinctive and contained very informative features. For example, the N*H* proton shows a broad signal in the δ 8.3-8.5 region, while complex **3d** showed an additional multiplet in the δ 8.59-8.60 region characteristic of a naphthalenic proton. ^{13}C signals of note include doublets featuring fairly large coupling constants for the *C*–Ni moiety (136 ppm, $^2J_{P-C}$ = 36 Hz) and

C–O moiety (168 ppm, $^2J_\text{P-C}$ = 14 Hz), whereas the other aromatic C nuclei showed smaller $J_\text{P-C}$ values (2-4 Hz).

Single crystal X-ray diffraction studies were carried out for all of the new Ni-TEMPOH complexes. The crystal data, structure refinement details, and lists of the most important bond distances and angles are presented in the electronic supporting information of this article (**Tables S1** and **S2**). The molecular diagrams for the new complexes are presented in **Figure 1** and briefly described below.

3a

3b

3c

3d
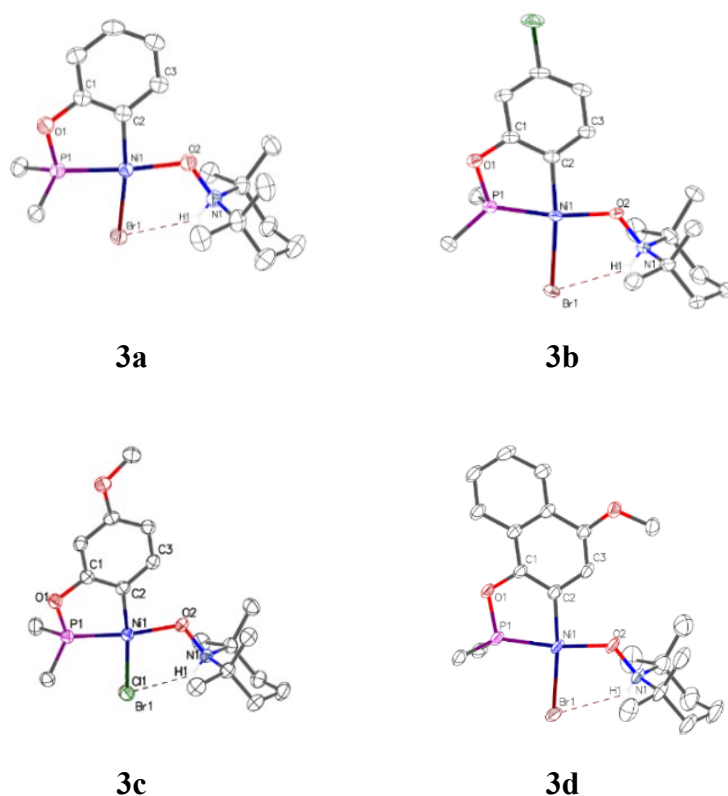
Figure 4. 1. Molecular diagrams of complexes **3a-3d**. Thermal ellipsoids are shown at the 50% probability level. Hydrogen atoms and the Me groups of the i-Pr substituents have been omitted for clarity.

In their solid states, **3a-d** display a slightly distorted square planar coordination geometry around the central nickel atom, with trans and cis angles of 170-174° and 83-98°, respectively. In all four complexes, the Ni atom sits less than 0.04 Å above the mean coordination plane defined by the four ligating atoms. All the Ni–P, Ni–C, and Ni–Br distances lie within the normal range of previously reported cyclonickellated complexes.[63–69] Similarly, the Ni–O distances in these TEMPOH complexes are very similar to the corresponding distances reported for previously reported Ni-TEMPOH complexes (1.89-1.92 vs 1.8927(7) and 1.8890(8) Å), but somewhat shorter than the corresponding distances in reported four-coordinate Ni(II)-methoxide complexes (1.932 Å).[70,71]

Other important structural parameters for analyzing M-TEMPO complexes include the N–O bond distance and sum of the C–N–X angles (X= O or C). Comparing the values of these parameters found in the solid states of M-TEMPO complexes vs. free TEMPO$^\bullet$ helps establish whether the TEMPO moiety is in its reduced or open-shell state, [TEMPO]$^-$ vs [TEMPO]$^\bullet$, respectively.[72] In the case of complexes **3a-d**, we found that the N–O distances of 1.39-1.40 Å and Σ(C–N–X) values of 339-344° are quite comparable to the corresponding parameters found in previously reported complexes featuring a M–TEMPOH moiety, *viz.* 1.384(1), 1.391(2), and 1.405(1) Å, and 340° in Captain's Ni complexes; 1.396(3) and 1.406(3) Å, and 339° in Hayton's Fe complexes; and 1.423 Å and 336° in the Ir-TEMPOH complex reported by Bas de Bruin. It is, therefore, reasonable to conclude that the TEMPOH moieties in **3a-d** are anionic ligands featuring pyramidal N moieties.

Another interesting feature of the solid-state structures of the Ni-TEMPOH complexes **3a-d** is the N---H---Br interactions. The observation of such H-bonding interactions in the solid state confirms the assignment of the broad and downfield signals observed in the ^{1}H NMR spectra of these complexes to the N–H moiety. We found Br–N distances of 3.17-3.21 Å that are somewhat shorter than the corresponding distance of 3.31 Å found in a broad survey of reported structures containing Br---H–N bonding interactions. The Br---H---N angles of 140-144° are also comparable to the mean value of 154° from the reported structures.

Characterization of the new adducts 5a, 6a, and 7a. The new adducts **5a-7a** were obtained as brown or yellow powders/crystals following work-up, and used them for full characterization of these diamagnetic complexes. The ^{1}H NMR spectrum of **5a** displays the characteristic signals for the phosphinite protons: four partially resolved multiplets for the inequivalent aromatic protons, a complex multiplet at ca. 2.3 ppm for the P–C*H* proton, and two clearly resolved doublets of doublets for P–C*H*$_3$ protons. Also observed are four broad signals in the 2.4-3.5 ppm range, which were attributed to the methylene moieties of morpholine; we speculate that these broad signals originate from the conformational flipping of morpholine. The signal anticipated for the N*H* proton is presumably obscured by the P–C*H* multiplet at ca. 2.3 ppm.

The above data implied that the ^{1}H NMR spectrum of this compound was consistent with the structure proposed for **5a**. On the other hand, the ^{31}P{^{1}H} NMR spectrum of **5a** revealed a surprise: instead of finding one singlet, we observed two resonances, a major singlet at ca. 196 ppm and a minor one at ca. 193 ppm; the integration ratio of these two singlets was 100:8 (**Figure S4. 47**). Several attempts aimed at removing the extraneous signal by re-crystallization of the sample were unsuccessful. Indeed, repeated synthesis of **5a** gave new batches for which the ^{31}P NMR spectra showed the same two peaks, but with different integration ratios (**Figure S4. 48**). Based on similar observations made with closely related adducts

of the the phosphinite-based cyclonickelated and pincer complexes $\{\kappa^P,\kappa^C\text{-}(i\text{-Pr})_2PO\text{-}(C_6H_4)\}Ni(Br)L$[41] and $\{\kappa^P,\kappa^C,\kappa\text{-}2,6\text{-}(i\text{-Pr}_2PO)_2\text{-}(C_6H_3)\}NiBr,$[35,73–76] we believe that the presence of two singlets, as opposed to one, in the $^{31}P\{^1H\}$ NMR spectra of **5a** signifies that our isolated products contain mixtures of the Ni–Br and Ni–Cl analogues of this compound.[77] This hunch was confirmed when the said chloro derivative was found to be the main component of the crystalline lattice of the single crystals isolated during the purification process (vide infra).

In the case of complex **6a**, the $^{31}P\{^1H\}$ NMR spectrum was consistent with the solid-state structure, showing a major singlet at ca. 195 ppm (**Figure S4. 57**). Some features of the ^1H and $^{13}C\{^1H\}$ NMR spectra pertaining to the cyclonickellated phosphinite ligand were also unsurprising and similar to the corresponding signals observed for **5a**. On the other hand, the signals observed for imidazole protons and carbons did not correspond to our expectation based on the symmetry properties of **6a** in the solid state (vide infra). Indeed, given the inequivalence of the two imidazole moieties in **6a**, in principle one would expect to observe two sets of three $C_{sp2}H$ signals for each of the two inequivalent imidazole moieties, whereas the ^1H and $^{13}C\{^1H\}$ NMR spectra of **6a** showed only one set of signals. For instance, the ^{13}C signals appeared at δ 139 (d,$^3J_{CP}$= 2.7 Hz), 129 (s) and 116 (s), whereas there was only one NH signal in the ^1H NMR spectrum. These observations suggest the equivalence of both moieties, or an averaging of their signals, which implies that the main species in solution is the charge-neutral mono-imidazole adduct.

To gain insight into this unexpected finding, we treated a C_6D_6 solution of the dimeric precursor **1a** with 2 equiv of imidazole to directly generate 2 equiv of the charge neutral imidazole adduct shown in **Scheme 4. 5**, without proceeding via the η^1-TEMPOH derivative **3a**. The ^1H and $^{31}P\{^1H\}$ NMR spectra of the sample were nearly identical to those of authentic samples of **6a**. Moreover, X-ray diffraction analysis performed on single crystals obtained from this sample corroborated the identity of the product as **6a**. These results validate the curious transformation of **6a** to its charge-neutral mono(imidazole) derivative in solution, implying the lower thermal stability of the cationic derivative in solution. Indeed, even in the solid state and inside the air-free atmosphere of a glovebox **6a** shows visible signs of decomposition at ambient temperature. This explains why, despite several attempts, we were unsuccessful in obtaining accurate combustion analysis results for solid samples of **6a**.

The NMR spectra of **7a** were, for the most part, consistent with the solid-state structure of this compound. Thus, the ^1H NMR spectrum displayed the characteristic signals of the TEMPOH moiety, including a broad singlet at ca. 7.8-7.9 ppm for the NH proton and two singlets at ca. 1.0 and 1.5 ppm attributed to the two, pairwise equivalent C(CH_3)$_2$ groups. The more downfield signal overlaps with one of the two sets of doublets of doublets (at ca. 1.5 ppm) attributed to the four pairwise equivalent Me groups

present in the i-Pr$_2$P moiety. The other set of doublets of doublets attributed to the PCHCH_3 protons resonates at ca. 1.2 ppm, whereas the two PCH protons give rise to a complex multiplet at ca. 2.5 ppm. Finally, the four aromatic protons gave rise to an interesting pattern of signals arising from H-H and P-H couplings: a doublet of doublets at ca. 6.78 ppm ($^3J_{HH}$ = 7.6, $^4J_{HH}$ = 1.5), two pseudo-triplets of pseudo-triplets (or doublets of doublets of pseudo-triplets) at 6.97 and 7.03 ppm ($^3J_{HH}$ ~ $^3J_{HH}$ ~ 7.6, $^4J_{HH}$ ~ J_{PH} = 1.5), and a doublet of pseudo-triplets a7 7.86 ppm ($^3J_{HH}$ = 7.6, $^4J_{HH}$ ~ J_{PH} = 1.6). The ^{19}F{^{1}H} NMR spectrum of **7a** showed a major singlet at -74.3 ppm, as well as two minor singlets at -74.7 and -75.0 ppm.

Single crystal XRD diffraction studies carried out on complexes **5a**, **6a**, and **7a** confirm the assigned structures. The pertinent bond distances and angles for these complexes are listed in **Table S3**, the molecular diagrams are shown in **Figure 2,** and the main structural features are described below.
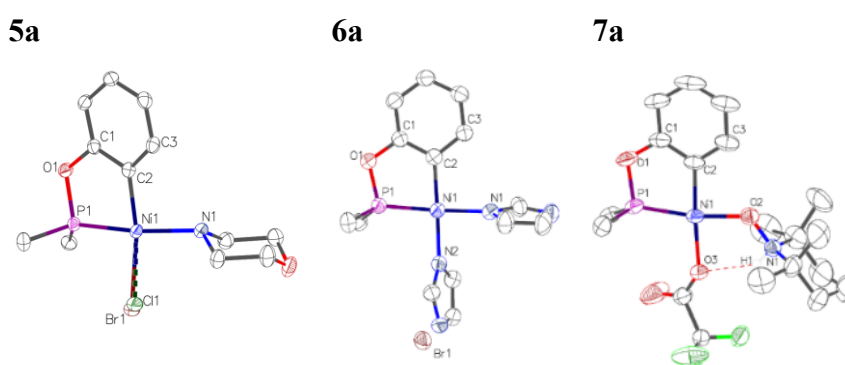
Figure 4. 2. Molecular diagrams for complexes **5a**, **6a**, and **7a**. Thermal ellipsoids are shown at the 50% probability level. For clarity, we have omitted in all three diagrams the H atoms and the Me groups of the i-Pr substituents, as well as the bromide anion in **7a**.

As was the case for complexes **3a-d**, the Ni atoms in complexes **6a-7a** adopt distorted square planar geometry featuring small angular distortions, as follows: cis angles of 93-96° (**5a**) to 83-95° (**6a**) and 82-102° (**7a**); trans angles of 165-169° (**5a**) to 175-176° (**6a**) and 170-175° (**7a**). The largest distances from the Ni center to the mean coordination plane defined by the four ligating atoms is seen in complex **5a** (0.06 Å). As mentioned above, the crystal lattice identified by X-ray analysis of the single crystals obtained for **5a** showed that it contained both the Ni–Br and Ni–Cl analogues in a 24:76 ratio. It is also worth noting that we found a molecule of imidazole co-crystallized with **6a**. The N$_{imine}$ moiety of this "free" imidazole displays H-interactions with the N–H moiety of the Ni-bound imidazole ligand trans to the aryl ligand, while additional nearly symmetrical H-bonds are also found between the bromide anion and N–H moieties of both the "free" imidazole as well as the imidazole ligand trans from the phosphinite ligand.

Comparison of bond distances reveals that Ni1–P1 bond distances are significantly longer in **5a-7a** compared to the TEMPOH complexes **3a-3d** reported herein (2.103-2.114 Å vs 2.091-2.099 Å). Complexes

5a and **7**a show Ni–C distances that are comparable to the corresponding distances in **3a-d**, whereas **6a** shows a longer distance (1.904 and 1.908 vs. 1.918 Å). As expected, the Ni–N_{sp3} distance in **5a** is longer than the corresponding Ni–N_{sp2} distance (trans from P) in **6a** (1.992 vs 1.930 Å), whereas the longest Ni–N_{sp2} distance is found for the imidazole moiety trans from C in **6a** (1.947 Å). The mean planes of the morpholine and imidazole ligands in **5a** and **6a** are nearly perpendicular to the mean coordination planes defined by the four ligating atoms in the respective complexes.

In the solid-state structure of in **7a**, the Ni–$O2_{TEMPOH}$ distance is in the same range as the corresponding distances in **3a-d** (1.902 vs 1.892-1.908 Å), whereas the Ni–$O3_{CF3CO2}$ distance is much longer (1.945 Å), presumably due to combined effect of the great trans influence of C_{ipso}, the electron-withdrawing properties of CF_3 and the N…H…O hydrogen bonding. It should also be noted that the Ni–$O3_{CF3CO2}$ distance found in **7a** is intermediate between the corresponding distances of 1.9674(19) Å [78] and 1.92-1.92 Å[79] reported for related Ni-OC(O)CF_3 compounds. Finally, the N1---O3 distance of 2.665(5) Å is also consistent with the presence of hydrogen-bonding interactions between the NH moiety of the TEMPOH ligand and the Ni-bound oxygen atom of the trifluoroacetate ligand. For comparison, a distance of 2.525 Å has been reported for similar N–H---O interactions in the metal-free pentachlorophenol adducts with substituted pyridines.[80]

4. 4. Conclusion

The original idea that inspired this study was the possibility that TEMPO$^\bullet$ might promote oxidation-induced C–O/C–N bond coupling in our cyclonickelated complexes. While this hoped-for reactivity failed to materialize, we ended up developing a simple route to a rare family of zwitterionic adducts featuring an η^1-TEMPOH-Ni(II) moiety. This was made possible by the surprisingly facile H-atom exchange between TEMPO$^\bullet$ and Et_2NOH to give TEMPOH, which converts the dimeric precursors **1a-1d** into the new TEMPOH adducts **3a-3d**. Solid state characterization of these compounds confirmed their zwitterionic character (partial negative and positive charges on the O- and N-moieties, respectively), as well as showing the presence of Br---H–N H-bonding. A number of tests also provided some insight into the lability of the Ni–O_{TEMPOH} bond in **3a**, showing that it can be displaced to varying degrees by N-based nucleophiles acetonitrile, morpholine, and imidazole, whereas other nucleophiles such as PPh_3, DMSO, and alkenes proved ineffective in driving the substitution equilibrium.

We also found that a number of oxidants lead to decomposition of the TEMPOH complexes **3**, whereas the potentially a one-electron oxidant AgOC(O)CF_3 simply displaced the bromide ligand in **3a** to give the new trifluoroacetate derivative **7a**. There are some indications that excess quantities of this salt can also displace TEMPOH from **7a**, in addition to causing a gradual oxidative decomposition, but these

reactivities have not been confirmed and remain poorly understood. Future efforts in our laboratory will be directed at more fully investigating the ligand exchange reactivities of the TEMPOH complexes, as well as reactivities with electrophiles such as alkyl and benzyl halides.

4. 5. Associated content

Supporting Information. Supplementary Information (ESI) available: synthetic procedures, NMR spectra, single crystal structure data and additional figures. CCDC 2287044(**3a**), 2287046 (**3b**), 2287047 (**3c**), 2287048 (**3d**), 2287049 (**5a**), 2287050 (**6a**), 2287104 (**7a**), 2309506 (piperidinium trifluoroacetate). For ESI and crystallographic data in CIF or other electronic formats see DOI: xxxxxxxx

4. 6. Author information

Corresponding Author

* E-mail: zargarian.davit@umontreal.ca

4. 7. Conflicts of interest

The authors declare no conflict of interest.

4. 8. Acknowledgement

Reactions of cyclonickelated complexes with hydroxylamines and TEMPO: isolation of new TEMPOH adducts of Ni(II) and their reactivities with nucleophiles and oxidants

Rajib K. Sarker, and Davit Zargarian*

Département de chimie, Université de Montréal, Montréal (Québec), Canada H3C 3J7

zargarian.davit@umontreal.ca

RECEIVED DATE (to be automatically inserted after your manuscript is accepted if required according to the journal that you are submitting your paper to)

a. General experimental considerations

All manipulations were carried out under a nitrogen atmosphere using standard Schlenk techniques and an inert-atmosphere box. The transfer/addition of all liquid reagents/reactants was performed with BRAND Transferpette® micropipettes (20-200 µL and 100-1000µL). Reported volumes should be considered to be within ±7 µL (for > 200 µL transfers) and ±3 µL (for < 200 µL transfers) of the measurements, with a >99% confidence level.[81] Solvents (CH_2Cl_2, DCM, tetrahydrofuran, THF, acetonitrile, MeCN, toluene, etc.) were dried by passage over a column of activated alumina, collected under nitrogen, and stored over 3 Å molecular sieves inside transfer/storage flasks equipped with high vacuum valves (Straus flasks). Et_3N was dried over CaH_2. The Ni^{II} precursor $[(i\text{-PrCN})NiBr_2]_n$ used throughout this study was prepared as reported previously.[35,82] Other reagents were purchased from Sigma-Aldrich or FisherSci and used without further purification.

The NMR spectra were recorded at 500 MHz (^1H), 125.72 MHz (^{13}C), and 202.4 MHz (^{31}P). Chemical shift values are reported in ppm (δ) and referenced internally to the residual solvent signals (^1H and ^{13}C: 1.94 and 118.26 ppm for CD_3CN; 7.26 and 77.16 for $CDCl_3$; 7.16 and 128.06

for C_6D_6) or externally (^{31}P: H_3PO_4 in D_2O, $\delta = 0$). The minimal precision of the NMR spectra was found to be 0.3 Hz for ^1H, 0.7 Hz for ^{13}C and 2 Hz for ^{31}P.

Single crystals of complexes **3a-3d** and **7a** were grown from Et_2O solutions cooled to -35 °C. Whereas complex **5a** was grown from DCM-Hexane mixture and complex **6a** was grown from DCM-Et_2O mixture. The crystallographic data for all structures were collected on either a Bruker Microsource (Cu radiation) or a Bruker Venture Metaljet (Ga radiation) via the Bruker APEX II or APEX III[83] software packages. Cell refinement and data reduction were performed using SAINT.[84] An empirical absorption correction, based on multiple measurements of equivalent reflections, was applied using the program SADABS or TWINABS.[85] The space group was confirmed by the XPREP[86] routine in APEX. The structures were solved in OLEX[87] using the SHELX[88] suite and refined by full-matrix least squares with SHEXL. All non-hydrogen atoms were refined with anisotropic displacement parameters, whereas hydrogen atoms were set in calculated positions and refined via the riding model, with thermal parameters being 1.5 times that of the carbon bearing the H in question. All Thermal ellipsoid plots were drawn using OLEX.

b. Procedures for the synthesis of Ni-TEMPOH complexes 3a-3d

[{κ^P,κ^C-(i-Pr)$_2$PO-(C$_6$H$_4$)}Ni(Br)(TEMPOH)], 3a. A 25 mL Schlenk flask containing 10 mL of DCM was charged with dimer [{κ^P,κ^C-(i-Pr)$_2$PO-C$_6$H$_4$}Ni(μ-Br)]$_2$ (95 mg, 0.137 mmol, 1.00 equiv) and Et_2NOH (27.5 µL, 0.273 mmol, 2.00 equiv). The resulting mixture was stirred overnight under inert atmosphere at room temperature. To this mixture was added TEMPO (43 mg, 0.273 mmol, 2 equiv) and the stirring was continued under the same conditions for 3 h. The final reaction mixture was placed under vacuum to remove all volatiles, and the resulting sticky yellow solid residue was treated with ca. 1 mL of Et_2O, filtered and the filtrate kept at -35 °C overnight. Brown crystals were separated and washed with cold hexane. Yield: 106 mg, 0.211 mmol, 77%. ^1H NMR (400 MHz, 20 °C, C_6D_6): δ 1.10 (s, 6H, CCH_3), 1.11 (br s, 6H, CH_2), 1.25(dd, 6H,$^3J_{HP}$ =14.3, $^3J_{HH}$ =7.0, CHCH_3), 1.54 (dd, 6H,$^3J_{HP}$ =17.1, $^3J_{HH}$ =7.2, CHCH_3), 1.75 (s, 6H, CCH_3), 2.24 (sept, 2H, PCH, J_{HH} = 7.1), 6.91 (dd, 1H, C3$_{Ar}$-H, $^3J_{HH}$ = 7.7, $^4J_{HH}$ = 1.1), 7.03 (t, 1H, $^3J_{HH}$ = 7.4, C4$_{Ar}$-H),), 7.09 (t, 1H,$^3J_{HH}$ = 7.3, C5$_{Ar}$-H),7.93 (d, 1H, C6$_{Ar}$-H, $^3J_{HH}$=7.6), 8.48 (br s, 1H, NH). $^{13}C\{^1H\}$ NMR (125.72 MHz, 20 °C, C_6D_6): δ 16.06 (s, 1C, CHCH_3), 17.16 (d, 2C, J_{PC} = 1.5, CHCH_3), 18.71 (d, 1C, J_{PC} = 3.9, CHCH_3), 20.69 (s, 2C, CCH_3), 28.81 (d, 2C, J_{PC} = 26.5, PCH) , 30.14 (s, 2C, CCH$_3$), 37.21 (s, 3C, CH$_2$), 66.27 (s, 2C, CCH$_3$), 110.05 (d, 1C, J_{PC} = 13.0,

C3$_{Ar}$), 120.48 (d, 1C, J_{PC} = 2.3, C4/5$_{Ar}$), 126.64 (s, 1C, C5/4$_{Ar}$), 134.28 (d, 1C, J_{PC} = 35.8, C1/6$_{Ar}$), 134.83 (d, 1C, J_{PC} = 3.9, C6/1$_{Ar}$), 167.64 (d, 1C, J_{PC} = 13.4, C2$_{Ar}$). ^{31}P{^{1}H} NMR (202.4 MHz, 20 °C, C$_6$D$_6$): δ 201.49 (s, 1P). Anal. calc. for C$_{21}$H$_{37}$BrNNiO$_2$P: C, 49.94; H, 7.38; N, 2.77. Found: C, 49.72; H, 7.32; N, 2.72.

[{κ^P,κ^C-(i-Pr)$_2$PO-(5-Cl-C$_6$H$_3$)}Ni(Br)(TEMPOH)], 3b. A 25 mL Schlenk flask containing 10 mL of DCM was charged with TEMPO (36 mg, 0.230 mmol, 2.00 equiv) and Et$_2$NOH (23.1 μL, 0.230 mmol, 2.00 equiv). The resulting mixture was stirred for 20 min under inert atmosphere at room temperature, followed by addition of the dimeric precursor [{κ^P,κ^C-(i-Pr)$_2$PO-(5-Cl-C$_6$H$_3$)}Ni(μ-Br)]$_2$ (88 mg, 0.115 mmol, 1 equiv) and continued stirring for 2 h under the same conditions. The final reaction mixture was placed under vacuum to remove all volatiles, and the resulting sticky dark brown solid residue was treated with ca. 1 mL of Et$_2$O, filtered and the filtrate kept at -35 °C overnight. Brown crystals were separated and washed with cold hexane. Yield: 57 mg, 0.106 mmol, 46%. ^{1}H NMR (400 MHz, 20 °C, C$_6$D$_6$): δ 1.03 (s, 6H, CCH_3), 1.08 (br s, 6H, CH_2), 1.18 (dd, 6H, $^3J_{HP}$ =14.5, $^3J_{HH}$ =6.9, CHCH_3), 1.48 (dd, 6H,$^3J_{HP}$ =17.2, $^3J_{HH}$ =7.3, CHCH_3), 1.70 (s, 6H,CCH_3), 2.16 (ps oct, 2H, PCH, $^3J_{HH}$ = 7.0), 6.95 (d, 1H, C6$_{Ar}$-H, $^4J_{HH}$ = 2.0), 7.05 (d, 1H,$^3J_{HH}$ = 8.3, C3$_{Ar}$-H),), 7.74 (dd, 1H,$^3J_{HH}$ = 8.3, $^4J_{HH}$ = 1.6, C4$_{Ar}$-H), 8.35 (br s, 1H, N-H). ^{13}C{^{1}H} NMR (125.72 MHz, 20 °C, C$_6$D$_6$): δ16.00 (s, 1C, CHCH_3), 17.02 (d, 1C, $^2J_{PC}$= 1.7, CHCH_3), 18.55 (d, 2C, $^2J_{PC}$= 3.7, CHCH_3), 20.59 (s, 2C, CCH_3), 28.79 (d, 1C, $^2J_{PC}$= 26.4, PCH) , 30.10 (s, 2C, CCH$_3$), 37.17 (s, 1C, CH$_2$), 66.32 (s, 2C, CCH$_3$), 110.65 (d, $^2J_{PC}$= 26.4, 1C, C6$_{Ar}$), 120.45 (d, 1C, $^2J_{PC}$ = 2.1, 1C, C3$_{Ar}$), 131.90 (s, 1C, C5$_{Ar}$), 132.69 (d, J_{PC} = 36.1, 1C, C1$_{Ar}$), 135.41 (d, 1C, J_{PC} = 4.07, 1C, C4$_{Ar}$), 167.56 (d, J_{PC} = 14.4, 1C, C2$_{Ar}$) . ^{31}P{^{1}H} NMR (202.4 MHz, 20 °C, C$_6$D$_6$): δ203.02 (s, 1P). Anal. calc. for C$_{21}$H$_{36}$BrClNNiO$_2$P: C, 46.75; H, 6.73; N, 2.60. Found: C, 46.57; H, 6.81; N, 2.53.

[{κ^P,κ^C-(i-Pr)$_2$PO-(5-OMe-C$_6$H$_3$)}Ni(Br)(TEMPOH)], 3c. A 25 mL Schlenk flask containing 10 mL of DCM was charged with TEMPO (29 mg, 0.186 mmol, 2.00 equiv) and Et$_2$NOH (18.7 μL, 0.186 mmol, 2.00 equiv). The resulting mixture was stirred for 20 min under inert atmosphere at room temperature, followed by addition of the dimeric precursor [{κ^P,κ^C-(i-Pr)$_2$PO-(5-OMe-C$_6$H$_3$)}Ni(μ-Br)]$_2$ (70 mg, 0.093 mmol, 1 equiv) and continued stirring for 2 h under the same conditions. The final reaction mixture was placed under vacuum to remove all volatiles, and the resulting sticky dark brown solid residue was treated with ca. 1 mL of Et$_2$O, filtered and the filtrate

kept at -35 °C overnight. Brown crystals were separated and washed with cold hexane. Yield: 44 mg, 0.082 mmol, 43%. ^{1}H NMR (400 MHz, 20 °C, C_6D_6): δ 1.10 (s, 6H, CCH_3), 1.12 (br s, 6H, CH_2), 1.27 (dd, 6H, $^3J_{HP}$ =14.4, $^3J_{HH}$ = 7.0, CHCH_3), 1.57 (dd, 6H, $^3J_{HP}$ = 17.0, $^3J_{HH}$ =7.2, CHCH_3), 1.77 (s, 6H, CCH_3), 2.25 (ps oct, 2H, $^3J_{HH}$ = 7.1, PCH), 3.39 (s, 3H, OCH_3), 6.65 (d, 1H, C3$_{Ar}$-H, $^4J_{HH}$ = 2.6), 6.73 (dd, 1H, $^3J_{HH}$ = 8.5, $^4J_{HP}$ = 2.0, C6$_{Ar}$-H), 7.78 (dd, 1H, $^3J_{HH}$ = 8.6, $^4J_{HH}$ = 1.7, C4$_{Ar}$-H), 8.48 (s, 1H, N-H). ^{13}C{^{1}H} NMR (125.72 MHz, 20 °C, C_6D_6): δ 16.07 (s, 1C, CHCH_3), 17.17 (d, 1C, $^2J_{PC}$= 1.5, CHCH_3), 18.71 (d, 2C, $^2J_{PC}$ = 3.9, CHCH_3), 20.66 (s, 2C, CCH_3), 28.75 (d, 1C, $^2J_{PC}$= 26.3, PCH), 30.17 (s, 2C, CCH$_3$), 37.21 (s, 3C, CH$_2$), 54.86 (s, 1C, OCH$_3$), 66.25 (s, 2C, CCH$_3$), 97.06 (d, $^2J_{PC}$ = 13.9, 1C, C3$_{Ar}$), 106.77 (s, 1C, C6$_{Ar}$), 123.30 (d, 1C, $^2J_{PC}$ = 37.7, 1C, C5$_{Ar}$), 134.67 (d, J_{PC} = 4.3, C4$_{Ar}$), 160.42 (s, 1C, C1$_{Ar}$), 167.69 (d, J_{PC} = 14.9, 1C, C2$_{Ar}$) . ^{31}P{^{1}H} NMR (202.4 MHz, 20 °C, C_6D_6): δ 200.80 (s, 1P). Anal. calc. for $C_{22}H_{39}BrNNiO_3P.Et_2O$: C, 51.26; H, 8.11, N, 2.30. Found: C, 51.06; H, 7.61; N, 2.62.

[{κ^P,κ^C-(i-Pr)$_2$PO-(4-MeO-C$_{10}$H$_5$)}Ni(Br)(TEMPOH)], 3d. A 25 mL Schlenk flask containing 10 mL of DCM was charged with TEMPO (26 mg, 0.167 mmol, 2.00 equiv) and Et_2NOH (16.8 µL, 0.167 mmol, 2.00 equiv). The resulting mixture was stirred for 20 min under inert atmosphere at room temperature, followed by addition of the dimeric precursor [{κ^P,κ^C-(i-Pr)$_2$PO-(OMe-1-Nap)}Ni(μ-Br)]$_2$ (71 mg, 0.083 mmol, 1 equiv) and continued stirring for 2 h under the same conditions. The final reaction mixture was placed under vacuum to remove all volatiles, and the resulting sticky dark brown solid residue was treated with ca. 1 mL of Et_2O, filtered and the filtrate kept at -35 °C overnight. Brown crystals were separated and washed with cold hexane. (Yield: 50 mg, 0.086 mmol, 51%). ^{1}H NMR (400 MHz, 20 °C, C_6D_6): δ 1.12 (s, 6H, CCH_3), 1.14 (br s, 6H, CH_2), 1.28 (dd, 6H, $^3J_{HP}$ =14.3, $^3J_{HH}$ =7.0, CHCH_3), 1.58 (dd, 6H, $^3J_{HP}$ = 17.2, $^3J_{HH}$ = 7.2, CHCH_3), 1.79 (s, 6H, CCH_3), 2.29 (ps oct, 2H, PCH, $^3J_{HH}$ = 7.1), 3.86 (s, 3H, OCH_3), 7.33 - 7.38 (m, 2H, C$_{Ar}$-H), 7.46 (d, 1H, $^3J_{HH}$ = 1.5, C$_{Ar}$-H),), 8.15 - 8.19 (m, 1H, C$_{Ar}$-H), 8.54 (br s, 1H, N-H), 8.59 - 8.64 (m, 1H, C$_{Ar}$-H). ^{13}C{^{1}H} NMR (125.72 MHz, 20 °C, C_6D_6): δ 16.09 (s, 1C, CCH$_3$), 17.20 (d, 1C, $^2J_{PC}$= 1.7, CHCH_3), 18.74 (d, 2C, $^2J_{PC}$= 3.9, CHCH_3), 20.53 (s, 2C, CCH$_3$), 28.94 (d, 1C, $^2J_{PC}$= 26.3, PCH), 30.24 (s, 2C, CH$_2$), 37.22 (s, 1C, CCH$_3$), 55.32 (s, 1C, OCH$_3$), 66.36 (s, 2C, C), 109.47 (d, $^2J_{PC}$ = 4.3, 1C, C6$_{Ar}$), 122.07 (d, 1C, $^2J_{PC}$ = 12.4, 1C, C$_{Ar}$), 122.41 (s, C$_{Ar}$), 122.73 (s, C$_{Ar}$), 124.08 (s, C$_{Ar}$), 125.52 (s, C$_{Ar}$), 126.16 (s, C$_{Ar}$), 148.20 (d, J_{PC} = 3.0, C$_{Ar}$), 156.03 (d, 1C, J_{PC} = 13.8, C2$_{Ar}$). ^{31}P{^{1}H} NMR (202.4 MHz, 20 °C, C_6D_6): δ 199.38 (s, 1P). Anal. calc. for $C_{26}H_{41}BrNNiO_3P$: C, 53.36; H, 7.06; N, 2.39. Found: C, 53.26; H, 7.10; N, 2.38.3.

c. Procedures for the synthesis of complexes 5a, 6a, & 7a.

[{κ^P, κ^C-(*i*-Pr)$_2$PO-(C$_6$H$_4$)}Ni(Br)(C$_4$H$_9$NO)], 5a. Method A: A 25 mL Schlenk flask containing 10 mL of DCM was charged with TEMPO (43 mg, 0.274 mmol, 2 equiv) and Et$_2$NOH (27.6 µL, 0.274 mmol, 2 equiv). The resulting mixture was stirred for 20 min under inert atmosphere at room temperature, followed by addition of the dimeric precursor [{κ^P, κ^C-(*i*-Pr)$_2$PO-C$_6$H$_4$}Ni(μ-Br)]$_2$ (95 mg, 0.137 mmol, 1 equiv), continued stirring for 20 min under the same conditions before adding morpholine (236 µL, 2.74 mmol, 20 equiv) and continued stirring for 2 h as before. The final reaction mixture was placed under vacuum to remove all volatiles, and the resulting sticky solid residue was treated with ca. 1 mL of DCM and filtered. The filtrate was layered with hexane and finally the filtrate was kept at -35 °C overnight. Brown crystals were separated and washed with cold hexane. **Method B:** A 25 mL Schlenk flask containing 10 mL of DCM was charged with the dimeric precursor [{κ^P, κ^C-(*i*-Pr)$_2$PO-C$_6$H$_4$}Ni(μ-Br)]$_2$ (95 mg, 0.137 mmol, 1 equiv) and morpholine (236 µL, 2.74 mmol, 20 equiv). This mixture was stirred for 2 h and then placed under vacuum to remove all volatiles. The resulting sticky solid residue was treated with ca. 1 mL of DCM and filtered. The filtrate was layered with hexane and finally the filtrate was kept at -35 °C overnight. Brown crystals were separated and washed with cold hexane. Yield: 58 mg, 0.132 mmol, 48%.

^{1}H NMR (400 MHz, 20 °C, C$_6$D$_6$): δ 1.21 (dd, 6H, $^3J_{HP}$ = 14.6, $^3J_{HH}$ = 7.0, CHC*H*$_3$), 1.53 (dd, 6H, $^3J_{HP}$ = 17.1, $^3J_{HH}$ = 7.2, CHC*H*$_3$), 2.19 - 2.36 (m, 3H, overlap of N-*H* and PC*H*), 2.45 (br s, 2H, C*H*$_2$), 2.76 (br s, 2H, C*H*$_2$), 3.28 (br s, 2H, C*H*$_2$), 3.50 (br s, 2H, C*H*$_2$) 6.68 (d, 1H, $^3J_{HH}$ = 7.6, C3$_{Ar}$-*H*), 6.87 (tt, 1H, $^3J_{HH}$ = 6.2, $^4J_{HH}$ = 1.2, C4/5$_{Ar}$-*H*), 6.91 (dd, 1H, $^3J_{HH}$ = 7.9, $^4J_{HH}$ = 1.3, C6$_{Ar}$-*H*,), 7.05 (tt, 1H, $^3J_{HH}$ = 7.5, $^4J_{HH}$ = 1.4, C5/4$_{Ar}$-*H*). ^{13}C{^{1}H} NMR (125.72 MHz, 20 °C, C$_6$D$_6$): δ17.10 (d, 2C, J_{PC} = 1.8, CHC*H*$_3$), 18.81 (d, 2C, J_{PC} = 3.3, CHC*H*$_3$), 28.9 (d, 1C, J_{PC} = 27.1, P*C*H), 47.37 (s, 2C, *C*H$_2$), 68.01 (s, 2C, *C*H$_2$) , 111.24 (d, 1C, J_{PC} = 12.6, *C*4/5$_{Ar}$), 121.46 (d, 1C, J_{PC} = 2.3, *C*5/4$_{Ar}$), 127.29 (s, 1C, *C*6$_{Ar}$), 133.43 (d, 1C, J_{PC} = 3.2, *C*3$_{Ar}$), 135.05 (d, 1C, J_{PC} = 32.1, C1$_{Ar}$), 168.29 (d, 1C, J_{PC} = 12.9, C2$_{Ar}$). ^{31}P{^{1}H} NMR (202.4 MHz, 20 °C, C$_6$D$_6$): δ 196.03 (s, 1P), 193.06 (s, 1P); integration ratio 100:8. Anal. calc. for C$_{16}$H$_{27}$Br$_{0.93}$Cl$_{0.07}$NNiO$_2$P: C, 44.49; H, 6.25; N, 3.22. Found: C, 44.29; H, 6.19; N, 3.28.

NB: We believe that the minor ^{31}P singlet at 193.06 ppm is due to the presence of the Ni-Cl analogue of **5a** that originates from the presence of the corresponding Ni-Cl analogue in the

specific batch of dimeric precursor **1a** used for this synthesis. Previous experience with this family of complexes has shown that the dimeric precursors **1** obtained from the C-H nickelation of the aryl phosphinite ligands R_2OPAr often contain variable amounts of its Ni-Cl analogues if R_2OPAr are contaminated with HCl•NEt$_3$ generated during their preparation from ArOH, ClPR$_2$, and NEt$_3$.

[{κ^P,κ^C-(*i*-Pr)$_2$PO-(C$_6$H$_4$)}Ni(imidazole)$_2$][Br], 6a. Method A: A 25 mL Schlenk flask containing 10 mL of DCM was charged with TEMPO (34 mg, 0.219 mmol, 2 equiv) and Et$_2$NOH (22.0 μL, 0.219 mmol, 2 equiv). The resulting mixture was stirred for 20 min under inert atmosphere at room temperature, followed by addition of the dimeric precursor [{κ^P,κ^C-(*i*-Pr)$_2$PO-C$_6$H$_4$}Ni(μ-Br)]$_2$ (76 mg, 0.110 mmol, 1 equiv), continued stirring for 20 min under the same conditions before adding imidazole (30 mg, 0.439 mmol, 4 equiv) and continued stirring for 1 h as before. The final reaction mixture was placed under vacuum to remove all volatiles, and the resulting sticky yellow solid residue was treated with ca. 1 mL of DCM and Et$_2$O mixture, filtered and the filtrate kept at -35 °C overnight. Brown crystals were separated and washed with cold hexane. **Method B:** A 25 mL Schlenk flask containing 10 mL of DCM was charged with the dimeric precursor [{κ^P,κ^C-(*i*-Pr)$_2$PO-C$_6$H$_4$}Ni(μ-Br)]$_2$ (76 mg, 0.110 mmol, 1 equiv) and imidazole (30 mg, 0.439 mmol, 4 equiv). This mixture was stirred for 2 h and then placed under vacuum to remove all volatiles. The resulting sticky yellow solid residue was treated with ca. 1 mL of DCM and Et$_2$O mixture, filtered, and the filtrate kept at -35 °C overnight. Brown crystals were separated and washed with cold hexane. Yield: 66 mg, 0.137 mmol, 62%.

^{1}H NMR (400 MHz, 20 °C, C$_6$D$_6$): δ 1.30 (dd, 6H, $^3J_{HP}$ = 14.5, $^3J_{HH}$ = 7.0, CHCH_3), 1.63 (dd, 6H, $^3J_{HP}$ = 17.2, $^3J_{HH}$ = 7.2, CHCH_3), 2.40 (ps oct, 2H, PCH, $^3J_{HH}$ = 7.1), 5.96 (br s, C$_{Ar}$-H), 6.30 (td, 1H, C3$_{Ar}$-H, $^3J_{HH}$ = 7.7, $^4J_{HH}$ = 1.3), 6.68 (tt, 1H, $^3J_{HH}$ = 7.3, J_{HH} = 1.1, C4/5$_{Ar}$-H), 6.92 (dd, 1H, $^3J_{HH}$ = 7.9, $^4J_{HH}$ = 1.3, C6$_{Ar}$-H), 7.00 (tt, 1H, $^3J_{HH}$ = 7.8, $^4J_{HH}$ = 1.4, C5/4$_{Ar}$-H), 7.13 (br s, C$_{Ar}$-H), 7.20 (br s, C$_{Ar}$-H), 8.56 (br s, 1H, N-H). ^{13}C{^{1}H} NMR (125.72 MHz, 20 °C, C$_6$D$_6$): δ17.16 (d, 2C, J_{PC} = 1.8, CHCH_3), 18.87 (d, 2C, J_{PC} = 3.4, CHCH_3), 28.82 (d, 2C, J_{PC} = 27.1, PCH), 110.48 (d, C, J_{PC} = 12.9, C6$_{Ar}$) , 115.80 (s, C, C_{Ar}), 121.11 (d, C, J_{PC} = 2.3, $C$4/5$_{Ar}$), 126.88 (s, C, $C$5/4$_{Ar}$), 128.84 (s, C, C_{Ar}), 135.72 (d, C, J_{PC} = 33.9, C1$_{Ar}$), 136.87 (s, C, C$_{Ar}$), 138.95 (d, C, J_{PC} = 2.6, C3$_{Ar}$), 168.38 (d, 1C, J_{PC} = 13.3, C2$_{Ar}$). ^{31}P{^{1}H} NMR (202.4 MHz, 20 °C, C$_6$D$_6$): δ 194.93 (s, 1P).

[{κ^P,κ^C-(*i*-Pr)$_2$PO-(C$_6$H$_4$)}Ni(OCOCF$_3$)(TEMPOH)], 7a: A 50 mL Schlenk flask containing 10 mL of DCM was charged with TEMPO (42.8 mg, 0.274 mmol, 2 equiv) and Et$_2$NOH (27.6 µL, 0.274 mmol, 2 equiv). The resulting mixture was stirred for 20 min under inert atmosphere at room temperature, followed by addition of the dimeric precursor [{κ^P,κ^C-(*i*-Pr)$_2$PO-C$_6$H$_4$}Ni(μ-Br)]$_2$ (95 mg, 0.137 mmol, 1 equiv),), continued stirring for 20 min under the same conditions before adding AgOCOCF$_3$ (60.5 mg, 0.274 mmol, 2 equiv) and continued stirring for 2 h as before. The final reaction mixture was placed under vacuum to remove all volatiles, and the resulting sticky yellow solid residue was treated with ca. 1 mL of Et$_2$O, filtered and the filtrate kept at -35 °C overnight. Yellow crystals were separated and washed with cold hexane. Yield: 57.5 mg, 0.107 mmol, 39%) ^{1}H NMR (400 MHz, 20 °C, C$_6$D$_6$): δ 1.05 (s, 6H, CC*H*$_3$), 1.15 (br m, 6H, C*H*$_2$), 1.19 (dd, 6H, $^3J_{HP}$ =13.2, $^3J_{HH}$ =7.0, CHC*H*$_3$), 1.49 (dd, 6H, $^3J_{HP}$ =18.5, $^3J_{HH}$ =7.3, CHC*H*$_3$), 1.52 (s, 6H, CC*H*$_3$), 2.48 (dm, 2H, PC*H*, $^2J_{HH}$ = 7.1, J_{HH} = 2.3), 6.78 (dd, 1H, C3$_{Ar}$-*H*, $^3J_{HH}$ = 7.6, $^4J_{HH}$ = 1.5), 6.97 (pstpst, 1H, $^3J_{HH}$ ~ $^3J_{HH}$ ~ 7.4, $^4J_{HH}$ ~ J_{PH} = 1.1, C4/5$_{Ar}$-*H*), 7.03 (pstpst, 1H, $^3J_{HH}$ ~ $^3J_{HH}$ ~ 7.3, $^4J_{HH}$ ~ J_{PH} = 1.6, C5/4$_{Ar}$-*H*), 7.74 (pstd, 1H, $^3J_{HH}$ ~ $^3J_{HH}$ ~ 7.6, J_{PH}=1.6, C6$_{Ar}$-H), 7.86 (br s, 1H, NH). ^{13}C{^{1}H} NMR (125.72 MHz, 20 °C, C$_6$D$_6$): δ15.91 (s, 1C, CHC*H*$_3$), 16.95 (d, 2C, J_{PC} = 3.5, CHC*H*$_3$), 19.00 (d, 1C, J_{PC} = 5.7, CHC*H*$_3$), 19.74 (s, 2C, CC*H*$_3$), 29.16 (d, 2C, J_{PC} = 24.4, P*C*H) , 29.59 (s, 2C, CC*H*$_3$), 37.46 (s, 3C, *C*H$_2$), 65.60 (s, 2C, *C*CH$_3$), 110.08 (d, 1C, J_{PC} = 12.0, C3$_{Ar}$), 120.41 (d, 1C, J_{PC} = 2.2, C4/5$_{Ar}$), 127.03 (s, 1C, C5/4$_{Ar}$), 134.90 (d, 1C, J_{PC} = 3.3, C6$_{Ar}$), 160.59 (d, 1C, J_{PC} = 35.8, C1$_{Ar}$), 168.47 (d, 1C, J_{PC} = 12.0, C2$_{Ar}$). ^{19}F{^{1}H} NMR spectrum of **7a** (C$_6$D$_6$): -74.3 (s). ^{31}P{^{1}H} NMR (202.4 MHz, 20 °C, C$_6$D$_6$): δ 199.84 (s, 1P). Anal. calc. for C$_{23}$H$_{37}$F$_3$NNiO$_4$P: C, 51.33; H, 6.93; N, 2.60. Found: C, 50.46; H, 7.45; N, 2.56.

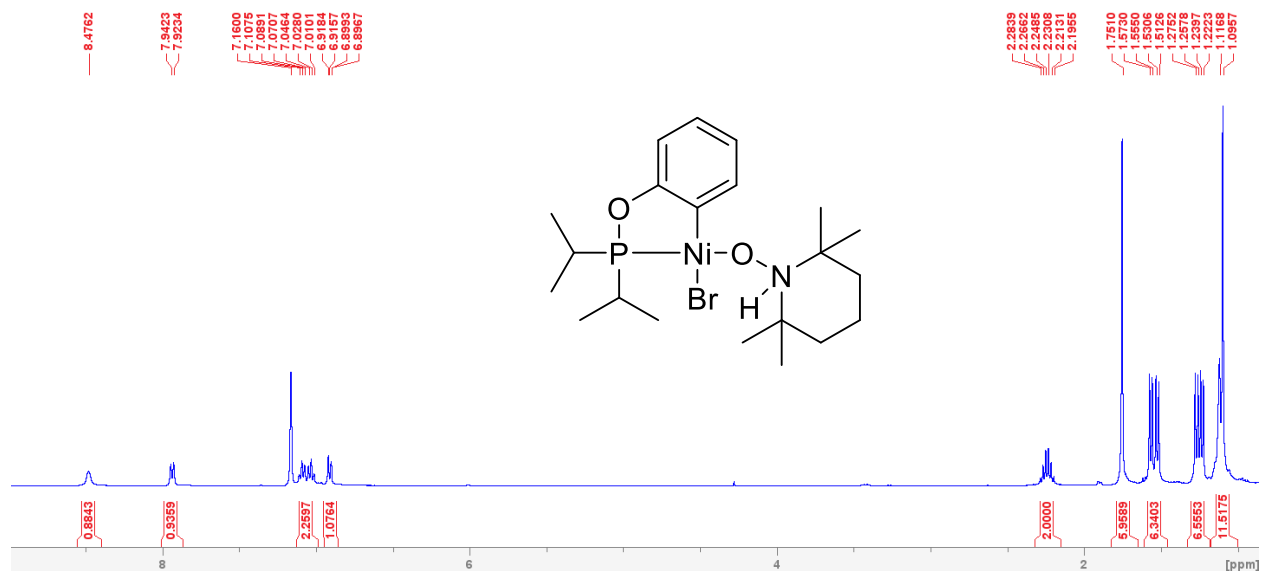## d. NMR spectra of characterized compounds

Complex **3a**

Figure S4. 1. Full ^{1}H NMR spectrum of **3a** in C$_6$D$_6$.

Figure S4. 2. The expanded aliphatic region of the ^{1}H NMR spectrum of **3a** in C$_6$D$_6$.
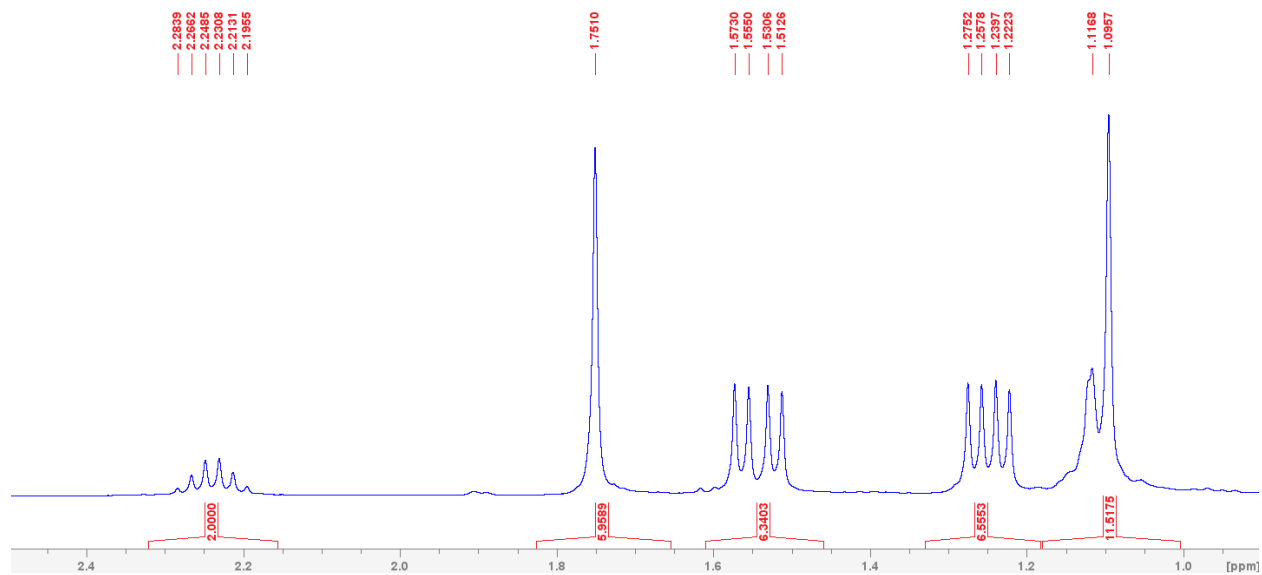
Figure S4. 3. The expanded aromatic region of the ^{1}H NMR spectrum of **3a** in C$_6$D$_6$.
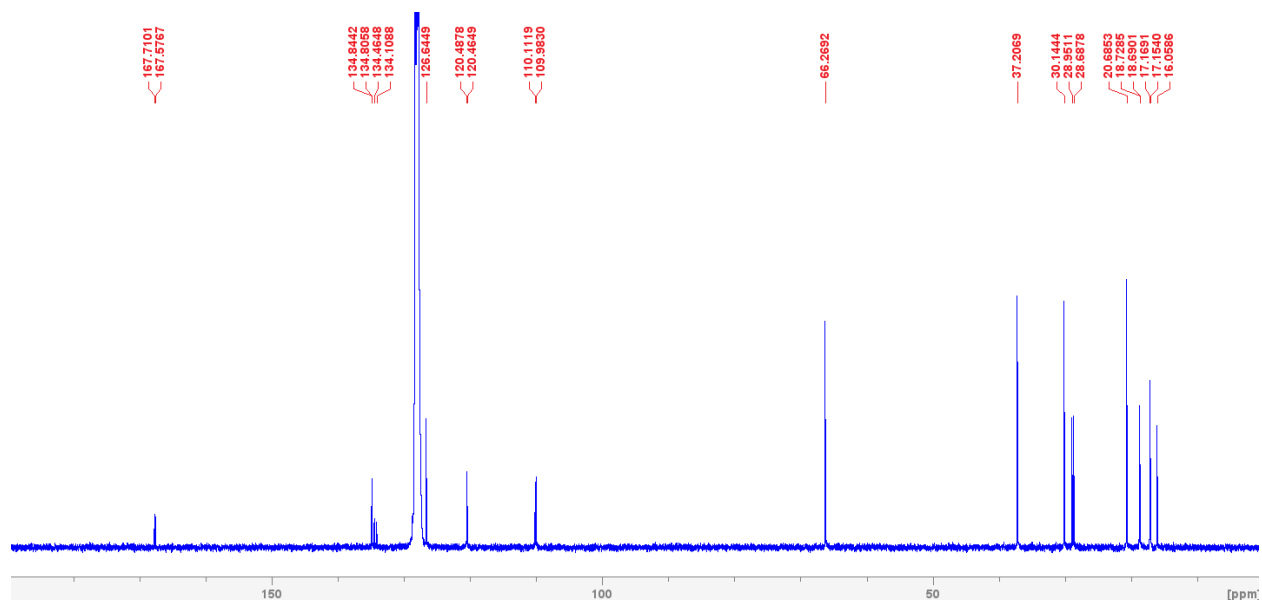
Figure S4. 4. Full ^{13}C{^{1}H} NMR spectrum of **3a** in C$_6$D$_6$.
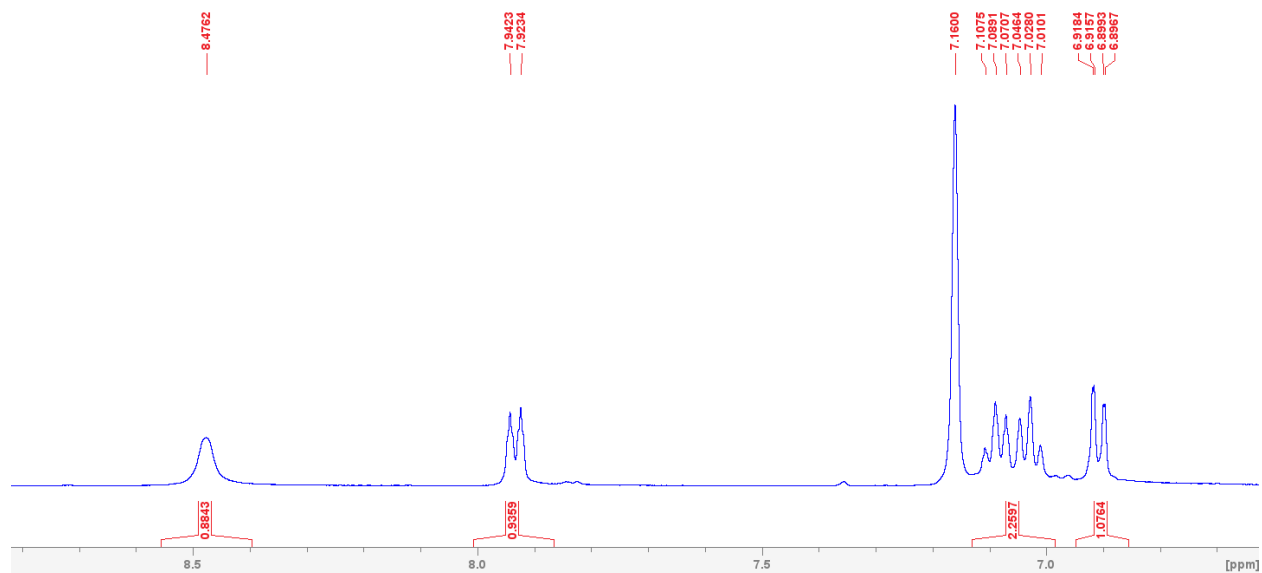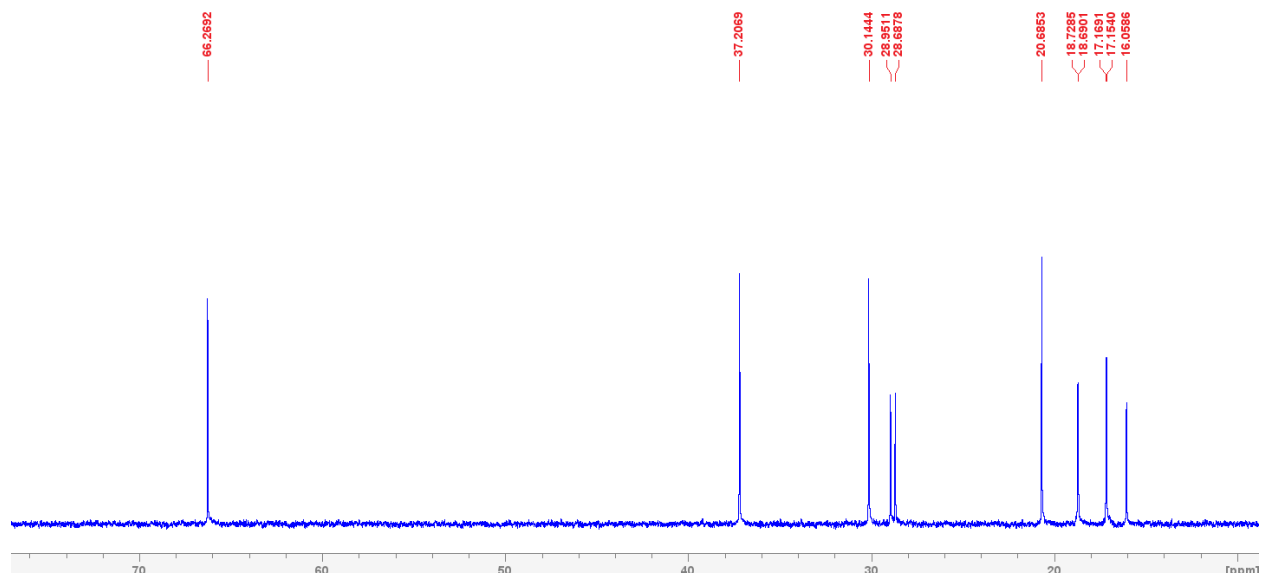
Figure S4. 5. The expanded aliphatic region of the $^{13}C\{^1H\}$ NMR spectrum of **3a** in C_6D_6.
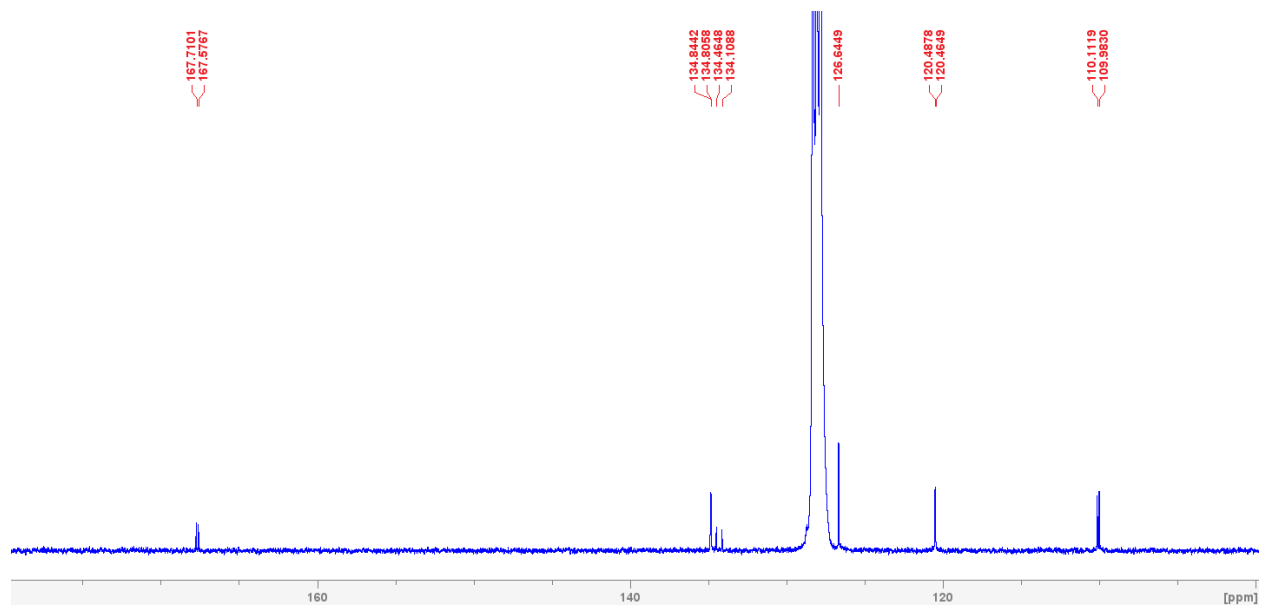
Figure S4. 6. The expanded aromatic region of the $^{13}C\{^1H\}$ NMR spectrum of **3a** in C_6D_6.
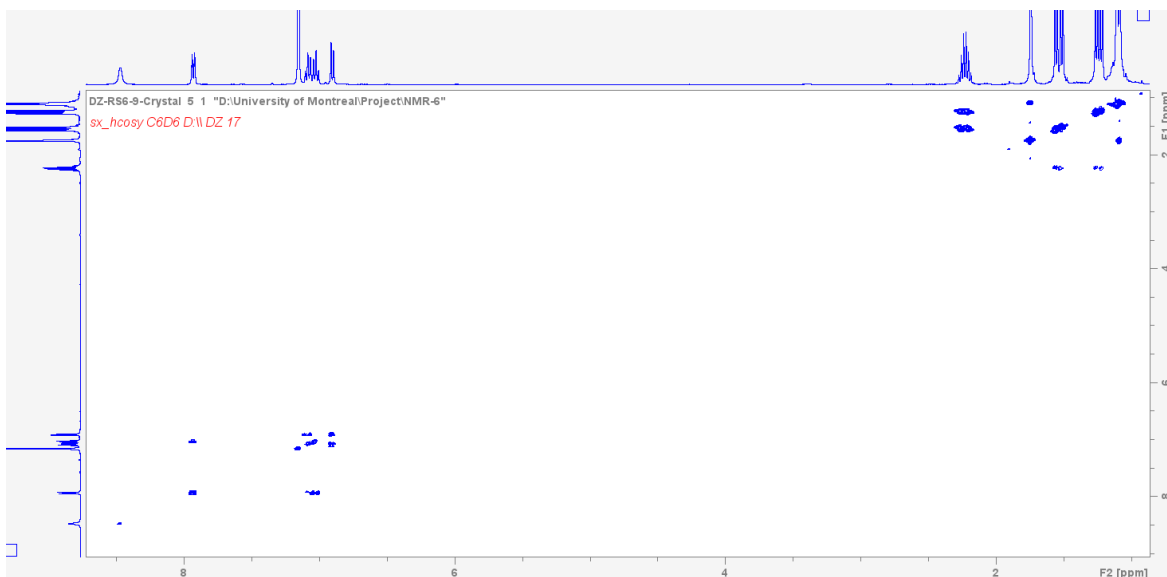
Figure S4. 7. Full ^{1}H-^{1}H COSY NMR spectrum of **3a** in C$_6$D$_6$.

Figure S4. 8. Full HSQC-edited NMR spectrum of **3a** in C$_6$D$_6$.
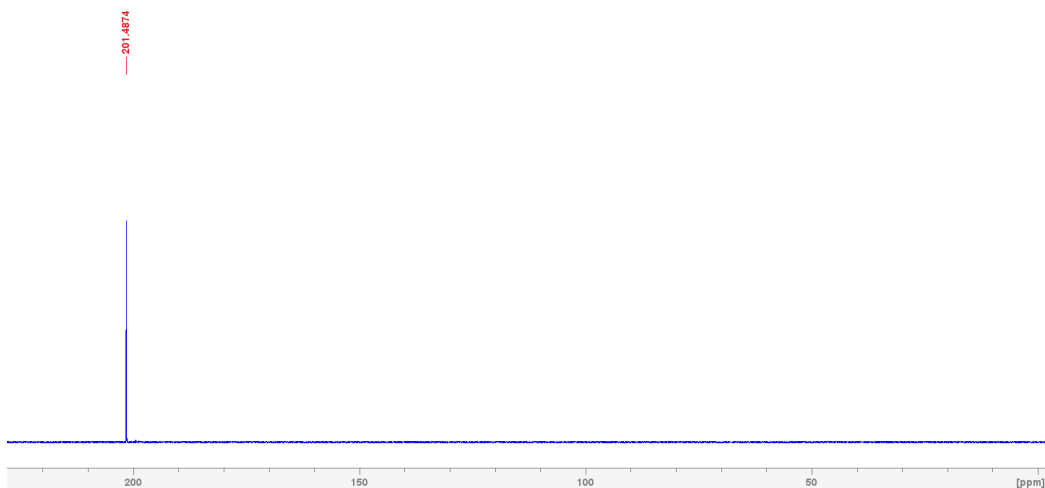
Figure S4. 9. $^{31}P\{^1H\}$ NMR spectrum of **3a** in C_6D_6.
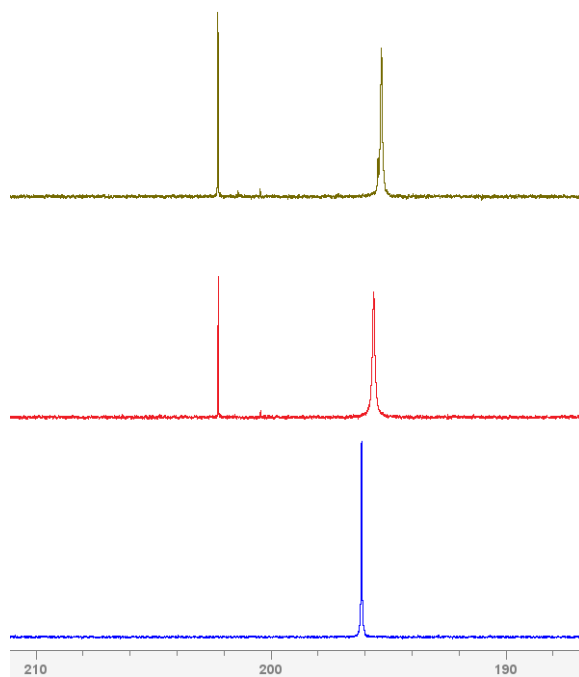
Figure S4. 10. $^{31}P\{^1H\}$ NMR spectra of an acetonitrile solution of **1a** containing (from bottom to top) 0, 2, and 3 equiv of added TEMPOH (Ni:TEMPOH= 1:0, 1:1, 1:2).
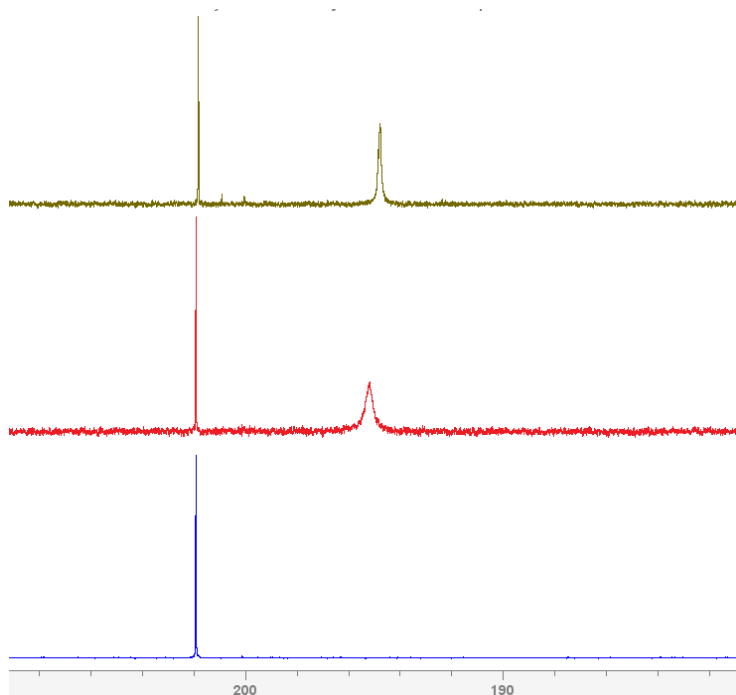
Figure S4. 11. $^{31}P\{^1H\}$ NMR spectra of a DCM solution of **1a** to which were added, successively, 2 equiv of added TEMPOH (blue trace, Ni:TEMPOH:NCMe= 1:1:0), 600 equiv of MeCN (red trace, Ni:TEMPOH:NCMe= 1:1:300) and 2 more equiv of TEMPOH (brown trace, overall Ni:TEMPOH:NCMe= 1:2:300).
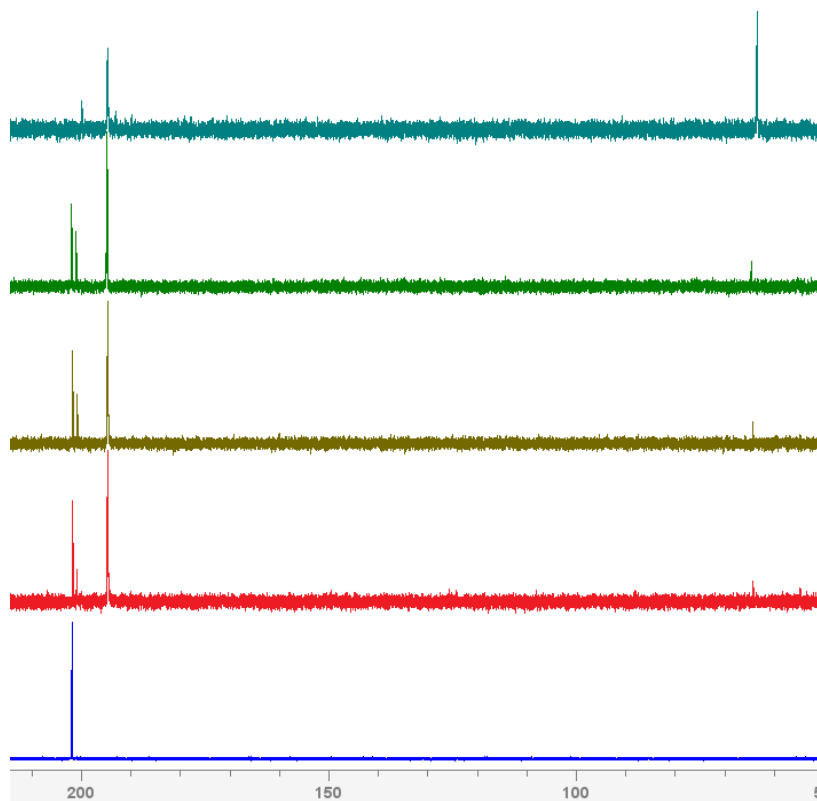
Figure S4. 12. $^{31}P\{^1H\}$ NMR spectra of a DCM solution of **1a** to which were added, successively, 10 equiv of TEMPOH (blue trace, Ni:TEMPOH:NCMe = 1:5:0), 600 equiv of MeCN (red trace, Ni:NCMe = 1:5:300), 2 more equiv of TEMPOH (brown trace, Ni:TEMPOH:NCMe = 1: 6:300), and 4 more equiv of TEMPOH (green trace, Ni:TEMPOH:NCMe= 1:8:300). The sample was then allowed to stand for 3 days before a final spectrum was recorded (gray-blue trace).

Complex **3b**

Figure S4. 13. Full ^{1}H NMR spectrum of **3b** in C$_6$D$_6$.

Figure S4. 14. The expanded aliphatic region of the ^{1}H NMR spectrum of **3b** in C$_6$D$_6$.

Figure S4. 15. The expanded aromatic region of the ^{1}H NMR spectrum of **3b** in C_6D_6.

Figure S4. 16. Full $^{13}C\{^1H\}$ NMR spectrum of **3b** in C_6D_6.

Figure S4. 17. The expanded aliphatic region of the $^{13}C\{^1H\}$ NMR spectrum of **3b** in C_6D_6.
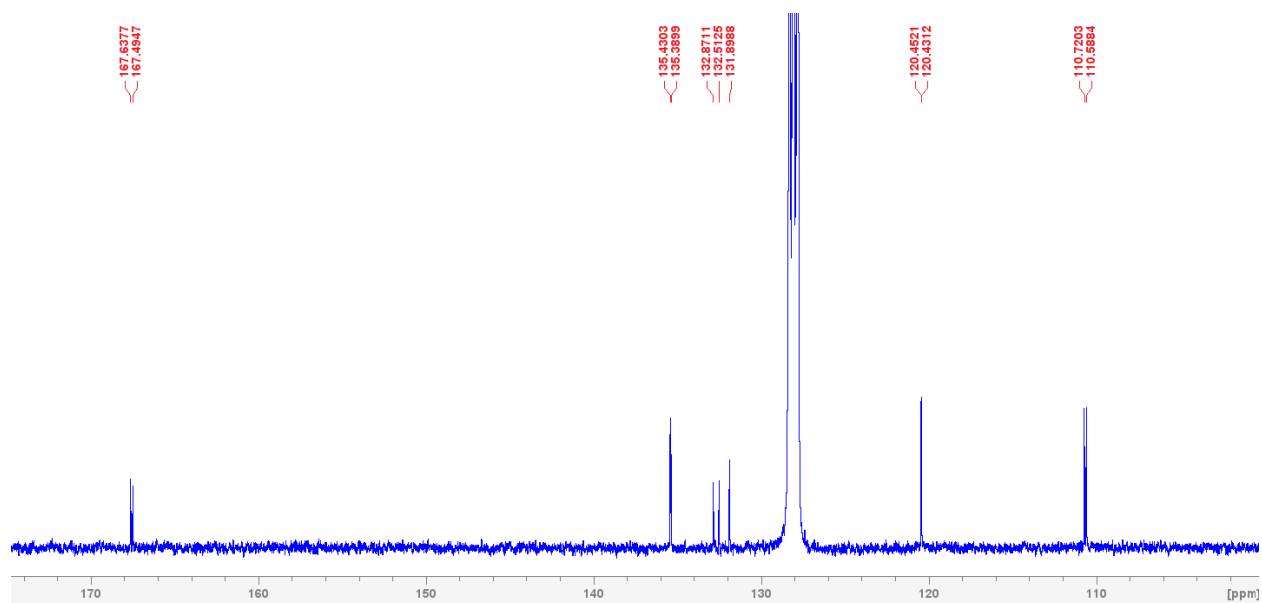
Figure S4. 18. The expanded aromatic region of the $^{13}C\{^1H\}$ NMR spectrum of **3b** in C_6D_6.
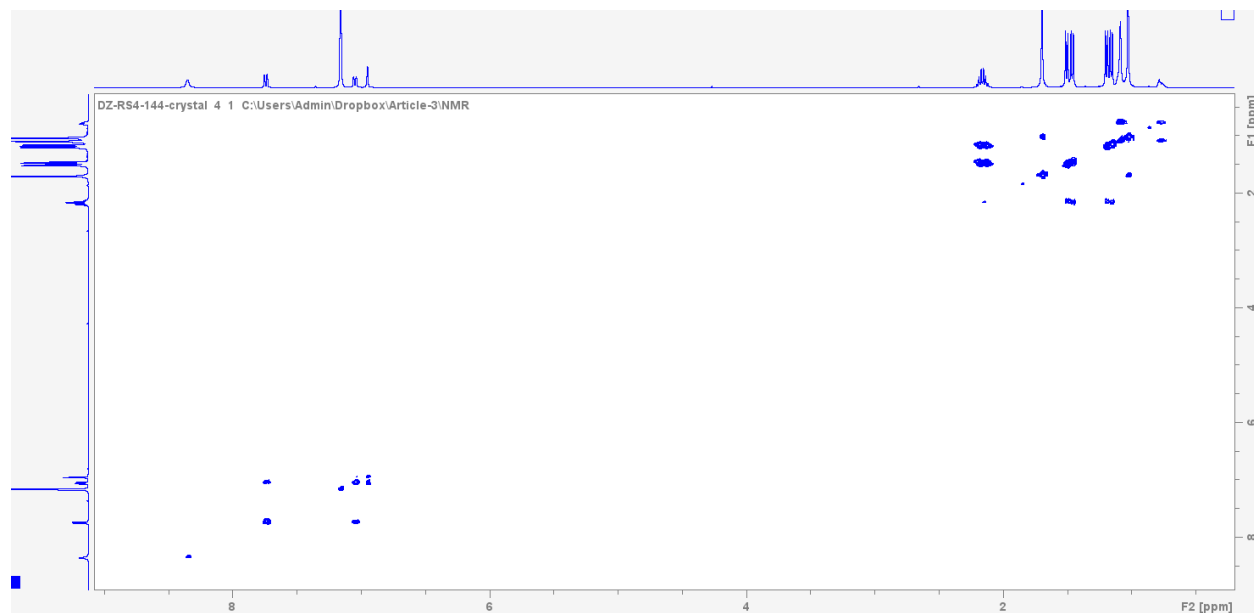
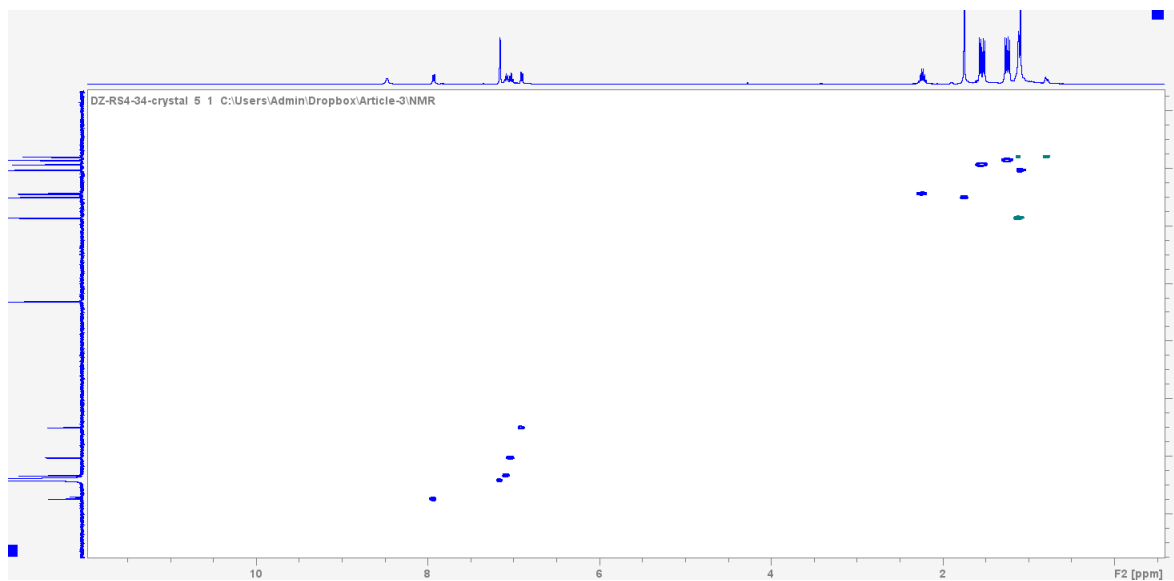**Figure S4. 19.** Full ^{1}H-^{1}H COSY NMR spectrum of **3b** in C_6D_6.
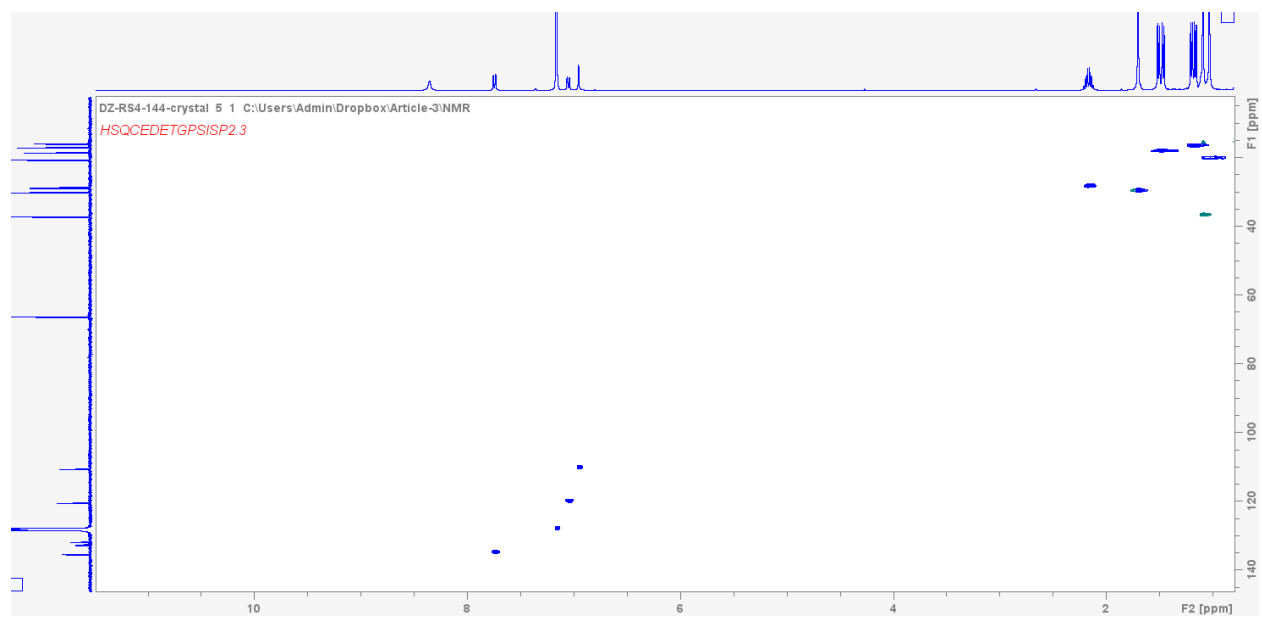
**Figure S4. 20.** Full HSQC-Edited NMR spectrum of **3b** in C_6D_6.
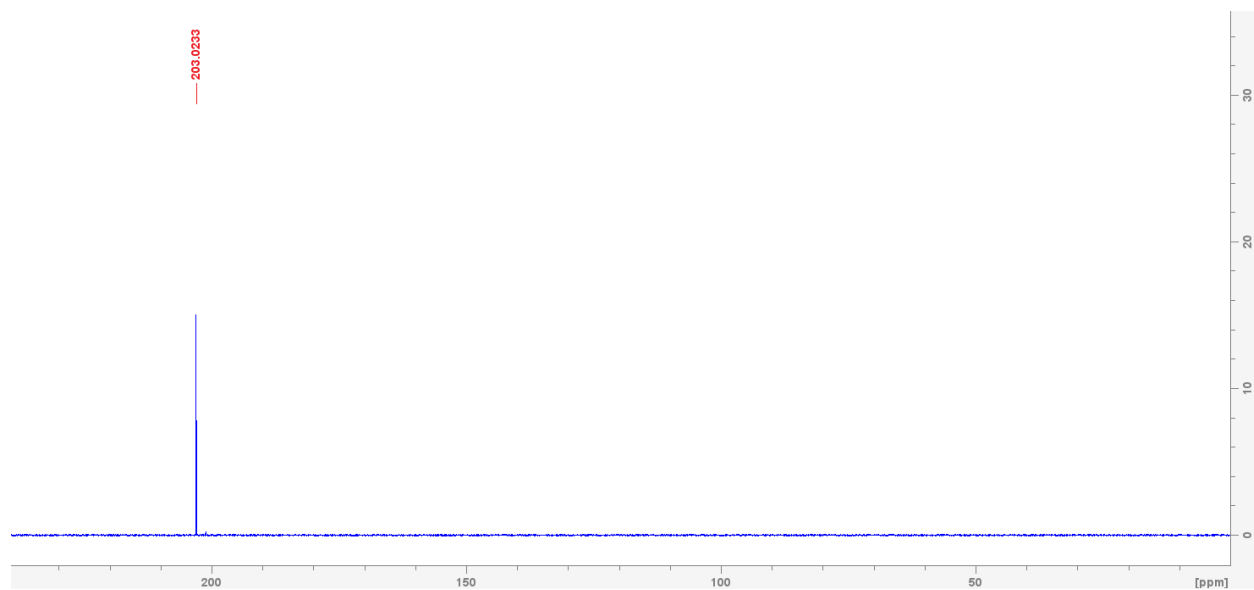
Figure S4. 21. $^{31}P\{^1H\}$ NMR spectrum of **3b** in C_6D_6.

Complex **3C**

Figure S4. 22. Full ^{1}H NMR spectrum of **3c** in C$_6$D$_6$.

Figure S4. 23. The expanded aliphatic region of the ^{1}H NMR spectrum of **3c** in C$_6$D$_6$.

Figure S4. 24. The expanded aromatic region of the ^{1}H NMR spectrum of **3c** in C_6D_6.

Figure S4. 25. Full $^{13}C\{^1H\}$ NMR spectrum of **3c** in C_6D_6.
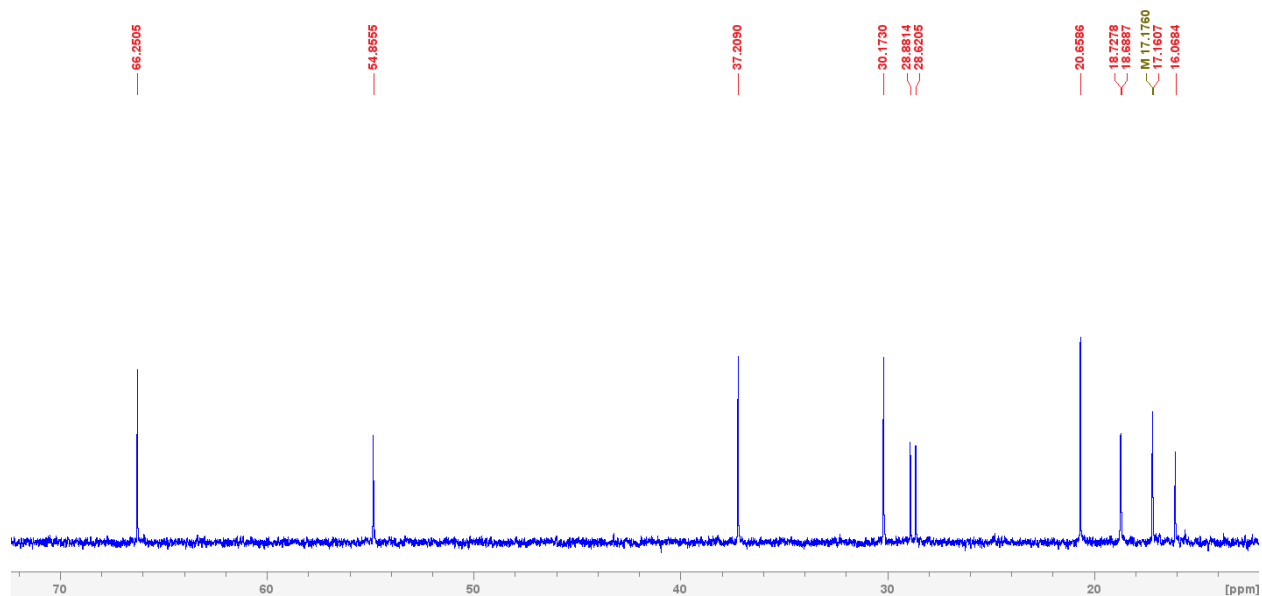
Figure S4. 26. The expanded aliphatic region of the $^{13}C\{^1H\}$ NMR spectrum of **3c** in C_6D_6.

Figure S4. 27. The expanded aromatic region of the $^{113}C\{^1H\}$ NMR spectrum of **3c** in C_6D_6.

Figure S4. 28. Full HSQC-Edited NMR spectrum of **3c** in C$_6$D$_6$.
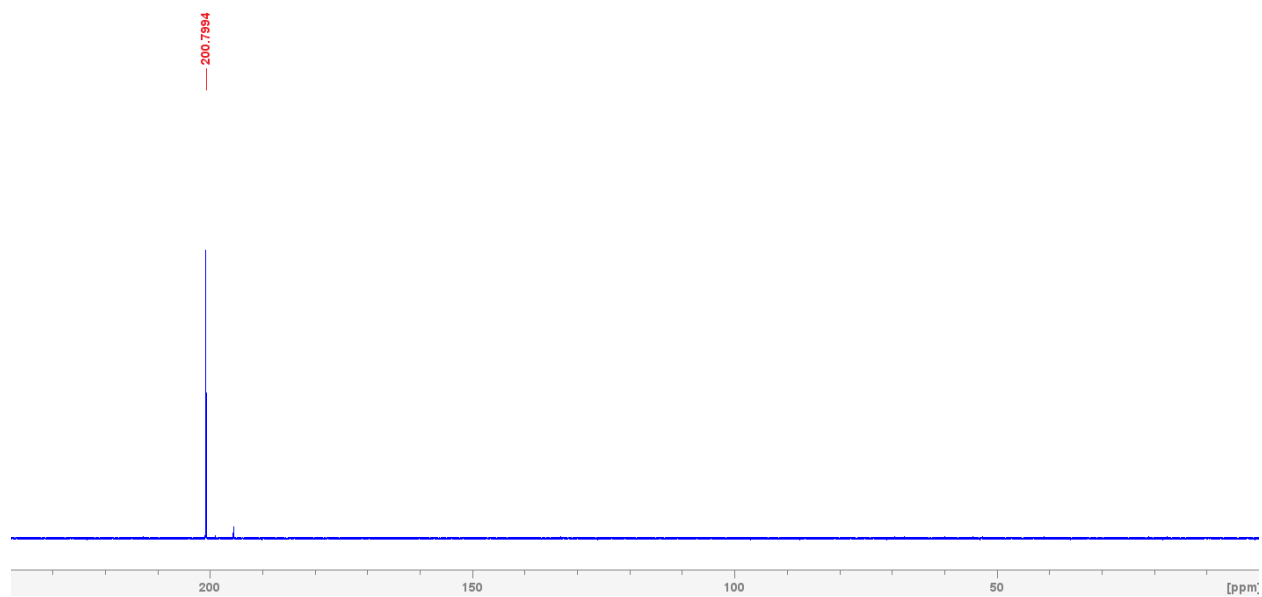
Figure S4. 29. ^{31}P{^{1}H} NMR spectrum of **3c** in C$_6$D$_6$.
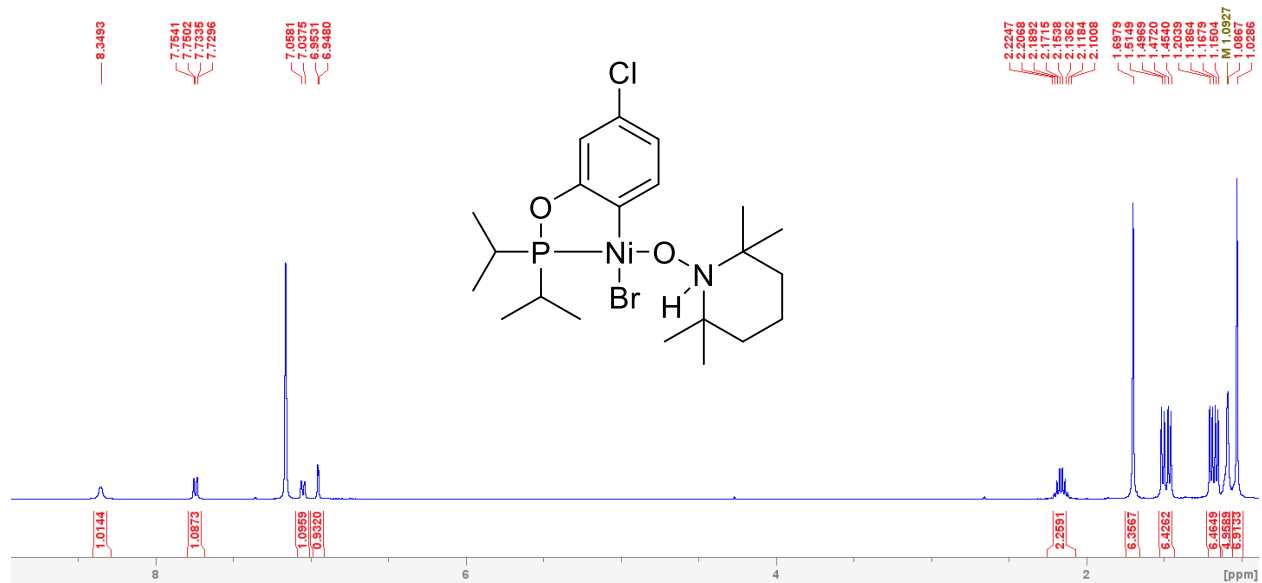
Complex **3d**
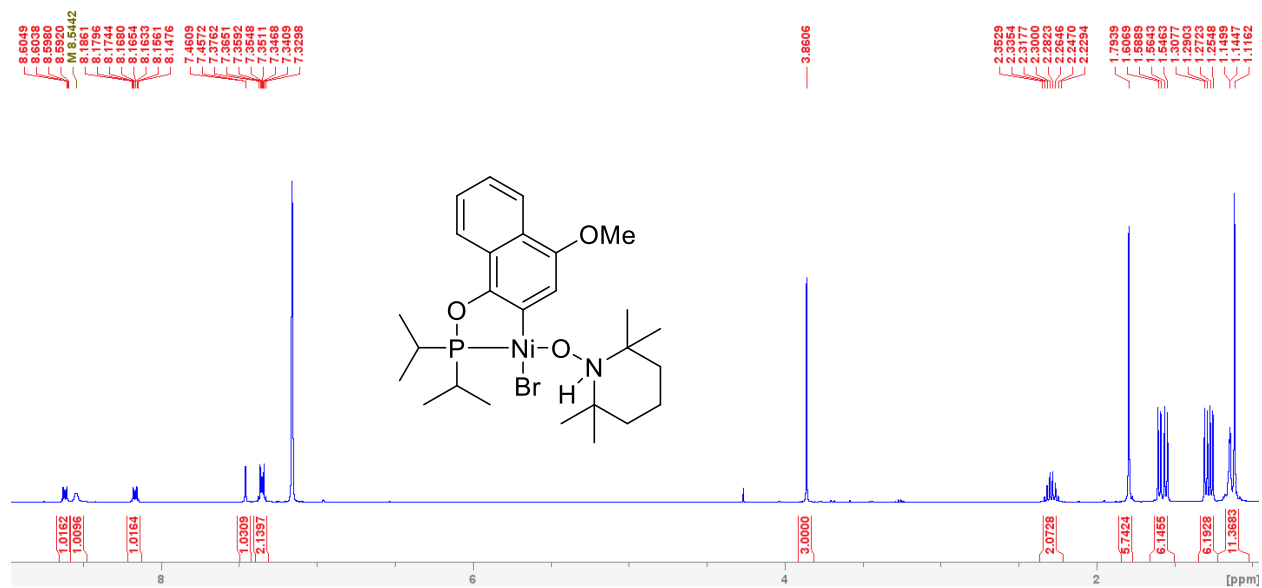
Figure S4. 30. Full ^{1}H NMR spectrum of **3d** in C_6D_6.
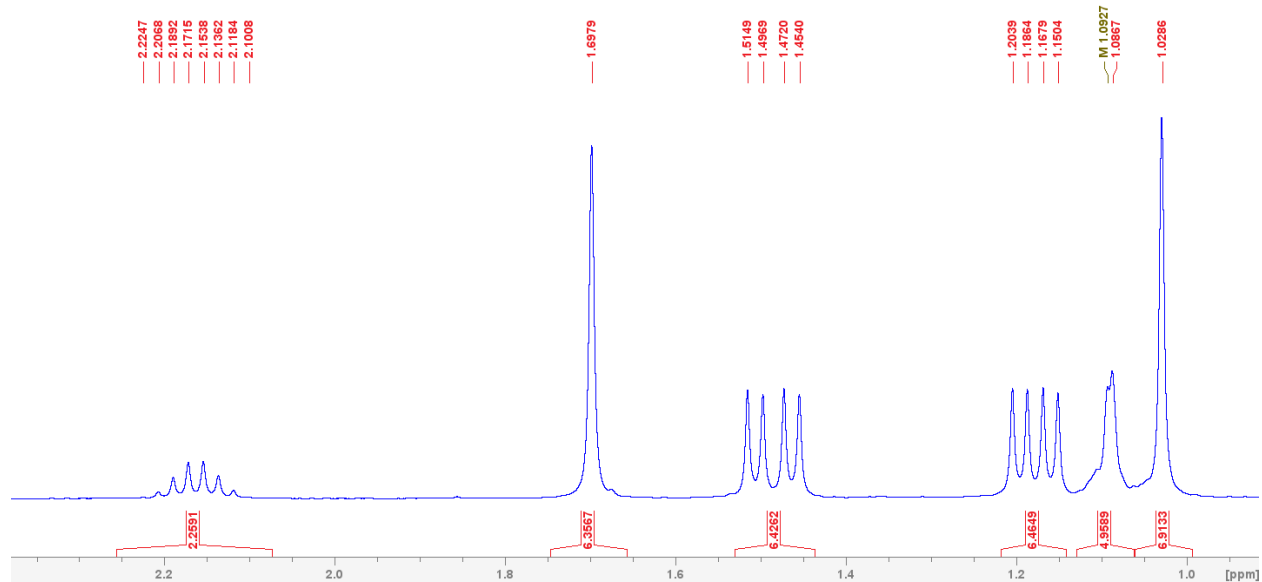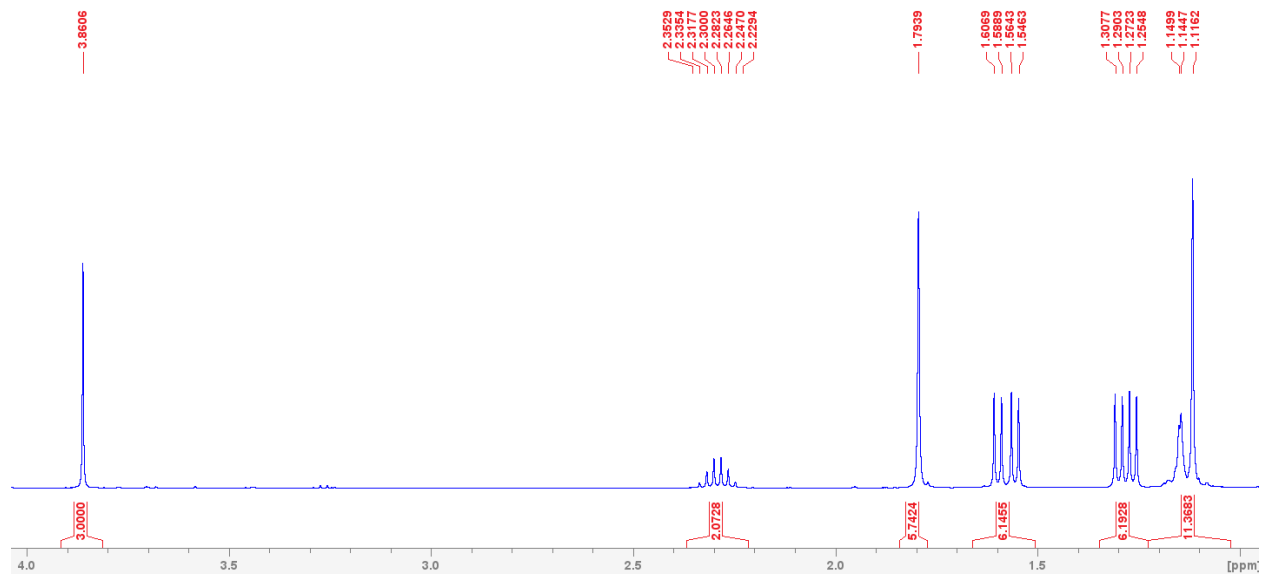

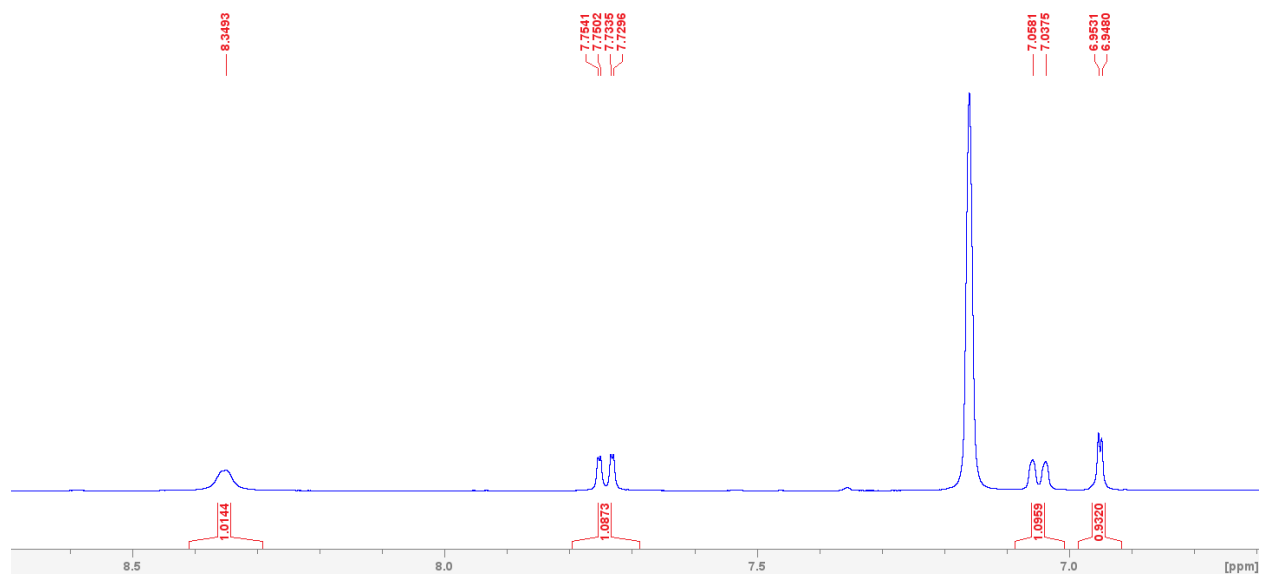**Figure S4. 31.** The expanded aliphatic region of the ^{1}H NMR spectrum of **3d** in C_6D_6.
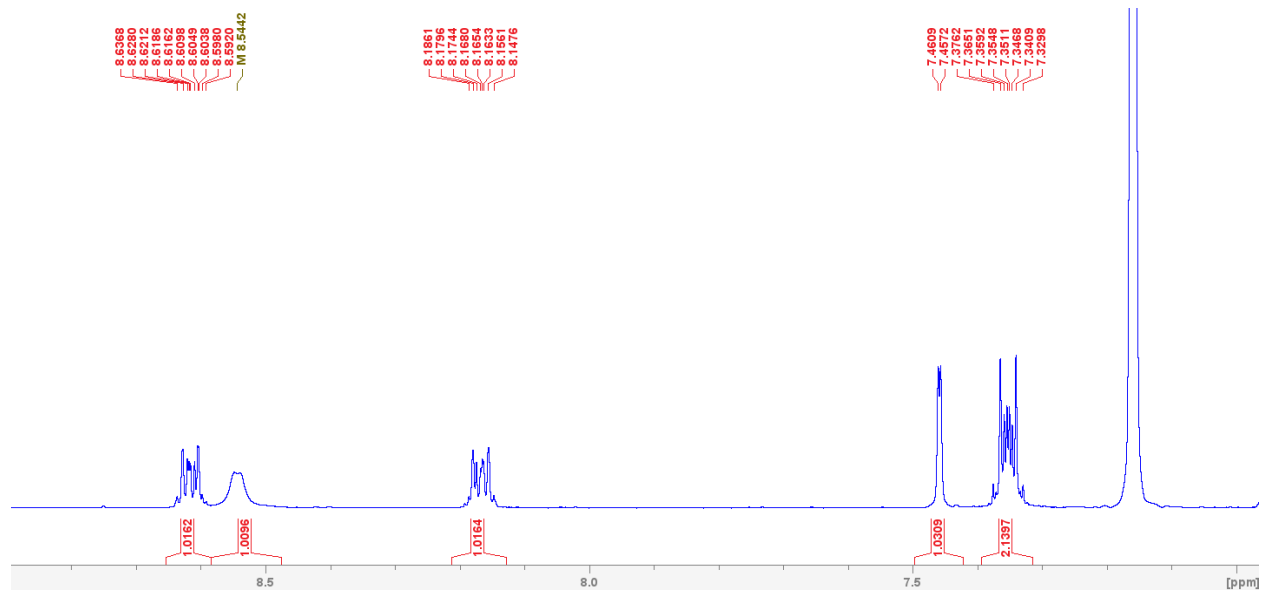
Figure S4. 32. The expanded aromatic region of the ^{1}H NMR spectrum of **3d** in C_6D_6.
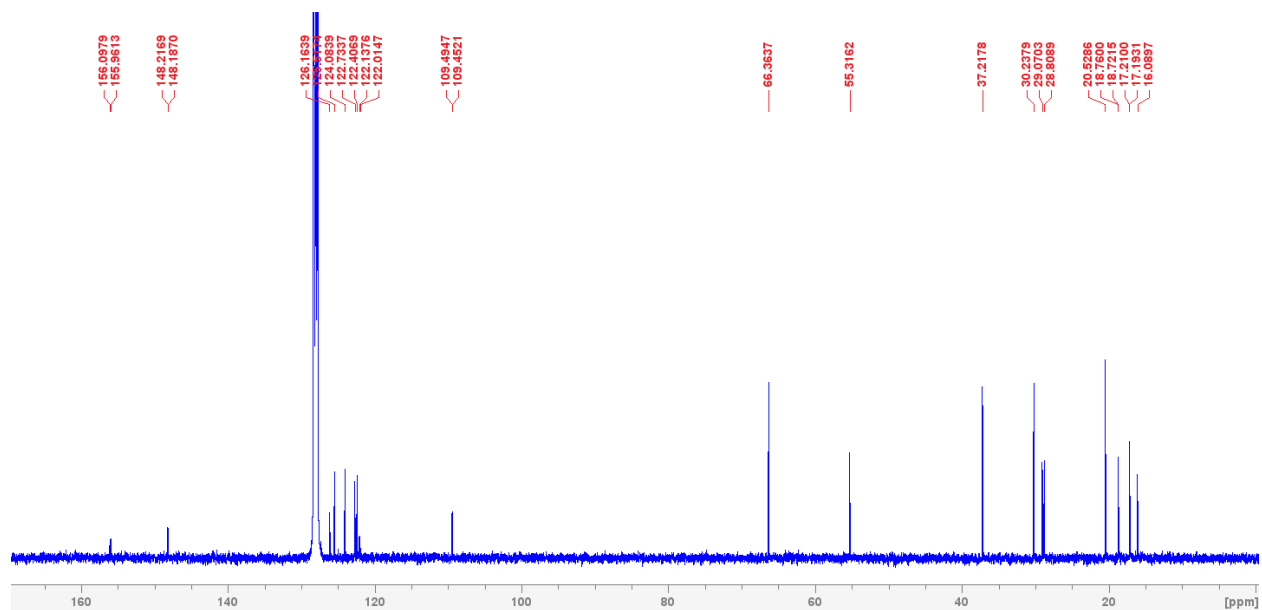
Figure S4. 33. Full $^{13}C\{^1H\}$ NMR spectrum of **3d** in C_6D_6.
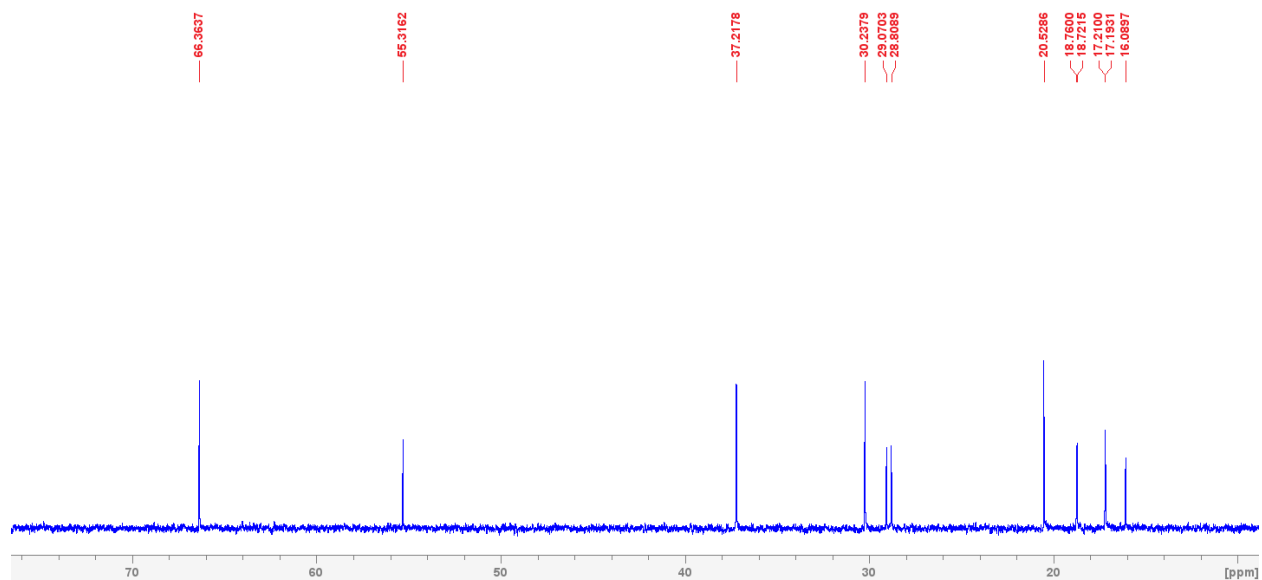
Figure S4. 34. The expanded aliphatic region of the $^{13}C\{^1H\}$ NMR spectrum of **3d** in C_6D_6.
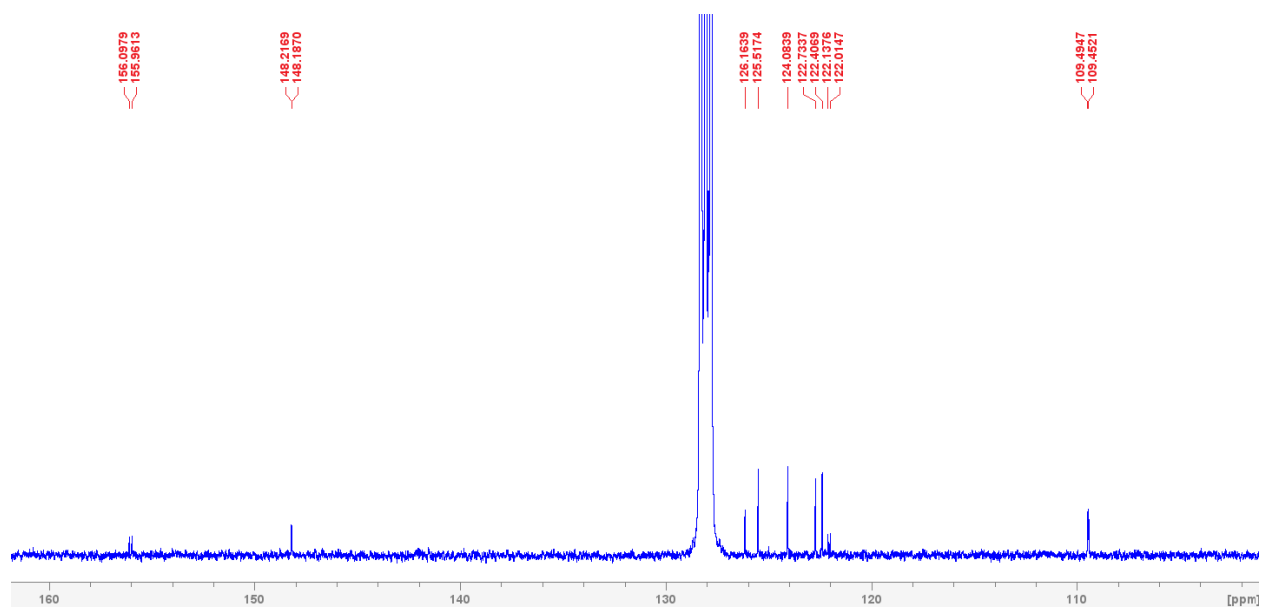
Figure S4. 35. The expanded aromatic region of the $^{13}C\{^1H\}$ NMR spectrum of **3d** in C_6D_6.
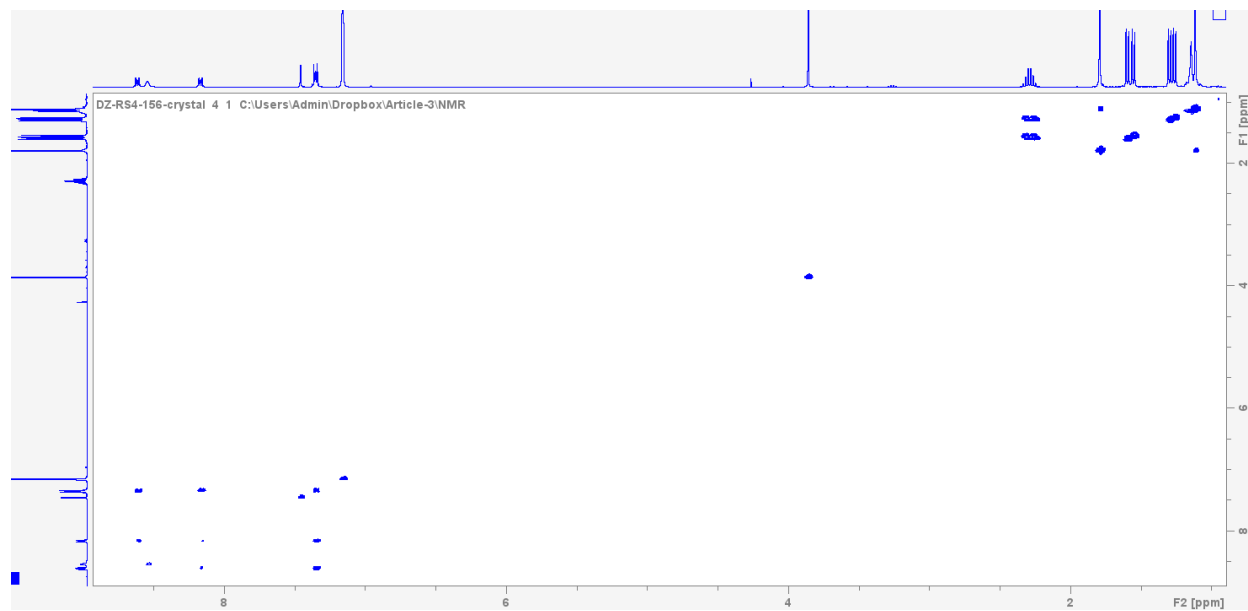
Figure S4. 36. Full ^{1}H-^{1}H COSY NMR spectrum of **3d** in C_6D_6.
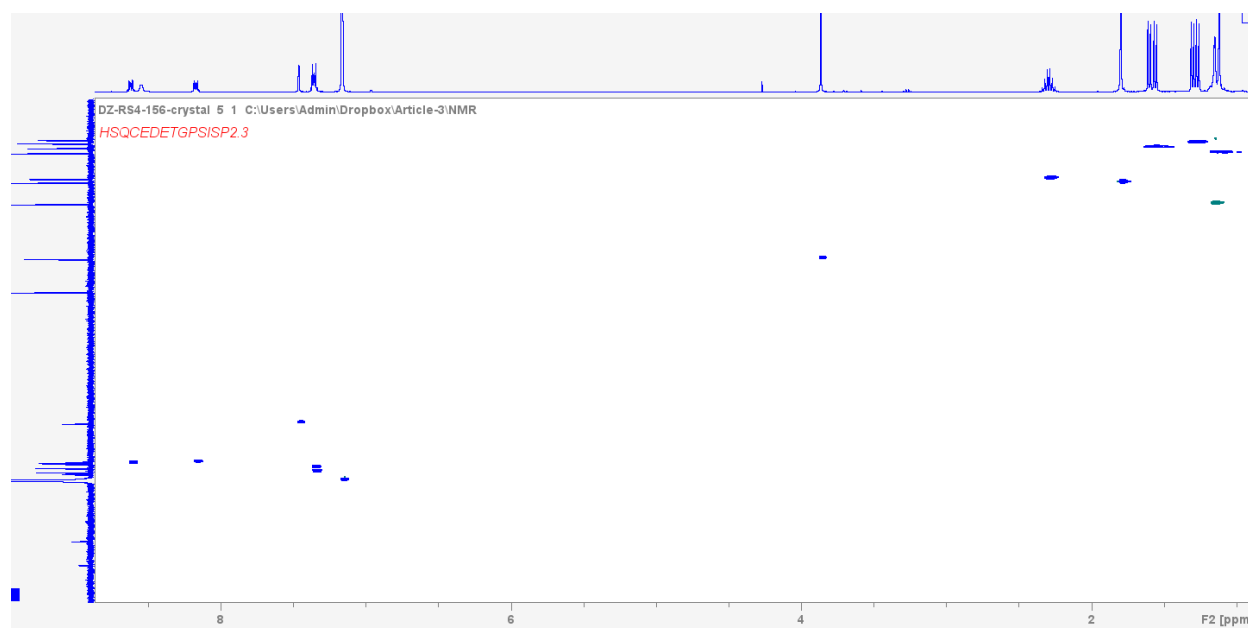
Figure S4. 37. Full HSQC-Edited NMR spectrum of **3d** in C_6D_6.
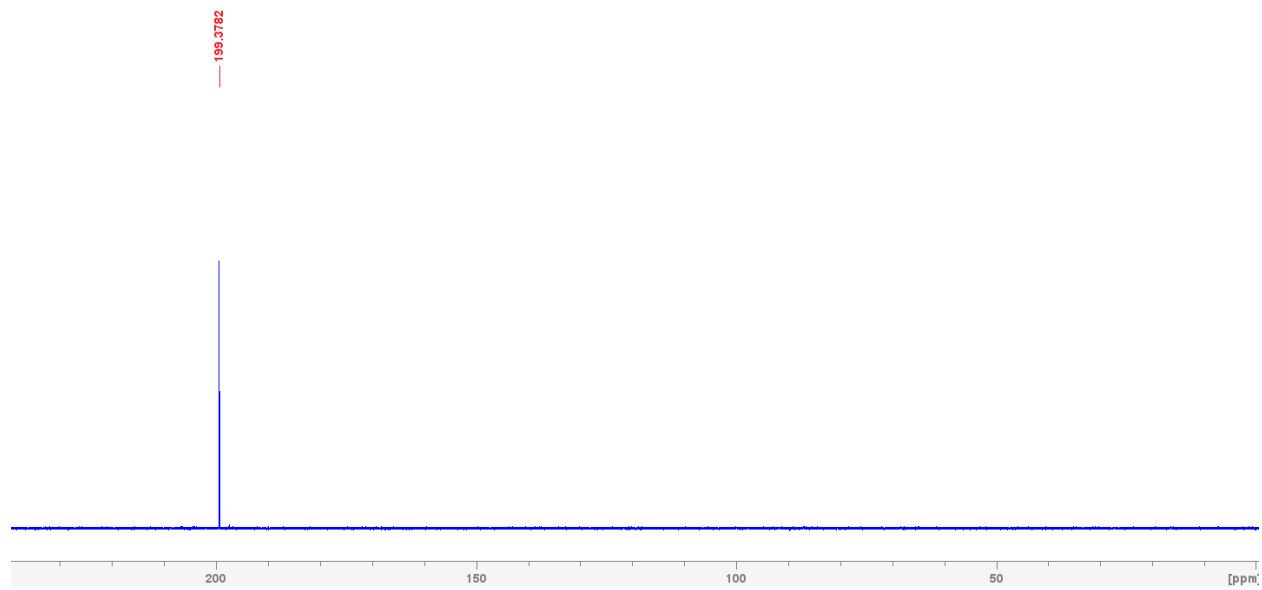
Figure S4. 38. $^{31}P\{^1H\}$ NMR spectrum of **3d** in C_6D_6.

Complex **5a**
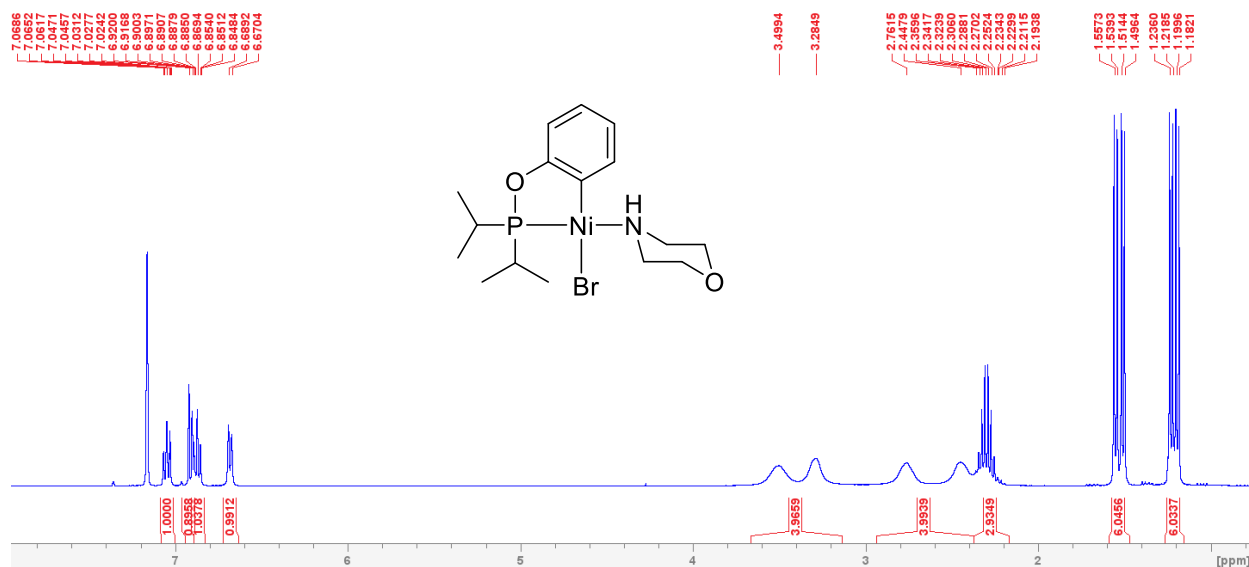
Figure S4. 39. Full ^{1}H NMR spectrum of **5a** in C$_6$D$_6$.
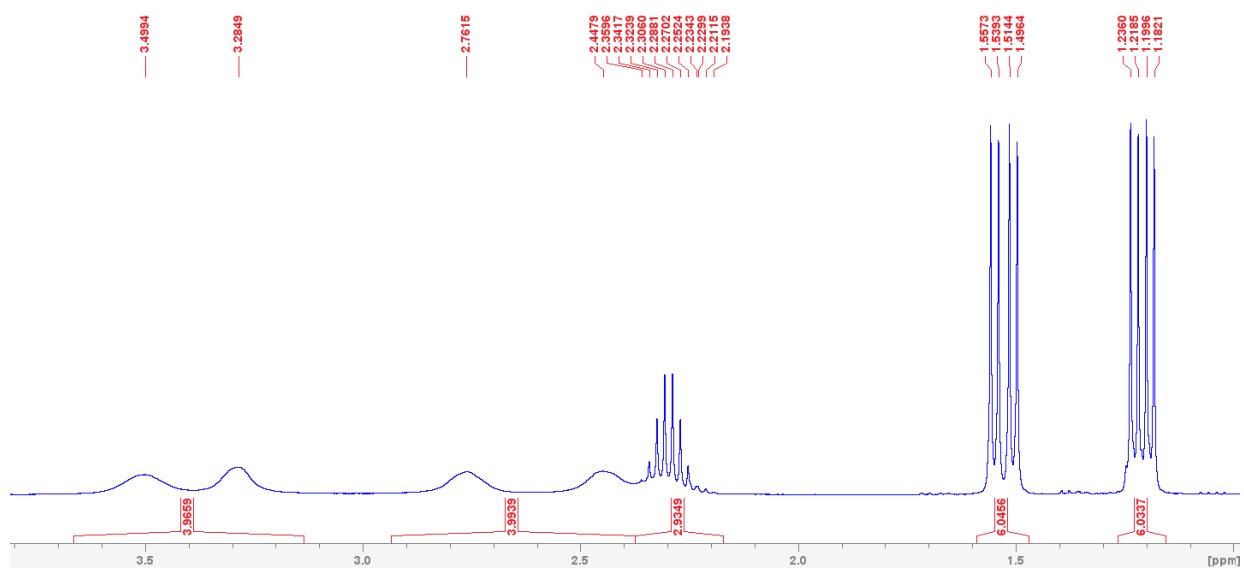
Figure S4. 40. The expanded aliphatic region of the ^{1}H NMR spectrum of **5a** in C$_6$D$_6$.
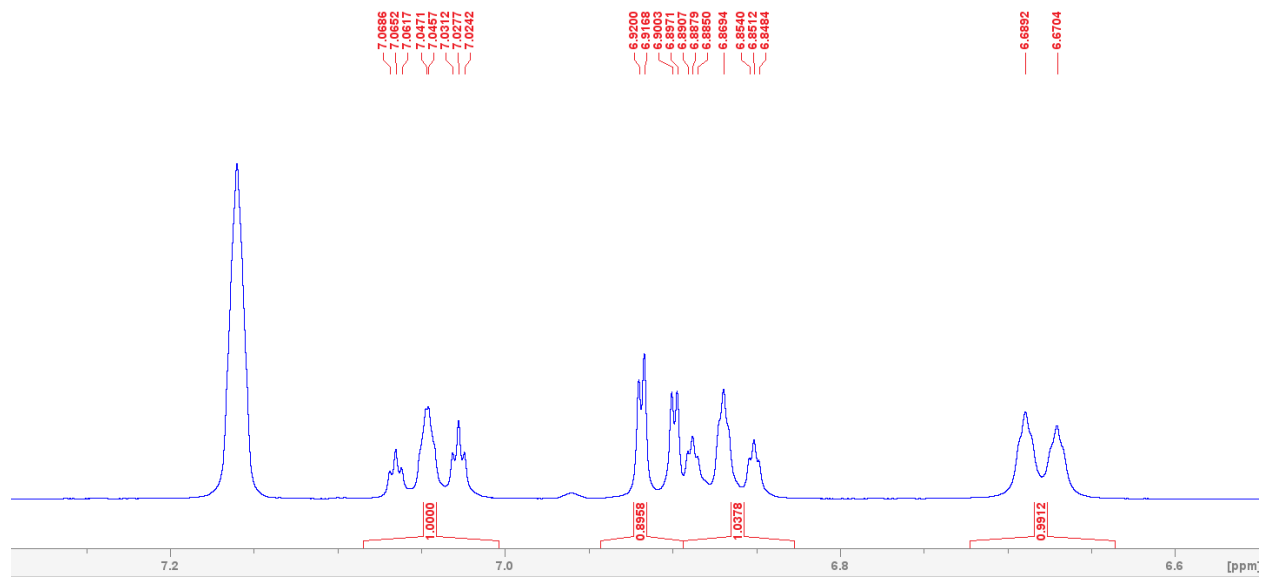
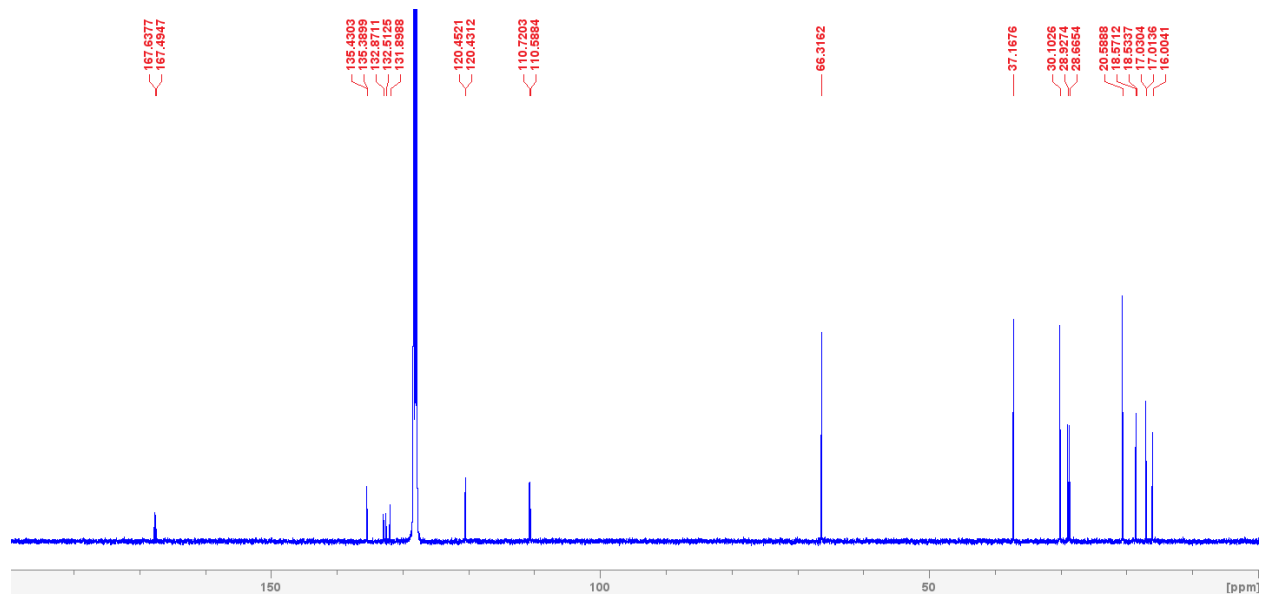**Figure S4. 41.** The expanded aromatic region of the ^{1}H NMR spectrum of **5a** in C$_6$D$_6$.
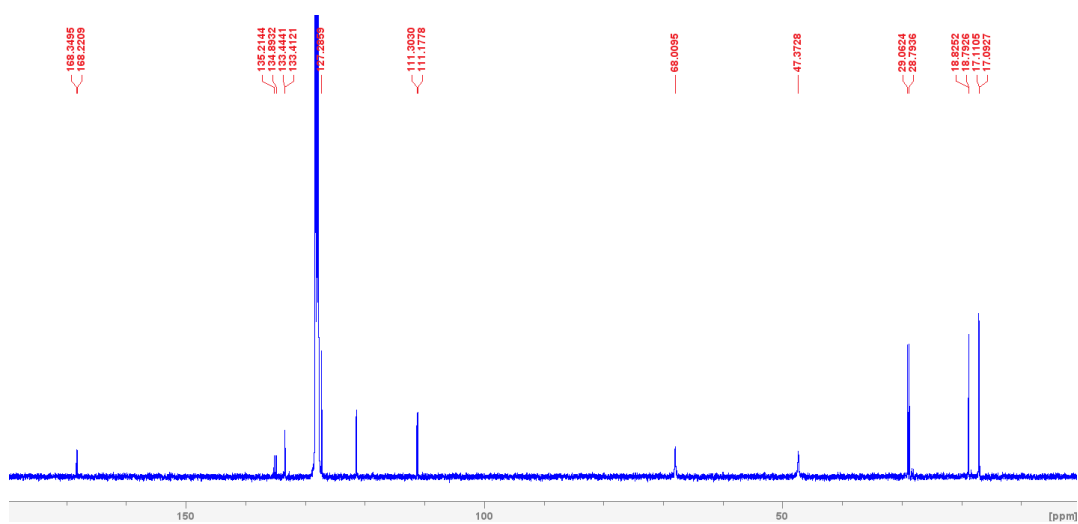
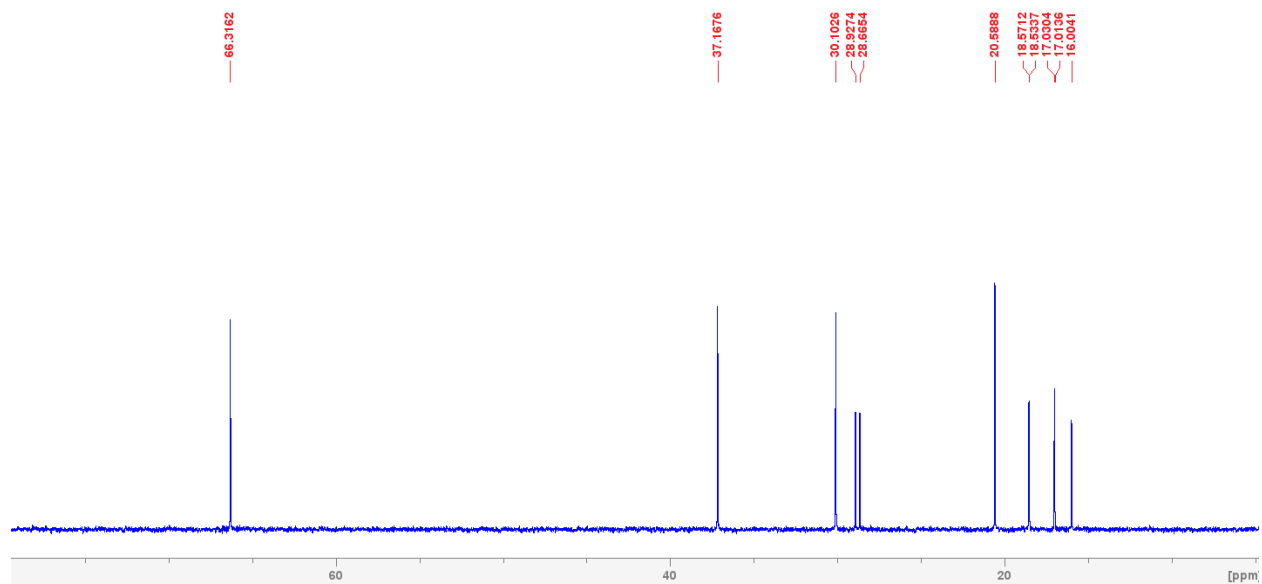**Figure S4. 42.** Full ^{13}C{^{1}H} NMR spectrum of **5a** in C$_6$D$_6$.
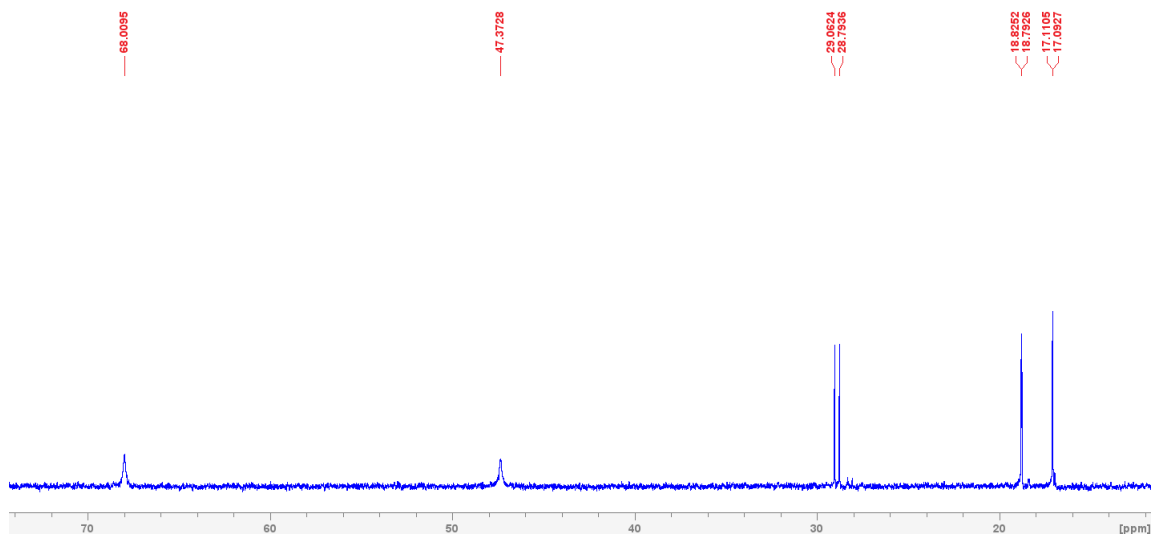
Figure S4. 43. The expanded aliphatic region of the ^{13}C{^{1}H} NMR spectrum of **5a** in C$_6$D$_6$.
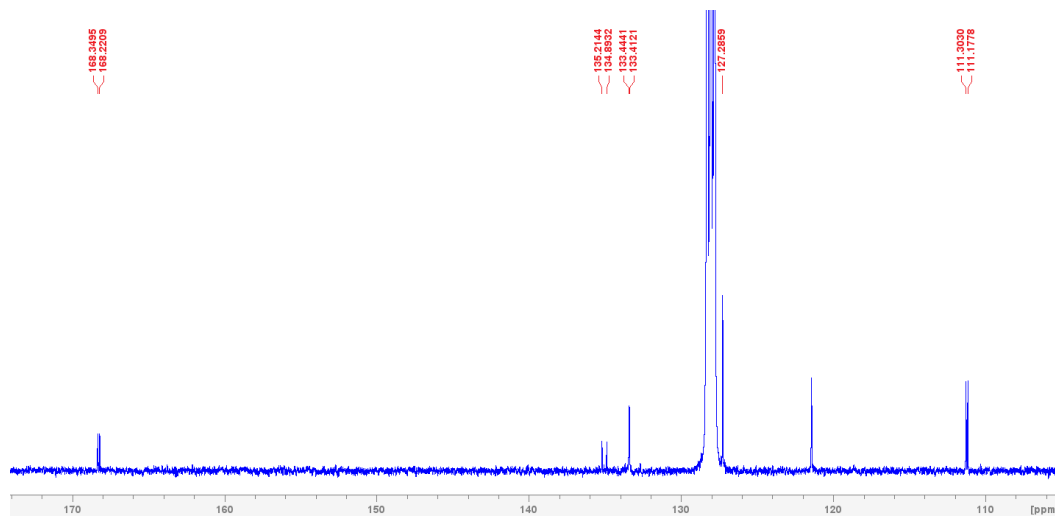
Figure S4. 44. The expanded aromatic region of the ^{13}C{^{1}H} NMR spectrum of **5a** in C$_6$D$_6$.
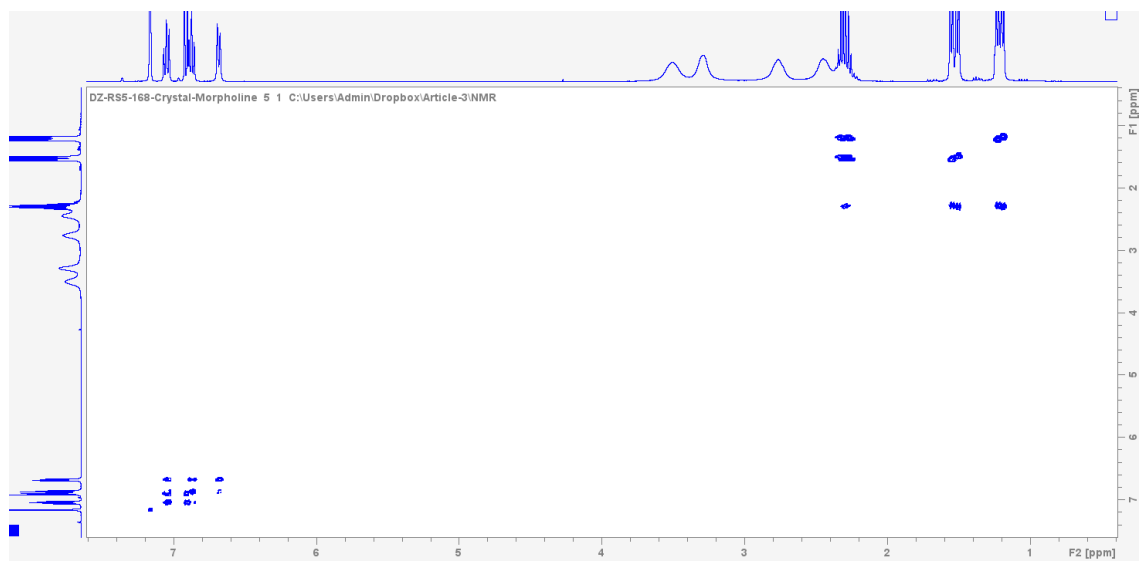
Figure S4. 45. Full ^{1}H-^{1}H COSY NMR of complex **5a** in C_6D_6.
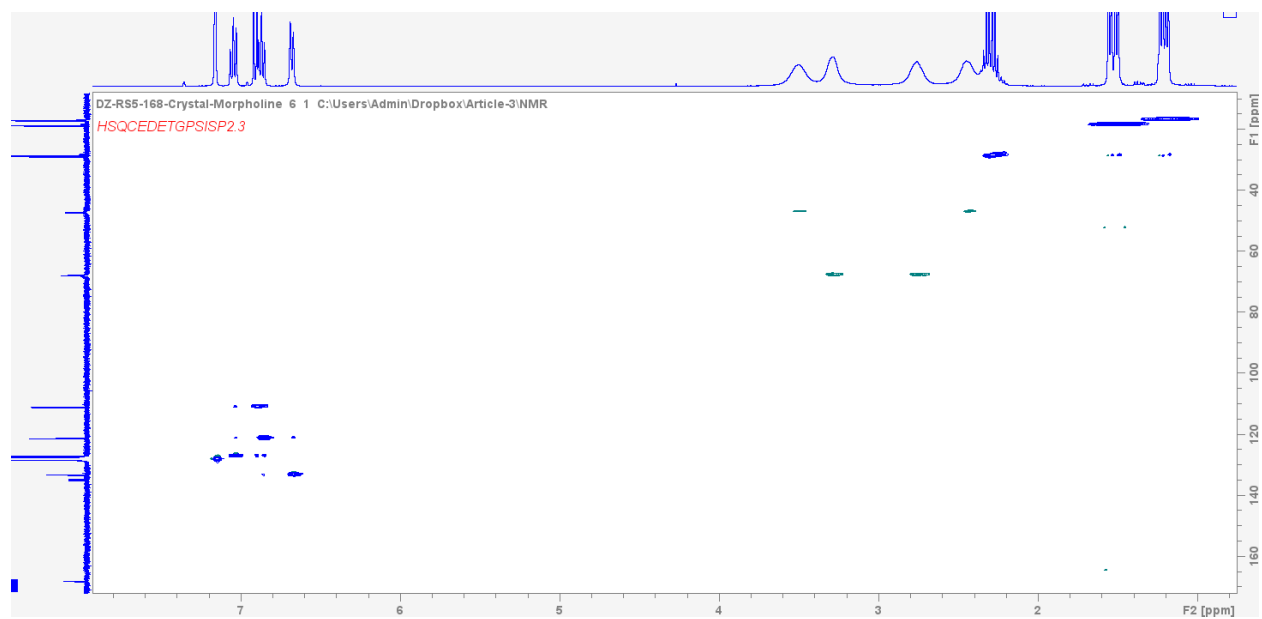
Figure S4. 46. Full HSQC- Edited NMR of complex **5a** in C_6D_6.
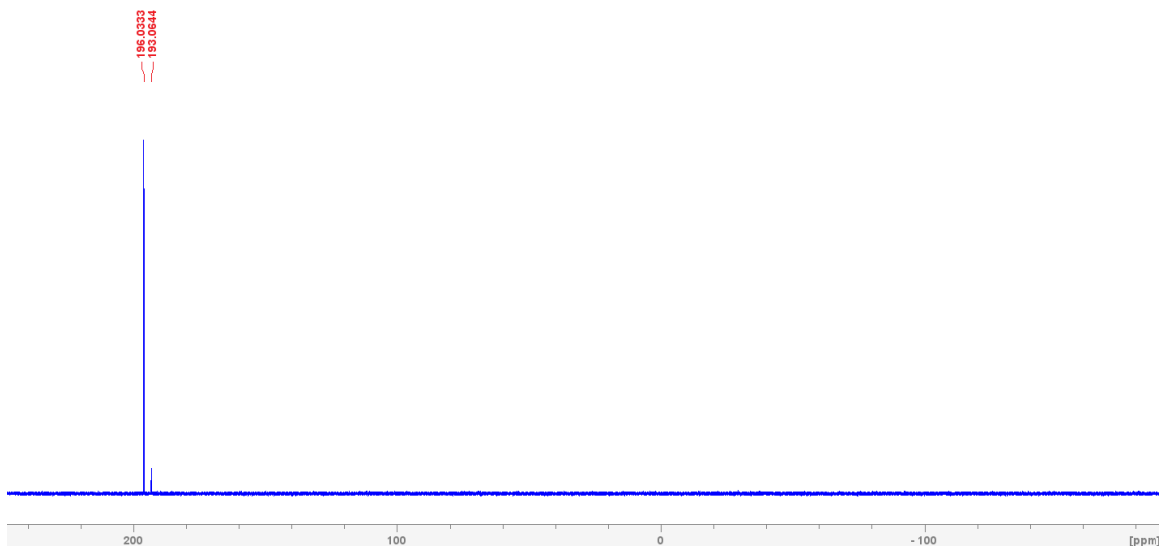
Figure S4. 47. Full ^{31}P{^{1}H} NMR spectrum of **5a** in C_6D_6.
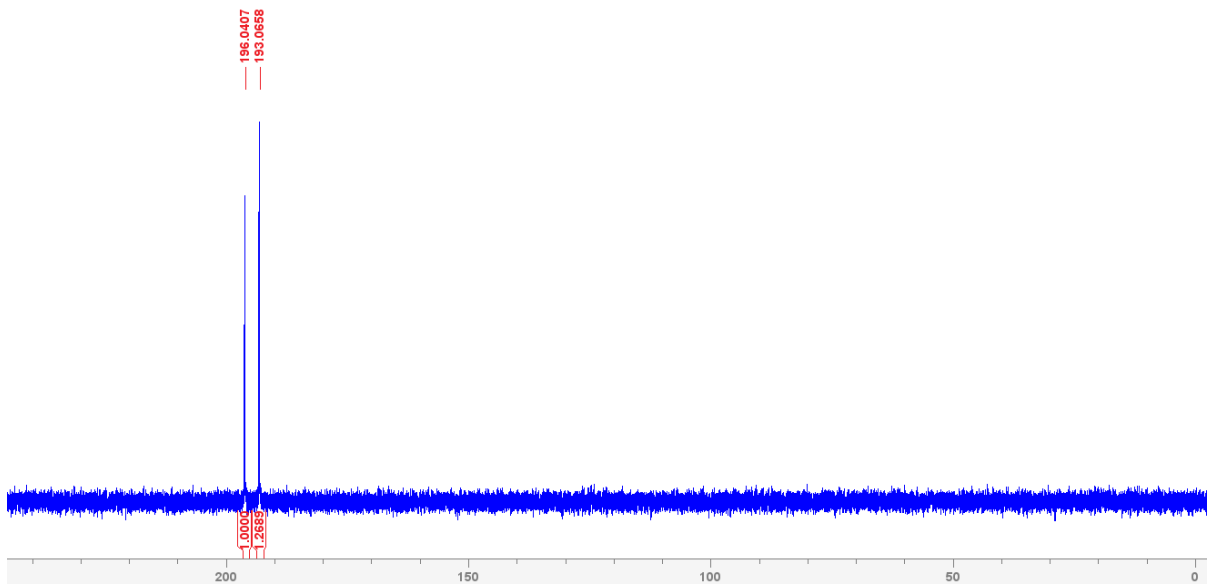
Figure S4. 48. Full ^{31}P{^{1}H} NMR spectrum of **5a** in C_6D_6 from a different batch.

Complex **6a**
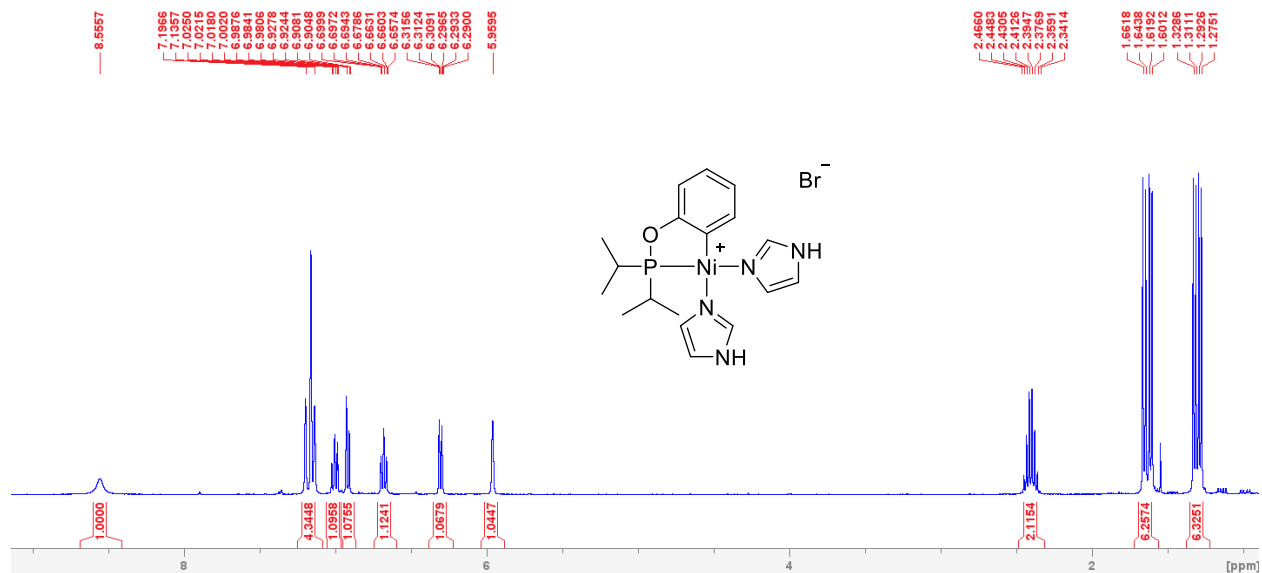
Figure S4. 49. Full ^{1}H NMR spectrum of **6a** in C_6D_6.
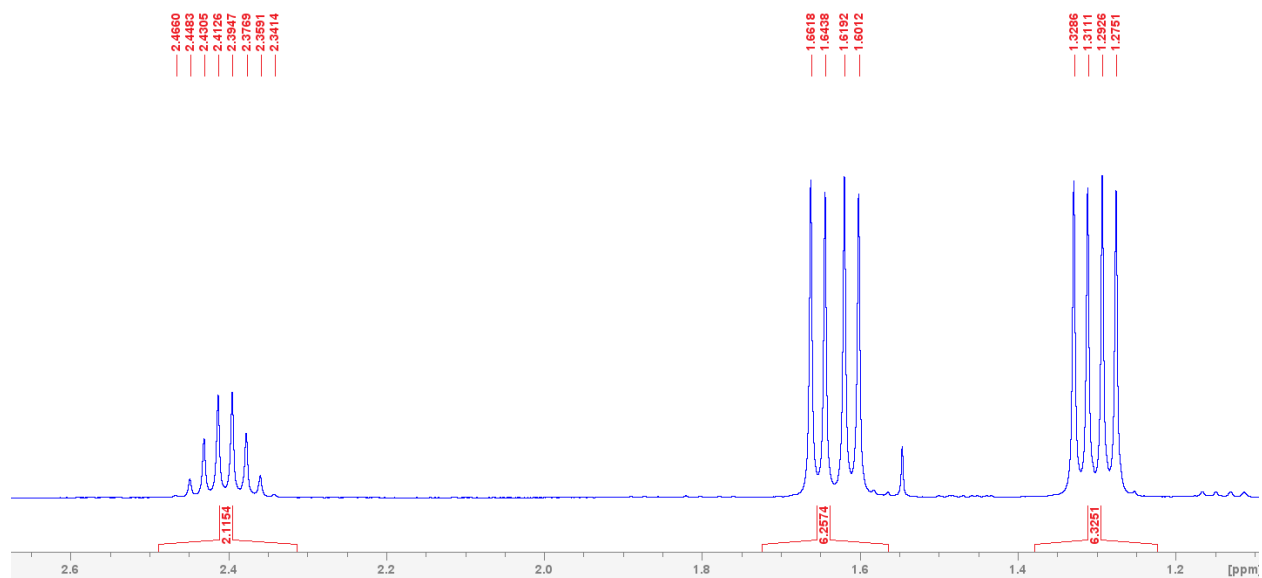
Figure S4. 50. The expanded aliphatic region of the ^{1}H NMR spectrum of **6a** in C_6D_6.
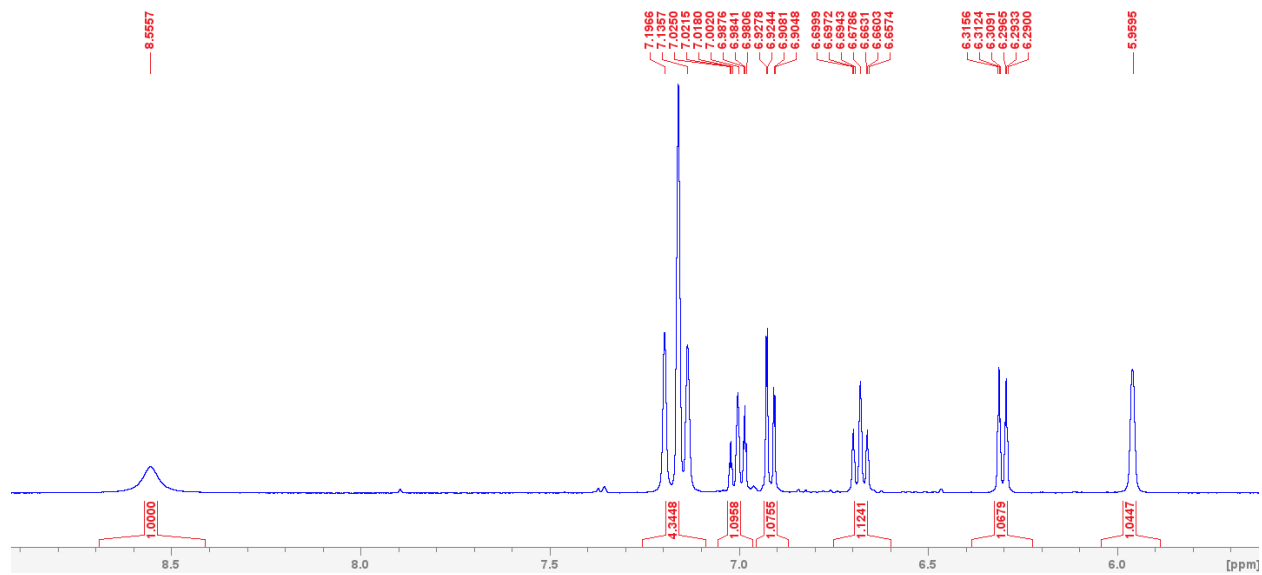
Figure S4. 51. The expanded aromatic region of the ^{1}H NMR spectrum of **6a** in C_6D_6.
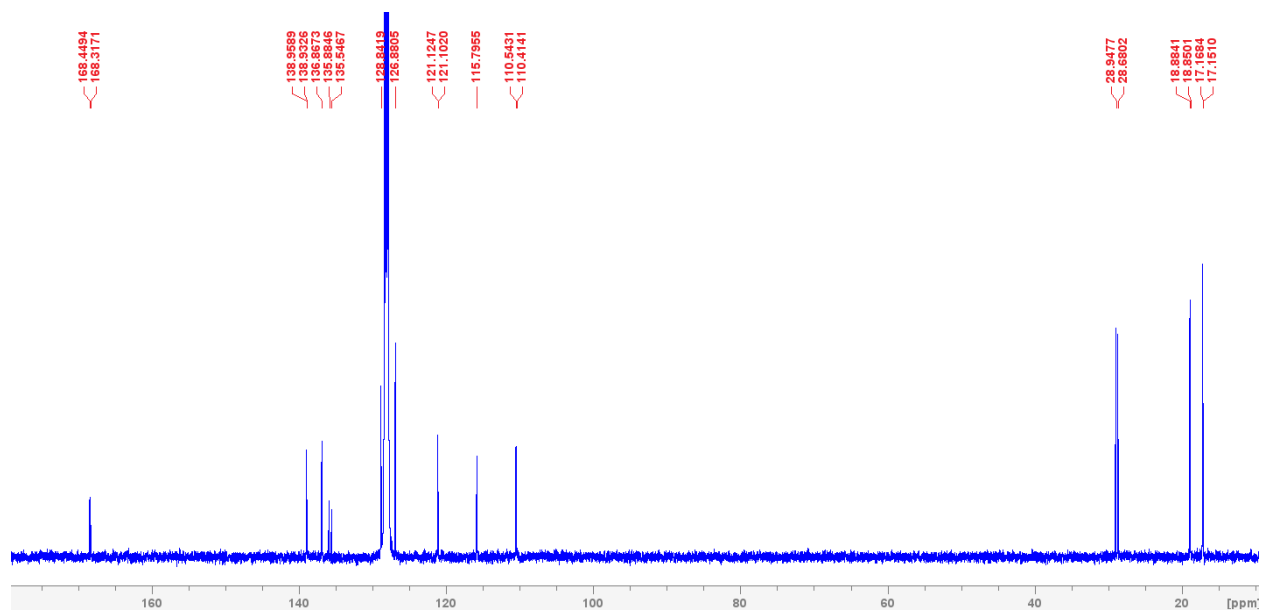
Figure S4. 52. Full $^{13}C\{^1H\}$ NMR spectrum of **6a** in C_6D_6.
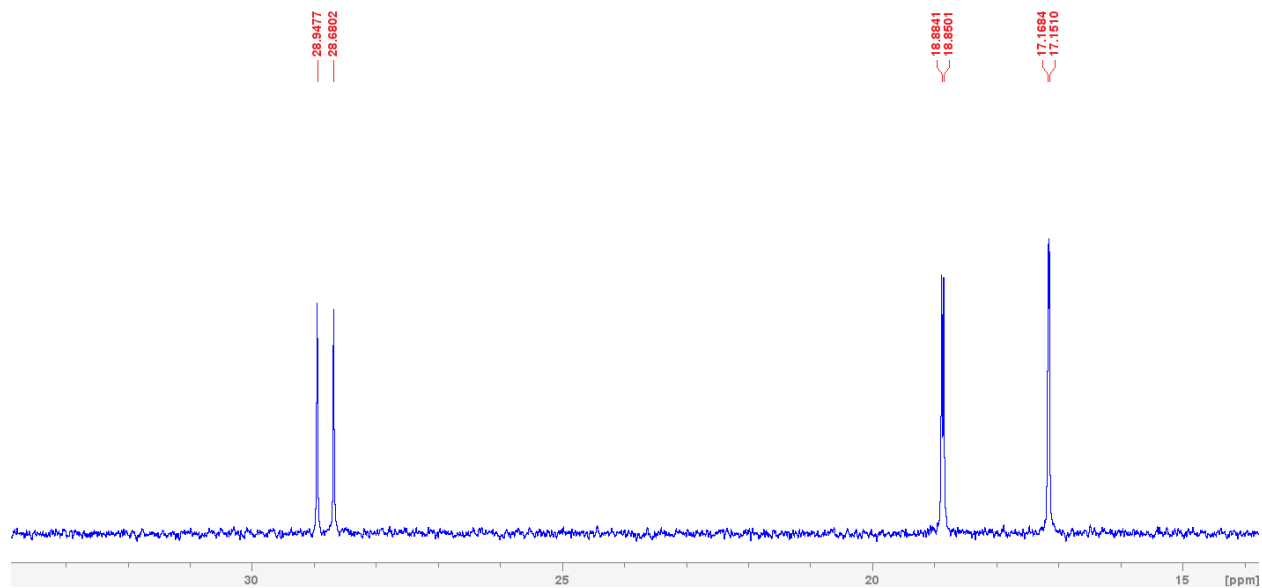
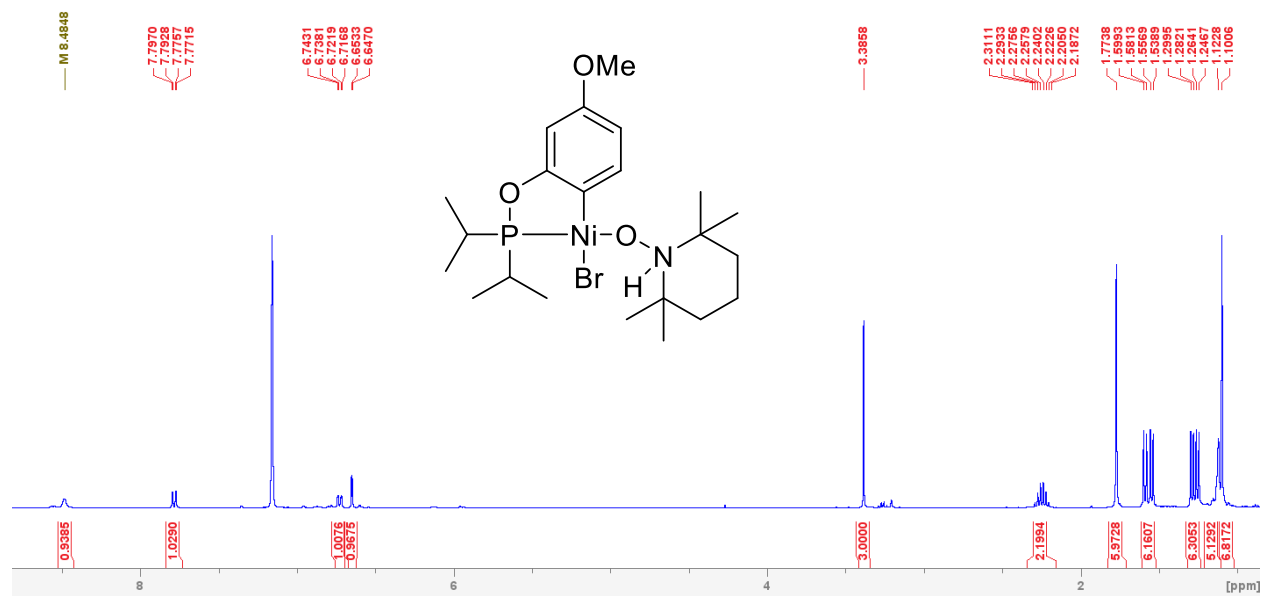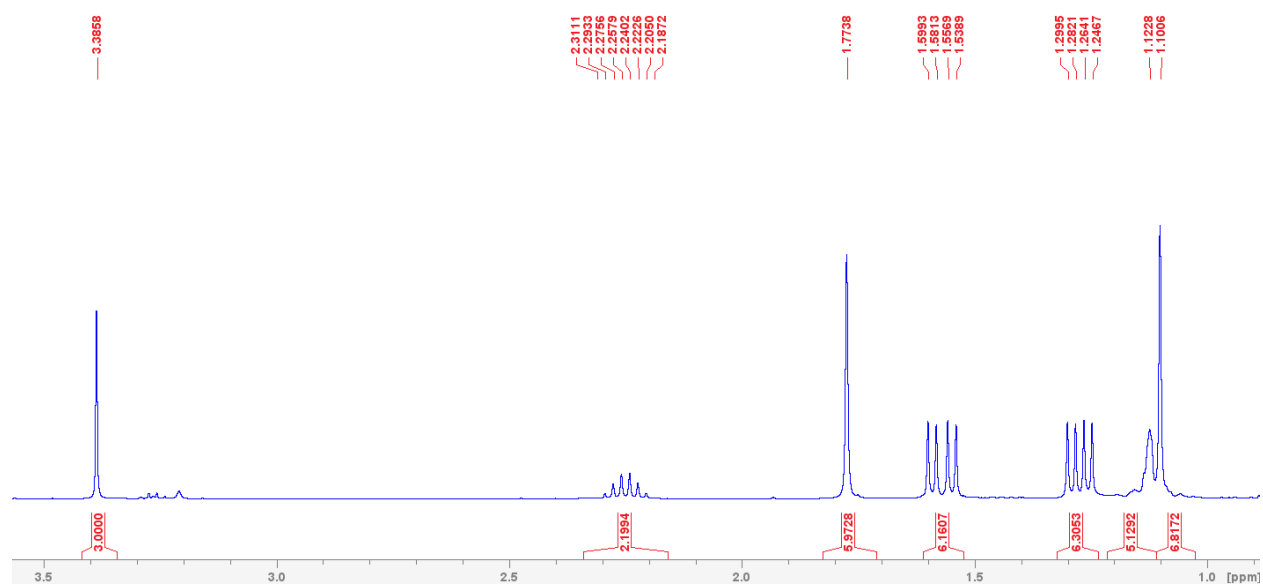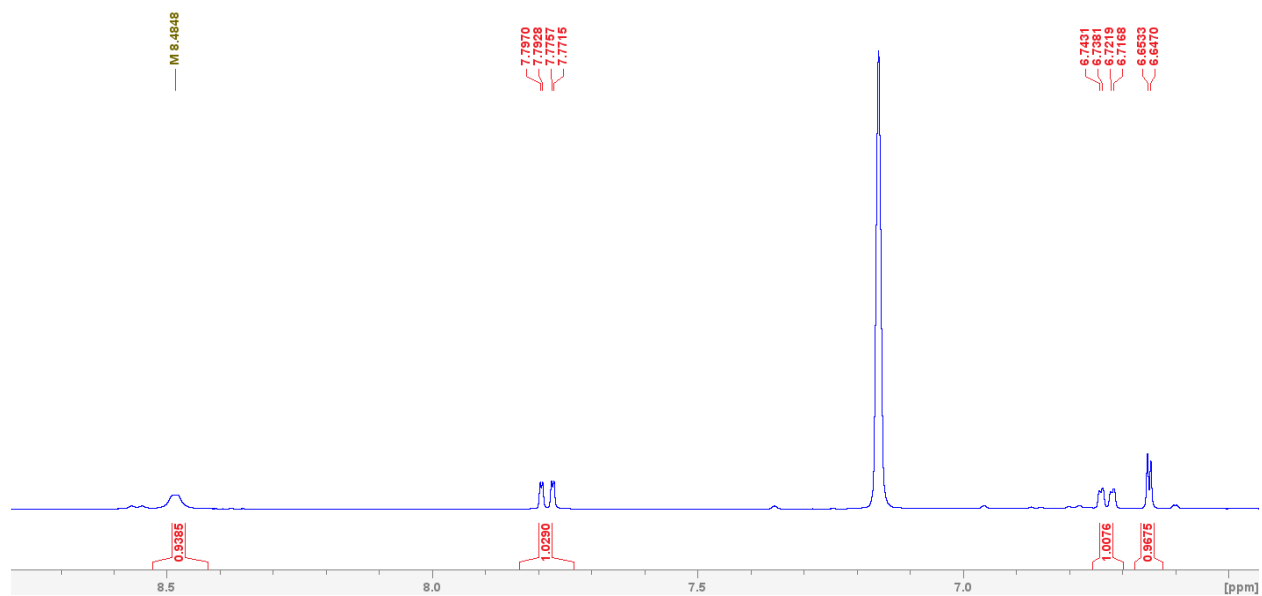**Figure S4. 53.** The expanded aliphatic region of the $^{13}C\{^1H\}$ NMR spectrum of **6a** in C_6D_6.
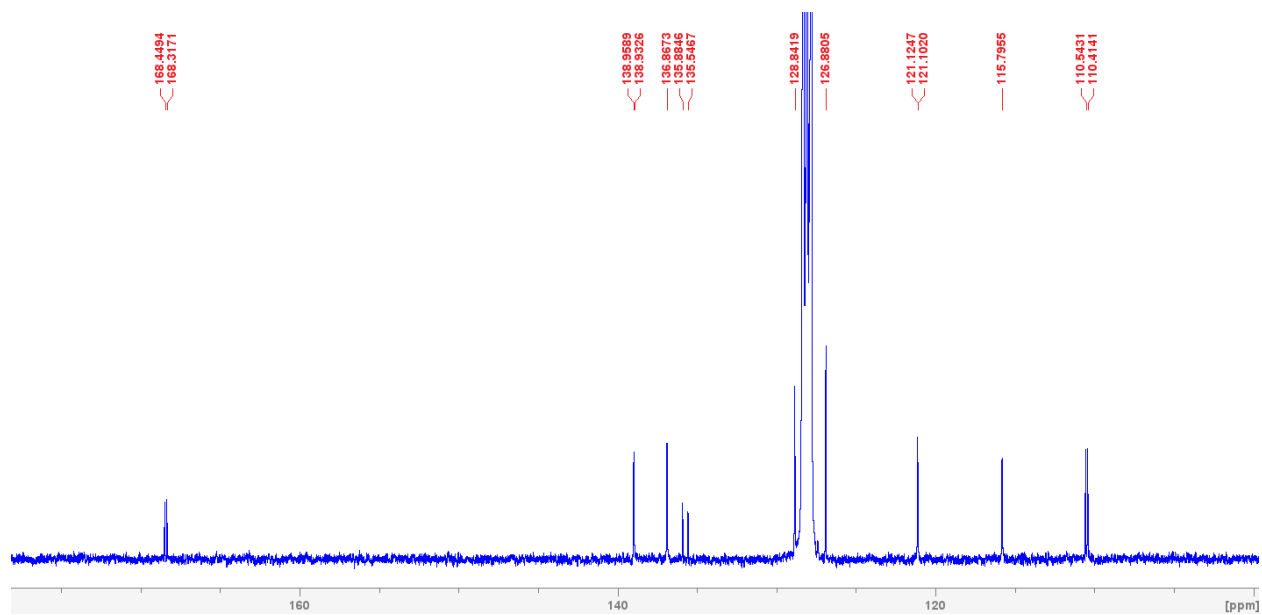
Figure S4. 54. The expanded aromatic region of the $^{13}C\{^1H\}$ NMR spectrum of **6a** in C_6D_6.
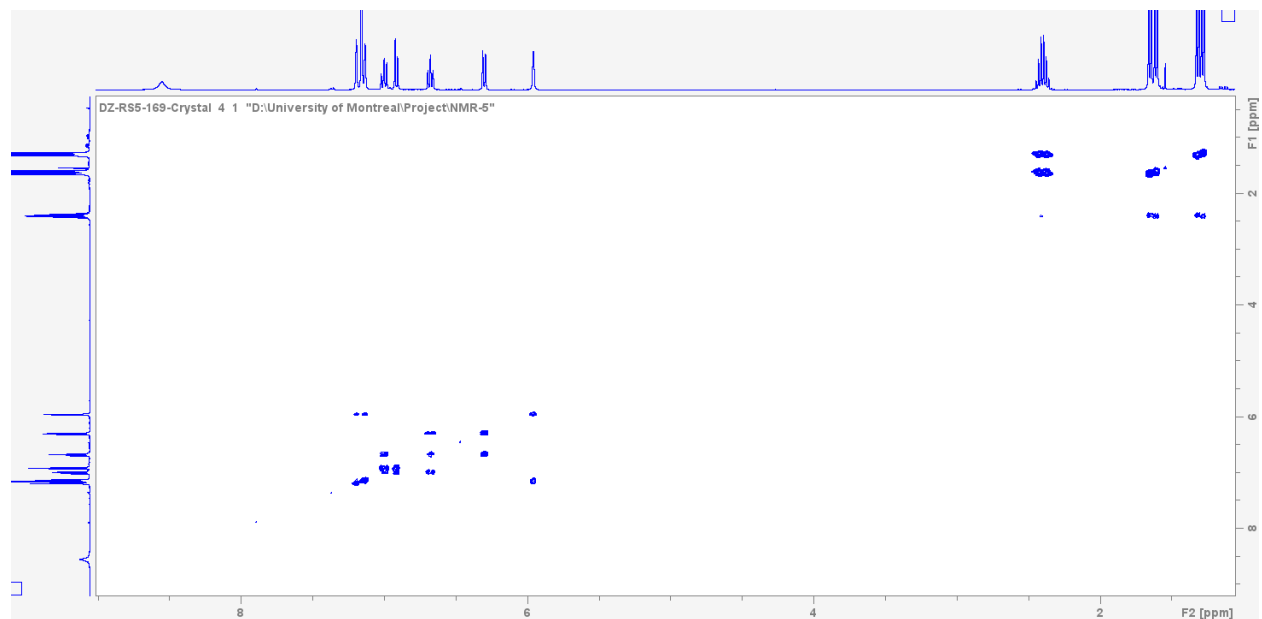
Figure S4. 55. Full ^1H-^1H COSY NMR spectrum of **6a** in C_6D_6.
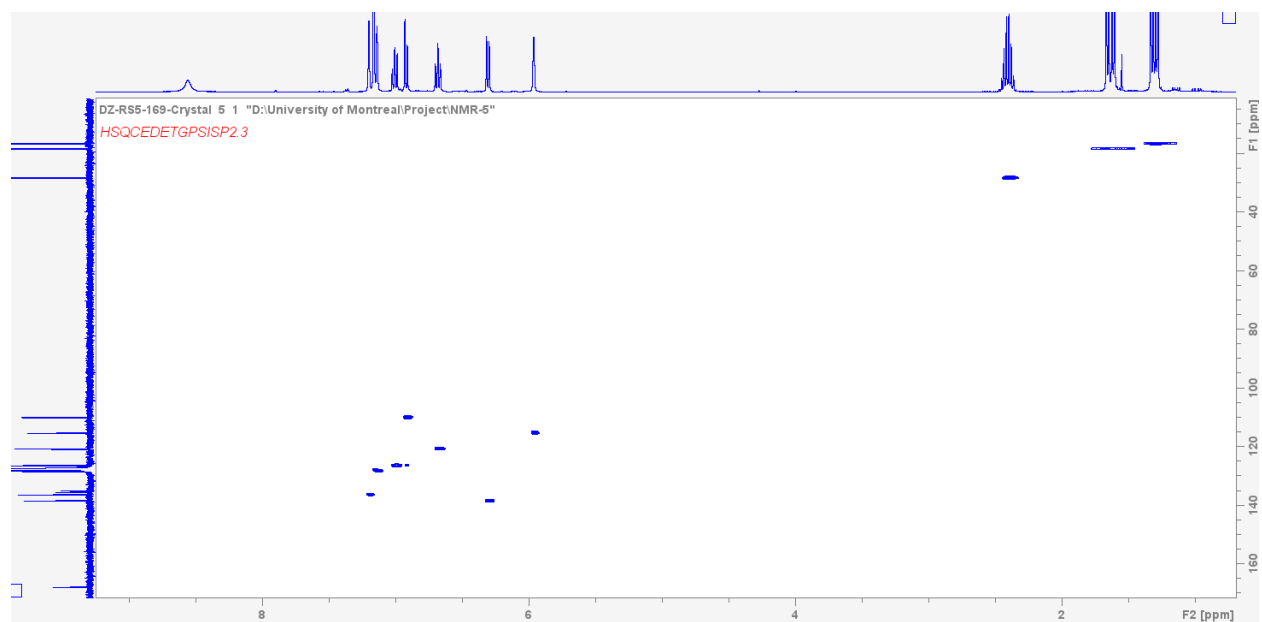
Figure S4. 56. Full HSQC-edited NMR spectrum of **6a** in C_6D_6.
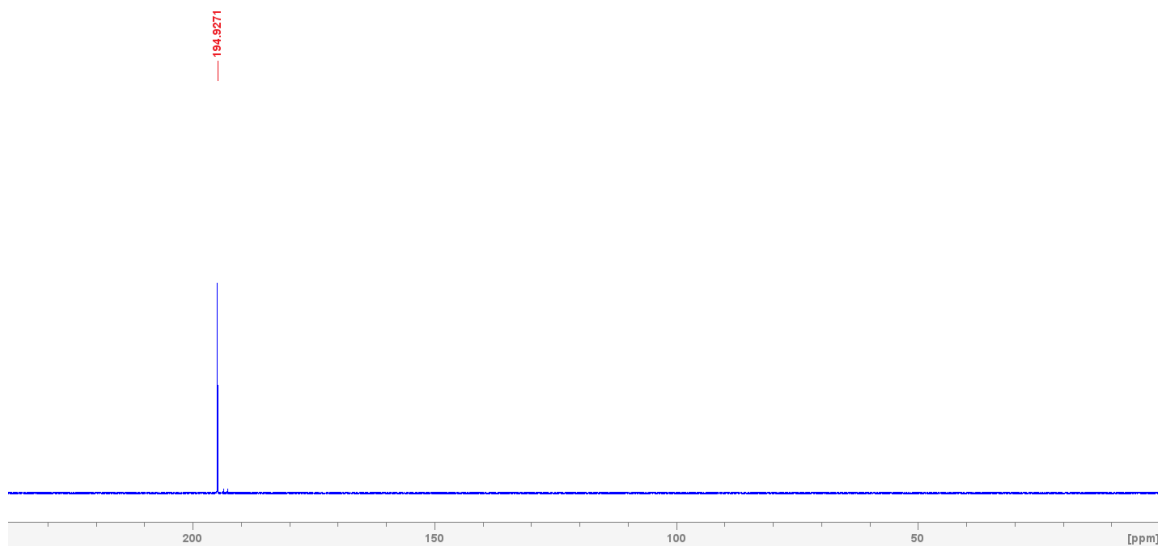
Figure S4. 57. $^{31}P\{^1H\}$ NMR spectrum of **6a** in C_6D_6.
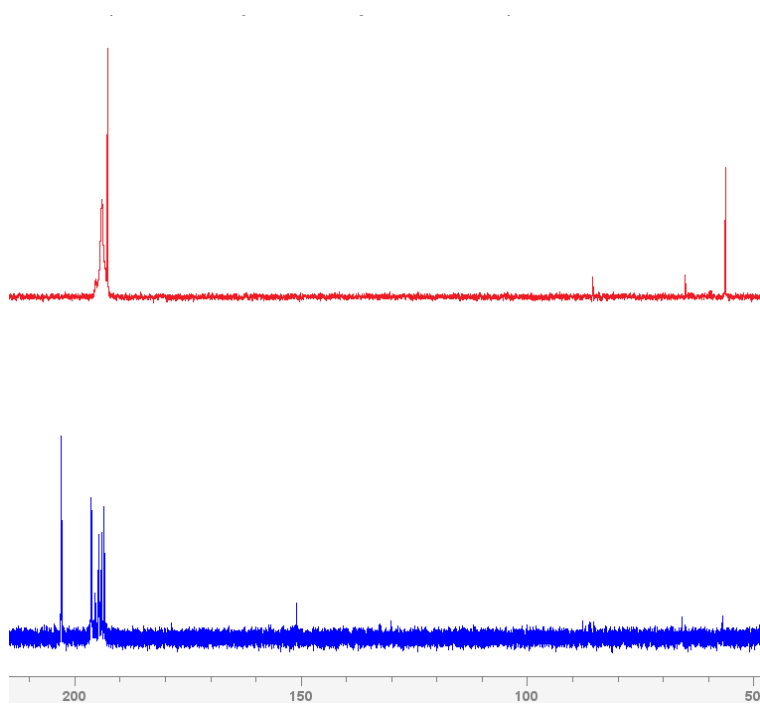
Figure S4. 58. $^{31}P\{^1H\}$ NMR spectra of **3a** with 1 equiv (blue trace) and 2 equiv (red trace) of imidazole in CH_2Cl_2.
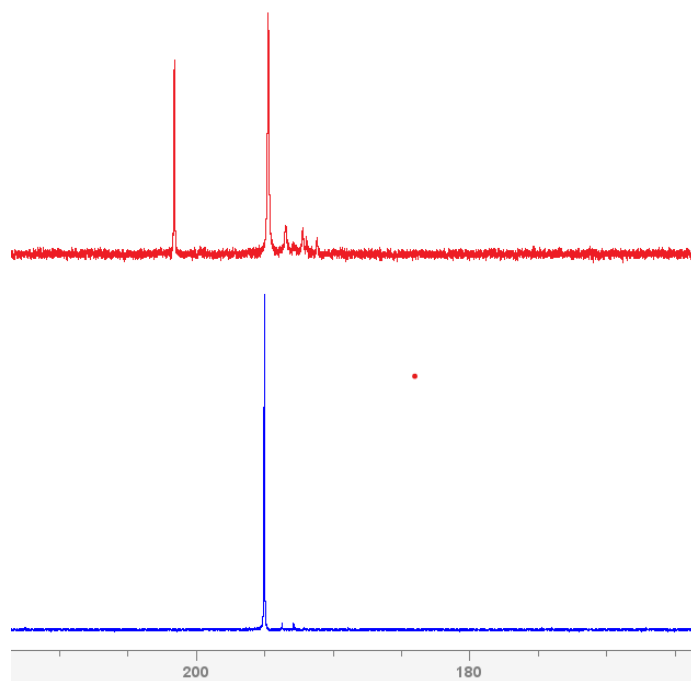
Figure S4. 59. ^{31}P{^{1}H} NMR spectra of **1a** with 2 equiv (blue trace) of imidazole and 2 equiv (red trace) of TEMPOH (Ni:imidazole:TEMPOH= 1:1:1) in CH$_2$Cl$_2$.

Complex **7a**
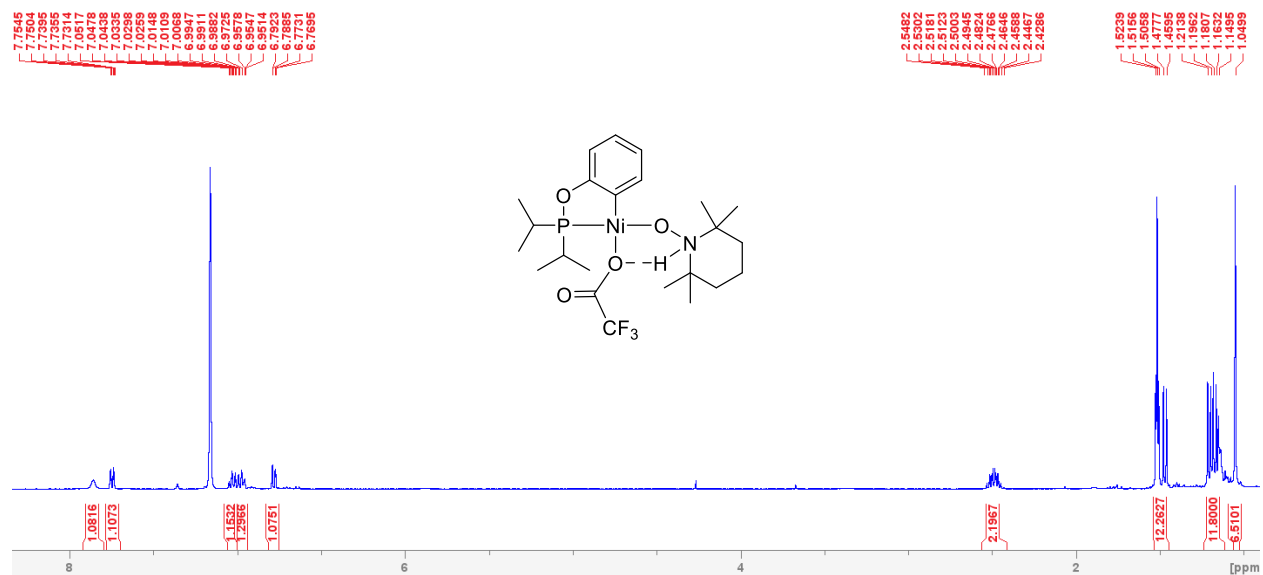
Figure S4. 60. Full ^{1}H NMR spectrum of **7a** in C_6D_6.
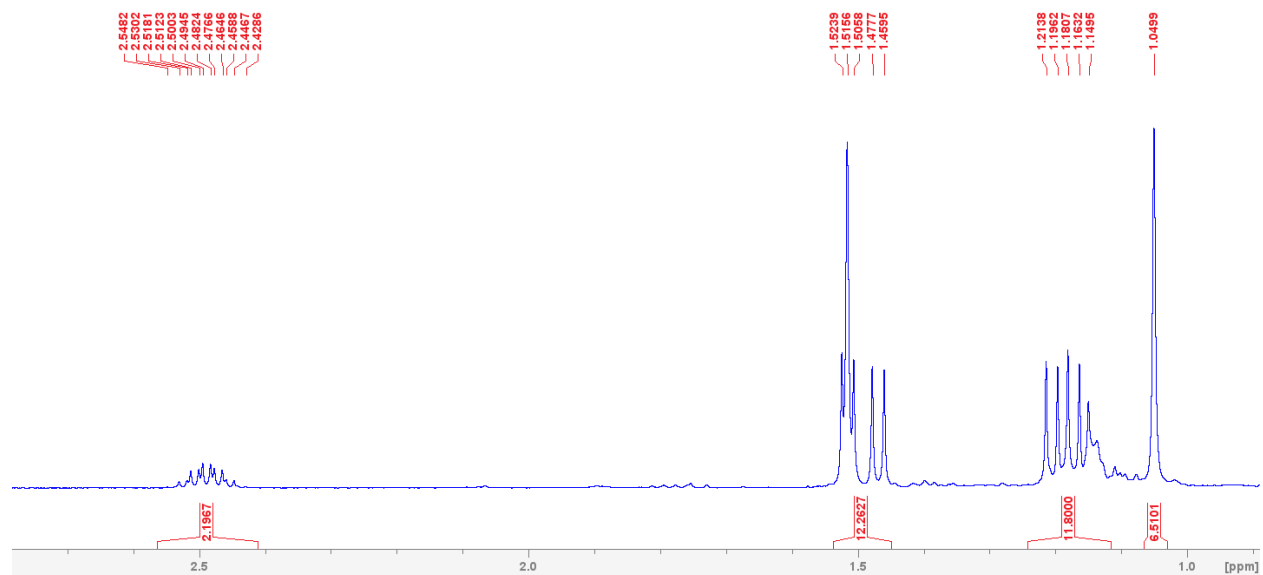
Figure S4. 61. The expanded aliphatic region of the ^{1}H NMR spectrum of **7a** in C_6D_6.
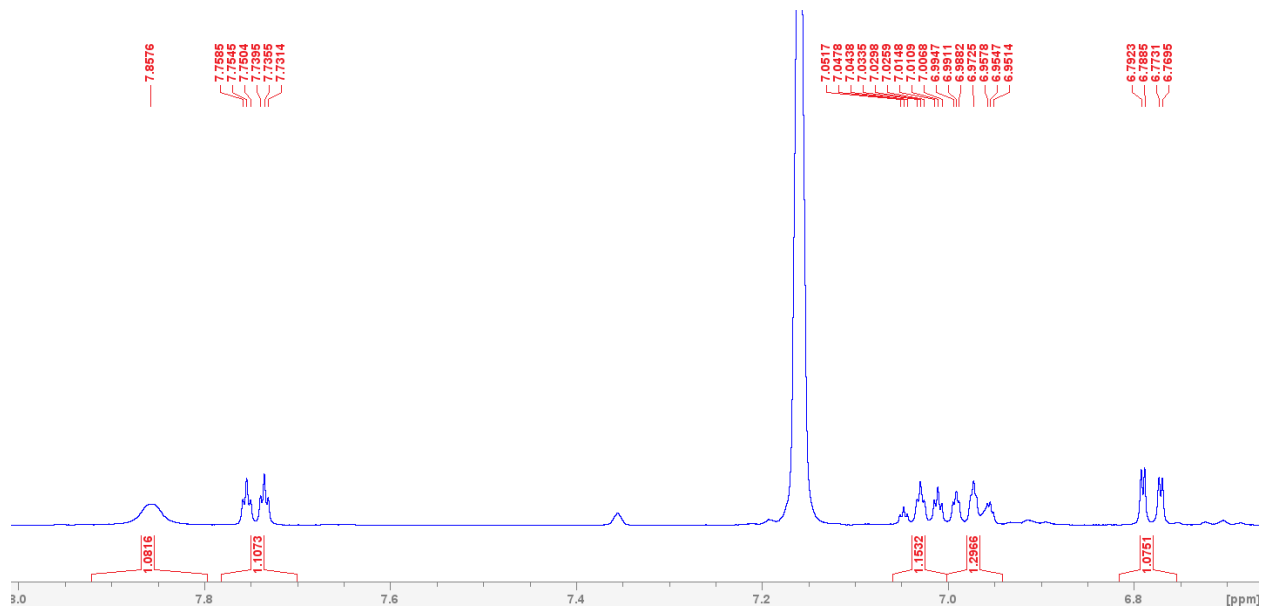
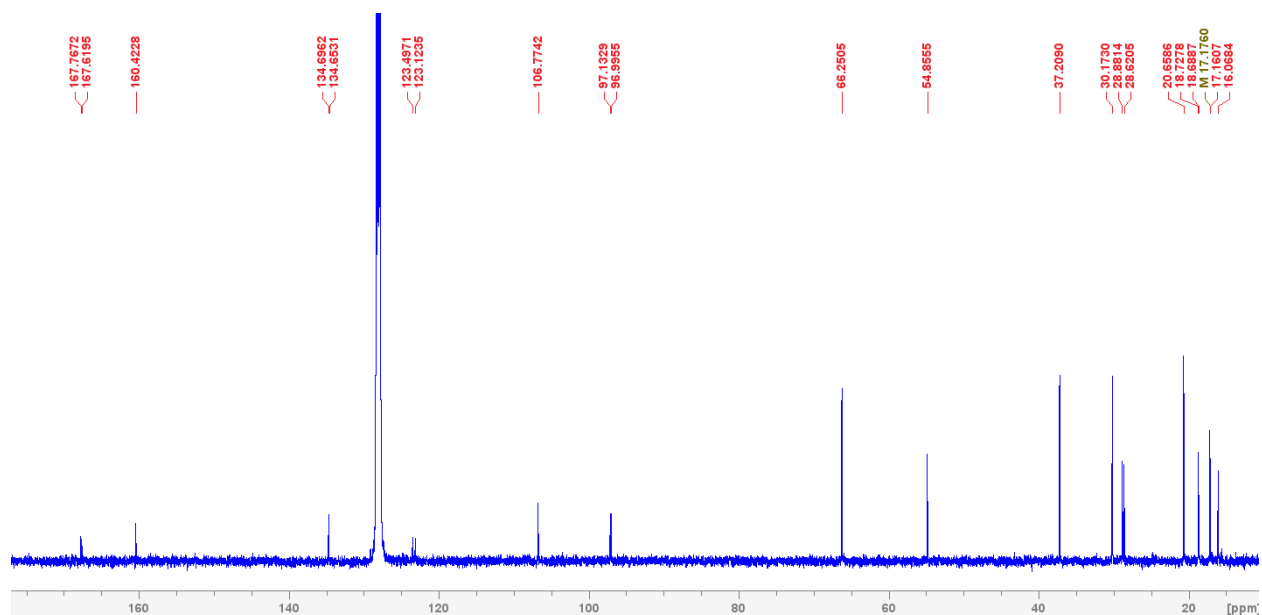**Figure S4. 62.** The expanded aromatic region of the ^{1}H NMR spectrum of **7a** in C$_6$D$_6$.
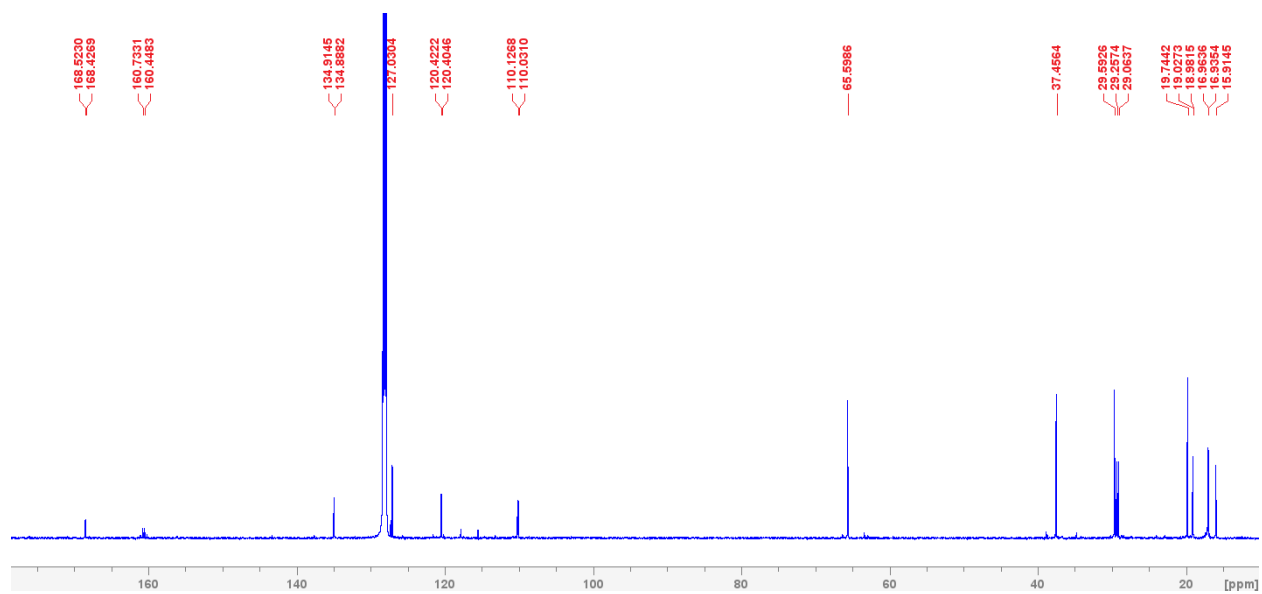
Figure S4. 63. Full ^{13}C{^{1}H} NMR spectrum of **7a** in C$_6$D$_6$.
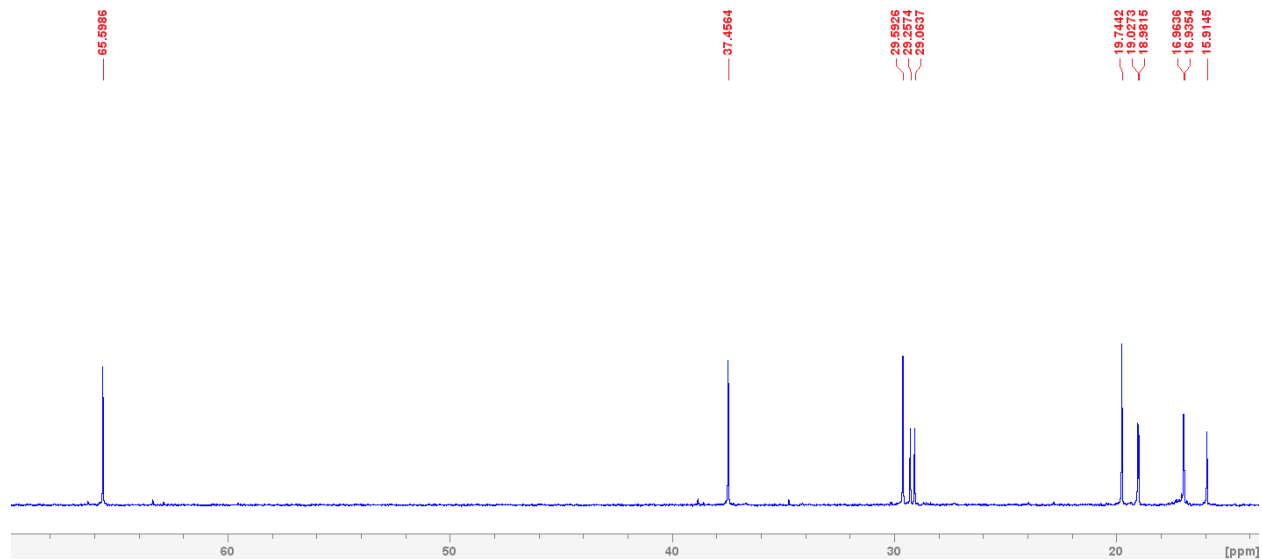
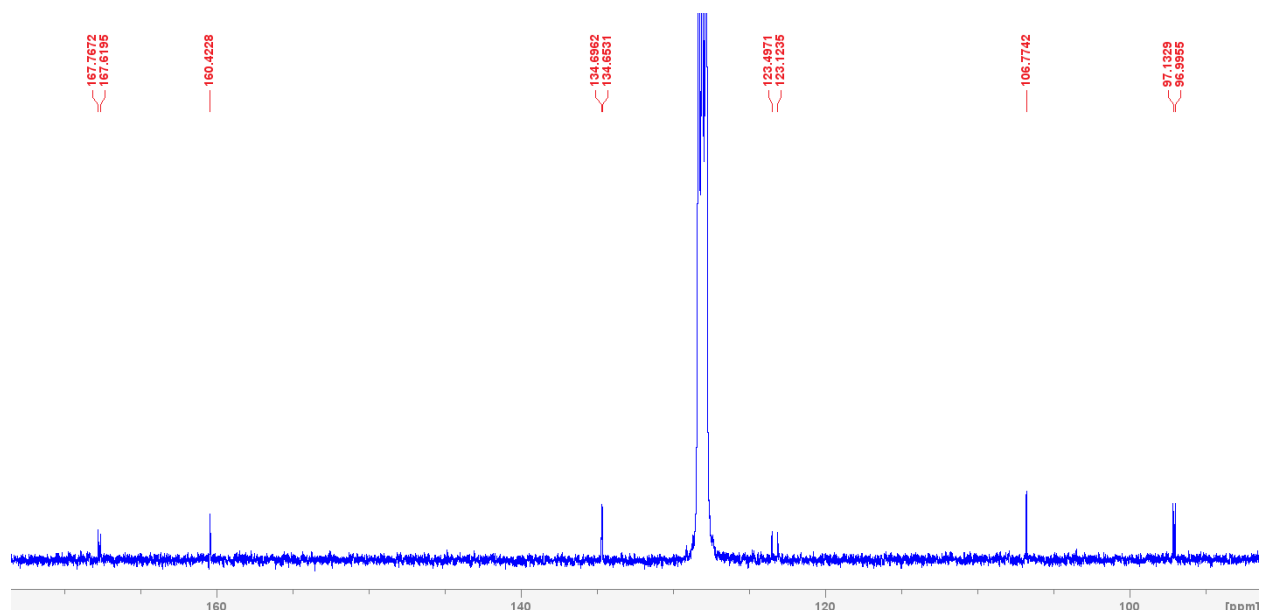**Figure S4. 64.** The expanded aliphatic region of the $^{13}C\{^1H\}$ NMR spectrum of **7a** in C_6D_6.

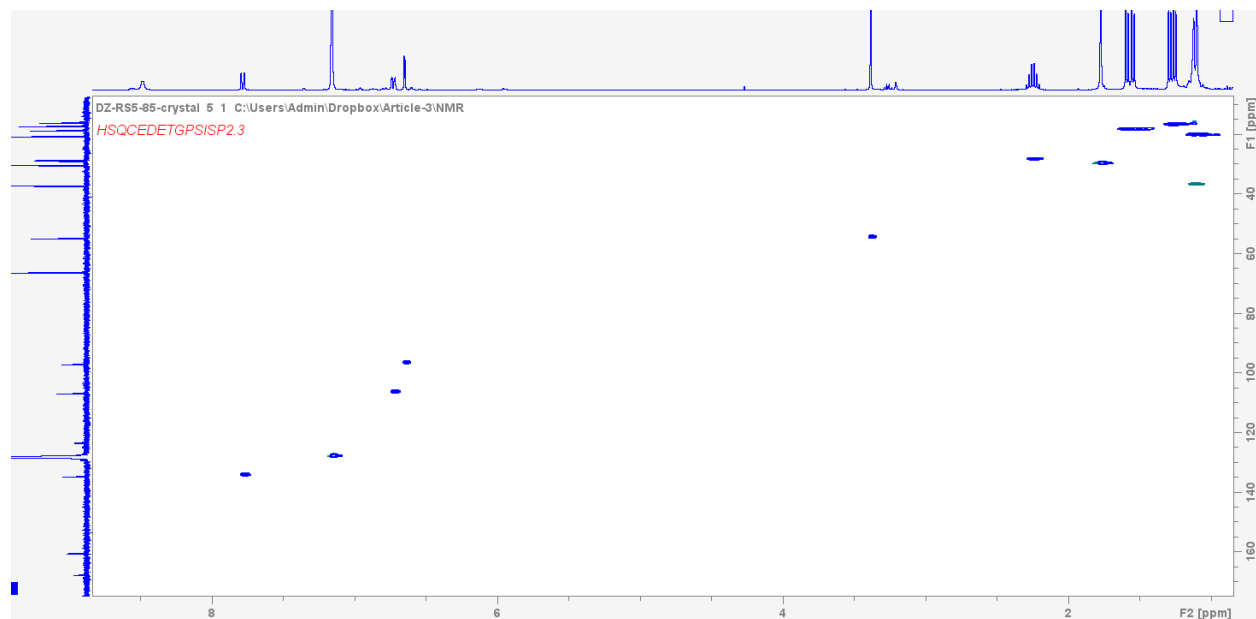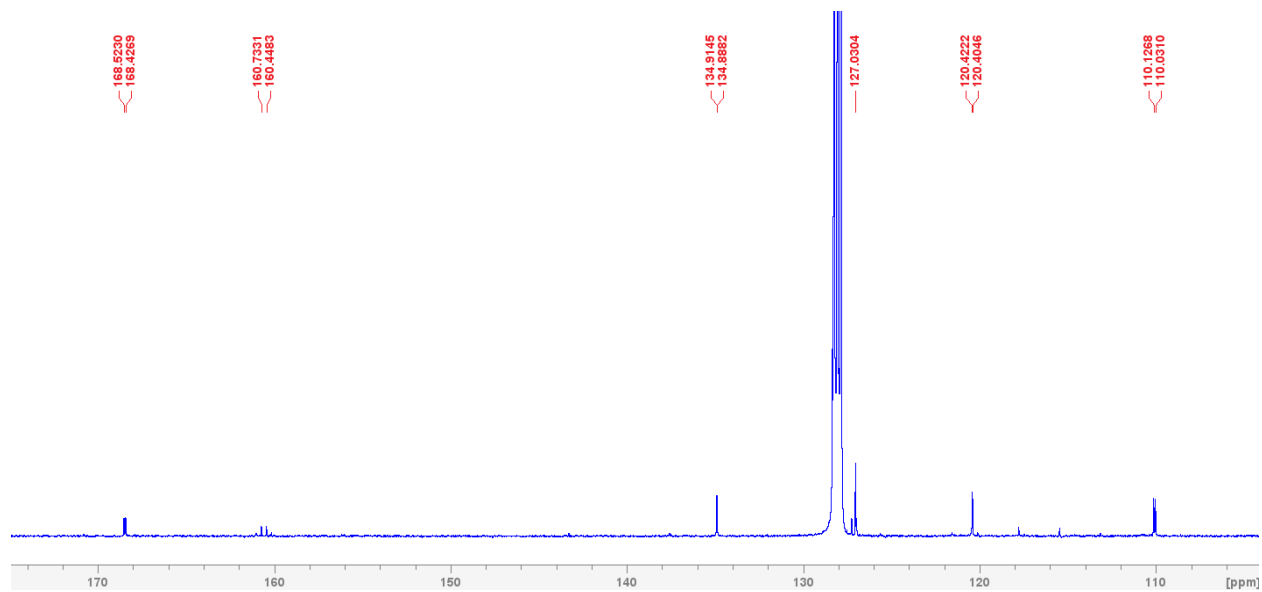**Figure S4. 65.** The expanded aromatic region of the $^{13}C\{^1H\}$ NMR spectrum of **7a** in C_6D_6.
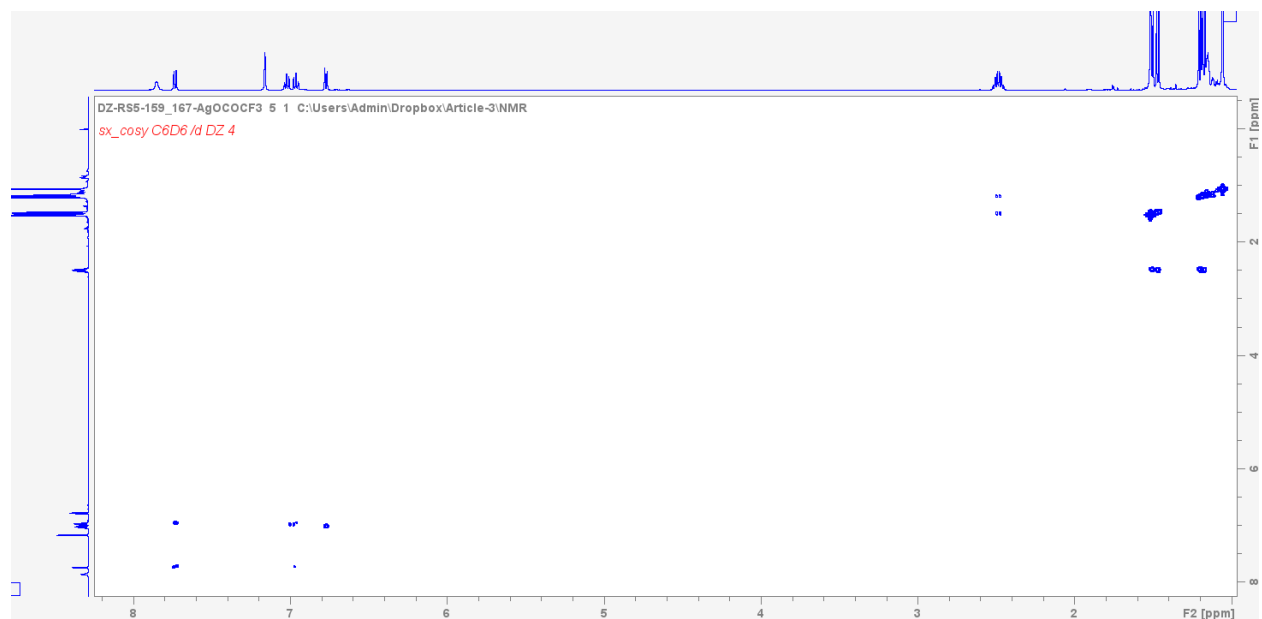
Figure S4. 66. Full ^1H-^1H COSY NMR spectrum of **7a** in C_6D_6.
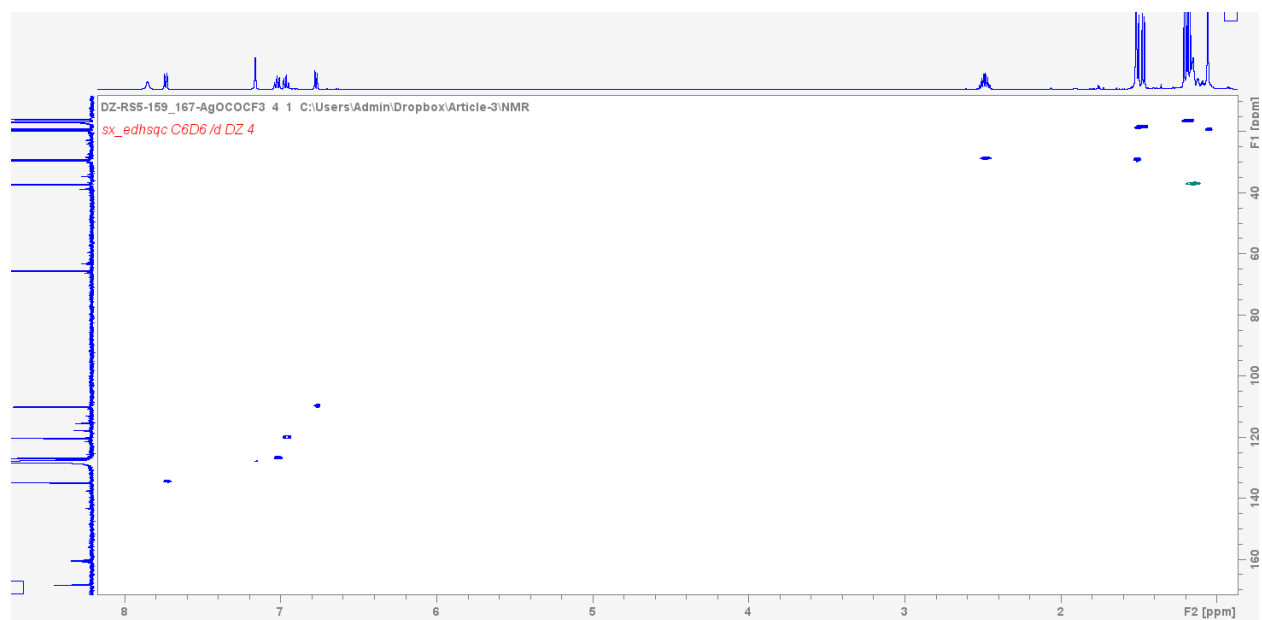
Figure S4. 67. Full HSQC-Edited NMR spectrum of **7a** in C_6D_6.
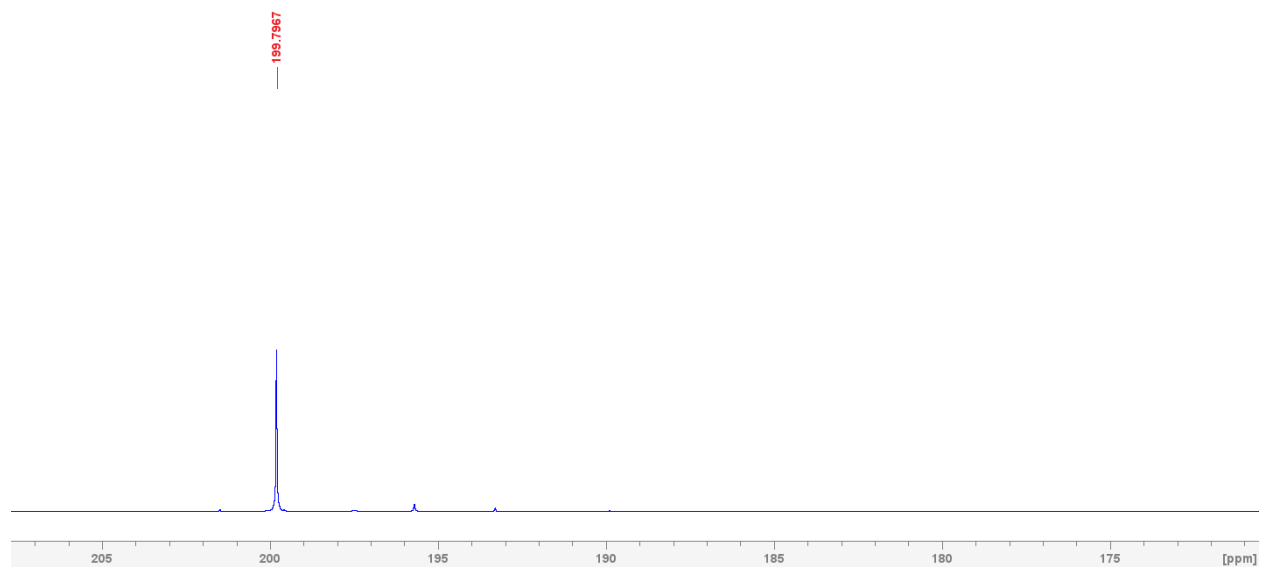
Figure S4. 68. Full $^{31}\text{P}\{^{1}\text{H}\}$ NMR spectrum of **7a** in C_6D_6.
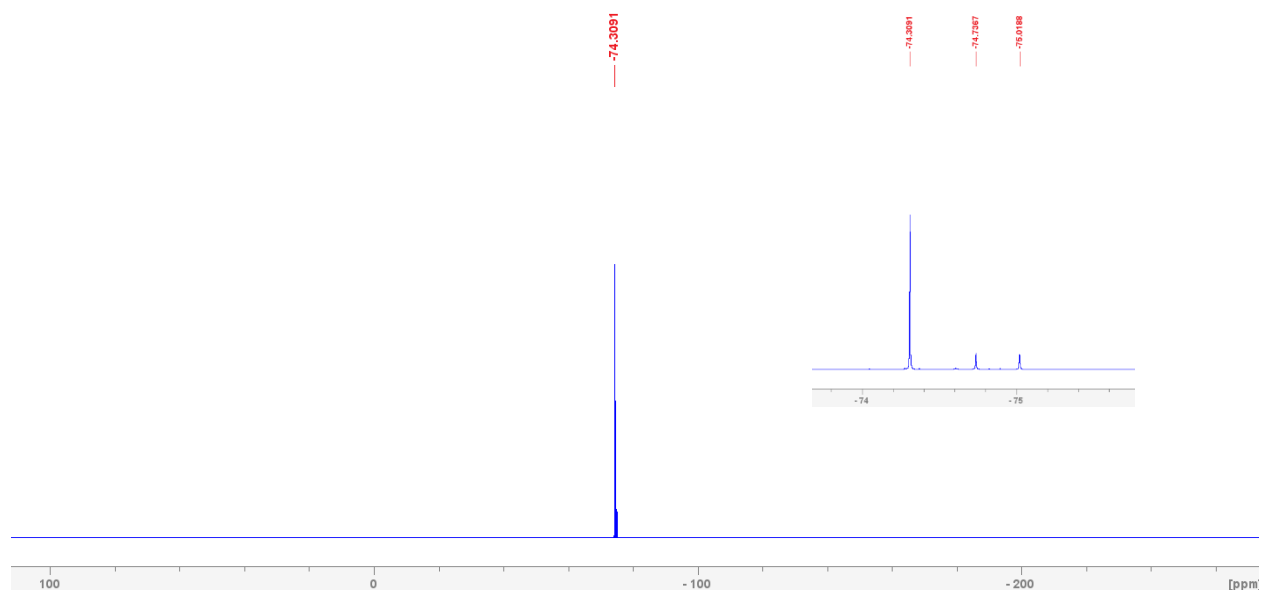
Figure S4. 69. Full $^{19}\text{F}\{^{1}\text{H}\}$ NMR spectrum of **7a** in C_6D_6.
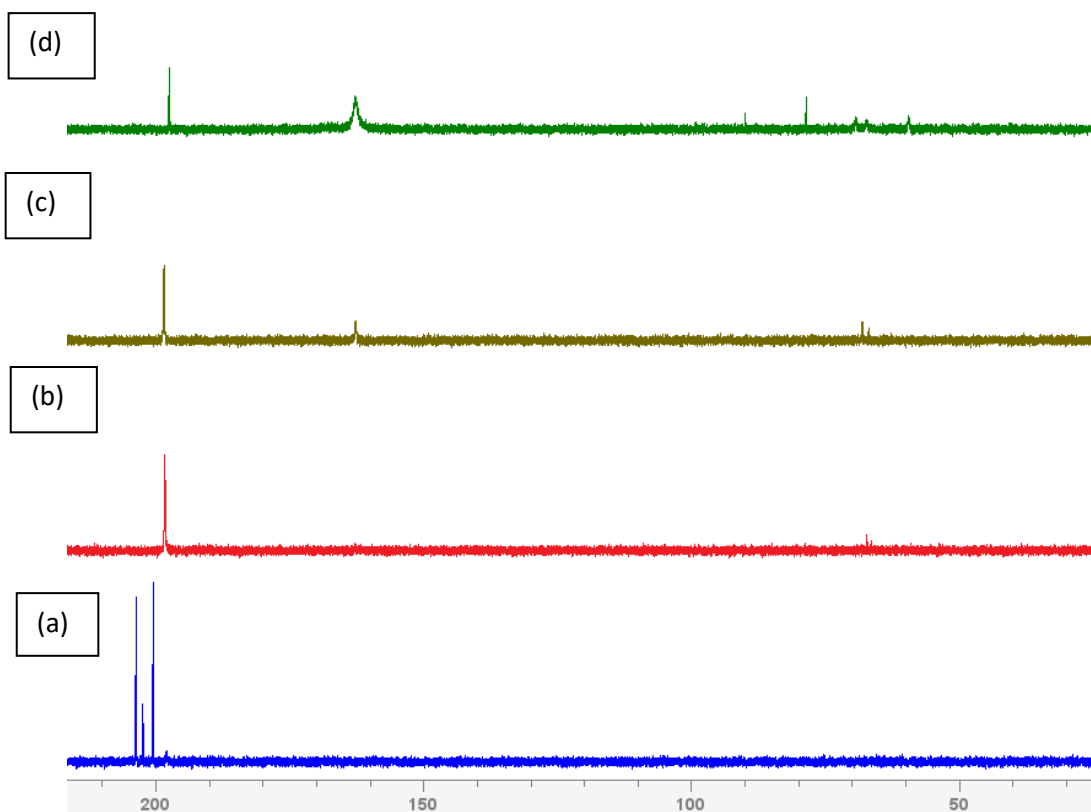
Figure S4. 70. $^{31}P\{^1H\}$ NMR (CH$_2$Cl$_2$) spectra of **3a** with various amounts of AgOCOCF$_3$: blue trace, a (1 equiv), red trace, b (3 equiv), brown trace, c (3 equiv, after 24h), green trace, d (4 equiv).
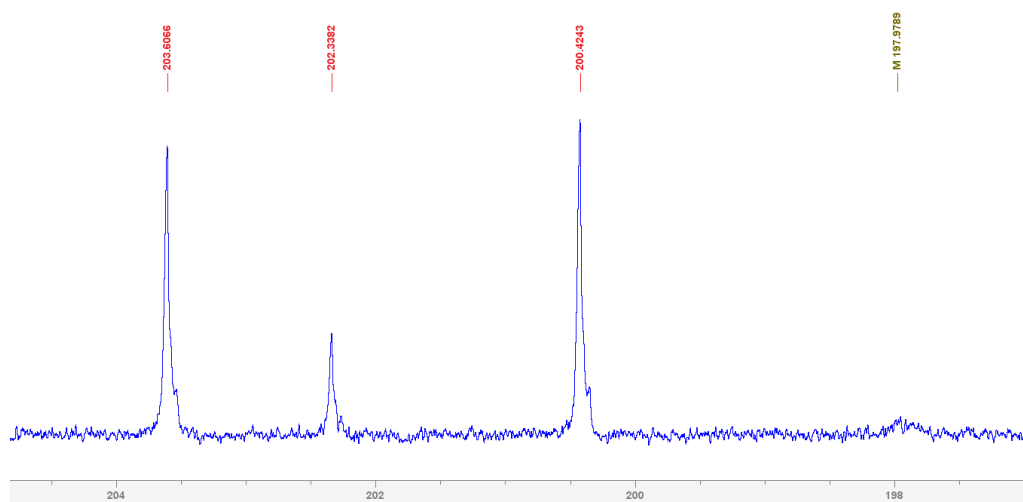
Figure S4. 71. $^{31}P\{^1H\}$ NMR spectra of **3a** with 1 equivalent of AgOCOCF$_3$ in CH$_2$Cl$_2$.
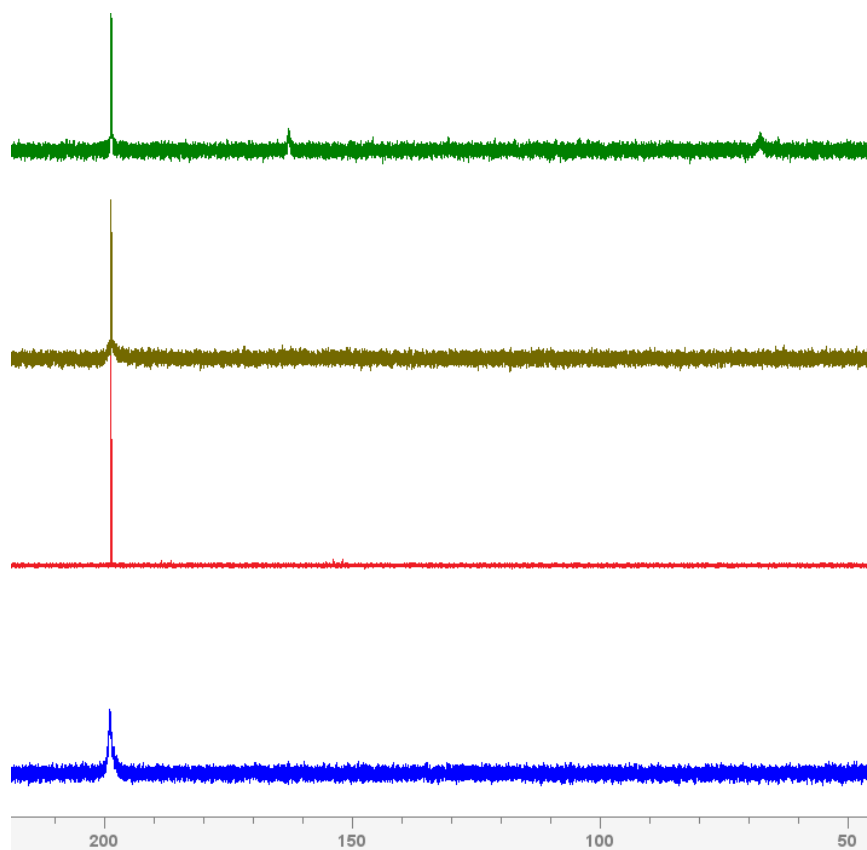
Figure S4. 72. $^{31}P\{^1H\}$ NMR spectra recorded for a DCM sample of **1a** to which were added successive quantities of AgOCOCF₃, as follows: blue trace, 0 equiv (199 ppm, FWHM ≈ 100 Hz); red trace, 2 equiv (196 ppm, FWHM ≈ 4 Hz); brown trace, 4 equiv (196 ppm, FWHM ≈ 9 Hz); green trace, 6 equiv (198 ppm, FWHM ≈ 21 Hz).
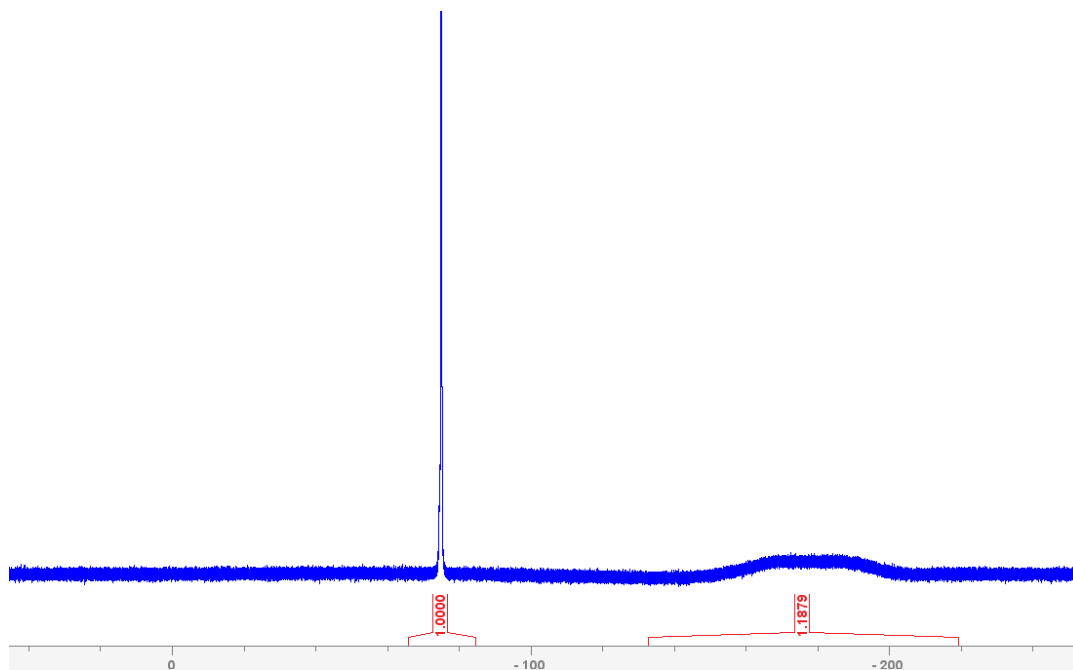
Figure S4. 73. ^{19}F{^{1}H} NMR spectrum of crude mixture of **3a** with 3eq of AgOC(O)CF$_3$ in CH$_2$Cl$_2$.
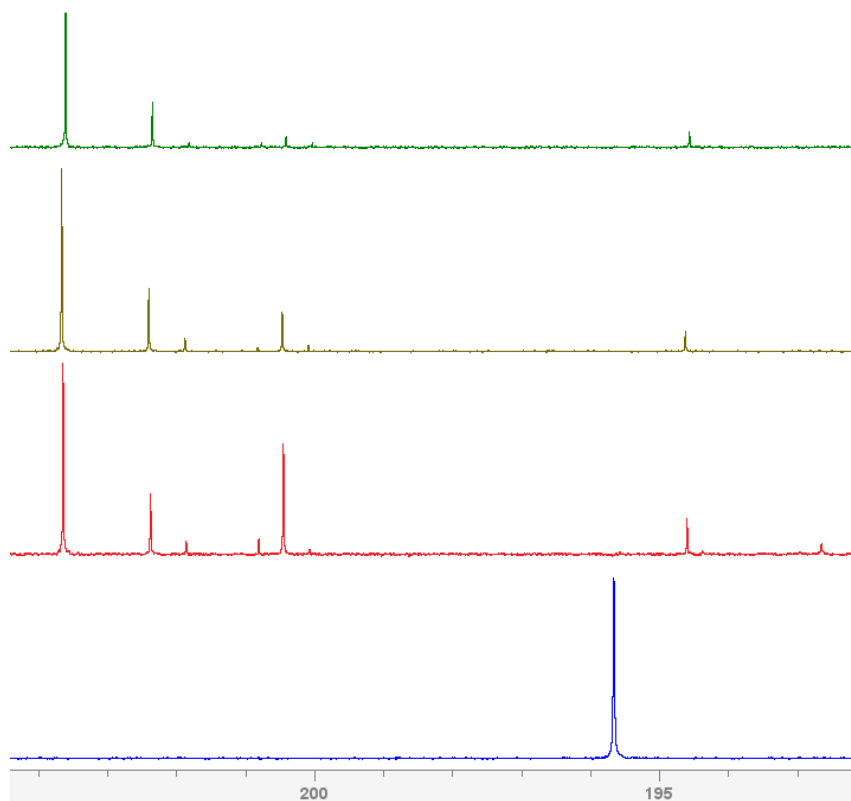
Figure S4. 74. $^{31}P\{^{1}H\}$ NMR spectra recorded for a DCM sample containing a mixture of **1a** and 2 equiv of AgOCOCF$_3$ (to generate a 1:1 ratio of Ni : CF$_3$COO) to which were added successive quantities of TEMPOH, as follows (bottom to top): blue trace, 0 equiv; red trace, 1 equiv; brown trace, 2 equiv; green trace, 4 equiv.
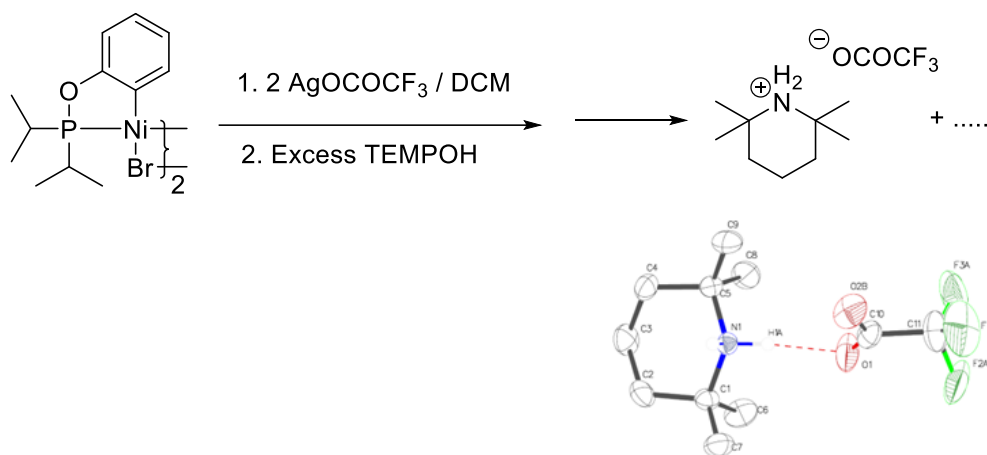
Figure S4. 75. Reaction scheme for formation of piperidinium trifluoroacetate and its molecular diagram. Thermal ellipsoids are shown at the 50% probability level. Hydrogen atoms have been omitted for clarity.

e. Crystallographic data tables

Table S4. 1. Crystal description and refinement indicators for compounds 3a-3c

	3a	3b	3c
chemical formula	$C_{21}H_{37}BrNNiO_2P$	$C_{21}H_{36}BrClNNiO_2P$	$C_{22}H_{39}Br_{0.25}Cl_{0.75}NNiO_3P$
crystal colour	brown	brown	brown
crystal size (mm)	$0.122 \times 0.175 \times 0.197$	$0.226 \times 0.331 \times 0.472$	$0.118 \times 0.149 \times 0.178$
index ranges	$-18 \leq h \leq 18$	$-19 \leq h \leq 19$	$-14 \leq h \leq 14$
	$-14 \leq k \leq 13$	$-14 \leq k \leq 14$	$-17 \leq k \leq 17$
	$-18 \leq l \leq 18$	$-18 \leq l \leq 18$	$-36 \leq l \leq 36$
Fw; F(000)	505.10; 1056	539.55; 1120.0	501.78; 2132.0
T (K)	150	150	150
wavelength (Å)	1.34139	1.34139	1.34139
space group	$P2_1/c$	$P2_1/c$	$P2_1/c$
a (Å)	15.1559(3)	15.8263(4)	11.9270(5)
b (Å)	11.6422(3)	11.6352(3)	14.1466(6)
c (Å)	15.0239(3)	14.8354(4)	29.5812(12
α (deg)	90	90)	90
β (deg)	117.4860(10)	114.5960(10)	98.950(2)
γ (deg)	90	90	90
Z	4	4	8
V (Å³)	2351.71(9)	2483.95(11)	4930.4(4)
ρ_{calcd} (g·cm^{-3})	1.427	1.443	1.352
μ (mm^{-1})	6.320	6.654	5.623
2θ range (deg); completeness	$5.718 - 113.912$; 0.992	$5.342 - 109.842$; 0.993	$5.262 - 109.846$; 0.988
collected reflections; R_σ	24417; 0.0290	30401; 0.0483	45605; 0.0268
unique reflections; R_{int}	4716; 0.0404	4668; 0.0640	9244; 0.0315
R1[a]; wR2[b] [I > 2σ(I)]	0.0266; 0.0705	0.0424; 0.1060	0.0284; 0.0721
R1; wR2 [all data]	0.0278; 0.0711	0.0469; 0.1078	0.0308; 0.0734
GOOF	1.087	1.095	1.029
largest diff peak and hole	0.33 and -0.79	0.91 and -0.96	0.67 and -0.46

[a] $R_1 = \Sigma(||F_o|-|F_c||)/\Sigma|F_o|$

[b] $wR_2 = \{\Sigma[w(F_o{}^2 - F_c{}^2)^2]/\Sigma[w(F_o{}^2)^2]\}^{\frac{1}{2}}$

Table S4. 2. Crystal description and refinement indicators for compounds **3d, 5a & 6a**.

	3d	5a	6a
chemical formula	$C_{26}H_{41}BrNNiO_3P$	$C_{16}H_{27}Br_{0.24}Cl_{0.76}NNiO_2P$	$C_{21}H_{30}BrN_6NiOP$
crystal colour	brown	brown	brown
crystal size (mm)	$0.236 \times 0.354 \times 0.388$	$0.083 \times 0.101 \times 0.168$	$0.088 \times 0.099 \times 0.117$
index ranges	$-15 \le h \le 15$ $-19 \le k \le 19$ $-17 \le l \le 18$	$-9 \le h \le 9$ $-30 \le k \le 30$ $-11 \le l \le 11$	$-11 \le h \le 10$ $-0 \le k \le 33$ $-0 \le l \le 12$
Fw; F(000)	585.19; 1220.0	401.18; 841.0	552.10; 1136.0
T (K)	150	150	150
wavelength (Å)	1.34139	1.34139	1.34139
space group	$P2_1/n$	$P2_1/n$	$P2_1/n$
a (Å)	12.4164(6)	7.7771(3)	9.1454(4)
b (Å)	16.3578(8)	24.7633(8)	27.5501(11)
c (Å)	14.9046(7)	9.4301(3)	9.8982(4)
α (deg)	90	90	90
β (deg)	112.769(2)	97.0120(10)	102.159(2)
γ (deg)	90	90	90
Z	4	4	4
V (Å³)	2791.3(2)	1802.53(11)	2437.97(18)
ρ_{calcd} (g·cm⁻³)	1.390	1.478	1.504
μ (mm⁻¹)	5.394	7.580	6.154
θ range (deg); completeness	$7.31 - 109.844$; 0.978	$6.21 - 109.74$; 0.969	$9.048 - 109.8$; 0.986
collected reflections; R_σ	20919; 0.0446	15394; 0.0252	42525; 0.0436
unique reflections; R_{int}	5133; 0.0493	3317; 0.0280	9390; 0.0664
R1[a]; wR2[b] [I > 2σ(I)]	0.0678; 0.1716	0.0275; 0.0697	0.0429; 0.1126
R1; wR2 [all data]	0.0687; 0.1735	0.0281; 0.0700	0.0445; 0.1149
GOOF	1.044	1.136	1.065
largest diff peak and hole	2.01 and -1.10	0.39 and -0.38	0.52 and -0.62

[a] $R_1 = \Sigma(||F_o|-|F_c||)/\Sigma|F_o|$
[b] $wR_2 = \{\Sigma[w(F_o^2-F_c^2)^2]/\Sigma[w(F_o^2)^2]\}^{1/2}$

Table S4. 3. Crystal description and refinement indicators for compounds **7a**.

	7a	**Piperidinium trifluoroacetate**
chemical formula	$C_{23}H_{37}F_3NNiO_4P$	$C_{11}H_{20}F_3NO_2$
crystal colour	yellow	yellow
crystal size (mm)	0.097 × 0.112 × 0.148	0.099 × 0.24 × 0.25
index ranges	$-18 \leq h \leq 19$ $-15 \leq k \leq 15$ $-17 \leq l \leq 17$	$-27 \leq h \leq 25$ $-11 \leq k \leq 9$ $-21 \leq l \leq 21$
Fw; F(000)	538.21; 1136.0	255.28; 1088.0
T (K)	150	150
wavelength (Å)	1.34139	1.34139
space group	$P2_1/c$	$C2/c$
a (Å)	15.7583(5)	19.9649(14)
b (Å)	12.7241(4)	8.3817(6)
c (Å)	14.1830(5)	15.8150(11)
α (deg)	90	90
β (deg)	115.546(2)	91.234(4)
γ (deg)	90	90
Z	4	8
V (Å³)	2565.82(15)	2645.9(3)
ρ$_{calcd}$ (g·cm⁻³)	1.393	1.282
μ (mm⁻¹)	4.797	0.632
2θ range; completeness	5.408 – 110.106; 0.993	7.706 –131.816; 0.985
collected reflections; R$_\sigma$	24214; 0.0735	29827; 0.0318
unique reflections; R$_{int}$	4845; 0.0835	3447; 0.0468
R1[a]; wR2[b] [I > 2σ(I)]	0.0568; 0.1171	0.0565; 0.1566
R1; wR2 [all data]	0.0942; 0.1291	0.0673; 0.1674
GOOF	1.050	1.058
largest diff peak and hole	0.39 and -0.42	0.45 and -0.28

[a] $R_1 = \Sigma(||F_o|-|F_c||)/\Sigma|F_o|$
[b] $wR_2 = \{\Sigma[w(F_o^2 - F_c^2)^2]/\Sigma[w(F_o^2)^2]\}^{1/2}$

Table S4. 4. Pertinent bond angles and distances for complexes **3a-3d** and **5a-7a**

	Ni1–C2	Ni1–P1	Ni1–Br1 or Ni1-Cl1	Ni1–O2/O3	Ni1–N	N-O2	C2-Ni1-Br1/ Cl1/N2/O3	P1-Ni1-N/O
3a	1.9017(18)	2.0905(5)	2.3897(3)	1.9045(12)		1.3973(18)	170.76(5)	171.64(4)
3b	1.9026(16)	2.0927(5)	2.373(8)	1.9132(11)		1.400(2)	174.0(2)	171.90(4)
3c	1.907(2)	2.0924(6)	2.3872(4)	1.8918(16)		1.3902(19)	172.14(8)	169.73(5)
3d	1.896(3)	2.0995(8)	2.3775(5)	1.908(2)		1.399(3)	173.99(9)	171.23(7)
5a	1.9076(18)	2.1026(5)	2.380(11)		1.9921(17)		168.6(3)	164.72(5)
6a	1.918(2)	2.1210(7)			1.944(2) 1.930(2)		175.45(9)	176.01(6)
7a	1.904(4)	2.1138(12)		1.945(3) 1.902(3)		1.390(4)	174.86(16)	169.95(9)

Table S4. 5. Pertinent bond angles and distances for complexes **3a-3d** and **7a**

	Br-N/ O3-N	N1–H1–Br1/ N1-H1-O3
3a	3.167	144.462
3b	3.167	144.121
3c	3.136	144.097
3d	3.190	139,480
7a	2.665	140.149

4. 9. References

(1)   Kakiuchi, F.; Kochi, T. Transition-Metal-Catalyzed Carbon-Carbon Bond Formation via Carbon-Hydrogen Bond Cleavage. *Synthesis (Stuttg)* **2008**, No. 19, 3013–3039. https://doi.org/10.1055/s-2008-1067256.

(2)   Ackermann, L. Carboxylate-Assisted Transition-Metal-Catalyzed C-H Bond Functionalizations: Mechanism and Scope. *Chem Rev* **2011**, *111* (3), 1315–1345. https://doi.org/10.1021/cr100412j.

(3)   Yamaguchi, J.; Yamaguchi, A. D.; Itami, K. C-H Bond Functionalization: Emerging Synthetic Tools for Natural Products and Pharmaceuticals. *Angewandte Chemie - International Edition* **2012**, *51* (36), 8960–9009. https://doi.org/10.1002/anie.201201666.

(4)   Ackermann, L. Metal-Catalyzed Direct Alkylations of (Hetero)Arenes via C-H Bond Cleavages with Unactivated Alkyl Halides. *Chemical Communications* **2010**, *46* (27), 4866–4877. https://doi.org/10.1039/c0cc00778a.

(5)   Chen, D. Y. K.; Youn, S. W. C-H Activation: A Complementary Tool in the Total Synthesis of Complex Natural Products. *Chemistry - A European Journal* **2012**, *18* (31), 9452–9474. https://doi.org/10.1002/chem.201201329.

(6)   Lyons, T. W.; Sanford, M. S. Palladium-Catalyzed Ligand-Directed C-H Functionalization Reactions. *Chem Rev* **2010**, *110* (2), 1147–1169. https://doi.org/10.1021/cr900184e.

(7)   Colby, D. A.; Bergman, R. G.; Ellman, J. A. Rhodium-Catalyzed C-C Bond Formation via Heteroatom-Directed C-H Bond Activation. *Chem Rev* **2010**, *110* (2), 624–655. https://doi.org/10.1021/cr900005n.

(8)   Huang, L.; Szewczyk, M.; Kancherla, R.; Maity, B.; Zhu, C.; Cavallo, L.; Rueping, M. Modulating Stereoselectivity in Allylic C(sp3)-H Bond Arylations via Nickel and Photoredox Catalysis. *Nat Commun* **2023**, *14* (1). https://doi.org/10.1038/s41467-023-36103-0.

(9)   It Should Be Noted, However, That Addition of Triazole to the Solutions of 2a Seems to Lead to Some Decomposition That Causes the Initially Clear Sample to Become Somewhat Cloudy. Filtration of These Cloudy Samples Gave Traces of a White Solid That Proved Intractable.

(10) Liu, Y. J.; Zhang, Z. Z.; Yan, S. Y.; Liu, Y. H.; Shi, B. F. Ni(II)/BINOL-Catalyzed Alkenylation of Unactivated C(sp3)-H Bonds. *Chemical Communications* **2015**, *51* (37), 7899–7902. https://doi.org/10.1039/c5cc02254a.

(11) Yan, Q.; Chen, Z.; Yu, W.; Yin, H.; Liu, Z.; Zhang, Y. Nickel-Catalyzed Direct Amination of Arenes with Alkylamines. *Org Lett* **2015**, *17* (10), 2482–2485. https://doi.org/10.1021/acs.orglett.5b00990.

(12) Li, Z.; Shi, H.; Chen, X.; Peng, L.; Li, Y.; Yin, G. Nickel-Catalyzed Regio- and Enantioselective Borylative Coupling of Terminal Alkenes with Alkyl Halides Enabled by an Anionic Bisoxazoline Ligand. *J Am Chem Soc* **2023**, *145* (25), 13603–13614. https://doi.org/10.1021/jacs.3c01040.

(13) Aihara, Y.; Chatani, N. Nickel-Catalyzed Reaction of C-H Bonds in Amides with I_2: Ortho-Iodination via the Cleavage of C(sp2)-H Bonds and Oxidative Cyclization to β-Lactams via the Cleavage of C(sp3)-H Bonds. *ACS Catal* **2016**, *6* (7), 4323–4329. https://doi.org/10.1021/acscatal.6b00964.

(14) Yoshikai, N.; Matsumoto, A.; Norinder, J.; Nakamura, E. Iron-Catalyzed Chemoselective Ortho Arylation of Aryl Imines by Directed C-H Bond Activation. *Angewandte Chemie - International Edition* **2009**, *48* (16), 2925–2928. https://doi.org/10.1002/anie.200900454.

(15) Wen, J.; Zhang, J.; Chen, S. Y.; Li, J.; Yu, X. Q. Iron-Mediated Direct Arylation of Unactivated Arenes. *Angewandte Chemie - International Edition* **2008**, *47* (46), 8897–8900. https://doi.org/10.1002/anie.200802526.

(16) Liu, W.; Cao, H.; Lei, A. Iron-Catalyzed Direct Arylation of Unactivated Arenes with Aryl Halides. *Angewandte Chemie - International Edition* **2010**, *49* (11), 2004–2008. https://doi.org/10.1002/anie.200906870.

(17) Gao, K.; Yoshikai, N. Cobalt-Catalyzed Arylation of Aldimines via Directed C-H Bond Functionalization: Addition of 2-Arylpyridines and Self-Coupling of Aromatic Aldimines. *Chemical Communications* **2012**, *48* (36), 4305–4307. https://doi.org/10.1039/c2cc31114c.

(18) Gao, K.; Yoshikai, N. Regioselectivity-Switchable Hydroarylation of Styrenes. *J Am Chem Soc* **2011**, *133* (3), 400–402. https://doi.org/10.1021/ja108809u.

(19)   Gao, K.; Yoshikai, N. Cobalt-Catalyzed Ortho Alkylation of Aromatic Imines with Primary and Secondary Alkyl Halides. *J Am Chem Soc* **2013**, *135* (25), 9279–9282. https://doi.org/10.1021/ja403759x.

(20)   Shacklady-Mcatee, D. M.; Dasgupta, S.; Watson, M. P. Nickel(0)-Catalyzed Cyclization of N - Benzoylaminals for Isoindolinone Synthesis. *Org Lett* **2011**, *13* (13), 3490–3493. https://doi.org/10.1021/ol201248c.

(21)   Ogata, K.; Atsuumi, Y.; Shimada, D.; Fukuzawa, S. I. Nickel-Catalyzed Three-Component Coupling between Aryl Aldehydes, Norbornenes, and Silanes Leading to Indanols through Aromatic C-H Bond Activation of Aryl Aldehydes. *Angewandte Chemie - International Edition* **2011**, *50* (26), 5896–5899. https://doi.org/10.1002/anie.201101468.

(22)   Shiota, H.; Ano, Y.; Aihara, Y.; Fukumoto, Y.; Chatani, N. Nickel-Catalyzed Chelation-Assisted Transformations Involving Ortho C-H Bond Activation: Regioselective Oxidative Cycloaddition of Aromatic Amides to Alkynes. *J Am Chem Soc* **2011**, *133* (38), 14952–14955. https://doi.org/10.1021/ja206850s.

(23)   Nakao, Y.; Kanyiva, K. S.; Hiyama, T. A Strategy for C-H Activation of Pyridines: Direct C-2 Selective Alkenylation of Pyridines by Nickel/Lewis Acid Catalysis. *J Am Chem Soc* **2008**, *130* (8), 2448–2449. https://doi.org/10.1021/ja710766j.

(24)   Aihara, Y.; Chatani, N. Nickel-Catalyzed Direct Alkylation of C-H Bonds in Benzamides and Acrylamides with Functionalized Alkyl Halides via Bidentate-Chelation Assistance. *J Am Chem Soc* **2013**, *135* (14), 5308–5311. https://doi.org/10.1021/ja401344e.

(25)   Song, W.; Lackner, S.; Ackermann, L. Nickel-Catalyzed C-H Alkylations: Direct Secondary Alkylations and Trifluoroethylations of Arenes. *Angewandte Chemie - International Edition* **2014**, *53* (9), 2477–2480. https://doi.org/10.1002/anie.201309584.

(26)   Beattie, D. D.; Grunwald, A. C.; Perse, T.; Schafer, L. L.; Love, J. A. Understanding Ni(II)-Mediated C(Sp3)-H Activation: Tertiary Ureas as Model Substrates. *J Am Chem Soc* **2018**, *140* (39), 12602–12610. https://doi.org/10.1021/jacs.8b07708.

(27) Nadeau, B. E.; Beattie, D. D.; Lui, E. K. J.; Tewkesbury, M.; Love, J. A.; Schafer, L. L. Electronic Directing Group Modification for Improved Ni(II)-Mediated C(sp3)–H Activation: A Hammett Investigation of 8-Aminoquinoline . *Organometallics* **2023**, *42* (17), 2326–2334. https://doi.org/10.1021/acs.organomet.3c00199.

(28) Roy, P.; Bour, J. R.; Kampf, J. W.; Sanford, M. S. Catalytically Relevant Intermediates in the Ni-Catalyzed C(sp2)-H and C(sp3)-H Functionalization of Aminoquinoline Substrates. *J Am Chem Soc* **2019**, *141* (43), 17382–17387. https://doi.org/10.1021/jacs.9b09109.

(29) Dubois, M.-A.; Wang, R.; Zargarian, D.; Tian, J.; Vollmerhaus, R.; Li, Z.; Collins, S. Nickel Indenyl Complexes as Catalysts for the Dimerization and Polymerization of Ethylene. *Organometallics* **2001**, *20*, 663–666. https://doi.org/10.1021/om000872.

(30) Gareau, D.; Sui-Seng, C.; Groux, L. F.; Brisse, F.; Zargarian, D. Indenyl-Nickel Complexes Bearing a Pendant, Hemilabile Olefin Ligand: Preparation, Characterization, and Catalytic Activities. *Organometallics* **2005**, *24* (16), 4003–4013. https://doi.org/10.1021/om050285u.

(31) Groux, L. F.; Zargarian, D. Aminoalkyl-Substituted Indenylnickel(II) Complexes (H3:H0-Ind(CH$_2$)$_2$NMe$_2$)Ni(PR$_3$)X and [(H3. *Organometallics* **2003**, *22* (23), 4759–4769. https://doi.org/10.1021/om0341348.

(32) Groux, L. F.; Zargarian, D. Aminoalkyl-Substituted Indenyl-Nickel Compounds: Tuning Reactivities as a Function of the Pendant, Hemilabile Moiety. *Organometallics* **2003**, *22* (15), 3124–3133. https://doi.org/10.1021/om030241q.

(33) R. Vollmerhaus; F. B. Gariepy; D. Zargarian. Preparation and Characterization of Cationic Nickel Indenyl Complexes [(1-Methylindenyl)NiLL′] +. *Organometallics* **1997**, *16*, 4762–4764.

(34) Vabre, B.; Lambert, M. L.; Petit, A.; Ess, D. H.; Zargarian, D. Nickelation of PCP- and POCOP-Type Pincer Ligands: Kinetics and Mechanism. *Organometallics* **2012**, *31* (17), 6041–6053. https://doi.org/10.1021/om3003784.

(35) Vabre, B.; Lindeperg, F.; Zargarian, D. Direct, One-Pot Synthesis of POCOP-Type Pincer Complexes from Metallic Nickel. *Green Chemistry* **2013**, *15* (11), 3188–3194. https://doi.org/10.1039/c3gc40968f.

(36)   Lefèvre, X.; Spasyuk, D. M.; Zargarian, D. New POCOP-Type Pincer Complexes of Nickel(II). *J Organomet Chem* **2011**, *696* (4), 864–870. https://doi.org/10.1016/j.jorganchem.2010.10.019.

(37)   Vabre, B.; Deschamps, F.; Zargarian, D. Ortho Derivatization of Phenols through C-H Nickelation: Synthesis, Characterization, and Reactivities of Ortho-Nickelated Phosphinite Complexes. *Organometallics* **2014**, *33* (22), 6623–6632. https://doi.org/10.1021/om500938u.

(38)   Mangin, L. P.; Zargarian, D. C-H Nickellation of Phenol-Derived Phosphinites: Regioselectivity and Structures of Cyclonickellated Complexes. *Dalton Transactions* **2017**, *46* (46), 16159–16170. https://doi.org/10.1039/c7dt03403b.

(39)   Mangin, L. P.; Zargarian, D. C-H Nickelation of Aryl Phosphinites: Mechanistic Aspects. *Organometallics* **2019**, *38* (7), 1479–1492. https://doi.org/10.1021/acs.organomet.8b00899.

(40)   Mangin, L. P.; Zargarian, D. C-H Nickelation of Naphthyl Phosphinites: Electronic and Steric Limitations, Regioselectivity, and Tandem C-P Functionalization. *Organometallics* **2019**, *38* (24), 4687–4700. https://doi.org/10.1021/acs.organomet.9b00660.

(41)   Sarker, R. K.; Mangin, L. P.; Zargarian, D. Reactivities of Cyclonickellated Complexes with Hydroxylamines: Formation of κO-Hydroxylamine and κN-Imine Adducts and a κO, κN-Aminoxide Derivative. *Dalton Transactions* **2023**, *52* (2), 366–375. https://doi.org/10.1039/d2dt02979k.

(42)   Sarker, R. K.; Zargarian, D. Cyclonickelated Complexes Featuring a Terminal or Bridging Triazole. *Inorganica Chim Acta* **2024**, *559*. https://doi.org/10.1016/j.ica.2023.121772.

(43)   Ryland, B. L.; Stahl, S. S. Practical Aerobic Oxidations of Alcohols and Amines with Homogeneous Copper/TEMPO and Related Catalyst Systems. *Angewandte Chemie - International Edition* **2014**, *53* (34), 8824–8838. https://doi.org/10.1002/anie.201403110.

(44)   Ma, Z.; Mahmudov, K. T.; Aliyeva, V. A.; Gurbanov, A. V.; Pombeiro, A. J. L. TEMPO in Metal Complex Catalysis. *Coord Chem Rev* **2020**, *423*. https://doi.org/10.1016/j.ccr.2020.213482.

(45)   Isrow, D.; Deyonker, N. J.; Koppaka, A.; Pellechia, P. J.; Webster, C. E.; Captain, B. Metal-Ligand Synergistic Effects in the Complex Ni(H$_2$-TEMPO)$_2$: Synthesis, Structures, and Reactivity. *Inorg Chem* **2013**, *52* (24), 13882–13893. https://doi.org/10.1021/ic401296f.

(46) Isrow, D.; Captain, B. Synthesis and Reactivity of a Transition Metal Complex Containing Exclusively TEMPO Ligands: Ni(H$_2$-TEMPO)$_2$. *Inorg Chem* **2011**, *50* (13), 5864–5866. https://doi.org/10.1021/ic2007342.

(47) Scepaniak, J. J.; Wright, A. M.; Lewis, R. A.; Wu, G.; Hayton, T. W. Tuning the Reactivity of TEMPO by Coordination to a Lewis Acid: Isolation and Reactivity of MCl$_3$(H1-TEMPO) (M = Fe, Al). *J Am Chem Soc* **2012**, *134* (47), 19350–19353. https://doi.org/10.1021/ja309499h.

(48) Nguyen, T. A. D.; Wright, A. M.; Page, J. S.; Wu, G.; Hayton, T. W. Oxidation of Alcohols and Activated Alkanes with Lewis Acid-Activated Tempo. *Inorg Chem* **2014**, *53* (21), 11377–11387. https://doi.org/10.1021/ic5018888.

(49) Hetterscheid, D. G. H.; Kaiser, J.; Reijerse, E.; Peters, T. P. J.; Thewissen, S.; Blok, A. N. J.; Smits, J. M. M.; De Gelder, R.; De Bruin, B. Ir^{II}(Ethene): Metal or Carbon Radical? *J Am Chem Soc* **2005**, *127* (6), 1895–1905. https://doi.org/10.1021/ja0439470.

(50) Walroth, R. C.; Miles, K. C.; Lukens, J. T.; MacMillan, S. N.; Stahl, S. S.; Lancaster, K. M. Electronic Structural Analysis of Copper(II)-TEMPO/ABNO Complexes Provides Evidence for Copper(I)-Oxoammonium Character. *J Am Chem Soc* **2017**, *139* (38), 13507–13517. https://doi.org/10.1021/jacs.7b07186.

(51) Nutting, J. E.; Rafiee, M.; Stahl, S. S. Tetramethylpiperidine N-Oxyl (TEMPO), Phthalimide N-Oxyl (PINO), and Related N-Oxyl Species: Electrochemical Properties and Their Use in Electrocatalytic Reactions. *Chemical Reviews*. American Chemical Society May 9, 2018, pp 4834–4885. https://doi.org/10.1021/acs.chemrev.7b00763.

(52) Indeed, Work-up of the Reaction Mixtures Always Gave a Sticky and Intractable off-White Solid in Addition to TEMPOH Complexes.

(53) Luzyanin, K. V.; Kukushkin, V. Y.; Haukka, M.; Pombeiro, A. J. L. The First Example of Re(IV)-Mediated Nitrile-Hydroxylamine Coupling. *Inorg Chem Commun* **2006**, *9* (7), 732–735. https://doi.org/10.1016/j.inoche.2006.04.010.

(54) The Original Synthesis of Complex 5a from the Dimeric Pre-Cursor 1a and Morpholine Was Conducted in the Context of an Earlier Study Conducted in Our Laboratory: Racine, R.; Mangin, L. P.; Research Internship Report, Univeristé de Montréal, 2017.

(55) Mougang-Soumé, B.; Belanger-Gariépy, F.; Zargarian, D. Synthesis, Characterization, and Oxidation of New POCN$_{imine}$-Type Pincer Complexes of Nickel. *Organometallics* **2014**, *33* (21), 5990–6002. https://doi.org/10.1021/om500529e.

(56) Cloutier, J. P.; Zargarian, D. Functionalization of the Aryl Moiety in the Pincer Complex (NCN)Ni^{III}Br$_2$: Insights on Ni^{III}-Promoted Carbon-Heteroatom Coupling. *Organometallics* **2018**, *37* (9), 1446–1455. https://doi.org/10.1021/acs.organomet.8b00103.

(57) Cloutier, J. P.; Rechignat, L.; Canac, Y.; Ess, D. H.; Zargarian, D. C-O and C-N Functionalization of Cationic, NCN-Type Pincer Complexes of Trivalent Nickel: Mechanism, Selectivity, and Kinetic Isotope Effect. *Inorg Chem* **2019**, *58* (6), 3861–3874. https://doi.org/10.1021/acs.inorgchem.8b03489.

(58) Cloutier, J. P.; Vabre, B.; Moungang-Soumé, B.; Zargarian, D. Synthesis and Reactivities of New NCN-Type Pincer Complexes of Nickel. *Organometallics* **2015**, *34* (1), 133–145. https://doi.org/10.1021/om5010176.

(59) Spasyuk, D. M.; Zargarian, D.; Van Der Est, A. New POCN-Type Pincer Complexes of Nickel(II) and Nickel(III). *Organometallics* **2009**, *28* (22), 6531–6540. https://doi.org/10.1021/om900751f.

(60) Spasyuk, D. M.; Gorelsky, S. I.; Van Der Est, A.; Zargarian, D. Characterization of Divalent and Trivalent Species Generated in the Chemical and Electrochemical Oxidation of a Dimeric Pincer Complex of Nickel. *Inorg Chem* **2011**, *50* (6), 2661–2674. https://doi.org/10.1021/ic1025894.

(61) Polukeev, A. V.; Tasić, M. Oxidation-Induced C-H Bond Activation in Iridium Pincer Complexes. *Dalton Transactions* **2023**, *52* (22), 7701–7708. https://doi.org/10.1039/d3dt00903c.

(62) This Side-Product Was Obtained as Follows: Two Equiv of AgOC(O)CF$_3$ Were Added to a DCM Solution of the Dimer 1a, Followed by Filtration to Remove AgBr, Adding Excess TEMPOH, and Stirring at r.t. for Two Days. The Final Reaction Mixture Was Then Evaporated, Extracted into

Et$_2$O and Cooled to -35 °C to Give a Small Crop of Crystals Which Were Identified by XRD Analysis as Pyridinium Trifluoroacetate. See ESI for Structural Details.

(63) Vabre, B.; Petiot, P.; Declercq, R.; Zargarian, D. Fluoro and Trifluoromethyl Derivatives of POCOP-Type Pincer Complexes of Nickel: Preparation and Reactivities in SN2 Fluorination and Direct Benzylation of Unactivated Arenes. *Organometallics* **2014**, *33* (19), 5173–5184. https://doi.org/10.1021/om500472b.

(64) Vabre, B.; Canac, Y.; Lepetit, C.; Duhayon, C.; Chauvin, R.; Zargarian, D. Charge Effects in PCP Pincer Complexes of Ni^{II} Bearing Phosphinite and Imidazol(I)Ophosphine Coordinating Jaws: From Synthesis to Catalysis through Bonding Analysis. *Chemistry - A European Journal* **2015**, *21* (48), 17403–17414. https://doi.org/10.1002/chem.201502491.

(65) Hao, J.; Vabre, B.; Zargarian, D. Reactions of Phenylhydrosilanes with Pincer-Nickel Complexes: Evidence for New Si-O and Si-C Bond Formation Pathways. *J Am Chem Soc* **2015**, *137* (48), 15287–15298. https://doi.org/10.1021/jacs.5b10066.

(66) Hao, J.; Mougang-Soumé, B.; Vabre, B.; Zargarian, D. On the Stability of a POC$_{sp3}$OP-Type Pincer Ligand in Nickel(II) Complexes. *Angewandte Chemie - International Edition* **2014**, *53* (12), 3218–3222. https://doi.org/10.1002/anie.201310386.

(67) Hao, J.; Vabre, B.; Mougang-Soumé, B.; Zargarian, D. Small Molecule Activation by POC$_{sp3}$OP-Nickel Complexes. *Chemistry - A European Journal* **2014**, *20* (39), 12544–12552. https://doi.org/10.1002/chem.201402933.

(68) Hao, J.; Vabre, B.; Zargarian, D. POCOP-Ligated Nickel Siloxide Complexes: Syntheses, Characterization, and Reactivities. *Organometallics* **2014**, *33* (22), 6568–6576. https://doi.org/10.1021/om500916d.

(69) Lapointe, S.; Vabre, B.; Zargarian, D. POCOP-Type Pincer Complexes of Nickel: Synthesis, Characterization, and Ligand Exchange Reactivities of New Cationic Acetonitrile Adducts. *Organometallics* **2015**, *34* (14), 3520–3531. https://doi.org/10.1021/acs.organomet.5b00272.

(70) Cámpora, J.; Palma, P.; Del Río, D.; Conejo, M. M.; Alvarez, E. Synthesis and Reactivity of a Mononuclear Parent Amido Nickel Complex. Structures of Ni[C$_6$H$_3$-2,6-(CH$_2$P^{i}Pr$_2$)$_2$] (NH$_2$) and

Ni[C$_6$H$_3$-2,6-(CH$_2$P^{i}Pr$_2$)$_2$](OMe). *Organometallics* **2004**, *23* (24), 5653–5655. https://doi.org/10.1021/om049312r.

(71)   Cámpora, J.; Matase, I.; Palma, P.; Álvarez, E.; Graiff, C.; Tiripicchio, A. Monomeric Alkoxo and Amido Methylnickel(II) Complexes. Synthesis and Heterocumulene Insertion Chemistry. *Organometallics* **2007**, *26* (15), 3840–3849. https://doi.org/10.1021/om7002909.

(72)   Capiomont, P. A.; Lajzerowicz-Bonneteau, J. Acta1974. *Acta Crystal* **1974**, *B30*, 2160–2166.

(73)   Pandarus, V.; Castonguay, A.; Zargarian, D. Ni(II) Complexes Featuring Non-Metallated Pincer-Type Ligands. *Dalton Transactions* **2008**, No. 35, 4756–4761. https://doi.org/10.1039/b802222d.

(74)   Pandarus, V.; Zargarian, D. New Pincer-Type Diphosphinito (POCOP) Complexes of Nickel. *Organometallics* **2007**, *26* (17), 4321–4334. https://doi.org/10.1021/om700400x.

(75)   Hao, J.; Vabre, B.; Zargarian, D. POCOP-Ligated Nickel Siloxide Complexes: Syntheses, Characterization, and Reactivities. *Organometallics* **2014**, *33* (22), 6568–6576. https://doi.org/10.1021/om500916d.

(76)   Lapointe, S.; Zargarian, D. On the Mechanism of Ni(II)-Promoted Michael-Type Hydroamination of Acrylonitrile and Its Substituted Derivatives. *Dalton Transactions* **2016**, *45* (40), 15800–15810. https://doi.org/10.1039/c6dt02105k.

(77)   See the ESI Section for a Plausible Explanation for the Origin of the Ni-Cl Analogues of 5a.

(78)   Dudkina, Y. B.; Fayzullin, R. R.; Lyssenko, K. A.; Gubaidullin, A. T.; Kholin, K. V.; Levitskaya, A. I.; Balakina, M. Y.; Budnikova, Y. H. Cyclometalated Nickel Complexes as Key Intermediates in C(sp2)-H Bond Functionalization: Synthesis, Catalysis, Electrochemical Properties, and DFT Calculations. *Organometallics* **2019**, *38* (6), 1254–1263. https://doi.org/10.1021/acs.organomet.8b00536.

(79)   Huynh, H. V.; Koh, C. H. M.; Nguyen, V. H. Heteroleptic Nickel(II)-DiNHC Complexes and an Unusual "reverse" Carbene-Transfer Reaction to Silver(i). *Dalton Transactions* **2017**, *46* (34), 11318–11326. https://doi.org/10.1039/c7dt01912b.

(80)   Steiner, T.; Majerz, I.; Wilson, C. C. First O-H-N Hydrogen Bond with a Centered Proton Obtained by Thermally Induced Proton Migration. *Angewandte Chemie - International Edition* **2001**, *40* (14), 2651–2654. https://doi.org/10.1002/1521-3773(20010716)40:14<2651::AID-ANIE2651>3.0.CO;2-2.

(81)   Post-Facto Calibration of the 100-1000 ML Micropipette with 20 ∈ 500 ML Aliquots of Deionized H2O Revealed That We Must Allow an Accuracy (Systematic Error) of +4 ML and a Precision of ±3 ML for Our Measurements, with > 99% Confidence. The 20-200 ML Micropipette Was Calibrated by the Same Procedure, with 150 ML Aliquots, and Revealed an Accuracy of +0.3 ML and a Precision of ±3 ML for Our Measurements, with > 99% Confidence.

(82)   Vabre, B.; Spasyuk, D. M.; Zargarian, D. Impact of Backbone Substituents on POCOP-Ni Pincer Complexes: A Structural, Spectroscopic, and Electrochemical Study. *Organometallics* **2012**, *31* (24), 8561–8570. https://doi.org/10.1021/om3009475.

(83)   Bruker (2012). APEX2 / Bruker (2016) APEX3, Bruker AXS Inc., Madison, WI, USA.

(84)   Bruker (2012). "SAINT Integration Software for Single Crystal Data", Bruker AXS Inc., Madison, WI, USA. (a).

(85)   (A) G. M. Sheldrick (1996). SADABS/TWINABS. University of Göttingen, Germany. (b) Bruker (2001). SADABS/TWINABS. Bruker AXS Inc., Madison, Wisconsin, USA. Bruker (2012). Data Preparation and Reciprocal Space Exploration Program, Bruker AXS Inc., Madi-Son, WI, USA.

(86)   Bruker (2012). Data Preparation and Reciprocal Space Exploration Program, Bruker AXS Inc., Madison, WI, USA.

(87)   A: O. V. Dolomanov, L. J. Bourhis, R. J. Gildea, J. A. K. Howard and H. Puschmann. "OLEX2: A Com-Plete Structure Solution, Refinement and Analysis Program". J. Appl. Cryst., 2009, 42, 339-341. https://doi.org/10.1021/acs.inorgchem.3c01236.

(88)   Sheldrick, G. M. SHELXT - Integrated Space-Group and Crystal-Structure Determination. *Acta Crystallogr A* **2015**, *71* (1), 3–8. https://doi.org/10.1107/S2053273314026370.

# 5. 1.   Chapter-5-Summary and proposals for future studies

5. 1. Summary

This thesis encompasses the reactivities of a family of phosphinite-based nickelacyclic complexes with the following substrates: 4-Amino-4H-1,2,4-triazole; the hydroxylamines Et$_2$NOH, (PhCH$_2$)$_2$NOH, and H$_2$NOCH$_2$Ph; and the hydroxylamines Et$_2$NOH and Ph(H)NOH in the presence of TEMPO. Thes investigations meant to test the idea of inducing C—N functionalization of the aryl moieties in the nickelacyclic complexes, an idea inspired by the previously observed reactivity of our nickelacyclic complexes with halophosphines. Thus, we had anticipated that homolysis of the relatively labile N—O bond in hydroxylamines would generate reactive Ni-amido or aminyl intermediates which might then lead to C—N coupling. Instead, we observed a range of reactivities depending on (a) whether or not the hydroxylamine substrate was protected at its OH moiety, (b) whether the aryl moiety of the cyclonickellated complex had a non-H substituent, and also (c) the type of N-substituent.

The most consistent reactivity observed for all four cyclonickellated precursors was formation of the (BnO)H$_2$N→Ni adducts. In contrast to the uniform reactivity seen with BnONH$_2$, the reactivities with unprotected hydroxylamines depended strongly on the Ni precursor as well as on the reaction solvent. In CH$_2$Cl$_2$, the unsubstituted precursor **1a** (**Scheme 5.1**) formed O-bound adducts initially that reacted further to give two different products depending on the N-substituent of the substrate, the zwitterionic hydroxylamine oxide [$\{\kappa^P,\kappa^C$-(i-Pr)$_2$PO-C$_6$H$_4\}\{\kappa^N$-Et$_2$NOH$\}$NiBr] with R'' = Et, and the κ^O,κ^N- aminoxide **3a** with R'' = CH$_2$Ph. A third type of reactivity observed in our study was the formation of the imine adducts **2a-2d** (**Scheme 5.1**) from the acetonitrile reaction of hydroxylamines with the Ni precursors possessing a non-H substituent on their aryl moieties. These findings established that hydroxylamines are stronger ligands than MeCN toward Ni(II). In addition, the N lone pair of (BnO)NH$_2$ is a better nucleophile than the O lone pair. Also, a number of literature precedents and experimental observations have allowed us to rationalize the transformation of hydroxylamines into imines via a nucleophilic attack on the in-situ generated acetonitrile adduct. A DFT analysis of a model reaction has also provided support for this scenario.

This mechanistic study proves that there is a net dehydration of hydroxylamine leading the formation of imine complex. It should be noted, however, that an alternative radical pathway cannot be ruled out for the formation of the imine adduct **2b** as a minor side-product (2-20%) when dimer **1c** was treated with Et_2NOH in CH_2Cl_2, toluene, or C_6D_6. Overall this study develop an effective method of generating Ni(II)-imine complex through dehydration of hydroxyl amine.
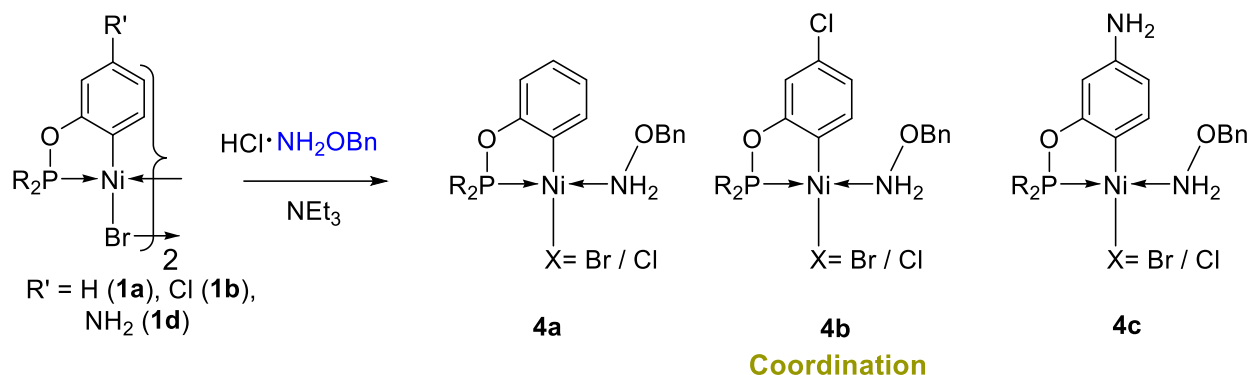
Scheme 5. 1. Reactivities of nickelacyclic precursor with nucleophiles: formation of imine complexes
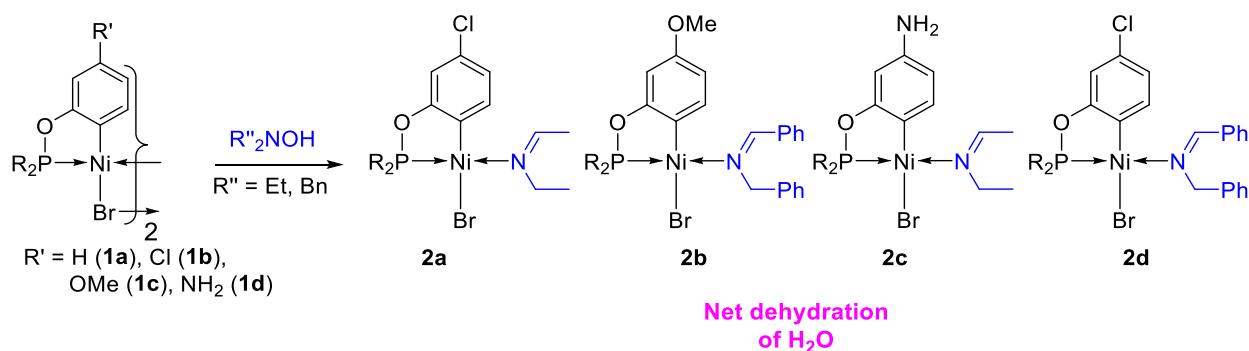
Scheme 5. 2. Reactivities of nickelacyclic precursor with nucleophiles: formation of aminoxide and zwiterioninc complexes
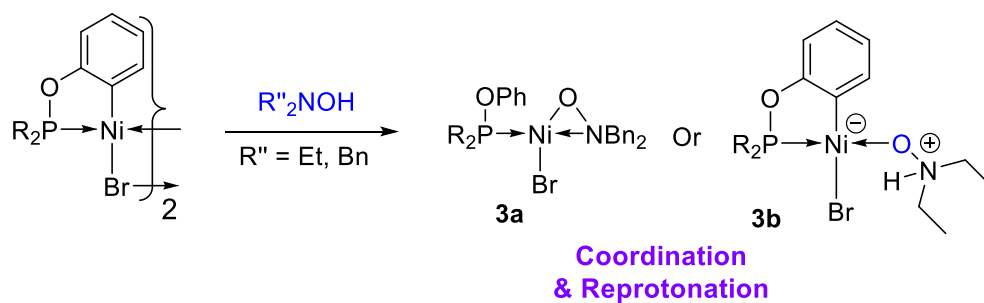
Scheme 5. 3. Reactivities of nickelacyclic precursor with nucleophiles: formation of Ni−NH₂−OBn adducts

4a **4b** **4c**

Coordination

The investigations involving 4-Amino-4H-1,2,4-triazole has yielded five new mono- and dinuclear Ni(II) adducts. While this outcome diverges from our initial objectives, the obtained results hold significant promise. Initially, we aimed to cleave the N−N bond within triazole, analogous to the O−N bond cleavage observed with hydroxylamine nickelacycles. This was expected to lead to a reductive elimination process, generating an aminated product. Contrary to this anticipation, triazole replaces acetonitrile MeCN and coordinates with nickel via its aromatic N lone pair, resulting in the formation of a triazole adduct.

Scheme 5. 4. Formation of Ni(II)-triazole adducts

5a **5e**

5b **5c** **5d**
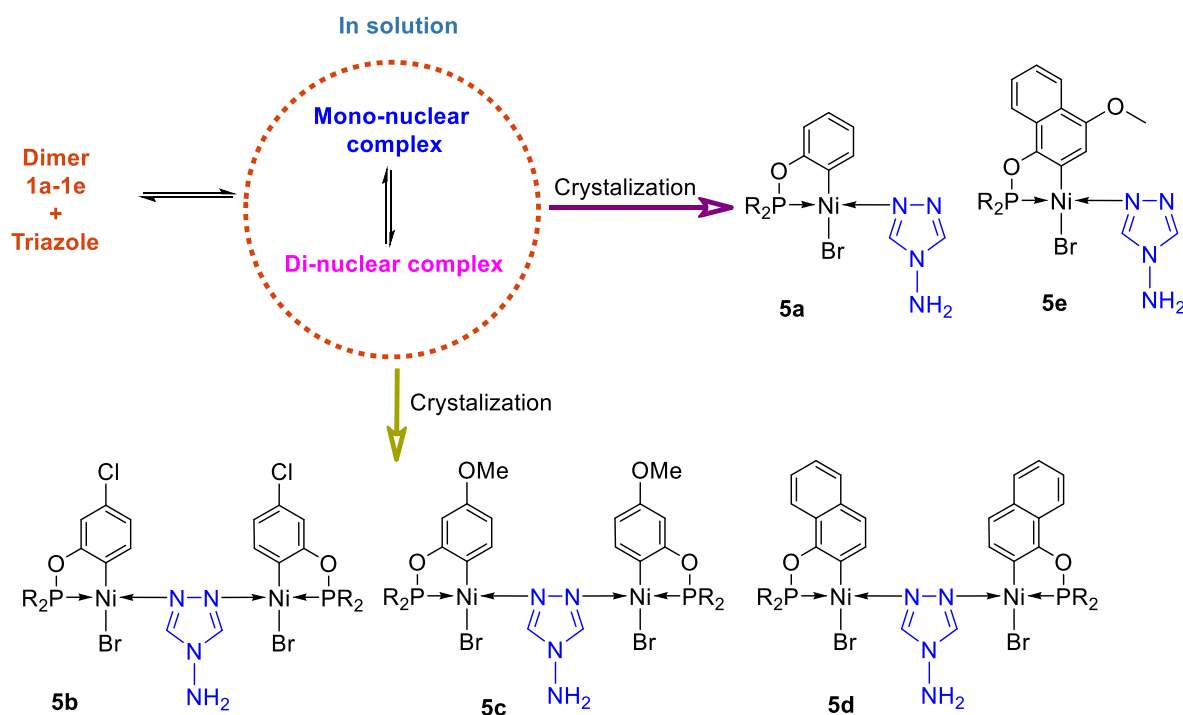
The successive addition of triazole to a MeCN solution of dimeric precursor **1a** indicates an equilibrium among the acetonitrile adduct (**1a**-NCMe), mononuclear and the dinuclear triazole adducts. Remarkably, the data indicates that while the mononuclear species is the exclusive product obtained through crystallization, it does not represent the predominant species in solution at ambient temperature. In contrast, when a substituted dimeric precursor (**1b-1d**) was subjected to treatment with triazole, crystallographic analysis showed the formation of a dinuclear Ni-Triazole-Ni adduct. The reasons for this variation between dimeric precursors **1a** and **1e** forming mononuclear adducts and dimer **1b-1d** forming dinuclear species remain to be elucidated (**Scheme 5.4**).

It is noteworthy that all previously reported Ni-triazole adducts are coordination complexes featuring only Ni-heteroatom linkages (Ni−O, Ni−O, Ni−Cl, etc.). Thus, the triazole complexes isolated in this study represent the first known examples of organonickel adducts with triazole, characterized by Ni−C bonds. Additionally, compounds **5a** and **5e** are rare instances of mononuclear complexes featuring terminal M-triazole moieties (**Scheme 5.4**). The influence of the triazole-to-Metal molar ratio, solvent selection, and concentration on the crystallization of mono- versus multinuclear adducts remains a subject of ongoing research efforts, with limited understanding to date. Future investigations will address this topic, along with insights into the observed decomposition reactivity between our Ni(II) precursors and 4-Amino-4H-1,2,4-triazole.

The primary objective of the study that explored the reactivities of our nickellacyclic complexes with hydroxylamines in the presence of TEMPO was to see if the oxidizing capabilities of the latter might induce the functionalization chemistry that was not observed in the absence of TEMPO. Contrary to our initial hypothesis, which postulated that TEMPO might facilitate oxidation-induced C−O bond functionalization in our cyclonickelated complexes, the results obtained did not support this proposition. Instead, the reaction with TEMPO resulted in the formation of zwitterionic TEMPOH derivatives, originating from the hydrogen abstraction between TEMPO and hydroxylamines. The structural analysis of these adducts in the solid state corroborated the anticipated properties of the O- and N-functional groups, revealing the presence of hydrogen bonding interactions involving the Br−H−N moieties.

Subsequent experiments elucidated the stability of the Ni−O$_{TEMPOH}$ bond in complex **6a**, demonstrating its vulnerability to displacement by relatively weak nucleophiles such as acetonitrile but not by others like PPh$_3$, DMSO, or alkenes. Moreover, various oxidants were found to induce decomposition of the TEMPOH complexes. Notably, the use of AgOC(O)CF$_3$, a potential one-electron oxidant, led to the formation of a novel trifluoroacetate derivative **7c** by displacing the bromide ligand in 6a. It is important to highlight that there are indications that excessive amounts of this salt may not only displace TEMPOH from **6a** but also trigger gradual oxidative decomposition, although these reactions have not been fully substantiated and remain poorly understood. Our forthcoming research in the laboratory will focus on exploring other reactivity patterns of the TEMPOH complexes, including their reactions with electrophiles such as alkyl and benzyl halides.

Scheme 5. 5. Synthetic route to form Ni(II)-TEMPOH complexes and their reactivity
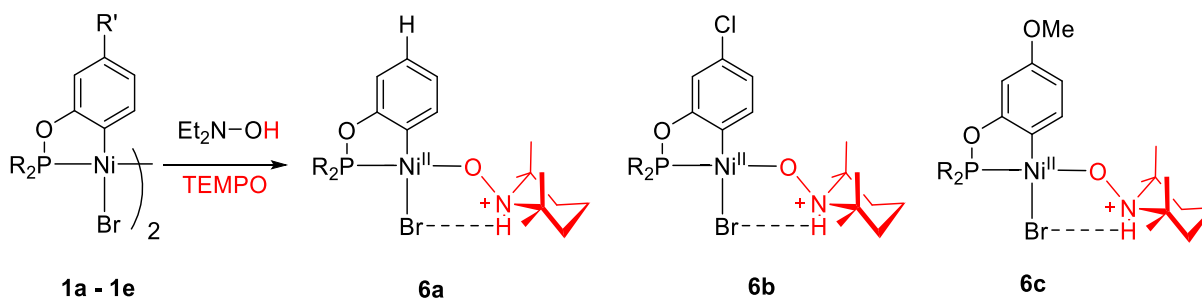

Scheme 5. 6. Reactivity of Ni(II)−TEMPOH complexes
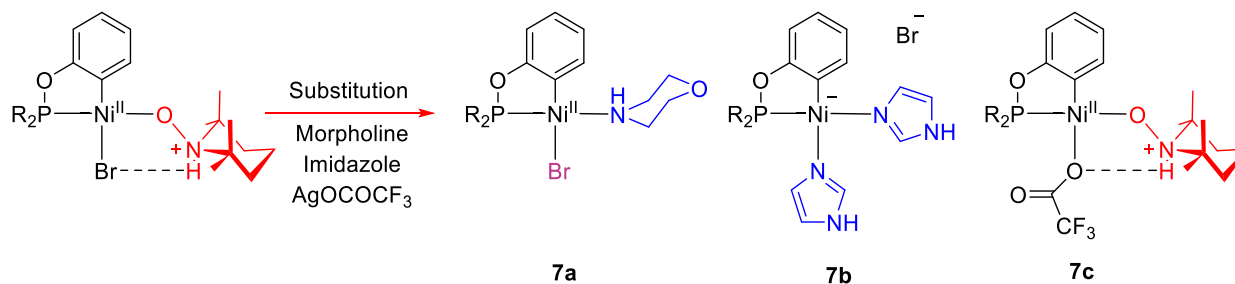
5. 2. Proposal for future studies

In our previous chapters, we detailed an optimized synthetic strategy for the preparation of cyclonickelated complexes derived from phenol- and arenol-derived ligands. Our investigations delved into the influence of reaction conditions on the crucial C−H nickelation step. Additionally, we demonstrated the feasibility of C−C and C−P functionalization when treating the cyclonickelated complexes with various electrophiles. However, we encountered a notable limitation: the cyclonickelated complexes failed to undergo reductive elimination, hindering our primary objective of functionalization through this pathway. This impediment appears to stem from the remarkable stability of the C−Ni bond within the nickelacyclic intermediate, which seems disinclined to engage in reductive elimination. To surmount this challenge, one plausible approach involves the introduction of oxidative conditions. Nevertheless, this route proves problematic as our system contains an O−P bond, susceptible to oxidation and resulting in system decomposition. Therefore, substituting the O−P bond with a C−P bond, by transitioning from a phosphinite system to a phosphine or amine system, may confer the requisite resilience to oxidation and subsequently enable reductive elimination to yield the functionalized product.

**Scheme 5. 7.** Future scope: changing the binding group
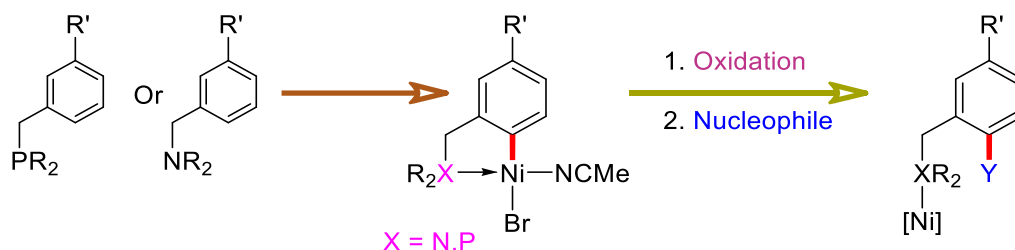
An alternative avenue to facilitate reductive elimination involves modifying the size of the nickelacyclic ring. The nickelacyclic intermediate under scrutiny currently exhibits a five-membered metallacycle, characterized by substantial energetic stability. Consequently, augmenting the chain length of the phosphinite arm can be anticipated to enlarge the nickelacyclic ring, rendering the C−Ni bond more reactive and, in turn, promoting reductive elimination.

Scheme 5. 8. Future scope: changing the nickelacyclic ring size
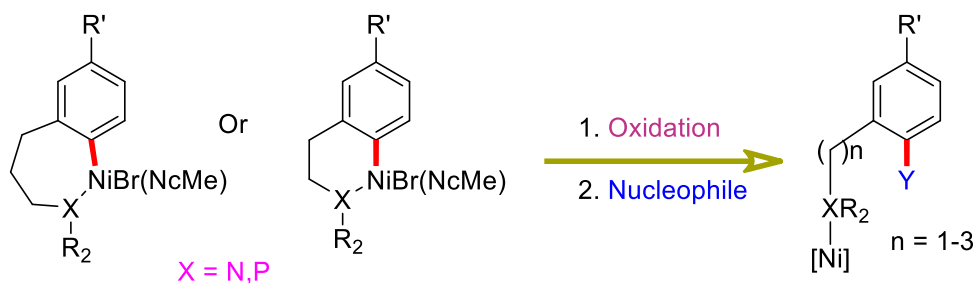
It is worth noting that the activation of aromatic Csp^2-H bonds is generally more facile compared to their aliphatic Csp^3-H counterparts. The activation of aromatic C−H bonds results in the formation of a highly stable C−M bond. Conversely, the activation of aliphatic C−H bonds necessitates elevated temperatures, yielding a considerably more reactive C−M bond. In the scope of this project, we focused exclusively on the activation of C−H bonds in aromatic phosphinites. Notably, the activation of phenolic substrates yields a stable C−M bond, but substituting these with alcoholic substrates may lead to the generation of a more reactive C−M bond, potentially resulting in distinct reactivity with coupling partners.

Scheme 5. 9. Future scope: exploring the reactivity of an aliphatic substrate
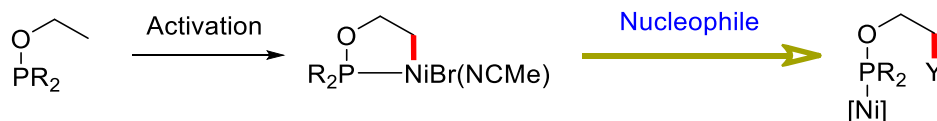
Previously, we observed the formation of a dimethylamine adduct when dimethylamine was treated with the nickelacyclic precursor through coordination of the N atom to the nickel center. Similarly, O-benzylhydroxylamine coordinated through its N lone pair to the nickel center, resulting in the formation of an adduct. Notably, both of these adducts contain a labile hydrogen atom attached to the N atom. Given that TEMPO has the capability to abstract a proton from a zwitterionic complex, it presents an intriguing avenue to investigate whether TEMPO can also abstract a proton or a hydrogen radical from these two adducts. This investigation opens an exciting pathway to explore the reactivity of these adducts with TEMPO and the potential formation of novel Ni(III) species or decomposition products.

Scheme 5. 10. Future scope: exploring the reactivity of dimethylamine adduct and benzyl protected hydroxylamine adduct with TEMPO